CRANFIELD INSTITUTE OF TECHNOLOGY

SCHOOL OF INDUSTRIAL SCIENCE

Ph.D THESIS

1982

C. J. ALLUM

Vol 1

The Characteristics and Structure of High Pressure (1-42 bars) Gas Tungsten Arcs

Supervisor: Professor R. L. Apps

Summary

The last decade has seen a considerable growth in the exploitation of deep sea mineral reserves. Accompanying these developments has come the need for suitable underwater repair and maintenance techniques. One such technique involves the use of fusion welding processes in localised dry high pressure environments created around weldments. Pressure chambers at Cranfield have been employed to simulate this situation. These have been used to investigate the influence of ambient pressure (1 to 45 bars) on gas-tungsten arcs.

The study has been of a basic nature with emphasis on arc characteristics and arc structure. Special attention is given to the argon TIG arc although helium TIG arcs and constricted argon-tungsten arcs have also been examined. Arc characteristics are reported in terms of arc appearance and modes, electrical characteristics and weld bead studies. The investigation of arc structure is concerned with gaining an understanding of observed characteristics. This has involved experimental and theoretical developments. Experimental techniques used include, electrostatic probes, calorimetry and the measurement of total power radiated from an arc. Models developed here have successfully explained many of the experimental findings and special emphasis has been directed at understanding gas flow in the column and arc stability.

Much of the work included in this thesis has implications for the development of underwater welding procedures. Results presented should also contribute to gaining a better understanding of arcs operating under normal ambient conditions. However, these aspects are not discussed in any detail as the main emphasis has been placed on documenting and explaining the influence of pressure on gas-tungsten arcs.

ACKNOWLEDGEMENTS

The author is indebt to many for help and co-operation during the course of this work. Most of the material presented here has been financially supported by the SERC (Marine Technology directorate), and this support is gratefully appreciated. Sub Ocean Services/Sub Sea Offshore are also thanked for permitting the use of their facilities for these experiments. It is a great pleasure to acknowledge the constant encouragement of Professor R. L. Apps and Professor H. C. Cotton and stimulating discussions with B. E. Pinfold. Professor A. E. Guile is also thanked for allowing the author access to his collection of literature on arcs. This project would not have been possible without the support of colleagues (past and present) from the underwater welding group at Cranfield and their assistance is gratefully acknowledged. Special thanks is due to John Holmes for his careful assistance with experimental work to D. Robinson for sample preparation and to R. Fry of the photographic department.

In preparing this thesis Ms. D. Rose (typing) and Mrs. S. Shevington (drawing office) have transformed a pile of untidy pages and drawings into the present form. This feat has been accomplished in a good natured manner and it is a great pleasure to acknowledge their contribution.

Without doubt this thesis would have not been completed without the tolerance and consistent encouragement of Sarah. This is deeply appreciated.

CONTENTS

1. INTRODUCTION

The stability of Tungsten Inert Gas (TIG) arcs has long been utilised for atmospheric welding applications. Associated with the recent interest in exploiting deep water mineral reserves, has come the need to extend the range of this process to higher ambient pressures. This requirement is the primary motivation behind the present investigation into the physical effects of pressure on TIG welding arcs.

The main deep sea use for welding is in the repair and maintenance of structures. Welding processes may be applied in such environments in three essentially different ways; wet welding, dry one atmosphere welding and dry high pressure welding. In wet welding the arc and weldment regions are surrounded by water. This technique is generally regarded as having prohibitive metallurgical implications. One atmosphere welding requires the construction of a pressure chamber capable of supporting the head of water equivalent to the welding depth around the region to be welded. Welding problems are then reduced to those experienced at the surface although this technique is often prohibitive on the grounds of economics and construction time scales. Dry high pressure welding is accomplished by surrounding the region to be welded with a gaseous envelope at a pressure equivalent to the welding depth. Such an approach obviates the need for a structure capable of withstanding pressures greater than a few P.S.I. and has few of the metallurgical implications associated with wet welding. Arc characteristics, however, are significantly affected by the high pressure environment.

The pressure dependence of arc characteristics has important stability, process and metallurgical implications. Very little information is presently available on the physical effects of pressure on TIG welding arcs and it was a primary aim of this work to obtain such information for the pressure range 1 to 45 atmospheres by operating TIG arcs in pressure chambers. The main arc form considered is the free burning argon-tungsten welding arc burning on steel. Experiments have also been performed in helium atmospheres, on water cooled anodes and with a constricted argon arc (plasma arc).

The approach adopted here has been to place the effect of pressure on argon-tungsten welding arcs at the centre of the investigation. Results obtained are by no means confined to hyperbaric welding. Indeed, pressure has been regarded as a variable that may be used to investigate the structure of one atmosphere arcs. Many of the conditions investigated here have a wider application than the welding arc. In this sense a broader class of arc phenomena is covered.

This investigation encompasses 'arc characteristics' and 'arc structural behaviour' under the conditions outlined above. It was found appropriate to discuss these aspects separately. 'Characteristics' is used here to represent bulk macroscopic behaviour and taken to encompass such aspects as arc appearance and modes, V-I characteristics and weld geometry. These are manifestations of interactions occurring on an essentially atomic scale. The structural investigation is not at this level but confined to separating the components of macroscopic properties. For example, the structure of the arc voltage is regarded as the spatial distribution of voltage. Structural investigations undertaken have been chosen primarily with regard to the characteristics obtained and are therefore largely concerned with dynamic effects and energy exchanges.

Results presented are predominantly of an experimental nature although a significant part of the thesis is concerned with theoretical developments. These have been made to extend the present theory of one atmosphere arcs and are also used to interpret behaviour observed at higher pressures. Emphasis has been placed on developing a theory for gas flow in the arc column that takes viscous and buoyancy effects into account as well as the arc current-self magnetic field interaction. This theory has also been used to investigate the arc column energy dissipation and stability.

2. Literature Survey

2. LITERATURE SURVEY

2.1. General Introduction

The phenomena of arcing belongs to a class of electrical discharge named from the upward buoyancy generated bow observed when such a discharge is initiated between horizontal electrodes. A precise definition of an arc discharge is rather difficult to give. Finkelnburc and Maecker (1) define an arc as "a discharge of relatively large current (greater than 1 amp) and low voltage, especially such with a low cathode drop (smaller than 20V)". Ecker (2) defines an arc discharge as "a self sustained conducting gas region between two electrodes in which each volume element is a closed system with respect to the charged particle balance". This modification specifically excludes externally heated cathodic arcs and favours thermal ionisation processes in the column. This definition makes no explicit statement about the cathode voltage drop. Guile (3) however, relates this to the excitation potential of the electrode vapour and defines an arc as "a discharge of electricity between two electrodes in a gas or in vapour from the electrodes, which has a voltage of the order of the excitation potential of the electrode vapour (of order 10V) and in which the current flowing can have any value almost without limit above a minimum which is about 100 mA". These definitions, with some reservation over the implied cathodic structure, are essentially similar.

A vast body of literature exists on phenomena falling within the above definitions. No attempt is made here to give an exhaustive account of this literature but the survey is intended to put into perspective aspects considered relevant to the present work. Welding arcs are generally characterised by further restrictions on the above definitions. In particular a welding arc must act as a stable source of heat within a given welding context. Many welding arcs are classified as 'free burning arcs'. This implies they are self stabilised by means of current generated plasma jets (4). Such arcs must operate at currents high enough to overcome the disruptive effects of buoyancy forces which would otherwise dominate. The current at which this behaviour occurs is well above the minimum for an arc as defined by Guile and is taken here as about 30A. It is worth noting that in microplasma welding

applications much lower currents may be employed. However, these arcs are not 'free' and as such are regarded as a special category. At high currents plasma jets may act as a disruptive influence on the weld pool. This may be manifest by porous weld appearance or in the limit, a large and unmanageable pool. The limit is generally determined by the application and is taken here as being about 1KA (as may be found in submerged arc welding). Mass transfer further distinguishes welding arcs from other arc discharges. In non-consumable processes this is associated with plasma jets and the attendent motion of entrained shielding gas. Bulk electrode melting accompanies this behaviour in consumable processes.

In keeping with the approach outlined in the introduction, an attempt is made to highlight areas where a better understanding of one atmosphere arcs may be obtained by considering the pressure dependence of a particular quantity. Considerable attention is therefore focused on the one atmosphere TIG arc. However, limited information is available above this pressure and the behaviour of arcs at elevated pressures is reviewed separately (see section 2.6). This literature review considers the characteristics and structural aspects of the arcs separately. A degree of overlap between these descriptions has been found unavoidable. In some cases it has been found appropriate to delay particularly specific discussions until later sections.

The structure of an arc may be separated into three distinct regions conventionally known as the anode, cathode and column regions. These differ to such an extent that the structure of each is discussed separately. Weld pool behaviour is included in the present review of the anode region of an arc. A further subdivision is thought appropriate in view of gross differences at the anode between arcs supporting weld pools and those not (i.e. water cooled anodes). Anode structures in the presence and absence of a pool are therefore considered individually.

2.2. Arc Characteristics

The most readily measured arc properties are arc current (I), arc voltage (V) and hence arc power (I.V). Arc power mirrors many phenomena occuring on a structural level and is therefore of much

interest. However, this is a bulk property and says little about the nature of individual structural contributions. Further considerations are therefore required to decide the significance of this quantity in welding. Many investigations have shown or implied that great care must be taken over the measurement, experimental specification and meaning associated with arc voltage (see ref. 5). Indeed there are fundamental problems associated with this measurement that exist at a number of levels. Because arc voltage is a result of interactions occuring on a structural level, this necessarily includes all energy exchanges occurring within the arc and electrode regions between the points of measurement. In consumable electrode welding this includes the complicated resistive behaviour of the electrode from the contact tube to the arc as well as a time dependent arc contribution. In non-consumable welding the nominal resistance of the rod electrode is usually small (5). However, there is evidence (2,6,7) to suggest that the voltage is a function of the thermodynamic state of the rod electrode and therefore a function of welding time. This evidence is associated with hysterisis behaviour observed in the arc voltage as the arc current is increased from a given level and then decreased to the same level for an otherwise nominal arc condition. Further complications arise with the concept of a nominal arc condition as the arc condition is to an extent dependent on the electrode condition and electrode erosion may be occuring at some rate (ref.5.).

The above considerations imply that the reproducibility of a given arc voltage measurement requires the identification and control of all variables associated with the system. This is never achieved in practice. It has been noted (2,3) that many early investigations under apparently identical conditions produced substantially different results. In some cases, this resulted from the arc voltage being associated with the voltage across the power supply terminals and thereby including line losses. However, more fundamental problems of reproducibility have been recognised and associated largely with the existence of different arc modes for an otherwise nominal set of conditions (6,7,8). Indeed, changes in arc mode are often characterised by abrupt changes in arc voltage (6,9). These changes in arc mode are usually associated with a change in the visual appearance of the arc (6,7,9), although it is

possible that visually indistinguisable arc forms may on other criteria represent different modes of behaviour. In consumable welding, mode changes occur when the metal transfer mechanism changes from a low frequency globular transfer to a high frequency spray over the current range of a few amps. In TIG welding the arc may adopt a constricted cathode spot mode (CSM) or the more diffuse normal mode (NM) (7) although other hybrid cathodic appearances have also been reported (6). The former mode is associated primarily with pointed electrodes whereas the latter often occurs on rounded electrodes. An appreciation of this general state of affairs is important and leads to the realization that any universal theory must account for this kind of behaviour. The most successful attempt at such an account is due to Ecker (2) who has shown that the physical laws embodied in the theories of quantum mechanics, statistical mechanics and electrodynamics can only be simultaneously satisfied if such abrupt changes do occur. These calculations are represented by Ecker's 'Existence-diagrams'. Unfortunately, the application of these ideas to the laboratory situation involves not only enormous mathematical problems, but more importantly, a lack of knowledge about the important physical parameters of a given system. Changes in arc mode are not confined to the rod electrode and can also be seen at the anode (9,10) in electrode negative TIG welding.

It is often reported that the current enters the anode through a constricted region known as the anode spot (e.g. 11). This behaviour appears to be by no means universal as may be seen from current density distributions measured at the anode (see section 2.3.2). Arc appearance is often diffuse for high current argon arcs on water cooled copper anodes. At lower currents the arc may contract and enter the anode through one or more highly constricted regions (10). These are normally in motion, moving in an erratic manner across the anode giving rise to unstable and assymetrical arc appearance. In some cases plasma jets eminating from the anode have been reported (8,9). Anode and cathode jets then compete to give an assymetrical column. This behaviour may occur at high currents in the presence of oxide layers (8) or when the anode is moving at very high speeds (9). The onset of this behaviour at the anode has previously been investigated with respect to arc current and length, gas composition, anode composition and surface

condition, and anode motion. It is found that below some critical current (dependent on the above factors) the arc moves in a discrete manner over a moving anode. This may give rise to a discontinuous weld bead of discrete and equally spaced melted regions (9). However, the only systematic studies that appear to have been made are by Reeve-Saunders (9) on high speed anodes and by Singh (12) on anodes moving at speeds normally encountered in welding applications. Reeves-Saunders found that the onset of this behaviour is often associated with an increase in arc voltage on high speed modes although Singh did not comment on this correlation. The observed dependence on anode composition suggests that vapourised anode material is probably contributing to this behaviour. These experimental studies suggest the possibility of the current entering the anode of a welding arc through a number of discreete and mobile sites. The stable and diffuse behaviour of the anode root could then be the result of this time averaged behaviour.

The above considerations indicate that there are limits to the absolute reproducibility of welding arc results. This means that careful experimental techniques must be applied in determining arc properties and that absolute comparisons between reported results are limited by the range of variables that must coincide. Perhaps the most serious problem concerns the identification of variables. Contemporary literature contains reports that fail to acknowledge the existence of what might be called first order variables such as gas flow rate in hyperbaric welding (see section 2.6). On a secondary level, experimental procedures such as electrode grinding directions may have an effect. This type of dependence can, however, be standardised or allowed for. Far more important are the unknown variables! Recent theoretical investigations (13) have shown that the passage that welding current takes to earth can change liquid metal motion in the weld pool from being of a single toroidal type to a double toroidal type. The implication is that the route taken by the current to earth must be considered along with material composition and arc behaviour in determining weld pool behaviour.

The determination of TIG voltage-current (V-I) and voltage-length (V-l) characteristics has been regarded as important by a number of workers

(6,7,8) and considerable attention has been given to an accurate determination of these. The V-I characteristic is found to be of a highly non-Ohmic nature and exhibits a negative slope at low currents before assuming a positive slope between 50A and 200A at atmospheric pressure (5). This behaviour may be empirically described by Nottingham's (14) relationship:

$$V = aI + \frac{b}{I^n} + c \qquad (1)$$

where a, b, c and n are constants for a given welding situation. The first term is of an Ohmic nature and the third term is associated with purely electrode effects (sum of the fall voltages) at high currents. The second term represents a modification to the fall behaviour at low currents and accounts for an increase in the cathode fall voltage with decreasing current. Goldman (15) 1963, attempted a quantitative explanation of this behaviour but concluded that factors influencing V-I could not be assessed with sufficient accuracy.

The position of the minimum voltage is strongly influenced by arc mode and for argon TIG arcs has a lower value in the NM than the CSM (8,7). At low currents the NM exhibits a higher voltage than the CSM. This behaviour is reversed at currents of above about 100 Amps (7,5). As might be expected from Nottingham's relationship, arc length affects the position of the turning point of the V-I curve. For very short arcs (less than 2mm) the current at which the minimum voltage occurs increases with decreasing arc length (8,7). For longer arcs no influence of current is felt. This last finding is contrary to Nottingham's relation which indicates that the current associated with the minimum voltage obeys an almost inverse square relationship with arc length if the coefficient 'a' is proportional to l (see below). It is found that the gradient of the positive arm of the V-I curve increases with increasing arc length (7). Nottingham's relation predicts this behaviour. There are, however, complicating factors. This effect is more pronounced for characteristics obtained by a measurement technique employing decreasing as opposed to increasing currents (hysterisis effect) and is stronger in the CSM than the NM (7).

Behaviour described above is largely confined to Argon arcs although there is evidence to suggest it also occurs in neon, xenon and krypton arcs (5). In helium the positive arm and turning point are found to be less pronounced. Less information is available for helium and a number of anomalies exist within the reported literature. Savage et al (23) find the V-I characteristic to be continuous and with a low positive slope occuring above an ill defined minima in the region of 150A. Results have also been reported that show a discontinuity at 150A (5). Here the voltage falls by 5V. The nature of the discontinuity is such that the voltage is a multi-valued function of current. This behaviour could possibly be the result of a change in arc mode. However, the arc mode is not specified. The shape of the V-I characteristic is determined primarily by the behaviour of the cathode and column contributions. The latter is a complicated function of convective, conductive and radiative energy losses from the column. Arc temperatures (7) and plasma flow velocities (4) are found to be higher for the CSM than the NM. It is therefore to be expected that the column contribution increases more quickly with current in the CSM than the NM. This is in agreement with behaviour reported above but a detailed understanding of the positive arm of the V-I curve has yet to be gained. The negative arm of V-I is far more complicated in nature than the expression given by Nottingham indicates. At low currents, where the arc contribution is small, the curve mirrors the dependence of the sum of the fall voltages (V_o) on arc current. At low arc currents V_o must clearly fall with increasing current. This behaviour is sensitive to the mode of arc behaviour and is often interpreted primarily in terms of the cathode fall voltage decreasing with arc current (15). There is evidence (7) to suggest that at high currents (for a given mode) the sum of the falls becomes only weakly dependent on current and arc length. Experiments with probes (1) indicate that the cathode fall voltage is insensitive to arc length and it would then appear that the anode fall is not substantially affected by arc length.

Many experiments have been performed to investigate the nature of the V-ℓ characteristic (6,8,16,17). These results indicate that the relationship is essentially linear for short arcs. At longer lengths in argon the gradient decreases. This decrease is not observed

in helium (17). In one reported case (16) the gradient is found to be negative for very short arcs (∿ 1mm). Considerable caution must be taken when interpreting behaviour at very short arc lengths as the effective arc length is probably significantly different from the work piece - electrode separation set prior to arc initiation. It is known that the electrode expands towards the anode on heating. Electrode erosion is also occuring. Further confusion is introduced by the effect of plasma climb on the electrode. In practice arc length is almost invariably associated with the electrode separation before arc ignition. For short arcs the V-ℓ gradient is substantially independent of arc current over the range 100-1000 Amps (5) and has a value of about 0.8 V/mm in argon (5,16,17). In helium this gradient is 1.5-2 V/mm. The zero arc length intercept of the V-ℓ curve is generally found to lie in the range 7-10 volts for argon arcs (5), and increases only marginally with arc current over the range employed in TIG welding (5). The intercept is also dependent on arc mode being lower for the NM than the CSM (5). The value of V_o obtained in this manner is often associated with the sum of the fall voltages for all arc lengths (16,17). However, the possibility of the sum of the fall voltages changing with arc length must also be considered (1,5,7).

A detailed investigation by Olsen (7) suggests that V_o may increase slightly with arc length for arcs on water cooled copper anodes (see section 2.3.2).

The substantially linear nature of the V-ℓ curve has often been interpreted as being indicative of a uniform electric field strength in the column. More detailed investigations (see section 2.3.1) show that this is not the case and that a highly non-uniform field exists. At best the slope of the V-ℓ curve may be regarded as an average value of the field strength (E) (7).

General arc characteristics reported above vary in detail depending on many variables. Electrode vertex angle is found to influence arc voltages for CSM arcs (19) - sharper electrodes produce higher voltages. Account must also be taken of anode composition (see section 2.3.2), electrode composition and diameter (18) shielding gas flow rate and gas purity, and workpiece travel speed. Attention should also be given to

the general conditions under which experiments are conducted. This has been recognised by a number of workers (8) who have performed experiments in purpose built chambers. In this manner atmospheric contaminants have been almost completely excluded from the arc region. In particular, it is then possible to operate an arc in a nominally still atmosphere as a shielding gas flow is no longer essential.

The effect of a cathodic constriction on the electrical characteristics of TIG type welding arcs has received little systematic attention. It is known, however, that in such systems the arc voltage increases. Experiments (20) have shown that the increase depends strongly on the constriction aperture size and the gas flow rate through the constriction. Such arcs are not 'free' and obtain mass in a manner other than by entrainment. It is therefore to be expected that the energy structure and hence the arc voltage will be different in character to that observed in TIG welding arcs. It is characteristic of such arcs that electric field strength is higher in the vicinity of the constriction than in the arc column (20). The effect of a constriction is to produce an essentially column like arc of a more stable nature. These arcs do not exhibit the same diversity of arc modes as found in TIG welding but do have peculiarities e.g. double arcing from oxide layers on the copper orifice.

The fundamental importance of the information discussed above is that any general arc column theory must explain such observations. It is therefore worthwhile examining the influence of other variables such as ambient pressure and gravitational field on this behaviour. In non-consumable electrode arc welding particular emphasis should be given to the restricted working range ($300 \gtrsim I \gtrsim 50A$) and to the influence of these characteristics on weld bead characteristics. The latter discussion is deferred until Section 2.4.

2.3. Structure of the Arc Column

The column is taken here as the space between the electrodes with the exception of regions within about 0.1mm (21) of each electrode. In reality, transitional regions will exist between the column and electrode regions and so the three arc subdivisions discussed here can only be

regarded as giving an approximate description. This point is discussed more fully by Ecker (81). The lateral extent of the arc column region is taken as the space over which the influence of the arc is felt and includes the non-current carrying heat affect zone adjacent to the current carrying core.

The column is perhaps the best understood of the three arc zones and has received much attention. Many papers have investigated column forms that are not appropriate to welding. In particular the long, wall stabilised column channel model (essentially two dimensional) has been extensively investigated. This has yielded much useful information on the temperature dependence of thermodynamic properties and an understanding of power dissipation in such a column. The cylindrical column is quite unlike the short arcs of point-plain geometry employed in welding. Despite obvious differences there are many features of interest in cylindrical column arcs. The present discussion is divided into two sections in an attempt to assess this literature. In the first a survey of general arc column properties is undertaken and in the second the literature on welding arc columns is reviewed.

2.3.1. General

The most striking feature of the column is that of high current transport through small areas (typically $10^7 A/m^2$). This is achieved by virtue of a degree of ionization (few per cent) being associated with high column temperatures. In this state the arc column is a thermal plasma as the degree of ionization required for current transport is primarily maintained by collisions (1). An essential feature of a plasma is that every volume element greater in size than the Debye length (λ_D) is closed with respect to charge conservation and that the extent of the system is greater than λ_D where (21)

$$\lambda_D = \left(\frac{\varepsilon_o KT}{n_+ e^2}\right)^{\frac{1}{2}} \qquad (2)$$

e, electronic charge; k, Boltzmann's constant; ε_o, permittivity of free space; $n_+(T)$ is number of positive ions per unit volume and given by the Saha equation; T, temperature.

λ_D is typically of order a few μm's (21) for an argon arc and may be used as a rough estimate of the extent of the fall regions in which charge neutrality no longer applies (21). The above expression assumes that collisions occur frequently enough for the electron and heavy particle temperatures to have the same value, i.e. T. This is normally (21) taken to be a good approximation at pressures above about 0.1 bar although deviations may occur near the electrodes where high temperature gradients exist. Here a two temperature plasma model is required. Most arc column models make use of single temperature gas properties and consequently implicitly assume equilibrium (the term 'equilibrium' as used here will be identified with the less stringent condition of local thermodynamic equilibrium, LTE).

The column is composed primarily of neutral particles, electronics, singly ionized particles and photons although a few multiply ionized particles will exist (21). With the exception of photons these particles move with random motions and obey Maxwellian distributions (21). Photons obey Bose-Einstein statistics and are usually assumed to be in equilibrium with the other particles, i.e. have the same temperature. Photons give rise to a continuous arc spectrum with discrete lines characteristic of the elements within the arc. The intensity of these lines are often used as the basis for arc column temperature measurements. The basic mechanisms responsible for arc column radiation are associated with free-bound transitions, bound-bound transitions, free-free transitions and the acceleration of charges in the fields of other charges (17). Only bound-bound transitions give rise to discreet lines.

The externally applied electric field superimposes a drift motion on the otherwise random movement of charged particles. Electrons move towards the positive terminal and positive ions towards the negative electrode. Most of the current (∿98%) (1) is carried by the electrons in view of the higher mobility of these particles. Further bulk motions may be superposed on this behaviour. This can occur if the arc is burning in a strong gas flow as in plasma welding. In a free arc the interaction of the arc current with the self magnetic field (4) can also generate flow. The result of these motions is to produce a current flow that may be characterised by the current density ($\underline{J}$) and

written as (22)

$$\underline{J} = \sigma\underline{E} + \sigma\underline{U}\wedge\underline{B} \qquad (3)$$

σ, the electrical conductivity, is determined by the gas composition, pressure and temperature. $\underline{E}$ is the electric field strength, $\underline{B}$ the self-magnetic field and $\underline{U}$ the bulk velocity of motion. The last term represents the induced e.m.f. resulting from bulk flow transporting charges across field lines. A relationship between $\underline{J}$ and $\underline{B}$ may be furnished from Maxwells equations (see for example 22):-

$$\nabla\wedge B = \mu_o\underline{J} \qquad (4)$$

where μ_o is the permeability of free space. An estimate of the importance of the induced e.m.f. may be obtained by using equation (4) to relate $\underline{B}$ to $\underline{J}$. It is then found that the second term in equation (3) is negligible when

$$E >> \frac{\mu_o . I . U}{2\pi R} \qquad (5)$$

where I is the arc current and R the electrical radius. Taking an unfavourable case for an argon plasma arc, i.e.

$$I = 10^2 A,\ U = 10^3 m/s,\ R = 10^{-3} m$$

gives $E >> 20V/m$

The average axial E is found experimentally to be about 800V/m for an argon TIG arc and is expected to be higher for plasma arcs. As the induced e.m.f. is only a few per cent of this term it will be neglected in all future considerations. Therefore

$$\underline{J} \simeq \sigma\underline{E} \qquad (6)$$

It then follows that current flows along electric field lines and has a density largely determined by the radial distribution of electrical conductivity. Values of σ as a function of temperature are available for argon (e.g. 24). However, discrepancies do exist between values reported by various workers. σ is a strong function of temperature below about 12,000K. Above 16,000K the temperature dependence is small

as most particles are then at least singly ionized. This suggests that the electrical boundary of an arc is sharp although in practice vapourisation will influence this behaviour. The saturation effect further suggests only a slight tendency for preferential current paths through regions above 16,000K (25).

Many workers have taken the axial electric field to be much greater than the radial. In this approximation equation (6) may be integrated giving:-

$$I = E_Z \int_0^R \sigma . 2\pi r dr \qquad (7)$$

The left hand side may be used to define a mean radial conductivity $< \sigma >$ i.e.

$$< \sigma > = I/\pi R^2 E_Z \qquad (8)$$

This is a simple example of the application of integral expressions to arcs (see 26). The right hand side of this expression can be estimated by suitable photographic estimates of R and by simple electrical measurements. Hence a mean conductivity temperature (T_σ) can be established. This has often (17,27) been found to be a useful measurement.

The temperature distribution within an arc column is normally evaluated by spectroscopic means, although electrostatic probe techniques have also been applied (28). The precise distribution is found to depend on many variables. However, these may be interpreted in terms of effects on the local radiation, convection and conduction balance within the column. The steady state differential form of the local energy balance (1) is

$$\rho C_p \ \underline{U}.\underline{\nabla T} + \nabla(-\kappa \nabla T) + W = \sigma E^2 \qquad (9)$$

where ρ, C_p and κ are the gas density, specific heat and thermal conductivity respectively. $\underline{U}$ is the gas velocity and W is the net radiation (absorption - emission) balance for a unit of arc volume. The left hand terms represent respectively convection, conduction and nett radiation. The right hand side is the Joule heating source term and

represents energy that must be provided to cater for these losses. This expression is not closed with respect to the temperature field and more information must be provided. In particular, the gas properties and radiation terms are functions of temperature. In the general case, electric field E is known to be a strong function of the axial co-ordinate (7). Perhaps the most difficult factor to account for is the convection term, as the flow field is also required. $\underline{U}$ involves the solution of the momentum equations which in a steady state vector form are (1):

$$\rho(\underline{U}.\underline{\nabla})\underline{U} = -\underline{\nabla}p + \eta\nabla^2\underline{U} + \underline{F} \qquad (10)$$

The inertial term is on the left hand side while effects of pressure (P), viscosity (η) and body forces (F) are on the right. $\underline{F}$ includes a component ($\underline{J}\wedge\underline{B}$) due to the interaction of the arc current with the self-magnetic field. In general a gravitational body force must also be included (29). $\underline{F}$ then becomes

$$\underline{F} = \underline{J}\wedge\underline{B} + (\rho-\rho_\infty)\ \underline{g} \qquad (11)$$

where ρ_∞ is the density of the cool surrounding gas and $\underline{g}$ the acceleration due to gravity.

Here $\underline{B}$ is related to $\underline{J}$ by the Maxwell equation previously introduced. Further relations must also be satisfied. These are the conservation of mass, current and field line expressions:

$$\nabla(\rho\underline{U}) = 0, \quad \nabla\underline{J} = \nabla\underline{B} = \nabla\underline{E} = 0 \qquad (12)$$

This formidable set of equations has not been solved for boundary conditions appropriate to the welding situation. However, solutions have been obtained using simplifying assumptions and these provide an important insight into column behaviour.

The simplest solutions of these equations consider arcs in the absence of convection and radiation. Conduction is then the only mechanism contributing to heat transfer. For a long cylindrical plasma (channel model) the equations reduce to the Elenbass-Heller (8) equation

$$-\frac{1}{r}\frac{d}{dr}\left(\kappa r\frac{dT}{dr}\right) = \sigma E^2 \qquad (13)$$

Equation 13 has no analytic solution (30) for realistic forms of K (T) and σ(T) but numerical solutions have been obtained. These show that the radial temperature field expands as the core temperature increases (30). This has been taken to imply that an arc column increases in diameter with increasing current. The general form of the distribution is such that temperature falls off radially in argon arcs with a gradient of about 4×10^6K/m although dissociation peaks may appear in nitrogen arcs (8). The inclusion of a radiation term is found to flatten the profile (17). However, only very approximate techniques have been employed in accounting for W. The term W is normally assumed (17,31,32, 33) to be a thermodynamic property (function of temperature, pressure and composition) and further assumptions about arc composition, equilibrium and self absorption within the arc, and adjacent gas are normally made. Emmons (33) has experimentally determined the radiative source strength of an argon plasma as a function of temperature. Evans and Tankin (31) have performed similar measurements. Bauder (32) has shown how such data may be used to determine the radiation from an arc at any pressure from the data obtained at one atmosphere if the temperature profile is known at the required pressure. Experiments involving channel arcs have been used to obtain data on the temperature dependence of thermal and electrical conductivities (33) i.e. K is found by integrating the Elenbass-Heller equation and examining the temperature dependence of the radial temperature gradient at the tube wall. These values have been compared with those computed using various plasma models and reasonable agreement is found. Perhaps the most difficult property to investigate is that of viscosity. This measurement requires a knowledge of both the flow and temperature fields. Considerable disagreement exists between the predicted and measured high temperature behaviour of this quantity in argon (24,34,35).

The simplest flow situation investigated is that where the stream lines are parallel to the isotherms. No convection of heat then occurs (i.e. there is no temperature gradient down a streamline) and so the Elenbass-Heller equation still applies. In most situations of practical importance streamlines do cross isotherms and so convection must be considered. It is often found suitable to deal with such situations by means of integral techniques. Essentially, this reduces to

investigating the axial dependence of the average radial value of a property. This significantly reduces the mathematical complexity of the problem and allows a comparison with experimental values by means of measuring suitable 'characteristic areas'. Cowley's development (26) of this approach for arc applications has included the time dependent behaviour of an arc burning in a gas flow within a nozzle.

In many treatments the equations are further simplified by assuming the existence of boundary layer flow. This approximation is suggested by the highly directional, jet like, appearance of the column. In the boundary layer limit the momentum equations have been integrated (4, 26) and an expression for the momentum flux (F) through the arc obtained i.e.

$$F = \int_o^R \rho v_z^2 \, 2\pi r dr = \frac{\mu_o I^2}{4\pi} \ln \left(\frac{R}{R_o}\right) \qquad (14)$$

Where R_o is the radius of the arc at the Cathode and R the radius at some down stream position z. This expression was first obtained by Maecker (4) for a diverging arc with a uniform radial current density at a given axial position. Cowley (26) later found this to hold for less stringest conditions on the current density. A root mean square estimate of the axial flow velocity can be obtained from this result i.e.

$$U_{rms} = \left(\frac{F}{\rho \pi R^2}\right)^{\frac{1}{2}} = \frac{I}{2\pi R} \cdot \left(\frac{\mu_o}{\rho} \ln \frac{R}{R_o}\right)^{\frac{1}{2}} \qquad (15)$$

It should be noted that the rms value of the axial velocity increases with current and generally decreases with ambient pressure although the dependence of arc radius on these parameters tends to reduce the indicated change i.e. R increases with current and decreases with pressure.

Recently Ramakrishnan et al (36) have developed a model for the high current arc based on an integral formulation of the boundary layer equations. Results are mainly applicable to long (cm's) high current arcs (KA). This theory assumes the velocity distribution to have a given functional form, the arc shape to be parabolic and the current density profile flat.

Numerical calculations then deduce the axial dependence of arc temperature, electric field strength, velocity and mass flow rate. Strong axial variations in the electric field and axial mass flow rate were observed. Axial velocities were found to fall with arc length while the axial temperature changed only slowly. Calculations were performed primarily for 2.16KA arcs assuming laminar and turbulent values for the transport coefficients (η and κ). Experimental comparisons were made principally with Bowmans 2.16KA arc (37), and good agreement was obtained when turbulent transport properties were used. The results describe an arc with strong radial entrainment near the cathode and essentially straight line but turbulent motion in the column. Turbulence has the effect of increasing axial mass flow rates while axial velocity falls faster than in the laminar case. This model indicates that axial temperatures and electrical field strengths increase slowly with current below 1KA. However, the arc radius increases strongly with increasing current. Hill and Jones (38) have examined turbulent effects experimentally in low current (10-60A) arcs and also find the electric field to increase with mass flow rate when turbulent effects become significant. Again the arc is found to form two axial zones, one in which strong entrainment occurs and another where flow is essentially straight line.

The stability of arc columns has received little attention, but there is evidence (39) to suggest that stability is governed by similar mechanisms as in free jets. The work by Howatson and Topham (39) on arcs burning in converging nozzles in accelerating flows suggests that instabilities can be generated in a shear layer between the cold and hot flows. The arc flow is always found to be stable for column Reynolds numbers less than 100 for 100 Amp arcs in Nitrogen.

Lowke (40) has given a very approximate analysis of free burning arcs over the range 1A to 10KA. This model regards natural convection as dominating below about 30A and convection induced by the current self magnetic field interaction above this value. Results indicate that behaviour is transitional near 100A having features common to both. Particularly interesting to the present work are the predicted pressure dependencies of arc radius, electric field and temperature at both high (10KA) and low (10A) currents. For a 10A arc in air the electric field

and temperature are found to increase with pressure while arc radius falls very strongly. For a 10KA arc in air the temperature falls with increasing pressure but the radius is almost independent of pressure.

Very little has been stated above about the nature of the 'current - self magnetic field' interaction responsible for generating flow in high current arcs. This important feature requires comment. Maecker (4) was the first to give an interpretation of this behaviour. Maecker considered the flow to be generated by an axial 'magnetic pressure gradient' existing in a diverging column. The model neglects viscosity and is essentially one dimensional in nature. A simple mathematical treatment of the momentum equation with a flat radial current distribution then gave an essentially Bernoullian expression:-

$$\frac{\rho U_z^2}{2} + \frac{\mu_o I J}{4\pi} = \text{constant} \qquad (16)$$

where the constant applies to the axial stream line. The second term on the left hand side is often called the 'magnetic pressure' where J is the current density at some axial position. The current density at the cathode (J_o) is normally taken as being much larger than at the anode. The value of u_z at a large distance from the cathode can then be obtained from equation (16) and written as:-

$$U_z = \left(\frac{\mu_o I J_o}{2\pi\rho}\right)^{\frac{1}{2}} \qquad (17)$$

The cathodic current density is often taken as having only weak I dependence. U_z then increases as $I^{\frac{1}{2}}$ and decreases $1/p^{\frac{1}{2}}$ (if the cathodic current density is independent of pressure). Meackers model also indicates that the velocity rises continuously with increasing axial position tending asymtotically towards the above value. Clearly this behaviour will be modified by viscous forces. Lancaster (41) broadened this treatment to include viscosity but neglected pressure gradients. The result was very similar in form to that obtained for a free jet with a magnetic point source of momentum at the origin. However, the identification of the appropriate point source momentum strength is by no means clearly defined. Such an approach predicts v_z to fall as $1/z$ with axial distance (z) and to be infinite at the origin..

Chang et al (42) have recently given a similar treatment based more directly on the free jet equations. The application of such results to welding arcs is of doubtful value in view of singular behaviour at the cathode and the inherently short arcs to which such results must be applied. This general class of self-magnetic field driven flows was given further consideration by Shercliff (43) in 1970. He emphasised that flow resulted essentially from the none vanishing curl of the $\underline{J} \wedge \underline{B}$ body force i.e. that part of $\underline{J} \wedge \underline{B}$ that cannot be balanced by a pressure gradient and is therefore free to generate a flow in a liquid or gas. As such, the flow is essentially three dimensional and has no two dimensional counterpart. For example, no flow is generated in an infinitely long (no end effects) triangular wedge type arc (see figure I) despite the divergence of current from apex to base. Shercliff considers the flow generated by a point source entering a homogenous semi-infinite inviscid medium. The important feature of the solution is that $v_z \alpha 1/z$ and has much in common with the free jet solution. However, this solution has a zero on the axis of symmetry (in spherical polar co-ordinates). One significant difference is the predicted dependence of axial velocity on gas density and hence ambient pressure. This feature isn't found in the free jet solution. Further work has been done by Sozou (44,45,46,47,48) who finds that the inclusion of viscosity leads to finite values on the axis below a given Reynolds number. More recently work by Andrews and Craine (13) and Atthey (49) who consider the effect of this force in weld pool behaviour, suggests that the axial discontinuity is a result of the point source assumption. The above models do not consider in a realistic manner the situation found to exist in a welding arc, where arc lengths are short, currents moderate and current densities finite and variable across the arc. Further, the homogenous nature of the medium in which the flow is taken to occur prohibits the analysis of buoyancy forces or the heat affected zone adjacent to the arc. The need for such an analysis is regarded as important in view of the significant part played by gas flow in arc behaviour and the possible effects this may have on weld pool behaviour.

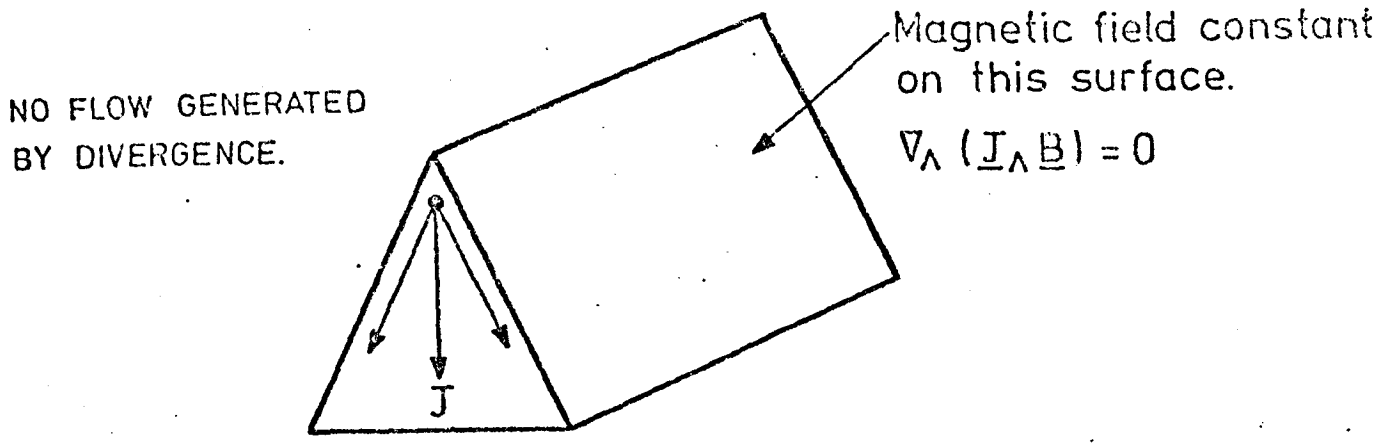

(a) Long, diverging wedge shaped arc.

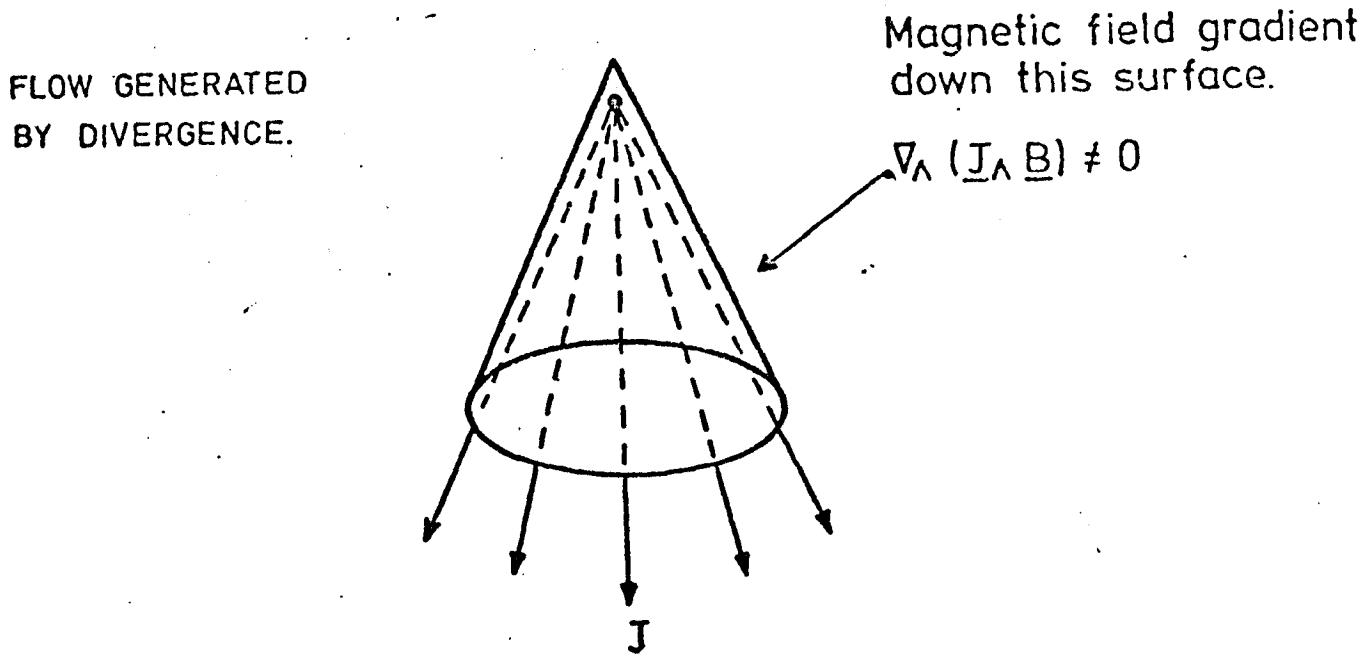

(b) Diverging conic arc.

FIG. 1. FLOW GENERATION IN DIVERGING ARCS.

2.3.2. The Column of a Welding Arc

Welding arcs are short (less than 1cm and typically a few mm's), divergent (point to plane), and carry moderate currents. These features mean that electrode characteristics (e.g. structure, geometry, vapourization etc) are likely to influence arc behaviour. Convective effects are expected to be strong although arcs may also have features associated with the transitional nature (see section 2.3.1) of the current range used in welding. Such effects have not been accounted for in existing theories and so most of the available information is of an experimental nature. The two important variables characterising column behaviour are temperature and velocity. These have received extensive treatment although a general energy balance predicting arc voltage, or arc column stability has yet to be given.

2.3.2.1. Temperature Field

Temperature may be measured in terms of changes in the behaviour of physical properties sensitive to such an influence. Properties used in practice are the intensity of a spectral line, thermal velocity of particles, refractive index, the number density of positive ions or electrons, or changes in the speed of sound. Values obtained by these measurements on a given arc will only coincide if local thermodynamic equilibrium applies. If this is not the case the 'temperature' obtained will relate in some manner to the particular property being investigated. It is the author's view that in themselves temperature measurements are not particularly important. Great importance is, however, to be attached to the use of such measurements in describing the physical state of the arc. This requires integrating and differentiating experimentally obtained profiles to obtain relevant arc properties such as the distribution of conductive heating and the part played by this in the total energy balance. Very few papers appear to use temperature results in this manner and in cases where this has been done inconsistencies have sometimes been revealed (17). Many papers have obtained temperature distributions for welding arcs (primarily argon TIG) but considerable discrepancies exist between reported results. These results and the methods of measurement are now reviewed.

Electrostatic probe devices have long been used (50) for the measurement of temperature in low pressure discharges. Here a fine wire is voltage-biased with respect to the plasma and so attracts a current as it is swept quickly through an arc. The size of current has to then be related to the plasma charge density. This is generally a known function of temperature and so the temperature distribution can be deduced (28). However, the relationship between the probe current and plasma charge density depends on the mechanism of current capture by the probe. In low pressure arcs, plasma is not significantly disturbed by a probe and so the 'random flux' current is collected. It has been pointed out (51) that this may not apply to higher pressures. Gick et al (28) have used a negatively biased probe (drawing a positive ion current) to plot the isothermal structure of a 100A, atmospheric Argon TIG arc above a vapourizing steel anode. Results were analysed using an essentially low pressure probe theory. In this manner the temperature near the cathode was found to be about 12,000K. The temperature profile had linear radial and axial gradients. These results have been challenged on a number of grounds. Glickstien (17) has pointed out that the profiles obtained produce axial electric field gradients a quarter of those to be expected. Clements and Smy (51) have raised doubts about the probe current capture mechanism. They supposed the probe to be depleting adjacent plasma of ions and thereby capturing current by a diffusion dominated mechanism. However, Allum et al (52) have shown such an approach to predict impossibly high current levels. Allum et al (53) have used probes to investigate plasma welding arcs. In this work a correction was applied to low pressure probe theory to account for the chilling effect of a probe on surrounding plasma. Self-consistent electrical properties were then obtained from experimental temperature profiles and an axial value of about 17,000K was indicated near the cathode of the 200A argon plasma arc investigated. However, doubts remain over the interpretation of probe signals.

Optical methods of measuring arc temperature are mainly concerned with investigating the intensity (I) of a spectral line (or lines) emitted by an arc. Theory (1) gives

$$I = \frac{NA}{4\pi} h\upsilon \qquad (18)$$

where h is Plancks constant; ν, the frequency of radiation and A the transition probability. The number (N) of atoms per unit volume in a given excited state is:

$$N = N_o \frac{W_e}{W_o} \exp - \left[\frac{E_e - E_o}{KT}\right] \qquad (19)$$

K is Boltzmanns constant, W the partition function, E the excitation energy and the suffixes e and O refer to excited and ground states.

This expression suggests a number of methods for measuring T. These rely on measuring the relative or absolute intensity of radiation. The absolute method considers just one line. For this an accurate knowledge of A and N are required as well as an absolute measure of the line intensity. Relative methods consider ratios of line intensities.. It is clear from the above expressions that a considerable amount of information is required to evaluate T. Mechev & Eroshenko (57) have examined possible sources of error in specifying this data and conclude that such errors are responsible for many of the anomolies existing in the literature. Further, the state of the plasma must be assumed i.e. N is taken to obey Maxwell - Boltzmann statistics. This is a prerequisite of LTE.

The optical techniques indicated above have been reviewed on a number of occasions (1,57) and so only the results of applying these methods to welding arcs will be given further consideration. Olsen (7) performed the pioneering work in TIG type arcs (operating on a cooled copper anode). For a 5mm, 200A argon arc he found temperatures (measured spectroscopically) above 20,000K near the cathode. This figure corresponds with an ionization level of about 90%. Just above the anode surface the temperature fell radially from 13,000K on the axis to 10,000K at the periphery. Results obtained were used to compute axial changes in the electric field and current density from expressions previously introduced (see 2.3.1). Olsen discussed thermal equilibrium and concluded that the fractional differences between electron and heavy particle temperatures is at most 20% near the cathode and 0.1% near the anode. More realistic welding situations (vapourising anode) have recently been considered by Glickstein (30). He measured the axial temperature for a

100A, 2mm argon TIG arc on a steel anode. A value of 11,000K was obtained near the cathode (~10% ionization) and approximately 8000K near the anode. This arc contained metal vapour in the form of Mn, Ni and Cr and in view of the low ionization potentials of these elements it was expected that the arc might behave as a metal type arc. However, Glickstein subsequently performed otherwise identical measurements on water cooled copper anodes and obtained similar results. The experiments of steel anodes were, however, associated with a larger scatter (10-30%) than those on copper anodes. Shaw (55) has also performed experiments on steel (mild and stainless) anodes and finds low temperature (5,000K) metal vapour (Mn) present in the arc, although the axial position at which these lines are found is undefined. This finding is supported by the work of Mills (56) who also obtained the radial temperature distribution. Axial symmetry of the temperature profile was not found and this was explained in terms of pool behaviour. Further experiments are clearly required to determine whether LTE may be taken to apply in the important region near the anode. Glickstein's (30) results have a similar axial magnitude as those of Gick et al and indicate that despite effects of vapourization, temperatures twice those expected for metal arcs exist. Unfortunately, no radial comparison is available between these results.

Erokhin A. A. et al (86) investigated the effect of electrode vertex angle on arc temperature. These workers found parabolic radial temperature distributions that became steeper with decreasing vertex angle. This is in qualitative agreement with measurements made by Petrie and Pfender (58) who investigated the intensity of a spectral line as a function of operating time. As the electrode tip geometry was lost the axial temperature was observed to fall. There is a need for more information concerning electrode effects on arc structure. In particular the effect of electrode diameter has yet to be considered.

Arc temperature is found by Glickstein (30) to increase with current in a linear manner and at a rate of 18.8 K/A. Mechev and Eroshenko (54) find a lower value of 9 K/A. Heat conduction is strongly dependent on temperature gradients. For the short 2mm arc, axial gradients of about

2×10^6 K/m have been measured (30). This is more than twice the value found for the 8mm arc of Gick et al (28). The radial gradient of Gick's arc was of a substantially linear nature with a gradient also of about 10^6 K/m. This is to be compared with a value of 4×10^6 obtained from a simple conductive model of the column by Glickstein. Kobayashi and Suga (59) performed similar experiments on a 100A, 6mm atmospheric argon TIG arc above a water cooled anode. Their results are substantially higher than those obtained by Gick et al and Glickstein. These workers found typical average axial temperatures of order 15,000K. This number increased slightly with increasing arc current and had a value of about 13,000K near the anode. Cathode temperatures were of order 18,000K. This paper also investigated the effect of shielding gas flow rate on temperature. No influence is observed for the range 5 l/min to 20 l/min. Shaw (55) also reports a similar result.

More recently laser techniques have been employed to investigate temperature fields (60). This approach examines the electron density by Thompson scattering of laser light. In this way the electron temperature can be measured from data available on electron density. Further a localised volume of space can be investigated. Using this technique it should therefore be possible to examine the validity of LTE. Spectroscopic results obtained by the same authors are in good agreement with these measurements near the centre of the column. This indicates that LTE exists in the column. In both spectroscopic and probe methods a cord of the arc is examined and data then has to be reduced, by means of an Abel transform, to the true radial distribution. Such a reduction requires the assumption of cylindrical symmetry and is known (61) to be susceptable to small errors in input data. Significant axial errors may then result from uncertainties near the boundary. These uncertainties are by passed because the local nature of the laser measurements. Results obtained by this method at the mid-plane of a 100A, 10mm argon TIG arc on a water cooled anode are $10{,}500 \pm 1{,}500$K. Temperatures measured by the same workers using spectroscopic techniques indicate values of about 13,000-15,000K at the cathode and 10,000K at the anode. These were used by the authors in conjunction with velocity field data, to determine mass flow and current density maps of the column.

Experiments with the constricted argon plasma arc have been performed by Allum et al (52) and more recently by Tao and Pavelic (62). The last workers investigated temperature profiles in the constriction of a low current (75A-135A) plasma gun. The maximum temperature recorded was 8,000K. These temperatures are thought to be impossibly low on the grounds that such temperatures could not support the current actually passing through the arc column. Earlier plasma temperature measurements in argon (20) with higher currents and flow rates have yielded values of order 30,000K in the constricting duct. However, enthalpy considerations indicate such values to be impossibly high. Recently (63) the influence of orifice geometry has been examined. This, coupled to plasma gas flow rate is expected to exert a significant influence. It is found, not unexpectedly, that converging nozzles give higher temperature columns than straight or diverging nozzles.

An analysis of published data by Simonik and Pangilskaya (64) has found that temperature is strongly dependent on the ionization potential (V_I) of a plasma and varies with current in accordance with:-

$$T = 591\ V_I\ I^{0.087}$$

where I is the arc current.

Results presented above refer mainly to argon arcs. However, the last expression described very roughly the behaviour as a function of gas ionization potential. Clearly helium arcs will have temperatures many times those of metal vapour arcs. In molecular gases (e.g. N_2) effects not mentioned above may become significant i.e. dissociation peaks have been observed (8). It can be seen from results described above that large discrepancies exist that cannot be reasonably accounted for by changes in arc behaviour and probably result from measuring techniques. Mechev and Eroshenko (57) have considered in depth the discrepancies reported in the literature. These workers have applied a number of optical techniques to the measurement of a given arcs temperature and conclude that the experimental procedures adopted account for many discrepancies. In particular they consider a 100A, 10mm argon arc and find that the careful application of a number of techniques yields an axial value of about 13,000K at the mid plane.

Few theoretical models of the temperature structure of TIG type arcs exist. These are mainly channel type models where convection is neglected. Of particular interest is a model of this type developed by Glickstein (17). Here the effects of metal vapour (aluminium) and radiation are taken into account for argon and helium arcs. It is found that beyond a given level of fractional vapour to gas composition a substantial reduction in arc temperature may occur. This has a complicated effect on the distribution of current. However, flow effects are also expected to influence the distribution of thermal energy in an arc, i.e. by directly modifying the temperature field through the introduction of convection, by influencing the migration of metal vapour from anode to column (1,65) affecting the entrainment of atmospheric contaminants, and by influencing arc stability. Literature concerned with these aspects of column structure is now considered.

2.3.2.2. Flow Field

Gas flow in arcs has been investigated experimentally by a number of workers. Wienecke (66) in 1955 observed the motion of gas in a 200A, 5cm, carbon arc burning in air. Bowman (37) has considered higher current arcs (2.16KA). His technique involved observing the force exerted by the arc on small spheres, traversing its path. However, the only directly measured velocity field appropriate to the argon-tungsten welding arc situation is that obtained by Seeger and Tiller (60). They considered a 100A, 10mm argon arc between a pointed tungsten electrode and a water cooled copper anode. Laser techniques were employed by these workers to obtain velocity field maps. A number of other workers (58,67) have reported less comprehensive results primarily by inferring the flow field from pressure measurements made at the electrodes.

Perhaps the most directly relevant single result (no velocity field is given) to the welding situation is that reported by Chang et al (42). They report that a stroboscopic investigation has given a value of 120m/s at the mid-plane of a 2mm, 200A argon TIG arc. However, no further details are given. A less direct method, making use of radiation and electric field strength measurements has been employed on high current (10KA) arcs by Strachan and Barrault (68). These workers deduced the

axial dependence of average velocity (radially averaged) by making use of an integrated form of the energy equation. This technique has not been applied to a welding arc situation. Results obtained using the methods outlined above are described below. A detailed theoretical understanding of these has yet to be given.

Velocity field maps (60,66,36) indicate that within the arc, the flow is essentially straight line and substantially parallel to the axis (60). Strong radial entrainment is found to exist near the cathode although this becomes weaker in downstream regions. Very little quantitative data exists for regions outside the column although flow visualization techniques (69) indicate that turbulent conditions may well exist in many experimental arrangements.

The axial velocity is generally found to fall with increasing distance from the cathode (66,37) although peaked distributions with maxima occurring away from the cathode have been reported (58,68). Such behaviour has been reported for welding arcs (58) and for arcs at much higher currents (68). This contrasts the predicted monotomically increasing behaviour of the inviscid model of Maecker or the monotomically decreasing behaviour of viscous dominated models. Other researchers (60) found velocity to fall slowly with axial distance from the cathode for moderate arc currents (~100A). At higher currents substantially steeper fall offs have been reported (37). The latter behaviour is sharper than that expected for laminar flow and has been attributed to turbulent motion (36) within the column. Very little information exists on the radial dependence of velocity in a welding arc. However, Seeger and Tiller (60) find that velocity is of a rounder peak nature and tends smoothly to the free stream flow. A similar Gaussian type profile has also been found at higher currents by Bowman (37).

Comments made above refer specifically to the form of the velocity distribution. In magnitude axial velocities are of the order 100m/s. An axial value of 105m/s is found at the mid-plane of the arc investigated by Seeger and Tiller (60). This compares with a value of 120m/s reported by Chang et al (42) at the mid-plane of a 2mm, 200A argon arc. Manometric techniques employed by Schoek (67) indicate axial

free stream values near the anode of a TIG arc to range from 218m/s for a 5mm, 150A arc to 52m/s for a 9mm 50A arc. No systematic set of experiments has yet been conducted to examine the influence of arc length, electrode geometry, arc current or gas composition on flow velocities.

Much higher velocities can be obtained by constricting the arc near the cathode as in plasma welding. The mechanisms of mass capture by the arc is then different in nature than that for the free burning arc. Metcalfe and Quigley (70) have considered such a situation and associate the flow velocity V with the mass flow rate ($\dot{m}$), orifice area (A) and density ρ of plasma gas by

$$V = \dot{m}/\rho A \qquad (20)$$

However, this approach is far from satisfactory as it is assumed that the arc fills the orifice and that the temperature field is known in this region. In practice, a cold gas flow will separate the arc from the nozzle wall giving rise to the so called thermal pinch effect. Despite these short comings it serves to indicate the existence of velocities of order 10^2-10^3m/s for realistic mass flow rates. There is a need for further research to clarify mechanisms occurring in this situation. In particular, no detailed understanding exists of the interaction between motion generated by the 'current-self magnetic field' and that generated by forcing gas through an orifice.

Gas flow may significantly influence weld structure and acts as a mechanism for the transfer of heat within the column. The latter effect is expected to play an important role in determining the electrical characteristics of an arc.

2.3.2.3. Electric Field

The total power appearing in an arc column is given by $I.V_c$ where V_c is the voltage drop across the column. V_c may be found by subtracting the sum of the fall voltages (V_o) from the process voltage (V). Clearly V_c is dependent on arc length. The linear nature of V-l plots previously noted (see section 2.2) suggests that a more suitable form for V_c is E.l

where E is the electric field strength as given by $(V-V_o)/\ell$. Values of E obtained in this manner are characterised by gas composition and are only weakly dependent on arc current. This behaviour has been discussed in section 2.2. The linear nature of the V-l curve suggests that the voltage gradient within the column (local value of E) is also uniform having a similar value near the anode to that near the cathode. However, this is not the case. Experiments using electrostatic probes (1) to measure the local voltage of an arc column have found that E has a very strong axial dependence. The distribution of E has also been found (7) by integrating temperature profiles and using the known dependence of the electrical conductivity on temperature (i.e. by applying equation 8). Olsen (7) finds that E has a value of 4 V/mm near the cathode of a 200A argon. A value of only 0.8 V/mm is found near the anode of the same arc. Theoretical investigations have also predicted this type of behaviour. Dennery (71) solved Laplaces equation with boundary conditions suitable to a point - plain geometry and found E to have an axial dependence. His approach was of an essentially electrostatic nature and no account was taken of physical processes occurring between the electrodes. Glickstein (17) has shown that similar behaviour may be predicted from a channel model taking account of only conductive and radiative losses. This model essentially involves calculating E (using Ohm's law) from a channel model temperature field. These models show that the observed electric field behaviour may be qualitatively explained without even considering convective effects. In view of the dependence reported above it is quite remarkable that column voltage increases almost linearly with arc length (see 2.2). Such behaviour has yet to be explained.

Local processes within the column produce a demand for electrical power that also has a strong spatial distribution. The energy appearing per unit volume of the column is $\underline{E}.\underline{J}$ where $\underline{J}$ is the local current density. This term is often called the 'source' term and represents local column power dissipated by conduction, convection and radiation. Using Ohm's law this may be rewritten as σE^2 or J^2/σ. Olsen's results would then indicate power dissipation per unit volume to be over 50 times greater near the cathode than anode. Even Glickstein's lower temperature channel model (i.e. no divergence) indicates a factor of 40. The more realistic welding situation considered by Seeger and Tiller (60) may be

used to infer a value of similar order. Unlike E, the current density has a strong radial dependence giving rise to strongest power dissipation on the axis. Gvozdetskii (72) has calculated J from temperature measurements and obtains a Gaussian type profile. Gaussian behaviour may also be inferred from the column current density map of Seeger and Tiller (60). This behaviour is somewhat surprising in view of the sharp electrical boundaries anticipated as a result of the temperature dependence of electrical conductivity. It has been pointed out (72,73) that vapourization, particularly near the anode, may give rise to an increase in J and thereby affect the local energy density.

A proper understanding of the electrical and energy structure of an arc column can only be given in terms of the parts played by radiative, convective and conductive contributions. Direct measurements of these contributions are difficult to obtain and very few experimental results exist. Existing radiation measurements for TIG arcs are concerned mainly with total arc radiation measurements while enthalpy flows are inferred from flow fields. No direct measurement of conductive losses from the column exists and it is difficult to see how such a measurement could be made.

2.3.2.4. Enthalpy Flow

Literature reviewed here suggests that convection is very strong near the cathode of a free burning arc. It is therefore expected that a strong enthalpy flow is developed in this region where cold entrained gas is heated to arc temperature. Seeger and Tiller (60) have obtained a mass flow map of a 100A, 10mm argon arc. They find the mass flow rate ($\dot{m}$) for this arc to be about 60mg/s. These results may be used to estimate convective dissipation ($\dot{m}.h$) in the column. Using an enthalpy (h) value of 6MJ/kg (70) at 10,000K gives 360W for this contribution. The total power appearing in the column (I.E.ℓ) can also be estimated and is found to be about 800W. On this basis convection accounts for about 45% of the column dissipation. Clearly this mechanism is significant and probably dominant. Quigley et al (65) have estimated the mass and enthalpy flows in an 8mm, 100A argon arc using Maeckers flow theory and the temperature field obtained by Gick et al (28). They find a flow rate of 37mg/s. Using an arc temperature of 7,000K they

find an enthalpy flux of 130W ($\pm$60W). 130W must be regarded as a low estimate in view of the low arc temperature used. The upper limit of this estimate (190W) is thought more appropriate to a 10,000K arc. Uncertainties still exist due to the use of Maeckers flow theory and arc dimensions inferred from Gick's work. Within this framework it can be deduced that about 30% of the arc column power is expected to appear as enthalpy flow. This percentage is not discussed by Quigley et al although they do emphasise that only about 10% of the total process power appears in this form. Enthalpy flow is developed primarily near the cathode. It is therefore expected to play a more important role in the short arcs used for welding than indicated by the above long arc estimates of 30% and 45%. The remainder of the column power is dissipated as radiation and conduction.

2.3.2.5. Radiation

Measurements of the bulk radiation properties of welding arcs have been made on only a couple of occasions (15,67). Goldman (15) used a small blackened copper disc (mass-18.6gms) situated behind a quartz window to measure this property calorimetrically. This was placed at a distance of 7.84cm from the arc. His results indicated that about 12% of the total arc power appeared as radiation for an argon TIG arc. However, no attempt appears to have been made to estimate the contribution to disc heating made by the electrodes and background regions. This figure (i.e. 12%) represents a substantial fraction of the power appearing in the arc column, i.e. about 50% of the column power for a 3mm, 100A arc. Schoek (67) employed a commercially available radiometer to make a similar measurement. He found the arc to represent a spherically symmetric point source radiating 20% of the total arc power in the case of argon arcs. Figures for Helium and nitrogen arc were much lower (between 2 and 4%). Schoek's argon radiation measurements would appear to represent an unacceptably high level of radiation which approaches 100% of the power appearing in the arc column.

Radiated power is observed to increase with both current and arc length and Goldman (15) finds radiation to increase linearly with arc power. In the constricted argon plasma arc, radiation of up to 20% (74) of the total arc power have been reported. This is not unreasonable in view of the higher power appearing in the arc column of such an arc. Estimates by Nestor (75) put the radiated power entering the anode as at most 12% for argon and 3% for Helium. These values represent small fractions of the total arc power. Estimates of the arc power appearing as radiation have also been made by Quigley et al (65). They assume the arc to be a surface radiator and associate an emissive value (ε) with the arc surface where ε is such that $0.400 > \varepsilon$ (per cm) > 0.001. Radiation from very high current arcs (KA's) has received more attention than that from welding arcs. It is reported by Stracham and Barrault (68) to vary with current and arc length as $1.27\ I(1 + 0.32\ell).\ell$ (watts) where ℓ is the arc length of cm's.

For a 100A, 3mm TIG arc this gives 43W, or expressed as a percentage of the total power this is about 4% (or 18% of column power).

The spatial distribution of radiation from a welding arc has not yet been considered. However, Bennett and Harlan (76) have considered the spectral distribution of radiant energy over a limited range of wavelengths and investigated the dependence of this on elements in the base metal.

Literature reviewed in this section indicates that all three energy transfer mechanisms are likely to be of importance in welding arcs but much more information is required to gain a detailed understanding of this region.

2.4. Structure of the Anode Region

The anode region is taken in the present review as encompassing a small region of the arc just above the plate surface (~1μm) and that region of the plate affected by or effecting the arc. In the practical welding situation a very complicated interaction generally occurs between arc and weld pool components of the anode region defined above. This is largely associated with melting and vapourization processes. For this

reason many experimenters have sought an understanding of a simpler situation in which no bulk melting occurs. This usually corresponds to an experimental arrangement employing a water cooled anode. Many features of this situation are also to be found in the less well understood practical welding situation. It is instructive to discuss these situations separately.

2.4.1. Structure of the Anode Region when No Significant Melting Occurs

2.4.1.1. The Anode Sheath and Fall Voltage

The general form of the V-I characteristic previously reviewed suggests that a significant fraction of the arc voltage is dropped in a very short distance adjacent to the electrode surfaces. The component near the anode surface is known as the anode fall voltage (V_a) and the spacial distance over which this occurs is called the anode fall or anode sheath. The region to be associated with the anode fall has, however, caused some confusion in the literature. This point is returned to later. In this region the properties of the arc column must change to match the radically different characteristics of the anode surface. It is therefore expected that strong gradients (21) or physical properties exist in this region e.g. gradients in temperature and particle number densities. The positive nature of the anode surface attracts electrons and repells positive ions. A region of negative space charge is then established as very little ion generation (1) occurs in the sheath and no ions are emitted by the anode (except under special circumstances (77)). The structure of this region may then be examined with the aid of Poissons equation i.e.

$$\nabla \underline{E} = \rho/\varepsilon_o \qquad (21)$$

where ρ is used here to signify the charge density i.e. $\rho = (n_+ - n_-).e$ where n is the number density of positive (n+) or negative (n-) particles. A general description of this region using Poissons equation (and other relevant expressions) has been found difficult although estimates of the extent of the region have been obtained by assuming the existence of collisionless behaviour (21). In this situation Child-Langmuir type expressions are obtained i.e.

$$d \simeq \left(\frac{2\varepsilon_o}{q}\right)^{\frac{1}{2}} \cdot \left(\frac{8e}{m}\right)^{\frac{1}{2}} \cdot \frac{V_a^{\frac{3}{4}}}{J^{\frac{1}{2}}} \qquad (22)$$

Here d is the extent of the collisionless region, V_a is the voltage across the region, J is the current density and m is the electronic mass. The above expression is simplistic in the sense that it neglects the initial velocities (3) of particles at the column end of the sheath edge. Despite this it may be used to establish an order of magnitude for sheath dimensions. Using suitable values of V_a and J, d is estimated as several μm's (67). This is similar in magnitude to the electron mean free path and therefore the collisionless assumption would appear justifiable. Another estimate (28) of the sheath extent may be obtained by supposing particles to obey Boltzmann type distributions in the sheath. This approach is the opposite of that above, and yields a value given by the Debye length (λ_D) (see equation 2). λ_D is also found to be of order μm's (21,28). These values indicate anode fall electric field strengths of about 10^6 V/M which are 10^3 times greater than in the column. For the purpose of establishing the above order of magnitude estimates, the anode fall voltage was taken as a few volts. This estimate is not close enough for considerations involving energy transfer to the anode (a point returned to later in this section after a more general review of V_a). In establishing the Child-Langmuir expression the existence of V_a was assumed and attributed to a charge imbalance. However, Finklenburg and Maecker (1) attribute the existence of V_a principally to ion generation that must occur in the anode fall to maintain current continuity. These ions must also be accelerated so as to attain the arc column temperature by the time they reach the sheath edge (1). Anodic vapourization is likely (1) to influence V_a (by reducing V_a) through the supply of low ionization potential material. It is noted that under such conditions the Child-Langmuir expression predicts an increase in V_a as current density also increases. The mechanism given by Finklenburg and Maecker would tend to indicate decreasing values for V_a as the arc current increases and cathodic jet action increases i.e. strong plasma jets would tend to prohibit the loss of ions from this region and high currents encourage vapourization. Indeed in the limit, when cathodic jet convection is strong enough to prohibit the migration of ions from the sheath no anode fall should be required (1,65,70,78). By the same token the anode fall voltage should increase as the arc contracts at the anode and strong anode jets are generated. The above considerations indicate that V_a is generally dependent on anode composition and temperature and

flow fields immediately in front of the anode.

The existence of a more or less free fall region for electrons adjacent to the anode gives rise to a significant increase in the effective temperature of electrons whereas heavy particles experience a decrease in temperature (21). Conditions are therefore such that a two temperature plasma model is required to describe this region as LTE no longer even approximately describes the behaviour. The implications of this have not been seriously considered in the literature as all heat transfer studies have assumed single temperature gas properties. Recently Kannapan and Bose (35) have obtained the two temperature (T_- and T_+) dependence of thermal conductivity, electrical conductivity and viscosity for argon plasma's. These results differ significantly from single temperature plasma properties. For example, the single temperature coefficient of thermal conductivity may be in error by two orders of magnitude near the anode.

Physical behaviour at the anode is strongly influenced by the anode fall voltage, current density and characteristics of gas flow in this region. These factors have been investigated experimentally by many workers. An upper limit estimate of V_a is readily obtained from the sum of the fall voltages ($U_o \simeq 8V$ for argon and 10V for helium). The contribution V_a makes to U_o has been investigated primarily by electrostatic probe (1,78) and calorimetric techniques (79,16,67,75,80). Probe measurements (78) for argon arcs on copper anodes indicate that V_a falls as the arc length decreases and current increases. Similar trends have been obtained in calorimetric studies (67,16,80) where V_a is obtained from energy balance considerations. Both methods involve significant uncertainties. In probe estimates a contact potential between probe and plasma must be allowed for Busz-Peuckert and Finkelnburg (78) estimate that uncertainties of order $\pm 2V$ may be involved in this estimate. In calorimetric studies all other contributions to anode heating are required. This introduces uncertainties associated with temperature and flow conditions in the vicinity of the anode. In some early estimates (16,79) the existence of plasma jets and thereby convective heating was not known and hence not accounted for. Also considerable uncertainty seems to have surrounded the choice of work function

adopted e.g. for copper Schoek (67) adopted a value of 3.6eV. This is nearly leV lower than values presently used and results in anode fall measurements being about 1V higher than they would otherwise be. Comparisons between results obtained by these techniques are not strictly allowed as, it seems that these voltage measurements do not refer to the same physical quantity. Calorimetric results refer to the real 'anode fall' voltage as represented by the energy gain of an electron in this region. Probe techniques ofter refer to a voltage measured some distance from the outer anode surface i.e. Busz-Peuckert and Finkelnburg (78) refer to the anode fall voltage obtained by determining the potential about 1mm ahead of the anode with a probe of 0.3mm diameter. Such a measurement therefore includes a contribution from the contraction region as well as the real 'anode fall'. Probe measurements should therefore be regarded as giving upper limits to V_a. This has been acknowledged by the authors (Busz-Peuckert and Finkelnburg) and discussed by Ecker (81). Direct comparisons between such results have, however, been made by Milner et al. (80) and Schoeck (67). A further technique for estimating V_a is to obtain the voltage distribution within an arc from temperature measurements (i.e. the electrical conductivity is integrated radially). This approach has been used by Olsen (7). However, considerable uncertainties must exist in temperatures measured very close to the anode. Despite these uncertainties Busz-Peuckert and Finkelnburg have found V_a to fall with increasing temperature, becoming nearly zero at 20,000K for argon. These workers (78) also note that up to a 2V change in V_a may be obtained for argon arcs on water cooled copper anodes by simply changing the flow rate of coolant through the anode. This observation is important as most experiments do not quote the coolant flow rate. Such behaviour is readily understood in terms of anodic vapourization. Anode fall values have been used by a great many workers in estimating heat input to the anode. It seems generally accepted that V_a is probably about $2(\pm 1)$V for a nominal argon TIG welding arc and about 3-4V for the corresponding helium arc. V_a is used so frequently in the literature that an exhaustive survey of values adopted by various workers for TIG type arcs is inappropriate. A sample of values is shown in table 1.

Date (Year)	Author	Ref. (No.)	Arc Type	Gas Comp.	Anode Comp.	Va (Volts)	Comments
1954	Busz-Peuckert	(78)	TIG	Ar	Cu	7 ± 2	Probe method sensitive to arc length
1954	Lancaster	(16)	TIG	Ar	Cu	2 - 3	Calorimetric (30-100A)
1955	Apps & Milner	(79)	TIG	Ar	Fe	1.8	Calorimetric
1959	Wilkinson & Milner	(8)	TIG	Ar	Cu	1.5 - 3	Calorimetric
1974	Quigley et al	(65)	TIG	Ar	Fe	2	
1974	Metcalf & Quigley	(70)	Plasma	Ar	Fe	0 - 2	
1979	Glickstein	(17)	TIG	Ar	Fe	3	
				He	Fe	4.5	
1979	Mills	(166)	TIG	Ar	Fe	2.1 - 2.4	
			TIG	He/(25% Ar)	Fe	2.7 - 3.0	
1982	Wasink	(167)	MIG	Ar	Fe	0	Heat balance calculations

Table 1 Survey of Anode Fall Data Used (or experimentally obtained) in the Literature

2.4.1.2. Anode Current Density

The distribution of current at the anode is important as this plays a large role in determining the distribution of electronic heating at the surface. This has been investigated on a number of occasions (75,67,82) using a split water cooled copper anode arrangement consisting essentially of two electrically isolated segments separated by a small gap. The distribution of current can be obtained by monitoring the current to each anode segment as the arc is moved from one segment to the other. Radial distributions of current are found by Abel transforming (61) the experimental data. This transformation essentially changes a line geometry to a circular geometry under the assumption of radial symmetry. Errors in boundary location may lead to significant errors (83) in axial J values. This has been overcome (83) by the use of a technique that amplifies the current signal near the arc boundary and so allows a more accurate location of this boundary. Less elaborate techniques are available (83) for obtaining the axial current density if it is known that the distribution is of a Gaussian form. A number of Russian researchers (83,84) have found this is to be the case for argon arcs. However, the nitrogen arc considered by Guile et al (82) exhibits an axial plateau in current density and a very steep fall to the boundary (top hat type distribution). Experiments (67,75,83,84,72) on argon arcs indicate characteristic axial values of current density at the anode of order 10-30 A/mm^2. Values of up to 580 A/mm^2 (82) have been found with nitrogen arcs on high speed (8m/s) rotating anodes. No explanation has yet been offered for this difference in behaviour. However, nitrogen arcs (unlike argon arcs) have dissociation cores (8) and appear narrower in cross-ection (80). Higher column current densities are then expected in N_2 than A_r. The significantly higher values found for nitrogen arcs may be due in part to the experimental technique used since high anodic speeds may produce a constricted anode root (9). Observations on high speed anodes concern a single anode root whereas the slow moving anode records only time averaged behaviour over a far larger number of root site life times. This could also explain the difference in current densities. Measurements on melting anodes (84) have recently been made by inserting insulating mica sheets in the pool path. Results indicate current densities larger by a factor of two than those obtained on copper anodes for an equivalent arrangement.

This is attributed to the influence of vapourization. Current density has been measured (67) using a small point probe situated in, and isolated from, a plain anode. Good agreement with the split anode technique is reported. Mechev et al (85) find a point probe to be an unstable current collector. Nestor (75) has investigated the distribution of current at the anode of argon and helium arcs. The anode spot behaviour is less pronounced than in nitrogen. Nevertheless, Nestor finds current distributions that are slightly more peaky than given by the Gaussian distribution.

Experiments (86) have shown that current density is dependent on cathodic conditions were the axial value falls with increasing electrode vertex angle. The distribution also appears more parabolic (86) than Gaussian at large vertex angles. In many experiments a 'flat' is given to the pointed electrode. The diameter of such a flat (86) has a marked effect on current density for flat diameters below 1mm although no influence on 'flat diameter' is noticed between 1 and 1.5mm. No experiments appear to have been performed to examine the influence of electrode diameter. Changes in electrode geometry during arcing may also result in a decrease in axial current density. This makes it inherently difficult to specify current densities accurately.

Current density has been observed to fall with increasing arc length (83) and Gvozdetskii (83) also reports that J falls with increasing current. Nestor (75), however, finds current density to initially increase with current before becoming independent and falling at higher currents (near 150A).

2.4.1.3. Arc Force, Gas Flow and the Distribution of Pressure at the Anode

Flow conditions strongly influence the arrival of heat at the anode and of transfer to the surface. The force associated with the flow (and the distribution of this force (i.e. pressure)) may influence behaviour in the pool and consequently weld properties. In particular, high arc pressures may lead to a significant depression of the pool surface. This may further act to modify heat transfer and flow patterns within the pool. Liquid metal motion may be flow dependent even when a

depression is not formed i.e. as a result of shear stress exerted by the flow at the free surface. Flow may also modify the distribution of electrical power by changing the power balance (i.e. V_a, J and E). A further effect of flow is to influence arc composition through the entrainment of atmospheric contaminants.

Flow conditions at the anode have been investigated primarily by observing the distribution of pressure on water cooled copper anodes or the total reaction force at the anode (not necessarily cooled). These experimental techniques give only limited information about the influence of flow on the weld pool. This further emphasises the need for a model describing flow conditions in the arc and relating these to conditions at the arc boundaries. The most commonly employed method (67,86,80,87,58) is to connect a small hole in the anode to a manometer. This registers pressure when an arc is passed over the hole. Such a technique relies on measuring a number of discrete pressure points in order to obtain the distribution. A number of Russian papers (58,89,90) have reported continuously recorded distributions obtained with transducer type devices. These methods have been used to examine the influence of arc and electrode characteristics on the form taken by the pressure distribution, axial values and radial extents, and the total force exerted on the anode (found by integrating pressure distributions). Before reviewing these findings it is appropriate to consider in more detail the nature of these measurements. The measured value is of course an average over the area of the hole or slit. Errors associated with this are expected to be small for hole diameters of less than 1mm e.g. for a distribution width of 3mm a mean error of 5% is associated with a hole diameter of 1.3mm. The system used by Schoeck (67) employed a hole of 0.5mm diameter and measured distribution widths of order 5mm. Averaging errors are therefore expected to be negligible in this situation. A more important error is associated with the response time (due to inertial effects) of the manometer system. This is dependent on arc speed over the hole and manometer geometry. Very few papers actually give these details although a number discuss the limitations of this technique (86,87,89,90). The pressure measured by this method has two components, a static pressure

associated with a local increase in ambient pressure and a dynamic pressure (often called gaskinetic pressure) associated with the flow. On the axis of an arc this becomes the stagnation pressure. It is not necessary to know the static pressure component if the quantity of interest is the total force. The influence of this term should, however, be considered if the stagnation pressure is to be used to calculate flow velocity. Schoeck (67), using Maeckers theory, estimates this term to be about 3% of the measured stagnation pressure for a 100 Amp, 6mm arc. Values substantially larger than 3% are expected for shorter arcs with Gaussian type current distributions and vapour pressure components.

If the total force is measured directly by a balance type technique (91,92) then $\underline{J} \wedge \underline{B}$ generated motion produced in the liquid pool will also contribute to the momentum balance. When comparing values obtained by these two methods this interaction must be taken into account, a point discussed at some length by Erokhin (87).

The major variable affecting measured stagnation pressures and the total arc froce (F) is arc current. It is generally found (87,88,91), that the force varies quadratically with current ($F \alpha I^2$) although linear behaviour ($F \alpha I$) has also been reported (92). The proportionality factor is found to be a function of arc length, gas composition, electrode geometry and electrode polarity. Erokhin (87) gives an account of early work by Creedy reporting F to fall with the square root of arc length ($F \alpha 1/\sqrt{\ell}$, this was found for short arcs, $\lesssim$3mm, running for short times - less than one second). More recent experiments (91) report a weaker dependence on arc length. Savage et al (92) report a 40% fall in F over the length range 1 to 9mm for 300A argon and helium arcs. Much smaller decreases (less than 15%) have been reported by Russo et al (91) for similar arcing conditions. It is generally found that the effects of arc length becomes less important with increasing arc current (see Erokhin (87)). However, further systematic experimentation would appear necessary to obtain a deeper understanding of this behaviour as only isolated accounts exist.

Russo et al (91) have investigated the effect of electrode vertex angle and flat geometry on F. They find F to decrease slightly with

increasing vertex angle and flat diameter. Systematic measurements on the effect of electrode diameter have yet to be reported, although in a recent review of the literature Erokhin (87) suggested that F should decrease as the electrode diameter increased. However, this deduction is based on a comparison of an early measurement using a 2mm electrode with contemporary measurements using a 5mm electrode.

A number of workers (91,92) have reported that no significant differences exists between values of F obtained in helium and argon. However, it has been reported by Kotov et al (88) that higher values are obtained in helium. This result must be treated with some reservation as large scatter is exhibited in results presented by these workers.

The form of the anodic pressure distribution has been found to be of a Gaussian type by most workers using manometric techniques (see 87). However, bilateral exponential distributions have been reported (89) using transducer type techniques where pressure is continuously monitored. This type of distribution exhibits a discontinuity in gradient at the axis and is therefore thought to be unlikely. The maximum pressure has been observed (67) to increase with current and decreasing arc length. This last finding is not always reported. Reports also exist (58) of the maximum pressure increasing at short arc lengths and subsequently decreasing with further increases in arc length. It is also found that the maximum pressure is greater in electrode negative polarity than in electrode positive and has intermediate values in AC welding (88). This behaviour is observed for both helium and argon arcs. Electrode geometry (86) influences maximum pressure which is observed to increase with decreasing vertex angle. It is known that electrode geometry deteriorates (58) during the welding cycle that such a deterioration results in a fall in the maximum pressure. As in current density measurements, such behaviour is a limiting factor for experimental accuracy and reproducibility. Again no direct information is available on the influence of electrode diameter.

A number of workers (58,67,80) have used stagnation pressure (P_o) measurements of the type discussed above to obtain values for the free

stream axial velocity (V_∞) outside the flow boundary layer at the anode. Using Bernoullis equation they then find

$$V_\infty = \left(\frac{2P_o}{\rho}\right)^{\frac{1}{2}} \qquad (23)$$

where ρ is the gas density near the anode.

This expression assumes the static contribution to be negligible. It is interesting to note that such an expression predicts much higher velocities for helium arcs than argon arcs. This contrasts the ball shaped nature of helium arcs which suggests that only weak plasma streaming occurs. In such a situation, where a highly constricted anode spot is often observed, the static pressure may play a significant role. The omission of a correction to P_o may then lead to significant errors.

Schoeck (67) has gone one step further and deduced that the flow velocity a distance S from the axis and at the outer edge of the boundary layer of the flow along the anode surface is

$$V_S = V_\infty \sqrt{1 - \frac{P}{P_o}} \qquad (24)$$

where P is the pressure measured at S. It is then found that V_S increases linearly with distance near the stagnation point. This approach has been used to obtain data for the heat transfer coefficient across the anode surface. However, as Helmoy (93) has pointed out, the action of viscosity must be considered if the realistic situation is to be approached.

2.4.1.4. Heat Transfer to the Anode

Factors discussed above influence the total and distribution of heat entering the anode. Essentially there are two components; electronic heating-related to the flow of electrons into the anode and Gas heating associated with heat transferred from the hot neutral gas including arc column radiation. Other components must in general be added to account for heat losses from the anode i.e. radiation or vapourization. The last terms are negligible for strongly cooled surfaces. Electronic heating is the result of thermal energy gained by electrons in the

column, energy gained by acceleration in the field of the anode fall and electronic potential energy of condensation (see below). The last term is the potential energy an electron gives up on entering the Fermi Surface of a conductor. These terms, in reverse order, may be written respectively as

$$Q_e = I(\phi + \beta V_a + V_T) \tag{25}$$

where Q_e is the total electronic heating, ϕ - the anode work function V_a - the anode fall voltage and V_T an equivalent voltage contribution due to electronic thermal energy. β is a factor accounting for energy lost by electrons due to collisions in the sheath. For steel and copper $\phi \simeq$ (4.3- 4.5) eV. The factor β is generally taken as unity i.e. no energy transfer to metal particles in the sheath. Quigley et al (65) have considered the energy lose by an electron during an electron - heavy particle collision. They find this to be $2 M_-/M_+$ where M_- is the electron mass and M_+ the heavy particle mass. This indicates that a great many collisions are required to change β significantly from unity. Mean free path - sheath thickness considerations reported here indicate that at most only a few collisions occur. It has also been pointed out by Schoeck (67) that even when collisions become significant some of the energy lost by electrons to heavy particles is transferred to the anode by the heavy particles. Considerable confusion seems to exist in the literature concerning the expression for V_T. Many papers (e.g. 65, 80) take this as

$$V_T = \frac{3kT}{2e} \tag{26}$$

where k is Boltzmann's constant and T is the difference between the electronic temperature in the arc and in the anode. This expression is based on the equipartion law for a monotonic gas. However, a rigorous statistical mechanics approach (94) shows that the factor of 3 should be replaced by a factor of 5 i.e.

$$V_T = \frac{5kT}{2e} \tag{27}$$

The magnitude of V_T depends very much on conditions existing near the anode i.e. vapourization, and arc temperature and this is discussed more thoroughly in latter sections. For the present purposes it is

sufficient to take V_T as about 1eV for argon arcs and 2eV for helium. Remembering that V_a for these gases has values of 2eV and 4eV respectively gives Q_e/I ~ 7.5eV for argon and 10.5eV for helium. In both cases it would appear that the work function effect dominates although this is only a marginal effect in helium.

The distribution of this heating is given by replacing I with J, the current density. Comments previously made about J can therefore be applied to this situation. Thus the distribution of electronic anodic heating is influenced, for example, by electrode vertex angle. The total heat entering the anode (Q) is the sum of Q_e and a gas component Q_g. Attempts have been made to separate these components by measuring the distribution of Q and the distribution of Q_e i.e. the distribution of Q_g then follows. The earliest attempt was by Milner et al (80) who used an arrangement consisting of three electrically isolated and separately cooled anode segments of annular geometry. They concluded that less than a quarter of the anode energy comes from the gas component. The radial distribution has subsequently been measured by Nestor (75). Nestor moved an arc slowly from one anode segment to the other using a split plate anode arrangement. The current and coolant temperatures to each block were continuously monitored. Such a technique relies on the relative movement of arc and anode being slow enough to ensure thermal equilibrium conditions to exist. Nestor found a speed of 0.01mm/s to be sufficient. Schoeck (67) has used a technique that increments discretely the position of the arc relative to the splitting plane. The reported reliability of data obtained by these techniques is surprising due to a number of factors. Firstly, to obtain a profile Nestor continuously ran an arc for 20 minutes. Other research (58) indicates that electrode degradation during this time introduces significant changes in arc properties. Further doubts concern thermal leaks between the blocks over such extended time periods and the amenability of resulting distributions to Abel transformation as the thermal boundary is ill defined (75). This may introduce significant errors (83) into axial heat flux results. It is generally found (67,75) that the distribution of heat is wider than that of current and that this increases with increasing arc current. Results obtained by Schoeck (67) indicate that the intensity of gas heating changes very slowly with the

radial co-ordinate being substantially flat over the central region of the arc. This increases with current from about 7 W/mm^2 at 50A (5mm argon arc) to about 13 W/mm^2 at 150A. Results given by Nestor (75) suggest a far more peaked distribution of arc heating with a value of about 10-20 W/mm^2 at 100A and 6.3mm arc length. Nestors results also show that the intensity of heating is much lower for the NM arc than the CSM arc. A number of theoretical investigations (80,65,67,70,94, 95,96) have been concerned with gas heating at the anode of a welding arc. These have relied heavily on the use of dimensionless numbers to characterise heat transfer. This technique has previously been widely used to investigating non-current carrying flows. However, a degree of uncertainty is associated with the identification of comparable flow characteristics in current carrying situations. It is customary in low temperature situations where no diffusion or chemical activity occurs, to describe heat transfer to a surface by

$$Q = \int_{\text{surface}} K.\left(\frac{dT}{dx}\right|_{x=0} \cdot \quad dS \qquad (28)$$

where dS is an elemental area of the surface and $\left(\frac{dT}{dx}\right|_{x=0}$ is the temperature gradient normal to the surface and at the surface (i.e.x=0). This integral may be expressed in terms of non-dimensional parameters (97) describing the flow field, temperature field and gas properties. Convection is accounted for through the effects of flow on the temperature gradient. It can then be seen that convective transfer essentially employs a conductive mechanism at the surface. However, Quigley et al (65) have supposed that both conduction and convection occur. Indeed, they find that conductive transfer is twice that from convection. On the basis of classical transfer theory it would appear that these workers have doubly counted the effect of conduction at the surface. Further uncertainties exist in the estimates made by these workers. The surface temperature gradient employed for estimating conductive transfer was obtained from Gick et al (28) who used an electrostatic probe technique to find temperature profiles. It is known that the chilling effect of a probe on the arc produces low temperature measurements. Also realistic temperatures near the anode cannot be found using this technique due to the limits within which a probe can

physically approach the anode and the presence of metal vapour in this region. This point has been dealt with by the authors (98) in a subsequent paper modifying the distribution reported in 1973. An estimate of Q also requires a knowledge of K and the area over which significant transfer occurs. Quigley et al assume this diameter to be about 3mm for a 100 Amp arc. Experimental work by Nestor (75) and Schoeck (67) indicates that a value of nearer 10mm is appropriate. The coefficient of thermal conductivity has components associated with electron, ion and neutral constituents. It is not clear from the literature whether the total conductivity should be used in estimating neutral heat transfer from the above expression for Q, or whether the electronic and ionic components should be subtracted and included in a separate term. The above comments indicate that close estimates of convective heat transfer based on the above approach are difficult to make.

Q_{cv} has often been expressed as (70,67,21,80)

$$Q_{cv} = K.Nu.A.\frac{\Delta h}{Cp.L} \qquad (29)$$

where L is a characteristic flow length, A area of heat transfer, Δh enthalpy difference between the free stream and anode plate temperatures. Nu, the Nusselt number. Nu is related to gas and flow properties by

$$Nu = B.Re^{1/2}.Pr^{1/3} \qquad (30)$$

B is an empirical constant having a value of about 0.7. Actual values used have been 0.8 (90), 0.76 (21), 0.7 (67), 0.8 $\pm$40% (65) and 0.76 (70). R_e is the Reynolds number of the flow and P_r the Prandtl number. This expression has been applied to both TIG and plasma welding situations. It is important to note that heat transfer in welding arcs is not driven purely by temperature gradients as implied by the above expression for Q_{cv}. Electric field and diffusion gradients must also be accounted for. No rigorous investigation of these effects in welding arcs appears to have been made although such effects have been considered (96,95,21) for other arcing arrangements. It is normally implicitly assumed that such phenomena are accounted for by evaluating

parameters in Q_{cv} at a mean enthalpy temperature (T*) given by

$$h(T^*) = \frac{h(T_\infty) + h(T_o)}{2}$$

where T_∞ and T_o are temperatures at the free stream - boundary layer interface and anode surface respectively. Analysis based on the above expressions indicates that between 15-28% of the heat received by the anode in TIG welding (67) comes from the gas heating. In plasma welding (70) figures of over 60% have been found. Within the above frame work for evaluating Q_{cv} three further uncertainties exist. These concern the identification of A and L; the evaluation of gas properties; and the flow field. Milner et al (80) associate A with the area of a circle the radius of which is the arc 'diameter' at the anode. Metcalfe and Quigley (70) use the 'arc radius' to identify A. The terms 'arc radius' and 'diameter' are difficult to know apriori - particularly as the heat affected arc zone diameter is likely to be significantly different from the current carrying diameter. Also recent research has shown that K is strongly influenced by whether or not LTE exists. In the absence of LTE, K may be increased by two orders of magnitude. This may then result in at least an order of magnitude error in Q. Even if this considerable uncertainty is put to one side the local composition is a matter of some speculation. The last uncertainty listed above is concerned with the flow velocity which is usually estimated from Maeckers inviscid theory. In view of this situation emphasis should be directed at experimental measurements of Q_{cv}.

Radiative contributions to anode heating have been estimated by a number of workers (67,65,15,75) by considering the total radiation from the column. These estimates are generally below 5% (for TIG arcs) and dependent on surface conditions. For highly reflective surfaces (i.e. a weld pool or shiney metal surface) most of the incident energy is reflected. More energy is absorbed if the surface is oxidised or blackened by for instance condensing metal vapour. In plasma welding radiative transfer may be significant (70), particularly in cases where a keyhole is formed. It is worth noting that the radiative contribution is not necessarily of a positive nature. In the case of a large weld pool more energy may be emitted than is absorbed.

Energy can be lost from the pool by vapourization. Quigley et al (65) have shown that this term has an almost exponential dependence on the central pool temperature. For a central pool temperature of 2,500K and a pool radius of 2mm it is found that 33W is lost by evaporation. However, this figure doubles for every 100K rise in temperature. Quigleys calculation was performed for iron. In a realistic welding situation with a steel workpiece elements with lower vapourization temperatures may significantly modify this behaviour.

Information given above shows that most of the anode energy comes from the electronic contribution in TIG welding and that the gas contribution is difficult to account for. In plasma welding where more energy appears in the column, gas heating is the dominant term. For many welding applications it is important to know the percentage of process power entering the anode (process efficiency). This can of course be found from a knowledge of the components discussed above and the total arc power. Many experiments have for this reason been concerned with measuring the total power input to the anode. Before reporting these experimental results it is noted that electronic heating accounts for about 750W for a short 100 Amp argon TIG arc.. A typical voltage for such an arc is 10-11 volts indicating that 70-75% of the process power reaches the anode on the basis of electronic heating alone. This figure must represent a minimum process efficiency and reflects the fact that very little (in this case ~250W or 25%) of the process power appears in the column of a TIG arc.

Many experiments (41,15,75,79,80,99,100,101) have been performed to determine process efficiency. These are mainly concerned with water cooled copper anode measurements although a few experiments have also considered situations with stationary (100) (conduction limited) and moving weld pools (79,99). Dry calorimetric methods have also received attention (100). This last technique uses the transient response of a thermocouple situated well away from the weld region. In most experiments very few details of the calorimetric arrangements are given. This is significant as it has been found (78) that the coolant flow rate can affect the anode fall voltage and therefore the total heat flow to the anode. In general efficiencies of 75 to 85% are obtained although

values as high as 95% (80) and as low as 60% (99) have been reported. High values (>90%) are usually associated with low arc powers, i.e. very little power then appears in the column. These indicate that the cathode receives very little nett power. This has been confirmed experimentally (16,80) and is associated with transpiration cooling by electrons leaving the cathode. This energy is then deposited at the anode by virtue of the work function effect.

It is generally found that anode power increases in a similar manner to arc voltage so that efficiency is substantially independent of process power, decreasing only slightly with arc current (15,80,100). This behaviour has been reported for a wide range of experimental situations including high speed rotating anodes (101).

Experiments recently reported by Ghent et al (99) indicate the arc efficiency to have a stronger power dependence than given above varying from 85% at 1KW to 60% at 3KW. These results were obtained on a water cooled anode with a moving weld pool. However, this appears to be an isolated result and may stem from the experimental arrangement employed. These authors placed a conical heat receptor around the arc to monitor radiation and heat swept away by the effluent gas. This could lead to a possible source of arc disturbance. Further, with a moving heat source at the anode, steady state heat transfer may not be attained. In contrast to this result, experiments (100) investigating the weld bead situation using dry calorimetric techniques have observed only small deviations from the water cooled copper anode situation.

The weak dependence of arc efficiency on arc power suggests that the anode power increases in proportion to arc current and length. This is indeed found to be the case (15,16,80). Such a result further suggests that gas heating is more or less directly proportional to arc current although the arc length dependence cannot be as readily deduced without assuming the anode fall to be independent of arc length. Experiments (16) indicate anode heating to be linearly dependent on arc length for short are lengths (<3mm) where only small changes in V_a are likely to occur. An explanation of this behaviour requires a deeper understanding of gas heating mechanisms. The only general theoretical treatments of arc

efficiencies are by Quigley et al (65) TIG arcs and Metcalfe and Quigley (70) for plasma arcs. Quigley et al consider a 8mm, 100 Amp, argon TIG arc and obtain an efficiency of 45% ($\pm$10%). This figure is significantly lower than experimental values. This is thought to be due to an over estimate of arc voltage (16V was used and this would imply E $\simeq$ 1V/mm) and low estimates of convective heating and the anode fall voltage for such an arc. The arc length employed is also rather impractical and would suggest efficiencies below those normally encountered in welding.

2.4.2. Structure of the Anode when Melting Occurs

In section 2.4.1. the structure of the anode region was considered under the condition that no bulk melting occurred. It is of course the nature of a welding situation that melting does occur. The literature reviewed in 2.4.1. indicates that the existence of a weld pool affects arc characteristics near the anode primarily through the existence of metal vapour. In this section emphasis is placed on how arc heating and other anodic effects influence melting behaviour. Weld pool behaviour is determined by arc characteristics, weld metal composition and 'other factors'. 'Other factors' must be taken to include plate geometry (in particular plate thickness), power source characteristics (especially dynamic response) and earthing arrangements. However, it is by no means clear at present that all other variables have been identified.

A great deal of effort has been directed over the years at describing weld bead geometry in terms of heat input to the weldment. For this reason importance has been placed on determining the process efficiency. Melting is usually assumed to occur by means of conductive heat transfer within the pool. Results obtained by this approach have been successful in describing many of the qualitative aspects of weld structure, particularly on thin plate (102). This model is highly amenable to mathematical techniques and may be described by the heat conduction equation. Wells (103) has shown that general solutions obtained by Rosenthal (104) (see also Carslaw ans Jaeger (105)) can be simplified

and used to relate weld bead geometry to heat input. For an infinitely thick plate he finds that:-

$$q = \pi d K T_m \left(1 + \frac{\nu . d}{5\alpha}\right) \qquad (31)$$

where q is the heat input as given by $\eta.IV$ where η is the process efficiency, ν the welding speed and d the weld width. K, α and T_m are material properties of the plate representing thermal conductivity, diffusivity and melting temperature respectively. This expression may also be applied to other isotherms where d then becomes the new isothermal width. The above expression takes no account of Latent heat effects or the temperature dependence of material properties. Further, the arc is regarded as a point source and no fluid motion within the pool is allowed for. The only arc feature is then associated with the total heat q entering the anode, i.e. the structure of the heat source has no effect on weld geometry. This theory predicts (102) weld shape to be of 'tear drop' geometry with circular cross section. The effect of Latent heat absorption at the front face of a weld pool and liberation at the rear is known to accentuate this prediction (79). However, a precise mathematical formulation has yet to be given. The structureless heat source assumed above is known to be at odds with experience as finger type penetration is often experienced in arc welding. Despite these problems the isothermal structure of the weldment outside the pool is reasonably well described by this theory (104).

Departures from purely conductive heat transfer models are expected because weld pool motion does occur (49). This may contribute to the melting process by directly transporting heat from the arc interface to the fusion boundary. Motion in the pool may be generated by a number of mechanisms i.e. interaction of current passing through the pool with the associated self magnetic field (46,43,49), by surface tension gradients (106) and by arc force at the pool surface (107). Such interactions are very complex and have only been considered for idealised experimental or theoretical arrangements.

The origin of motions generated by the 'current - self magnetic field' force is similar to that occurring in the arc column. i.e. for diverging three dimensional current fields there will exist a component of the

$\underline{J} \wedge \underline{B}$ force that cannot everywhere be balanced by a pressure field and hence motion may occur (48). A number of mathematical treatments (e.g. 43,49,46) have been concerned with idealised forms of this situation. Shercliff (43) first considered (1970) motion generated in a semi-infinite inviscid fluid by a stationary current source entering through a point on the surface. He found that a fluid jet was generated away from the point of current entry and that mass entered the jet near the origin by flow tangential to the surface. For a closed system this would give rise to circulation. Such motion may be time dependent so that a fluid element is continuously accelerated until steady state is achieved or flow break down occurs. It has been conjectured that such an instability (43) may even be responsible for drop detachment in MIG welding. However, it is noted that in consumable arc welding such time scales must be compared with 10^{-2} secs at the wire tip where drop detachment occurs. At the pool the time scale is given by the time between melting and solidification i.e. 1 sec. Shercliff did not consider the time development of flow. The only time dependent analysis is by Sozou and Pickering (48) who find flow time scales to be dominated by the parameter λ identified below

$$\lambda = (\nu t)^{\frac{1}{2}}/r \qquad (32)$$

where ν is the diffusivity, t time and r a characteristic distance. Steady state flow is practically established when $\lambda \approx 0.2$. This value has been found by computer simulations of numerical solutions. For liquid steel flows $\nu \sim 1.3 \times 10^{-7}$ m^2/s. Using characteristic distances of 1mm for a wire tip and 5mm for a pool (with $\lambda \sim 0.2$) gives time scales of 0.3 s and 6 s respectively. Comparing these figures with those given above indicates that steady state conditions probably aren't reached in welding applications.

Equations obtained by Shercliff and Sozou exhibit singularities on the flow axis. Sozou (44) supposes the singularity in Shercliff's inviscid solution to result from neglecting viscosity. He finds that when viscosity is included, singularities are eliminated below a critical Reynolds number. More recently Andrews and Craine (13) and Atthey (49) have performed calculations for distributed current sources. They attribute singularities previously found to the assumption of a point

source of current. Andrews and Craine, and Atthey, have examined the effect of current (source) and departure (sink) positions from a hemispherical pool and find that the relative position of source to sink can change flow in a conduction limited pool from consisting of a single toroidal flow to a double toroidal flow. This indicates that pool structure may be dependent on earthing position. Work on weld pool motion is still at an early stage and has yet to be linked to energy considerations i.e. to compute pool shape and the relative parts played by conduction and convection. However, the possible none steady state nature of the flow posses quite formidable problems.

General considerations on weld bead formation must also take into account the roles of turbulence (108), buoyancy (109), surface tension and other surface forces (109). The limited experimental information available indicates that all of these factors may play a role.

A number of workers (109,110,111) have examined the influence of external magnetic fields on weld bead geometry. It has been found that more consistent (109) weld shapes can be achieved by the application of such a field. However, penetration (109) is reduced and it may be inferred from such work that the melting efficiency is generally lower than that obtained in the absence of externally applied magnetic stirring. The frequency of the imposed field is found (109,110) to have a profound effect on bead structure. This indicates that an interaction is occurring between imposed motions and indigenous motions.

Work has also indicated that surface tensional gradients (112) may produce motion in liquids. Workers (107) have examined the cooling behaviour of liquid wax and found similarities between solidification shapes obtained and those found in welding. Indigenous motions were investigated by Woods and Milner (113) who examined motion in a mercury bath, due to current entering at the surface. Further modelling has been performed by Russian workers (114) who considered motions in an electrolyte (NaCl solution). The fact that such modelling experiments have been performed reflects the magnitude of problems involved in investigating real weld pool situations where the most direct experimental information presently available is concerned with e.m. stirring studies. Indirect information

on the extent to which the above factors influence bead formation may be obtained by comparing experimental results with the predictions of conduction theory.

Many investigators (e.g. 79,115) have considered the influence of arc parameters on weld bead geometry. Geometry is found to be strongly dependent on heat input where arc current and gas composition are the most important variables. Welds formed in helium are deeper and of larger cross-sectional area than corresponding welds in argon. Increased penetration may also be achieved with small hydrogen additions (109). This behaviour is often interpreted in terms of higher heat inputs for such gas mixes. It has been found useful (116) to examine some of these effects using the concept of melting efficiency ($Z_\cdot$) where $Z_\cdot$ is defined by

$$Z_\cdot = \frac{\rho \langle CT+L \rangle \nu A}{I.V} \times 100\% \qquad (33)$$

ρ is the base metal density, $\langle CT + L \rangle$ is the heat required to just melt one gram of base metal, ν is travel speed and A is the cross-sectional area of the weld. The behaviour of $Z_\cdot$ may be predicted from conduction theory by manipulating equation (31) to give A. The result is readily shown to be

$$Z\ (\%) = \eta\, G. \left[\frac{1 + \theta - \sqrt{1 + 2\theta}}{\theta} \right] \qquad (34)$$

$$G = \frac{5^3}{2} \cdot \frac{\langle CT_m + L \rangle}{\langle CT_m \rangle}, \quad \theta = \frac{2\nu.I.V.\eta}{5\pi.\alpha.K.T_m}, \quad \alpha = \frac{K}{\rho C}$$

This expression predicts that melting efficiency increases with travel speed, heat input and process efficiency. The maximum value of Z can be seen to be ηG or about 60% for $\eta \simeq 80\%$. However, in most practical welding situations Z is between 5 - 30% being larger in helium than in argon. It is also interesting to note that Z decreases as the thermal conductivity increases (i.e. Z decreases as θ decreases).

Conductive theory predicts weld aspect ratios, width (W)/depth (D), of 2 on thick plate. In practice this is observed to depend on factors associated with heat source structure e.g. arc length, electrode vertex angle

(19, 117, 118) and the influence of vapourization on the anode root. This last effect has recently received much attention due to the variability of weld geometries obtained under apparently identical conditions. Metcalfe and Quigley (11) investigated the possibility of variability arising as a result of the influence of minor elements being vapourised from the pool but no firm confirmation of the mechanism was found. Ludwig (77) has observed that changes in the anode spot size can be brought about by the vapourization of Alkali elements. Chase and Savage (119) have found that differences in the concentrations of certain minor elements (aluminium and titanium) can produce varations in weld penetration and cross sectional area. These workers suggest that such elements (depending on whether they form a scum or remain in the pool) change the surface tension and modify pool motion. This behaviour was also observed to be associated with a change in arc appearance. Bennett and Mills (120) have considered the effect of the steel making process on weld bead aspect ratios, i.e. air melting, vacuum arc melting, electro-slag refining. They find the major influence to be the presence of aluminium, while they also find a tendency for higher aspect ratios at brighter manganese radiation line. Savitskii (84) has suggested that the partial pressure of vapourised trace elements may influence penetration. He also measured changes in current density produced by vapourization. Glickstein (121) has also reported that vapour from low ionisation potential trace elements may substantially change the current distribution. Mills (122) attempted to correlate weld bead shapes with the energy distribution in the arc. No correlation was found and it was suggested that differences in aspect ratios occur as a result of mechanisms within the pool.

Results of the type given above suggest that the correlation between weld bead properties and arc properties is very complicated and difficult at the present time to specify in detail.

Weld bead properties reported above are basically of a uniform nature along the direction of welding. However, it has been found (92,123) that periodic disturbances in bead shape may occur for certain combinations of arc current and travel speed in TIG welding. Such disturbances (known as humping) are also to be found in plasma welds (124) where the additional variable of plasma gas flow rate is involved.

2.5. Structure of the Cathode

The cathode is perhaps the least well understood region of a welding arc. This state of affairs exists largely because of the hostile environment hindering experimental studies and difficulties in giving a theoretical description. Nonetheless this region is of vital importance in determining arc behaviour. The most important characteristics are concerned with electrical phenomena occuring very close to the electrode surface.

Electrical behaviour may be qualitatively described as follows. Positive ions enter a sheath region from the contraction zone adjacent to the cathode. These are accelerated under the influence of the cathode fall field and collide with the surface. Kinetic energy is given to the cathode causing an increase in cathodic temperature. This promotes the emission of electrons thermonically. Electrons generated in this manner may then combine with incident ions causing a further release of energy (ionization energy) due to positive ion neutralization. However, an electron leaving the Fermi Surface of the cathode will take with it the work function of energy (this is a negative contribution to cathodic heating and gives rise to transpiration cooling). At the surface the entire current must be carried by electrons as positive ions cannot enter the lattice. Electron generation may also occur by 'Field Emission'. This process is made possible by very high electric field strengths (1,2, 81,125) existing in this region. Other processes such as photo ionization are also possible and these have been reviewed by Guile (3). The above description pays no account of accommodation phenomena (81), e.g. not all incident ions are neutralised. A general theoretical description of this region is extremely difficult and must take full account (81) of conditions existing in the contraction zone.

In the anode sheath only one kind of charge carrier is of importance i.e. the electron. It can be seen that both electrons and positive ions carry current through the cathode sheath. One of the most difficult questions concerns the relative importance of charge generation mechanisms and the fraction of current carried by each type of charge. These are thought to be strongly dependent on surface conditions (125) and material composition. Calculations show (3) that low boiling point materials cannot in general support enough thermionic emission to account

for arc current. This situation exists in consumable welding arcs. It is known from practical experience that the presence of oxygen may significantly influence emission behaviour for such arcs. Guile (125) has recently proposed a theory whereby high electric field strengths are generated by charging oxide layers on such surfaces. This in turn generates electrons by field emission.

In non consumable arcs of the type considered here, the cathode is usually composed of tungsten with possible additions of thoria, zirconia or cesium. It is then possible for thermionic emission to generate the arc current (3). This situation may be described theoretically by employing elements of the theories of statistical and quantum mechanics. If space charge and field effects are ignored then (see 3) current density is given by the Richardson-Dushmann equation:-

$$J = A.T^2 \exp\left(-\frac{B}{T}\right) \qquad (35)$$

where J is the electron current density (I/A_c), A_c being the cathode spot area. A and B are constants and ϕ is the electrode work function. T is the electrode temperature. The most difficult problem associated with the use of this expression is the identification of A_c. Upper limit estimates of this quantity are provided by suitable photographic records. Other estimates may be given by measurements of anode tracks (125) left when an arc is moved quickly over a cathode by magnetic means. Despite considerable uncertainties in A_c the above expression provides a measure of the minimum possible thermionic current density. This figure is of order 10^8 A/m^2 for tungsten. The addition of low work function elements such as thorium may significantly lower the effective work function of the cathode and thereby increase the maximum current density generated thermionically. Rough estimates of the electric field strength associated with this region can be obtained using the Child-Langmuir expression previously introduced. These are about 10^8 V/m for the above situation but significant uncertainties (3) are again associated with such estimates.

2.6. The Effect of Pressure on Welding Arc Behaviour

2.6.1. Introduction

Arcs have been operated at high ambient pressures for a variety of reasons. These are often associated with exploiting a change in arc behaviour observed at high pressures. In other cases the reason for going to higher pressure is one of practical necessity as in underwater welding (126). Arc luminosity may be increased by operating at high ambient pressure. This is a desirable feature when arcs are used as sources of illumination. The increased power appearing at high pressures is also exploited in wind tunnel gas heaters. Applications are also to be found in the electricity supply industry (gas blast circuit breakers). These arcs are long and of a transient nature. The properties of high pressure plasma are of some interest to astrophysicists, nuclear scientists and space engineers concerned with re-entry problems. High pressure laboratory plasmas (usually long and cylindrical) have been used to obtain such data (33). In manufacturing technology high pressure arcs have been investigated (127) with a view to increasing the energy density in fusion welding applications. Since the late 1960's investigations have been conducted into the use of high pressure arcs for underwater cutting (128) and welding (126) as applied to repair and maintenance. Shallow water applications include ship repair through to the dismantling of nuclear reactors (129). Deep water applications are necessarily confined to off-shore situations and the present considerations are primarily directed at this field of application. High pressure plasma applications are by no means confined to high ambient pressure environments. Low ambient pressure - high plasma pressure situations may also occur e.g. on the re-entry shield of a space vehicle as a result of the stagnation pressure effect.
The local pressure of an arc may also be increased by the interaction of arc current and self magnetic field (68). For arc currents of order 100 Amps this effect is small. However, this increases in accordance with the square law and may be of order 10 atmospheres in a 10KA arc (as used in the electricity supply industry).

Arcs have also been investigated (e.g. 130) at low pressures regarded here as less than 0.1 bars. These arcs are fundamentally different from high pressure thermal arcs as collision frequencies are low enough to

allow significant deviations between light and heavy particle temperatures. Behaviour near the electrodes is then substantially different from that at one atmosphere and above.

In this section a review is undertaken of literature concerned with the effects of pressure on TIG welding arcs. Other arc forms are considered where appropriate.

2.6.2. Influence of Pressure on TIG Arcs

Nearly all published work on high pressure TIG arcs is concerned with the characteristics of TIG arcs. Very little knowledge is presently available on the structure of such arcs. A number of papers have given accounts of aspects of TIG arc V-I characteristics (10,131,132,127). These are generally found to be of a similar form to those at one atmosphere exhibiting a negative arm at low currents and a positive arm at high currents. It is found that arc voltage increases with pressure and so the V-I characteristic is translated to higher voltages with increasing pressure. The minimum voltage position on the V-I curve is reported to be only weakly pressure dependent.

As at one atmosphere the V-ℓ characteristic (127) is substantially linear for short arcs. However, the gradient of this curve increases with pressure. Extrapolated values of the zero arc length voltage obtained from the intercept with the voltage axis are reported (133) to be only weakly pressure sensitive although a report (131) has been made of a pressure dependent V_o. This report is thought to involve inaccurate measurements because at one atmosphere a zero length voltage as low as 5V appears to occur. No information is available on the relative anode and cathode components of V_o and it is possible that one may be increasing as the other is decreasing. It has been found (18) possible to express the pressure dependence of the electric field strength (as given by the gradient of the V-ℓ curve) by

$$E = E_1 . p^n \qquad (36)$$

where E_1 is the field strength at one bar and p the pressure in bars. n is a positive number. Guile (18) has given a study of factors

influencing n for a wide variety of arc forms. Much of this work refers to very high pressure (up to 900 bars), long (cm's) high current (up to 40KA), transient (1 ms) arcs. A good deal of such work has been done by a Russian group (134,135,136,137,138,139) interested in heating dense plasmas to high temperatures while using relatively low power expenditures. Guile finds that E may also be influenced by arc current arc length, electrode material and translational speed of the arc. However, for TIG type arcs operating on the positive arm of the V-I curve, only small changes in V with I are observed for practical welding conditions. Also it is known that the V-1 curve decreases in slope with increasing arc length. If values are taken for short arcs the length dependence disappears. In welding applications arcs are moved slowly (< 10mm/s) and so convection losses due to cross flow are thought to be relatively unimportant compared to the effect of an axial shielding gas flow (~ 1 m/s). These considerations show that the simple expression given above is insensitive to many TIG arc variables. However, shielding gas flow should be considered as an additional variable. In nearly all reported cases shielding gas flow rates are not specified. Guile (18) indicates that n may be between 0.16 and 0.67 for the wide range of arc conditions examined. Much narrower limits are expected for the dependence of n on typical TIG type arc variables. Guile has examined the experimental voltage measurements of Burrill and Levin (140) for a 150 Amp MIG arc in Argon (2% oxygen) over the pressure range 4 to 22 atmospheres. These workers used wire diameters of 0.8, 1.2 and 1.6mm. It is deduced that E decreases with wire diameter and has a relatively high value (relative to other types of arc). This is associated by Guile with vapour jets causing strong convection within such arcs. The values of n obtained were 0.53, 0.45 and 0.43 for wire diameters of 0.8, 1.2 and 1.6mm's respectively. However, in obtaining these values Guile has applied a simple correction to the total arc voltage by assuming the sum of the fall voltages to be 20V. No account is taken of the change in arc mode (metal transfer mode with wire size) or the effect of Ohmic heating in the wire stick out. Both of these factors will complicate the interpretation of consumable arc voltages. It is also to be noted that the sum of the fall voltages for steel electrodes is likely to be less than 20V. This is asserted by observing that in short circuit welding arc voltages of below 20V may be obtained and that such voltages also involve a

component along the stick out that is not associated with V_o. Changes in this component will vary with wire diameter being largest for thin wires. This has not been taken into account by Guile and so the dependence of n on wire size may be associated with the wire stick out and not the arc.

Dynachenko and Olshanskii (127) have obtained a more complex expression for E than that given above. They also relate E to the arc current and diameter (d) by

$$E = \frac{K.p^n}{I^b.d^g}$$

where K,n,b and g are positive numbers. This relationship was found for argon TIG arcs. However, the arc diameter d is pressure dependent and so the real pressure dependence of E will be greater than indicated by n which they find to be 0.25. Comparison with other values is further complication by the fact that E is estimated from the long arc length gradient of arc voltage. Lower values are therefore to be expected.

For low current arcs Finkelnburg and Maecker (1) report values of n between 0.5 and 0.17. Weizel and Rompe (141) consider arcs with low degrees of ionization and find $n \simeq 0.5$. Values of 0.5 have also been found by Peters (142) for arcs in water vapour at pressures of up to 10^4 atmospheres, and by Bauder (27) for wall stabilised arcs.

Variations in reported values of n are to be expected and originate from the widely differing arc situations investigated, i.e. arc voltage and hence electric field strength varies with pressure as a result of the pressure dependence of energy transfer processes within the arc. For metal vapour arcs the degree of ionization required to maintain arc current is easily achieved in view of the low ionization potentials of arc constituents. In argon type arcs higher temperatures (higher than for metal arcs) must be achieved to maintain current flow. These are likely to be associated with larger energy losses and therefore higher values of n. It is found (143) that only small changes in arc voltage occur with increasing pressure for shielded metal arc and flux cored electrodes due to the presence of readily ionizable flux constituents.

Recent work (144) has shown that arc voltage is dependent on shielding gas flow rate in high pressure environments. The failure to specify shielding gas flow rates by many authors introduces further uncertainties into comparisons between electric field strengths reported above. Electric field strength is an important parameter because it may be used to specify the total arc voltage

$$\text{i.e.} \quad V = V_o + E.\ell = V_o + E_1 \, .\ell.p^n \qquad (37)$$

Such information is clearly useful from the operational aspect i.e. in helping to choose suitable open circuit voltages for power supplies, for estimating process power at a given pressure and for estimating arc lengths in operational situations (from arc voltages). E also characterises many physical phenomena within an arc column.

A number of workers (127,131,132,144)have reported changes in arc appearance with increasing pressure. Generally arcs are reported to undergo a reduction in cross-section and an increase in luminosity. This behaviour is also found at the cathode (144) where the 'plasma climb' effect on the electrode is less evident. Hence the current density must increase. It is also found that cathodic erosion (132) increases with pressure. This may give rise to a number of operational difficulties. These observations indicate a general increase in energy density and an increase in the importance of radiative transfer. At very high pressures radiation is reported (135) to be the dominant loss mechanism for long high current arcs.

Arc ignition is more problematic than at one atmosphere. At one bar arcs are often ignited by means of a high frequency transient discharge. At high pressures high frequency (HF) ignition is reported (131,132) to become increasingly more difficult (as the Pachen breakdown curve would predict). Indeed no HF ignition is reported (132) above about 10 atmospheres in argon and 4 in helium. For this reason a touch striking technique has often been employed. Arcs are then often struck on a carbon tab before running onto the workpiece.

One of the most significant effects of pressure on welding arcs is the deterioration in arc stability. Arc stability is of paramount importance

in welding where the heat source must have predictable and suitable characteristics.

Very little work has been reported on the stability of TIG arcs. However, it is known (146) that consumable arc systems may be stabilised by the addition of suitable low ionization fluxes and TIG arcs burning in helium and nitrogen atmospheres are observed (132) to be much less stable than those in argon. Instabilities are often associated with enhanced electrode erosion (132) in the former gases. The arc column may then flicker. In off shore environments TIG arcs are apparently more sensitive to magnetic influences (145). Electrode positive MIG welding arcs are found to be unstable at high pressures. On the other hand electrode negative MIG (10), which is almost unworkable at one atmosphere, is relatively stable at higher pressures. This seems to be one of the few examples of an arc system becoming more stable with increasing pressure. Coupled with the increase in electrode negative MIG stability is a fall in wire melting rate. A possible explanation of this behaviour is given by Allum et al (146) where it was shown that this could be due to the positive ions carrying a diminishing fraction of the cathode fall current with increasing pressure. Some work (147) has been conducted on the stability of long wall stabilised arcs in axial gas flows. This suggests that the mass flow rate of the gas in which an arc burns is of importance. Turbulence is observed with flow rates above 10g/s for 150 Amp wall stabilised argon arcs.

Very little has been reported about arc stabilization although Knagenhjelm (148) claims high frequency TIG power supplies have this effect. Christienson (149) notes that stabilization may be encouraged by introducing a component of swirl to an arc.

Arc characteristics are found to influence weld pool behaviour at high pressures. Work by Stalker and Salter (132) suggests that the welds become narrower and deeper with increasing pressure up to about 7 atmospheres. Above this pressure weld bead geometry changed little with pressure.. These workers attributed this behaviour to tungsten inclusions from an eroding cathode. This suggestion is thought unlikely as this should not significantly influence heat input. Matsunawa and

Nishiguchi (10) have measured calorimetrically the heat entering a steel anode over the range 1 to 7 bars. They observed an increase with pressure. However, the increase was less than that found for a cooled copper anode. This may be due to vapourisational effects although it is also noticed that the arc voltage was lower for the steel experiments. It can be inferred from this work that the efficiency of heat transfer falls with increasing pressure over the range 1 to 7 bars. Similar behaviour has been found for plasma arcs (150) in underwater cutting applications. Weld pool behaviour is influenced by pressure in a number of ways. Larger melted volumes are obtained for a given arc length and current. This is associated with an increase in process power or more specifically with an increase in the convective contribution to plate heating (10). An important operational observation of high pressure arc behaviour is that larger volumes of weld metal may be maintained in overhead welding. This may be associated with the force of the arc on the pool, changes in surface tension or changes in boiling point with pressure. These factors should also influence weld pool motion. Further effects should be noticeable due to an increase in current density i.e. effects such as an increase in the intensity of heating and weld pool convection.

Very little is known about the effects of pressure on the structure of TIG welding arcs, although some work does exist for other types of arc (27,141,135). It has occasionally been suggested that arc velocities and temperatures (152) increase with ambient pressure. These views would appear to be based entirely on the observation that high pressure TIG arcs are more constricted and luminous than at one atmosphere and as such has no experimental or theoretical foundation. Indeed Bauder (27) has found the temperature of a wall stabilised arc to fall with pressure. Theoretical modelling (36) of high current (10KA) long free burning arcs suggests the temperature may increase marginally with pressure. Significant temperature increases with pressure have been inferred by Russian workers (135) using long, high current transient arcs.

No experimental measurement of velocity fields exist for high pressure arcs. Inglis and North (152) imply that arc velocities should increase as a result of ambient pressure acting on the arc boundary. This

suggestion has no foundation in theory as the arc boundary is free and with no pressure gradient across it. Theoretical modelling work referred to above (36) suggests a decrease with increasing pressure in a manner described by $p^{-\frac{1}{2}}$.

2.7. Overview of Literature Survey

This survey has concentrated on aspects of arc behaviour of direct relevance to the present contribution. Therefore, the bulk of the literature has concerned short, medium current TIG type welding arcs operating at and above one atmosphere. Regions of potential interest have been outlined where a lack of data presently exists or where progress has been slow. Slow progress has in part been due to the formidable nature of some existing problems, e.g. behaviour of vapourizing pools and structure of the arc column. Arc characteristics are well documented at one atmosphere and a few papers concerned with higher pressures have appeared. However, more data is required on high pressure behaviour.

It has generally been found difficult to obtain detailed knowledge on arc structure. In view of this situation importance is attached to investigating the influence of all major variables on arc phenomena. Clearly the lack of information on the effect of ambient pressure leaves room for further potentially fruitful and important investigations. Pressure may also be used as a test for existing theories based largely on one atmosphere behaviour. In this manner a better understanding of one atmosphere arcs should be achieveable. In particular pressure offers a means of affecting arc power without changing arc length, current or gas composition. Arc stability is known to deteriorate with increasing operating pressure. It is thought important that this aspect is considered further as such a study should throw light on the important but rarely considered fundamental nature of arc stability. Despite these particular points the main aim of the present contribution is to obtain data on the behaviour of high pressure TIG arcs.

3. Experimental Investigation

3. Experimental Investigation

In this section the direction of the experimental investigation is described and discussed. It has also been found appropriate to explain the links with theoretical considerations and to outline the main aims and methods employed in these developments. A general description is given of procedures and materials as well as experimental details. This has involved a discussion of methods and procedures , accuracy and errors, and of design criteria. The interpretation of experimental measurements (but not of results) is also included in this section. Further details are to be found in section concerned with results and discussion of results.

3.1. Introduction

Experiments were performed between 1978-1982 in pressure chambers situated within the materials department at Cranfield Institute of Technology. Initial work was conducted in a chamber with a working pressure limitation of 19 bars and an internal volume of about $1m^3$ (see figure 2). This was the larger of the two chambers employed and simulated working depths of about 200m of water (typical North Sea bed depths). The smaller chamber (see figure 3) had an internal volume of about $0.2m^3$ and a maximum working pressure of 135 bars although ancillary equipment limited experimental investigations to about 45 bars.

Experiments were designed to investigate the characteristics and structure of TIG type arcs over the pressure range 1 to 45 bars where the terms 'characteristics' and 'structure' used above have the same meaning as defined in the Introduction.

Parameters were generally chosen to be similar to those used in practical welding where a typical argon TIG arc on steel is operated in the electrode negative mode with a current of order 100 Amps, an arc length near 3mm and a welding speed of about 2mm/s. Deviations from these conditions were employed to obtain a greater understanding of general behaviour. The range of variables investigated was often limited by other considerations such as arc stability. Experiments were performed in argon and helium environments and investigations were also undertaken to assess the

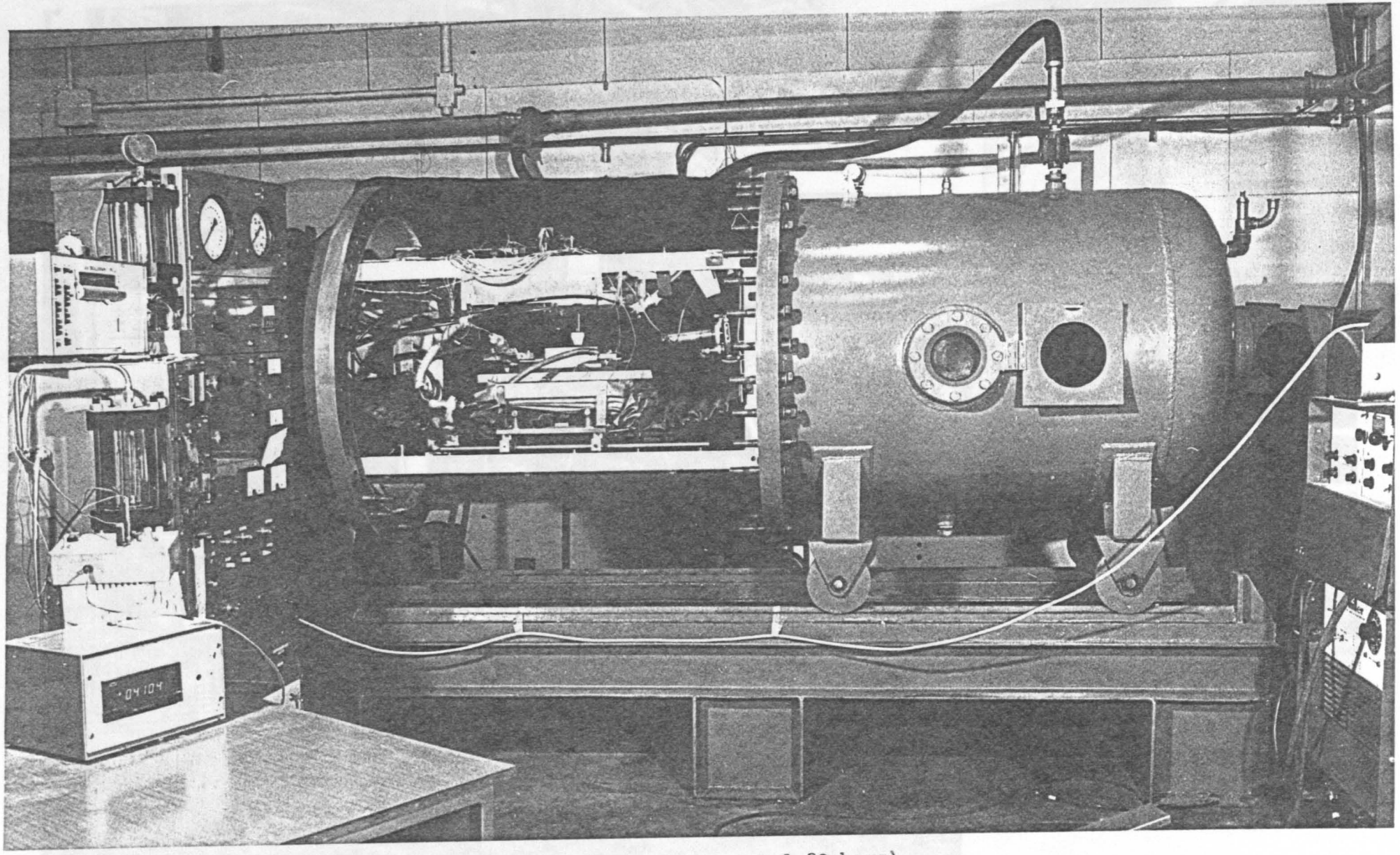

Figure 2 Chamber CI (operating range 1-20 bars)

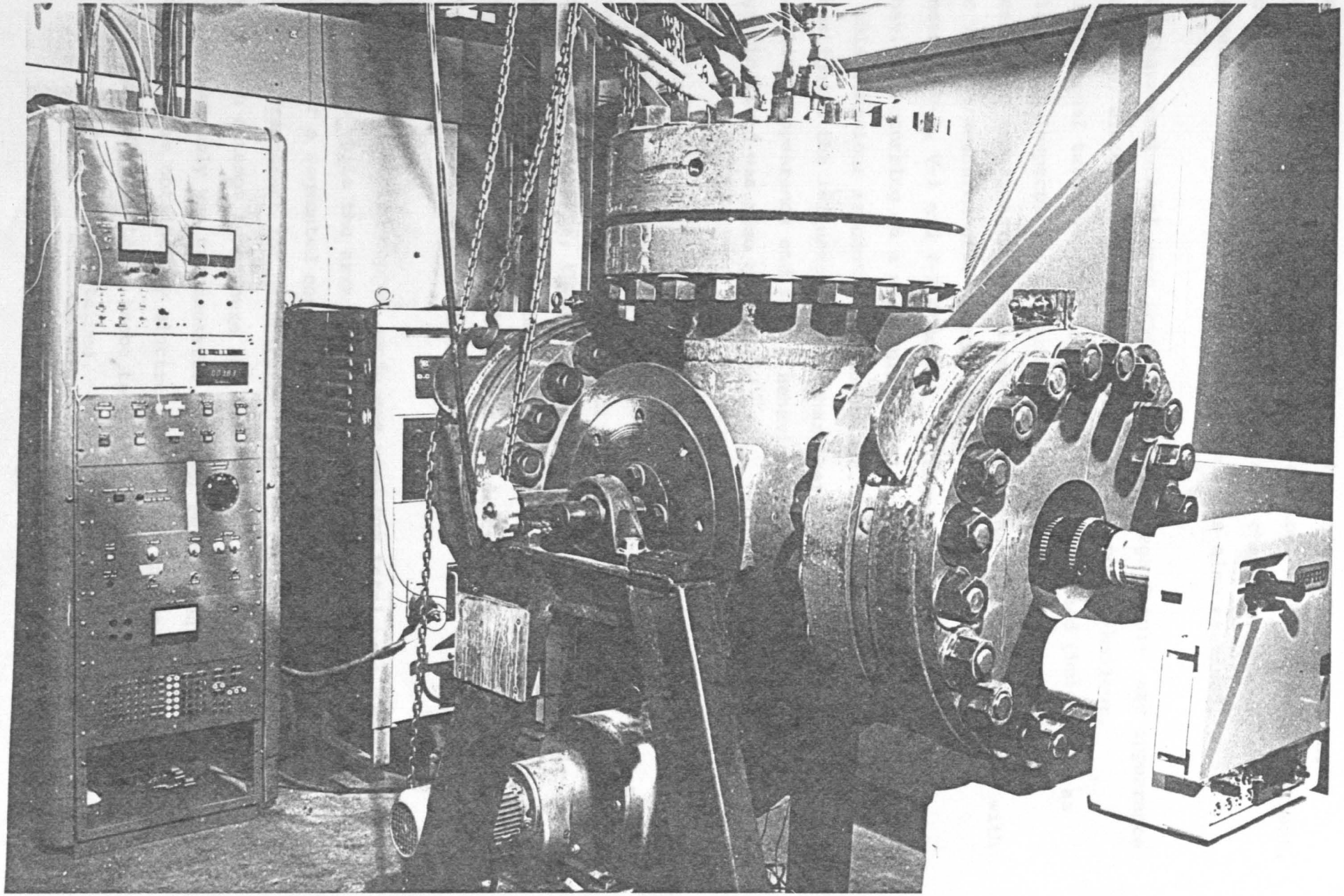

Fig.3 Chamber CII (operating range 1-135 bars)

influence of welding position on arc and weld pool behaviour. In all cases only electrode negative arcs were investigated. Experiments investigated the dependence of process behaviour on pressure arc current, arc length, shielding gas flow and electrode characteristics. The influence of a constriction at the cathode was also examined.

Arc 'characteristics' were investigated with regard to:- arc appearance and modes, electrical characteristics and weld pool behaviour. Observational techniques included still and high speed photography as well visual inspection. Of particular interest was the effect of pressure on arc appearance and mode. This behaviour was correlated with arc voltage measurements. Electrical characteristics principally concerned V-I, V-ℓ and V-P studies. Voltage characteristics mirror behaviour occurring on a structural level and so a detailed knowledge of this behaviour is considered important. Weld bead studies investigated the influence of arc characteristics on weld shape, stability, appearance and size. Behaviour in the presence of an applied magnetic field was also considered.

The arc 'structural' investigation was aimed at gaining a deeper understanding of observed arc 'characteristics'. This part of the study involved theoretical and experimental considerations. Experiments were basically of two types; those measuring behaviour at the anode and those concerned with arc column properties. Measurements at the anode investigated the total heat input and the distribution of arc current at the anode for a range of arcing conditions.

A single water cooled copper anode was used for total heat input measurements while the arrangement for measuring current densities consisted of a segmented copper anode. It was also found possible to use this arrangement for quantitative arc stability measurements. However, an attempt to measure the distribution of total heat using such an anode assembly was unsuccessful. Direct measurements of arc column properties were obtained by electrostatic probe and radiation monitoring techniques. Electrostatic probe technique allowed the axial distribution of column voltage to be obtained.

The main theoretical effort has been directed at understanding gas flow in the column of a TIG arc in a more comprehensive manner than is described by Maeckers theory. A model is developed based on the momentum, energy balance and Maxwell equations. This has given an insight into many of the experimentally observed aspects of arc behaviour.

3.2. General Equipment

The two pressure chambers used in this study are shown in figures 2 and 3 and will be referred to as CI and CII. The larger chamber, CI, had no positional capability, but CII could be rotated through 180^{o} to simulate any welding position. This was achieved by means of a chain and motor drive mechanism. Both chambers were closed by means of a series of high tensile bolts. These were tightened with a pneumatic torque wrench set at a torque suitable for the chamber operating pressure. CI could be undone by sliding one section of the chamber shell, on runners, away from the other section. In CII an overhead hoist was used to remove end sections and hence gain access to the chamber interior. In this chamber all three end flanges (see figure 3) could be unbolted and removed. Both chambers were equiped with viewing ports. These were perspex discs of about 50 mm's in thickness. CI had three ports, two situated in the side of the chamber and a further port situation centrally at one end of the chamber. CII had two ports situated at each end of the chamber. The detailed experimental arrangements employed varied from chamber to chamber and from experiment to experiment. Such details are given in later sections. Only general experimental considerations are reported in this section. These may be divided into chamber services (i.e. water, gas and electricity) and arrangements within a chamber. Basic facilities supplied to CI and CII were similar and are summarised schematically in figure 4. This figure indicates the services that were required by each chamber to perform the experiments reported here. However, the logistics varied between CI and CII. These differences are given where appropriate. Each chamber was provided with water, gas and electricity in a manner described below. Within each chamber work handling equipment was provided to manipulate the welding table and welding torch.

3.2.1. Electrical Connections

Welding power was supplied to the arc by means of high current terminals through the chamber shell and insulated from the shell. Three welding power supplies each with constant current V-I characteristic were used during the course of this experimental work. For arc stability work a highly rectified current source was used. This was obtained from a custom built transistorised power supply (ref.153) and an open circuit voltage (OCV) of about 40V. Because of the low OCV it was only possible to use this power supply for argon TIG work. The OCV was too low for high pressure helium TIG arcs and argon plasma arcs. Helium TIG arcs were investigated with a BOC Argon Arc (350A) set with an OCV of 65V while plasma arcs were operated with a Miller Gold Star (350A) Set of similar OCV. In all cases a contactor was employed and arc current was measured across a calibrated shunt. Arc voltage was monitored at the current entry and exit points from the shell. Negligible voltage drops were found to exist between these points and the connections to the torch and anode (less than 0.1V). Arc current and voltage were measured using calibrated moving coil meters and occasionally with Digital Voltmeters. Signals were simultaneously recorded on an ultra violet oscillograph (UVO), which allowed permanent records to be kept and time dependent effects to be quantified.

In plasma experiments a pilot arc of about 6 Amps was supplied between the electrode and copper orifice. This was given by a current limiting device employing a high OCV for arc striking purposes. Additional power supplies were required for torch and table motions. These supplied motors powering the respective motions (see work handling) and also transducers. Transducers were used to monitor table and torch motions and ten turn potentiometers were employed to vary torch and table speeds. Low current signals (e.g. transducer readings) from the chamber were brought out through a single point incorporating a 26 way 'Secon connector'.

FIG. 4 Schematic diagram of basic chamber services (additional services are used in plasma welding).

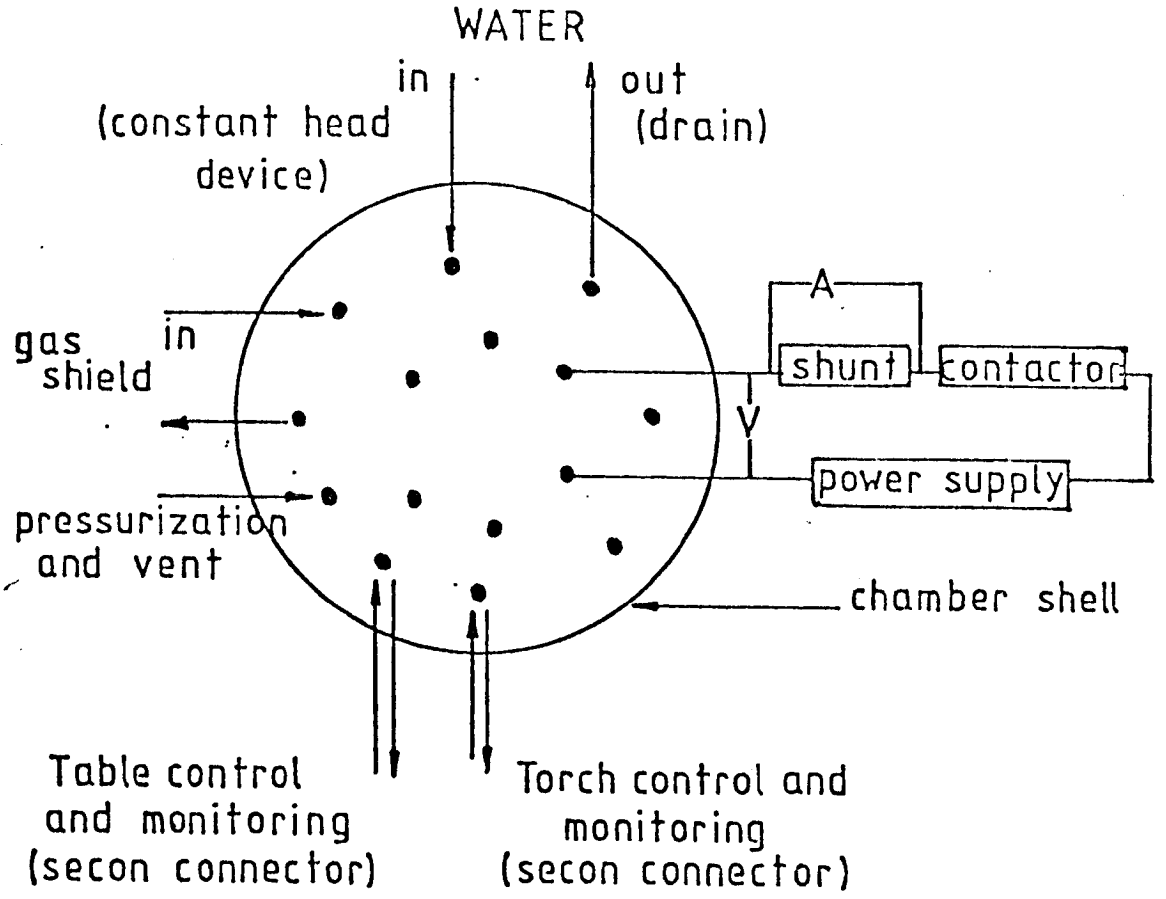

3.2.2. Water Ways

Water was supplied to each chamber for the purpose of cooling the plasma torch (when used) and also as a calorimetric fluid in heat transfer experiments. In plasma experiments the torch was cooled by a closed loop distilled water flow of 8 cuft/min, supplied by a Thermal Arc pump. However, a constant head device supplied water for calorimetric experiments. This was provided by a water tank situated about 20m above ground level. Water entered the chamber through two inlets (one for each copper block). This was then run off to a drain. Flow rates were measured at the drain end of the system by a container and timer method. High pressure water piping was employed to minimise the occurrence of pipe collapses within the chambers and needle valves were used to control flow rates.

3.2.3. Gas Ways

Gas was used for pressurizing the chamber and as shielding and plasma forming gas flows (in constricted arc welding). Standard BOC gas bottles of commercial purity were used in all cases. This arrangement required three gas lines. A further line was used to monitor chamber pressure. The pressurization line was also used for evacuating the chamber (with an Edwards vacuum pump) prior to pressurization and for venting after experimentation.

Gas flows to the arc were regulated by ball valve devices and monitored by tapered-tube and float flow meters (Rotameters) situated in specially made safety housings. Rotameters supplied by Platon were used throughout this work. These meters were calibrated for use at pressure using a technique described in appendix 1.

3.2.4. Work Handling (Torch and Table Motions)

In chamber I the welding torch had one degree of freedom in the Z direction (perpendicular to the table) while the work piece moved with the two degrees of freedom in the x and y directions. In chamber II the table had only an x motion capability (for reasons of space) and the torch moved in the y and z directions. The table and torch drives in

chamber I employed screw thread mechanisms in the x-y plane and a cog mechanism in the Z direction. For chamber II the table motion was driven by a chain while the y and z motions were by screw and cog mechanisms respectively (See fig.5). All motions were monitored with linear transducers and could be accurately controlled using ten turn potentiometers.

3.2.5. Welding Torches

An air cooled BOC TIG torch (T150A) of orifice diameter 13mm was used for TIG welding. This arrangement was kept throughout. However, torch mounting considerations in CII necessitated modifications to the torch body (see figure 21). A number of electrode sizes and compositions were adopted but in general electrode protrusion from the shroud was set at 6mm.

Plasma welding was performed using a thermal arc torch (model P8) (figure 6). This consisted essentially of a water cooled plasma orifice enclosed by a ceramic (aluminium oxide) shield cup. Plasma orifice diameters of 3.2 and 4.8mm's were employed. In all cases 4.8mm, 1% thoriated tungsten electrodes were used and situated within the orifice as shown in figure 7.

3.2.6. Anode Arrangements

Two different anode arrangements were employed. For weld bead studies, samples were bolted to a base plate. In calorimetric studies water-cooled copper anode arrangements were used. For weld bead experiments in CI the base plate consisted of a large steel slab. This was insulated from the rest of the chamber by a teflon sheet. A twin earth was attached to this base plate to counteract possible arc blow effects. For reasons of space and weight a titanium base plate was used in chamber II.

The water-cooled anode design evolved during the course of experimental work. Initially hollowed out copper blocks with bolted copper top pieces were used. These were found to leak at high pressures. The design was then modified to replace the bolts with soldered joints.

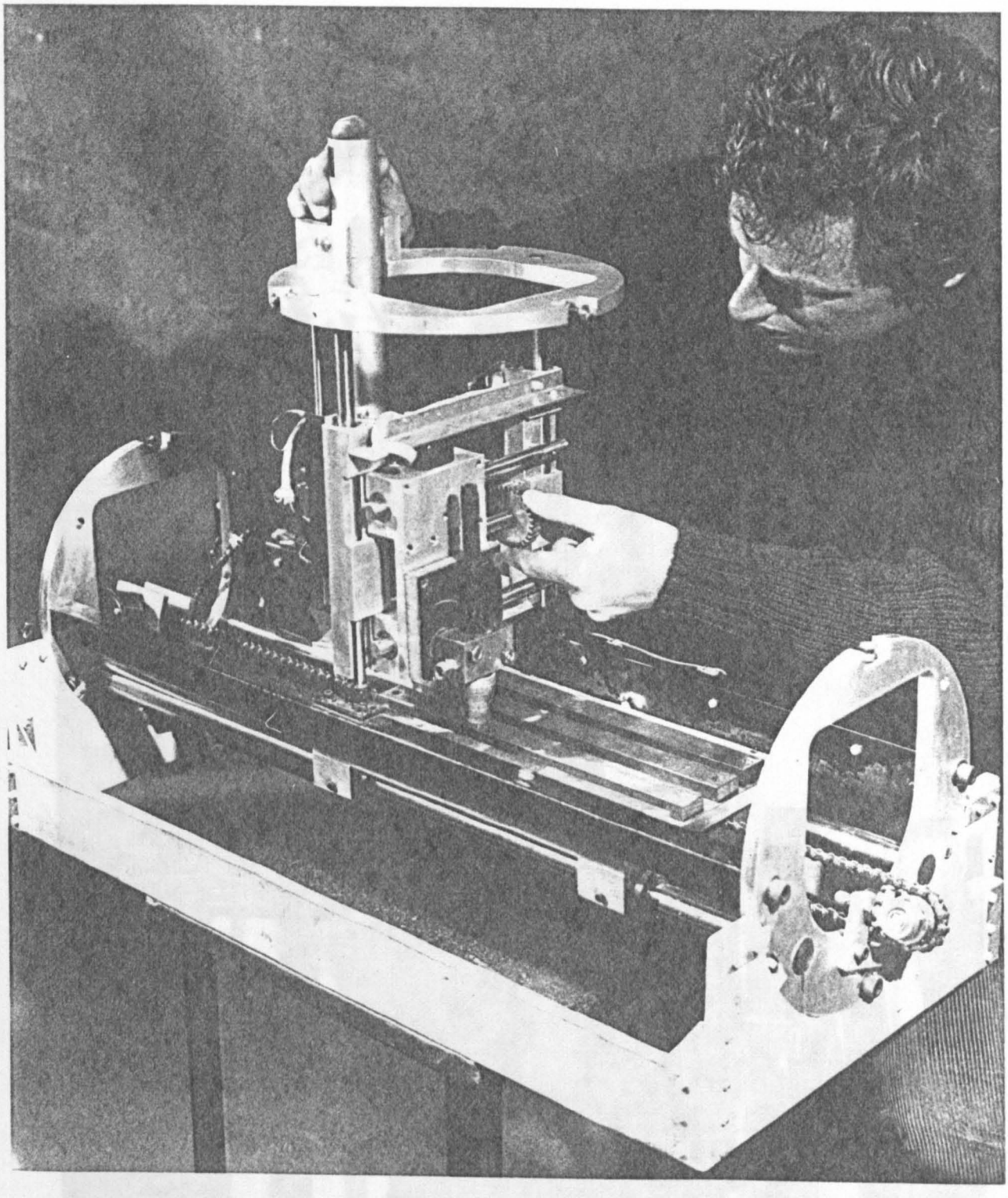

Figure 5 Torch and Table Arrangement with Chamber CII

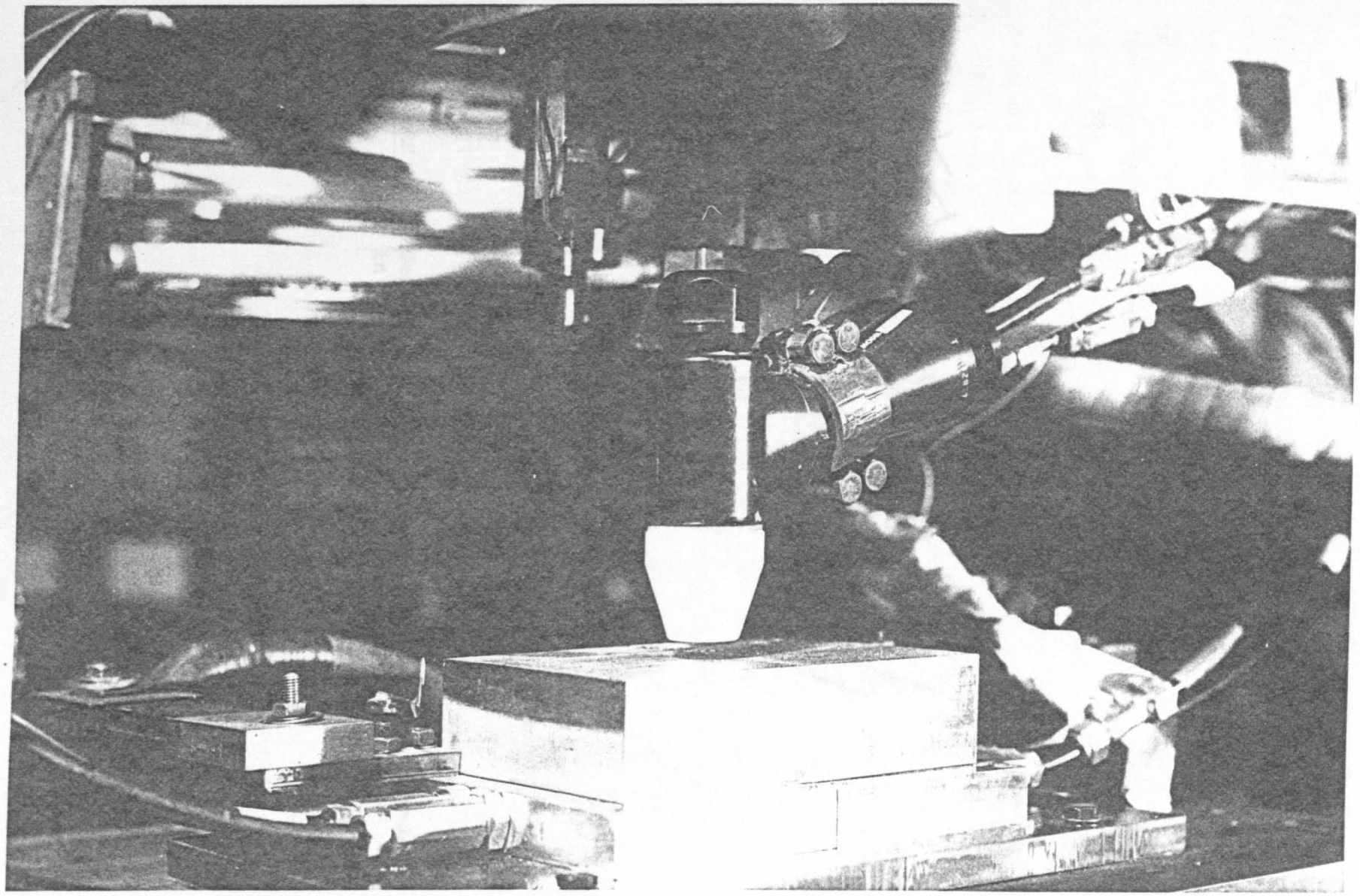

Figure 6 Plasma Torch Above a Split Water Cooled Copper Anode

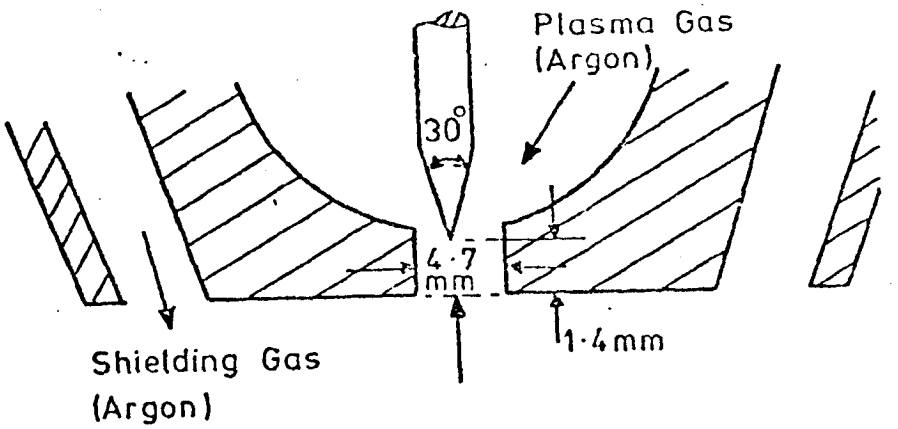

FIGURE 7 Geometry of Electrode Position at the Cathode in Plasma Welding

However, it was found that arc heating caused local leaks to again appear. In a latter development the top piece became a top hat bolted to a base plate. An 'O'-ring seal was also fitted at the base. This arrangement was satisfactory for all pressures investigated. A baffle was included within the block to aid mixing. The arrangement used for results presented here is shown in figure 6. Two blocks were employed for current density measurements. These were separated by an 'air' gap of 0.1mm and placed on a teflon base. This ensured that the blocks were electrically isolated. Only one block was used for total anode heating measurements. Heat transfer with steel anodes was investigated by placing steel discs in a recess on the surface of one anode segment modified form of that shown in figure 6.

3.3. General Procedures

Prior to each pressurization atmospheric contaminants were expelled from the chamber by evacuating to below 5 mbars. Subsequently, the chamber was raised to the required pressure ready for welding operations. The electrode was then slowly (0.1mm/s) lowered to the work until contact was made. Contact could be accurately monitored by measuring the circuit resistance which decreased abruptly on touch down. The arc length transducer was then zeroed. In this manner very accurate electrode-work piece distances could be set. Unfortunately, HF could not in general be successfully applied to arc striking. For this reason the arc was ignited by bringing in the contactor and welding power with the electrode in contact with the work piece. An arc was then struck by separating the electrodes at a low arc current (30A>). Arc current was subsequently raised to the desired value. During this procedure the arc was viewed through a port. If any noticable electrode damage or contamination occurred on striking the chamber was vented and the electrode replaced. The procedure described above is very much more accurate than the equivalent manual operation and electrode damage on striking was only very occasionally observed. In plasma welding the pilot arc was established by shorting the copper nozzle and tungsten electrode. The pilot arc was extinguished during welding and re-ignited just prior to the end of a weld. This procedure made use of the ignition technique only once per pressurization. After welding the electrode was again brought to the anode surface to examine for any loss of electrode

material that may have occurred during welding. Arcing was continuously observed visually through a welding screen and photographic images were taken.

Restrictions were placed on arc running time in chamber II. This was due to effects associated with heat build up and was particularly noticable in overhead welding, plasma welding and helium TIG welding. It was also found that the chamber pressure increased during the course of a weld for high heat inputs or high shielding gas flow rates. This necessitated fairly regular gas venting to maintain steady pressure conditions. Eight welds could be achieved per pressurization in CII and twice this number in CI. The turn round time per pressurization was such that, at best, two pressurizations per day could be achieved.

The absolute accuracy of specifying process parameters is difficult to assess. A general account must consider not only reading and instrument limitations but also the nature of the variable. Such considerations are given in following sections. However, instrument reading are shown below. These values are required for more general assessments of accuracy.

Property	Arc length mm	Arc Voltage V	Arc Current Amps	Pressure (PSI)	Gas Flow ..ℓ/min
Reading Error	$\pm$ 0.01	$\pm$ 0.05	$\pm$ 0.5	$\pm$ 2	$\pm$ 0.25

A number of photographic techniques were employed during these experiments. In CI is was possible to place a camera within the chamber (at a distance of about 0.7m from the arc). Arc images were then recorded using an f32 stop an 0.6 neutral density filter and a shutter speed of 1/1000 sec. Both black and white, and colour film were used to record arc images. The above settings were chosen to give reasonable representations of the electrical arc boundary (see section 4). Images of arc operating in chamber II were obtained from outside the chamber at a distance of about 0.8m from the arc using an f16 stop and 1/100s shutter speed. For experiments in this chamber (CII) high speed photographic methods were occasionally employed. The arc events investigated used film speeds of up to 500 frames a second with a Fastex ciné camera.

3.4. General Materials and Material Preparation

TIG weld bead studies were conducted on bright mild steel. This was obtained over a period of three years and hence did not come from a one single batch. Plasma weld bead experiments were performed on stainless steel (321/EN58B). Specimens were cut to length on the laboratory band saw and linished to remove surface layers. These were then degreased using 'Inhibisol' prior to being drilled ready for fixing on the base plate of the welding table. Specimen sizes were chosen to give bead fusion characteristics similar to those expected on a semi-infinite slab. It was found that for 100 Amp arcs samples of 25mm (width) by 13mm (thickness) were adequate when these were fixed on to the massive base plates previously mentioned (see Appendix 6). Generally specimen lengths were between 125mm and 375mm.

TIG weld bead specimens were cut and prior to etching polished on three grades of paper. Stainless steel samples were machine polished in the departmental workshop. It was found possible to obtain fusion and heat affected zone boundaries with an etchant of 5% nital for mild steel welds. Weld beads were subsequently examined at a magnification of about 10 on a Vickers microscope. This allowed weld profiles to be traced or photographed. Weld bead diameter and depth could then be measured directly while weld bead areas were measured using a planimeter.

3.5. Experimental Investigation of Arc Characteristics

Initial experiments were concerned with assessing variables with respect to their nature, significance and tolerance to pressure changes. It was quickly realised that the nature and order of significance of variables observed at one atmosphere, changed with increasing pressure. 'Significance' was judged at this stage in terms of effects on stability, arc voltage and weld appearance i.e.characteristic behaviour. Arc stability was generally found to decrease with pressure. This was associated with gross changes in arc appearance and fluctuations in arc voltage. Arc voltage became increasingly more sensitive to arc length and shielding gas flow at high pressures. However, the significance of electrode geometry in argon TIG welding appeared to play a smaller part than has been reported at one atmosphere. (See Literature Survey).

These early results indicated that special consideration had to be given to arc stability, arc length and shielding gas flow values. In an inert environment there is of course no requirement for a shielding gas flow and so this variable, on these grounds, can be eliminated. In many practical situations a water interface is present and humidity levels may be high enough for rain to fall within an enclosure. Other gases such as carbon monoxide may also be generated in the habitat. A shielding gas flow is then required to perform a function similar to that at one atmosphere. Arc shielding requirements demand arc and weld pool coverage. This is given principally by the volumetric flow rate of a shield. However, a constant volumetric flow rate implies an increasing mass flow rate with pressure. Arc stability problems may then arise (see section 6). For this reason, the significance of mass and volume shielding criteria could not initially be assessed. This led to somewhat arbitrary assignments of these values over the duration of expermentation. In many cases constant volumetric flows were maintained while in others no shielding flows was used. It was found that a constant flow meter setting gave flows between those of constant mass and constant volume (e.g. see appendix 1). For this reason constant meter settings were often employed across a range of pressures. Because of the uncertainties outlined above flows are often described in the text in terms of all three parameters.

The observed increase in arc voltage sensitivity to arc length meant that arc length settings had to be specified very accurately (this, of course takes no account of the 'effective arc length' - as already discussed in section 2). Arc length dependencies were generally obtained by systematically varying the arc length and thereby avoiding many of the more random factors which may enter results when arc length dependencies are inferred from less systematic sets of data. V-I characteristics were obtained by fixing the arc length and incrementing arc current. The necessity of adopting this procedure meant that many experimental conditions were repeated for different experimental sets. Comparisons between these results give an indication of the general degree of reproducibility. In all experiments the arc was allowed to run for a time of at least one minute. This ensured steady state arc and pool behaviour. Throughout these experiments the arc was visually

observed and results relating to peculiar arc forms were ignored (or considered separately). Unless otherwise stated measured voltages refer to the mean value as given by a moving coil instrument.

V-I and V-ℓ characteristics were obtained for TIG arcs (and for constricted argon TIG arcs) in argon and helium. These were examined for cooled copper anodes and for weld pool situations. In constricted arc experiments orifice diameter also influenced voltage characteristics. The influence of this was examined by performing experiments with two orifice diameters (3.2 mm and 4.8mm). Orifice damage occasionally occurred during arc running. Unfortunately, the orifice condition could not be observed during a pressurization but results were discarded in the event of significant orifice damage on opening the chamber. Experiments were also performed to examine the influence of other parameters on arc voltage e.g. electrode diameter, vertex angle, composition, inclination (down-hand or overhead), travel speed, shielding gas flow, stickout from the shroud and magnetic field.

CSM behaviour was found for all argon TIG experiments. Helium arc modes were more complicated. A 'self-pulsing' mode was observed under certain conditions (see section 4). High speed photographic techniques were used to investigate this behaviour in conjunction with fast UVO paper speed recordings of electrical characteristics. At low arc currents the previously reported (see literature survey) constricted anode form (Anode Spot mode) was found. Experiments were performed to investigate the pressure dependence of this behaviour for steel and chilled copper anodes. The procedure adopted was to systematically reduce the arc current until the onset of this behaviour was observed. These experiments were performed with moving anodes in the downhand and overhead positions. The arc voltage was simultaneously monitored and correlations between voltage and visual arc appearance were made. Arc images were obtained photographically by a procedure already described. From these images arc dimensions near the electrode regions and in the central part of the column were measured and expressed as functions of pressure and gas flow.

The range of the main variables used in the above investigations are outlined below with brief reasons for any limitations.

PROCESS: TIG	Range of Variable Investigated	Limitations to Investigation
PRESSURE (bar)	1-45 (argon) 1-15 (helium)	Pressure chamber/equipment limit arc stability, electrode erosion limit
I (Amps)	20-150	Stability - torch rating limits
ℓ (mm)	(1-2) - upwards	Pool contamination - power supply (OCV) limitation
Shield (ℓ/min)	0-15	15 ℓ/min is adequate at 1 bar
Electrode composition	1% - 2% thoriated	As at 1 bar
Electrode diameter (mm)	1.6 - 4.8	Electrode melting
PROCESS: Plasma (soft plasma - constricted TIG type arcs)		
PRESSURE (bar)	1-15 (argon)	CI pressure limit
I (Amps)	100-200	Soft plasma arc
Stand-off (mm)	5-15	Orifice/shield cup damage allow end to practical upper limit
Orifice diameters (mm)	3.2 - 4.8	Suitable for currents and flows reported here
Shield gas flow (ℓ/min)	20	Suitable values for 1 bar shielding
Plasma gas flow (ℓ/min)	2-10	Nozzle erosion at low and high end. Also rebounding plasma jet at high end

Table 2 Parametric Ranges

Weld bead studies were exclusively of the bead on plate type. These were conducted for argon and helium TIG arcs and argon plasma arcs. Weld lengths of at least 100mm were generally deposited and samples were taken near the middle of these runs. Throughout these runs arc conditions were monitored. Checks were made to investigate reproducibility and effects of pre-heat, by the arc and chamber atmosphere, on welds made towards the end of a pressurization. However, these influences were negligible. At very high pressures (above30 bars) weld bead appearance often suggested turbulent pool behaviour. It was then difficult to satisfactorily represent a weld bead by a given section of the weld.

The onset of this behaviour was investigated for a range of arc parameters. However, it was found possible to stabilise a pool by means of the magnetic field from a permanent magnet (see figure 8). Experiments using this magnetic field arrangement were conducted throughout the investigation. In plasma welding weld pool 'humping' was observed for certain combinations of arc current, travel speed and plasma gas flow rate. Operating envelopes defined by this behaviour were investigated at a given pressure by increasing the flow rate (the other two parameters being fixed) until the onset of this behaviour occurred.

A total of about 500 welds were performed, sectioned, polished, etched and analysed. Measurements of weld diameter, depth and fusion area were made on each. Similar heat affected zone (HAZ) measurements were also made. These were performed under conditions similar to those indicated in table 2. The observed behaviour was correlated with arc characteristics, mainly by means of melting efficiency measurements. The general relationships sought are shown in table 3.

WELD PROPERTY/ HAZ PROPERTY ⟹	MIXED PROPERTY	⟸ PROCESS CHARACTERISTIC
Width (w)		Ambient pressure
Depth (d)	Melting efficiency	Process
Area (A)		Arc current
Aspect ratio (w/d)	(Z)	Welding speed
	(see section 4)	Electrode characteristics
		Gas composition/flow rates
		Magnetic field

Table 3 Relationships between Weld/HAZ Properties and Process Characteristics

3.6. Experimental Investigation of Arc Structures

In this section methods employed for investigating arc structure are reported. The conditions and procedures used in these investigations are also described. Consideration is given to experimental design and special attention is payed to the interpretation and treatment of experimental measurements.

3.6.1. Anode Heating

Experiments were performed using a split water cooled anode to investigate the distribution of heating at the anode. These experiments were largely unsuccessful due to thermal leaks between the blocks. Further experiments to determine the total anode heating used just one water cooled copper segment. Heat transfer was extensively investigated for the range of conditions shown below:

i) Argon TIG arc on a copper anode.
ii) Plasma arc (argon) on a copper anode.
iii) Helium TIG arc on a copper anode.
iv) Argon TIG arc on a mild steel anode.
v) Helium TIG arc on a mild steel anode.

Further experiments were performed to investigate the influence of shielding gas flow and magnetic field strength on TIG arcs. Arcs on copper anodes were performed by simply running an arc on a cooled copper anode and monitoring the change in water temperature between inlet and outlet. Experiments with steel anodes were performed by placing a steel disc in a recess machined into the top face of a copper block. Before giving a detailed description of these situations a description of methods common to both experiments are reported.

A water cooled copper anode was placed on a tufnol base plate and supplied with water from a constant head device thereby ensuring a constant volumetric flow of water. The side walls of the copper anode were lagged using glass wool. Plastic water piping connected the block to the chamber inlet and exit water lines. Thermocouples were situated close to the copper block inlet and exit points and in the water flow within the plastic piping. The use of plastic piping reduced conductive heat losses and electrical pick up by the thermocouples. The thermocouples were themselves lagged to further limit heat losses or pick up from the atmosphere. Special attention had to be given to preventing chamber gas entering the water lines through the thermocouple connections. This problem was overcome by setting the thermocouple shafts in araldite.

FIG. 8 FIELD OF PERMANENT MAGNET.

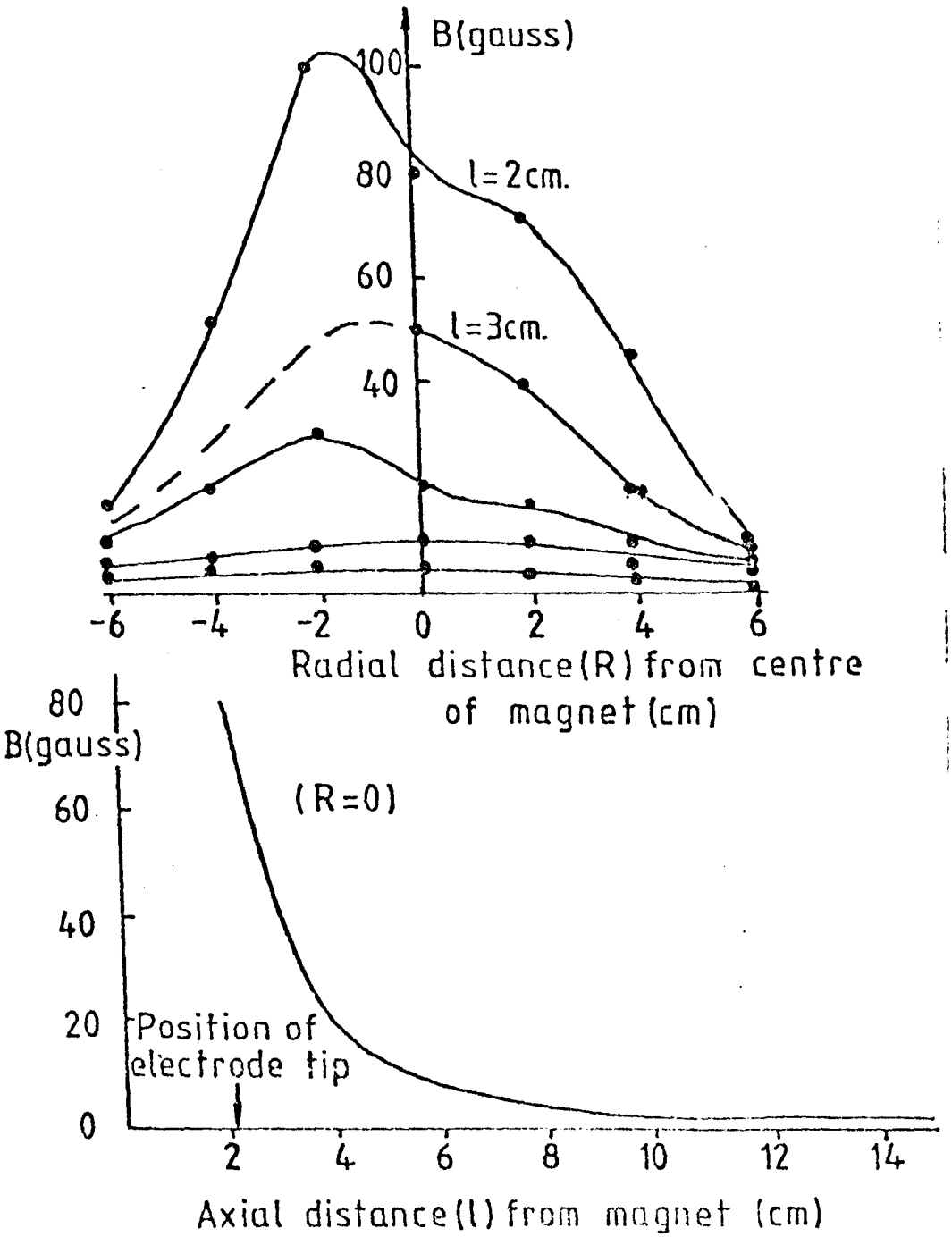

The thermocouples were calibrated and found to have substantially linear characteristics of 41 μV/°C over temperature range 0-100°C. The measurement of interest in this experiment was the difference between the inlet and outlet water temperatures (θ). Compatible thermocouples were therefore connected differentially so as to directly read this value. This method automatically eliminated the effects of changes in the chamber temperature with arc running time and reduced reading errors as only one reading was required. The value of θ was monitored at regular 10 second intervals on a DVM.

The coolant flow rate through the block could be varied by means of a needle value. However, at low flow rates it was found that the arc voltage was sensitive to the flow rate indicating that vapourization was influencing arc behaviour (and hence heat transfer efficiency) in some way. No noticable effect on arc voltage was observed for flow rates above 15g/s. In experiments reported here flows of order 50g/s were often used, giving temperature rises of about 5°C. The precise flow rate was measured by a container and timer method and checked on a number of occasions during the course of an experiment.

The arc was positioned centrally on the block and coolant temperature observed for a period of about 3 minutes. During this time the value of θ was regularly noted and an average value over the steady state period (θ_s) calculated (see figure 9). The total heat carried off by the coolant (Q) was then given by

$$Q = \dot{m}.C_p.\ \theta_s$$

Where $\dot{m}$, is the mass flow rate of water, and C_p is the specific heat of water at constant pressure. C_p is a function of temperature. For measurements made here a value of 4.18 J/Kg°C is appropriate (ref.154). Throughout these experiments arc voltage was also monitored. A detailed description of energy transfer processes could then be given in terms of the process and anode powers (see section 6.1).

Experiments for the range of parameters (i) - (v) were made by systematically changing arc length for a given current. This procedure was repeated for a number of currents. Reproducibility was checked on a

number of occasions and found to be good. (See results given below).

Special attention had to be given to the procedures employed using steel discs situated in the surface of a copper anode. Preliminary experiments were conducted to select a suitable disc size. With small diameter discs gross melting occurred. However, the main problem concerned disc thickness. For discs of 5mm in thickness melting occurred on the back face causing the disc copper contact area to be reduced to a small central region and the side walls. This problem did not occur with discs of 10mm's thickness. The final disc dimensions chosen were 30mm's diameter by 10mm's depth. These were machined so as to give a good fit which locked tight due to expansion when an arc was struck.

To test for heat losses, a copper disc was machined having the dimensions previously given. This was placed in the recess and a number of heat transfer experiments performed. Results from these tests were compared with those obtained on a copper block without a disc (see below). It can be seen that very similar results are found for copper both with and without a disc anode assembly.

Arcing	Arc on surface of copper anode			Arc on copper disc placed in a recess on the surface of a copper anode		
Arrangement ℓ=6mm, I=100A Argon, 1 BAR	P (KW)	Q (KW)	η (%)	P (KW)	Q (KW)	η (%)
No magnet	1.55 (1.48)*	1.23 (1.20)*	77 (81)*	1.42	1.11	79
Magnet (south face up)	1.55	1.11	74	1.55	1.11	74
Magnet (south face down)	1.69	1.28	76	1.52	1.14	75
Ave.	1.60	1.21	76	1.50	1.12	76

(* Results obtained on a separate occasion)

Slightly lower process power, P, (and hence anode power, Q) are observed for arc running on a disc. This is attributed to a small degree of disc lifting thereby shortening arc length. However, process efficiency is unaffected by this behaviour.

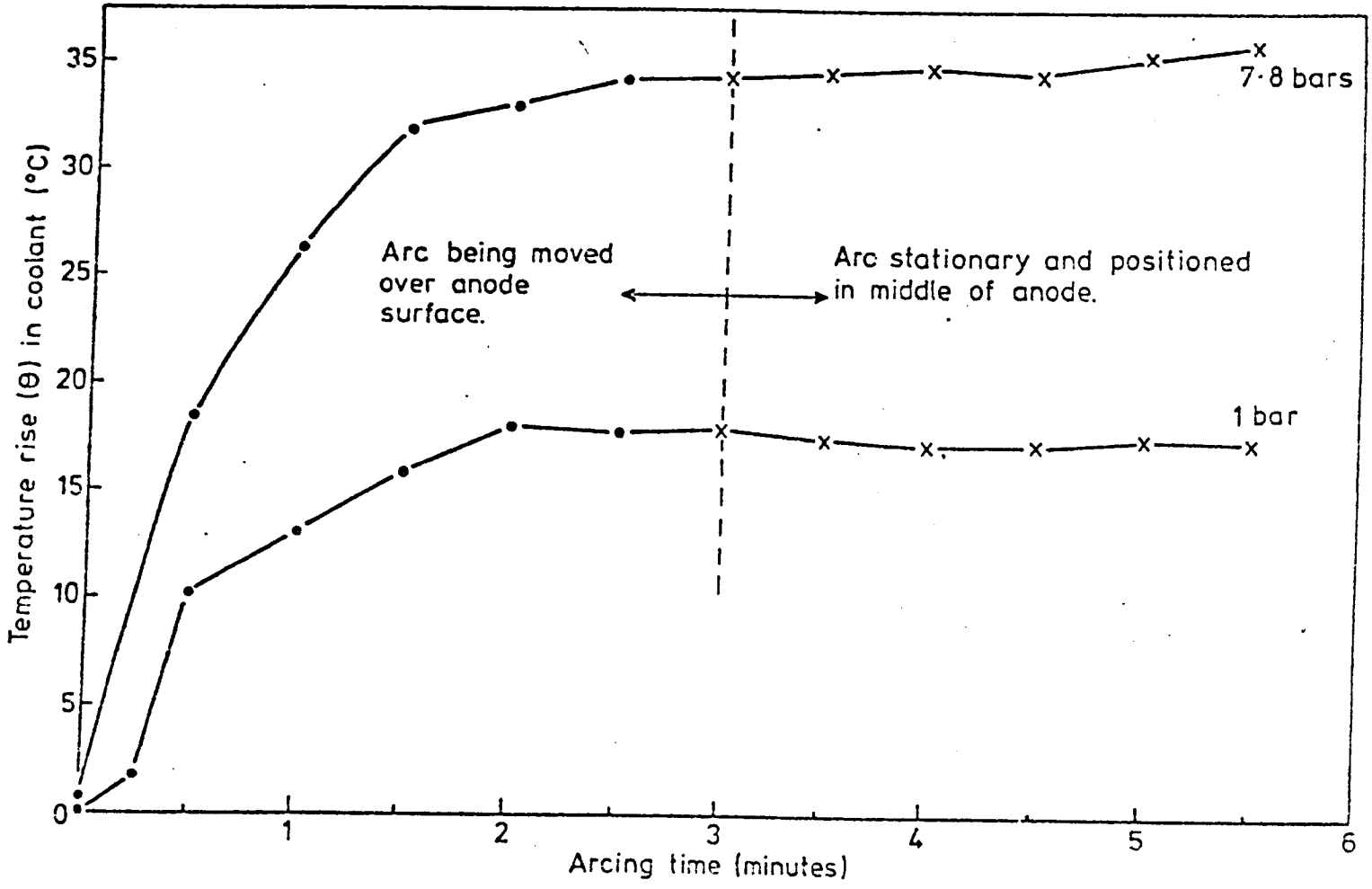

FIG. 9. TYPICAL COOLANT TEMPERATURE RISE AS A FUNCTION OF ARCING TIME ON A COPPER ANODE FOR CONSTRICTED TIG ARC.

Errors involved in obtaining Q are of a number of types. These are primarily associated with (i) reproducing a given arc condition (ii) measuring coolant flow rate and temperature rise (iii) the assignment of system constants i.e. thermocouple calibration and specific heat of water. The last error is of a systematic nature and in any case small. For a given arcing condition the error (ΔQ) in Q is then

$$\Delta Q = \pm Q \sqrt{\left(\frac{\Delta \dot{m}}{\dot{m}}\right)^2 + \left(\frac{\Delta \theta}{\theta}\right)^2}$$

To minimise the error ($\Delta \dot{m}$) in $\dot{m}$ measurements were made over a long period of time (60 ± 1)s and for large volumes (3000 ± 30) cm^3 i.e. $(\Delta \dot{m}/\dot{m}) \sim 0.026$ or less than 3%. The error ($\Delta\theta$) in θ is associated with fluctuations in temperature and an instrument reading error. This was estimated as $0.1^{o}C$. The lowest recorded values of θ for TIG were of order $2.5^{o}C$ while the largest were about $10^{o}C$. Thus

$$\text{(low Q)} \quad 4\% \gtrsim \frac{\Delta\theta}{\theta} \gtrsim 1\% \quad \text{(high Q)}$$

These figures indicate that $\Delta Q/Q$ is less than $\pm 5\%$ for the lowest heat inputs and less than $\pm 3\%$ for the highest i.e. Taking Q~ 1KW as a low heat input and Q $\sim$ 4KW as a high heat input gives the respective errors as $\pm 50W$ and $\pm 120W$. These estimates take it for granted that a given arc condition can be accurately reproduced. Quantifying this assumption is difficult but arc voltage changes may be reasonable taken as gauging reproducibility. At low pressures reasonably good reproducibility exists but this may deteriorate with pressure (see section 4) due to increases in column field strength and arc instabilities.

3.6.2. Distribution of Current at the Anode

3.6.2.1. Method

Measurements were made using the split copper anode arrangement previously described. The blocks were electrically isolated and separated by an 0.1mm air gap at the splitting plane. The current to each block was monitored by measuring the voltage dropped across calibrated shunts connected in the earth lines from each block (see figure 10). The procedure adopted was to move an arc uniformly (at a speed of 77mm/s) from one anode segment to the other while simultaneously

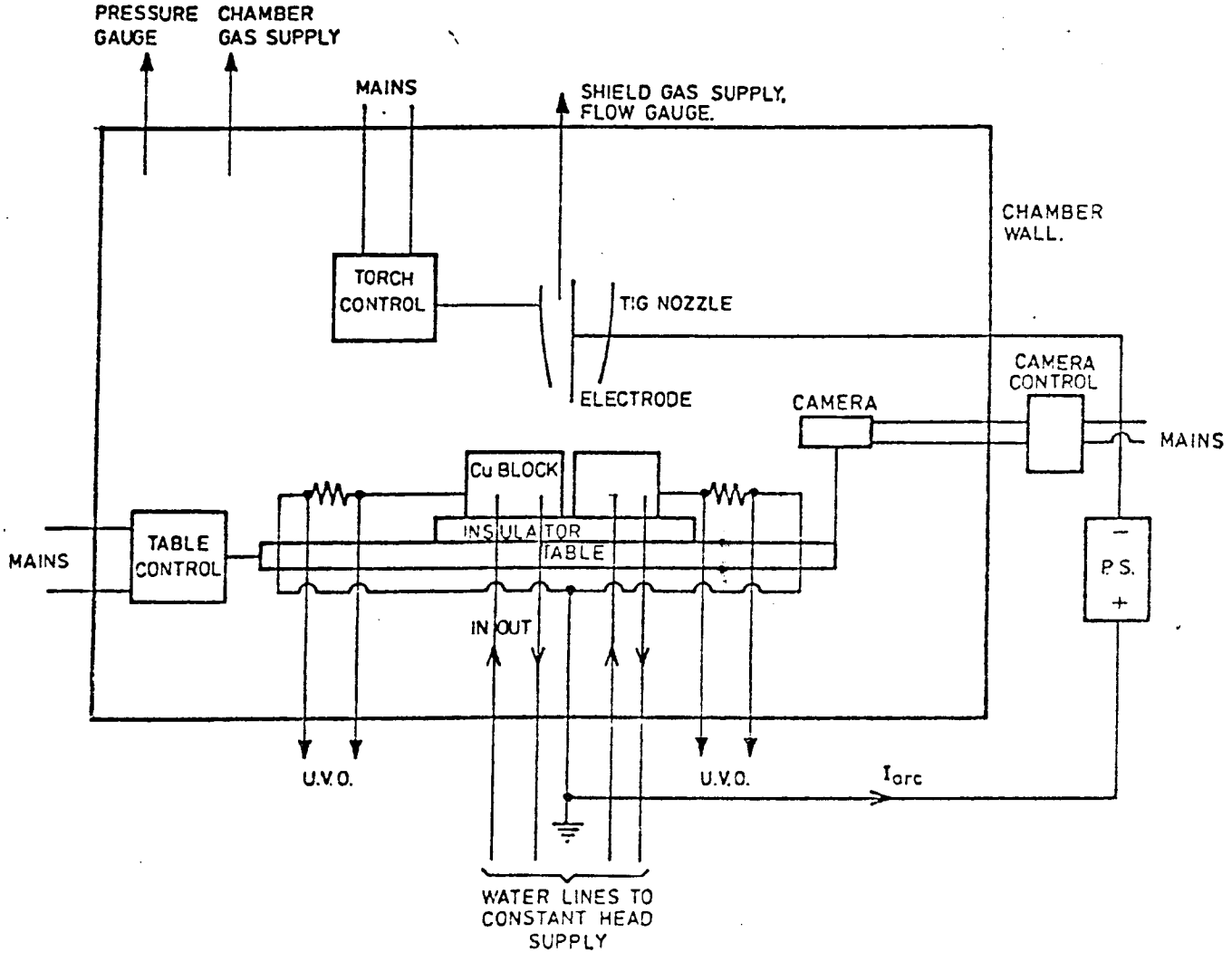

FIG.10 SCHEMATIC REPRESENTATION OF EXPERIMENTAL ARRANGEMENT.
(CURRENT DENSITY MEASUREMENTS)

recording the current to each block on a UVO. To increase the lateral UVO trace resolution, high paper speeds were employed (i.e. 200mm/s). In this manner traces of order 1m in length were obtained. A typical trace for a low shielding gas flow rate is shown in figure 11. It can be seen that the trace is symmetrical and that the arc moves smoothly over the slit. This indicates that the slit has no influence on measured current distributions. However, this was not always found to be the case. At low currents (50A>) the arc root moved in a discontinuous manner. This was often observed to give rise to a discontinuous current trace i.e. the current then appeared on one or other of the blocks but not on both. It should be noted that this observation provides a method of quantifying arc modes. At high shielding gas flow rates the arc current to each segment was found to have a fluctuating component (see section 3.6.3). For such cases a mean line was constructed through the oscillations. At very high shielding gas mass flow rates such an approach was not possible.

Throughout these experiments photographic arc images were taken perpendicular to the slit direction (i.e. along the line of motion) while visual observations were made along the slit direction. Arc boundaries obtained by photographic means were compared with those found electrically at the anode and found to be in reasonable agreement (see section 4). These electrical measurements provided a means of investigating changes in the behaviour of arc electrical boundary at the anode and of directly calculating the mean anodic current density. Current boundaries could be determined with a much greater accuracy than heat transfer boundaries previously reported. The boundary was taken to be associated with the position at which current fell below 0.3A. This is associated with a possible error of up to 5% (ref.83) in boundary location. The definition of the arc boundary was enhanced by using a transistorized power supply which had virtually no ripple but open circuit voltage limitations meant that this power supply could only be used for TIG experiments. Constricted TIG arcs were examined using a Miller power supply with much more current ripple. A mean line was then plotted through the ripple to obtain the average current (see figure 12).

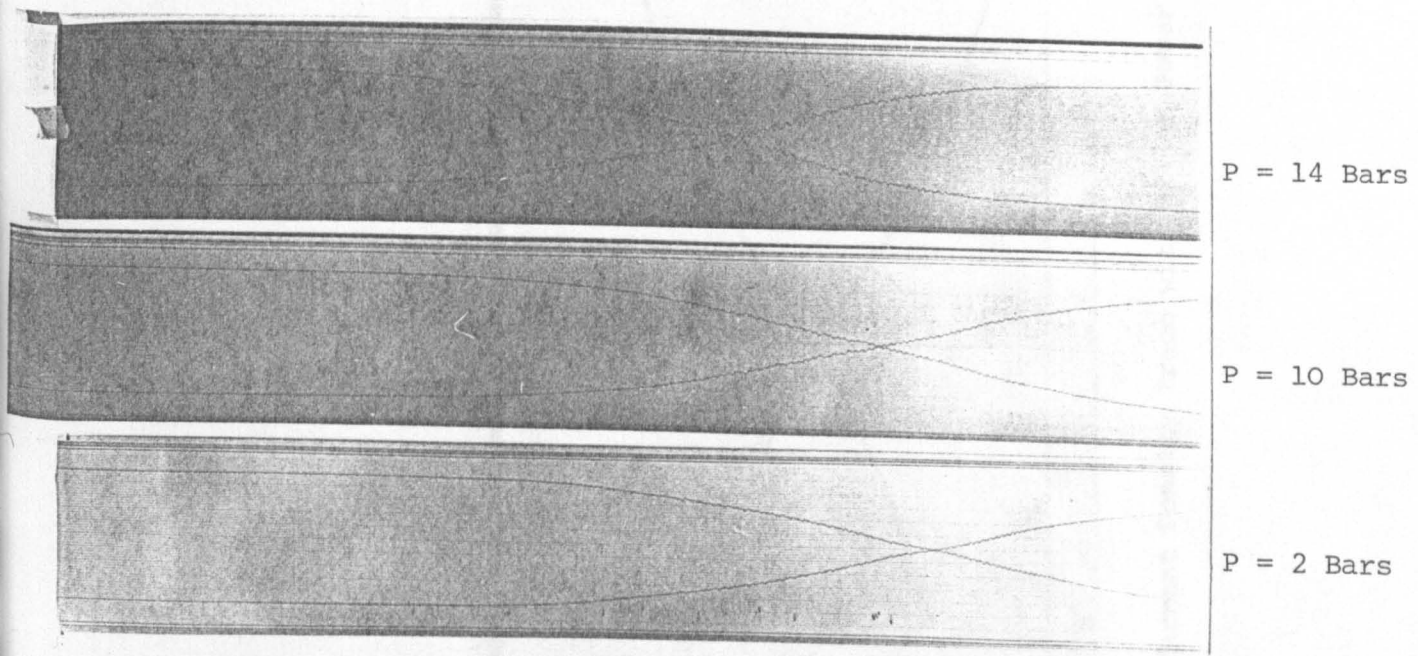

Figure 11 Typical UVO Traces Obtained During Current Density Measurements (No Shield)

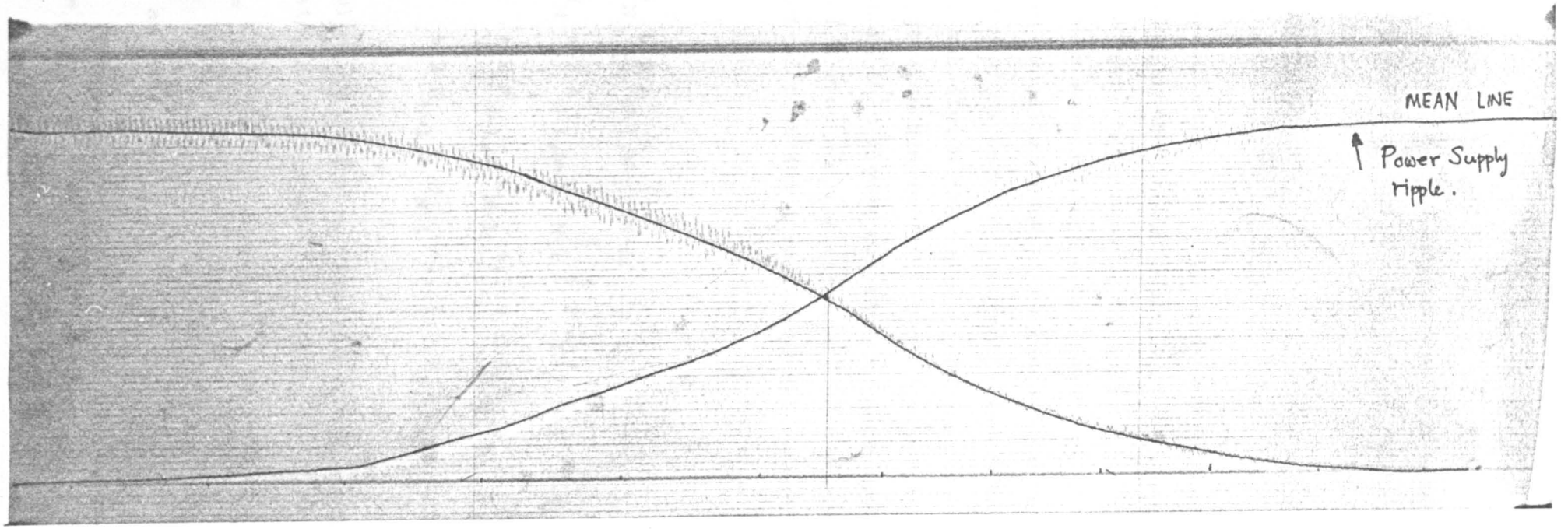

Figure 12 Arc Plasma (constricted TIG) Current Density Trace with Miller Power Supply

Experimental investigations of current density were confined to chamber C-I and therefore limited to pressures of below 19 bars. The main variables considered were ambient pressure and shielding gas flow rate. In these experiments secondary variables were regarded as arc length and current in TIG welding with the additions of shielding gas flow rate and orifice diameter in plasma welding.

3.6.2.2. Treatment of Experimental Measurements

The radial distribution of current may be obtained from experimental measurements by means of an Abel transformation. This transformation involves the use of integral techniques. However, it is found appropriate here to use a more intuitive approach. It is assumed, as usual, that the arc is radially symmetric. The arc is then considered as a series of N annular regions each of constant current density. Further divisions are made to sub-divide the current carrying zone into regions with co-ordinates (i,j) (see figure 13). The current (ΔI) through each of the N slices shown in this figure can then be expressed in terms of the current density of a ring and the areas Aij of the elements. A slice is defined as a region of constant j enclosing all values of $i \geq j$. Then

$$\begin{aligned}
\Delta I_N &= 2 A_{N,N} J_N \\
\Delta I_{N-1} &= 2 A_{N,N-1} J_N + 2 A_{N-1,N-1} J_{N-1} \\
\Delta I_{N-2} &= 2 A_{N,N-2} J_N + 2 A_{N-1,N-2} J_{N-1} + 2 A_{N-2,N-2} J_{N-2} \\
\Delta I_M &= 2 A_{N,M} J_N + 2 A_{N-1,M} J_{N-1} + \ldots + 2 A_{M,M} J_M \\
\Delta I_1 &= 2 A_{N,1} J_N + 2 A_{N-1,1} J_{N-1} + \ldots + 2 A_{1,1} J_1
\end{aligned} \qquad (38)$$

When the splitting plane is at i = M, then the total current (I_M) to the anode segment enclosing all elements with $i \geq M$ is

$$I_M = \Delta I_N + \Delta I_{N-1} + \ldots + \Delta I_M$$

This may be written as

$$I_M = 2 \sum_{i=M}^{i=N} \sum_{j=M}^{j=i} A_{ij} J_i \qquad (39)$$

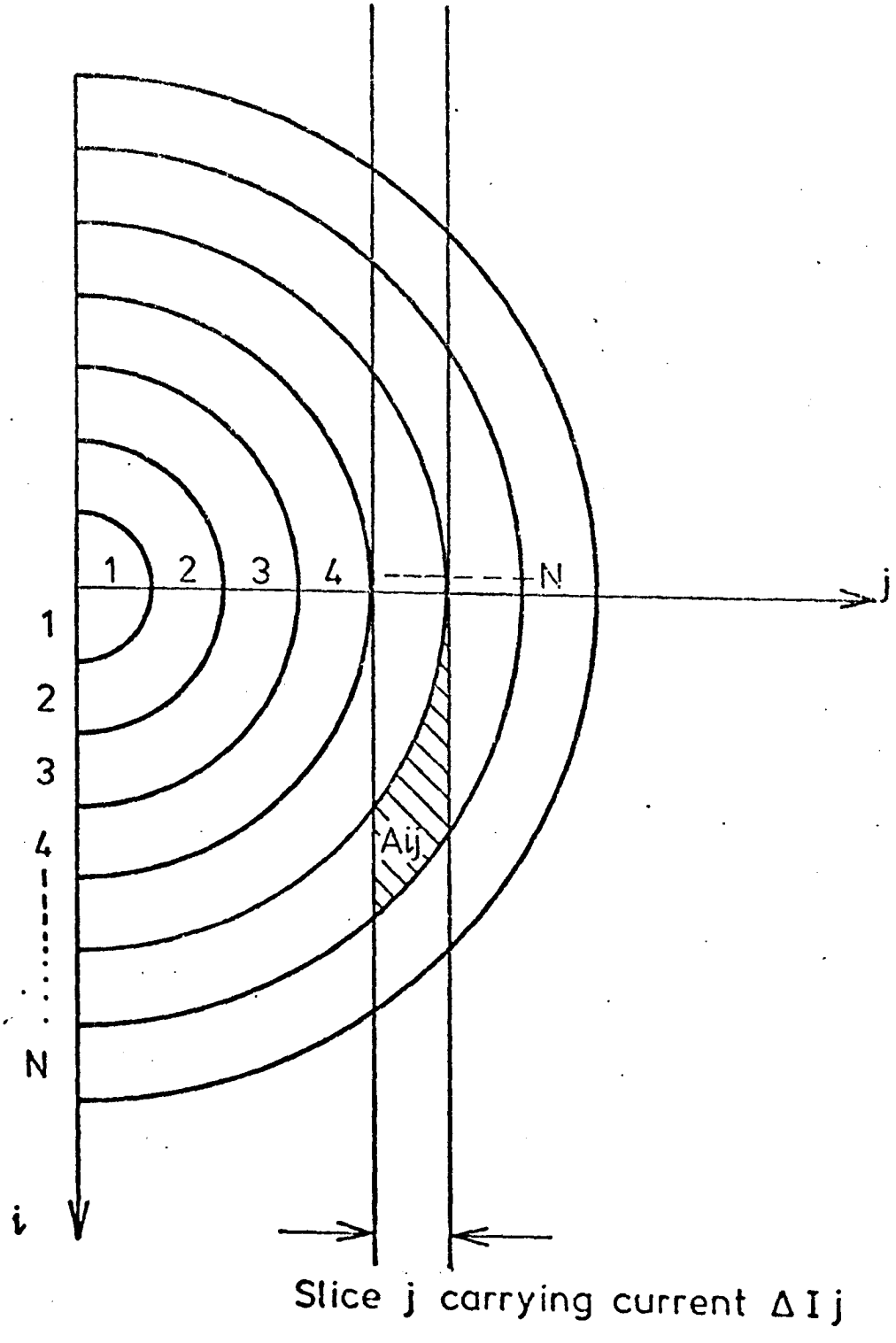

FIGURE13. ARC ZONES (i, j) USED FOR ABEL TRANSFORMING CURRENT DENSITY DATA

This expression is equivalent to a set of N simultaneous equations ($N \geq M \geq 1$) with N unknowns (J_i's for $N \geq i \geq 1$) and may therefore be solved for the J_i's if the I_M's are known. The area elements A_{ij} are obtained in appendix 2 for various values of N. The procedure employed was to divide the arc into N regions and measure the corresponding values of I_M at the centre of each region. The set of equations 38 were then solved for J using a programmable calculator. It was found that distributions were relatively insensitive to the value of N adopted. Measurements using N=5 and N=9 yielded similar results. N was therefore generally taken as 7.

Errors in the input data for I may lead to significant errors in the output, J. (i.e. because the solution of seven simultaneous equations is required). For this reason large scale data representations were employed. The lateral extent of a trace was of order 1m while current could be read to within 0.3%. This was possible because of the highly stable transistorized power supply used (as can be seen from UVO traces). In plasma experiments the degree of rectification was less. Checks on the consistency of the above technique were performed by integrating the experimental current distributions and comparing the current obtained with the set current. For numerical purposes the following approximation was employed:

$$I = \frac{\pi R^2}{N} \sum_{i=0}^{i=N} (2i+1)\, J_i \qquad (40)$$

Procedures described above make no assumptions about the current distribution other than to assume radial symmetry. It is often found that the distribution is of an approximately Gaussian nature (see section 6.2). This suggests a considerable simplification in the analysis of current density data. It is then found possible to obtain the distribution from one simple measurement i.e. the gradient of the current trace at the point where the centre of the arc crosses the splitting plane. This technique has also been used to examine current traces. A comparison with the previous results then provides a measure of deviations from Gaussian conditions. The simplification described above is now considered mathematically.

The current I(x) to a segment when the centre of the arc is at a distance x from the splitting plane (see figure 14) is given by geometric considerations as

$$I(x) = 2\int_{x}^{R} J(r).\cos^{-1}\left(\frac{x}{r}\right).r.dr \qquad (41)$$

where R is the arc radius. Differentiating equ.41 gives

$$\frac{dI(x)}{dx} = 2\int_{x}^{R} \frac{J(r).r.dr}{\sqrt{r^2-x^2}} \qquad (42)$$

Considering the gradient at the splitting plane (i.e. x=0 in equ.42) gives

$$\frac{dI}{dx}(o) = 2\int_{o}^{R} J(r).dr \qquad (43)$$

If J(r) is given a Gaussian form then

$$J(r) = J_o.e^{-ar^2}, \quad R \to \infty \qquad (44)$$

where J_o is the axial current density and 'a' describes the radial behaviour of the distribution. J_o and 'a' may be related by considering the total arc current (I). i.e.

$$I = \int_{o}^{\infty} 2\pi.J.r.dr = \frac{J_o.\pi}{a} \qquad (45)$$

Substituting 44 and 45 into 43 gives

$$\frac{dI}{dx}(o) = 2J_o\int_{o}^{\infty} e^{-ar^2}\,dr = \sqrt{I\,J_o} \qquad (46)$$

or re-arranging also gives

$$J(o) = \frac{1}{I}\left[\frac{dI(o)}{dx}\right]^2 \qquad (47)$$

This result has also been used to analyse current distributions (see section 6.2).

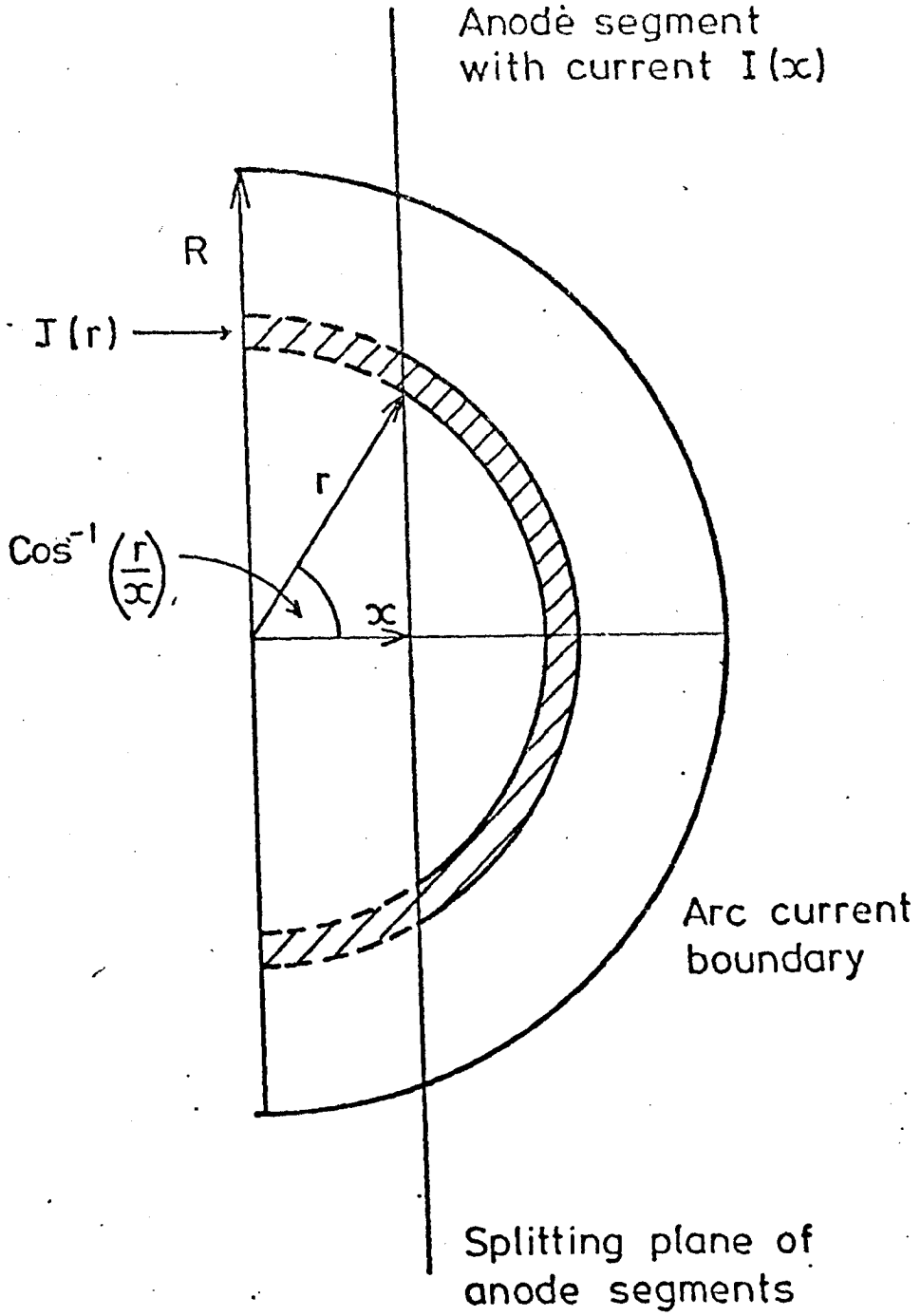

FIGURE 14. GEOMETRY USED FOR CALCULATING I(x)

3.6.3. Arc Stability

Arc stability is generally difficult to define and quantify. This is because of the many sided nature of stability. Stability may refer to behaviour in a particular region of an arc without affecting all other arc regions or it may refer to the behaviour of a particular arc property without significantly affecting all other arc properties. It is however, generally agreed that an arc column moving in an erratic manner is an unstable welding heat source. On classical grounds such behaviour is not regarded as unstable as the arc returns to its initial equilibrium position i.e. it oscillates without being extinguished. In this section arc column motions are investigated and 'stability' is quantified.

3.6.3.1. Method

Stability was quantified by measuring the movement at the anode of an arc root when an arc was subjected to the disturbing influences of pressure and shielding gas flow. The procedure was identical to that used for current density measurements and UVO traces obtained from that work are used here. At high shielding gas flow rates and ambient pressures UVO traces showed fluctuations in the current collected by each anode. These were associated visually and photographically (see figure 15) with a movement of the arc root over the anode surface. The arc root appeared diffuse and at no time exhibited the anode spot mode characteristic of low current arcs (or very high table speeds). This is supported by the generally smooth appearance of the traces, i.e. no discontinuous jumps from one segment to another. Fluctuations were found to increase with shielding gas flow rate (figure 16) at a given pressure and this behaviour became more marked at higher pressures. These factors were therefore taken to represent the causal behaviour of the observed phenomena.

3.6.3.2. Treatment of Experimental Measurements

Fluctuations in current to an anode segment are interpreted in terms of an oscillation of the arc perpendicular to the splitting plane. UVO traces contain information about this component of motion. In particular

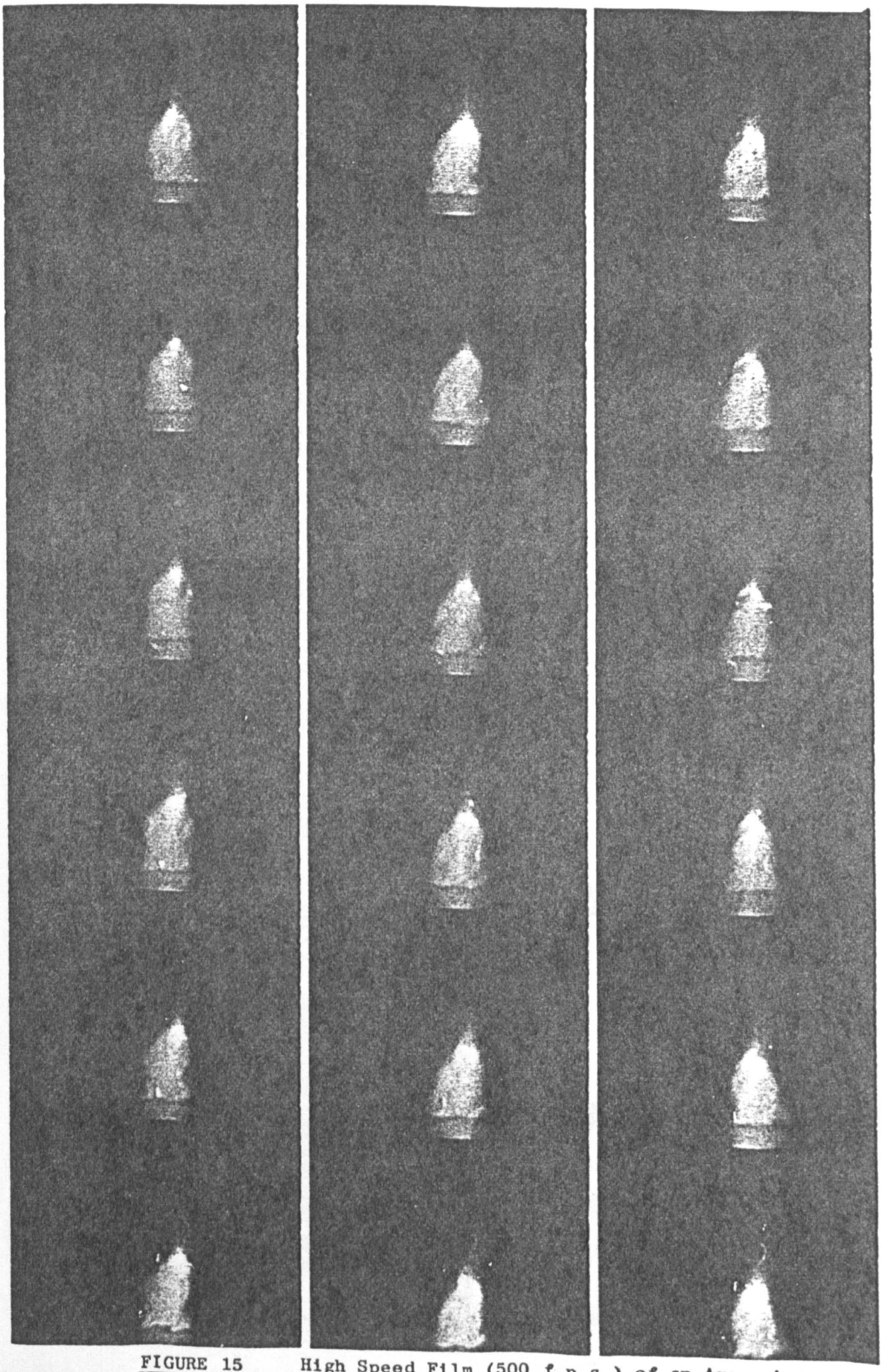

FIGURE 15 High Speed Film (500 f.p.s.) of an Argon Arc in a Turbulent Shielding Gas Flow on a Copper Anode (P = 14 bars, flow setting of 4, 100A, 5 mm)

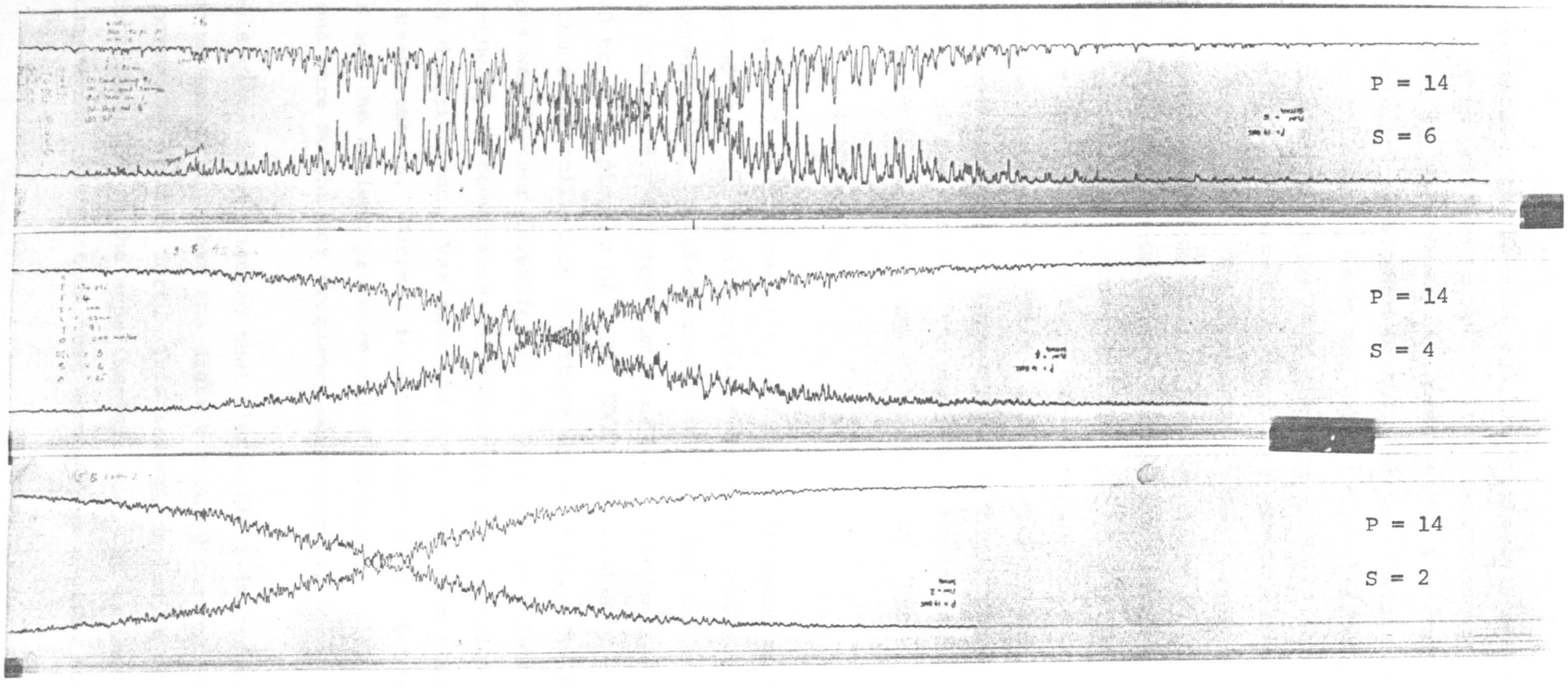

Figure 16 Influence of Gas Flow on the Appearance of UVO Traces Obtained During Current Density Measurements at 14 Bars

these traces contain information about the component of the oscillation amplitude perpendicular to the slit and the frequency spectrum of oscillations. It is possible to measure the instantaneous lateral displacement of an arc relative to its mean position if the assumption of cylindrical symmetry is assumed to hold for small disturbances. This assumption can be substantiated on the basis of results obtained here. An oscillation is taken to occur when the current moves through a constructed mean line, representing the time averaged current, and then back again (see figure 17). The frequency is then simply defined as the number of such oscillations divided by the time taken to cross the slit. Consider figure 18. The instantaneous current to a block at time t_1 has the same value as the mean current at time t_2. This indicates that the same area of the arc appears on the block at t_1 as would occur at time t_2 if no disturbances existed. This can only occur if the arc moves from its mean position by a distance ε in a direction perpendicular to the slit where ε is the distance the table would move in the time t_2-t_1. If V_T is the table speed and V_P the UVO paper speed then

$$\varepsilon = x_p . V_T/V_P$$

Where x_p is spatial separation of t_1 and t_2 in UVO paper units. It should be noted that the total displacement of the arc cannot be found as the component along the direction of the slit has no influence on the current monitored. A large number of measurements of x_p were taken of each UVO trace (typically of order 100). These values were used to calculate the mean oscillation amplitude for a trace. The form of the oscillations was further investigated by plotting oscillation amplitude against frequency of occurrence and comparing such distributions with the Poisson distribution. Variance was considered from standard deviation measurements. Correlations were then sought between these parameters and the ambient pressure and shielding gas flow. Similar correlations were sought for frequency measurements.

The analysis given above assumed that fluctuations in arc current were due to arc movements and that the distribution of current was unaffected by small movements of this sort. This assumption can be verified by further consideration of the experimental data. It is possible to predict the current fluctuation that accompanies a given arc movement if

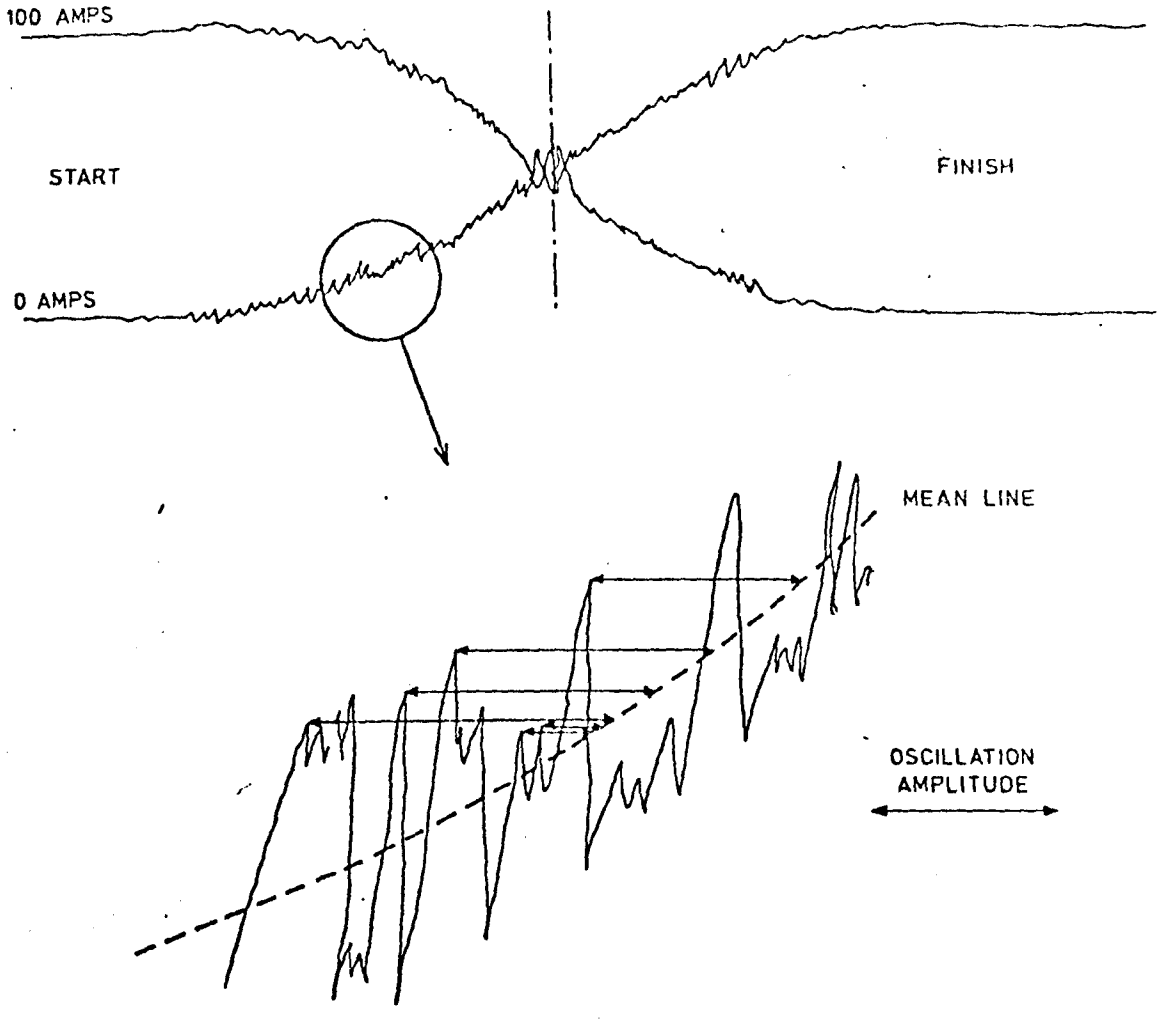

FIG. 17. SCHEMATIC OF U.V.O. TRACE INDICATING THE MEASUREMENT OF OSCILLATION AMPLITUDE USED HERE.

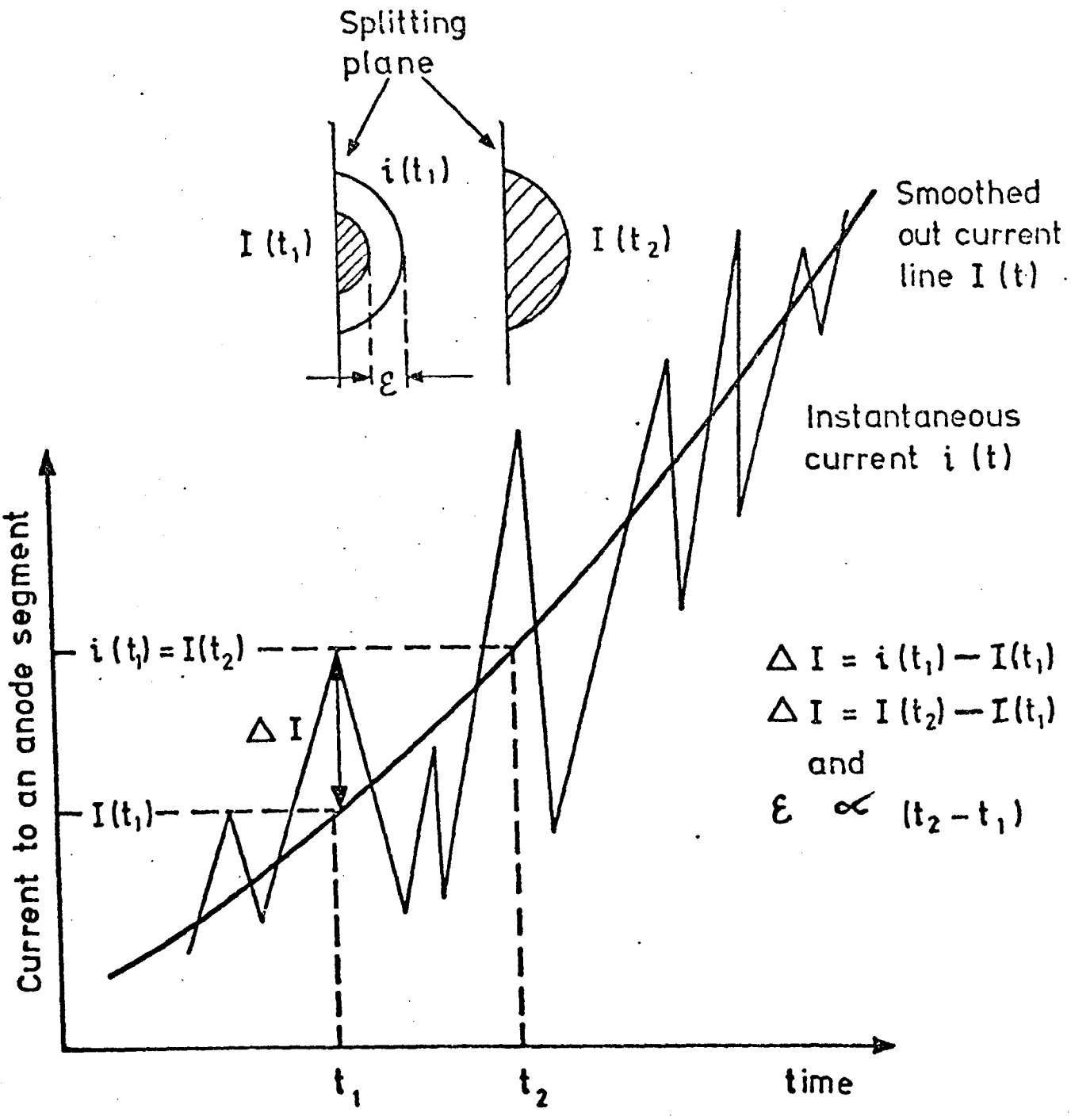

FIGURE.18. RELATIONSHIP BETWEEN CURRENT OSCILLATION AMPLITUDE AND ARC MOVEMENT.

the distribution of current is known. Current fluctuations are calculated here on the basis of experimentally observed arc movements and current density profiles. These results are then compared with the experimentally observed current fluctuations associated with the corresponding arc movements. The starting point for this analysis is equation 42 i.e.

$$\frac{dI(x)}{dx} = 2\int_x^R \frac{J(r).r.dr}{\sqrt{r^2-x^2}}$$

Integrating gives

$$I(x_1) - I(x_2) = 2\int_{x_2}^{x_1} dx \int_x^R \frac{J(r).r.dr}{\sqrt{r^2-x^2}} \qquad (48)$$

This expression gives the change in current to an anode segment when the axis of the arc is moved from the splitting plane distance x_2 to x_1. This is illustrated in figure 19. Clearly the left hand side may be interpretated as the fluctuation in current ($\Delta I = I(x_1) - I(x_2)$) when an oscillation of amplitude $\varepsilon = x_1 - x_2$ occurs. All of the factors on the right hand side of this expression are known and so ΔI can be calculated and compared to experimental values. A great many oscillations occur ($\sim$100) and so the evaluation of all traces using this expression would require thousands of long and detailed computations. A simplification is obtained by considering only those distributions that are found to be well represented by Gaussian profiles. The integral then becomes

$$\Delta I = 2J_o\int_{x_2}^{x_1} dx \int_x^R \frac{\exp(-ar^2)r.dr}{\sqrt{r^2 - x^2}} \qquad (49)$$

$$\therefore \quad \Delta I = 2J_o\int_{x_2}^{x_1} dx.\ \exp(-ax^2)\int_o^{\sqrt{R^2-x^2}} \exp(-aZ^2)\ dZ \qquad (50)$$

$$\therefore \quad \Delta I = \frac{J_o\sqrt{\pi}}{a}\int_{x_2\sqrt{a}}^{x_1\sqrt{a}} \exp(-Z^2)\ \mathrm{erf}\ (\sqrt{aR^2-Z^2})\ dZ \qquad (51)$$

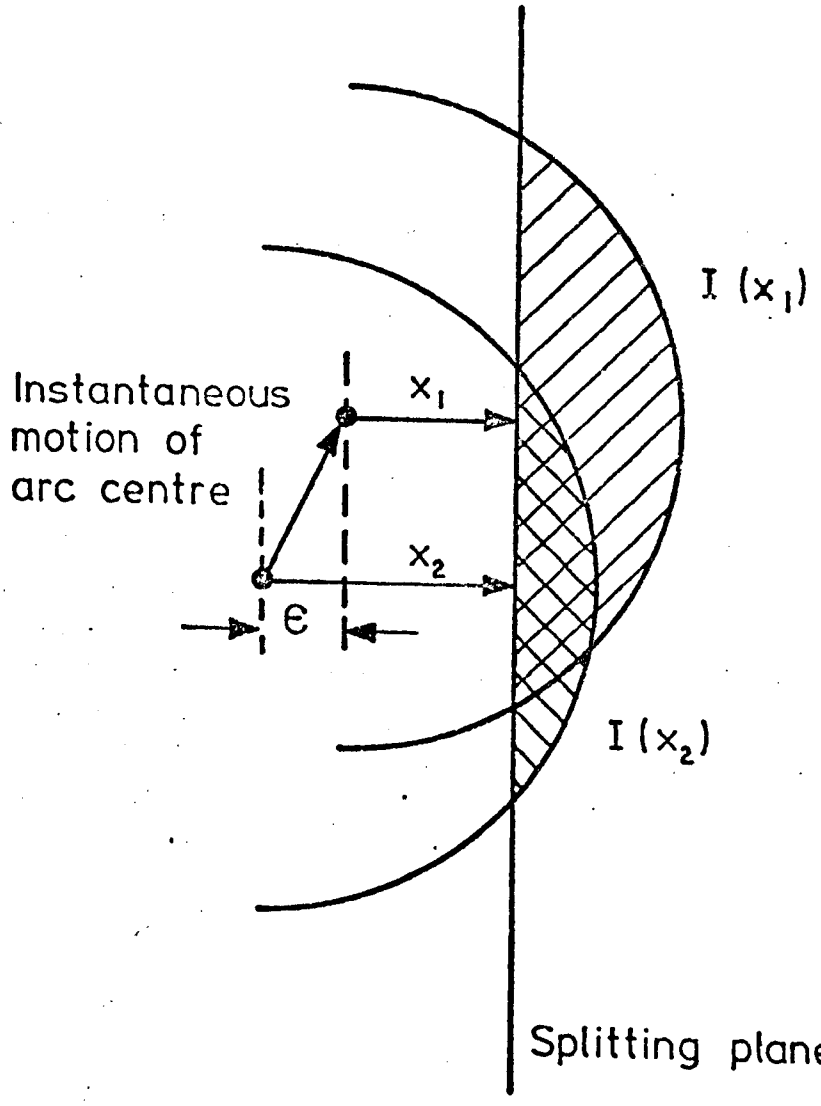

FIGURE 19. FLUCTUATIONS IN THE CURRENT TO AN ANODE SEGMENT.

Substituting for J_o and 'a' gives

$$\Delta I = \frac{I}{\sqrt{\pi}} \int_{x_2\sqrt{a}}^{x_1\sqrt{a}} \exp(-z^2)\ \mathrm{erf}\ (\sqrt{aR^2-z^2})\ dz \qquad (52)$$

The last factor in the integrand has well documented (e.g. see data of 105) properties and is known to become effectively unity when $(\sqrt{aR^2-z^2})$ is greater than 1.4 (the maximum error in this approximation is 5%). It is shown below that when suitable values of Z are chosen (i.e. suitable limits on x_1 and x_2) this expression may be replaed by unity. Consider again the total current flowing through the arc core and let the current within the circle R be I $(R \geq r \geq 0)$. Then

$$I(R \geq r \geq 0) = \int_o^R J.2\pi r dr = \frac{J_o \pi}{a} \ (1 - \exp(-aR^2)) \qquad (53)$$

$$\therefore \qquad I(R \geq r \geq 0) = I(1 - \exp(-aR^2)) \qquad (54)$$

If R is taken to represent a boundary through which 95% of the arc current flows then equation 54 gives

$$a.R^2 = \ln 20$$

Returning to the error function and substituting for aR^2 shows that it may be replaced by unity when

$$\ln 20 - z^2 \gtrsim 1.4 \qquad \text{i.e. } 1 \geq z$$

but $x_1\sqrt{a} \gtrsim z \gtrsim x_2\sqrt{a}$

Thus $1 \gtrsim x_1\sqrt{a} \gtrsim x_2\sqrt{a}$

Substituting for 'a' gives the condition for the error function approximation as

$$R/\sqrt{\ln 20} \gtrsim x_1 \gtrsim x_2$$

we can now write equation (52) as

$$\Delta I = \frac{I}{\sqrt{\pi}} \int_{x_2\sqrt{a}}^{x_1\sqrt{a}} \exp(-z^2)\ dz \qquad (55)$$

This may be written in terms of error functions. Substituting for x_1, x_2 and 'a' then gives

$$\Delta I = \frac{I}{2}\left[\operatorname{erf}\left\{\frac{(x+c)\sqrt{\ln 20}}{R}\right\} - \operatorname{erf}\left\{\frac{x\sqrt{\ln 20}}{R}\right\}\right] \qquad (56)$$

Experimental results have been analysed using expression 56 and in accordance with the analysis, only points within a distance of $R/(\ln 20)^{\frac{1}{2}}$ of the trace crossing point have been used (i.e. a little over a half of each trace).

A reasonably representative trace was picked (9,6 bars, Shield Setting 2) to calculate ΔI. Corresponding values of x and ε are given in Table 5 along with calculated and measured values of ΔI. Figure 20 shows this result graphically. It can be seen that good agreement exists between calculated and measured current fluctuations. This validates the analysis described above.

3.6.4. Electrical Structure of the Column

An electrostatic probe technique was used to measure arc voltage at local axial positions between the anode and cathode. The true arc voltage can then be obtained by subtracting a contact potential, existing between probe and plasma from measured values. Details of procedure adopted, experimental design and interpretation of probes traces are given below.

3.6.4.1. Experimental Design

The approach adopted was to sweep a fine tungsten (99.97% purity) probe through the arc and monitor the floating probe voltage with respect to the anode with a high impedance instrument. The experimental equipment consisted essentially of a probe radiating from the side of a circular tufnol turntable mounted on the axis of a small DC motor. Voltage was picked up by the carbon brush in contact with an annular brass disc situated in a recess within the table. Good electrical contact was ensured by spring loading and carbon brush. The signal was then examined on an oscilloscope fed into a transient recorder, stored, and subsequently played back onto a UVO recorder to obtain a permanent

No.	x** (mmx10^{-2})	ε** (mmx10^{-2})	†erfA (x10^{-1})	†erfB (x10^{-1})	I*(cal) (A)	I(measured) (A)
1	4.46	1.27	0.68	0.35	1.7	2
2	7.01	2.55	1.24	0.58	3.3	4
3	9.55	1.27	0.98	0.79	1.0	2
4	11.46	0.64	1.05	0.94	0.6	1
5	15.28	0.96	1.46	1.25	1.1	1.5
6	16.56	1.59	1.80	1.36	2.2	2.5
7	24.20	3.82	2.89	1.96	4.7	6
8	26.10	2.87	2.94	2.14	4.0	4.5
9	29.30	3.82	3.38	2.38	5.0	6
10	33.12	3.18	3.61	2.68	4.7	5
11	33.75	3.18	3.61	2.68	4.7	5
12	36.30	1.59	3.23	2.93	1.5	2.5
13	37.57	2.23	3.47	3.03	2.2	3.5
14	40.12	1.91	3.70	3.23	2.4	3
15	41.39	2.23	3.85	3.32	2.7	3.5
16	46.49	1.27	4.00	3.70	1.5	2
17	49.04	1.59	4.30	3.89	2.1	2.5
18	52.86	2.23	4.82	4.16	3.3	3.5
19	55.41	1.27	4.74	4.34	2.0	2
20	57.32	1.59	4.88	4.48	2.0	2.5
21	59.86	0.96	4.95	4.66	1.5	1.5
22	63.68	1.27	5.25	4.91	1.7	2.
23	65.59	1.59	5.52	5.05	2.4	2.5
24	68.78	2.55	6.02	5.25	3.9	4
25	72.60	1.91	6.06	5.49	2.9	3
26	70.42	2.55	6.46	5.72	3.7	4
27	78.33	1.27	6.28	5.83	2.3	2
28	80.88	2.23	6.75	5.99	3.8	3.5
29	82.15	1.27	6.39	6.07	1.6	2
30	83.43	1.59	6.65	6.13	2.6	2.5
31	85.34	1.59	6.81	6.26	2.8	2.5
32	86.61	1.27	6.78	6.30	2.4	2
33	87.25	1.27	6.86	6.35	2.6	2
34	91.71	2.55	7.50	6.59	4.6	4
35	93.62	1.27	7.15	6.68	2.4	2
36	94.89	2.23	7.62	6.75	4.4	3.5
37	99.35	0.06	7.13	6.98	0.8	1
38	99.98	0.06	7.28	7.00	1.4	1
39	102.53	0.06	7.42	7.13	1.5	1
40	105.72	1.27	7.81	7.28	2.7	2
41	108.90	1.27	7.89	7.42	2.4	2
42	110.81	1.27	7.97	7.51	2.3	2
43	113.36	0.06	7.76	7.61	0.8	1
44	114.00	1.91	8.27	7.63	3.2	3
45	115.27	2.87	8.73	7.68	5.3	4.5
46	116.54	1.59	8.31	7.74	2.9	2.5
47	119.09	1.27	8.36	7.83	2.7	2
48	121.00	1.91	8.44	7.90	2.7	3
49	123.55	1.27	8.51	7.99	2.6	2
50	127.37	3.18	9.05	8.14	4.6	5

Table 5 Predicted and measured current fluctuations on a split copper anode at 9.8 bars (flow setting 2)

* See equation 56

** x = position of an oscillation from centre of trace such that $(R/\sqrt{\ln 20}) \geq x + \varepsilon$, i.e. $1.36 \geq x + \varepsilon$

Electrical Radius of Current Distribution (R) = 2.36mm (see Fig.19)

** ε = oscillation amplitude at x (see Fig.19)

† A = $(x + \varepsilon)\sqrt{\ln 20/R}$

† B = $x\sqrt{\ln 20/R}$

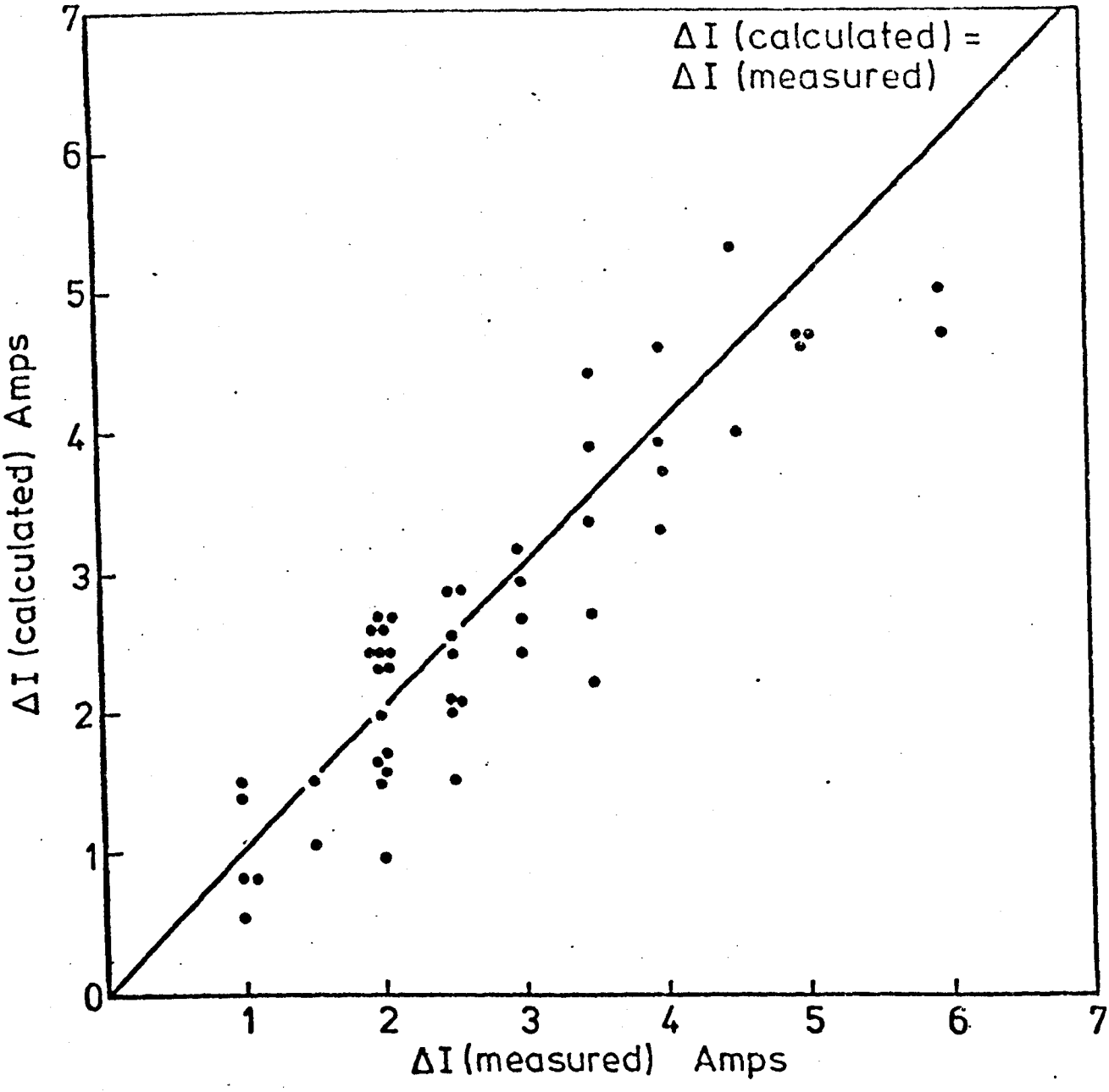

FIG. 20. PREDICTED AND MEASURED CURRENT FLUCTATIONS (ΔI) AT THE SPLITTING PLANE OF A COPPER ANODE. (ARGON TIG ARC, 100 AMPS, 3·2mm ARC LENGTH, 10 BARS, FLOW SETTING OF 4.)

record. This arrangement is shown in figure 21 and schematically in figure 22.

The probe passed through the arc in a planar manner (i.e. direction of motion is nearly the same on entry to the arc as at exit from the arc). To ensure this the distance between the turntable axis and that part of the probe entering the arc was maintained at more than 10 arc diameters. Probe stiffness was enhanced by encasing that part of the probe radiating from the table in a glass sleeve. High speed photographic studies confirmed that probe motion through the arc was essentially straight line. Throughout these experiments the table speed could be continuously varied by means of a ten turn potentiometer regulating the motor power.

The probe motor was mounted on the same vertical table as the welding torch so that the arrangement was fixed with respect to the welding torch.

3.6.4.2. Preliminary Investigations'

Tests were made to determine the effect of probe speed and size on measured probe voltages. It was found possible to employ a probe diameter of 0.2mm without encountering noticeable probe damage. This size was used in all experiments reported here. Voltage measurements were made for a range of probe speeds and examples shown in figure 23. At low speeds noticable probe ablation occurred and this was mirrored in the amplitude of the voltage trace. However, the voltage became independent of speed above about $0.5ms^{-1}$. This corresponds to a transit time through the arc of about 10ms. In subsequent tests the probe speed through the arc was greater than $1ms^{-1}$. This figure could be accurately recorded by measuring the interval between successive arc sweeps. Very good reproducibility was obtained for voltages measured at different arc sweeps (see figure 24). Probes are known to have a disturbing influence on arc properties. This is particularly noticeable for situations where a significant probe current is drawn. In the present situation much less than one milliampere was drawn and so only small disturbances are expected to occur. A measure of the disturbance is given by the effect of the probe on the total arc voltage. This was noticeable only near the cathode

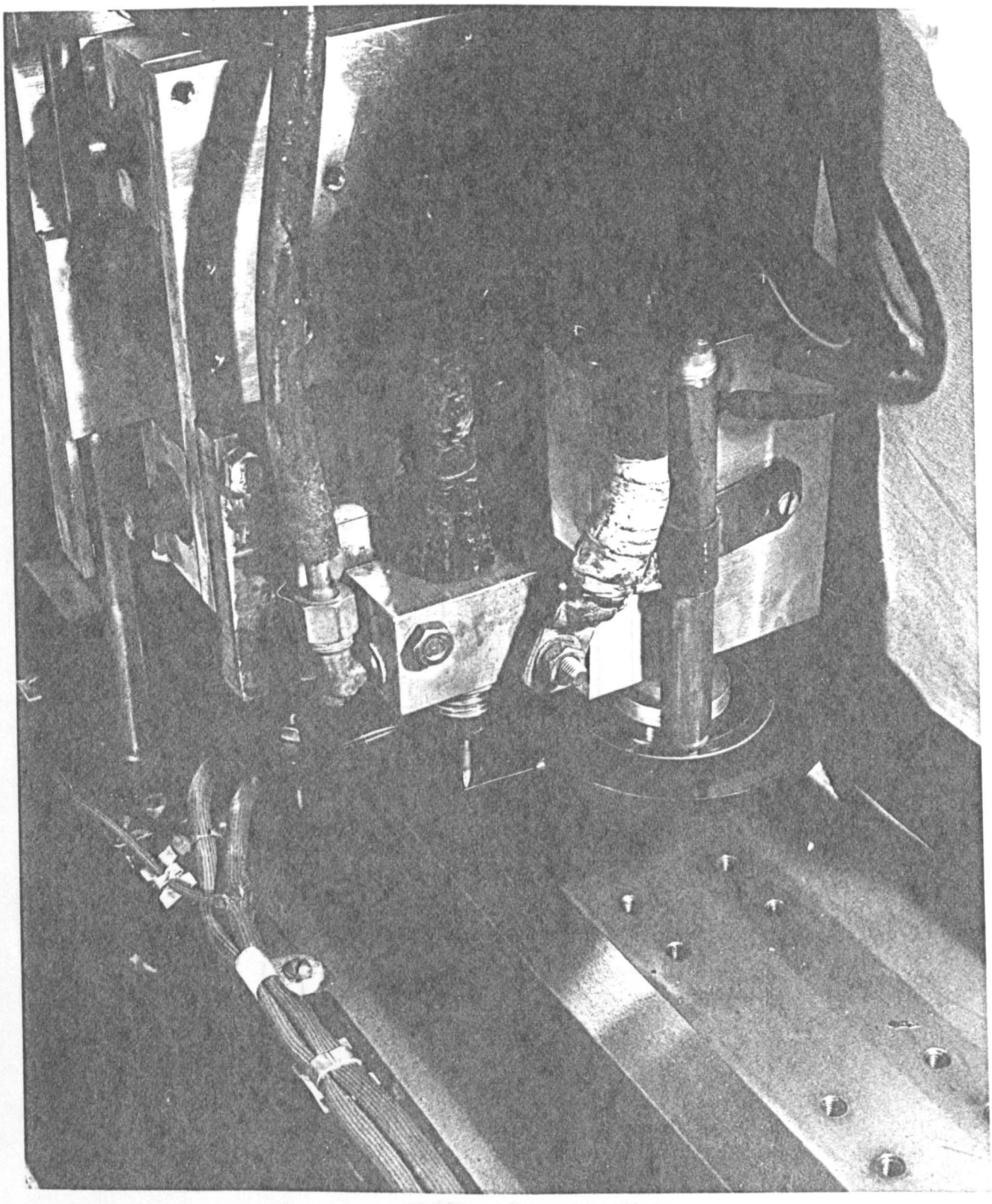

Figure 21 Electrostatic Probe Assembly

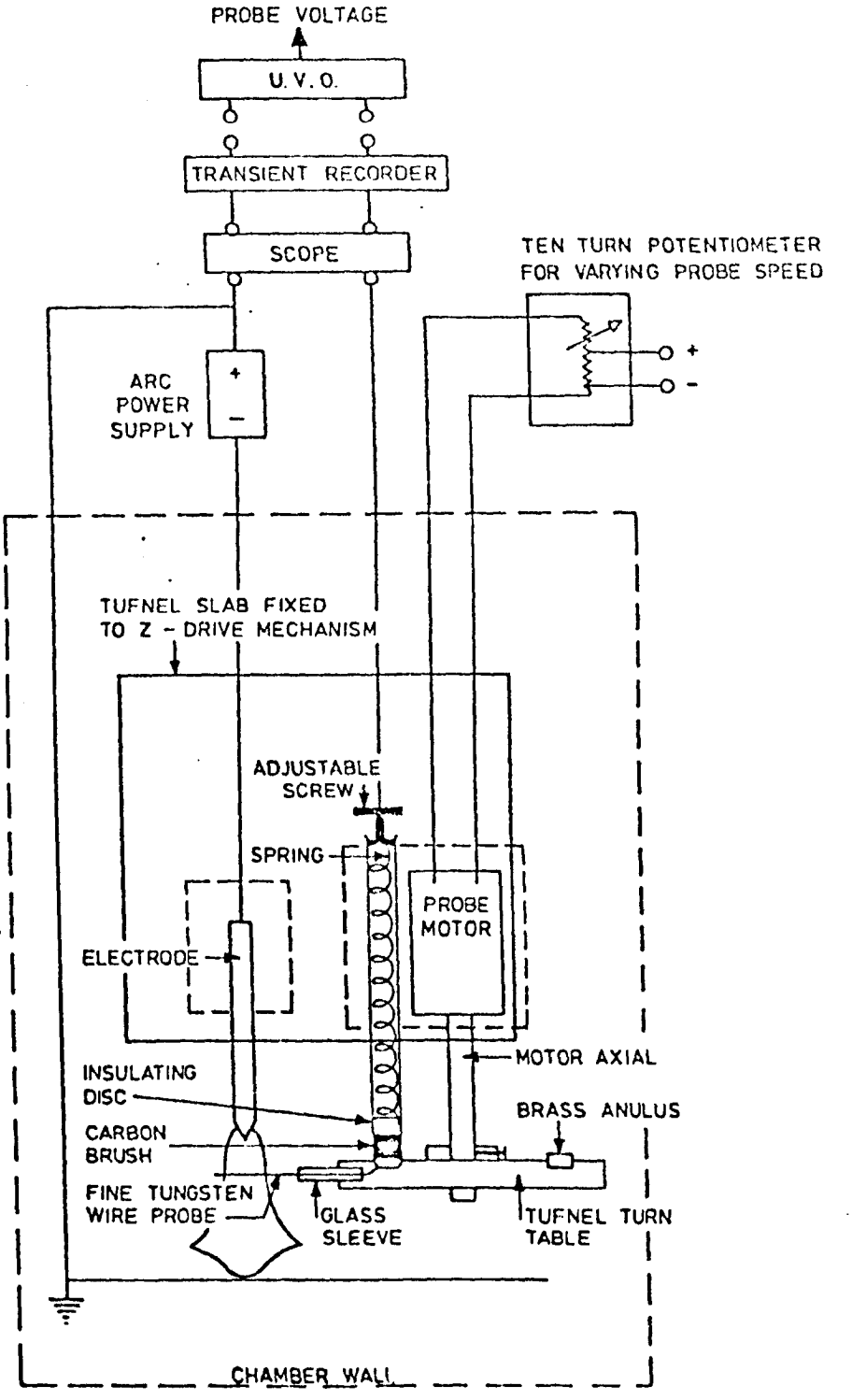

FIGURE22. SCHEMATIC DIAGRAM OF ELECTROSTATIC PROBE ARRANGEMENT.

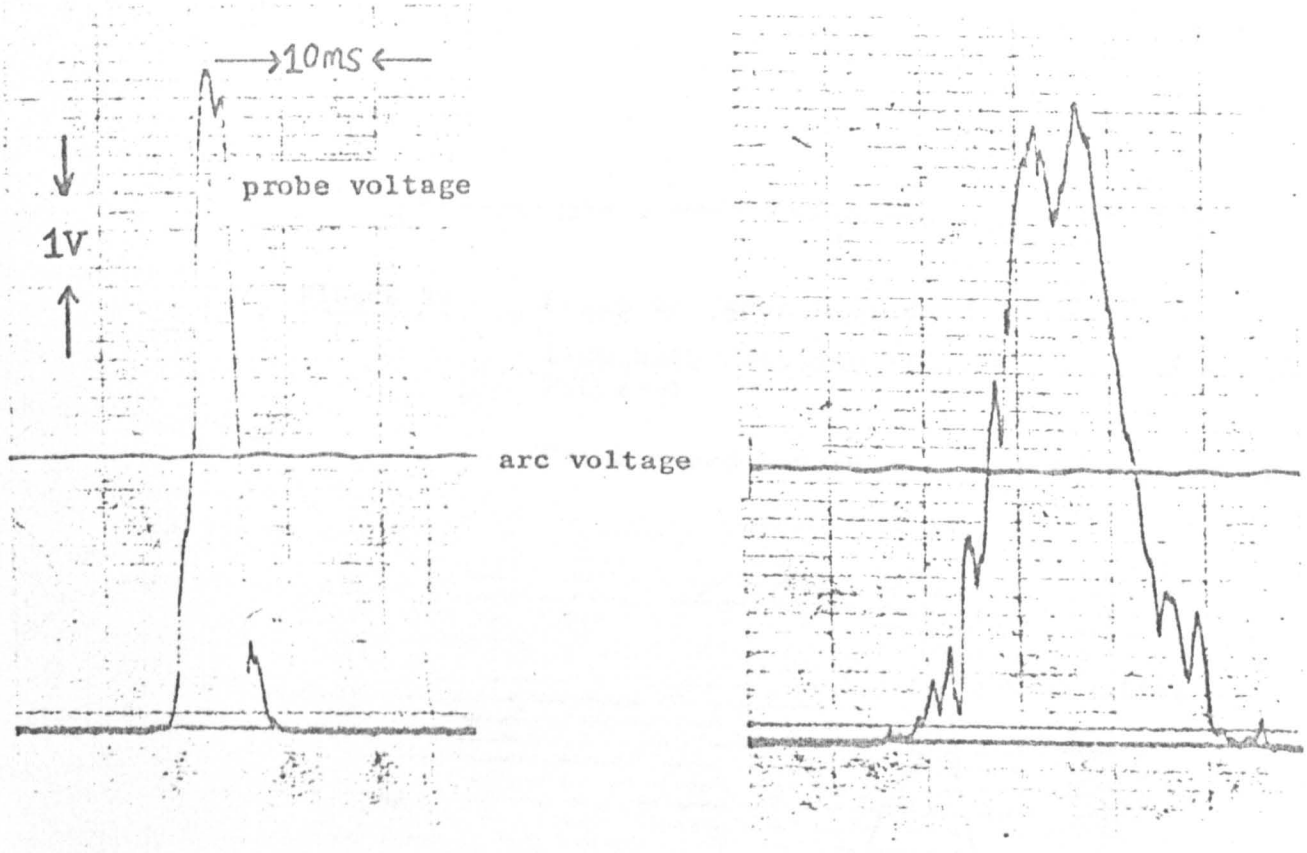

v = 0.49 m/s

v = 1.41 m/s

FIGURE 23 Influence of Probe Speed (v) on Trace Structure (same arc condition)

arcing conditions:

5mm, 100A, 15V, atmospheric argon arc

probe position: 1.5mm from cathode.

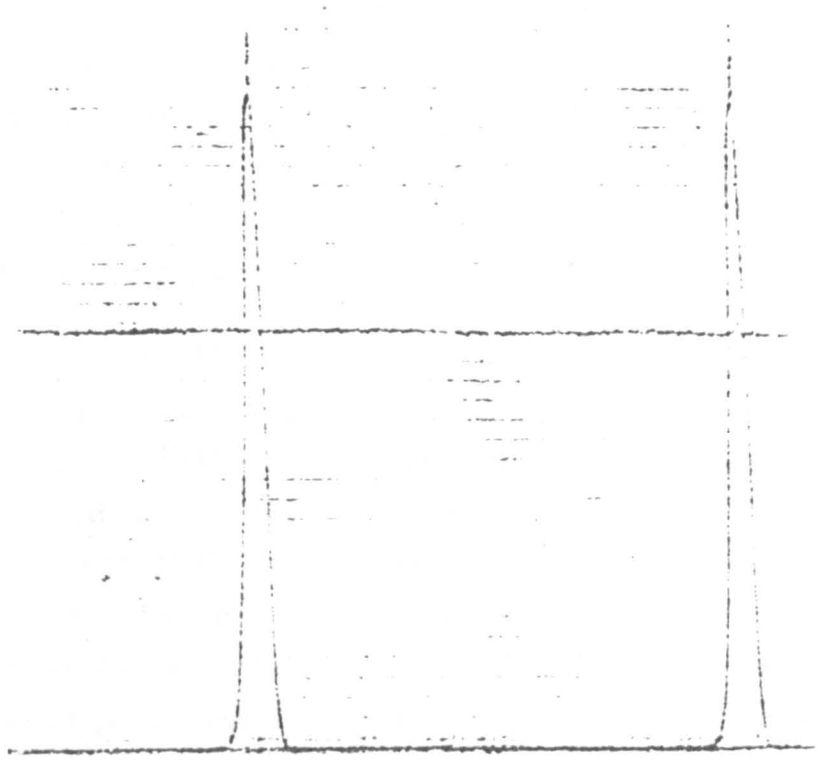

FIGURE 24 Sweep to Sweep Reproducibility

(1mm below cathode of a 3mm, 100A, atmospheric TIG arc)

Probe Speed = 0.96 m/s U.V.O. Paper Speed 100mm/s

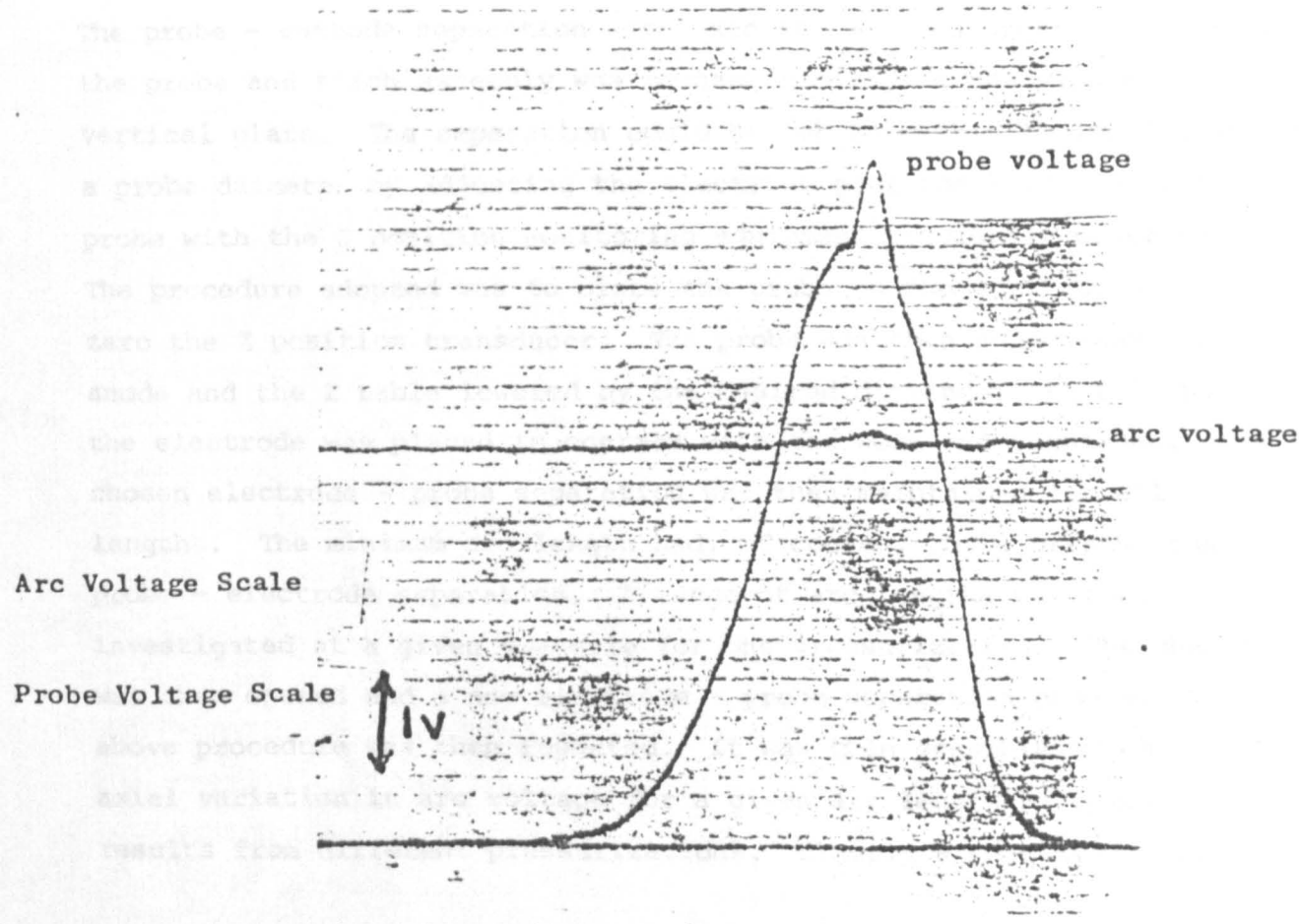

FIGURE 25 Influence of Probe on Arc Voltage

(1mm below cathode of a 3mm, 100A, atmospheric TIG arc)

U.V.O. Paper Speed 1000 mm/s Probe Speed = 0.96 m/s

(probe - cathode separations of 1mm, see figure 25). However, the properties of the plasma will change in the probe vicinity and so results must be corrected to allow for the resulting 'contact potential' (see section 3.6.4.4.).

3.6.4.3. Experimental Procedure

Measurements were made on 100 Amp argon TIG arcs over the pressure range 1-45 bars. Arc lengths of between 1 and 10mm's were investigated at every pressure. This entailed more than 150 experiments. Throughout these tests no shielding gas flow was used as resulting fluctuations in arc voltage made it difficult to achieve reproducibility (even on a sweep to sweep basis). Tests were performed in the presence of a weld pool at the anode (a few atmospheric tests on cooled copper were also made). The existence of a weld pool made it difficult to approach within 1mm of the anode. Below this arc length significant probe damage occurred. This was caused by collision with the pool or spatter from the pool. Occasionally, at very short arc lengths, electrical breakdown across the probe and anode sheaths was observed. This acted as a further limiting factor.

The probe - cathode separation was fixed for a given pressurization as the probe and torch assembly was mounted rigidly on the same moveable vertical plate. The separation could be set to within $\pm$0.1mm (to within a probe daimeter by adjusting the electrode position relative to the probe with the Z position monitoring equipment previously described). The procedure adopted was to place the probe on the work surface and zero the Z position transducer. The probe was then swung away from the anode and the Z table lowered by the desired distance. At this point the electrode was placed in contact with the work and tightened. The chosen electrode - probe separation was then maintained for all arc lengths. The minimum arc length had, of course, to be greater than the probe - electrode separation. A range of arc lengths was then investigated at a given pressure for one pressurization. The chamber was then opened and a new electrode - probe separation chosen. The above procedure was then repeated. It was then possible to obtain the axial variation in arc voltage for a given arc length by combining results from different pressurizations. Clearly a more systematic

procedure would have been to change the probe - electrode separation for a given arc length thereby monitoring this behaviour for a single arc. Arc to arc variations would have then been eliminated. This would have involved two independent Z motion capabilities. The cathode - probe distance was limited to within 2mm. For shorter distances the probe was often found to collide with the cathode. Even in situations where this did not occur considerable changes in the total arc voltage (up to 3V) were recorded as the probe passed through the arc (see figure 25). The first effect described above was attributed to electrode expansion which on this based is estimated as about 1mm.

3.6.4.4. Interpretation of Probe Signals

In these experiments the floating probe voltage was measured when practically no current is drawn by the probe. The voltage of interest is the local plasma voltage. These voltages differ by what might be regarded as a contact potential. The nature of this potential may be investigated by examining traces obtained and by considering the physical processes responsible for the potential.

The structure of a typical trace is such that at least two distinct regions may be identified, called here the central and outer regions. These are shown schematically in figure 26. The outer region extends over a distance of order 15mm and is typically a factor of three broader than the inner region. This region may be futher subdivided into 4 zones shown in figure 26. The inner region is characterised by only small changes in voltage (1V>) between the edge and centre. Near the cathode, central peaks are observed in this region (27). These disappear with increasing axial distances. Photographic arc images (see section 4) are found to be much smaller than the diameters obtained here with probes. However, the inner central zone is of the same magnitude as found photographically indicating that the central inner region is associated with the current carrying arc core and that the outer region is cooler and non-current carrying. This was substantiated by passing a negatively biased (-20V) probe through the arc and observing the region over which the probe collected positive ions. Such a procedure is similar to that used by Gick et al (28) and Allum et al (53).

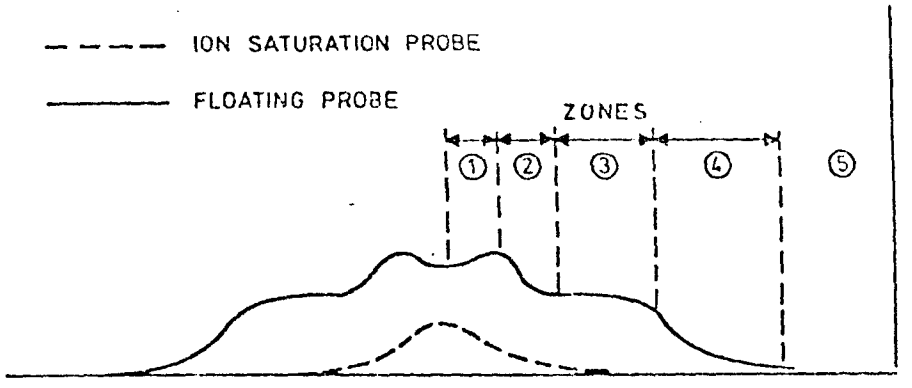

A. STRUCTURE OF PROBE TRACES

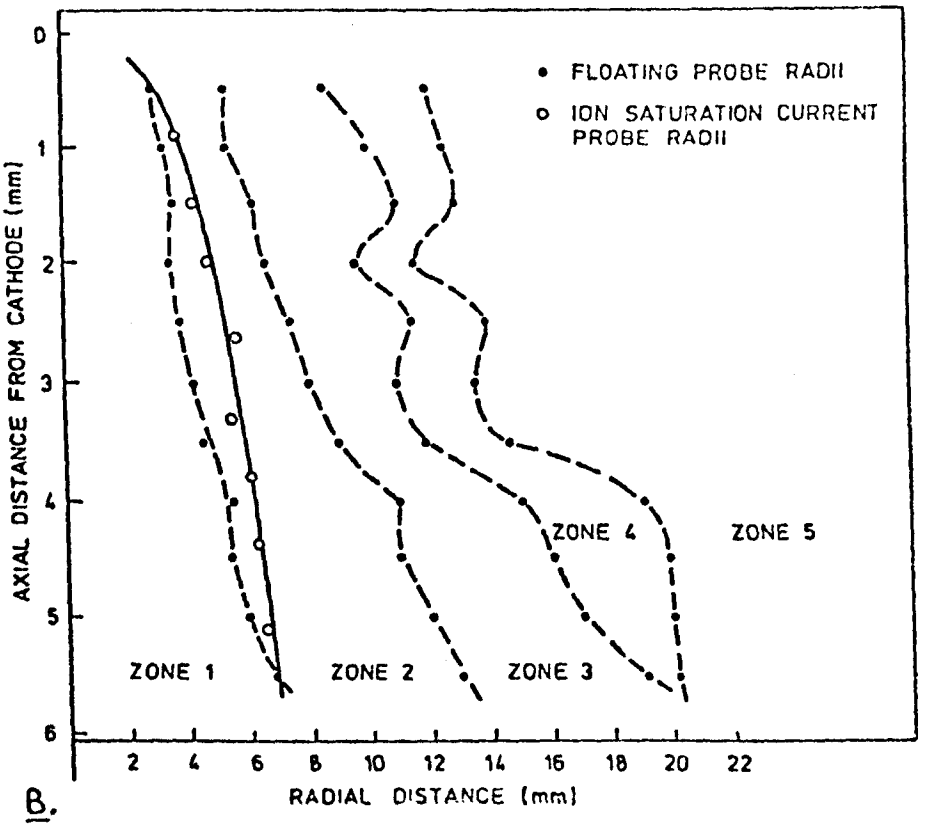

B.

FIG. 26. STRUCTURE OF ARC REVEALED BY ELECTROSTATIC ELECTROSTATIC PROBE MEASUREMENTS

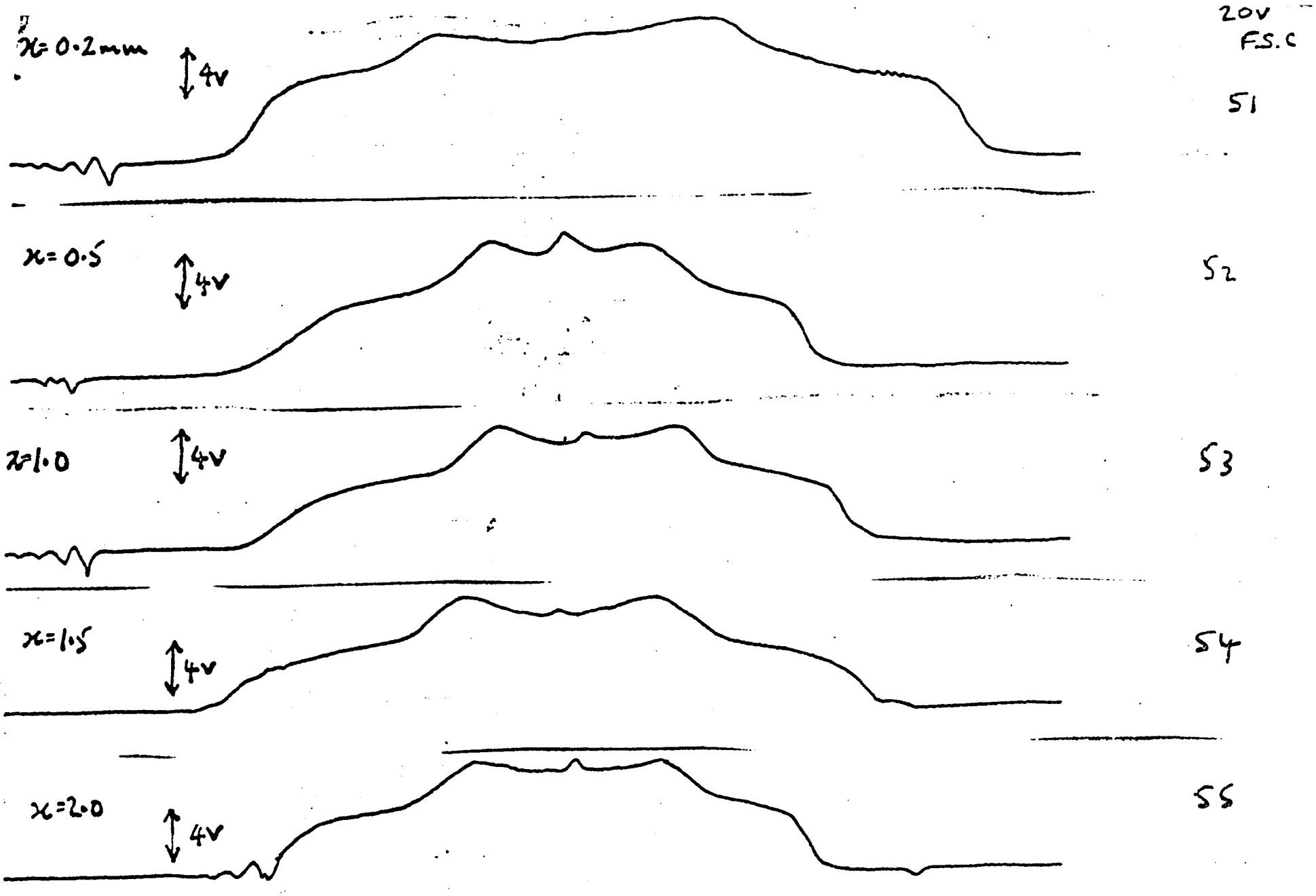

FIGURE 27 Floating Probe Signals

6mm arc (15V)

x = axial distance from cathode

100A, argon, 1 bar

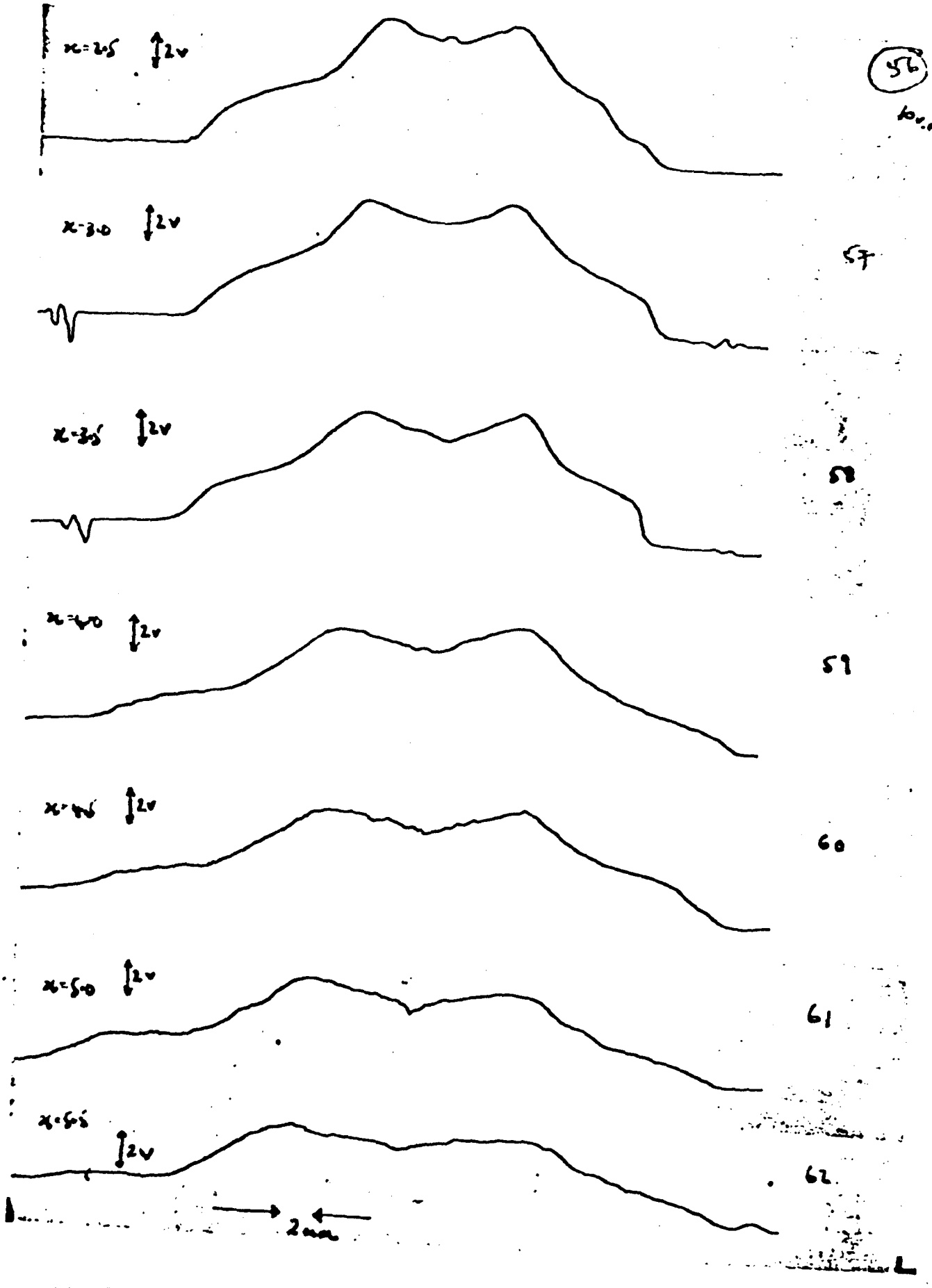

FIG.27 continued

to obtain temperature profiles for TIG and plasma welding arcs. It can be seen (figure 28) that the region over which significant positive ion concentrations exist corresponds with the central zone of floating probe traces. It is known that significant floating probe potentials may be recorded in flame plasma's where of course no current flows and temperatures are only of order 3000K (electron densities are 10^{15}-10^{18} per m^3). The structure revealed by the floating probe in the outer zone is therefore attributed to this type of behaviour. In this manner the extent of the outer zone is associated with the region over which the thermal influence of an arc is felt.

Experimental probe traces show that only small changes in voltage exist across the arc (i.e. radially). This substantiates the view that small radial field strengths exist and that current flow is predominantly axial. It is therefore permissible to express all experimental results in terms of the maximum value of arc voltage occurring in the central zone.

It is remarkable that the floating voltage changes little across the arc radius (see figure 27). Over this region plasma flow velocity is expected to change by one or two orders of magnitude while considerable changes in ionization density (two orders of magnitude) and temperature also occur. Radial variations are more extreme than those occurring axially. Further it is found that a three fold increase in probe speed (from 0.49m/s to 1.41m/s - see figure 23) has little influence on the probe voltage. These considerations indicate that the contact potential has the same value for all conditions existing across the arc and down the arc. It is therefore sufficient to apply a single correction factor to all measured voltages (at a given pressure) to obtain the true plasma potential. Further, the true plasma electric field strength is obtained by considering the axial gradient of experimental probe voltages. This is little influenced by contact potential effects and can be obtained directly. The independence of probe voltage and probe speed shows that emf's induced by cutting the arc magnetic field flux lines is negligible (Lense's law gives ≈ 40μV) and also that probe speeds are high enough to prohibit thermionic emission from the probe (cold probe).

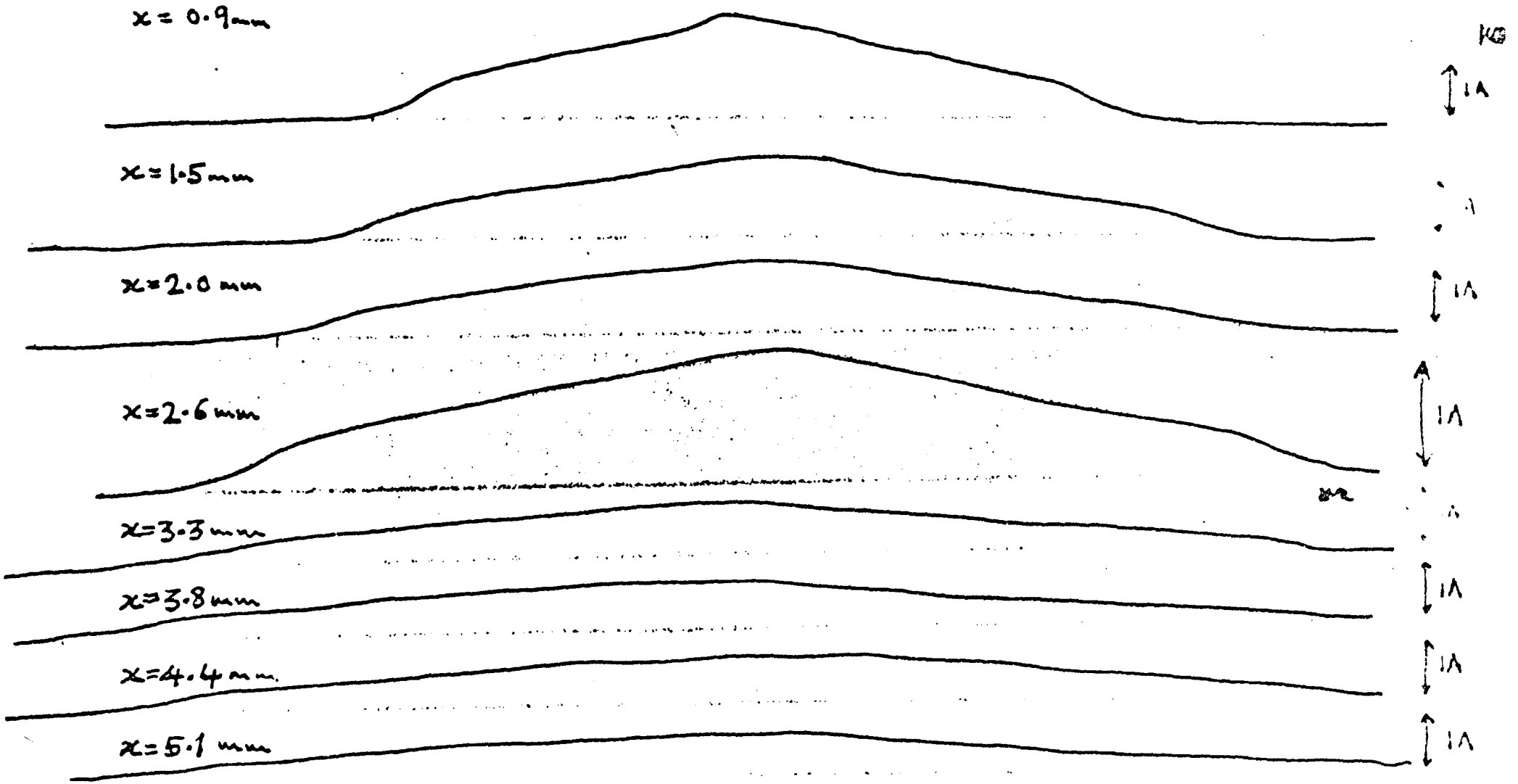

FIGURE 28 Ion Saturation Current Probe Traces

Arc conditions:
6.1mm length, 100 Amps, argon TIG arc on a steel anode

Probe conditions:
0.25mm diameter, -20V probe potential, 3.9 m/s transit speed

x = distance from cathode

Many workers have investigated the nature of the contact potential between probe and plasma. No universal theory exists and the present situation is found particularly difficult to analyse in an accurate manner. Physically the present situation is characterised by high pressure plasma flow over a cold probe in the 'thin-sheath' regime. The last characteristic simply means that hydrodynamic and temperature boundary layers around the probe are much thicker than the region over which electrical influences exists. The central questions concern the extent to which electron cooling occurs and the mechanisms of ion current generation. The probe cools the neutral flow and this in turn may influence the electron temperature near the probe. A detailed analysis will involve considerations such as plasma flow velocity, electron heavy particle collision frequency, probe radius and probe speed. These are considered below.

Clements and Smy (ref.155,156) have shown that the contact potential (ϕ_c) when no probe current is drawn can be written as

$$\phi_c = \frac{k}{e}(T_{e\infty} - T_{ep}) + \frac{k}{e}\int_{n_{ep}}^{n_{e\infty}} T_e \frac{dn_e}{n_e} \qquad (57)$$

where k is Boltzmanns constant, e the electronic charge; T_e electron temperature; and n_e the electron density. The suffices p and ∞ denote values at the probe surface and in the bulk plasma respectively. They also obtained a further expression indicating the conditions under which no electron cooling occurs. This is

$$\frac{M}{m} \cdot \frac{V}{C} > \frac{r_p}{\lambda_e} \qquad (58)$$

where M is the ion mass, m the electron mass, V is plasma flow velocity, C the mean neutral thermal velocity, r_p is probe radius and λ_e the electron-neutral mean free path. For argon at 10^4K.

$$\frac{M}{m} = 7 \times 10^{+4},\ \lambda_e \sim 3.10^{-6}\text{m},\ C \sim 5 \times 10^3\ \text{m/s}$$

Taking $V \sim 10^2$m/s and $r_p \sim 10^{-4}$m and substituting into equ.58 then gives

$$(\sim 10^3) \quad > \quad (\sim 30)$$

This indicates that electrons remain at the undisturbed plasma temperature. Detailed heat transfer calculations by Allum et al (53) have shown that the heavy particle temperature is depressed by between 1500K and 3000K.

These figures represent maximum cooling factors for electrons and substantiate the above conclusion.

Therefore by equation (57) ϕ_c now becomes:

$$\phi_c \simeq \frac{k}{e} T_{e\infty} \int_{n_{ep}}^{n_{e\infty}} \frac{dn_e}{n_e} \simeq \frac{kT_{e\infty}}{e} \ln \left(\frac{n_{e\infty}}{n_{ep}} \right) \qquad (59)$$

$$\text{or } \phi_c \simeq 0.9 \ln \left(\frac{n_{e\infty}}{n_{ep}} \right) \text{ volts} \qquad (60)$$

Under floating probe conditions the electron and ion currents must balance at the probe surface. This condition places a restriction on n_{ep} and links this parameter to the ion collection mechanism. This implies that Saha's thermodynamic expression (ref.1) cannot be used. An approximate analysis by Clements and Smy (156) suggests that the ion current isn't substantially affected by cooling. This is borne out by the temperature profiles obtained by Gick et al (28) using a random flux approach (i.e. no cooling). These workers used a low pressure theory and obtained temperatures of order 10^4K. This suggests that $n_{e\infty}/n_{ep} \sim 1\text{-}10$ but this value is not critical in the above estimate and indicates a value for ϕ_c of order one or two volts. The analysis given above is not significantly affected by pressure as it is found (see section 6) that only small changes in temperature occur with increasing pressure. The true plasma potential can therefore be obtained by applying a correction factor of about 1-2 volts to all results presented here. The probe assumes a negative potential with respect to the plasma (ref.155). Since probe measurements were made with respect to the anode the correction is applied by subtracting one or two volts from all measured values.

3.6.5. Arc Column Radiation Measurements

A thermopile type device was designed and constructed. This was used to measure radiation from high pressure (1-42 bars) argon and helium arcs burning above steel anodes. Details of this device, measurement procedures and the interpretation of results are given below.

3.6.5.1. Experimental Design

The experimental arrangement is shown in figure 29 and 31. This consisted of two blackened copper discs (1mm thick, 10mm in diameter, mass 4g) each situated at the end of long tubes. Measurements were made by aligning the assembly with the arc and shielding one of the discs from the influence of arc radiation. From the temperature response of each disc, it is found possible to account for all factors contributing to disc heating (including arc radiation). The basic idea was that the shielded disc experienced all heating influences except arc radiation. A comparison with the unshielded disc should therefore allow this factor to be identified.

The disc face pointing at the arc was lamp blacked with actelyne soot thereby providing a good approximation to a black body absorber with a nearly flat spectral response over much of the range of interest. The back face and edge of each disc were silvered to ensure that no radiant energy left through these sides. This was achieved by removing surface oxide layers by a sputtering technique and then using a vacuum deposition method to apply an even silver film with a thickness of about 900nm. All radiant exchanges could then be taken as occurring at the front face as silver is an almost perfect reflector in the infra red spectral region corresponding to disc temperatures. Cardboard shields were placed near (but not on) the back face of each disc to ensure that no radiation from the arc spectrum reached this face (see figure 30). Disc temperature measurements were made using thermocouples spot welded to the centre of the back face of each disc.

Background radiation from the chamber walls to a disc was minimized by placing the discs at the end of long cardboard tubes. To minimise internal reflections each tube was blackened. The outer surface of each tube was also blackened but for a different reason. This was done to optimise the thermal interaction with the surroundings and to standardise tube characteristics (see section 3.6.5.2). Both tubes were placed in contact and mounted symmetrically within the chamber (so as to be equally affected by the environment).. Conduction from the mountings was minimised by using a tufnol block mount. In all experiments (unless otherwise stated), discs were mounted at a distance of 7.8cm from the tube opening

and 20cm from the arc. Absolute thermocouple temperature measurements were made possible by placing the cold junction of each thermocouple in an insulated ice box situated within the chamber. This eliminated floating cold junction effects due to changes in ambient temperature. A permanent record of disc temperature as a function to time was obtained by displaying thermocouple readings on a UVO recorder with a very slow paper speed (0.2mm/s). Typical traces are shown in figure 32.

3.6.5.2. Behaviour and Theory of Disc Assembly

An understanding of disc behaviour has been obtained by analysing UVO traces such as those shown in figures 32. Sources of disc heating (or cooling), q_D are listed below and where possible quantified:

i) Radiant energy from arc (q_a)
ii) Background radiation (q_b) from weld pool, tungsten electrode and chamber walls
iii) Radiation emitted by tube walls (Σ)
iv) Natural convection within the tube ($-q_c$)
v) Radiation from the disc ($-q_{RD}$)
vi) Radiation from the atmosphere adjacent to the disc (q_{RA})
vii) Conduction from the disc mountings (q_K)

These are illustrated in figure 33. An energy balance gives

$$q_D = q_a + q_b - q_c + q_k + \Sigma + q_{RA} - q_{RD} \qquad (61)$$

Convective and radiative terms may be quantified in terms of known temperatures. For natural convection within the tube

$$q_c = K(T - T_A)^{5/4} \qquad (62)$$

and by Stefan's law

$$q_{RA} = \sigma.\varepsilon.A.T_A^4 \qquad (63)$$

$$q_{RD} = \sigma.\varepsilon.A.T^4$$

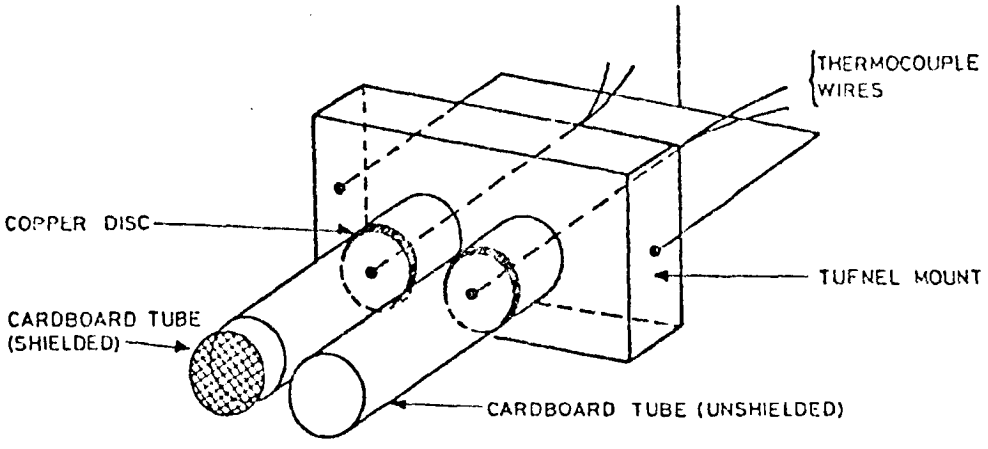

FIGURE 29. SCHEMATIC OF DISC ASSEMBLY.

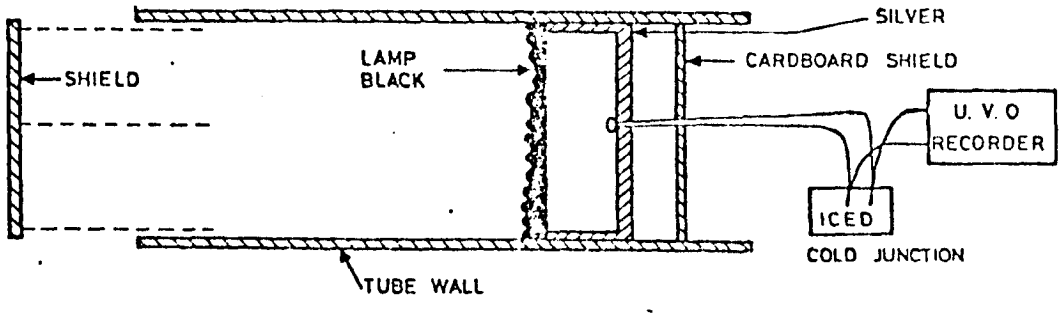

FIGURE 30. SIDE VIEW OF TUBE AND DISC.

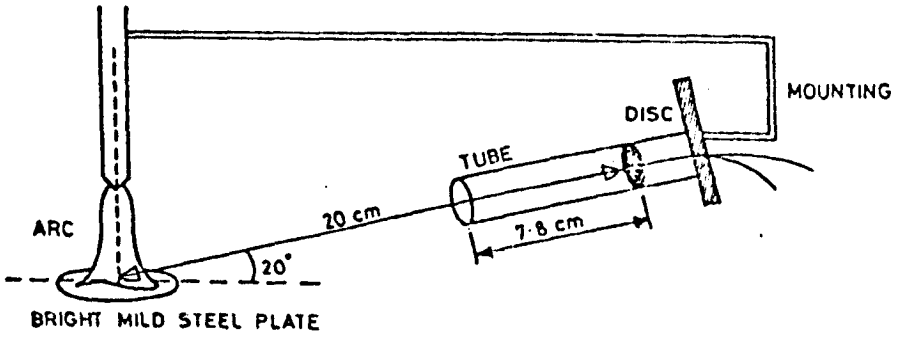

FIGURE 31. GENERAL ARRANGEMENT.

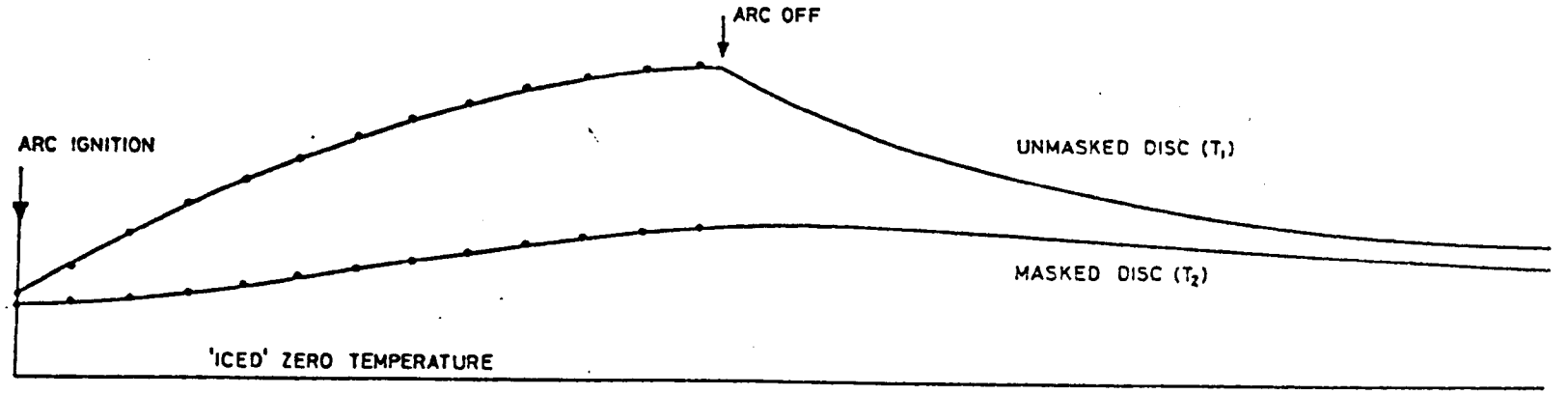

a) 1 Bar, 100 Amps, 6 mm arc length.

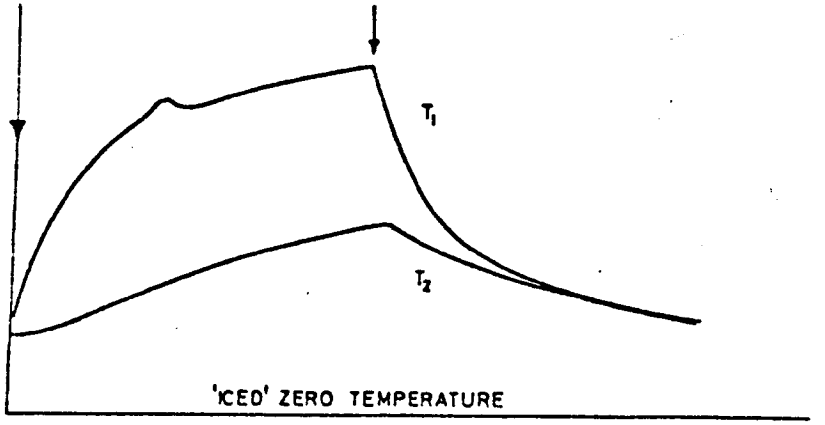

b) 42 Bars, 100 Amps, 6 mm arc length.

BOTH RECORDS HAVE THE SAME SCALE i.e.

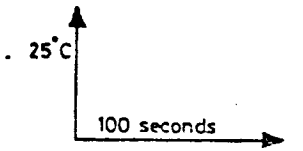

FIG 32. U.V.O. RECORDS FOR TIG RADIATION MEASUREMENTS IN ARGON.

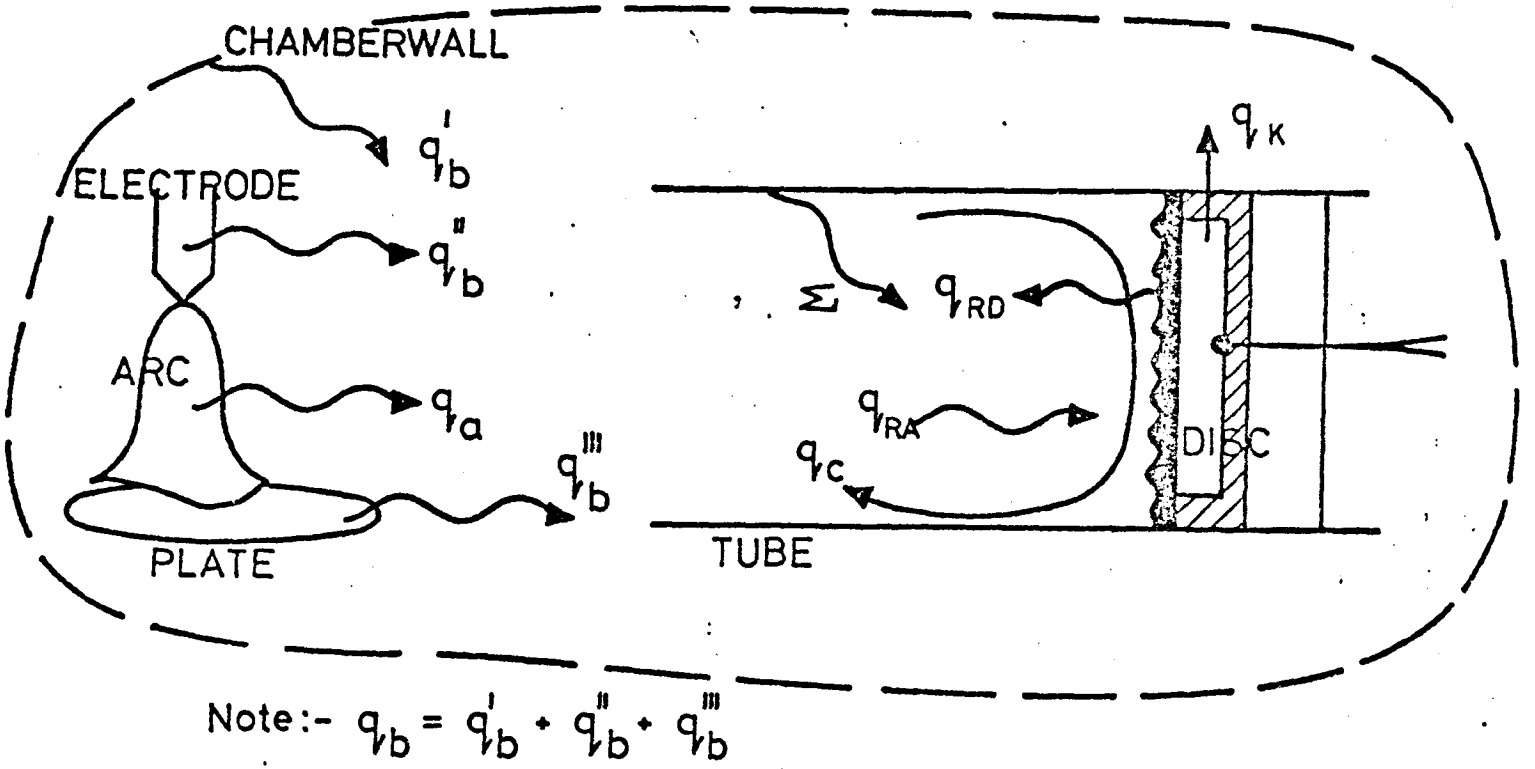

Note:- $q_b = q'_b + q''_b + q'''_b$

FIGURE33. SCHEMATIC OF ENERGY EXCHANGES BETWEEN DISC AND ENVIRONMENT.

where T is the disc temperature and T_A the ambient temperature near the disc.. K is a constant dependent on gas composition, disc geometry, disc surface conditions and disc orientation. ε is the emissivity of lamp black and A is the front face surface area of a disc. σ is Stefan's universal constant. Disc heating may also be quantified and written as

$$q_D = m.c. \frac{dT}{dt} \tag{64}$$

where m is disc mass and c the specific heat of copper. Combining equations 61-64 allows the energy balance to be written as

$$m.c. \frac{dT}{dt} = q + q_k + \Sigma - K(T - T_A)^{5/4} - \sigma.\varepsilon.A(T^4 - T_A^4) \tag{65}$$

where $q_a + q_b$ has been written as q. This equation has four unknowns (q, q_k, Σ and K). The behaviour of each disc is represented by

$$m.c. \frac{dT_1}{dt} = q + q_{K1} + \Sigma_1 - K(T_1-T_{A1})^{5/4} - \sigma\varepsilon A(T_1^4-T_{A1}^4) \tag{66}$$

and

$$m.c. \frac{dT_2}{dt} = q_{K2} + \Sigma_2 - K(T_2-T_{A2})^{5/4} - \sigma\varepsilon A(T_2^4 - T_{A2}^4) \tag{67}$$

where the suffix 1 refers to the open disc and the suffix 2 to the shielded disc. The difference equation formed is subtracting (66) and (67) is

$$m.c. \frac{d(T_1-T_2)}{dt} = q + (q_{K_1}-q_{K_2}) + (\Sigma_1-\Sigma_2) - K\Big[(T_1-T_{A1})^{5/4} - (T_2-T_{A2})^{5/4}\Big] - \sigma.\varepsilon.A\Big[(T_1^4-T_{A1}^4) - (T_2^4-T_{A_2}^4)\Big] \tag{68}$$

This equation can be simplified in a number of ways. The experimental design was such as to allow a number of approximations to be made on physical grounds. Firstly, the contact area between the disc and mounting was small and the mount material was chosen to be a poor conductor. Thermal conduction leakage is then expected to be small and it is therefore reasonable to write

$$q_D >> q_{K_1} \approx q_{K_2}$$

Secondly, chamber environment exerts the major influence on the thermal state of the tube walls and gas within the tube as the discs play only a small part in the tube wall energy balance. To improve the nature of this approximation each tube was painted black thereby enhancing absorption from the environment. This assumption is reasonable in view of the small surface area of the disc in comparison to that of the tube (∿5%) and the chamber walls (1%>>>). The above approximation essentially amounts to asserting that the tube walls receive the major part of their energy from the chamber gas and chamber walls. It then follows that both tubes (shielded and unshielded) are in a similar thermal state i.e.

$$\Sigma_1 \simeq \Sigma_2 \simeq \Sigma \text{ (say)}$$

and $$T_{A1} \simeq T_{A2} \simeq T_A \text{ (say)}$$

The last equation (68) can now be written as

$$m.c.\ \frac{d(T_1-T_2)}{dt} = q - K\left\{(T_1-T_A)^{5/4} - (T_2-T_A)^{5/4}\right\} - \sigma.\varepsilon.A(T_1^4-T_2^4) \quad (69)$$

For convenience the notation below is introduced

$$\Delta q_D = m.c.\ \frac{d(T_1-T_2)}{dt}$$

$$\Delta q_R = q_{R1} - q_{R2} \quad \text{where } q_R = q_{RD} - q_{RA}$$

$$\Delta N = N_1 - N_2 \quad \text{where } N = (T - T_A)^{5/4}$$

With this notation K may be expressed as below where the difference equation at time t has been subtracted from its initial value (i.e. at t = 0).

$$K = \frac{\Delta q_D(t=0) - \Delta q_D + \Delta q_R(t=0) - \Delta q_R}{\Delta N - \Delta N(t=0)} \quad (t \neq 0) \quad (70)$$

All factors appearing in this expression may be measured directly from UVO traces. Using values of K determined in this manner it is then possible to determine Σ from the behaviour of disc 2. q can then be found from the expression for disc 1 or from the difference expression below

$$q = \Delta q_D + K\Delta N + \Delta q_R \quad (71)$$

The procedure given above has been used to analyse traces shown in figures 32. Results are given in numerical form in tables 6 and 7. It can be seen that the value of K deduced by the above method varies little with time for both cases analysed. This is a strong justification of the above interpretation of disc behaviour. Further the overall accuracy of graphical measurements and computation is borne out by the small difference between Σ_1 and Σ_2 as given by the respective expressions. Similar measurements of K have been made for higher pressures. These are displayed graphically in figure 34. It can be seen that K increases in a regular manner with pressure. The observed pressure dependence is in good agreement with the square root behaviour for natural convection predicted by the Grasshoff number (i.e. the dimensionless number describing the behaviour of natural convection in terms of physical parameters). Values of q given on figure 37 have been determined using the last equation. In particular, the initial behaviour may be studied. Using equation 71 at t=0 gives

$$q = \Delta q_D(t=0) + K\Delta N(t=0) + \Delta q_R(t=0) \qquad (72)$$

If complete equilibrium existed at this time then

$$q = \Delta q_D(t=0) \qquad T_1 = T_2 = T_A$$

It is predicted by the theory and can also be seen from the traces that $q_{D2}(t=0) = 0$. Therefore, when equilibrium conditions initially exist:

$$q = q_{D1}\ (t=0) \qquad (73)$$

where q can be found from the initial gradient of the unshielded disc temperature trace as long as equilibrium conditions initially existed. This is readily checked with reference to tables 6 and 7.

At 1 bar $q = 0.227(W)$, $q_{D1}(t=0) = 0.219(W)$ i.e. $q-q_{D1}(t=0)=0.008$ (W)

At 42.6 bars $q = 1.180(W)$, $q_{D1}(t=0) = 1.109(W)$ i.e. $q-q_{D1}(t=0)=0.071$ (W)

These figures indicate that in the present cases an error of order 5% is made by using initial temperature gradients to estimate q. However, the absolute error is ten times lager at higher pressures due to the pressure dependence of K. It is found in general that prohibitively long times

	Measured Values DISC 1			Measured Values DISC 2			Difference: DISC1-DISC 2			Values Derived using equations 61 to 71					
time (secs)	T_1 (^oC)	q_{D1} (W)	q_{R1} (W)	T_2 (^oC)	q_{D2} (W)	q_{R2} (W)	Δq_D (W)	Δq_R (W)	ΔN ($^oC^{5/4}$)	$K \times 10^{-3}$ ($W/^oC^{5/4}$)	Σ_1 (W)	Σ_2 (W)	$\Delta\Sigma$ (W)	q_{C1} (W)	q_{C2} (W)
0	18.13	0.219		15.63	0	0	.219	.004	3.144	-	-	-	-	-	-
50	23.75	0.219	0.011	16.25	.019	.001	.200	.013	13.157	1.039	.023	.020	.003	.014	0.000
150	37.25	0.181	0.039	18.75	.043	.005	.138	.034	42.473	1.309	.058	.053	.005	.061	0.005
200	43.13	0.153	0.052	20.13	.057	.008	.096	.044	56.420	1.567	.081	.076	.005	.099	0.011
300	52.50	0.130	0.072	23.75	.057	.013	.073	.059	77.150	1.242	.092	.087	.005	.113	0.017
400	59.38	0.104	0.089	27.50	.057	.020	.047	.069	90.486	1.232	.109	.105	.004	.319	0.028
500	65.00	0.067	0.103	31.25	.037	.027	.021	.076	99.817	1.308	.118	.105	.013	.171	0.041
600	67.50	0.031	0.110	32.50	.017	.030	.009	.080	105.01	1.318	.101	.088	.013	.183	0.041

TABLE 6 Structure of Radiation Probe Trace (see figure 32) for the Arc Conditions:- 1 bar, 100 Amps, 6mm Argon Arc

Symbols are as defined in the text.
Ambient temperature near the disc is 15.63°C
Radiated power (q_a) = 0.227 (W)

$M = 4 \times 10^{-3}$ kg
$\varepsilon = 0.95$
$\sigma = 5.67 \times 10^{-8}$ $W\,M^{-2}\,K^{-4}$
$A = 3.14 \times 10^{-4}$ M^2
$C = 383$ J/kg^oC

	Measured Values DISC 1			Measured Values DISC 2			Difference: DISC 1-DISC 2			Values Derived using equations 61 to 71					
Time (secs)	T_1 (°C)	q_{D1} (W)	q_{R1} (W)	T_2 (°C)	q_{D2} (W)	q_{R1} (W)	Δq_D (W)	Δq_R (W)	ΔN ($^oC^{5/4}$)	$K \times 10^{-3}$ ($W^oC^{5/4}$)	Σ_1 (W)	Σ_2 (W)	$\Delta\Sigma$ (W)	q_{C1} (W)	q_{C2} (W)
0	20.63	1.109	0.007	16.25	0	0	1.110	0.007	6.336	-	-	-	-	-	-
25	37.50	0.855	0.039	17.50	0.075	0.002	0.765	0.037	44.303	8.342	0.105	0.088	0.017	0.0381	0.011
50	48.13	0.630	0.062	19.38	0.156	0.005	0.475	0.056	71.590	8.993	0.203	0.198	0.005	0.0681	0.037
75	55.63	0.402	0.079	21.96	0.153	0.010	0.250	0.069	89.82	9.579	0.256	0.248	0.008	0.945	0.085
100	60.63	0.301	0.091	24.63	0.153	0.014	0.149	0.077	100.29	9.499	0.310	0.302	0.008	1.088	0.135
125*	65.00			27.50											
150	63.13	0.101	0.098	29.38	0.124	0.023	0.023	0.075	97.68	11.172	0.399	0.426	0.027	1.370	0.279
175	65.63	0.138	0.104	31.25	0.096	0.027	0.041	0.078	101.38	10.512	0.448	0.433	0.025	1.376	0.310
200	68.50	0.101	0.112	32.50	0.096	0.029	0.005	0.083	107.85	10.153	0.469	0.456	0.013	1.426	0.331
225	69.38	0.066	0.114	34.38	0.106	0.038	0.040	0.081	106.03	9.998	0.444	0.513	0.069	1.434	0.374
250	70.63	0.066	0.118	36.25	0.106	0.036	0.040	0.081	105.377	10.067	0.501	0.568	0.067	1.487	0.426
275	72.50	0.049	0.123	38.13	0.106	0.040	0.057	0.083	105.725	9.750	0.504	0.607	0.103	1.502	0.461
300	72.50	0.044	0.123	39.38	0.106	0.043	0.062	0.080	103.322	10.060	0.547	0.659	0.112	1.550	0.510

* irregularity on trace

TABLE 7 Structure of Radiation Probe Trace (see figure 32) for the Arc Condition: 42 bars, 100 Amps, 6mm Argon Arc

Ambient temperature near disc is 16.25°C
Radiated power (q_a) = 1.18 W
Probe data is the same as given on table 6

are required between experiments to achieve good equilibrium conditions and so radiation results (see section 6) have been obtained using the equation for q with the determined pressure dependence of K (see figure 34).

Some of the results presented in tables 6 and 7 have been expressed in graphical form to depict the time dependence of the disc heating components at 1 bar and 42 bars (see figures 35 to 38). These figures show that the nett radiation term (q_R) is relatively small for both shielded and unshielded discs and decreases in importance with increasing pressure. It can also be seen that background tube heating (Σ) is important and as expected dominates for shielded discs. Natural convection is a significant term in all cases and dominant in unshielded tube situations. These figures show quite clearly that it is not permissible to assume that disc equilibrium is reached when the power radiated by a disc becomes equal to that received solely from arc radiation.

3.6.5.3. Relationship Between Radiation, q, Captured by Disc and that Emitted by Arc (Q_a)

Measurements reported so far have been concerned with deducing the relationship between disc heating and radiation emitted by the arc, weld pool/plate, electrode regions and chamber reflections. The objective is of course to relate disc heating to radiation solely from the arc. To obtain this relationship experiments at every pressure and current were performed over a range of arc lengths (2 to 10mm's). A typical result processed in the manner previously described is shown in figure 39. It can be clearly seen that for every current a zero arc length component exists. This component increases with arc current and is interpreted as the background radiation q_b.

$$\text{i.e. } q(\text{Limit as arc length} \rightarrow 0) = q_b \qquad (74)$$

This is substantiated on the ground that arc length has only a small influence on weld pool size (see section 4) and virtually no influence on cathodic behaviour (see section 6.4). Thus the radiation from these

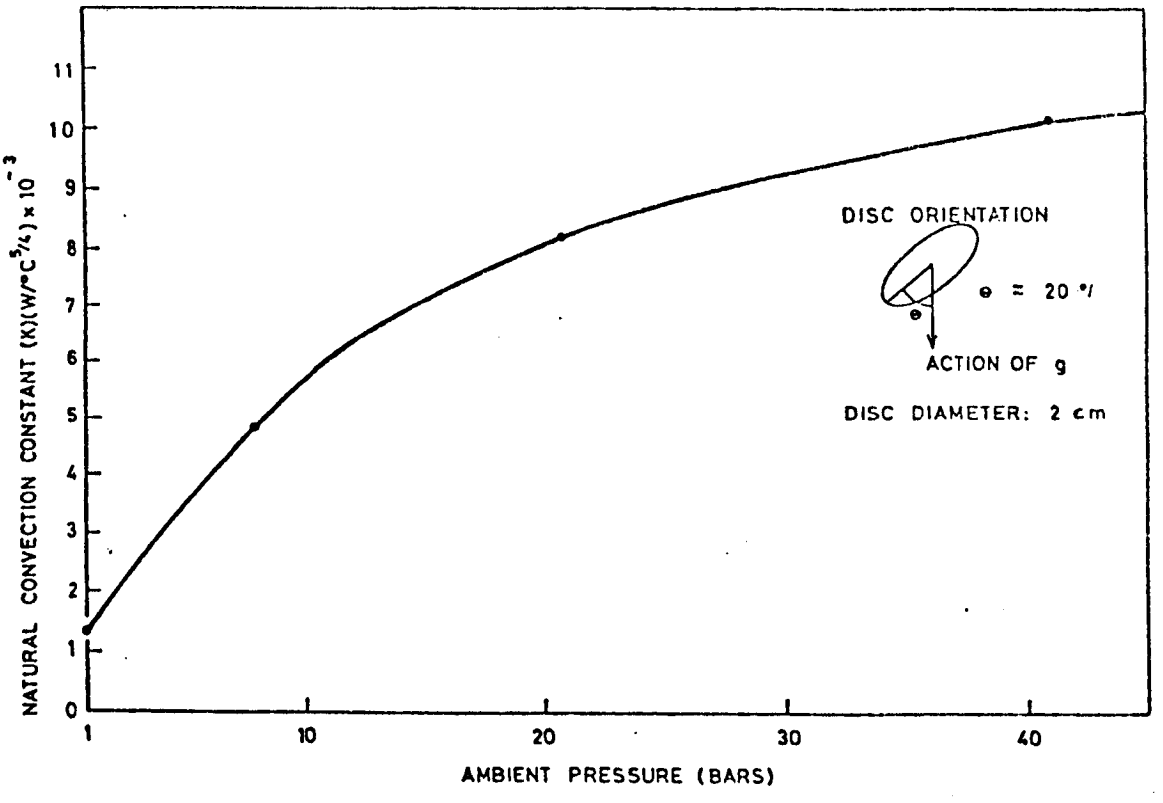

FIGURE 34. PRESSURE DEPENDENCE OF THE NATURAL CONVECTION FACTOR K FOR THE DISC GEOMETRY SHOWN.

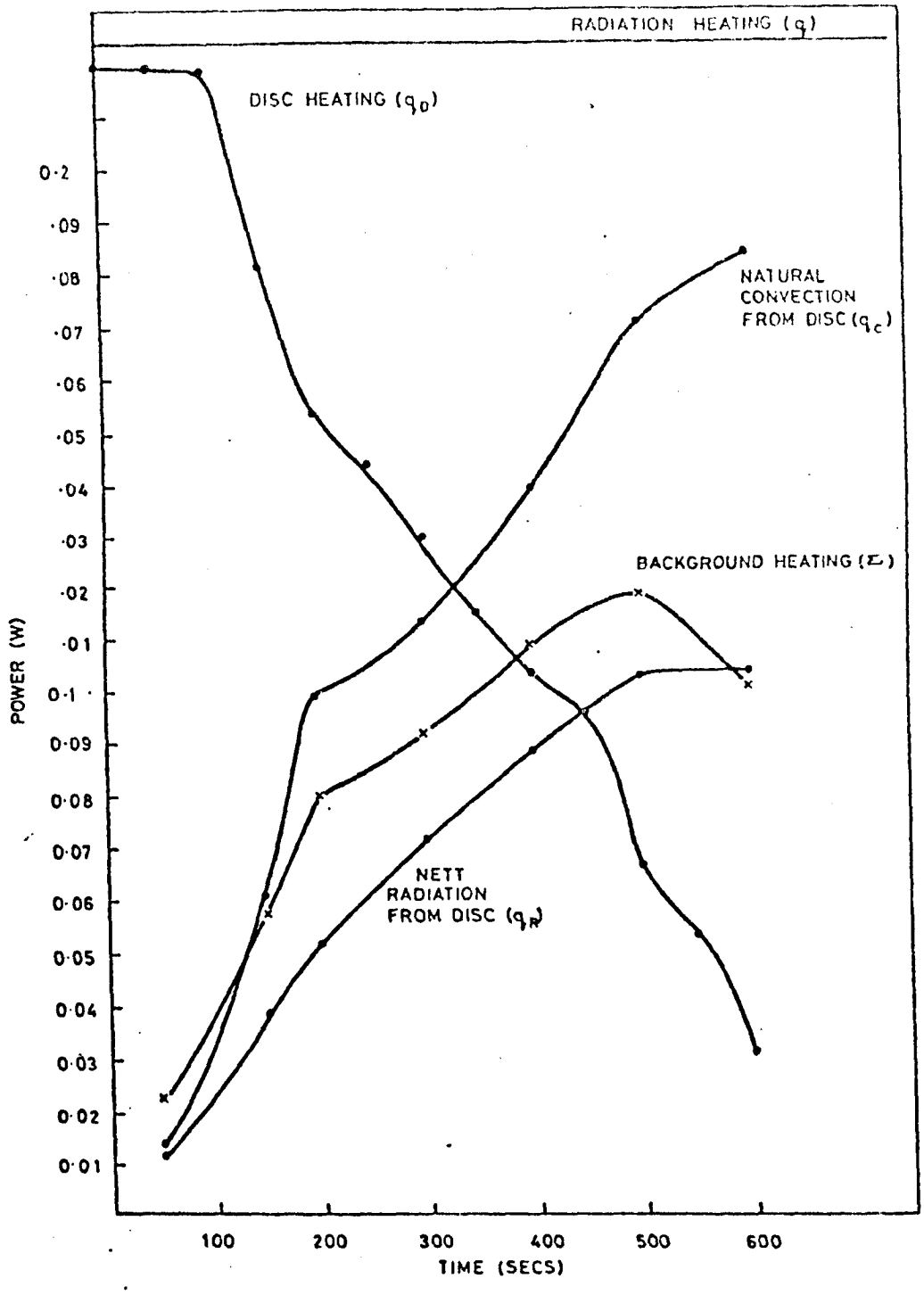

FIGURE 35 RESPONSE OF RADIATION PROBE RECEIVING ARC RADIATION AT 1 BAR (SEE TABLE 6 AND FIGURE 32d)

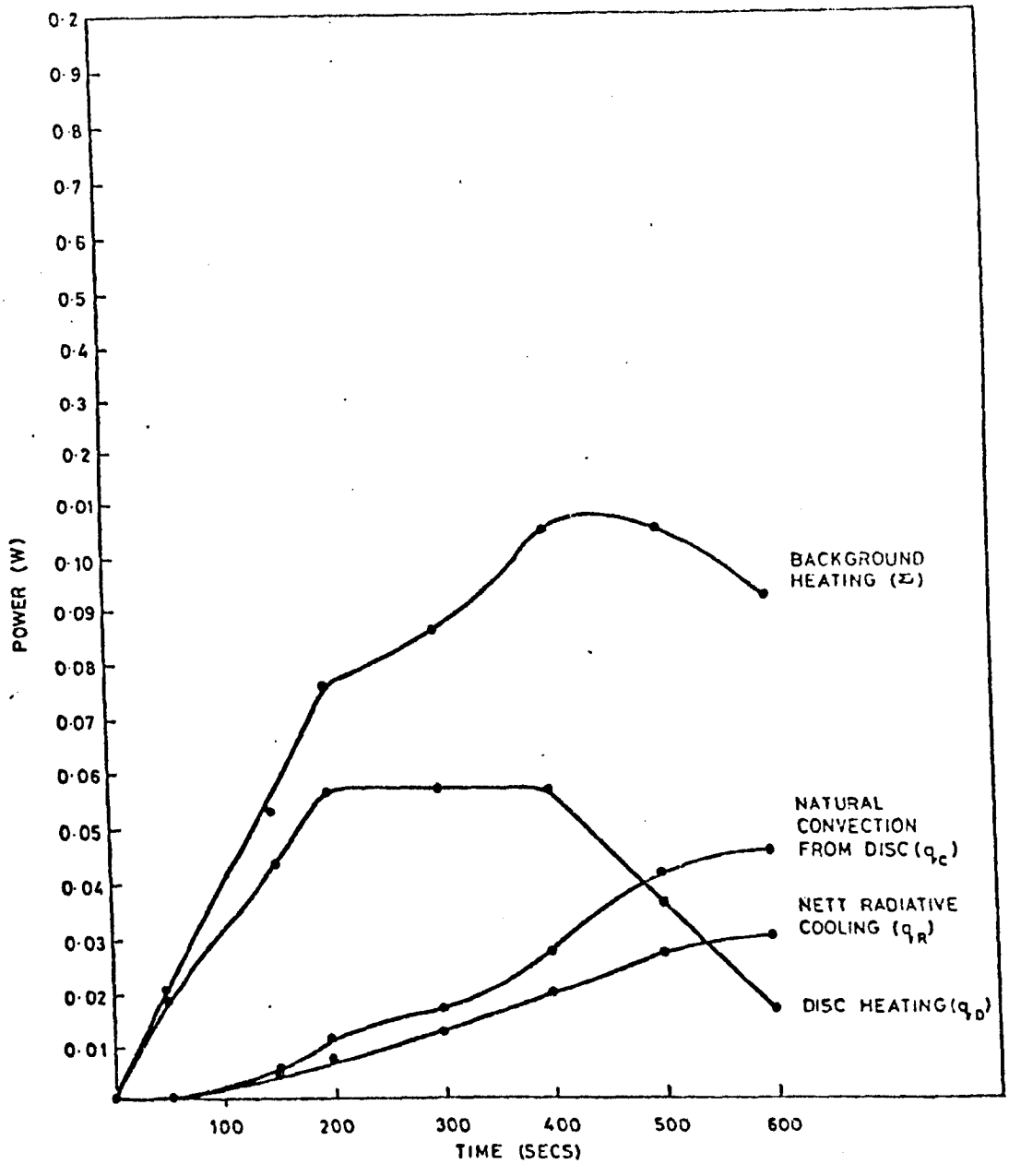

FIGURE 36 RESPONSE OF RADIATION PROBE SHIELDED FROM ARC RADIATION AT 1 BAR (SEE TABLE 6 AND FIGURE 32 a)

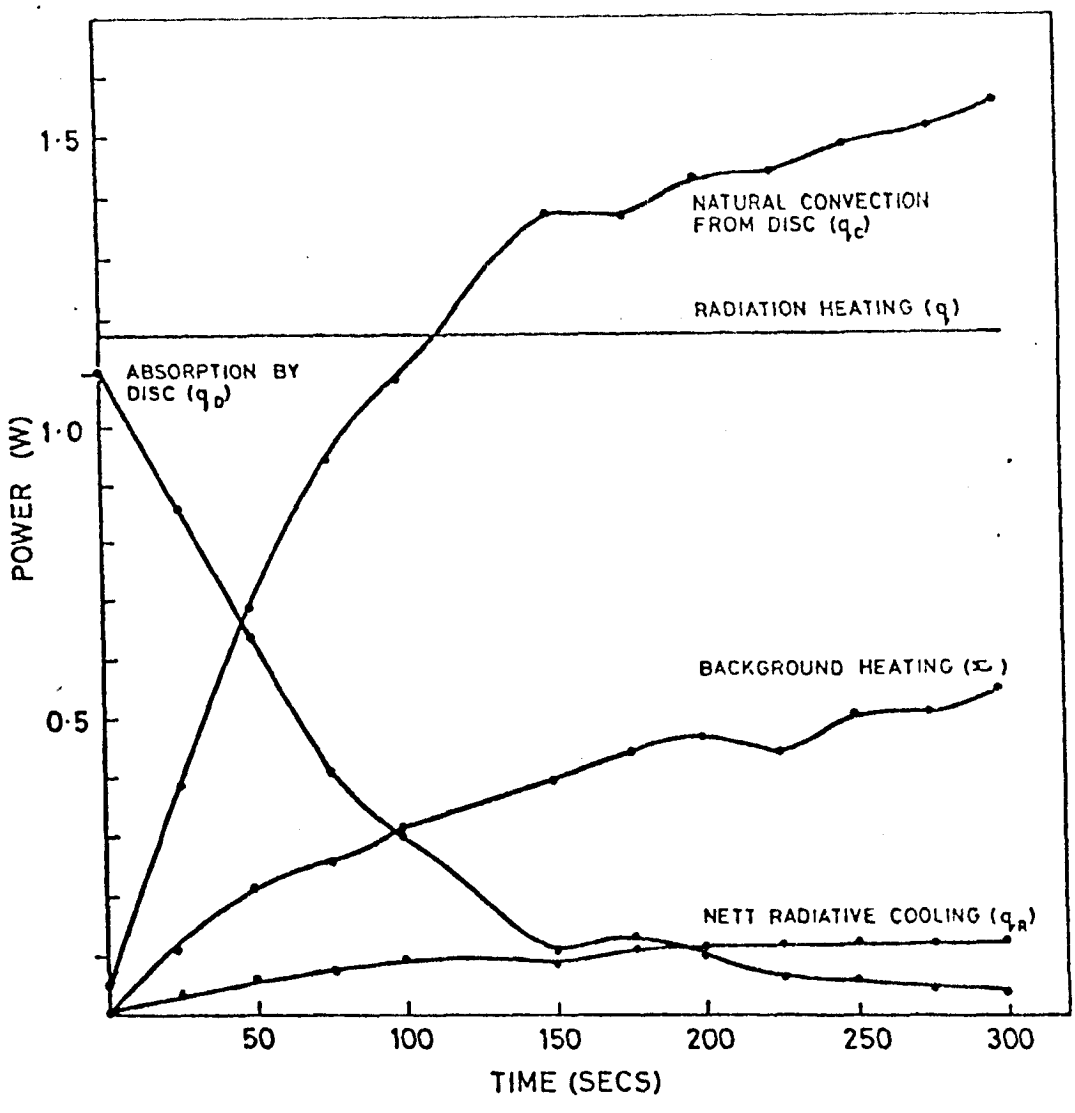

FIGURE 37. RESPONSE OF RADIATION PROBE RECEIVING ARC RADIATION AT 42 BARS (SEE TABLE 7 AND FIGURE 32b)

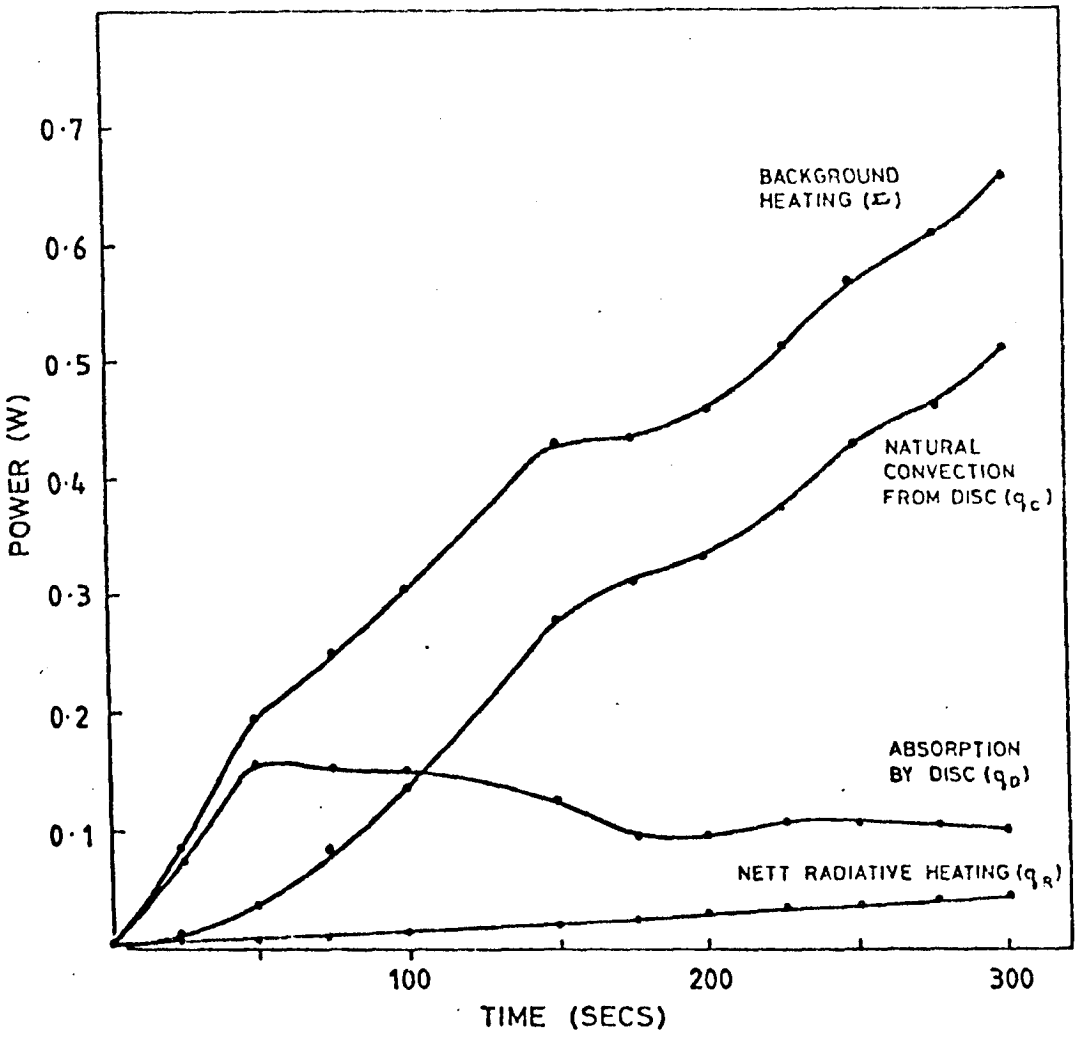

FIGURE 38. RESPONSE OF RADIATION PROBE SHIELDED FROM ARC RADIATION AT 42 BARS (SEE TABLE 7 AND FIGURE 32b)

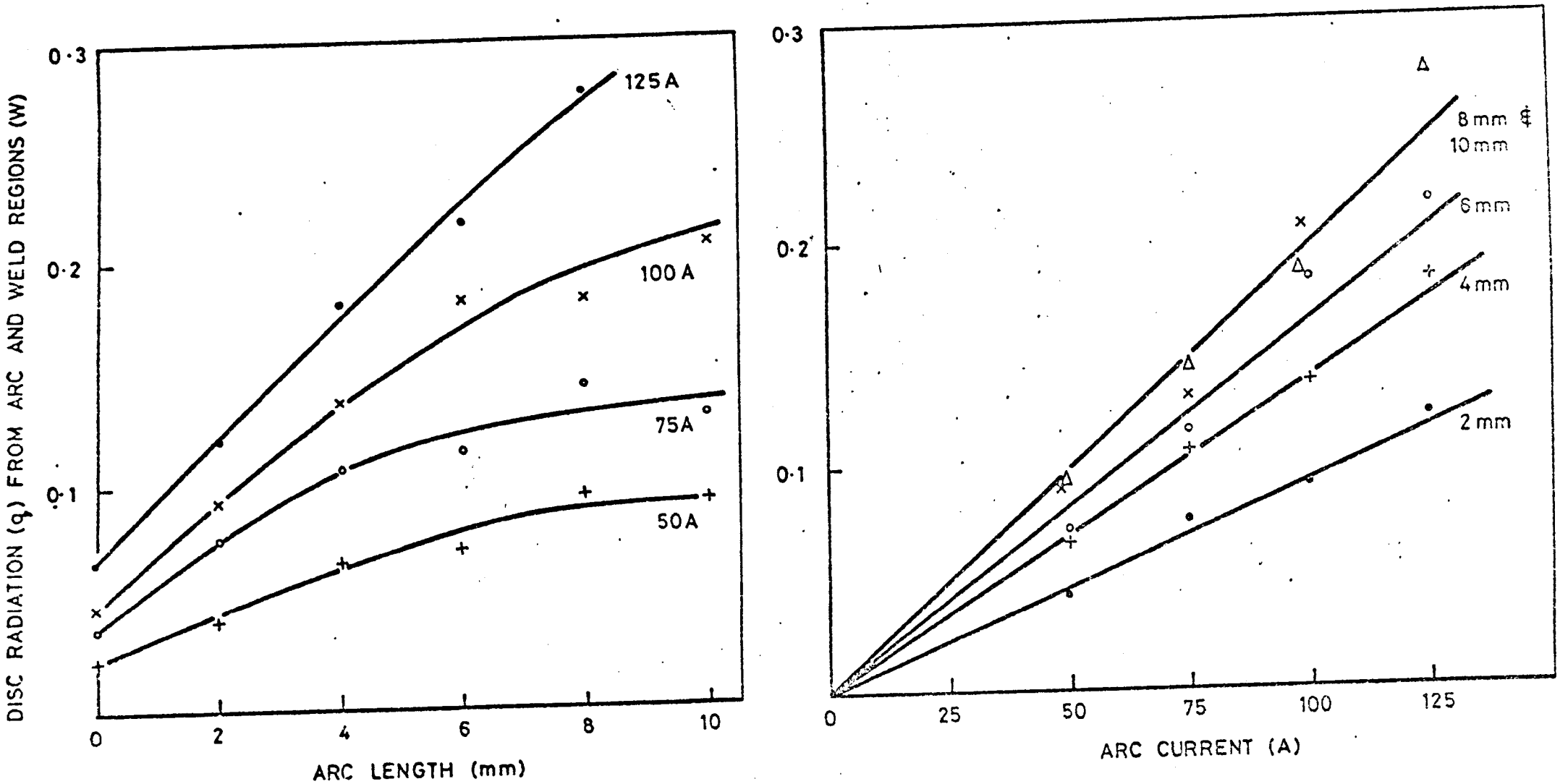

FIGURE 39. DISC RADIATION FROM THE ARC AND WELD REGIONS (1 BAR, ARGON)

regions is expected to be insensitive to arc length. Further the position of the disc within the tube was such that very little arc radiation reflected from the chamber walls entered the tube. The role of chamber wall reflections was further reduced by blackening the chamber walls. The large thermal mass of the chamber is then expected to give reasonable insensitivity to changes in arc length with regard to the radiation emitted/reflected by the walls. It is then reasonable to associate the zero arc length radiation received by a disc with the background radiation q_b. Under these circumstances

$$q_a = q - q_b \tag{75}$$

Values of q_a obtained in this manner have been used to deduce the true arc contribution to disc heating. It is important to note that single arc length measurements cannot produce good estimates of q_a as the background contributions remain unidentified. In the present experiments the zero arc length value has been experimentally found for each arc current and pressure investigated.

The arc contribution to disc heating must now be related to the absolute radiation emanating from the arc. For a point source (Q) radiating isotropically in all directions the radiation received (q_ℓ) by an area A of emissivity ε at a distance ℓ from the source is

$$q_\ell = \frac{Q.A.\varepsilon}{4\pi\ell^2} \quad (\text{when } \ell^2 >> A) \tag{76}$$

In the present situation the arc isn't radiating equally in all direction. This is due to reflections from the weldment. Consider an element within the arc to be radiating above a partially reflecting surface as shown in figure 40. An area 'A' will then receive additional radiant contributions that may be taken as coming from a virtual source of strength Q^1 situated at the same distance below the surface as the arc element is above the surface. When the collecting area is at a sufficiently large distance from the arc (see Appendix 3) the sources Q and Q^1 appear as a point source of strength $(Q+Q^1)$ situated on the plate surface. If α is the reflectivity of the plate then $Q^1 = \alpha Q$. The point source solution (76) now gives:

$$q_\ell = \frac{(1+\alpha).Q.A.\varepsilon}{4\pi\ell^2} \tag{77}$$

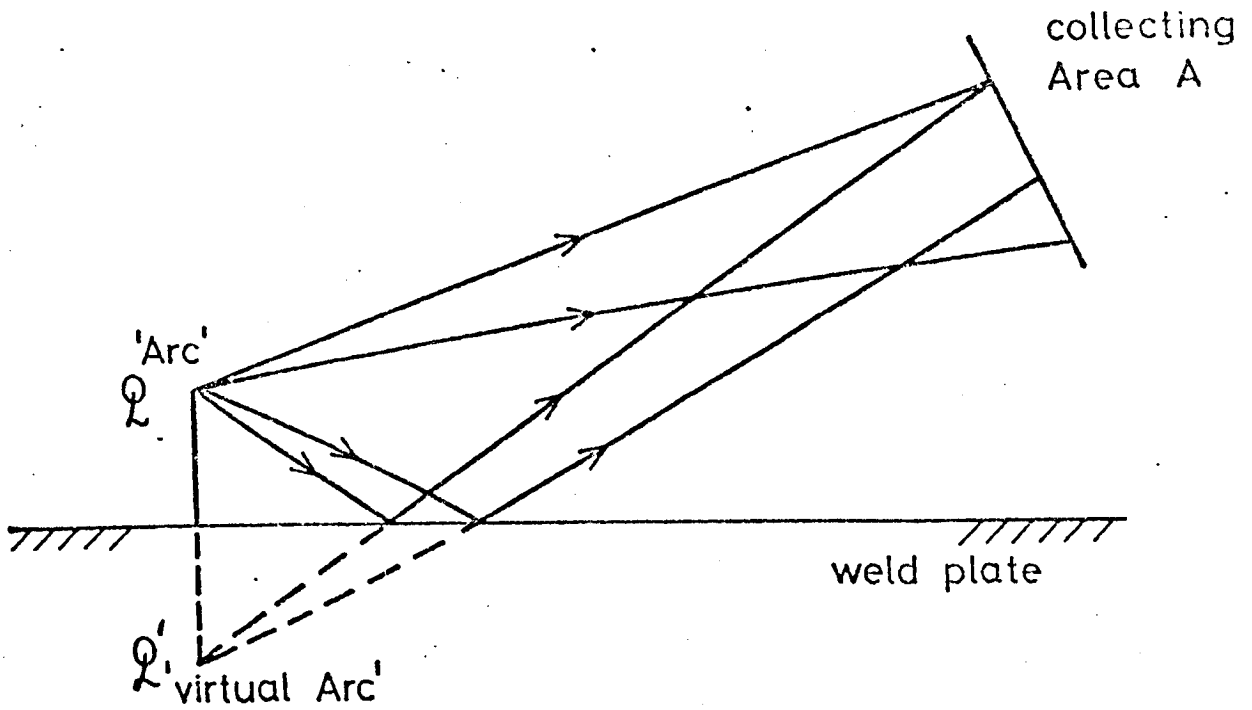

FIGURE 40. THE ARC AS A DIPOLE RADIATION SOURCE.

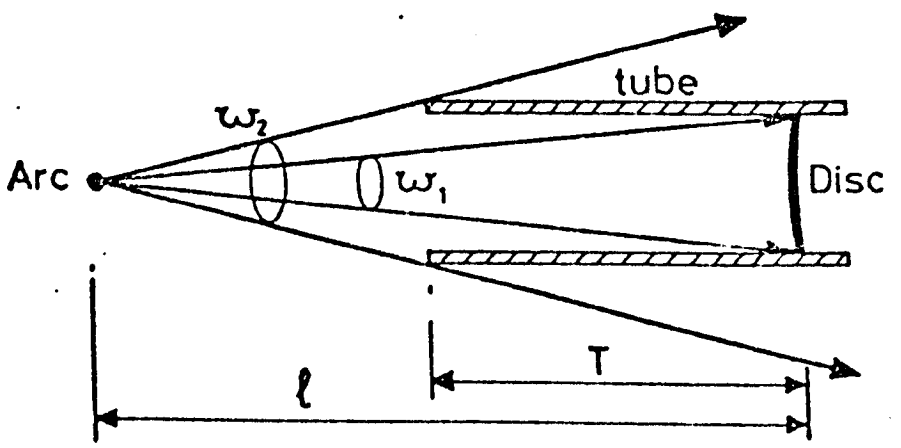

FIGURE 41. EFFECTIVE CAPTURE AREA OF DISC ASSEMBLY

Further complications arise because the disc and tube assembly is not equivalent to an absorbing body of area A situated a distance ℓ from the arc (see figure 41). Radiation from the solid angle ω_1 is directly incident on the disc. However, radiation from the larger solid angle ω_2 may also reach the disc by reflection within the tube. If β is the reflectivity within the tube (blackened) then simple geometric considerations may be used to show that the factor A/ℓ^2 used in equ.77 must be replaced by:

$$\frac{A}{\ell^2}\left\{1 + \beta\left\{\frac{\ell^2}{(\ell-T)^2} - 1\right\}\right\} \qquad (78)$$

where $(\ell-T)$ is the distance of the tube opening from the arc. This expression shows that the absolute power (Q) radiated by the arc is proportional to the arc power received by the disc (q_ℓ). The constant of proportionality depends on the geometry of the disc and tube and on surface conditions at the tube and plate.

The work piece represents a very complicated reflector. In the centre molten weld pool will give rise to high reflectivities. However, it is known (ref.157) that the reflectivity of a plain carbon steel is a complicated function of surface temperature and conditions. Both of these factors will vary considerably over the weldment. Near the pool a high temperature, heavily oxidised region will exist. α is then likely to be between 0.2 and 0.05 (ref.157). For the shiny, relatively cool metal beyond this region the same reference indicates a value of 0.75 to 0.9 for α. To obtain a reasonable estimate of α we regard the plate as being comprised of three zones; the pool of reflectivity α_1 and area a_1, a hot oxidised region of reflectivity α_2 and area a_2, and a cool outer shiny region of reflectivity α_3 and area a_3. A reflectivity (α) weighted in this manner is

$$\alpha = \frac{\alpha_1 a_1 + \alpha_2 a_2 + \alpha_3 a_3}{a_1 + a_2 + a_3}$$

For the present purposes we regard the width of annular regions two and three as being equal to pool radius. Then $a_3/a_1 = 5$, $a_2/a_1 = 3$ with reference to values previously given, reflectivities are taken as $\alpha_1 \simeq 0.95$, $\alpha_2 \simeq 0.05$, $\alpha_3 \simeq 0.80$

Then $\alpha \simeq 0.6$

No great accuracy is associated with this estimate ($\pm$0.2). With reference to equation 77 such an error contributes an uncertainty of order 10% in the absolute radiative arc output estimate.

Reflection within the tube is a simpler parameter to consider. Values of order 0.2 have been associated with the reflectivities of dull black surfaces. In the present case an experimental determination of β is also possible. Experimental measurements of q_ℓ have been made for a range of arc - disc separations (ℓ). The last equation in q_ℓ can then be solved graphically for Q and β i.e. Q is the intercept and $Q.\beta$ the slope (see figure 42). A linear least squares data fit gives:-

Slope of plot $(Q.\beta)$ = 25.37 W

Intercept (Q) = 118 W

$\therefore$ Reflectivity (β) = 0.215

This value of β is in good agreement with the expected value (about 0.2). Correction factors to the point source expression may now be calculated and combining expressions 77 and 78 allows Q to be written as

$$Q = \frac{4\pi\ell^2}{A}\ q_\ell \quad \{0.46\} \tag{79}$$

where values of T = 7.8cm, ℓ = 20cm and ε = 0.95 have been used in evaluating 78. Substituting for A and ℓ gives

$$Q = 733.6\ q_\ell \tag{80}$$

Finally, in absolute terms, the arc column radiation (Q_a) is given by

$$Q_a = Q - Q \text{ (zero arc length)}$$

which, using equation (80), gives

$$Q_a = 733.6\ (q_\ell - q_b) \tag{81}$$

There are many possible sources and type of error that may be involved in this expression. These may best be discussed be restating the detailed expressions on which the above value is based i.e.

$$Q = \frac{4\pi\ell^2}{A.\varepsilon.(1+\alpha)} \cdot \frac{q}{1 + \beta\left(\frac{\ell^2}{(\ell-T)^2} - 1\right)}$$

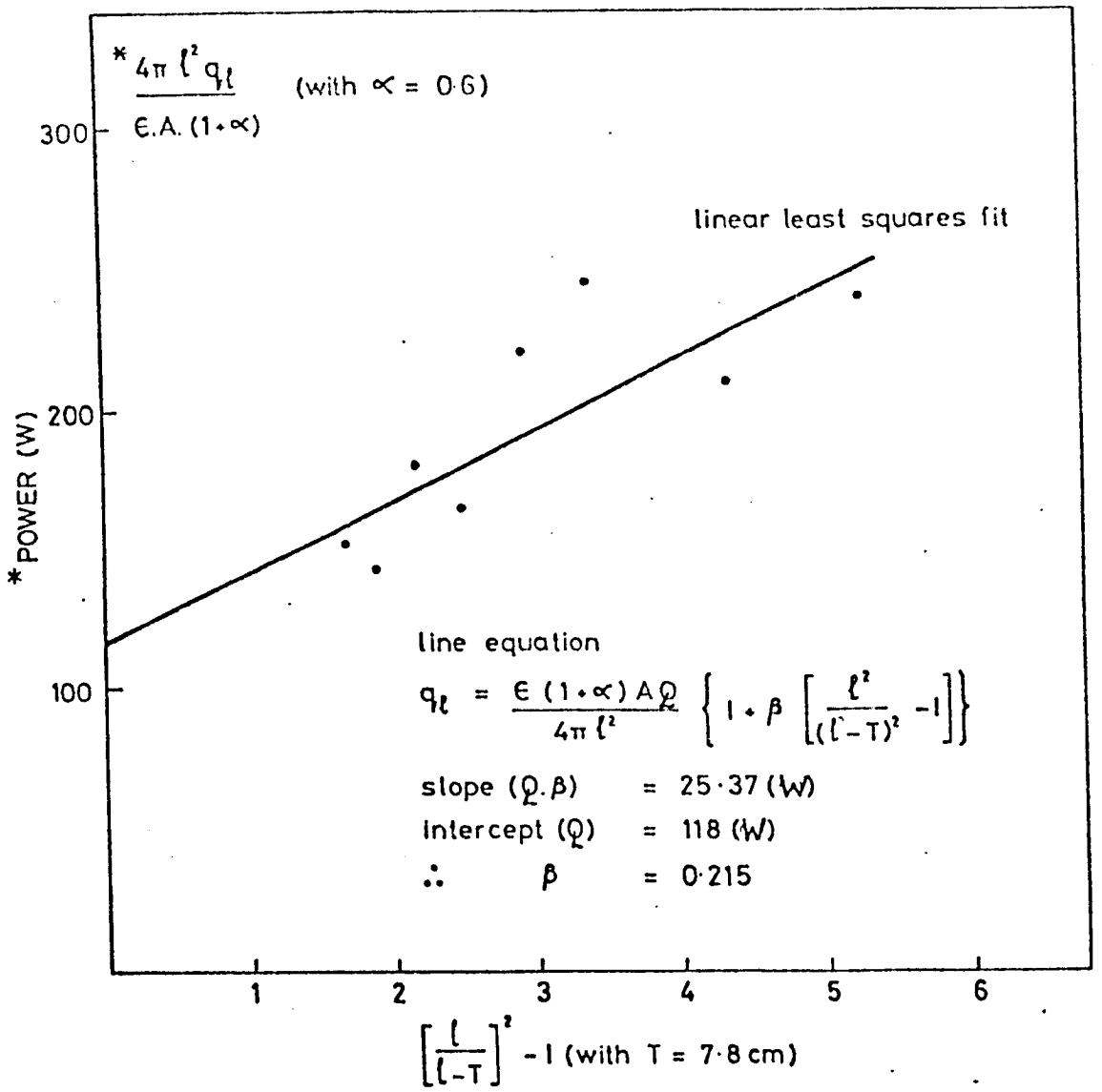

FIGURE 42 DETERMINATION OF TUBE REFLECTIVITY FACTOR β

$$q = \Delta q_D + K\Delta N + \Delta q_R$$

$$Q_a = Q - Q \text{ (zero arc length)}$$

The relative error between values of Q_a is given by the error in $(q-q_b)$ (other factors systemmatically enter all experiments). Considerations in section 3.6.5.2 indicate that q may be found to within about 5%. Graphical errors in determining q_b then indicate an error margin of about 10% in the relative magnitudes of Q_a values. The absolute error in Q_a is likely to be higher than this in view of uncertainties in α and β. Previous estimates indicate that α and β give rise to an error margin of $\pm$10%. The total error margin in Q is then 20%. The good degree of reproducibility obtained indicates that errors associated with arcing conditions and disc settings are generally small. On this basis it is concluded that an error margin of 25% is appropriate to absolute radiation values given here. While this estimate is probably over cautious, uncertainties associated with factors such as work piece surface conditions make closer absolute estimates difficult to justify. It should, however, be realised that the relative errors between results will be much smaller than 25% as many sources enter systematically into all measurements.

4. Results (Characteristics)

4. CHARACTERISTICS

Characteristics of the arc column and weldment are reported separately. Column behaviour is considered in terms of arc appearance, arc modes and electrical characteristics. Emphasis throughout this work has been placed on the behaviour of argon TIG arcs in the presence of a moving weld pool. A more general appreciation of the tungsten arc characteristics has been obtained by changing shielding gas composition and electrode (cathode and anode) characteristics. To this end experiments have also been performed in helium. Cathode geometry and composition have been varied and experiments have also been made with the constricted tungsten - argon arc (plasma arc), on water cooled copper anodes and with arcs operating above stationary conduction limited water cooled steel pools. The results of these are reported largely with respect to corresponding argon - steel experiments. This preserves the intended emphasis and reasons for performing such experiments.

Part 1 Arc Behaviour

4.1. Arc Appearance and Arc Modes

4.1.1. Argon TIG Arcs on Mild Steel Anodes

Conditions existing near the electrodes and in the column are sufficiently different to warrant separate descriptions. Results for the column, anode and cathode regions are therefore presented separately.

4.1.1.1. The Column

Visual observation of the influence of pressure on the arc column indicates that

(a) The luminous boundary becomes smaller with increasing pressure.

(b) Arc luminousity increases with pressure.

(c) The arc becomes more concentrated at the electrode tip often producing gross melting.

(d) Arc stability decreases with increasing pressure and becomes increasingly sensitive to shielding flow conditions.

These qualitative observations have been quantified and further explored by photographic techniques (still and high speed) and by experiments designed to measure specific arc properties (e.g. radiative output).

Arc photographs made from outside chamber (CII) using settings given in section 3 are shown in figure 43. Inspection of these photographs reveals that the outer penumbra in evidence at atmospheric pressure has disappeared by 2.5 bars. It can also be seen that the characteristic bell shape disappears with increasing pressure. This is associated with a decrease in column radius and arc contact area at the anode. At very high pressures (above 30 bars) erratic arc images were obtained (see also figure 44). This behaviour is partly due to refractive index effects within the chamber and not solely with arc behaviour. Such an association is substantiated in the basis of figure 45 showing the shape of a glowing electrode tip just after arc extinction. Behaviour of this sort made arc observation very difficult at pressures beyond 30 bars.

Photographic records of the arc boundary on copper anodes were made in conjunction with current density measurements (see section 6.2). Measurements were taken from arc images by projecting these onto a wall to enhance resolution. The results are shown in figure 46 and compared with electrical boundaries in section 6.2. It can be seen that the column contraction may be represented by a power law of the form

$$R = R_1 P^{-n} \qquad (82)$$

Where R_1 is the arc radius at 1 bar and R the value at pressure P. n is a positive number depending on shielding gas flow conditions and axial position. Near the cathode n ≈ 0.14. This value is 0.17 at the anode. When a strong shield is used n increases to 0.25. Behaviour of this type is discussed in following sections.

4.1.1.2. The Anode

Figure 46 indicates that the arc assumes a more contracted anodic form at pressures above one bar. Such behaviour is strongly dependent on arc current. At very low currents the arc can appear more constricted at the anode than the cathode (see figure 47). Under such condition the anode root

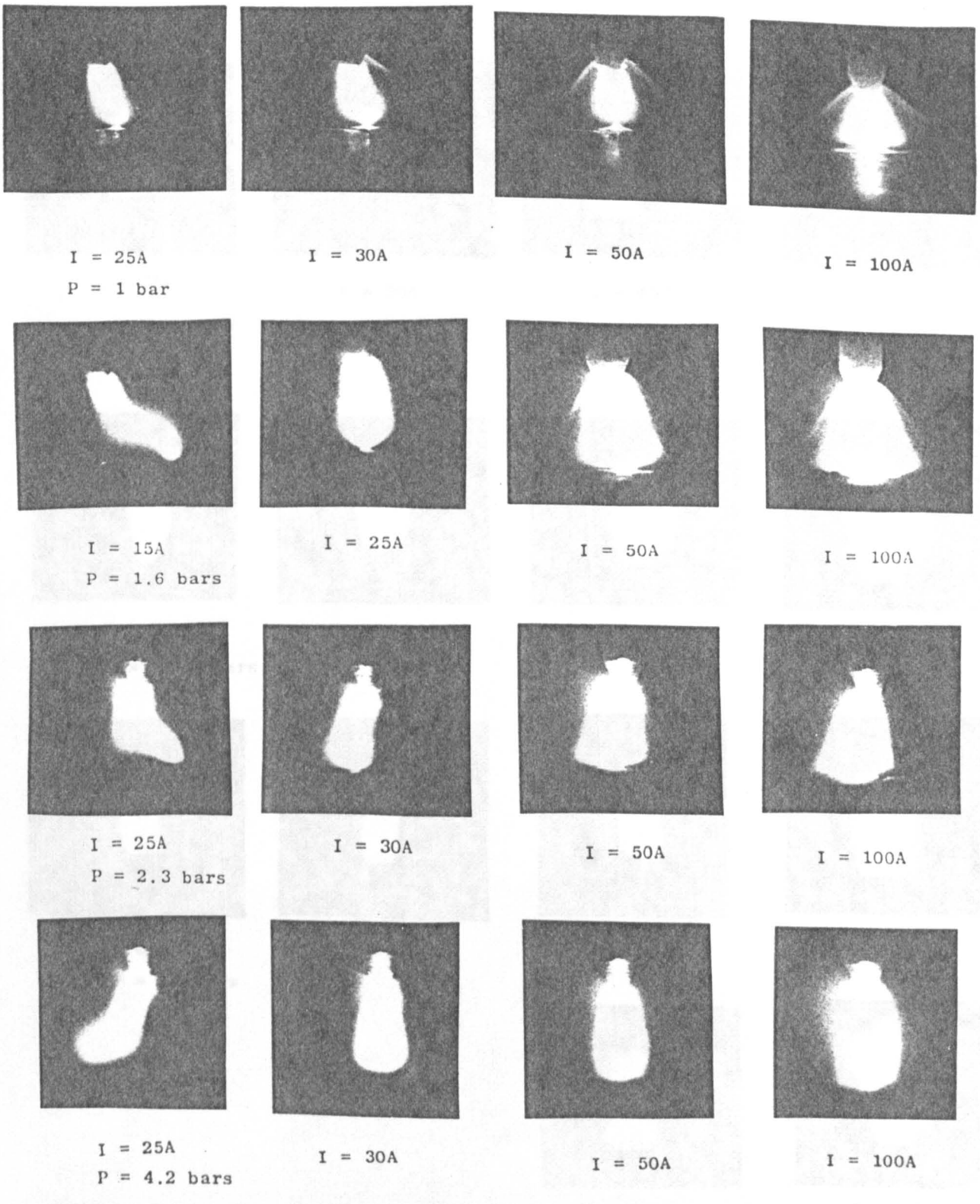

FIGURE 43 Influence of Arc Current and Pressure on Arc Appearance

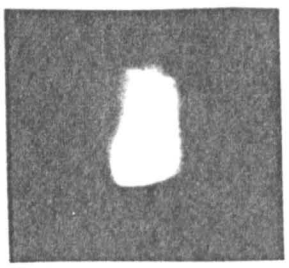

I = 25A

P = 7.8 bars

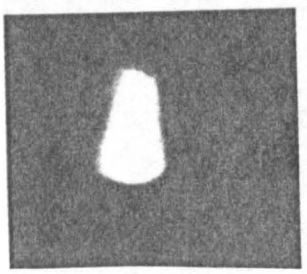

I = 30A

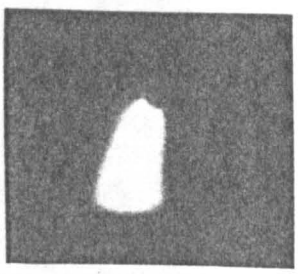

I = 50A

I = 100A

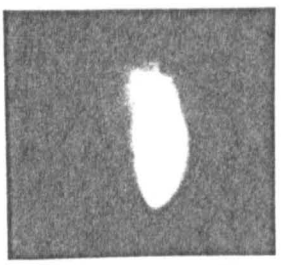

I = 30A

P = 14.2 bars

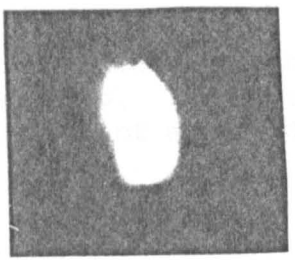

I = 35A

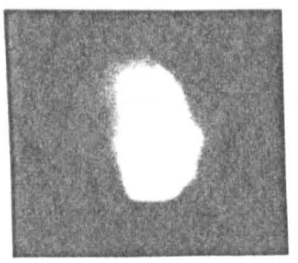

I = 50A

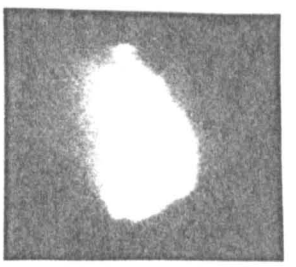

I = 100A

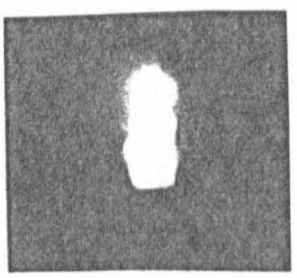

I = 30A

P = 28 bars

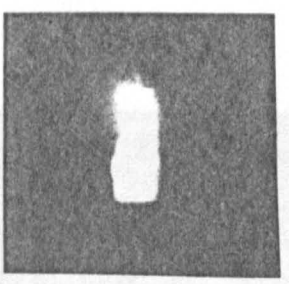

I = 35A

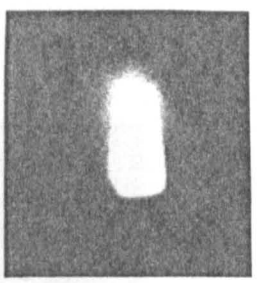

I = 50A

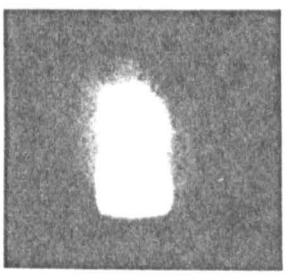

I = 100A

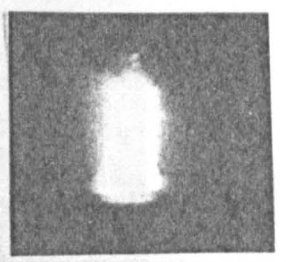

I = 50A

P = 42 bars

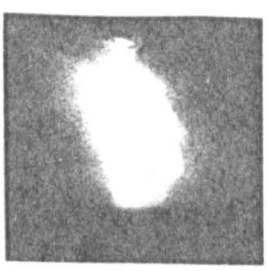

I = 100A

Figure 43b.

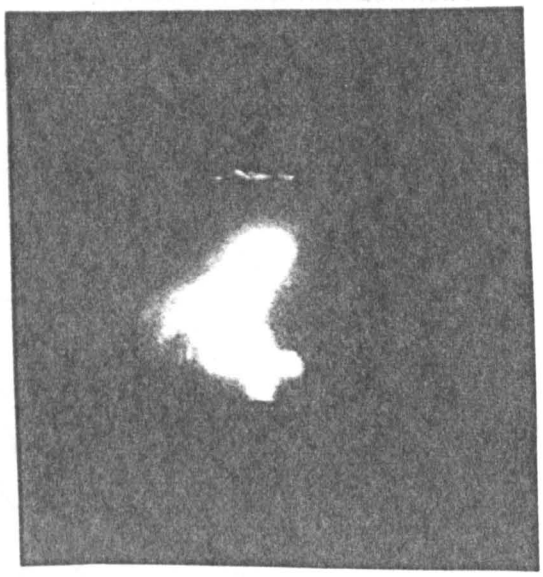

Figure 44 Arc Appearance Occasionally Observed at Very High Pressures. (42 bars, 100A, 5mm, no shield-viewing distance of about 70cm).

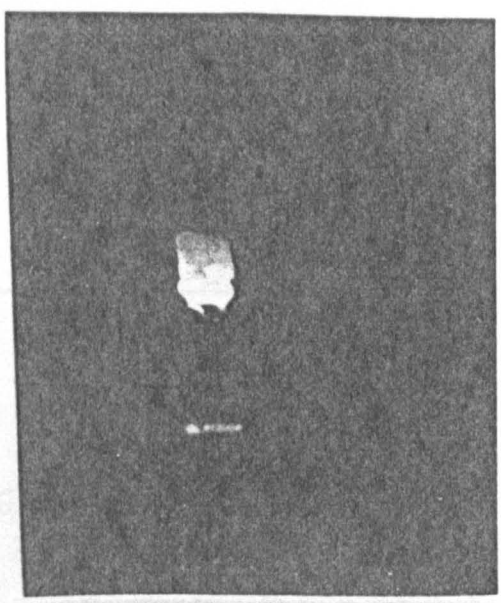

Figure 45 Appearance of Arc Shown in Fig.44 just after Arc Extinction

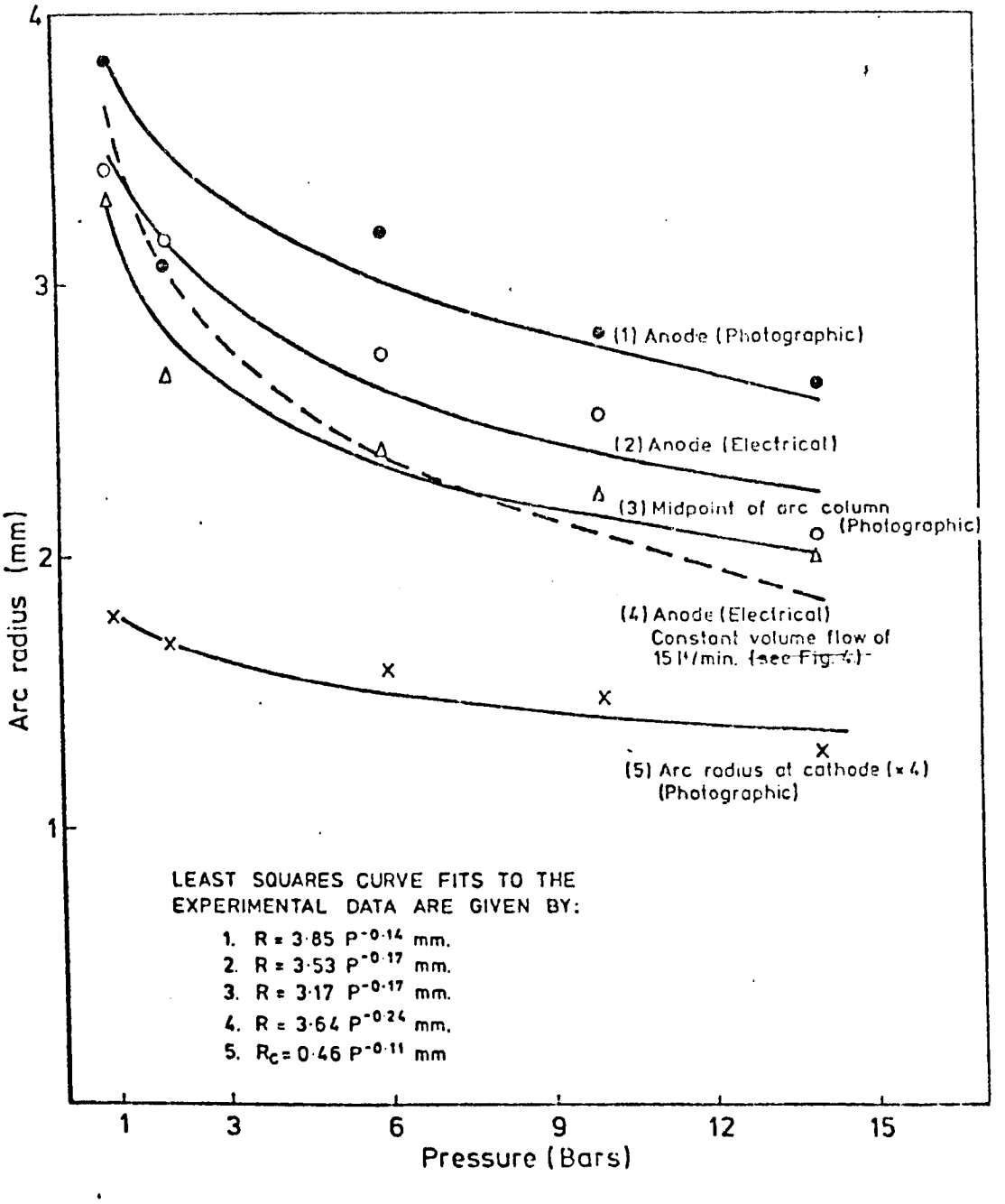

FIG.46. DEPENDENCE OF MEAN ARC RADIUS ON PRESSURE (AVERAGED OVER ALL FLOW VALUES)

moves discretely from one rooting site to another i.e. 'heel and step'. This behaviour may also give rise to an anode jet strong enough to repel the cathodic flow (see figure 48). It was generally observed that such behaviour was strongly current dependent which above some critical current gave way to the diffuse anodic form normally used in welding. The critical current (I_c) at which this change occurs have been examined. It is observed that (I_c) increases with arc length (see figure 49) but the pressure dependence is more complicated and depends critically on anode conditions (see section 5.2). At currents above I_c the arc often 'flickered' across the anode until some further current where a stable root appeared. In all cases this behaviour was associated with the negative arm of the V-I characteristic.

Experiments were also performed to examine the influence of buoyancy forces on anode spot behaviour i.e. by inverting the chamber and operating in the overhead position. In this position, no constricted anode mode occurred for pressures above 7.8 bars for the arc currents investigated (≥20A) - see figure 60..

4.1.1.3. The Cathode

Arc appearance at the cathode was associated with the cathode spot mode (CSM). It was observed that the 'plasma climb' effect became increasingly less evident above one atmosphere. This was particularly noticeable at 2.4 bars where the outer penumbra disappeared. Measurements of arc diameter at the cathode have been made and were presented in section 4.1.1.2. These show the luminous boundary to contract with pressure between 1 and 14.6 bars in a manner given by $P^{-0.11}$.

Gross electrode tip melting was often observed above 4.4 bars. Melting was generally confined to the tip for 3.2mm tungsten electrodes where a spherical molten zone formed (see figure 50). Such behaviour effectively destroys the pre-set tip vertex angle in place of a spherical geometry. More extreme behaviour was observed for smaller diameter electrode (2.4mm - 1% and 2% thoriated) where the complete electrode taper often disappeared during a short arcing time (figure 50).

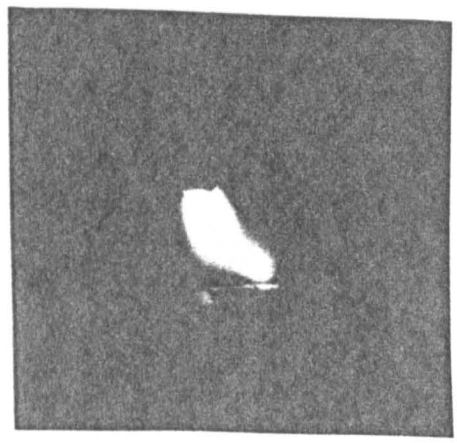

Figure 47 Highly Constricted Anode Root
(5mm, 20A, atmospheric argon)

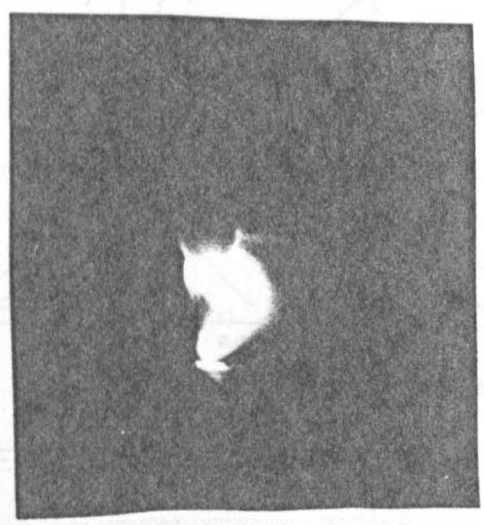

Figure 48 Anode Jet Repelling Cathode Jet (5mm 15A, atmospheric argon)

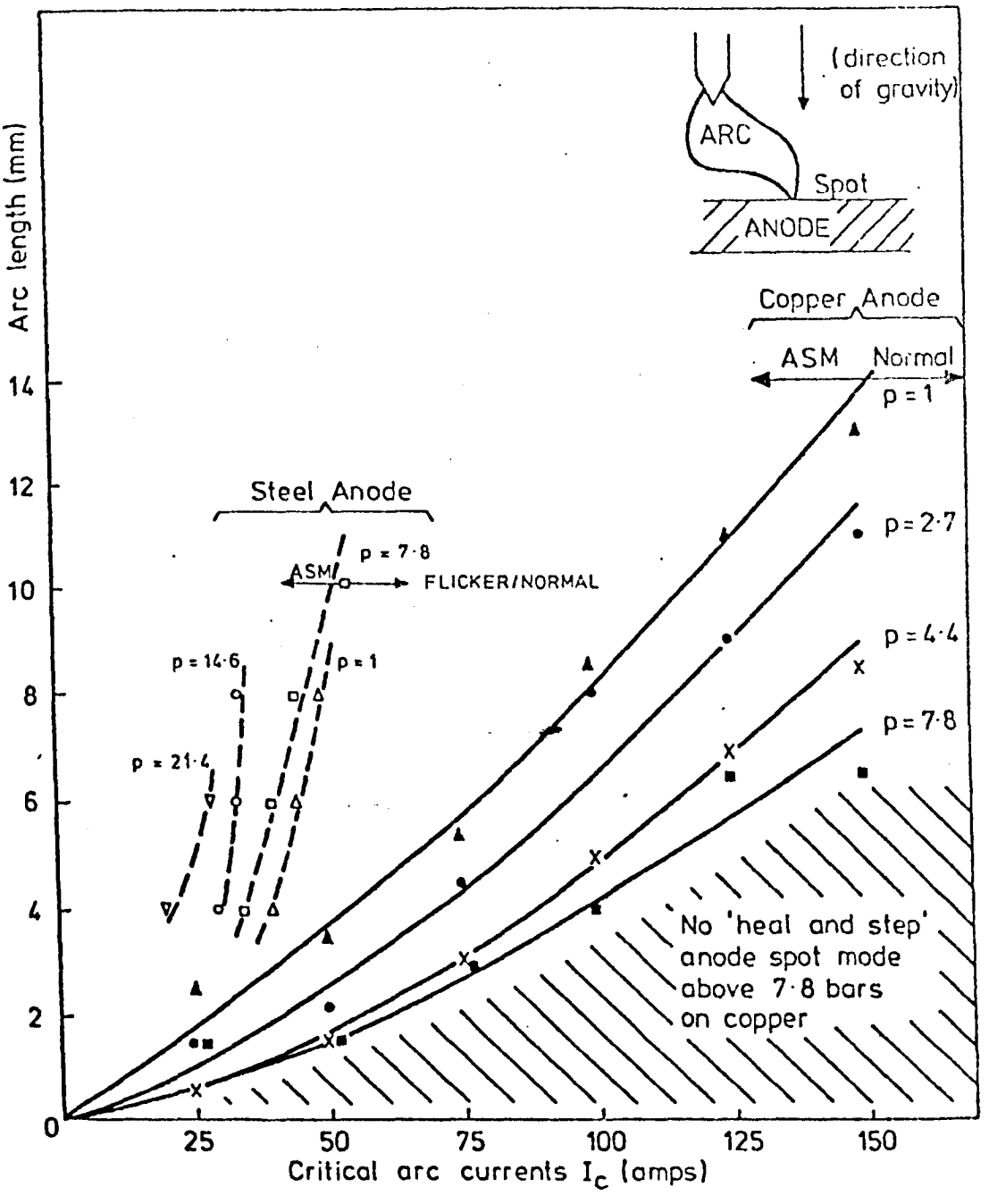

FIGURE 49. CRITICAL CURRENTS AT WHICH THE ANODE SPOT MODE OCCURS ON COPPER AND STEEL ANODES

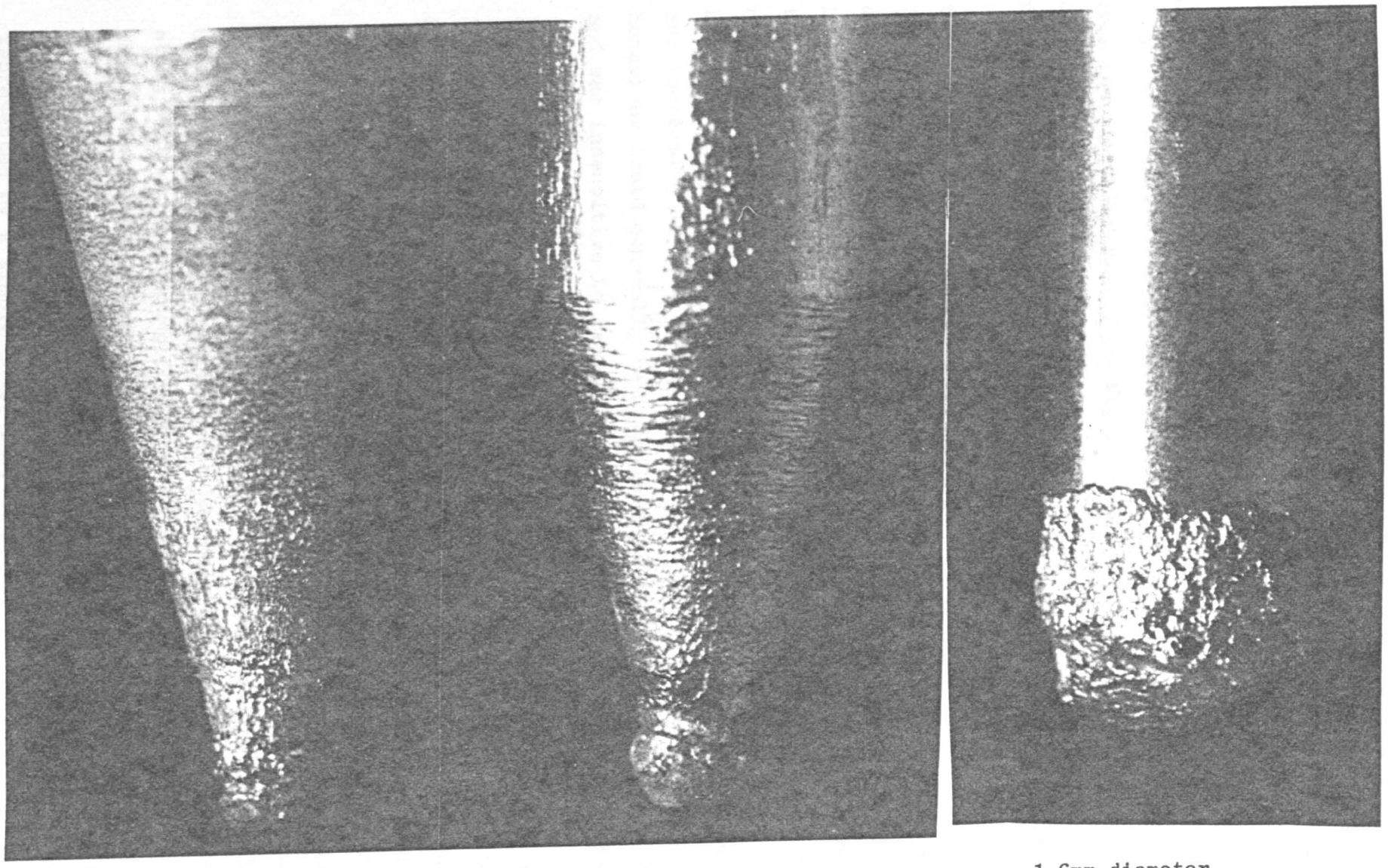

4.8mm diameter 3.2mm diameter 1.6mm diameter

Figure 50. Electrode erosion at high pressures (42 bar argon environment, 30^{o} angle, 1% thoriated, 100A)

4.1.2. Argon TIG Arcs on Cooled Copper Anodes

The column and cathode regions for TIG arcs on copper anodes appeared similar to those observed on steel anodes. Significant differences did, however, appear in low current anode rooting behaviour. For all pressures it was found that the anode spot mode transition current (for a given arc length) occurred at a higher current on copper than on steel. This behaviour is particularly sensitive to pressure and changes significantly over the first 7.8 bars (see figure 49). The tendency at any arc length is for I_c to double over this pressure range. The most remarkable feature of this behaviour is the direction in which pressure changes I_c. For steel anodes I_c is found to decrease with increasing pressure while for copper anodes I_c increases with pressure (for 7.8 bars > P). Beyond 7.8 bars no heel and step mode was observed on copper. The arc then adopts a more concentrated form and moves continuously across the anode. However, it is possible that anode spot behaviour still exists but is then localised within the root. This possibility is associated with the observed existence of spots dancing round the edge of the arc-plate boundary. Results reported above were obtained by fixing arc current and increasing arc length until heel and step behaviour occurred. This behaviour could generally be reproduced to within $\pm$0.5mm of arc length and was insensitive to travel speed over the range 0.5 to 5mm/sec.

The column of an argon arc on a copper anode appeared more sensitive to the influence of shielding gas flow than on steel anodes. At high pressures moderate volumetric flow rates (20 ℓ/min) often extinguished the arc. The arc was observed visually to flicker with increasing amplitude as flow rate was increased. This observation is quantified by experiments reported in section 6. Here a split copper anode arrangement is reported that allows the measurement of arc column oscillation amplitudes at the anode. The same arrangement has been used to measure the electrical arc boundary at the anode. These results along with corresponding photographic measurements are shown in figure 46. It can be seen that the results of the photographic technique are in good agreement with electrical measurements. Both indicate the arc column boundary to contract with pressure in a manner that is well represented by a simple power law.

4.1.3. Helium TIG Arcs on Mild Steel Anodes

At one bar short helium TIG arcs are characteristically ball shaped in geometry (see figure 51a). For long arc lengths this geometry becomes conic (51b). No central core is observed and arc rooting is through a well defined spot. At low currents (20 amps) the anode spot becomes highly constricted (figure 52). However, only one anode spot was ever observed and no heel and step motion occurred. This behaviour contrasts that of the atmospheric argon arc. Similar behaviour is also observed at chamber pressures of 1.7 bars and 2.4 bars. Quite different behaviour may occur at and above 4.4 bars. The arc then takes a conic form and spreads across the anode in a manner similar to the atmospheric TIG arc.. A central core region can also develop with a surrounding penumbra. At pressures of 14.6 bars jetting is so strong that a reflected flame is often in evidence at the anode (see figure 53). Cathode erosion is severe in helium arcs and electrode geometry is quickly lost at high pressures. Above 14.6 bars unacceptable levels of electrode erosion were experienced and so no experiments were made in this region.

At pressures as low as 10 bars it was found possible to produce an arc that flashed blue and red alternatively. This was accompanied by regular changes in arc current and voltage. An investigation of this behaviour was undertaken using high speed photography (500 fps) and high speed (200mm/s) UVO current and voltage recordings. Results are shown in figures 54. It can be seen that an intense central core exists during the 'red' period and that the arc diameter is smaller than during the 'blue' period. The photographic record shown in figure 54 indicates that the transition from red phase to blue phase is completed in a time of about 5ms (i.e. 3 frames). The period of the behaviour is about 20ms (50Hz) with approximately equal time in each phase. UVO traces show that the phenomena may also occur on longer time scales (e.g. 1Hz, 10Hz, 20Hz see figure 55). It can be seen that voltage and current pulse between high and low levels and that arc current is minimum when voltage is maximum.

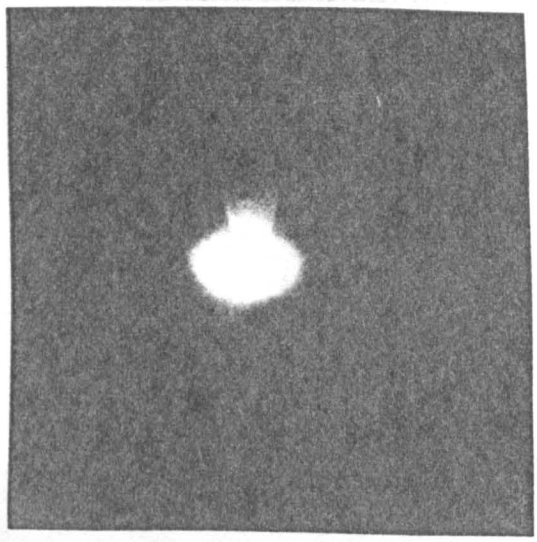

(a) Short arc (2mm)

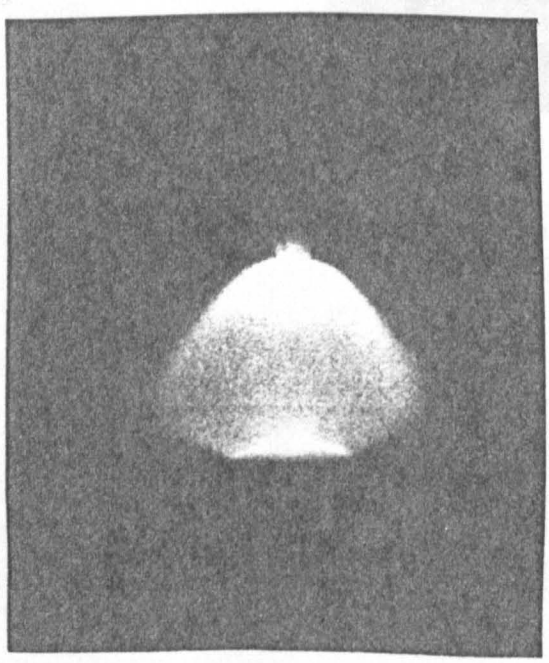

10mm

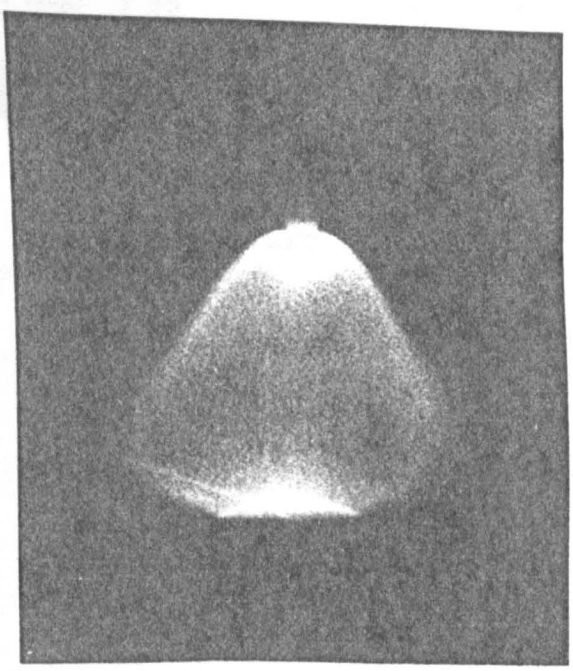

15mm

(b) Long arcs

Figure 51 Appearance of the 100A Atmospheric Helium TIG Arc

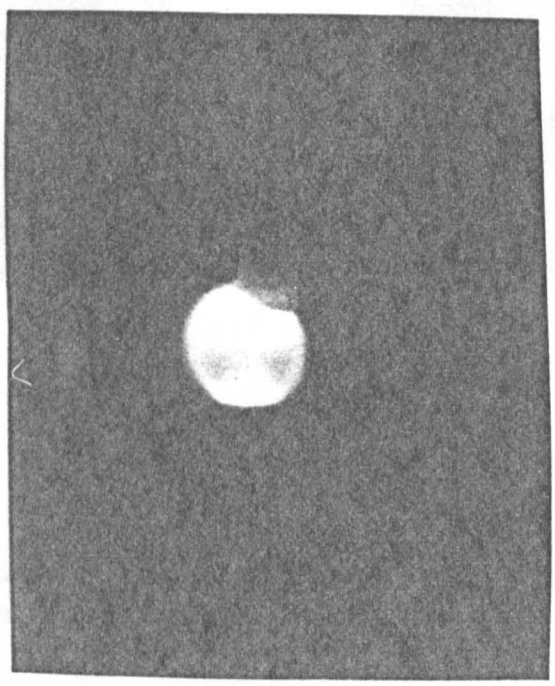

Figure 52 Constricted Anodic Form of Helium Arc
(20A, 1.7 bars (abs), 5mm arc)

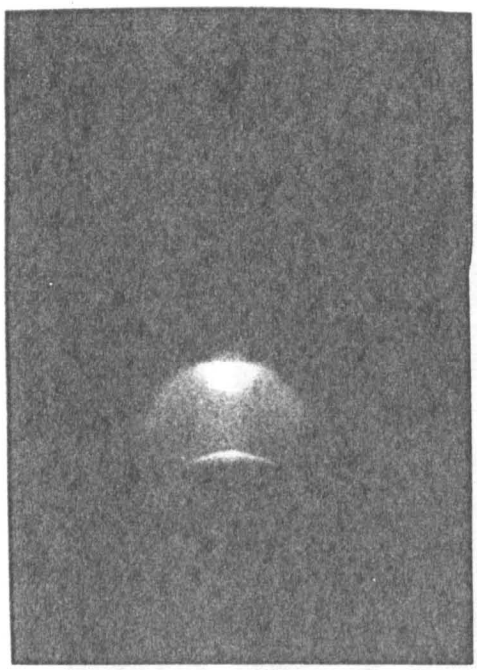

P = 1 bar

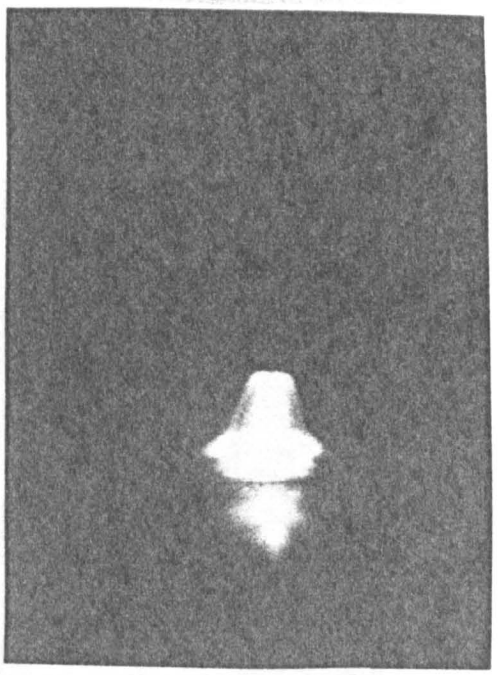

P = 14.6 bars

Figure 53 Reflected Anode Flame from a High Pressure (14.6 bars) Helium TIG Arc (5mm, 100A)

Note:- Behaviour at 1 bar is also Included for Comparative Purposes

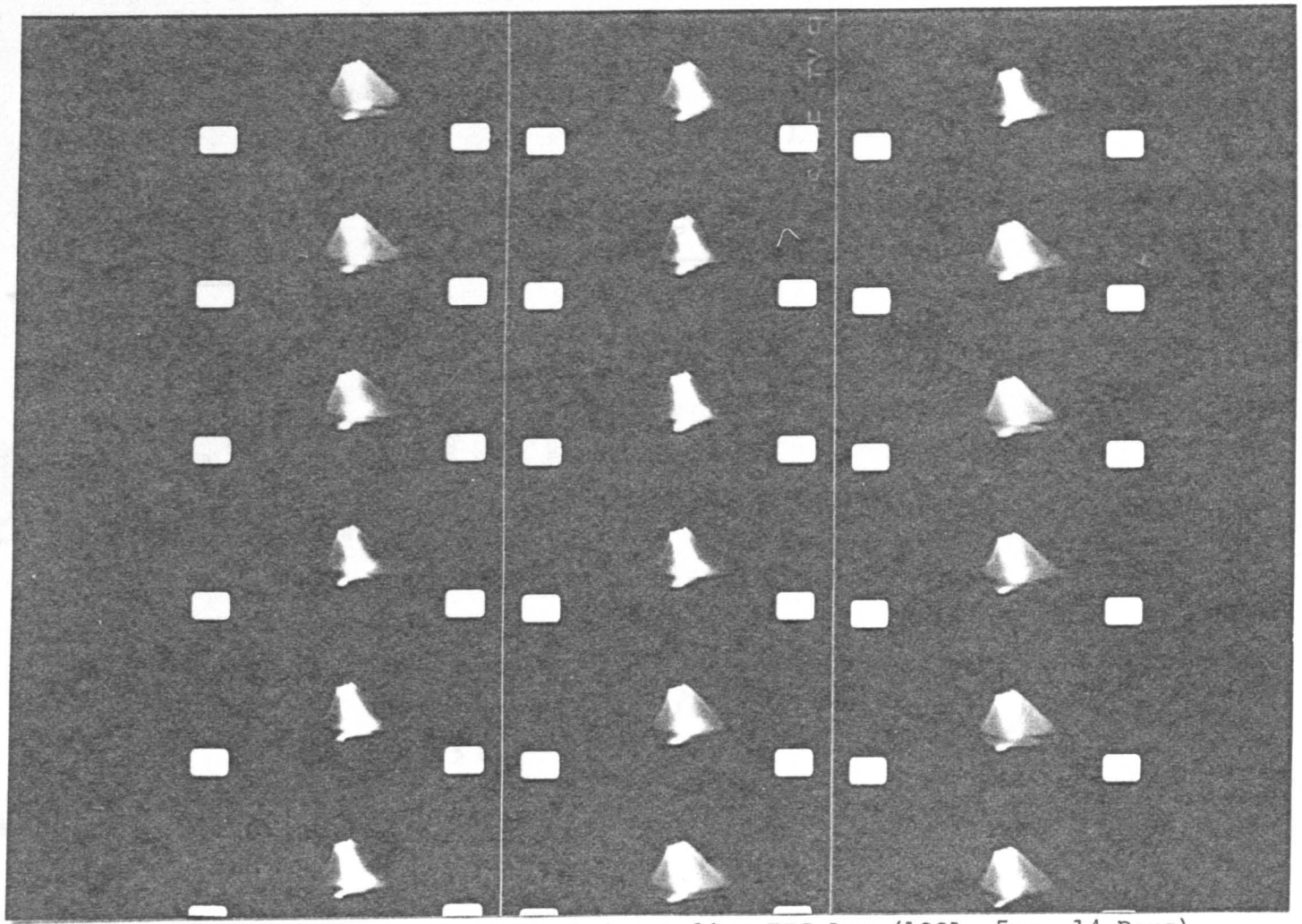

Figure 54 High Speed Film (500 fps) of Self Pulsing Helium TIG Arc (100A, 5mm, 14 Bars)

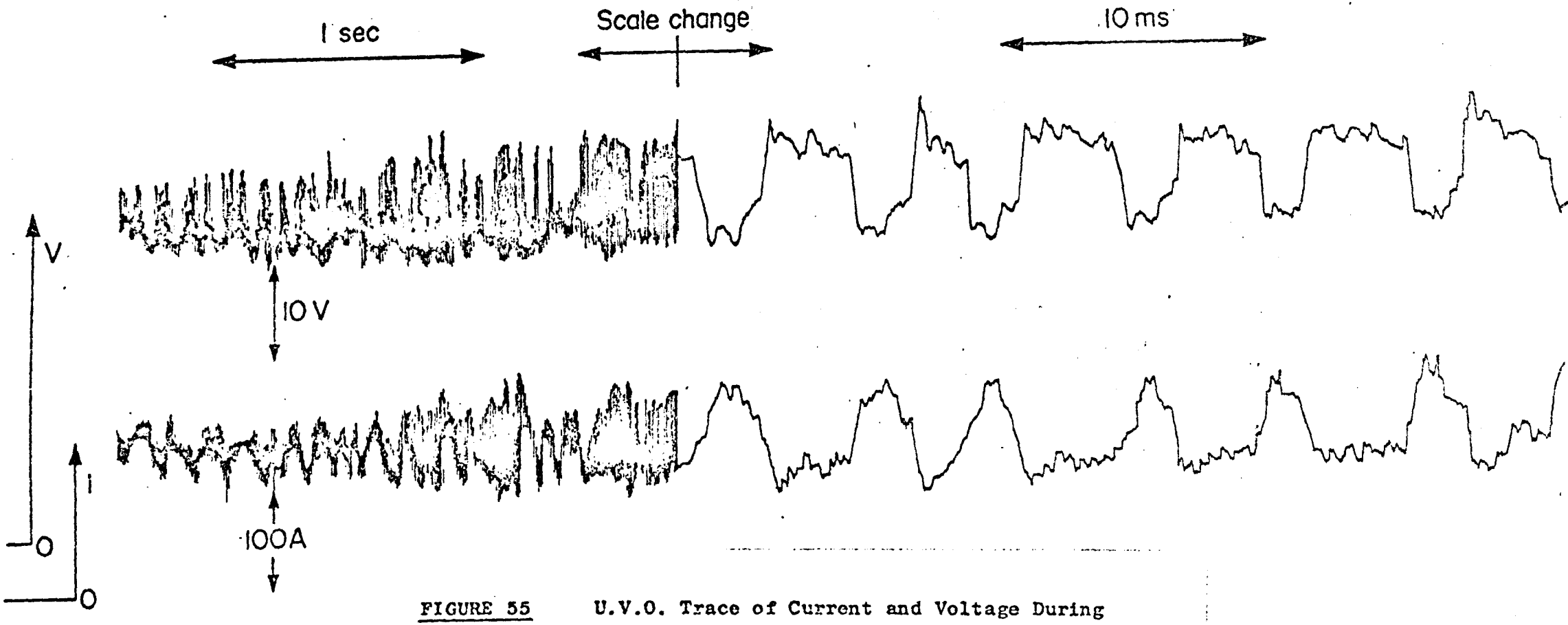

FIGURE 55 U.V.O. Trace of Current and Voltage During Pulsating Arc Behaviour (100A, 5mm helium arc, 14 bars)

4.1.4. Helium TIG Arcs on Cooled Copper Anodes

Arc stability was generally poorer than on steel anodes. Despite this, electrode erosion was less severe and the 'self-pulsating' mode was not encountered.

4.1.5. The Constricted Argon Tungsten Arc (Plasma Arc)

The constricted TIG arc was found to possess a high degree of stability over the pressure range 1 to 14.6 bars. This behaviour was observed for a wide range of plasma and shielding gas flow rates. However, cathodic erosion tended to increase with pressure and in extreme cases the aluminium oxide shield cup exhibited local melting. As in the unconstricted arc, a tendency for column contraction with increasing pressure was also noted. This behaviour was complicated by the influence of gas flow, orifice size and arc current. Photographic records were made of plasma arcs operating on stainless steel and copper anodes (see figure 56). The most noticeable difference between arc behaviour on these materials was the tendency of the arc to spread over the copper anode while remaining more localised on steel. Arc profiles traced from projected photographic (slide) images are shown in figure 57. It can be seen that the arc column contracts at atmospheric pressure with increasing plasma gas flow rate. Contraction is accompanied by an increase in extent of the region spreading across the anode. A similar but less pronounced contraction is observed at higher pressures. The spread of the arc across the anode is little influenced by flow and there is no evidence of a reflected anode flame.

4.2. Electrical Behaviour

4.2.1. Argon TIG Arcs

4.2.1.1. Voltage - Current Characteristics (V-I)

The general form of the V-I characteristic at high pressures is similar to that observed at 1 bar exhibiting a negative gradient at low currents and a positive gradient at high currents. It can be seen (figure 58) that the magnitude of arc voltage increases with pressure and that the effect of pressure diminishes as arc current is reduced. The last observation indicates that the effect of pressure is felt most strongly

Copper anode
I = 100A
P = 7.8 bars
Plasma Flow Setting: 1.5
4.8mm orifice
10mm arc

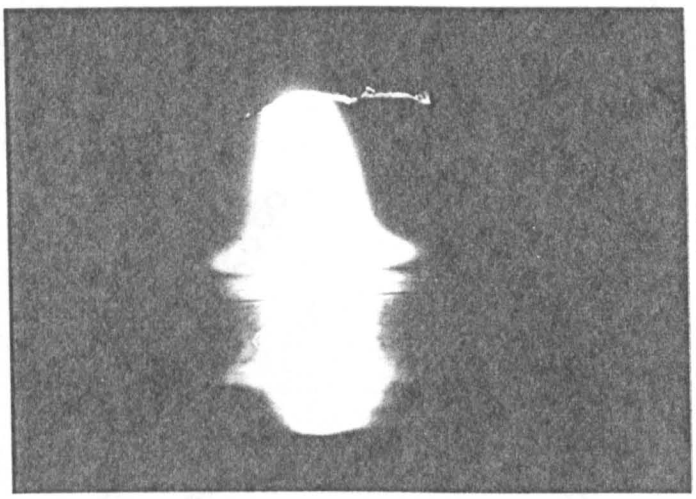

Copper anode
I = 100A
P = 1 bar
Plasma Flow Setting: 1.5
4.8mm orifice
10mm arc

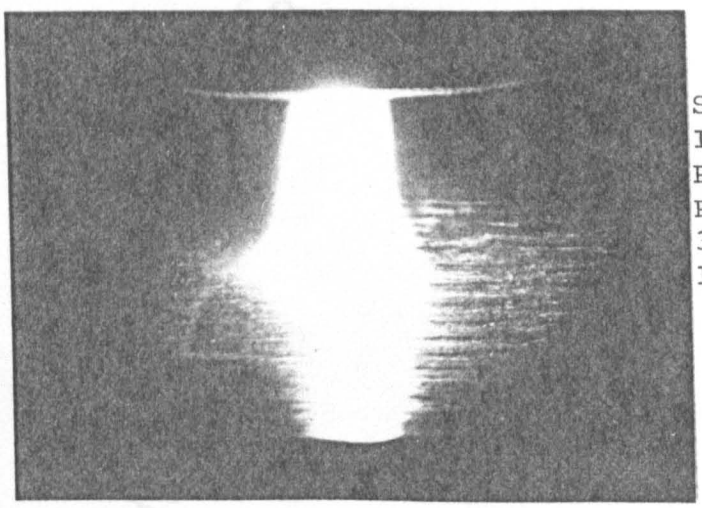

Steel anode
I = 100A
P = 7.8 bars
Plasma Flow Setting: 2.5
3.2mm orifice
10mm arc

Figure 56 Appearance of Plasma Arcs on Steel and Copper Anodes

FIG.57. The influence of gas flow and ambient pressure on arc profile in plasma welding.(Magnification of 12) 150A arc, 4·8mm. orifice.

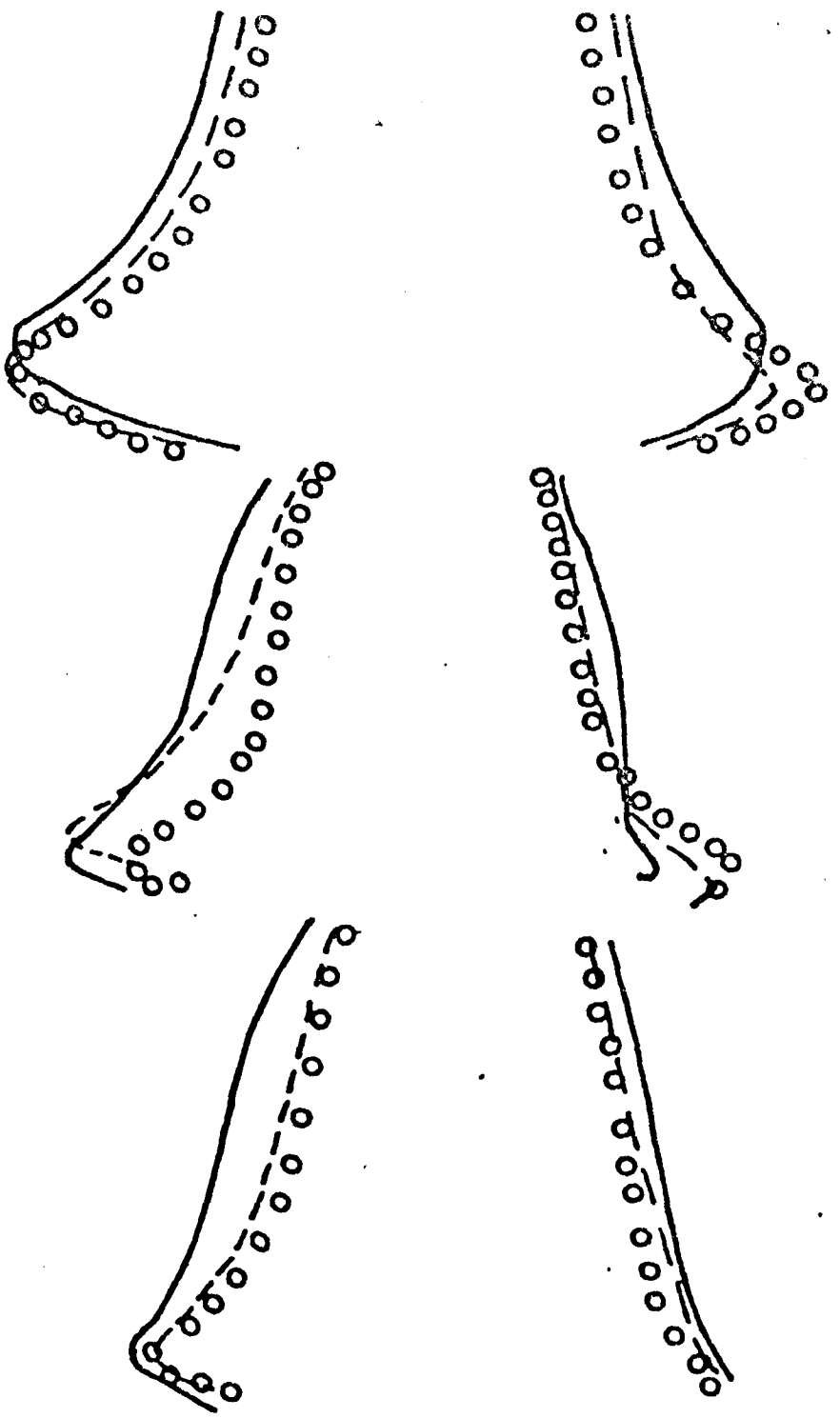

P=1 bar

P=4·4 bars

P=7·8 bars

S=1 ————

S=2 - - - - - - -

S=3 ooooooooo

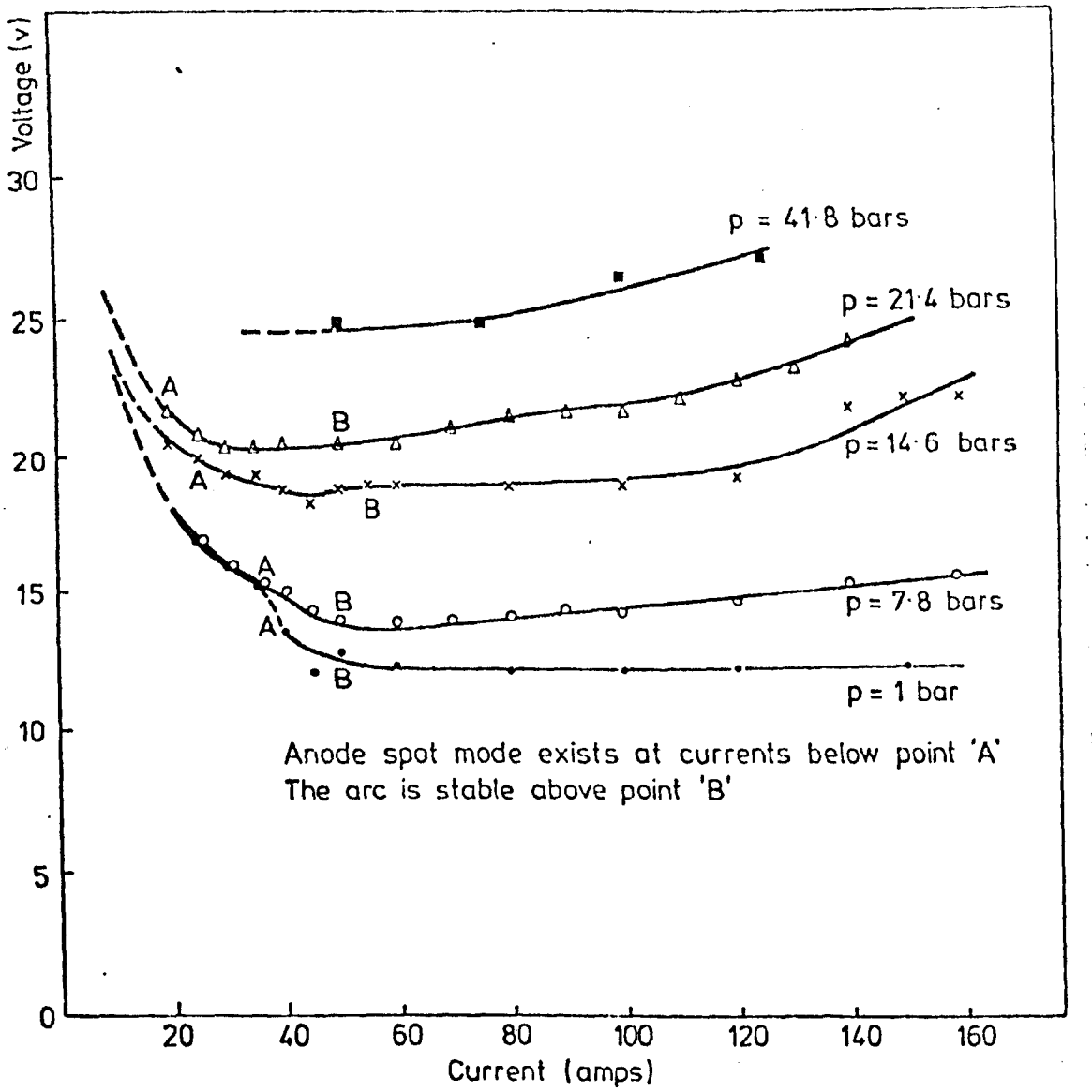

FIGURE 58. V-I CHARACTERISTICS OF A 4 mm ARGON ARC ON A MOVING STEEL ANODE (DOWNHAND)

in the column and not at the electrode regions. The characteristic has an ill defined minima that tends to move to lower currents with increasing pressure while the gradient of the positive arm increases with pressure. Experiments indicate that this gradient is a slowly increasing function of current and generally independent of arc length (see figure 59). The same figure shows that arc length has no significant effect on the position of V-I minima.

Arc appearance was also simultaneously recorded during the course of V-I experiments. Particular attention was given to recording the current at which the anode spot mode first occurs. The critical current (I_c) is denoted by 'A' on the respective graphs. This is followed by a transitional region during which the arc flickered before assuming the usual high current form, at a point denoted by 'B'. It can be seen that the point 'A' moves to lower currents with increasing pressure and occurs on the negative slope of the V-I curve. The critical current increases with increasing arc length (see figure 59). Experiments were also performed in the overhead position to examine the influence of buoyancy on I_c. Results are shown in figure 60 and 61. By comparing with figures 58 and 59.it can be seen that the arc voltage is slightly higher for this position than in the down hand position. One of the most interesting observations is the disappearances of the anode spot mode above 7.8 bars (for currents of 20A and greater). Voltage measurements shown in figures 60 and 61, exhibit a larger scatter than for down hand welding. This is possibly the result of enhanced convective motion within the chamber in overhead welding.

4.2.1.2. Voltage - Electrode Separation Characteristics (V-ℓ)

Many experiments were performed during the course of this work that involved systematically measuring V-ℓ characteristics e.g. calorimetric, radiation and weld bead experiments. These results are produced here. Derived values, such as the pressure dependence of electric field strength, are also analysed and discussed in this section. Experiments have been performed for a wide range of arrangements e.g. arcs above moving anodes with weld pools, arcs above stationary anodes with and without weld pools, arcs in strong flows, arcs in stagnant atmosphere, arcs on copper and in

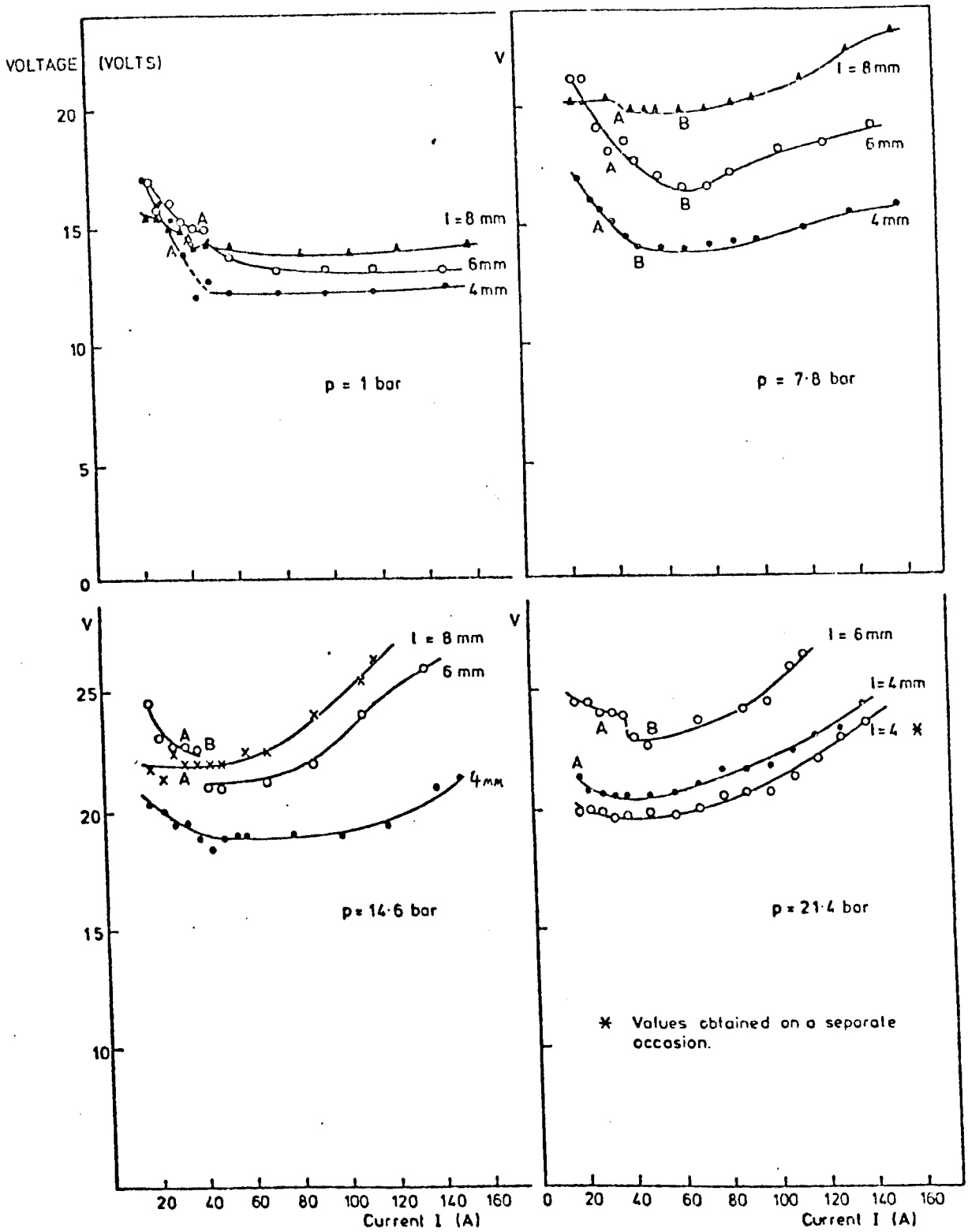

FIGURE 59. V-I CHARACTERISTICS OF ARGON ARCS ON A MOVING STEEL ANODE IN THE DOWNHAND POSITION.

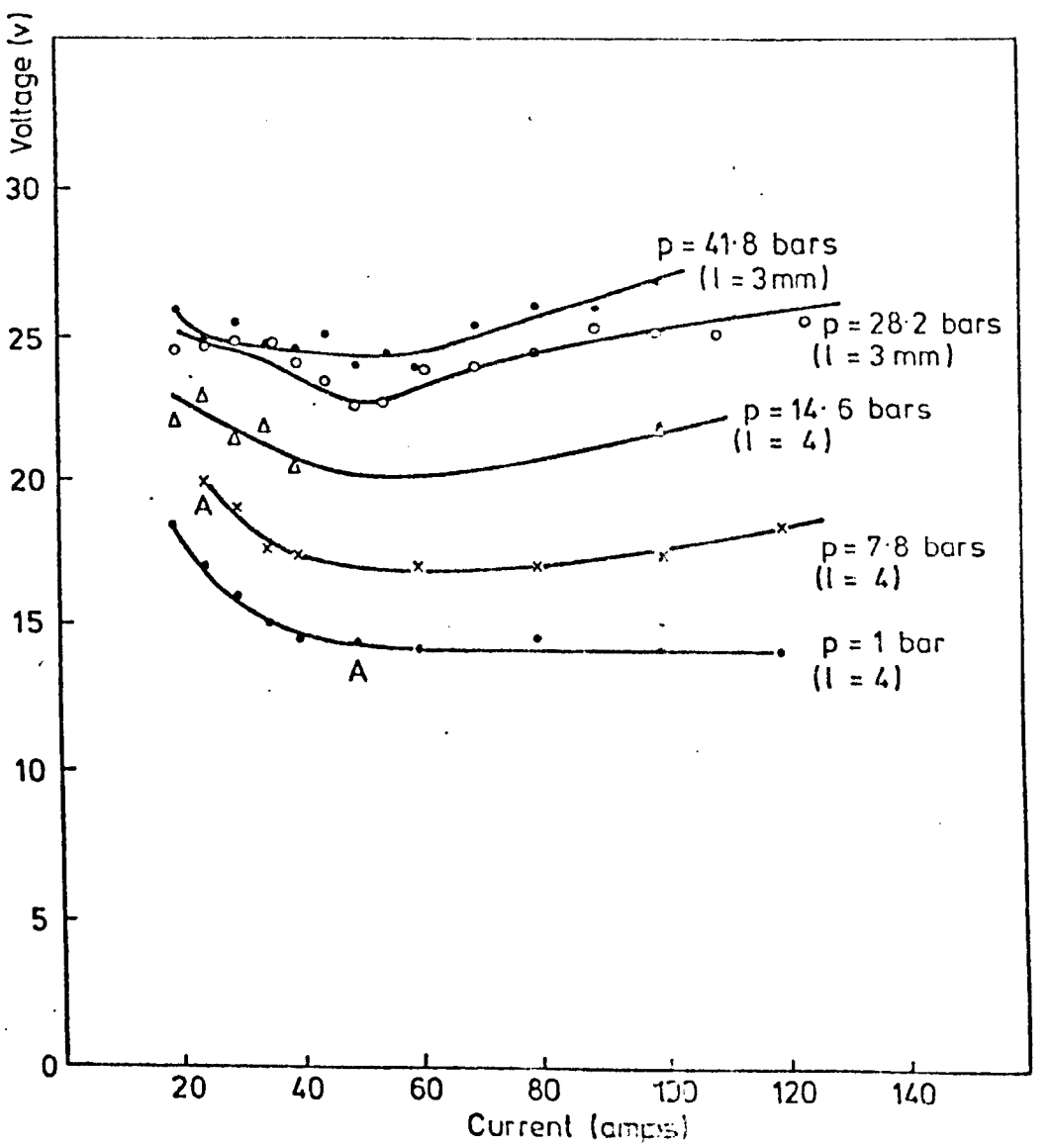

FIGURE 60. V - I CHARACTERISTICS OF ARGON ARCS A MOVING STEEL ANODE IN THE OVERHEAD POSITION

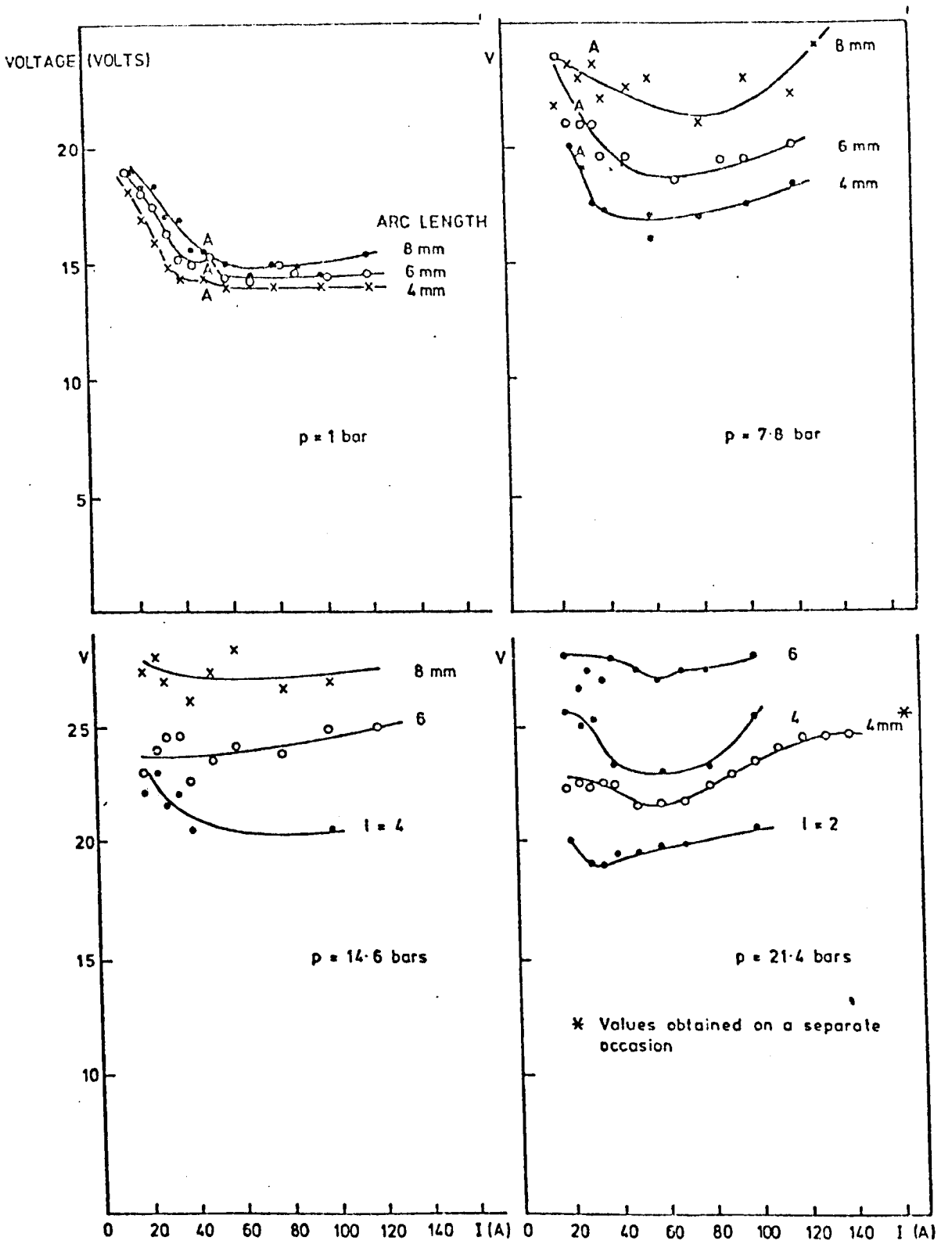

FIGURE 61. V-I CHARACTERISTICS OF ARGON ARCS ON A MOVING STEEL ANODE IN THE OVERHEAD POSITION.

helium and constricted arcs on copper and steel. In this section only argon TIG arcs are discussed.

Inspection of typical V-ℓ curves (see figure 62-67) indicates that the characteristic is substantially linear for currents above 75 Amps and arc lengths of 4mm's and less. At longer arc lengths the gradient sometimes (depending on the arrangement) falls. This is particularly noticeable for 50 Amp arcs and becomes more marked with increasing pressure e.g. (see figures 62 and 67). It is found that the zero electrode separation voltage is almost independent of ambient pressure. This indicates that the effect of pressure on arc voltage is confined to the column. Small changes in zero separation voltage (V_o) may be associated with the existence of plasma above the electrode tip even at zero electrode separation (at zero separation the effective arc length may be none zero). It can be seen from V-ℓ plots for argon arcs on steel anodes (see figures 62 - 65) that V_o is generally between 7 and 10 volts and typically 8 volts. Experiments on cooled copper anodes indicate that V_o is between 9 and 11 volts and typically 10 volts. These figures are largely insensitive to arc current over the range 50-125 Amps.

In view of the substantially linear nature of the V-ℓ characteristic it is realistic to relate the voltage of short arcs to the initial gradient of V-ℓ curves. The component of arc voltage appearing between the electrodes (column voltage = V_c) can then be written quite generally as

$$V_c = \ell.E \text{ (I, ambient pressure, gas flow, electrode characteristics)}$$

where ℓ is the electrode separation and E, the electric field strengths, is defined here by the initial voltage gradient. Values of E as a function of pressure for various combinations of arc current, gas flow and electrode characteristics are shown on log-log graphs in figures 68 - 73. It can be seen that the nature of these graphs is substantially linear. The functional form of E may therefore be reduced to:-

$$E = E_1 \, p^m$$

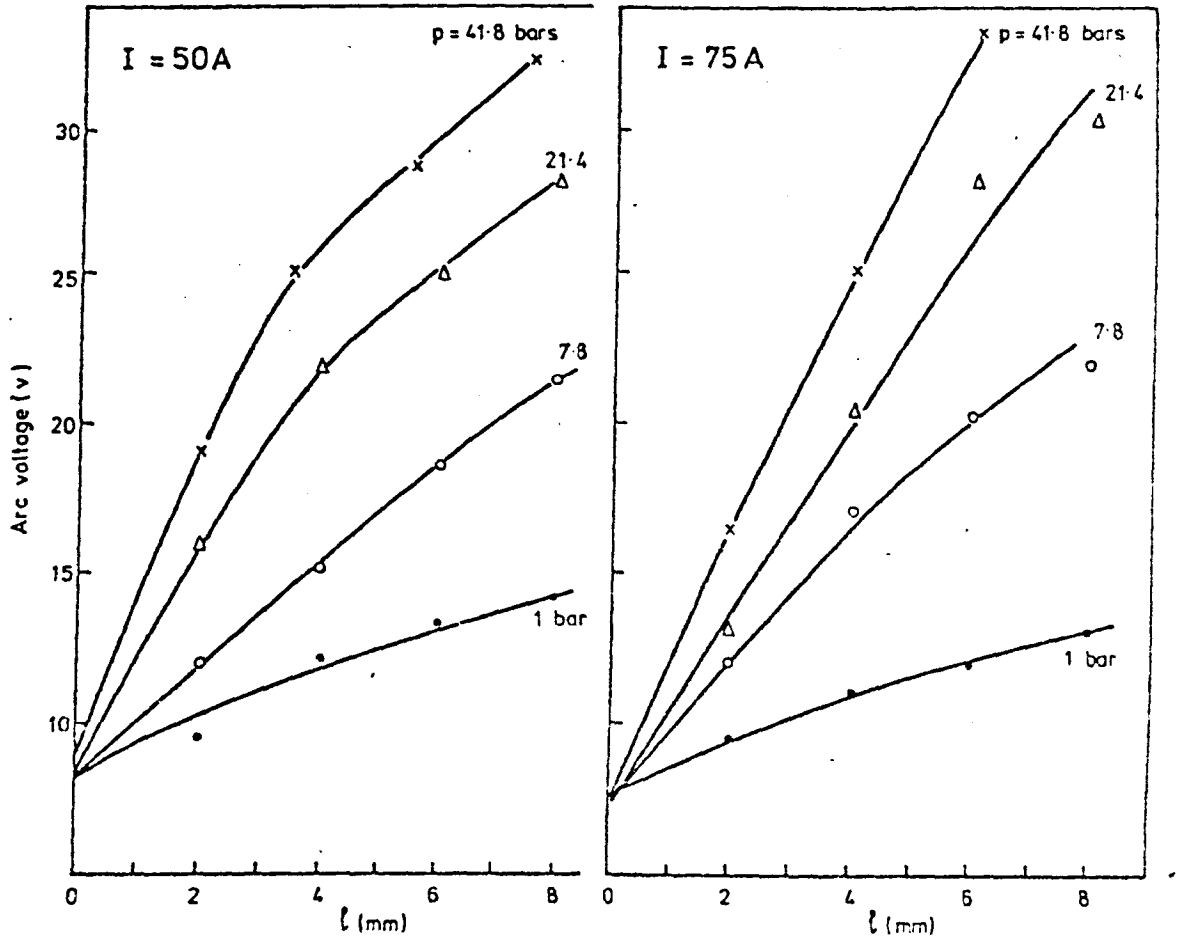

FIGURE 62. VOLTAGE DEPENDENCE ON ARC LENGTH (ℓ)
(ARGON TIG ARC ABOVE A MOVING STEEL ANODE
- SEE RADIATION MEASUREMENTS)

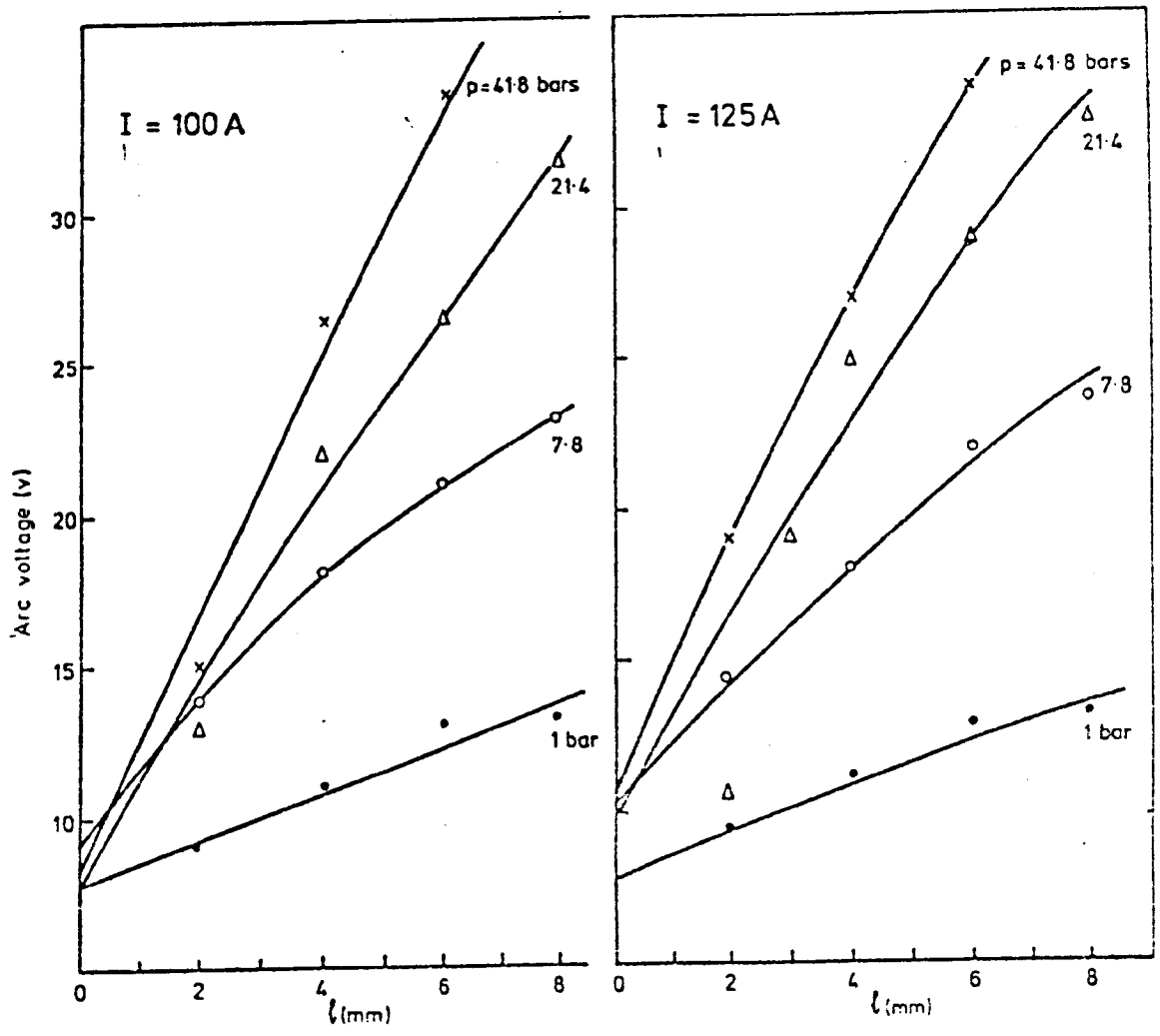

FIGURE 63, VOLTAGE DEPENDENCE ON ARC LENGTH (l)
(ARGON TIG ARC ABOVE A MOVING STEEL ANODE
– SEE RADIATION MEASUREMENTS)

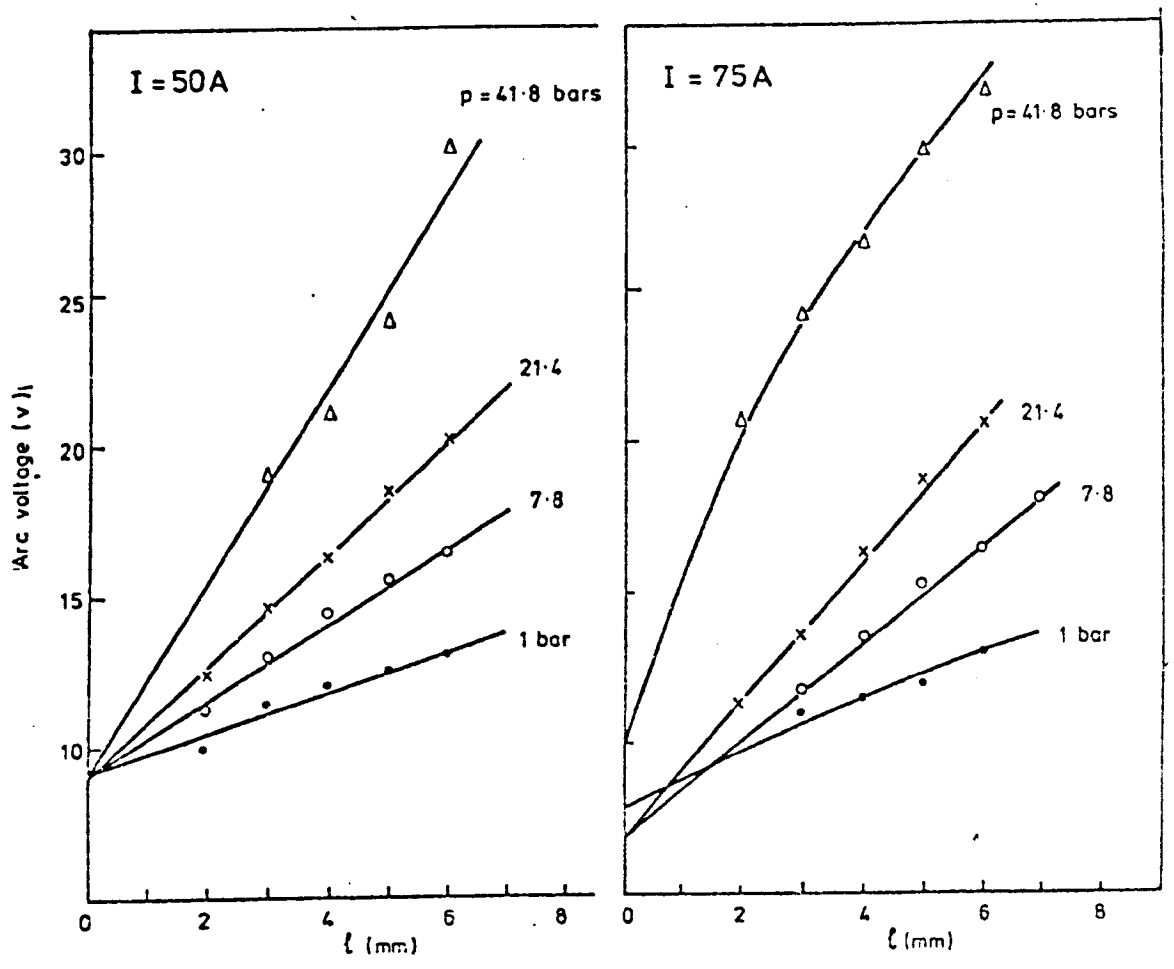

FIGURE 64. VOLTAGE DEPENDENCE ON ARC LENGTH (ℓ)
(ARGON ARC ABOVE A STATIONARY COOLED STEEL POOL
-SEE HEAT TRANSFER MEASUREMENTS)

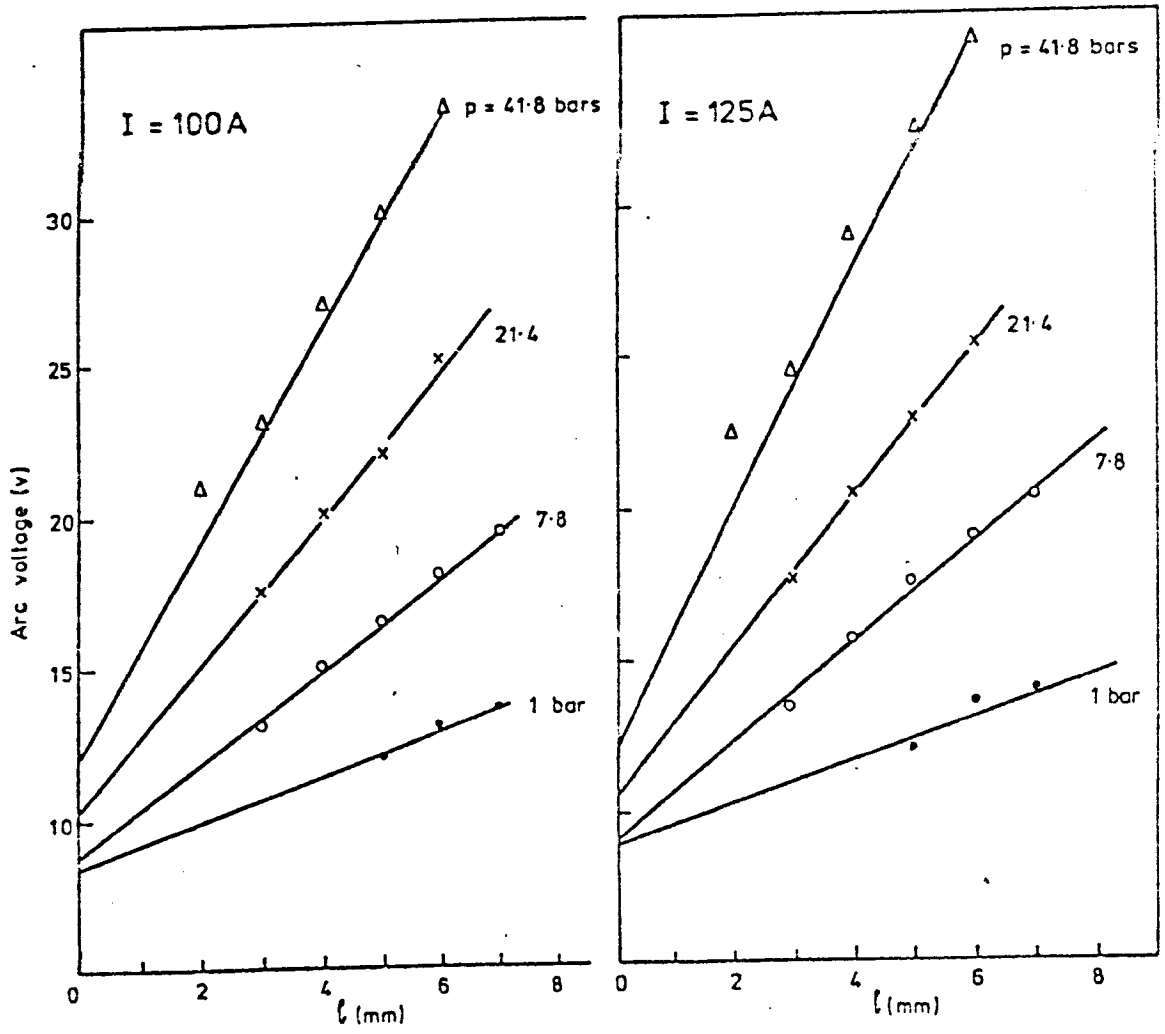

FIGURE 65. VOLTAGE DEPENDENCE ON ARC LENGTH (ℓ)
(ARGON ARC ABOVE A STATIONARY COOLED STEEL POOL
- SEE HEAT TRANSFER MEASUREMENTS)

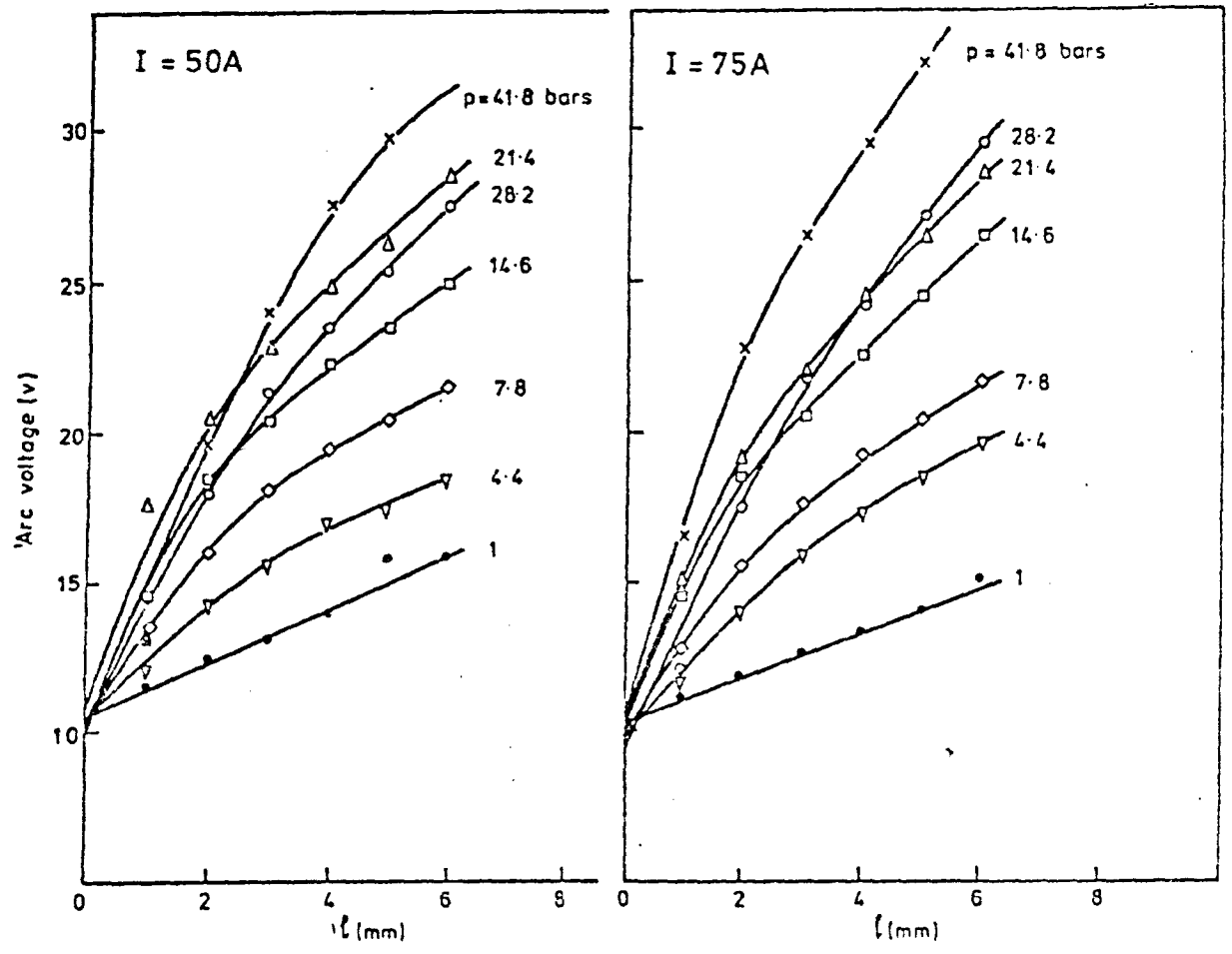

FIGURE 66. VOLTAGE DEPENDENCE ON ARC LENGTH (l)
(ARGON TIG ARC ABOVE A COOLED COPPER ANODE
– SEE HEAT TRANSFER MEASUREMENTS)

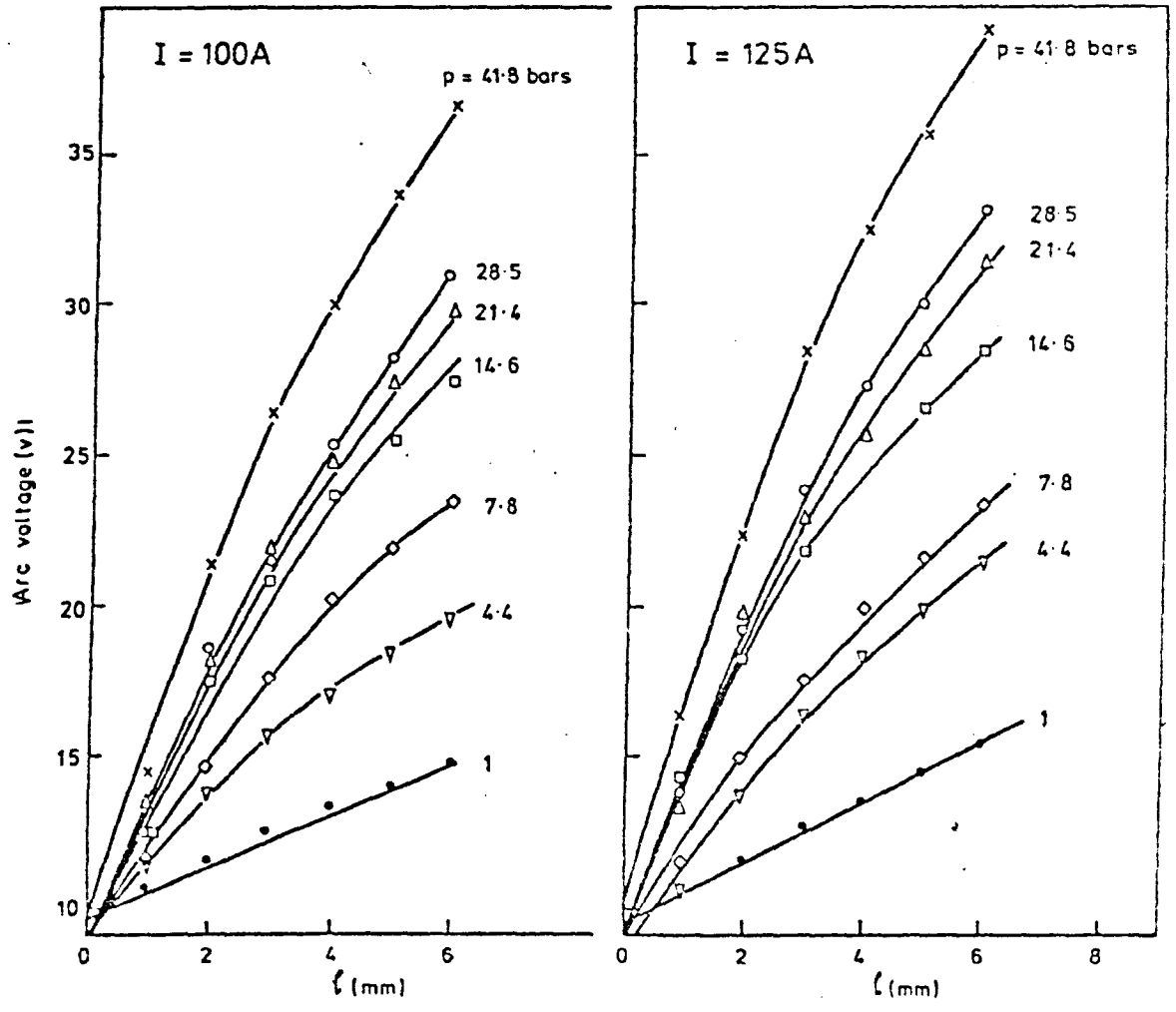

EIGURE 67. VOLTAGE DEPENDENCE ON ARC LENGTH (ℓ)
(ARGON TiG ARC ABOVE A COOLED COPPER ANODE
- SEE HEAT TRANSFER MEASUREMENTS)

where $E_1 = E_1$ (I, gas flow, electrode characteristics)

and $m = m$ (I, gas flow, electrode characteristics)

E_1 is the atmospheric field strength and m a positive number. Values of E_1 and m obtained for the arrangements investigated here are shown in table 8..

E_1 (V/mm)	m	Arc Current Conditions (A)	Shield Flow Conditions	Anode Composition and Motion	Tungsten Cathode Geometry	Experimental Arrangement
0.78	0.48	50,75,100, 125	Zero	Moving Steel Weld Pool	Tungsten 1% thoria 3.2mm dia. 60° vertex	Radiation measurements
0.70	0.43	50,75,100, 125	Zero	Stationary Cooled Steel Weld Pool	Tungsten 1% thoria 3.2mm dia. 60° vertex	Steel Disc heat transfer
0.85 0.85 1.00	0.49 0.51 0.49	50 100 125	Zero	Stationary Cooled Copper Plate	Tungsten 1% thoria 3.2mm dis.	Copper block heat transfer
0.70	0.50	100	Zero	Moving Steel Weld Pool	Tungsten 1%,2% thoria 3.2mm,4.8mm dia. 20-60° vertex	Weld bead stability studies
0.75	0.55	75,100	15ℓ/min at all pressures	Moving Steel Weld Pool		Weld bead studies

Table 8 Electric Field Strengths of Argon TIG Arcs

These figures (and respective graphs) show E and m to be substantially independent of current. For a wide range of conditions on steel anodes E and m can be represented by:

$$0.78 \geqslant E_1 \text{ (V/mm)} \geqslant 0.70$$

$$0.55 \geqslant m \geqslant 0.43$$

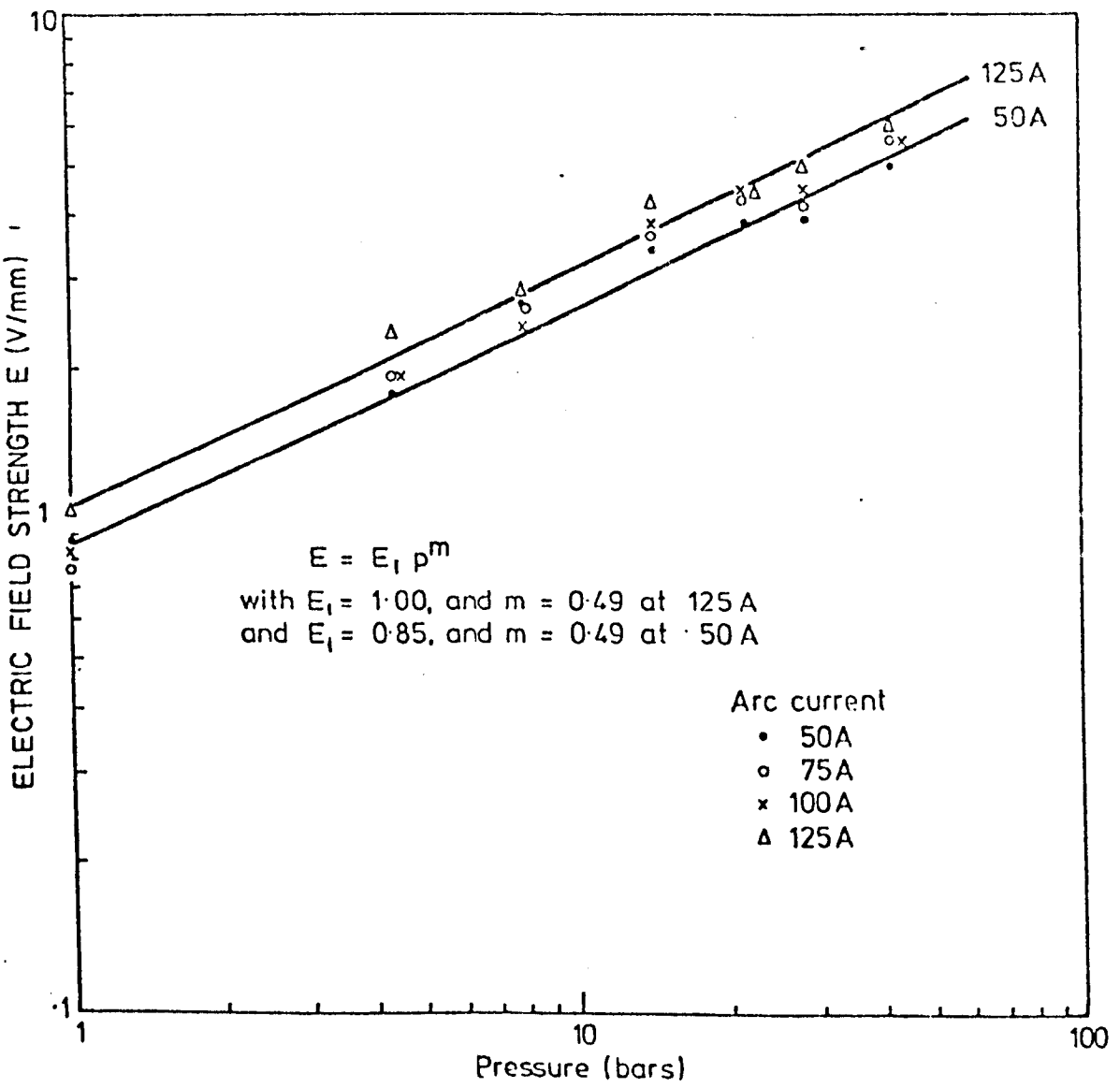

FIGURE 68. ELECTRIC FIELD STRENGTHS FOR ARGON ARCS ON A COOLED COPPER ANODE AT VARIOUS CURRENTS (SEE HEAT TRANSFER EXPERIMENTS)

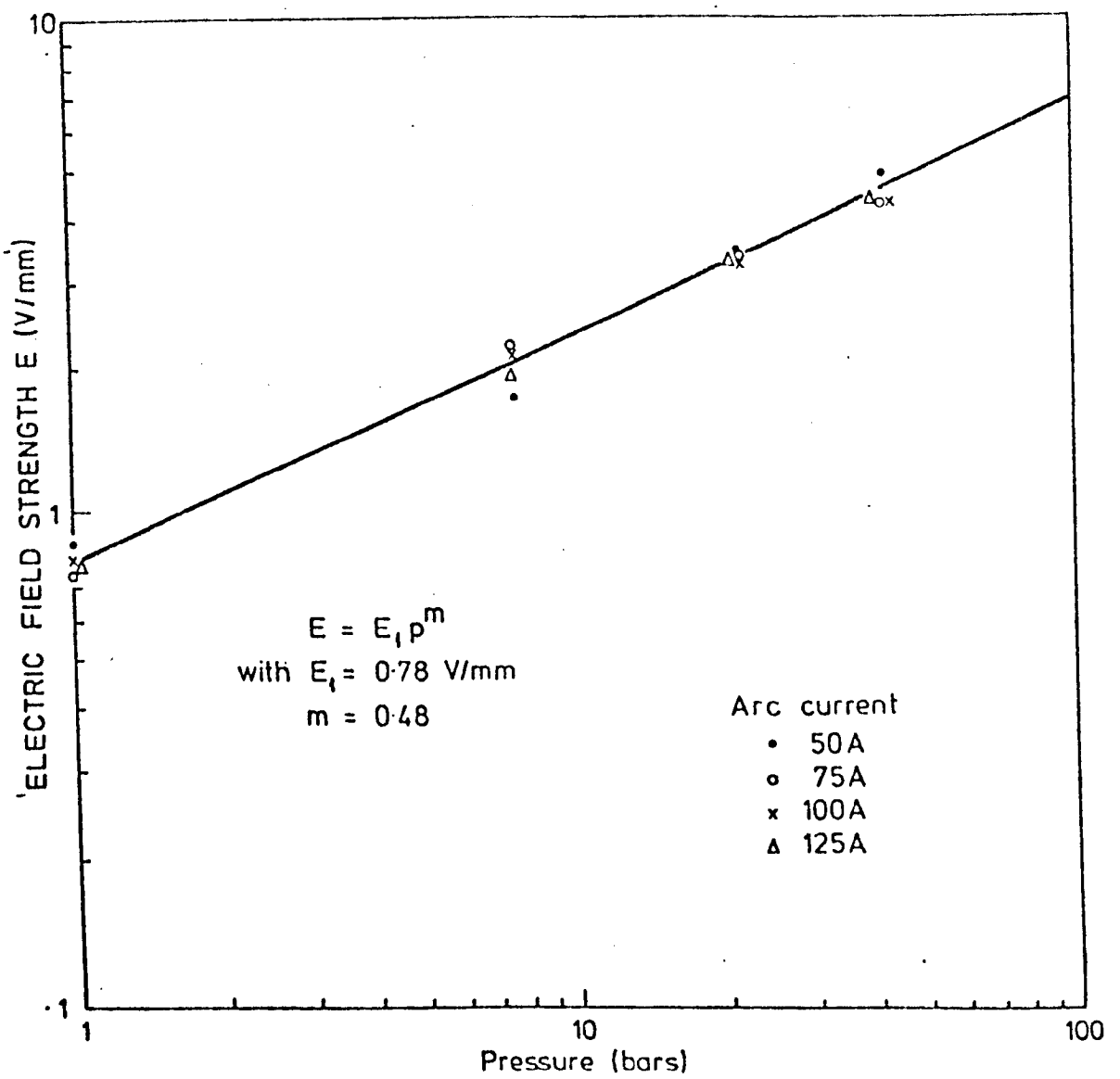

FIGURE 69. ELECTRIC FIELD STRENGTHS ON MOVING STEEL ANODES (SEE RADIATION MEASUREMENTS)

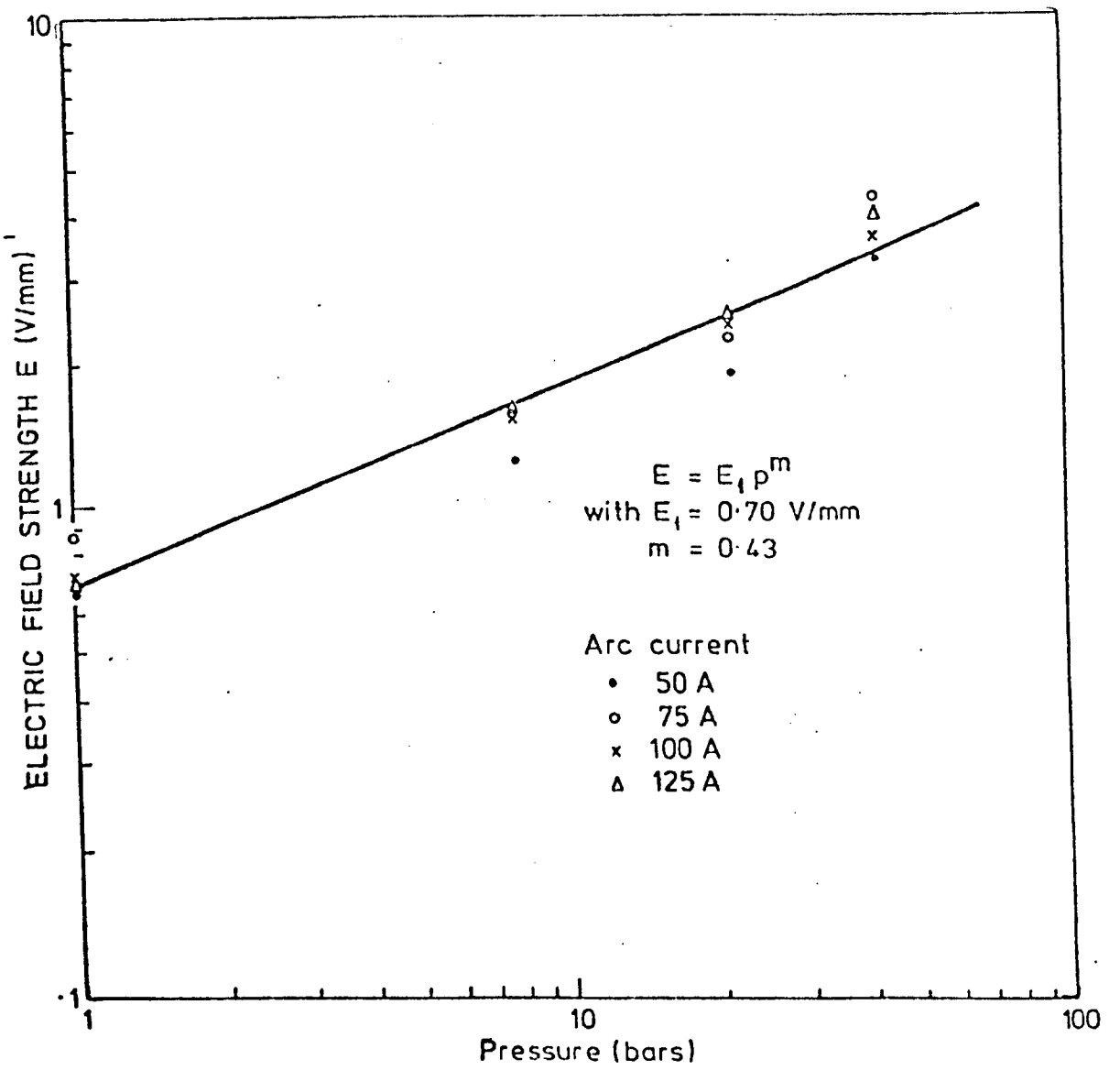

FIGURE 70. ELECTRIC FIELD STRENGTHS FOR ARGON ARCS ON COOLED STATIONARY STEEL ANODES (i.e. CONDUCTION LIMITED POOLS - SEE HEAT TRANSFER EXPERIMENTS)

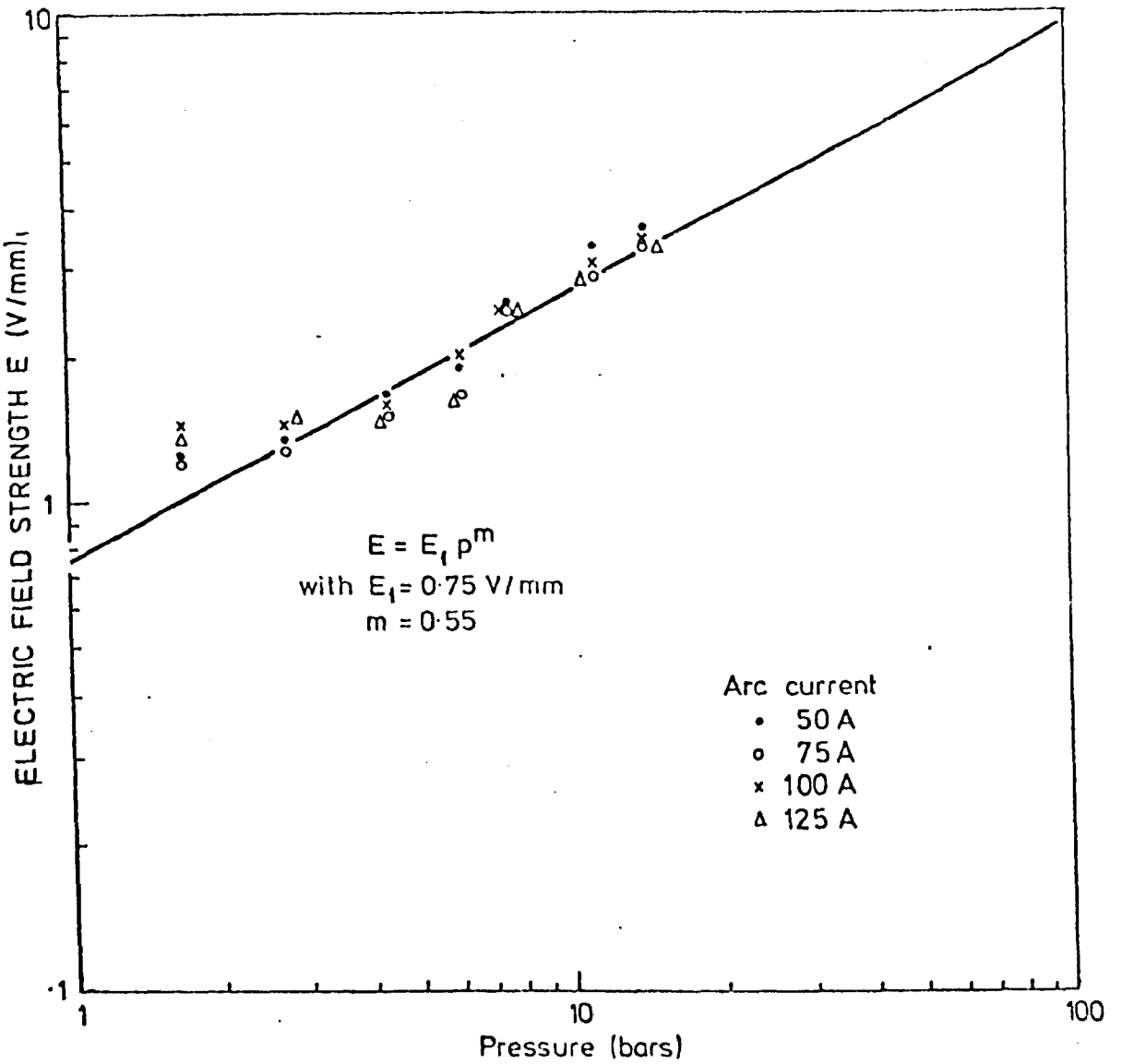

FIGURE 71. ELECTRIC FIELD STRENGTHS FOR ARGON TIG ARCS (GAS FLOW OF 15 l/min MOVING STEEL ANODE)

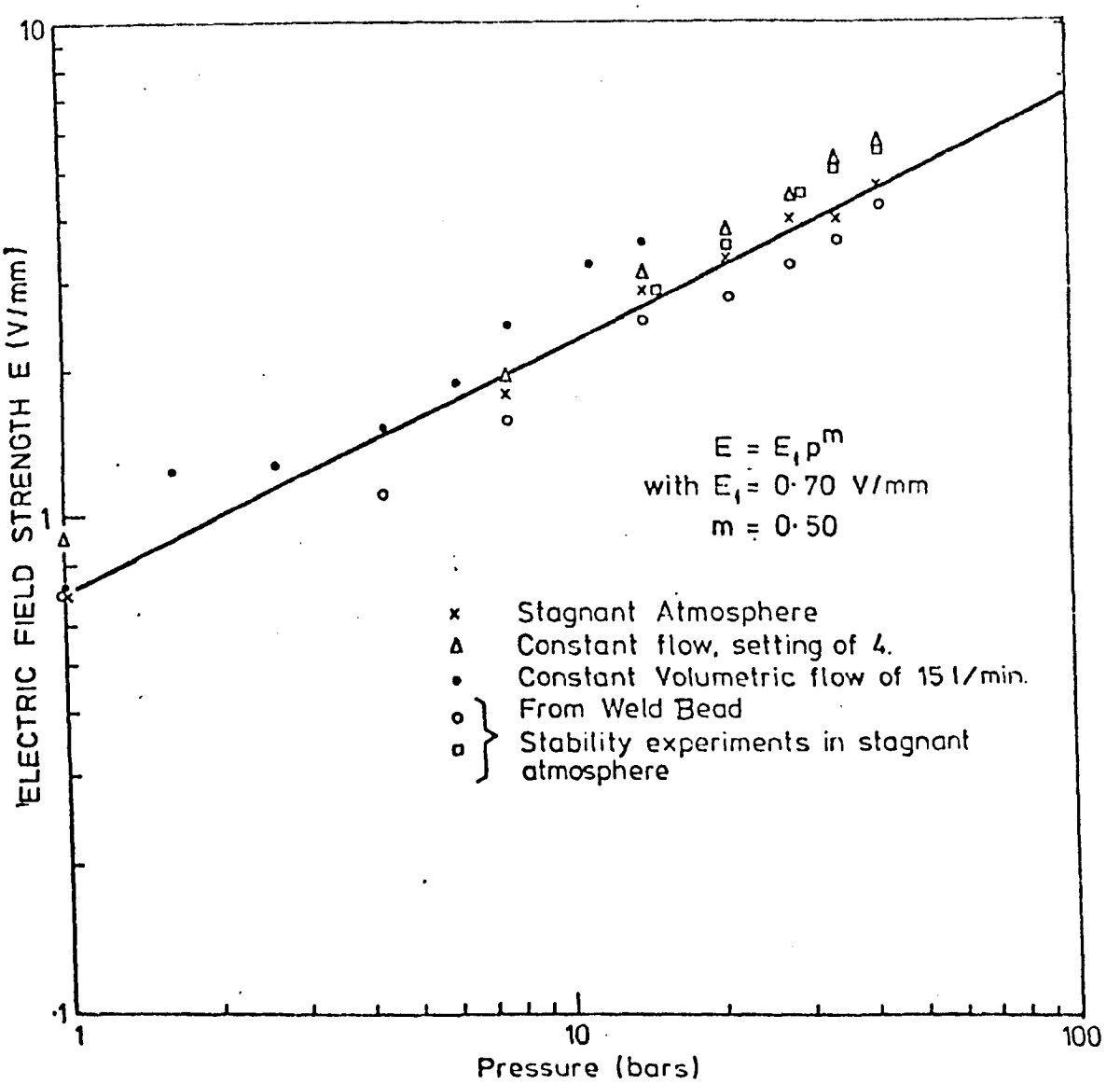

FIGURE 72. ELECTRIC FIELD STRENGTH FOR ARGON TIG ARCS (100 Amps) ON STEEL ANODES OBTAINED UNDER VARIOUS EXPERIMENTAL CONDITIONS

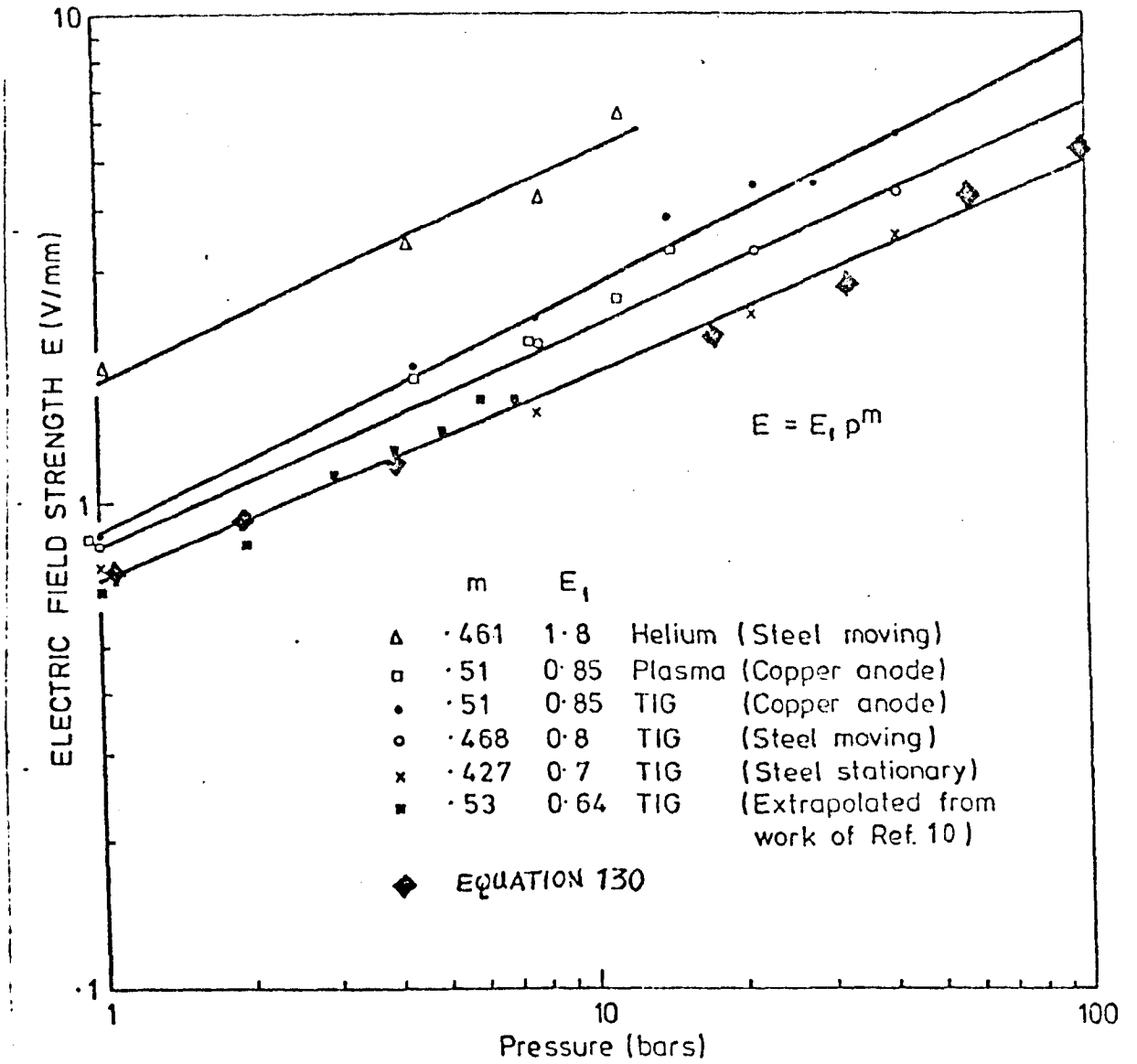

FIGURE 73. ELECTRIC FIELD STRENGTHS FOR A RANGE OF ARCING CONDITIONS.

The upper limit on m corresponds to arcs in strong gas flows where the voltage is expected to be higher (see section 4.2.1.3). The lower limit corresponds to a stationary conduction limited weld pool situation where vapourization is expected to reduce the arc voltage. A typical value of m for a weld bead situation in a low or zero gas flow is 0.5. The values of E_1 given above are in excellent agreement with those customarily associated with atmospheric TIG arcs. It can also be seen that there is good agreement between the values of m found with copper anodes ($0.51 \geq m \geq 0.49$) and the typical value of 0.5 for moving steel anodes. However, the atmospheric electric field strength is higher on copper (0.85 at 100 Amps). This behaviour is associated with the absence of gross anodic vapourization in copper arcs. The total arc voltage (V) may now be identified using equation (37) i.e.

$$V = V_o + E_1 . P^m . \ell$$

where V_o, E_1 and m are known. It is not possible (from the above experiments) to associate the constancy of V_o with the pressure independence of the anode and cathode falls. Additional experiments are required and these are reported in section 6.4. Further investigations will also be reported that attempt to understand the mechanisms responsible for column power loss at high pressures. Results presented in this section show that the power distribution in a high pressure TIG arc is fundamentally different from that found in an atmospheric TIG arc. Most of the power appears at the electrodes in atmospheric TIG arcs whereas most appears in the column for high pressure arcs. At least half of the process power appears in the column when

$$\ell . P^{\frac{1}{2}} \geq 10$$

Where ℓ is arc length in mm's and P the pressure in bars. Greater importance is therefore attached to understanding arc column behaviour at high pressure than at 1 bar.

4.2.1.3. Influence of Gas Flow on Electrical Characteristics

Many of the experiments reported so far have concerned arcs operating in the absence of a shielding gas flow. At one atmosphere a shield is required to perform obvious functions. In truely inert environments such

a flow is clearly not required. Despite this, it is of interest to understand the behaviour of arcs in gas flows at high pressures. In underwater welding environments the atmosphere although nominally inert may contain water vapour and other gases. A shield is then required to perform a function similar to that at 1 bar.

Gas flow rate exerts only a small influence on electrical characteristics at atmospheric pressure. This is not the case at high pressures. It has already been noted that gas flow may affect arc stability and arc diameter and it is also found that arc voltage is flow sensitive. At this point it is appropriate to discuss the choice of flow values (see also section 3.5). The flow meter was calibrated in a manner such that the volumetric flow rate (W) at any pressure could be given by

$$W = \frac{S}{\sqrt{P}} \ 10 \ \ell/\text{min} \quad \text{(see Appendix 1)} \tag{83}$$

Where S is a scale setting and P the pressure in bars. Thus a constant volumetric flow is maintained by increasing S with $\sqrt{P}$. This is regarded as a maximum setting procedure at any pressure. The mass flow rate (M) of shield is given by

$$M = \rho . W$$

$$\text{or} \quad M = \rho_1 . \ P . W$$

$$\therefore \quad M = \rho_1 . \ 10 . S . \ \sqrt{P} \tag{84}$$

Where ρ_1 is the shielding gas density at atmospheric pressure. This shows the mass flow rate to increase in direct proportion to pressure if the volume flow rate is held constant. Alternatively, if the shielding gas setting is held constant (i.e. volume flow rate reduced with $1/\sqrt{P}$) then the mass flow rate increases with $\sqrt{P}$. It should also be noted that the Reynolds number (R_e) of the shielding gas flow is

$$R_e = \frac{\rho \ v \ L}{\eta} \tag{85}$$

Where η is the viscosity, v the gas flow velocity and L the orifice diameter. 'v' may be readily related to M and it is then found that

$$R_e = \frac{4 \ M}{\pi L \eta} = \frac{40 \rho_1}{\pi L \eta} \ S\sqrt{P} \tag{86}$$

The Reynolds number increases with $S\sqrt{P}$ since viscosity is only weakly pressure dependent (158). It is this combination that will determine the degree of turbulence in the shielding gas flow i.e. the mass flow rate of the shield must be restricted if the shield is to be laminar at all pressures. This would mean reducing the shielding gas volumetric flow as 1/P. It can be seen from the above expression that arc stability and shielding gas flow stability are basically incompatible criteria at very high pressures. This is dealt with in more detail in section 6.3. On many occasions shielding gas flow rates are specified in this text in terms of S, but expressions given above may be used to convert this number into volumetric or mass flow rates (i.e. equations 83 and 84).

A series of experiments were conducted to examine the influence of shielding gas flow on arc voltage at high pressures (1 to 42 bars). Results expressed in terms of the laboratory co-ordinate S are shown in figure 74. These have been converted using equ.83 into volumetric flows where it is generally found that the influence of volumetric flow rate on voltage increases with pressure (see figure 75). Further experiments were performed to identify the arc region (or regions) affected by the shielding gas flow. For this purpose arc voltage was measured at a number of arc lengths, flow settings and pressures. The increase in voltage (ΔV) between the flow settings S=0 and S=4 is plotted against arc length for a number of pressures in figure 76. It can be seen that ΔV is approximately linearly related to arc length at any pressure and negligible for very short arc lengths at all pressures. i.e. these lines pass through the origin. The influence of shielding gas flow on arc voltage may therefore by associated with the column region and taken to increase linearly with arc length. Measurements taken from figure 74 indicate that the arc voltage has an approximately linear dependence on flow setting for a given pressure. A linear dependence on volumetric flow rate is also found (see figure 75). These results suggest that the arc voltage (V), written as the function $V(S,\ell,P)$, may be expressed by

$$V(S,\ell,P) = V(O,\ell,P) + S.\ell.F\ (P) \qquad (87)$$

Where F(P) is a function of pressure. The increase in field strength (ΔE) resulting from flow is therefore

$$E(S,P) = \frac{V(S,\ell,P) - V(O,\ell,P)}{\ell} = S.F(P) \qquad (88)$$

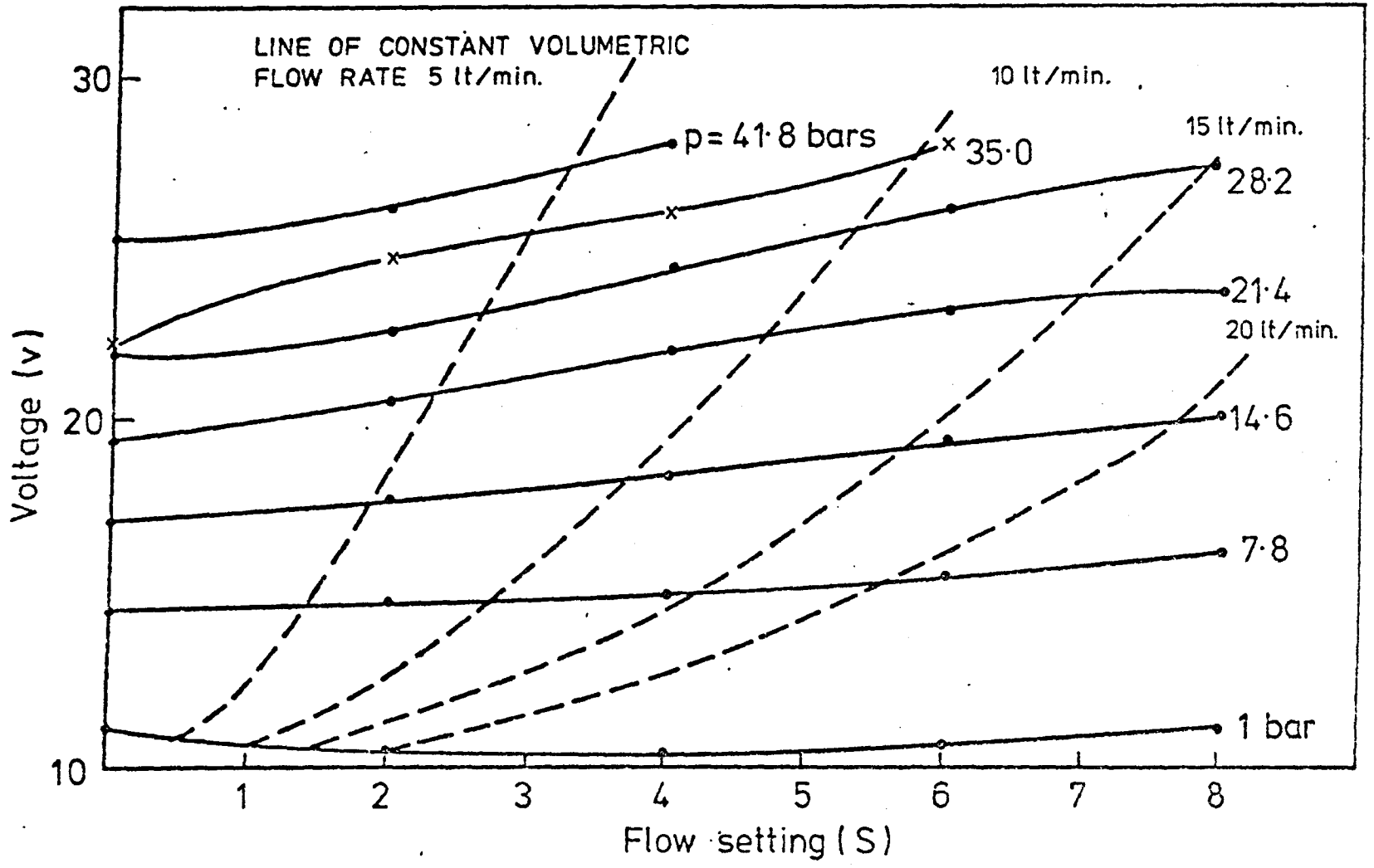

FIGURE 74. INFLUENCE OF SHIELDING GAS FLOW ON ARC VOLTAGE FOR 100 A 3 mm, ARGON TIG ARC ON A MILD STEEL ANODE.

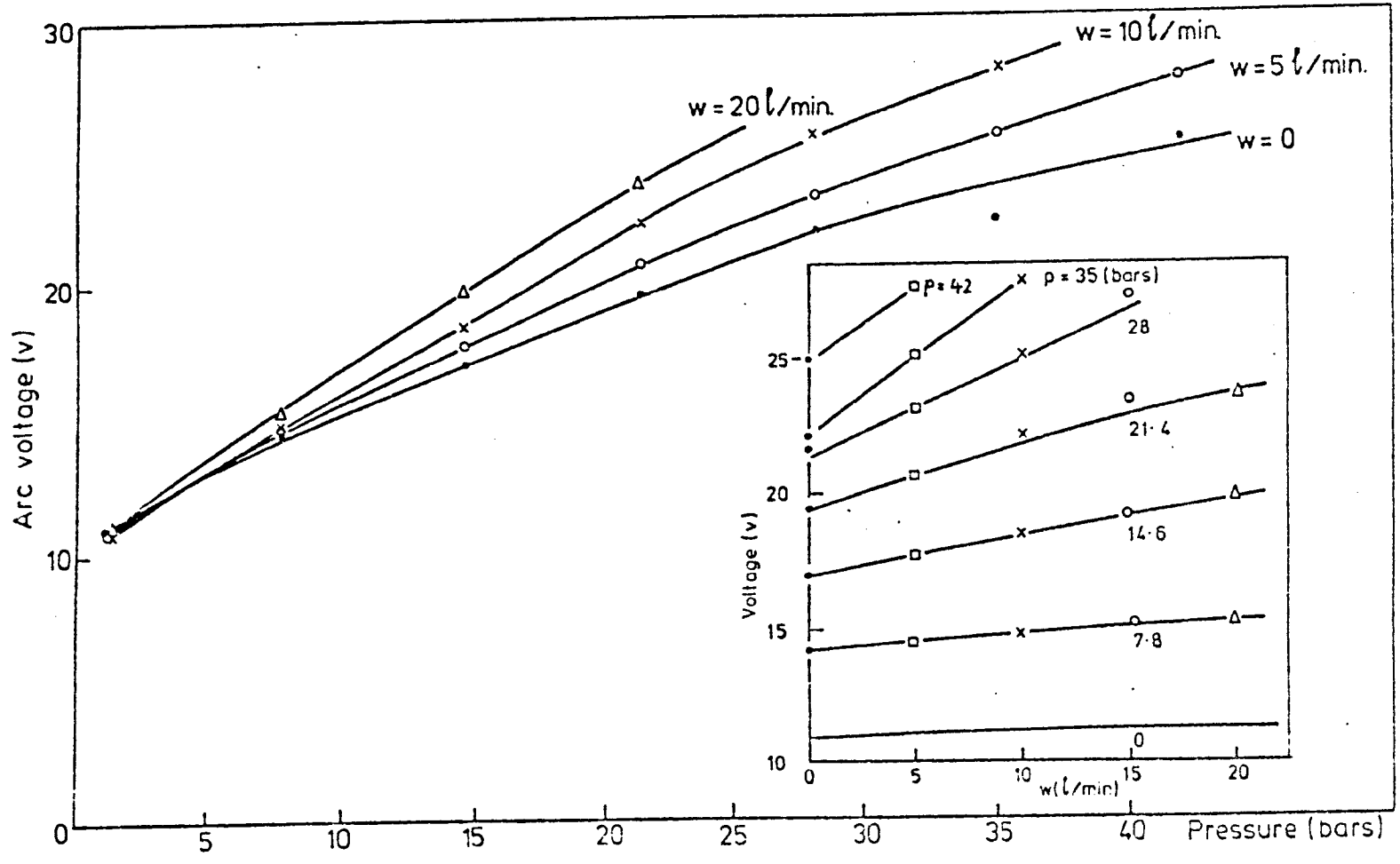

FIGURE 75. ARC VOLTAGE OBTAINED UNDER CONSTANT VOLUMETRIC (w) SHIELDING CONDITIONS (100A, 3mm ARGON TIG ARC ON A MOVING STEEL ANODE)

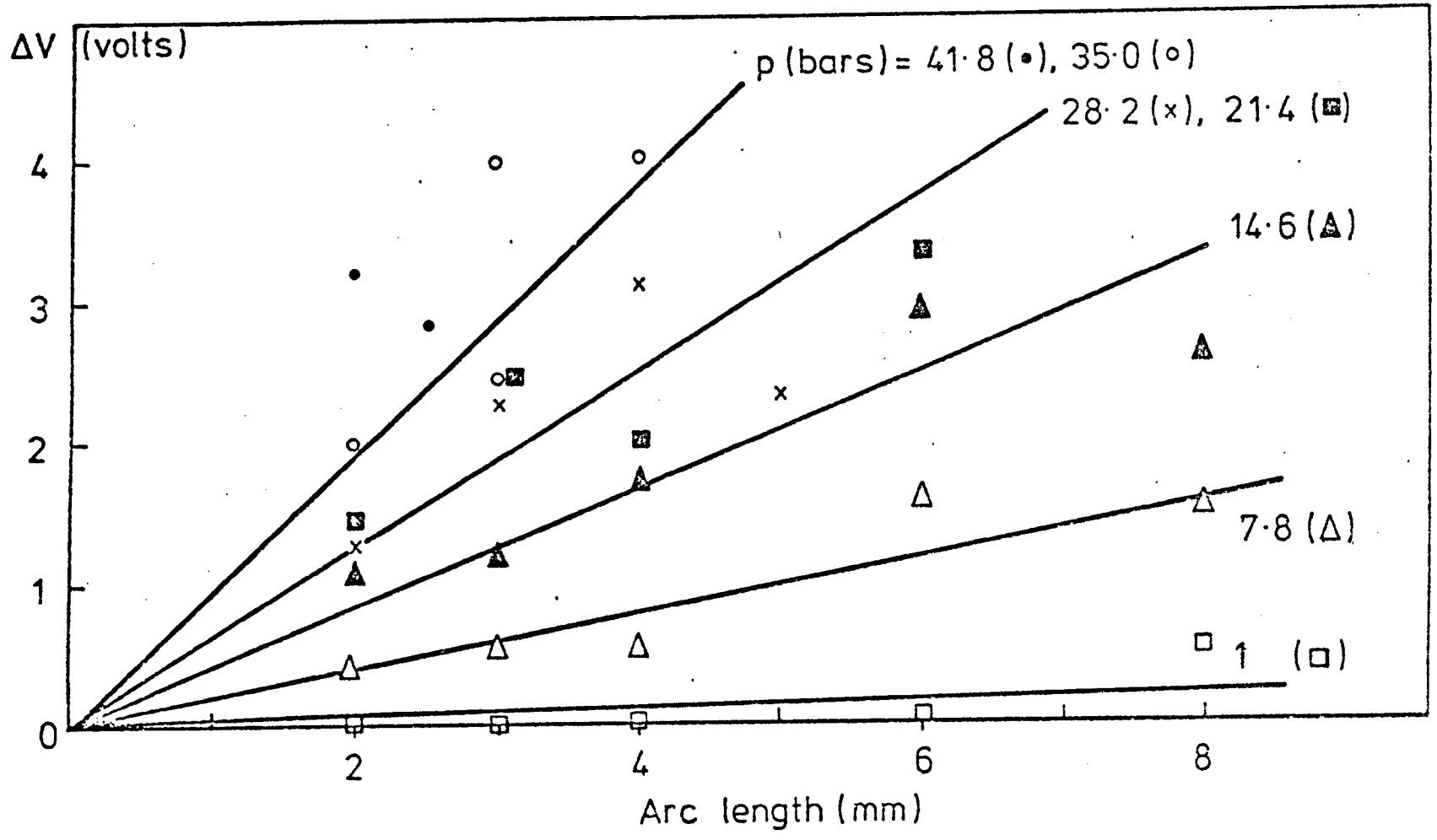

FIGURE 76. INFLUENCE OF SHIELDING GAS FLOW AND ARC LENGTH ON ARC VOLTAGE (ARGON TIG ARC ABOVE A MOVING STEEL ANODE)
ΔV is the increase in voltage when the shielding gas flow setting is increased from zero to 4

The value of E (4,P) has been obtained from figure 76 and is shown in figure 77. It can be seen from figure 77 that

$$\Delta E(4,P) = P/40 \tag{89}$$

Using equations 88 and 89 allows F(P) to be identified as F(P)=P/160. Substituting into 88 now gives

$$\Delta E(S,P) = \frac{S.P}{160} \tag{90}$$

Volumetric and mass flow representations of the data may be obtained by making use of equations 83 and 84. The results are:-

$$\Delta E(W,P) = \frac{W.P^{3/2}}{1600} \tag{91}$$

and

$$\Delta E(M,P) = \frac{M.P^{1/2}}{\rho_1.1600} \tag{92}$$

The arc voltage can now be written in a more general form than equation 37 i.e.

$$V(x,\ell,P) = V_o + E(P).\ell + \Delta E(x,P).\ell \tag{93}$$

where x represents the flow conditions (i.e. x=S, W or M) and E(P) is the zero flow condition field strength as previously found. The relative influence of flow conditions is determined by the ratio $\Delta E/E(P)$ defined here as θ. Equation 93 now becomes

$$V(x,\ell P) = V_o + E(P).\ell . (1+\theta) \tag{94}$$

θ may be further generalised with reference to equations 36 and 91 where

$$\theta = \frac{W.P^{3/2}}{1600.E_1.P^m} \tag{95}$$

taking $E_1 = 0.75$ (V/mm) and $m = 0.5$ (see section 4.2.1.2) gives

$$\theta = \frac{W.P}{1200} \tag{96}$$

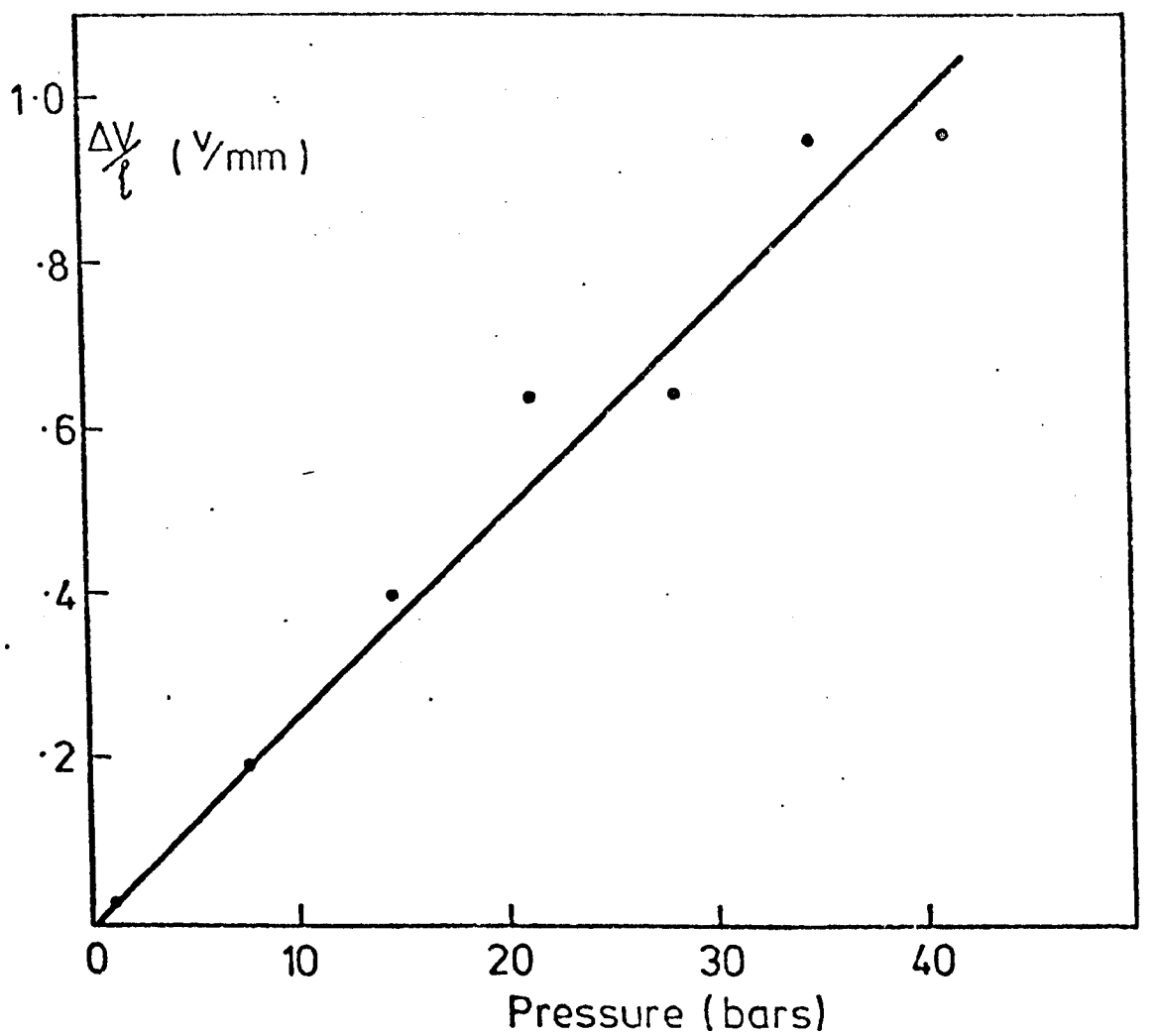

FIGURE 77. INCREASE IN ELECTRIC FIELD STRENGTH WHEN THE SHIELDING GAS FLOW SETTING IS RAISED FROM 0 TO 4 (SEE FIGURE 76)

Clearly θ is negligible at low pressures and for low flows at high pressures. However, θ may be significant in many realistic welding situations e.g. W = 1.0 ℓ/min at 40 bars gives θ = 0.33. The shielding flow then accounts for a quater (i.e. $\theta/1+\theta$) of the total power appearing in the column. A general plot of this nature is shown in figure 78. It can be seen that curves based on the expression for θ are in reasonable agreement with values measured directly from figure 74.

4.2.1.4. Influence of Anode Characteristics on Electrical Behaviour

Significant differences have already been noted between the behaviour of argon TIG arcs on copper and steel anodes but these are largely confined to the vicinity of the anode. It is found that the sum of the fall voltages is typically 2 volts greater on copper anodes than steel anodes. Higher arc column electric field strengths are also found on copper than on steel anodes. The total arc voltage is therefore greater because of higher anode fall and column components of voltage. This behaviour is presumably associated with vapourization.

4.2.1.5. Influence of Cathode Characteristics

Experiments were performed (see table 8) with a range of electrode vertex angles, electrode diameters and tungsten compositions (1% and 2% thoriated). The spread of voltages obtained using this range of variables is within the limits of experimental reproducibility and so it is concluded that arc voltage is not greatly influenced by electrode characteristics. The change in electrode geometry due to melting is thought to be partly responsible for this behaviour. Also, any small changes that may occur are likely to be lost in the strong pressure dependence of the field strength.

4.2.1.6. Influence of an External Magnetic Field on Electrical Characteristics

The use of magnets was prompted by the need to stabilise weld pool behaviour at high pressures. In experiments, the magnetic field was created by a permanent magnet concentrically situated around the electrode and having the field shown in figure 8. This magnetic field is found to exert no significant influence on arc voltage (certainly to within 5%) - see figure 79.

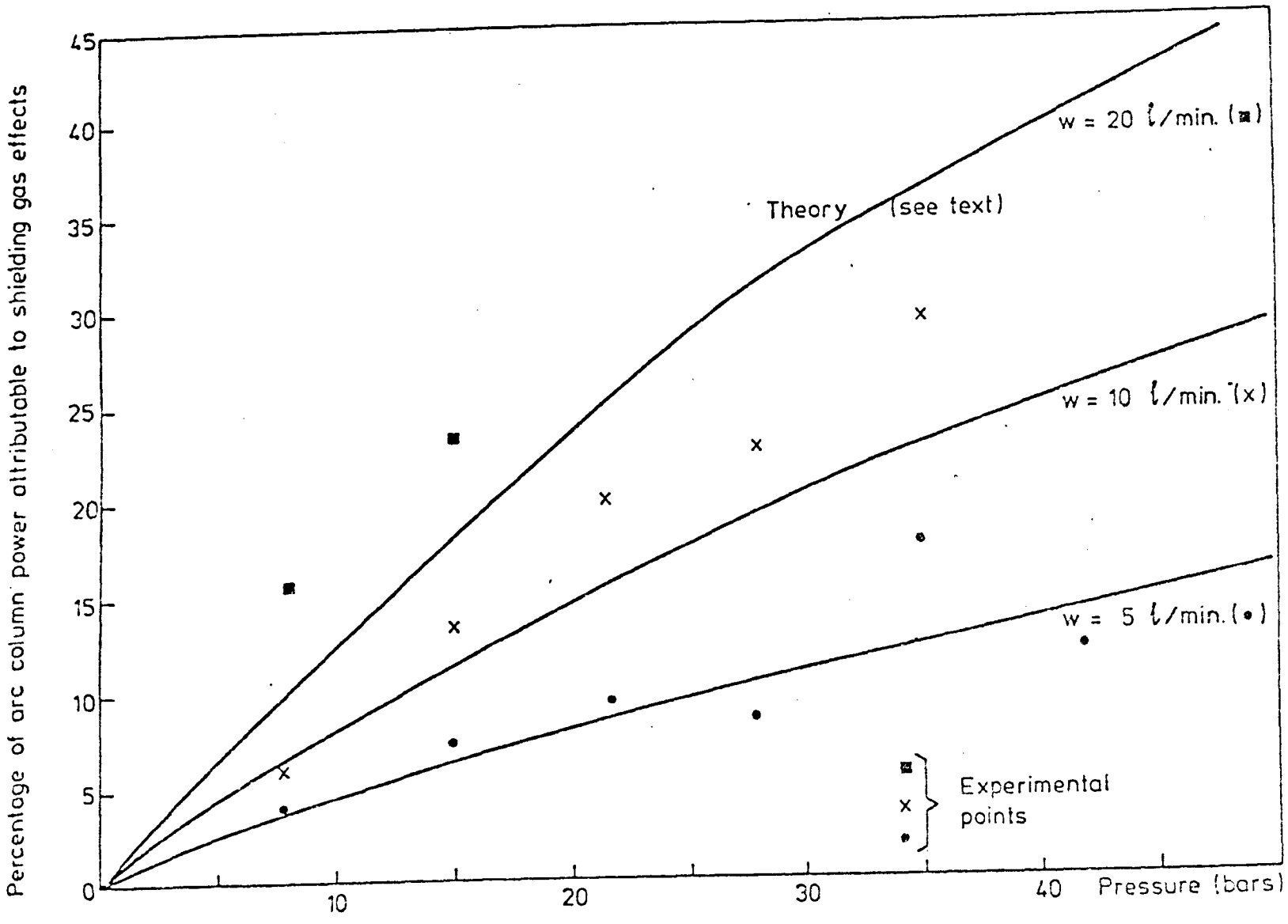

FIGURE 78. INFLUENCE OF GAS FLOW ON ARC COLUMN POWER ($I.V_c$)

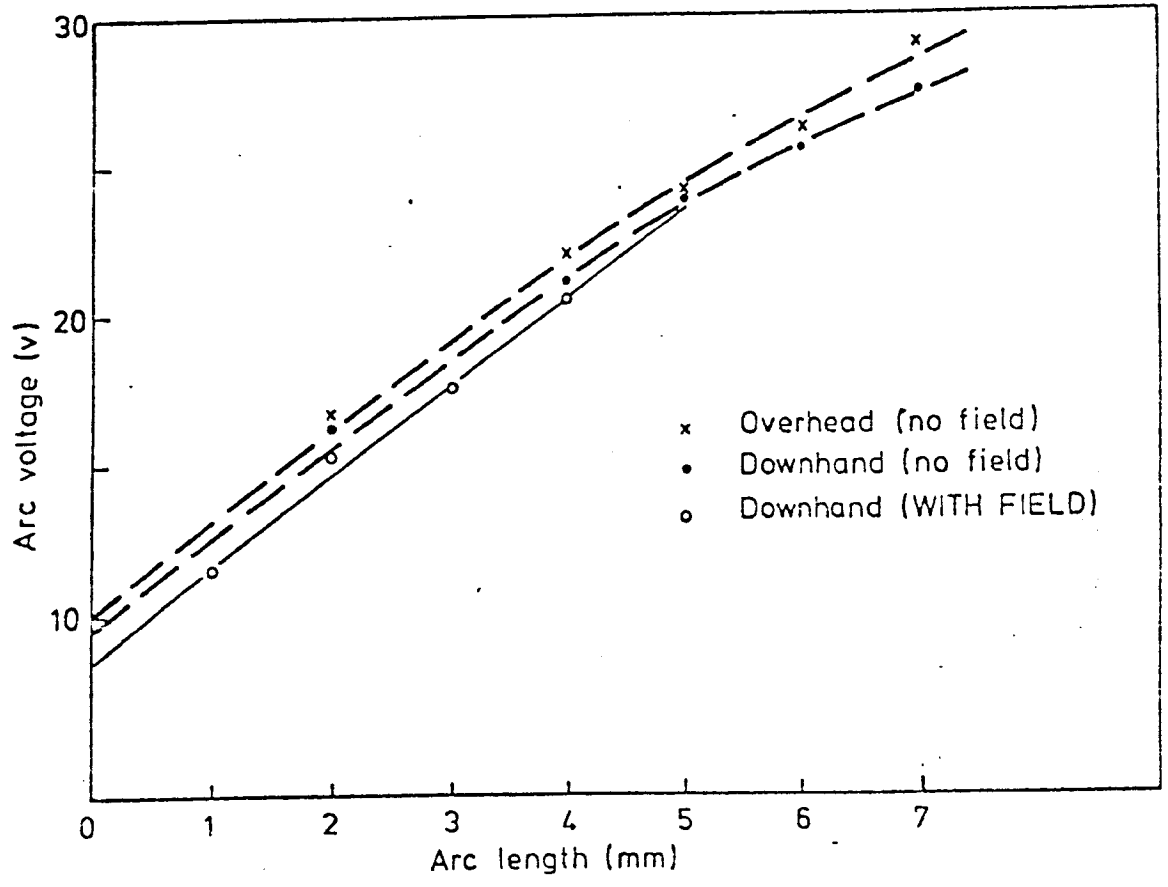

FIGURE 79 EFFECT OF WELDING POSITION AND MAGNETIC FIELD ON ARC VOLTAGE (100A, ARGON TIG ARC AT 21 bars ON A STEEL ANODE)

4.2.1.7. Influence of Welding Position on Arc Voltage

By rotating chamber CII it was possible to run arcs in any welding position. Experiments performed in different positions indicated that small differences in arc voltage exist. However, it was difficult to accurately specify this dependency due to small arc to arc variations. Measurements shown in figure 79 were made by rotating the chamber with an arc running - thereby avoiding arc to arc variations. These results indicate a slightly (perhaps 1 volt) higher voltage in overhead welding than in down hand welding.

4.2.2. Electrical Characteristics of Helium TIG Arcs

4.2.2.1. V-I Characteristics

The V-I characteristic of the helium TIG arc was found to be a decreasing function of current at all currents investigated. This behaviour is significantly different from that found in argon where a positive gradient occurs at high currents. It can also be seen from figures 80, 81 that higher voltages occur in helium than for argon. The nature of the V-I characteristics has the same form at all pressures and arc lengths investigated. However, it is interesting to note that the 'heel and step' anode root motion observed for argon (at low currents and for negative V-I gradients) is entirely absent. This was despite a highly constricted anode root in helium..

4.2.2.2. V-ℓ Characteristics

The results from a large number of experiments are shown in figure 82. It can be seen that V-ℓ is substantially linear with a voltage intercept of about 9-10 volts at all pressures. This behaviour is quite similar to that in argon but the V-ℓ curve has a gradient of order twice that found for argon. Values of E are shown in figure 73 where a comparison is given with a number of argon-tungsten arc arrangements. The pressure dependence of E compares well with that found in argon
i.e. $m = 0.46$ in helium and $E = 1.8P^{0.46}$ V/mm.

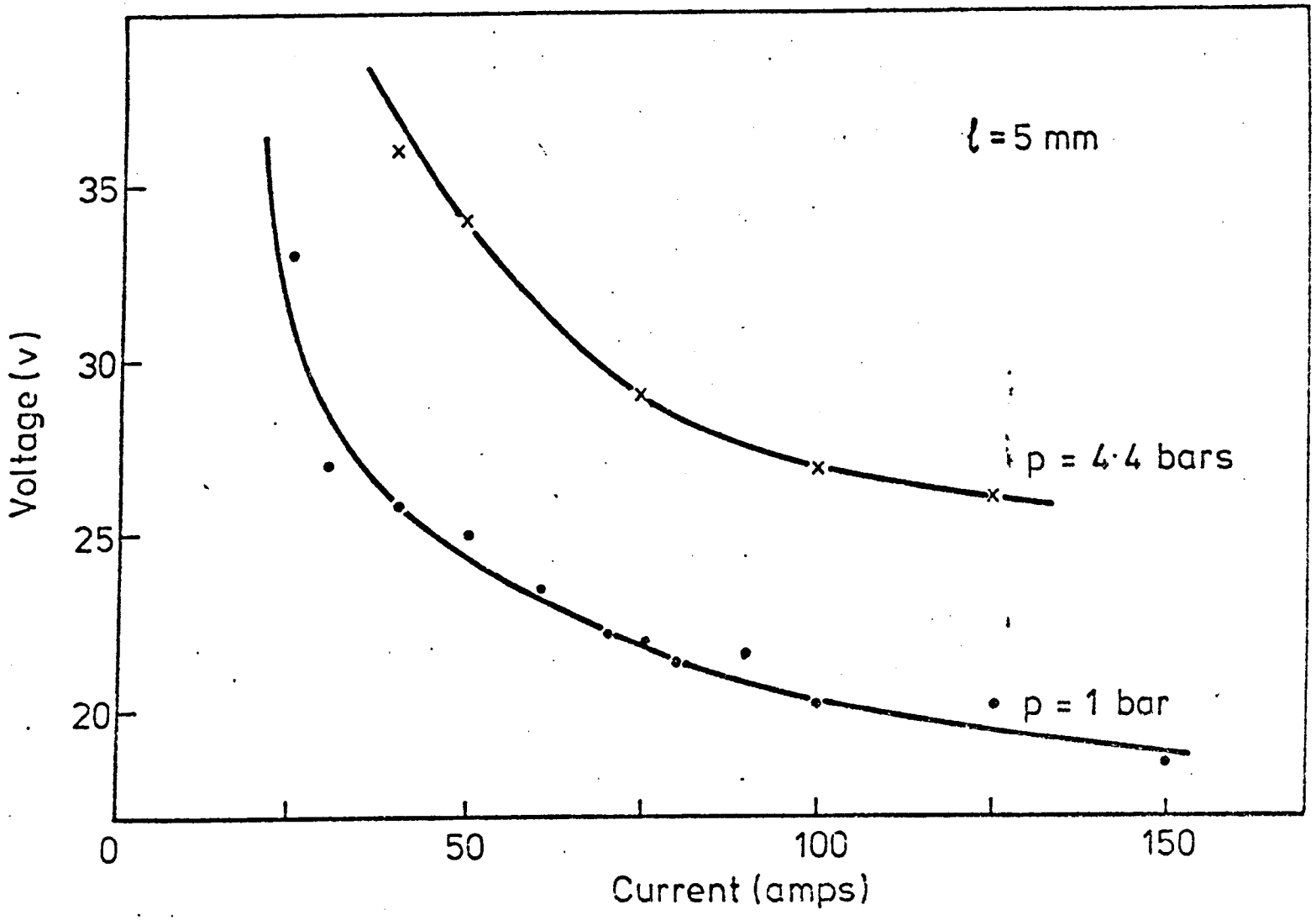

FIGURE 80. V-I CHARACTERISTIC FOR A 5mm HELIUM TIG ARC ON A STEEL ANODE

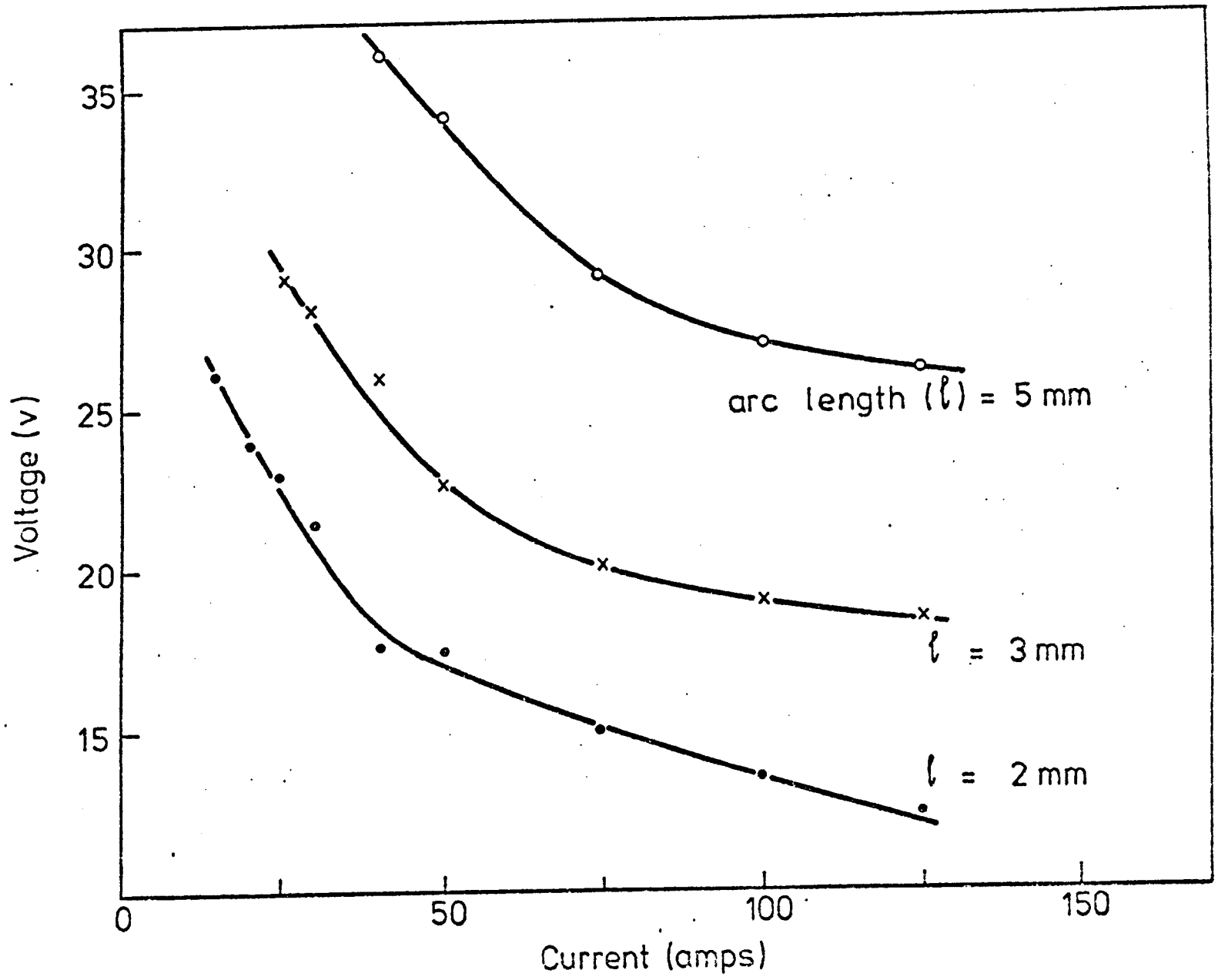

FIGURE 81. INFLUENCE OF ARC LENGTH ON THE V - I CHARACTERISTIC OF A HELIUM TIG ARC AT 4·4 bars

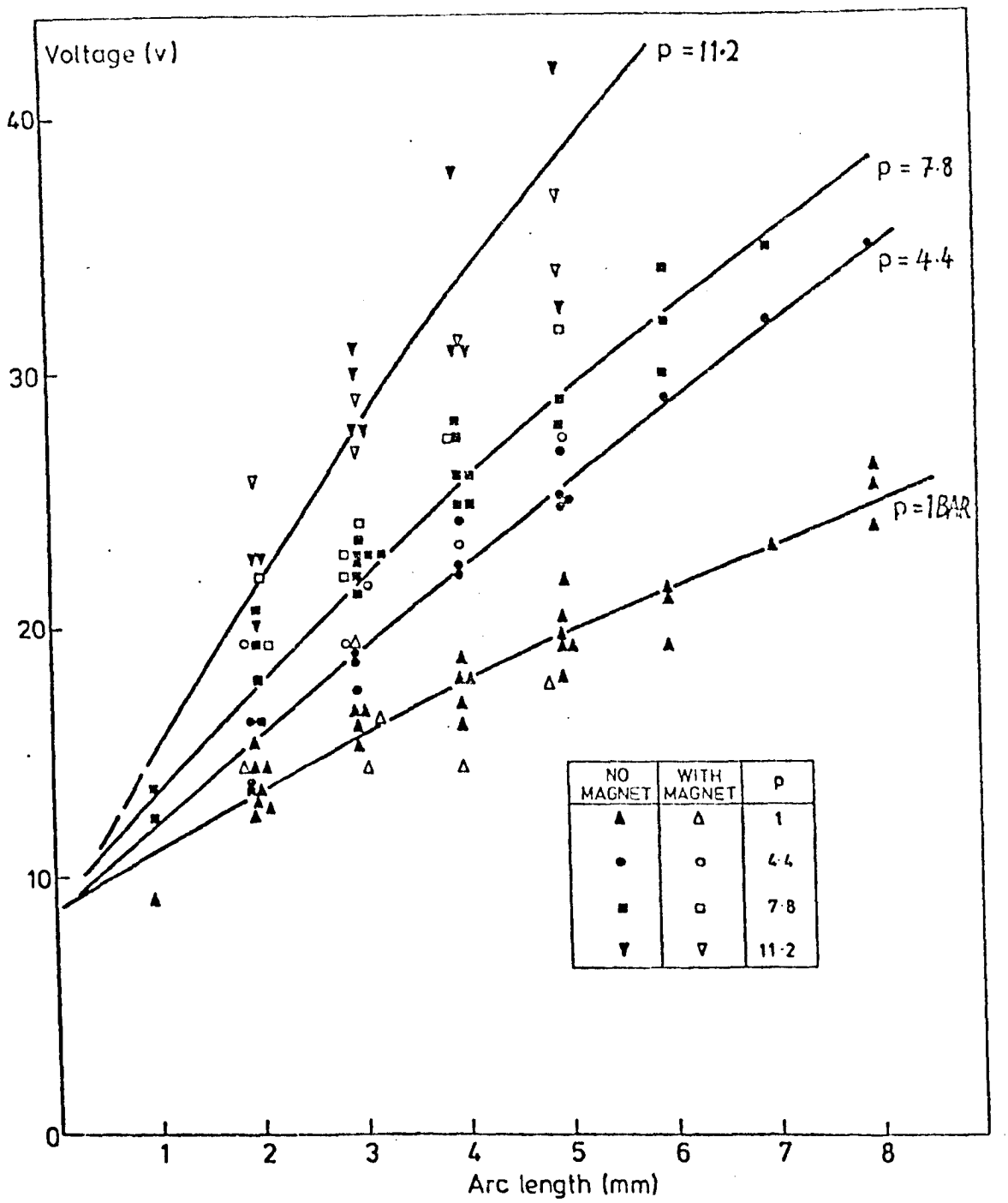

FIGURE 82. VOLTAGE ARC LENGTH CHARACTERISTICS OF 100 A HELIUM TIG ARCS ON MOVING STEEL ANODES

It can also be seen from figure 82 that significant scatter exists between voltage measurements from different experimental sets. This is associated with the combination of electrode erosion and high field strengths. For example at 11.2 bars, 1mm of electrode erosion would change arc voltage by more than 6 volts because E(11.2 bars) = 6.2 V/mm.

4.2.2.3. Electrical Characteristics of 'Self Pulsing' Helium Arcs

Photographic and electrical observations of the self pulsing helium arc have been given in section 4.1. An examination of arc current and voltage UVO traces reveals that the red phase is associated with a lower arc voltage and higher current than the blue phase (normal phase). This behaviour is associated with vapourization at the cathode. Tungsten vapourization provides a supply of low ionization material to the column and consequently a lower arc voltage is required. The increase in arc current is thought to result from the power supply V-I characteristic. This reasoning may explain the appearance of red and blue modes but further considerations are required to explain why these pulse with time i.e. why the red arc doesn't remain having once appeared. This is possibly explained by vapourizational cooling of the electrode where vapour leaving the electrode carries off energy. The electrode should then cool and in doing so inhibit further vapourization.

4.2.3. Electrical Characteristics of the Constricted Argon - Tungsten Arc

4.2.3.1. Characteristics

V-I characteristics of plasma arcs on steel and cooled copper anodes are shown in figures 83 and 84. At one atmosphere a plasma arc on a copper anode exhibits a weak minimum in V-I near 100A. Arc voltage changes slowly with current on either side of this minimum value. Similar behaviour is observed at 2.4 bars. For higher pressures voltage is an increasing function of current such that the gradient of the V-I characteristic increases with pressure - although a tendency exists for the V-I characteristic to saturate at high pressures. Measurements on steel anodes give lower respective voltages than those on copper anodes. The difference between these results is slight at atmospheric pressure but quite significant at higher pressures (see figures 83,84,88). However, the form of these curves is such that the gradients of V-I characteristics

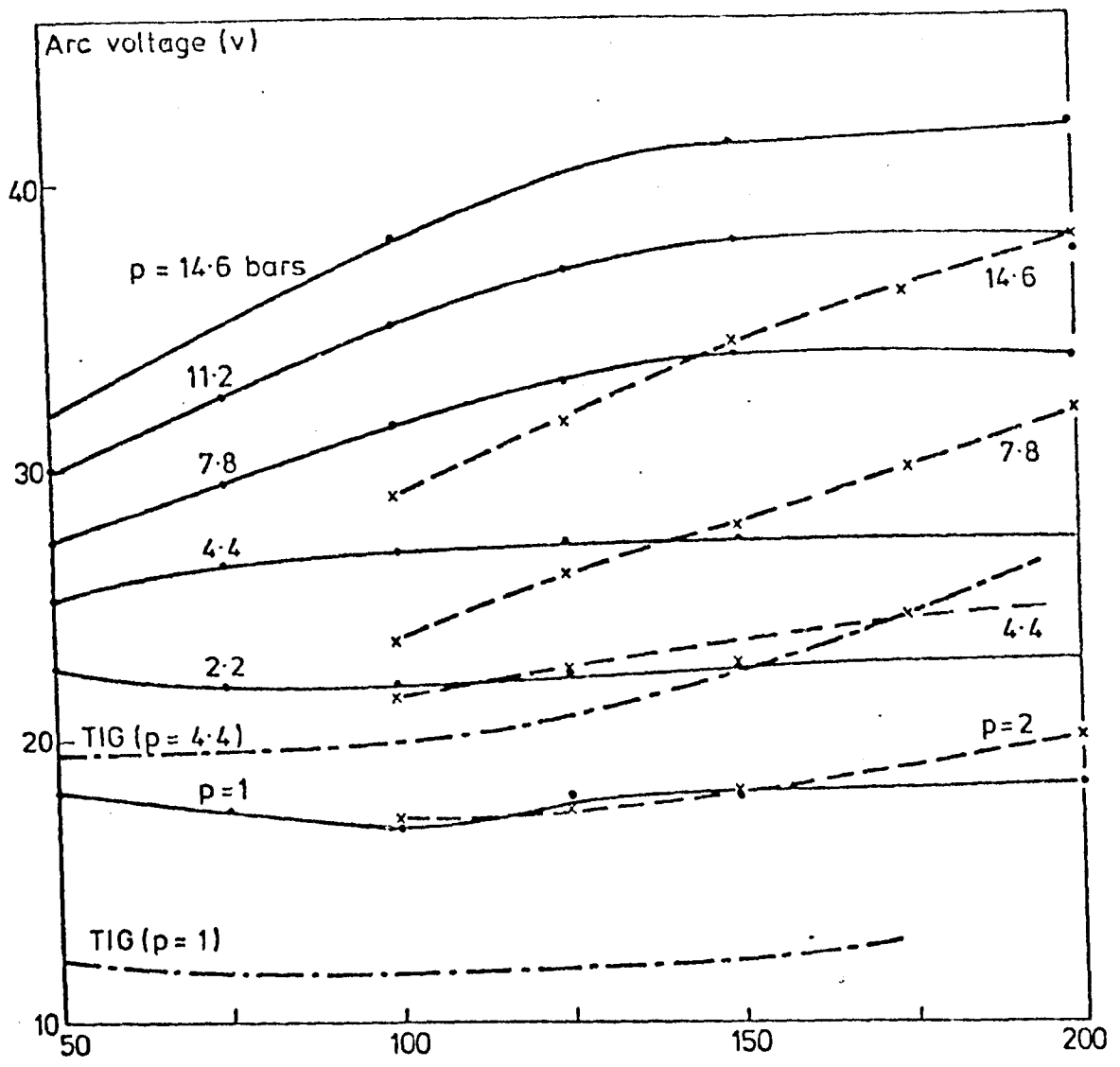

EXPERIMENTAL CONDITIONS

PLASMA	PLASMA	TIG
COPPER ANODE ———	STAINLESS STEEL ANODE —x—x—	MILD STEEL —·—
SHIELD FLOW SETTING 1	SHIELD FLOW SETTING 1	ARC LENGTH 8 mm
PLASMA FLOW SETTING 2	PLASMA FLOW SETTING 3	NO FLOW
ORIFICE DIAMETER 4·8 mm	ORIFICE DIAMETER 4·8 mm	
TUNGSTEN - WORK SEPARATION 10 mm	TUNGSTEN-WORK SEPARATION 10 mm	
TRAVEL SPEED 3·8 mm/s	TRAVEL SPEED 3·8 mm/s	

FIGURE 83. INFLUENCE OF A CONSTRICTING ORIFICE AND ANODE COMPOSITION ON THE V-I CHARACTERISTICS OF ARGON ARCS.

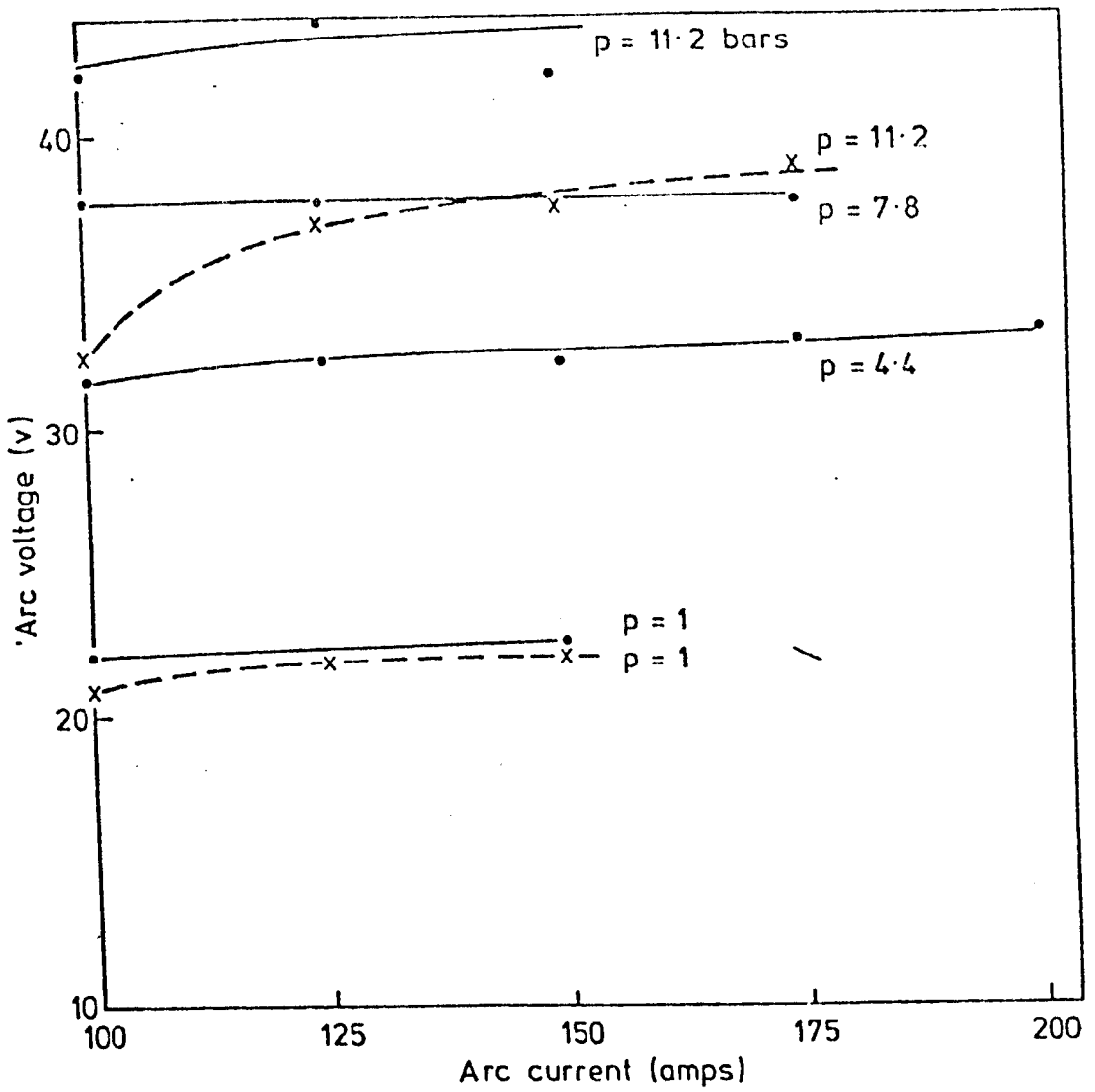

EXPERIMENTAL CONDITIONS

——— COPPER ANODE

– – – – STAINLESS STEEL ANODE (3·8 mm/s)

SHIELD FLOW SETTING 2

PLASMA FLOW SETTING 3

ORIFICE DIAMETER 3·2 mm

TUNGSTEN – WORK SEPARATION 10 mm

FIGURE 84. V – I CHARACTERISTICS OF CONSTRICTED ARGON TUNGSTEN ARCS ON COPPER AND STEEL ANODES

are similar for both anode materials. Results described above refer predominantly to an orifice diameter of 4.8mm's. Experiments have also been made for the case of a 3.2mm orifice. These are shown in figure 84. It is again found that at high pressures a significant difference exists between copper and steel anodes although this is not in evidence at low pressures. It can also be seen that substantially higher voltages exist for the smaller orifice than with the larger. The smaller orifice gives rise to V-I behaviour where voltage has only a weak current dependence at all pressures over the current range 100A to 200A. This behaviour corresponds to the saturation region observed with the larger orifice (but occurring here at lower currents).

Voltage measurements for plasma arcs are substantially higher than those for TIG arcs of similar length and current. For the purpose of comparison a few results from TIG experiments have been included in figure 83.

4.2.3.2. V-ℓ Characteristics

V-ℓ measurements are presented in figure 89 for plasma arcs on a cooled copper anode. The characteristics can be seen to be linear for arc lengths below 8mm. Above this the gradient decreases slightly. Extrapolating to zero arc length is not a reasonable procedure in plasma welding because of the influence of the constricting orifice. However, if allowance is made for an increase in field strength within the orifice (due to constriction) then the zero arc length voltage is again seen to be fairly insensitive to pressure changes. Column field strengths have been found from the short arc length gradient of V-ℓ curves. Results are shown in figure 73. It can be seen that 'soft' plasma arcs considered herehave electric field strengths similar to those obtained with TIG arcs.

4.2.3.3. Influence of Gas Flow on Electrical Characteristics

It is normal to employ two gas flows in plasma welding. The inner flow is through a constricting orifice and known as the plasma gas flow. The outer flow between the orifice and a shield cup, has the function of a shielding gas flow and is known as such. Results reported here are expressed mainly in terms of flow meter settings (Sp for plasma and S_S for shielding flow). Flow meter characteristics were such that the

volumetric flow (W) at any pressure could be represented by (see appendix 1)

plasma: $W_p = 1.s/\sqrt{P}$ ℓ/min

shield: $W_s = 10.s/\sqrt{P}$ ℓ/min

Expressions similar to those previously introduced in section 4.2.1.3 can then be found and used to convert to the respective mass flow rates. These have been used to construct the lines of constant mass flow shown on some diagrams.

The influence of plasma gas flow for plasma arcs on a copper anode is shown in figure 85. It can be seen that the voltage initially increases slowly with flow. The rate of increase then rises before an inflection point is reached and saturation occurs. Saturation is reached at lower flow rates for the larger orifice (despite the higher current). Saturation also tends to occur at lower flow settings as pressure is increased. The onset of voltage sensitivity to flow at about 0.25g/s (≃ 15 ℓ/min at 1 bar) for all pressures. However, saturation behaviour doesn't appear to correspond to any single mass flow rate. The difference between large and small orifice behaviour increases with flow at any pressure with only slight differences occurring at low flows. The flow range used for experiments with arcs on steel anodes was limited by the onset of weld pool 'humping' (see section 4.3.3). This gave an upper limit to usable plasma gas flow values. Welding became less sensitive to this type of behaviour with increasing pressure.

The voltage - gas flow relationship on steel anodes is more complicated than for copper anodes. However, similar trends may be identified. The small orifice (3.2mm) again exhibited a higher voltage than the larger (4.8mm) and saturated at low flows. In this situation saturation is not as clearly defined and may be accompanied by a decrease in arc voltage for further increases in gas flow. This is associated with behaviour at the weld pool i.e. vapourization and (or) a change in effective arc length due to the gas jet changing weld pool surface shape as in humping.

Shielding gas flow had no significant influence on arc voltage at any of the pressures investigated.

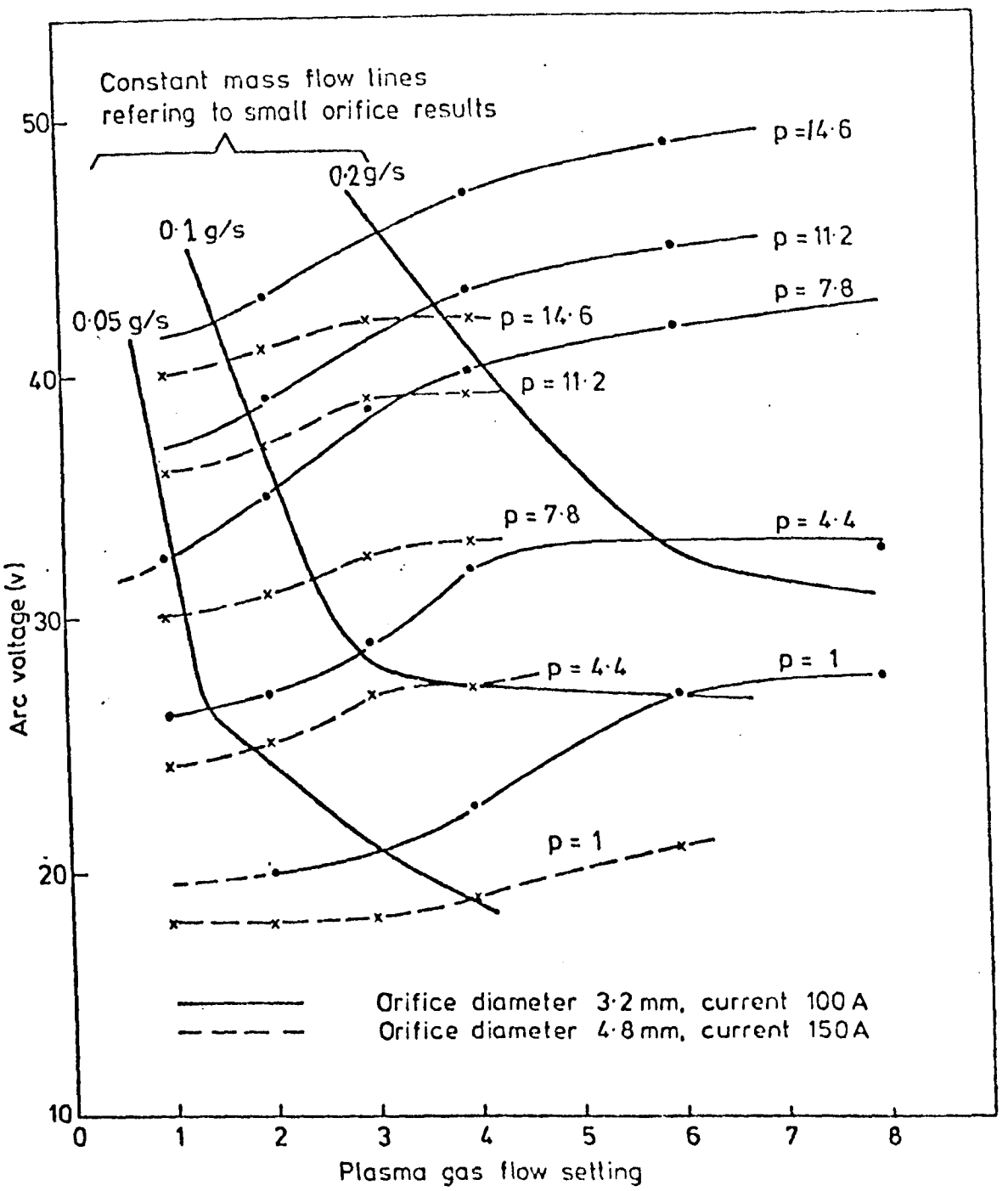

FIGURE 85. INFLUENCE OF GAS FLOW ON ARC VOLTAGE FOR THE CONSTRICTED TUNGSTEN ARC ON A COPPER ANODE (TUNGSTEN WORK SEPARATION OF 10 mm)

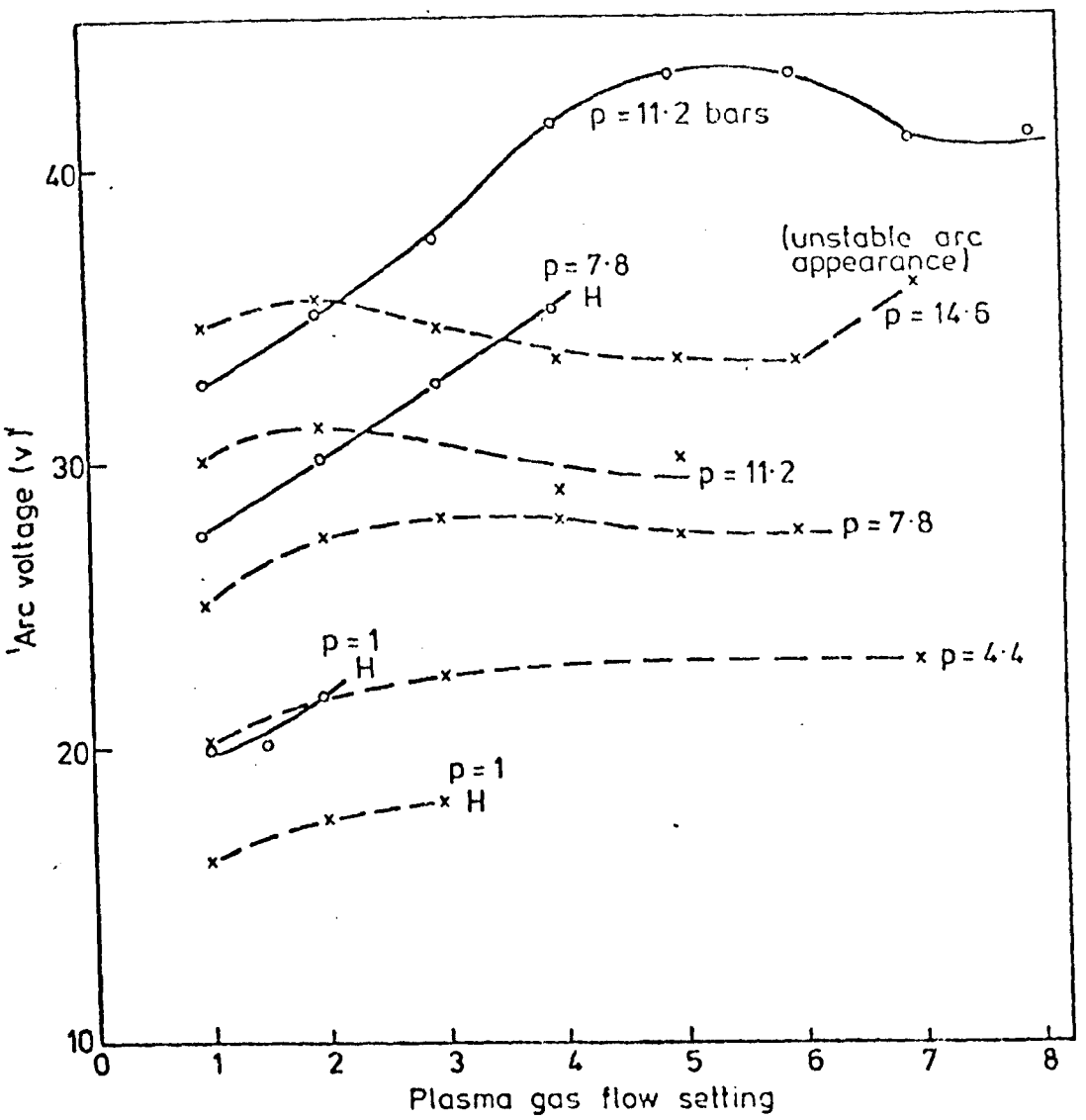

EXPERIMENTAL CONDITIONS

——— 3·2 mm ORIFICE DIAMETER
— — — 4·8 mm ORIFICE DIAMETER
SHIELD FLOW SETTING 1
TRAVEL SPEED 3·8 mm/s
H INDICATES THE ONSET OF HUMPING
CURRENT = 150 A
TUNGSTEN - WORK SEPARATION 10 mm

FIGURE 86. INFLUENCE OF GAS FLOW ON ARC VOLTAGE FOR THE CONSTRICTED TUNGSTEN ARC ON A STAINLESS STEEL ANODE

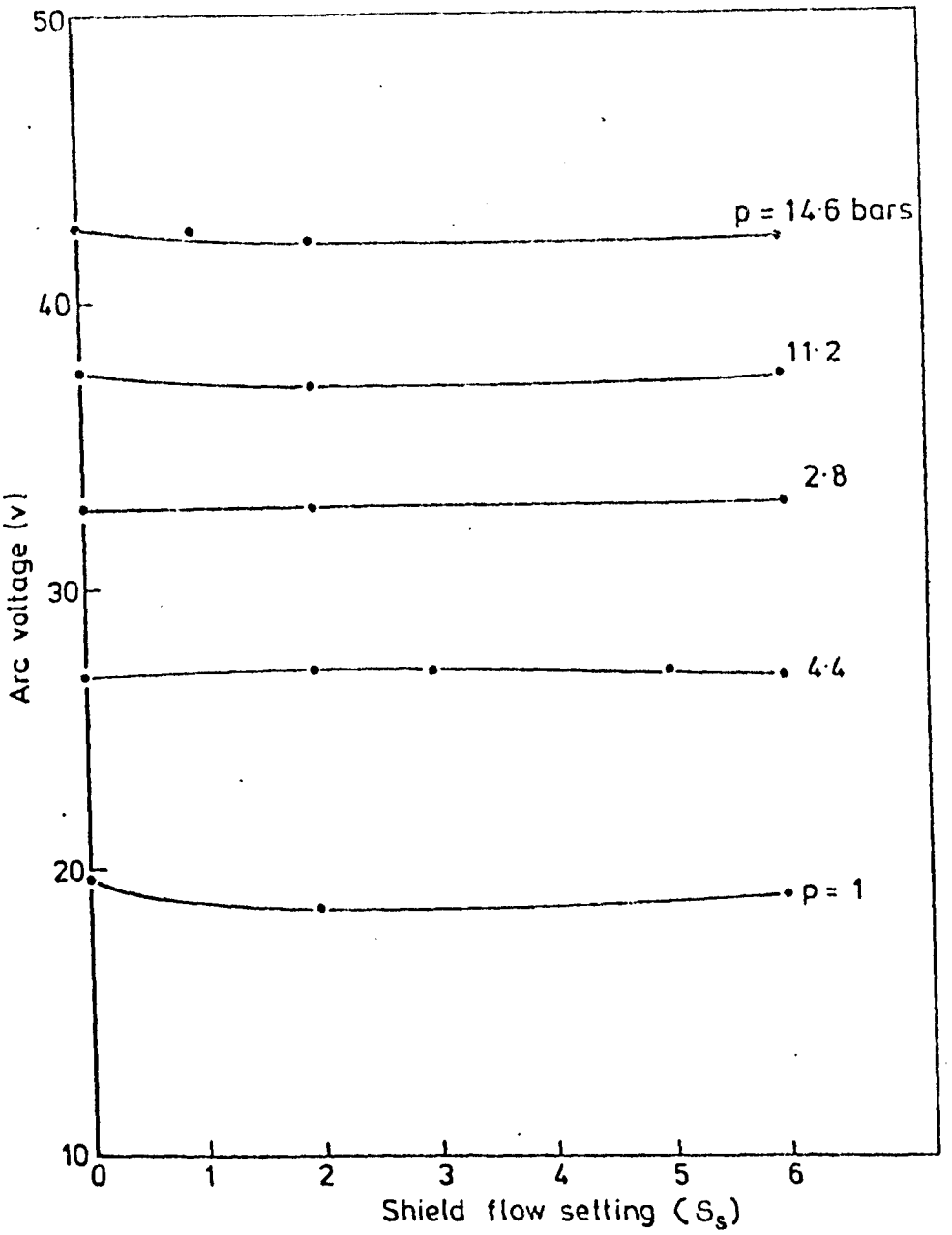

EXPERIMENTAL CONDITIONS

ORIFICE DIAMETER 4 8 mm
CURRENT 150 A
TUNGSTEN - WORK SEPARATION 10 mm
S_p = 3

FIGURE 87. INFLUENCE OF SHIELDING GAS FLOW ON ARC VOLTAGE FOR THE CONSTRICTED TUNGSTEN ARC ON A COPPER ANODE

4.2.3.4. Influence of Anode Characteristics

Results presented in figure 83 indicated that higher voltages are obtained on copper anodes than on steel. The difference between the respective voltages is shown in figure 88. It can be seen that this difference tends to increase over the first 10 bars. Very similar behaviour has been observed with TIG arcs (see section 4.2.1.4). For TIG arcs the difference in behaviour (ΔV) was attributed to the existence of higher zero arc length voltages (by about 2 volts) and larger column field strengths. Using expressions previously found for TIG arcs in still atmospheres we may write

$$\Delta V\ (C_u - F_e) = V(C_u) - V(F_e)$$

$$= V_o(C_u) - V_o(F_e) + \ell\left[E_1(C_u)P^{m(C_u)} - E_1(F_e)P^{m(F_e)}\right]$$

with $V_o(C_u) - V_o(F_e) = 2V$ (see section 4.2.1.2)

and $m(C_u) \simeq m(F_e) \simeq 0.5$

and $E(C_u) \simeq 0.85$ V/mm, $E(F_e) \simeq 0.75$ V/mm

$\therefore \Delta V(C_u - F_e) \simeq 2 + 0.1.\ell.\ P^{0.5}$

Clearly the difference increases with pressure and arc length. For the purpose of comparing TIG results with plasma results an arc length of 10mm is taken. The results is shown in figure 88. It can be seen that predicted TIG results are in reasonably good agreement with those found for plasma arcs. No great accuracy is claimed for the TIG expression given above but it is thought to show that similar phenomena are occurring in both the constricted and unconstricted arc.

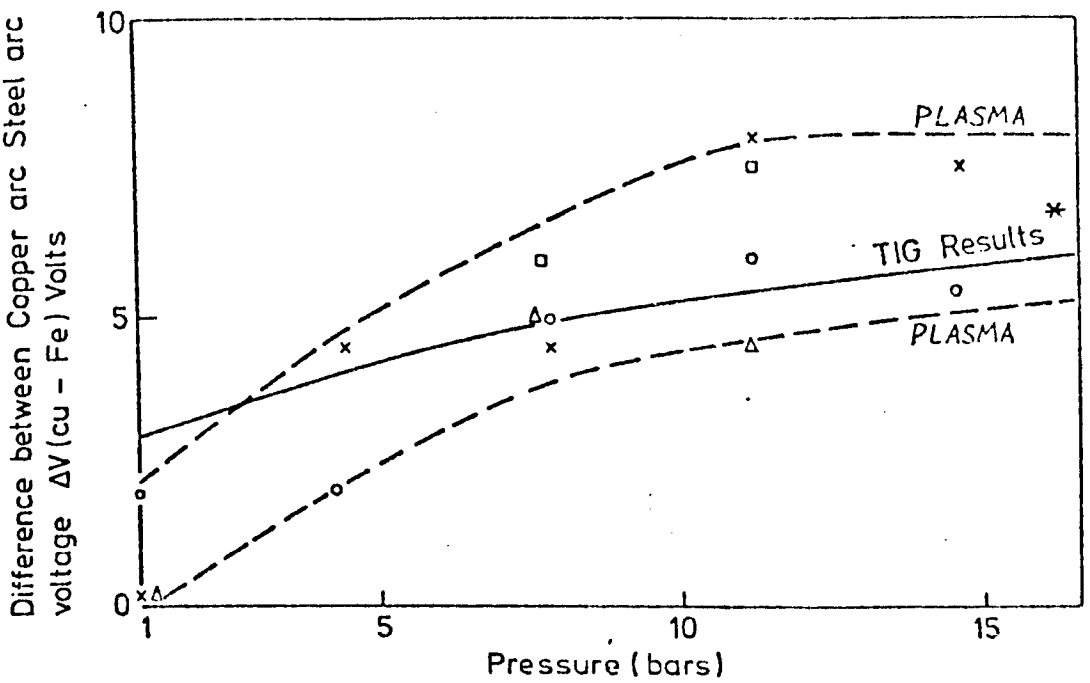

EXPERIMENTAL CONDITIONS

	PLASMA FLOW SETTING	ORIFICE DIAMETER mm
o	1	0·48
x	3	0·48
Δ	1	0·32
□	3	0·32

* TIG RESULTS (SEE EXPRESSION GIVEN IN TEXT)

FIGURE 88. INFLUENCE OF ANODIC COMPOSITION ON ARC VOLTAGE FOR THE CONSTRICTED ARGON-TUNGSTEN ARC (TUNGSTEN - ANODE SEPARATION OF 10 mm, 150 amps)

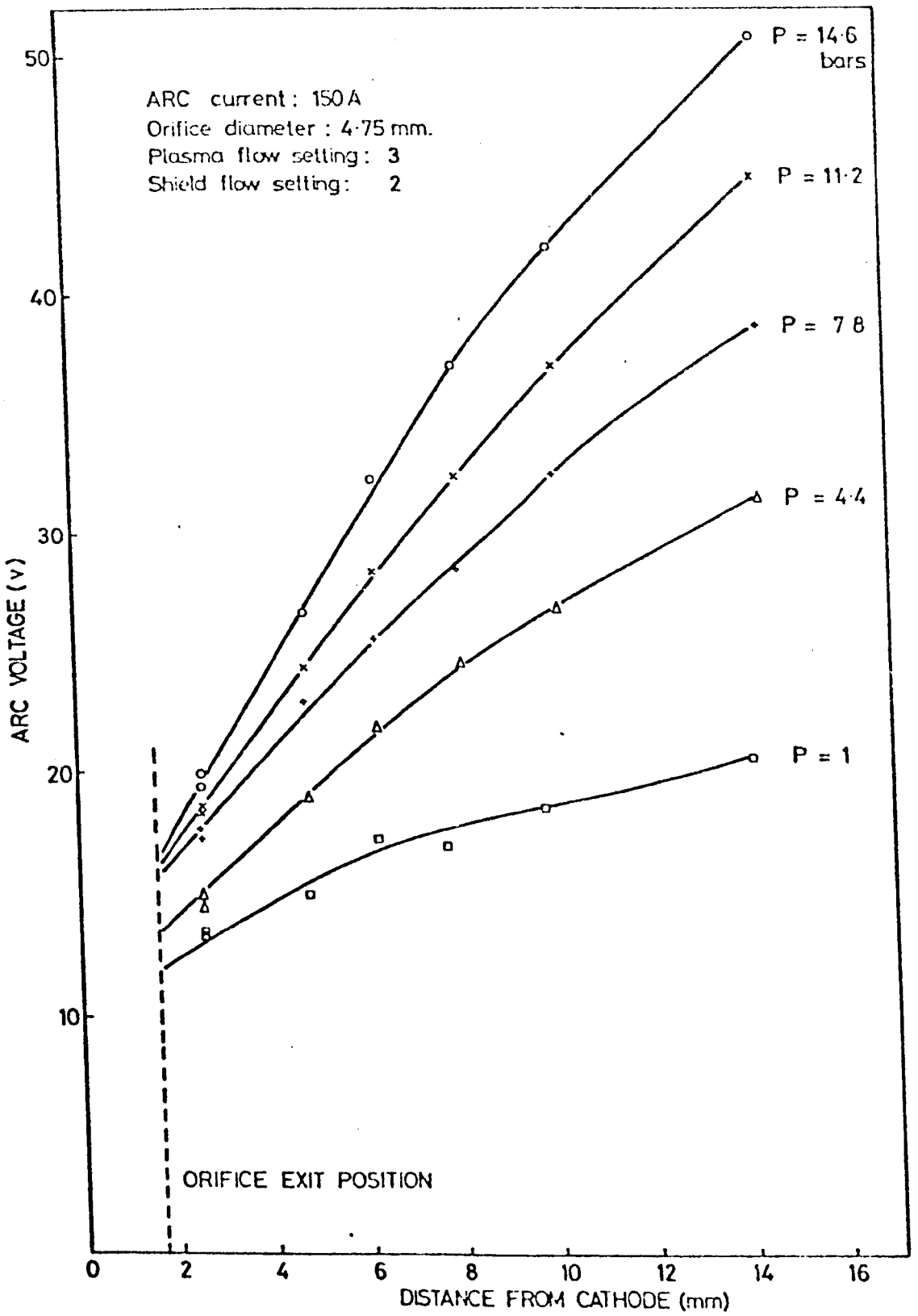

FIG.89. PRESSURE DEPENDENCE OF ARC PLASMA VOLTAGE.

Part 2 Weld Bead Characteristics

In this section weld bead characteristics are reported. Experiments have been performed for argon and helium TIG arcs and also for the constricted tungsten arc. Details of weld bead geometry and melting behaviour are given with respect to arcing parameters. As a prerequisite to this a more general description to weld bead stability, modes and symmetry is given.

4.3. Weld Bead Appearance

4.3.1. The Argon TIG Arc

The surface appearance of weld beads made using argon TIG arcs was generally good for pressures below about 30 bars. Above 30 bars beads often gave the impression of being associated with turbulent or unsteady molten pool behaviour. This form of behaviour was observed for a range of arc currents, arc lengths and electrode characteristics (see figures 90,91). It was found that weld bead surface appearance could be stabilised by means of the axial magnetic field of a permanent magnet (figure 92,93). The effect of such a magnetic field was not only to produce a straight weld bead track but also to give a very smooth surface appearance.

Sectioned weld beads showed a tendency to increase in depth and become more 'U' shaped over the first 10 bars or so (figure 94). This behaviour was associated with a high degree of symmetry but at pressures greater than 30 bars assymmetrical beads occurred. Symmetry could be regained by the application of a magnetic field but this was found to be accompanied by a decrease in weld bead penetration and a slight increase in bead width (96,97). The general behaviour was such that bead geometry was less sensitive to ambient pressure when a magnetic field was applied than without. In all of these experiments the heat affected zone's (HAZ) appear roughly semi-circular and largely unaffected by the application of a magnetic field.

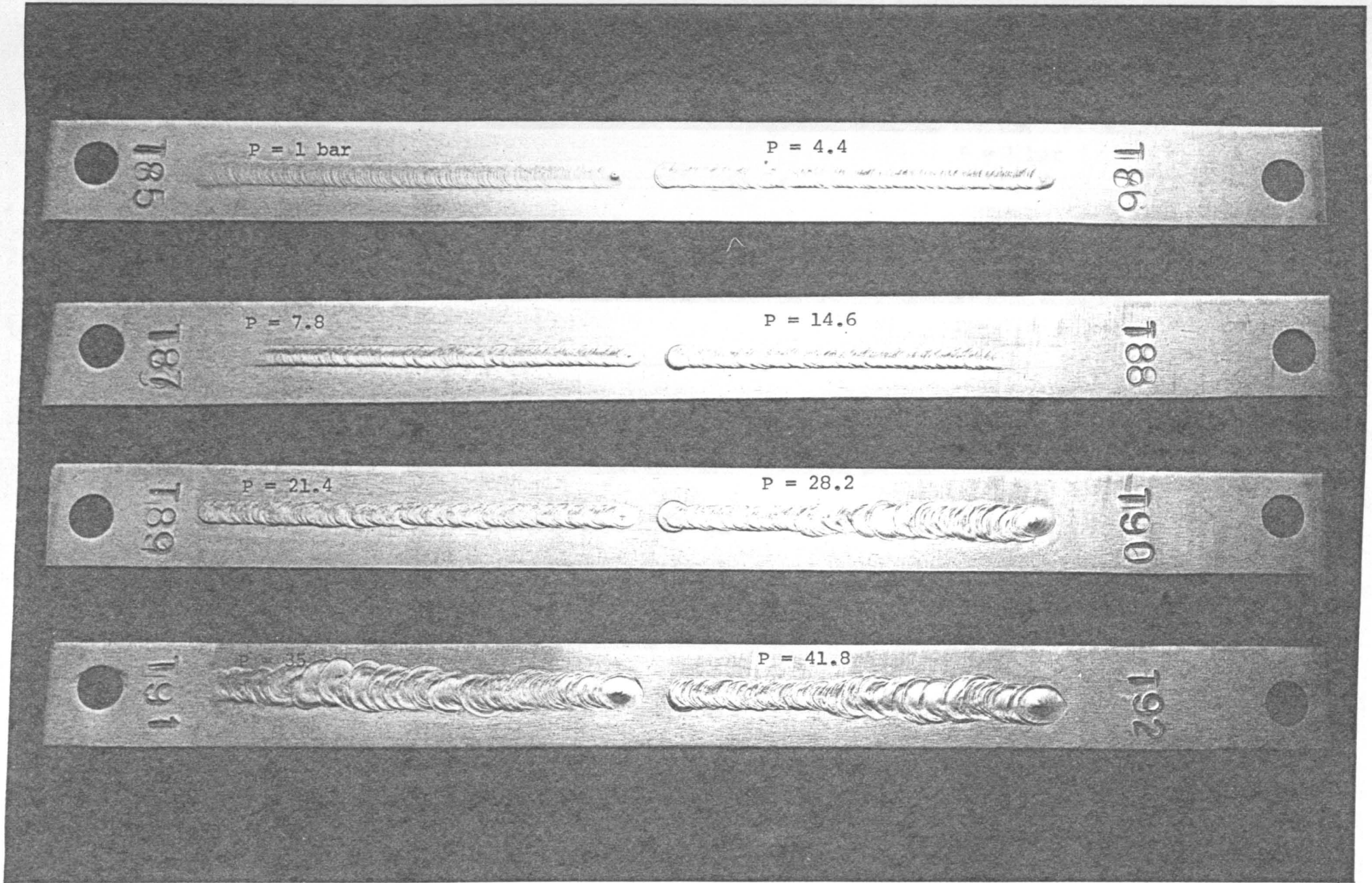

Figure 90 Stability of Argon TIG Weld Beads. (150A, 2mm arc with no shield on mild steel, welding speed of 1.4mm/s)

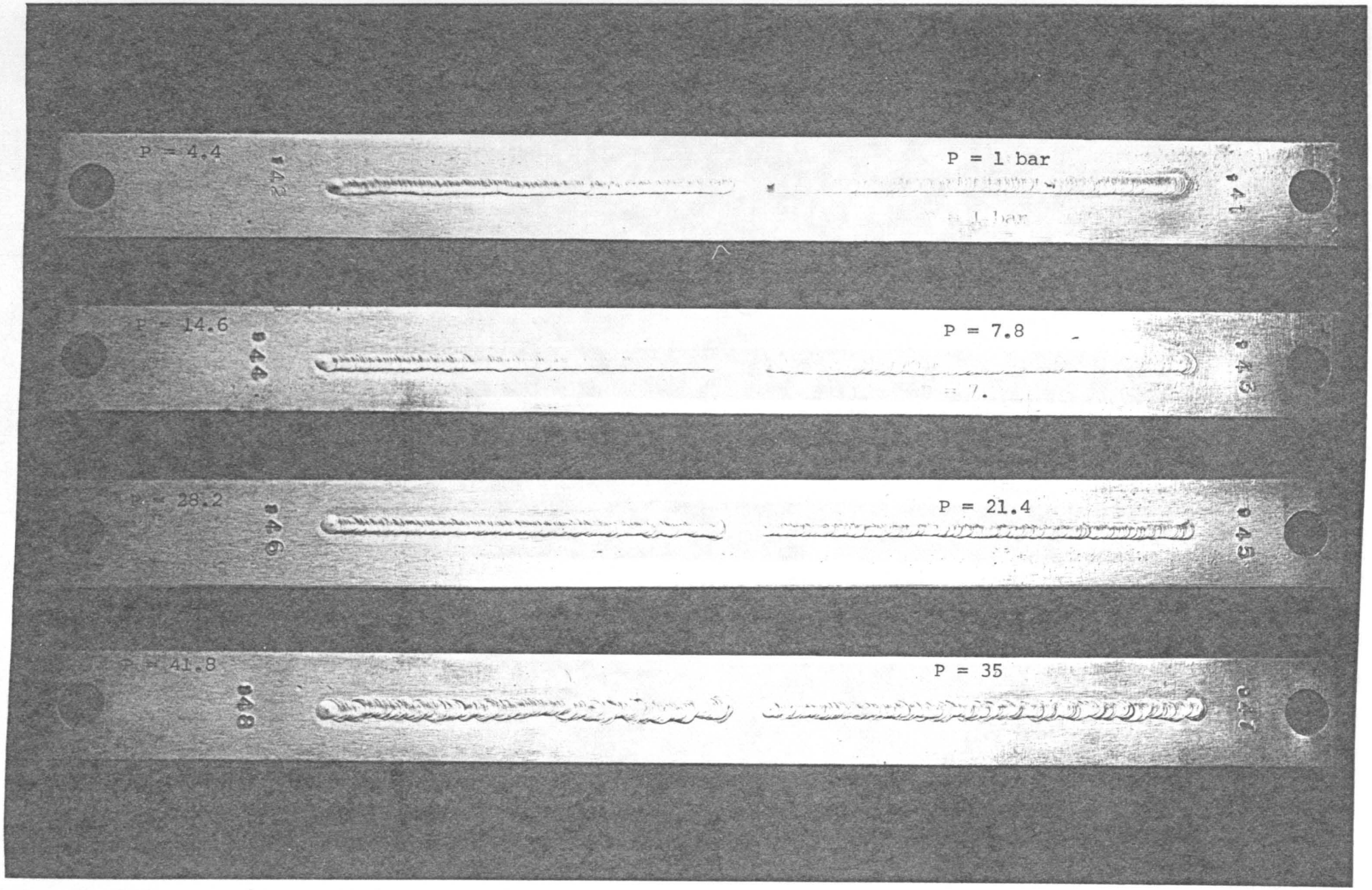

Figure 91 Influence of Ambient Pressure on Bead Appearance (100A, 2mm argon arc, travel speed = 1.38mm/s)

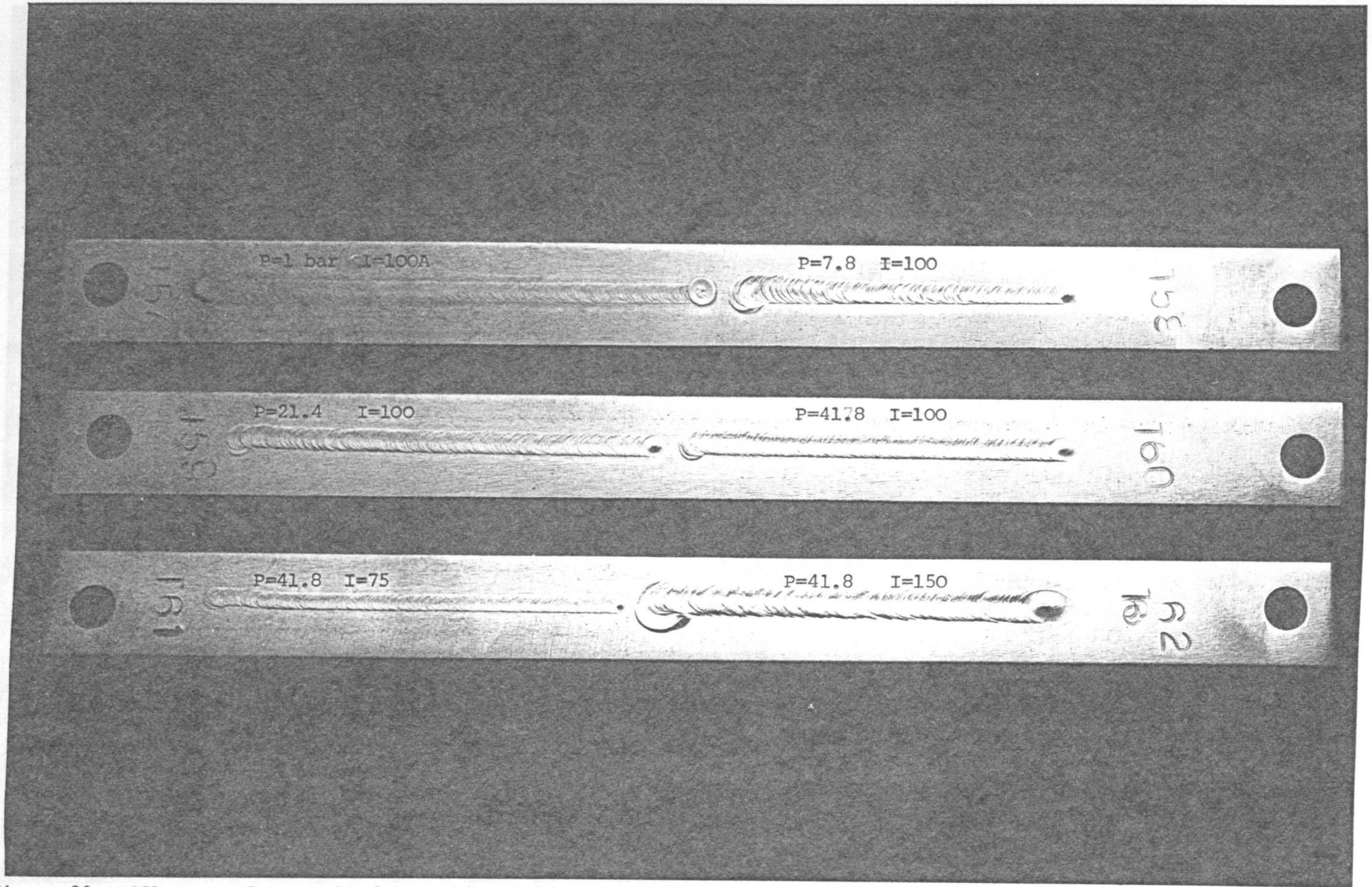

Figure 92 Influence of an Applied Magnetic Field on Bead Appearance. (arcing conditions: axial field with a strength of about 20 gauss near the work, arc length=2mm, travel speed=1.4mm/s, argon arcs, no shielding gas flow)

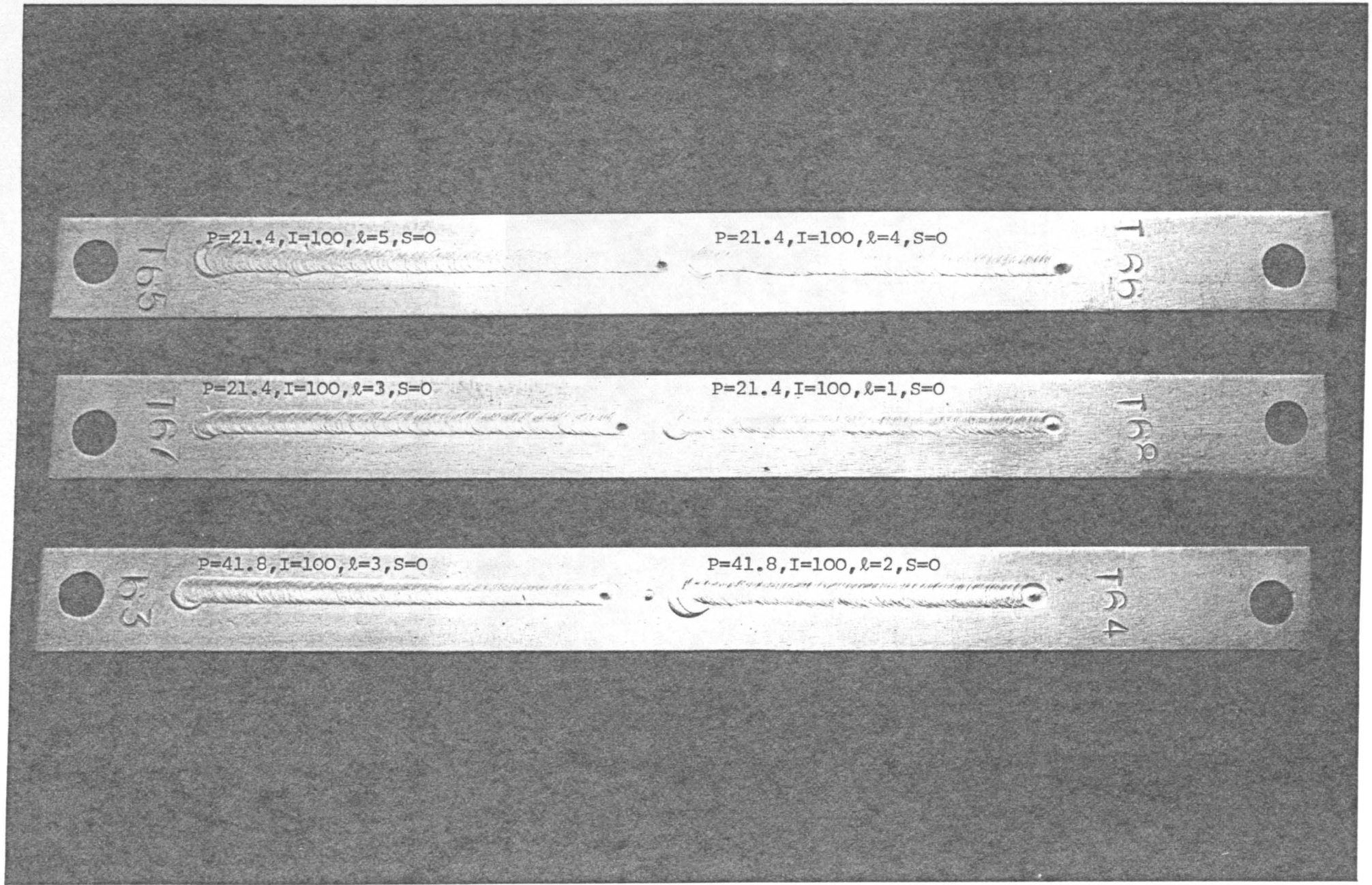

Figure 93 Influence of Magnetic Field on Bead Appearance (P=Pressure in bars, I=Current, ℓ=arc, length in mm and S = shield gas flow setting)

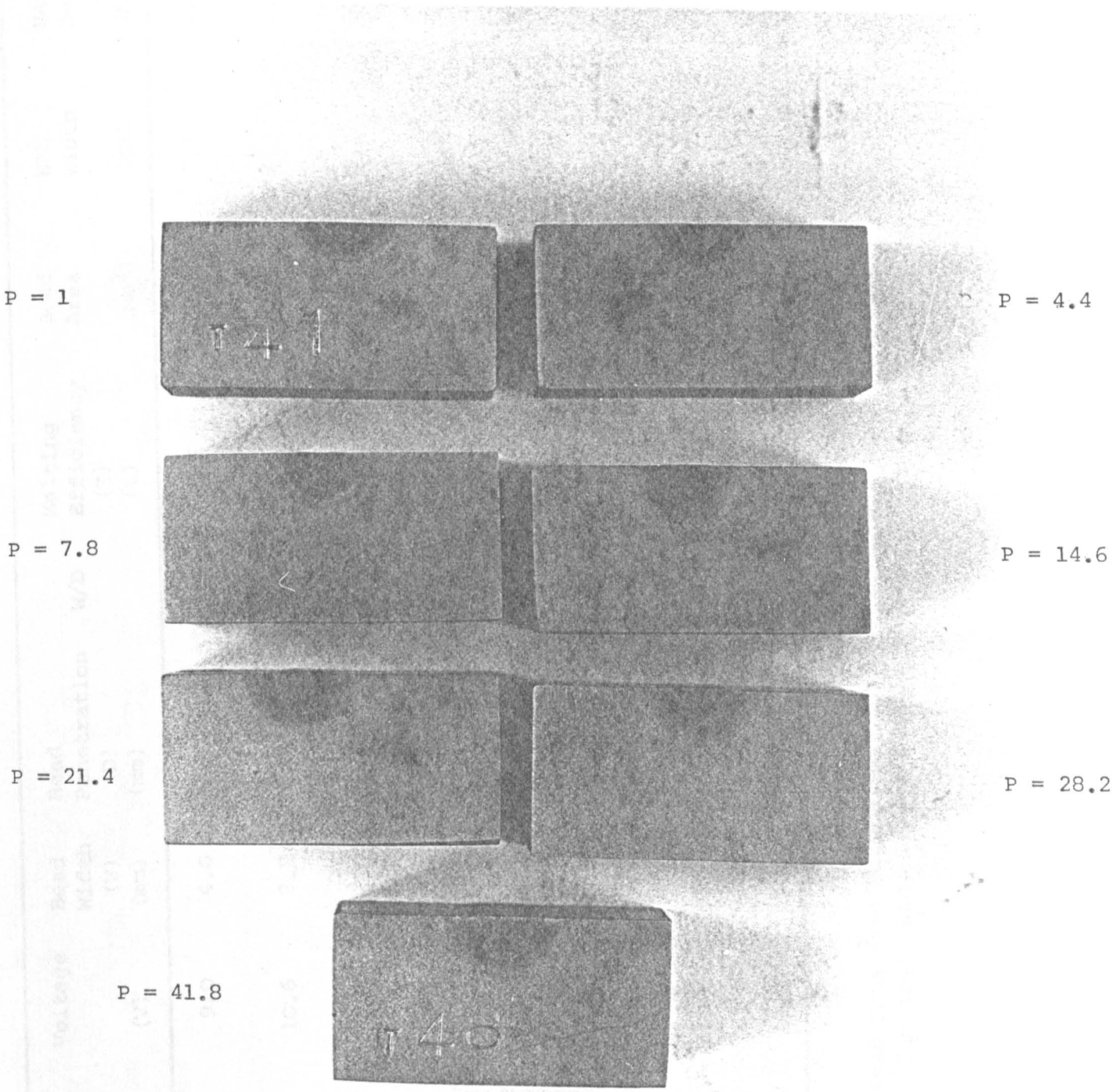

Figure 94 Influence of Pressure on Weld Bead Cross-Section
(magnification of 2.1)
(I = 100A, 2mm argon arc, table speed = 1.38 mm/s)

Sample No.	Pressure (bars)	Voltage (V)	Bead Width (W) (mm)	Bead Penetration (D) (mm)	W/D	Melting Efficiency (Z) (%)	Bead Area (mm^2)	HAZ Width (mm)	HAZ Depth (mm)
41	1	9.0	4.0	1.3	3.1	6.6	3.6	7.4	2.6
42	4.4	10.6	3.9	1.9	2.0	8.4	5.4	6.9	2.8
43	7.8	11.3	4.3	2.4	1.8	10.8	7.4	7.1	3.4
44	14.6	12.9	3.7	2.9	1.3	9.9	7.8	7.3	4.1
45	21.4	13.7	3.7	2.9	1.3	9.8	8.2	7.7	3.9
46	28.2	15.4	5.3	3.1	1.7	12.6	11.8	8.4	4.3
47	35.0	15.5	4.7	2.9	1.7	10.6	10.0	7.9	3.7
48	41.8	16.17	5.6	3.3	1.7	12.3	12.4	9.4	4.7

Weld Bead Data (see figure 94)
(100A, 2mm argon arc, 1.38mm/s table speed)

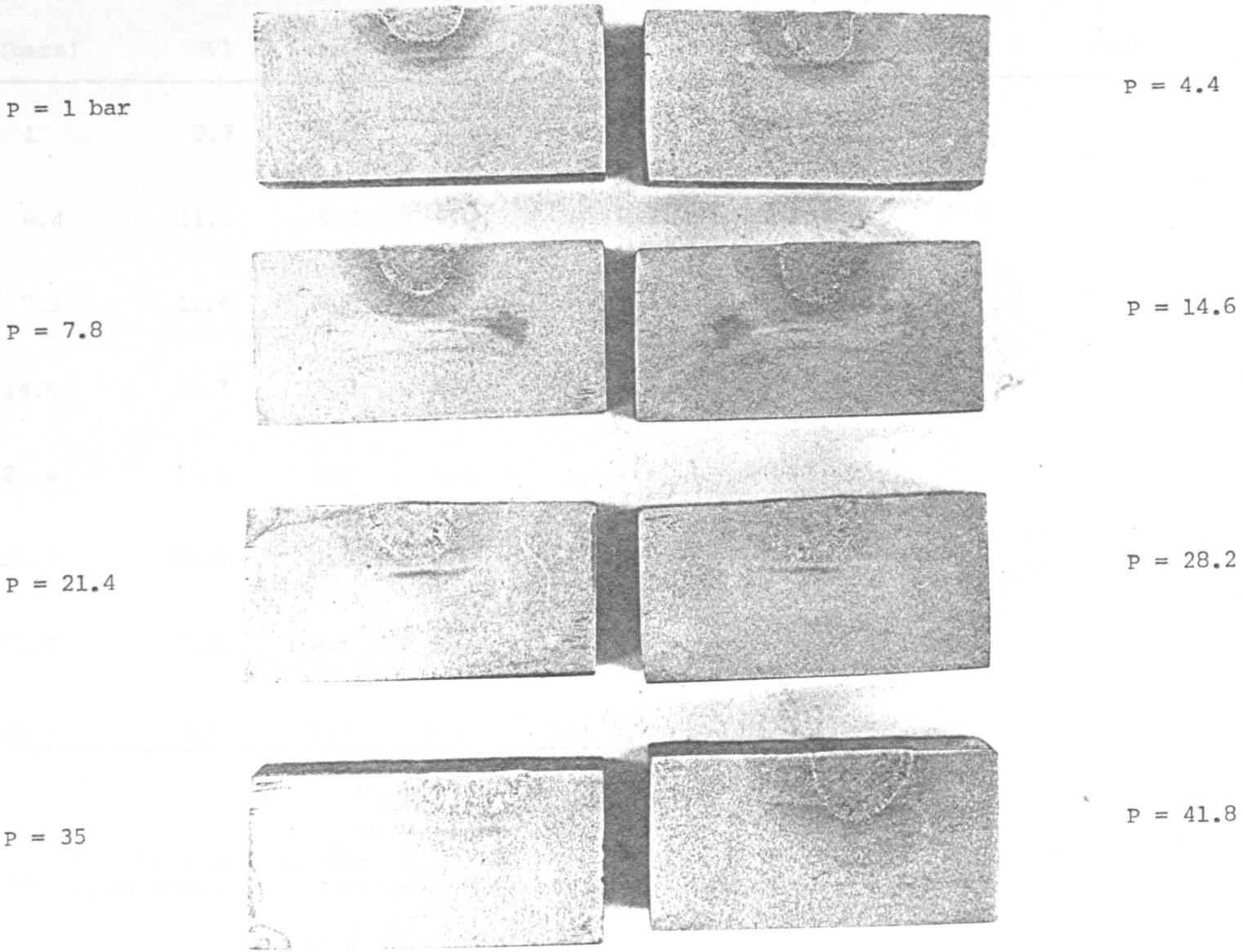

Figure 95 Influence of Pressure on Weld Bead Cross-Section (magnification of 2.1)
(I = 150A, 2mm argon arc, table speed = 1.38 mm/s)

Sample No.	Pressure (bars)	Voltage (V)	Bead Width (mm)	Bead Penetration (mm)	W/D	Melting Efficiency (Z) (%)	Bead Area (mm^2)	HAZ Width (mm)	HAZ Depth (mm)
49	1	9.7	6.1	2.7	2.3	14.0	12.4	11.6	5.0
50	4.4	11.3	6.0	4.0	1.5	17.4	18.0	10.4	5.6
51	7.8	11.4	6.6	3.4	1.9	16.7	17.4	10.9	5.9
52	14.6	13.7	5.3	4.4	1.2	14.5	18.2	12.7	7.3
53	21.4	15.3	7.7	4.1	1.9	15.0	21.0	13.7	6.6
54	28.2	18.0	7.0	4.6	1.5	14.6	24.0	15.9	7.9
55	35.0	19.5	9.6	3.0	3.2	12.7	22.6	16.7	7.3
56	41.8	21.0	8.3	5.0	1.7	16.2	31.0	17.6	8.9

Weld Bead Data (see figure 95)
(150A, 2mm argon arc, 1.38 mm/s table speed)

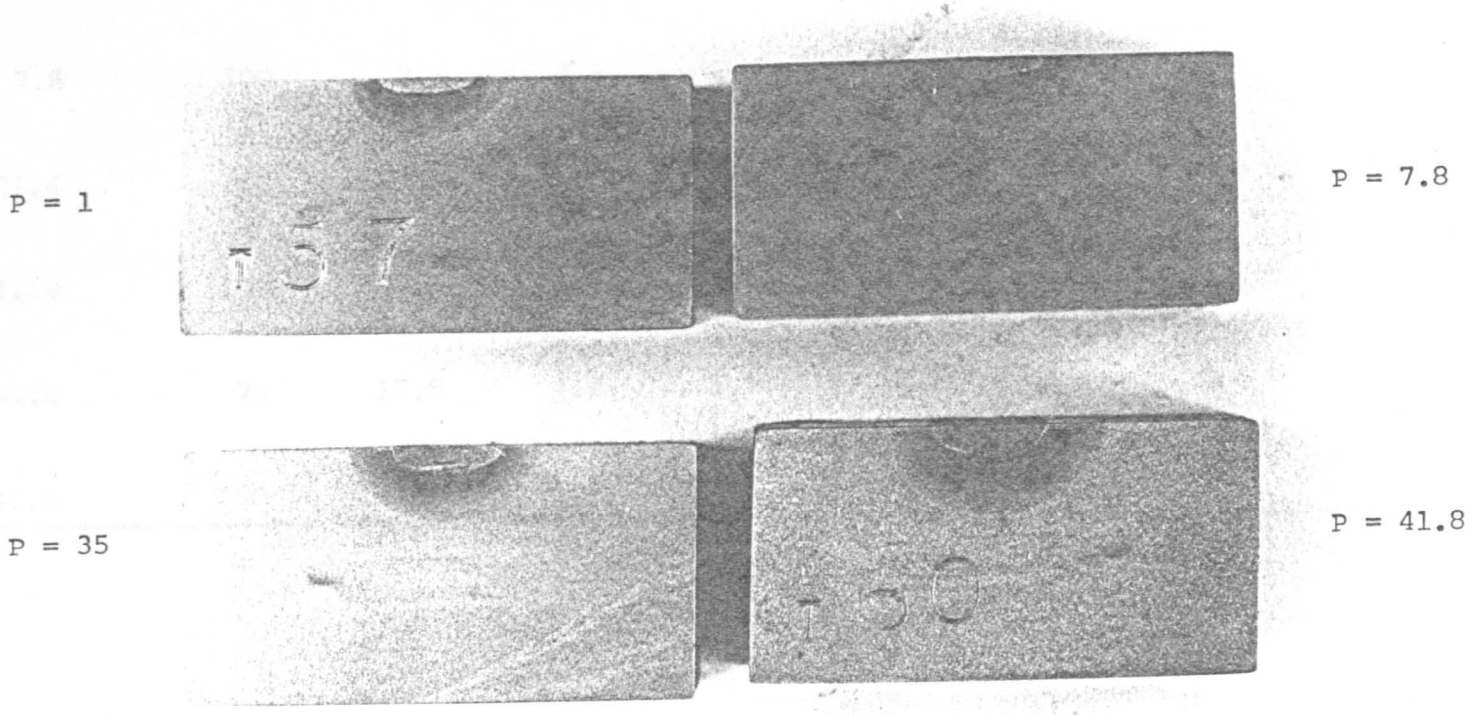

Figure 96 Influence of Ambient Pressure on Bead Profile when a Magnetic Field is Applied (I = 100A, 2mm argon arc, table speed = 1.38 mm/s, magnification = 2.1)

Sample No.	Pressure (Bars)	Current (A)	Voltage (V)	Bead Width W (mm)	Bead Penetration D (mm)	W/D	Melting Efficiency (Z) (%)	Bead Area (A) (mm^2)	HAZ Depth (mm)	HAZ Width (mm)
57	0	100	10.4	4.7	0.8	6	3.8	2.4	7.4	2.4
58	7.8	100	12.1	4.9	1.1	4.3	5.7	4.2	8.3	2.9
59	21.4	100	15.3	5.6	1.1	4.9	6.0	5.6	9.3	3.4
60	41.8	100	20.5	5.9	1.4	4.1	5.3	6.6	9.6	3.7
61	41.8	75	17.8	4.2	1.1	3.9	4.4	3.6	7.0	2.6
62	41.8	150	20.2	8.7	2.0	4.4	7.4	13.6	-	-

Weld Bead Data (see figures 96 and 97)
(Magnetic stirring applied to 2mm argon arcs)

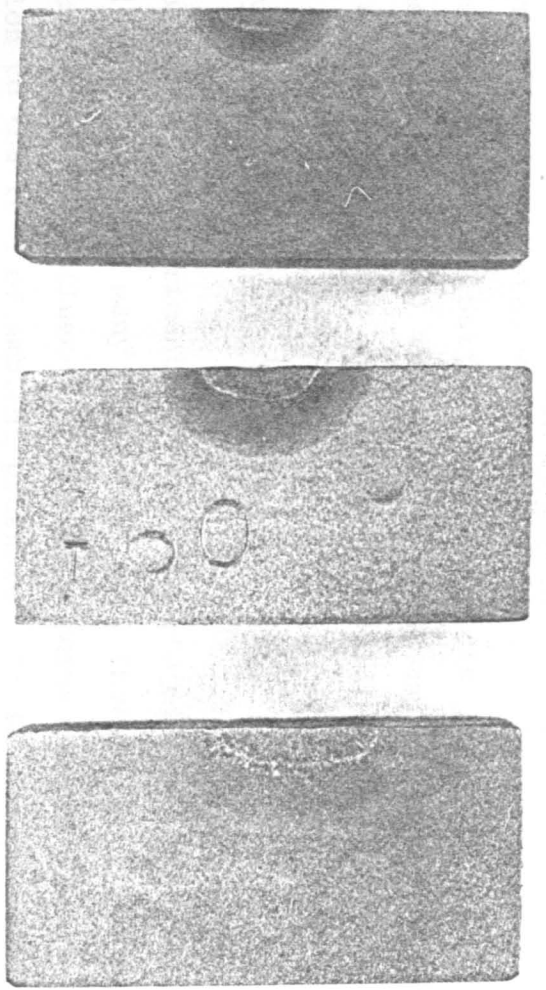

I = 75A

I = 100A

I = 150A

Figure 97 Influence of Arc Current on High Pressure (41.8 bars) Bead Profiles in the Presence of Magnetic Stirring (2mm argon arc, table speed = 1.38 mm/s, magnification of 2.1)

4.3.2. The Helium TIG Arc

Helium TIG arcs generally give deeper welds than the corresponding argon arcs. Aspect ratio as low as 0.9 have been obtained (see figure 98). Indeed it was observed that 'key holing' behaviour could occur at pressures of 11.2 bars and arc currents of 100 Amps (see figure 99). Other effects of increasing pressure were to produce significantly larger melted volumes and occasionally weld metal cracking (figure 100). This was generally associated with short arcs (2mm) at high pressure and could be predicted from the surface appearance of a bead (figure 100).

4.3.3. The Constricted Argon Arc

Experiments with soft constricted argon tungsten arcs on stainless steel produced weld bead sections with less symmetry (101) than those of TIG arcs. This was associated with larger width to depth ratios than those obtained for TIG arcs. Surface appearance was generally good although weld bead 'humping' (102) was found to occur at certain combination at plasma gas flow (S_p), arc current (I) and welding speed (v).

4.4. Argon TIG Arc Weld Bead Geometry

A large number of experiments have been performed over the pressure range 1 to 42 bars and many parameters were investigated. The text concentrates on the influence of the main parameters and gives particular attention to the role of ambient pressure. It is thought inappropriate to cross plot all combinations of these parameters (and combinations of these). For this reason emphasis is placed on parameter combinations of direct physical significance. These comments also apply to heat effect zone and melting characteristics reported in latter sections.

4.4.1. Weld Bead Penetration

Experiments with 1% and 2% thoriated electrodes were performed. No evidence was found to suggest that this variable affected penetration (e.g. see figure 103). Scatter between these results is therefore taken as an indication of reproducibility. It can be seen from figures 103 and 104 that penetration increases quickly with pressure over the first 15 bars. Further influences occur up to about 20 bars but penetration

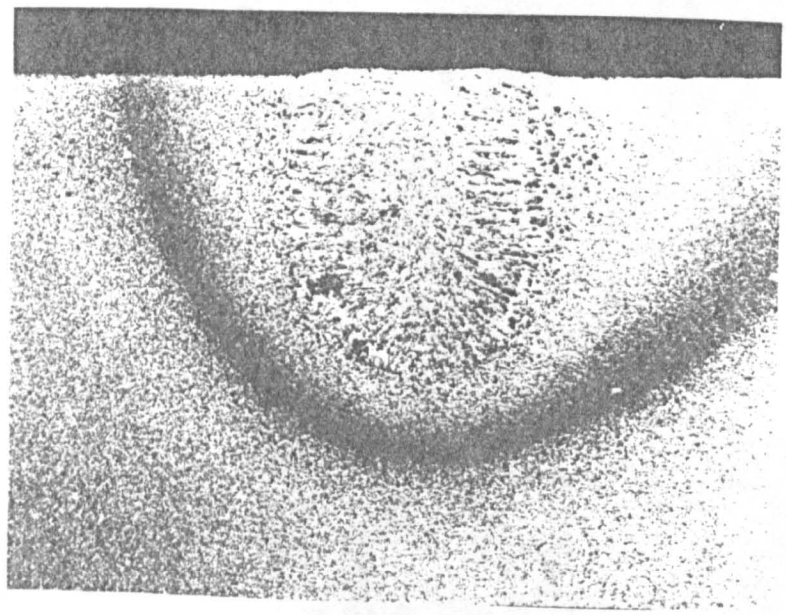

Fig. 98. High pressure helium TIG weld bead (aspect ratio: 0.9)

p = 14.6 bars, I = 100A, ℓ = 3mm travel speed = 1.38 mm s.

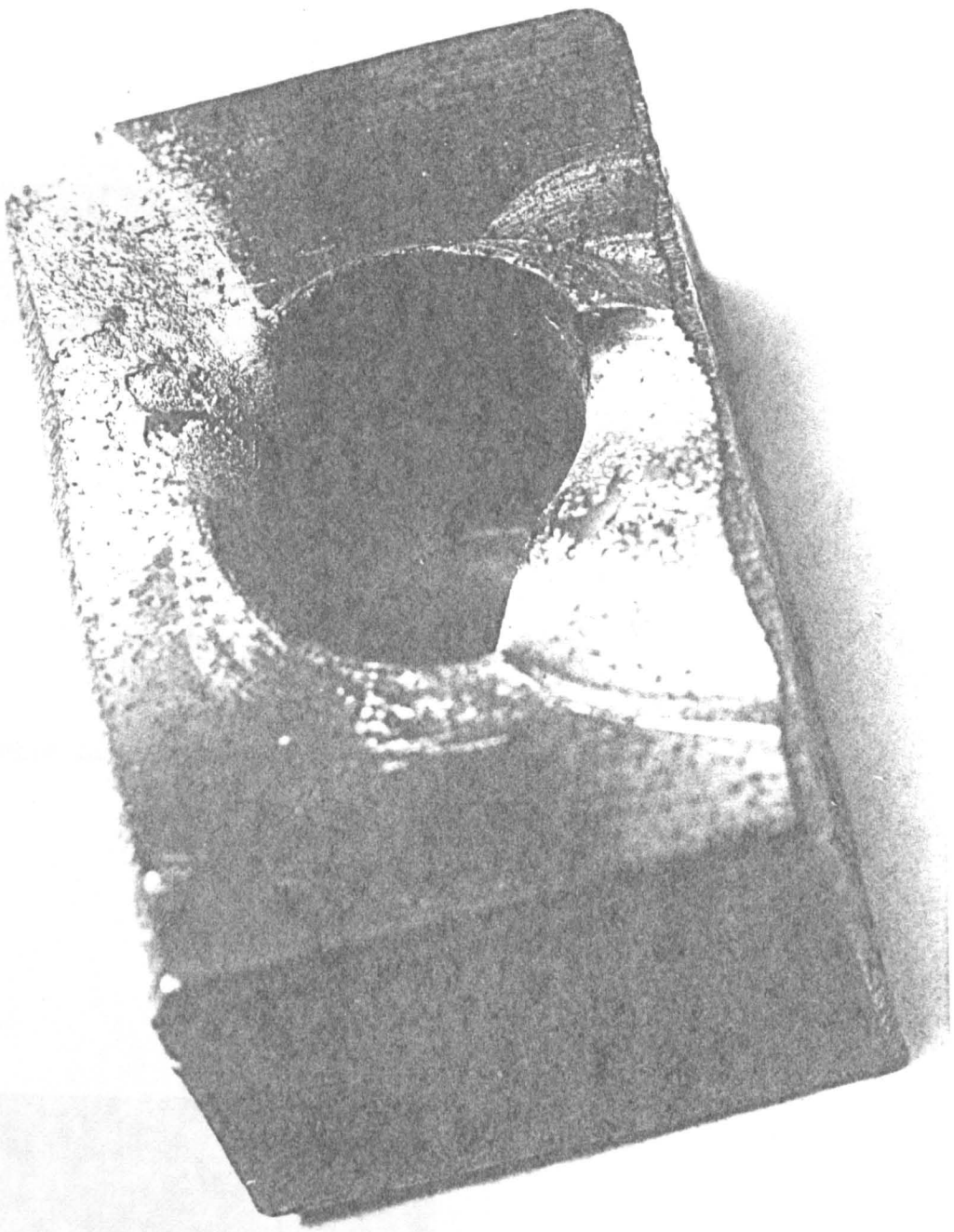

Figure 99 Keyhole Action Produced by a Helium TIG Arc at 15 Bars

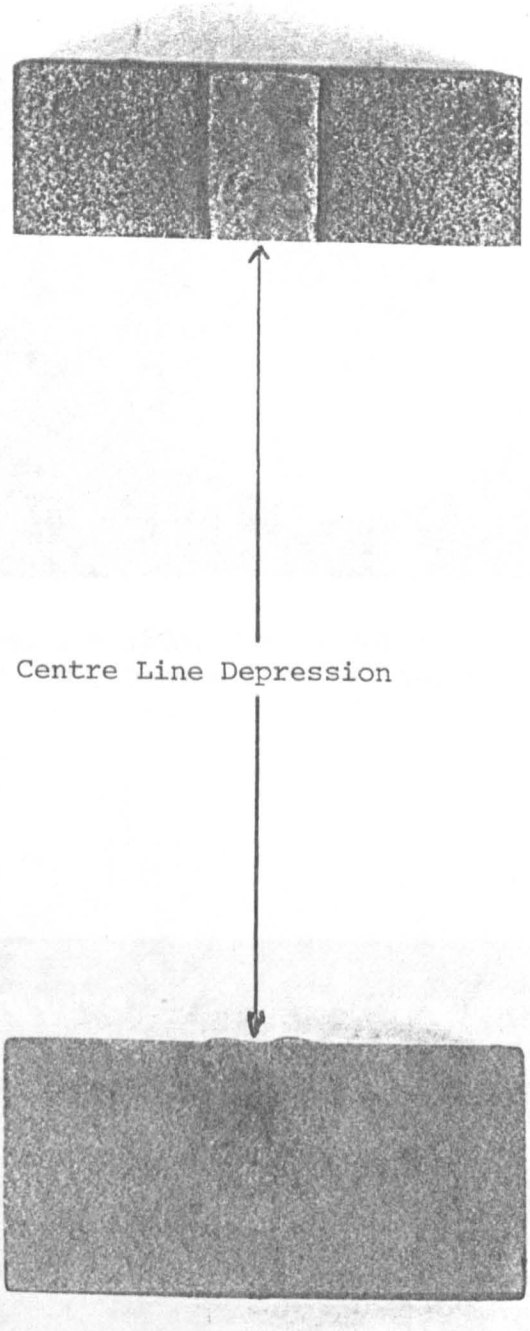

Figure 100 Weld Bead Crack for High Pressure Helium Arc (P = 11.2 bars, 2mm helium arc, 100A, 23 volts, travel speed = 1.38 mm/s)

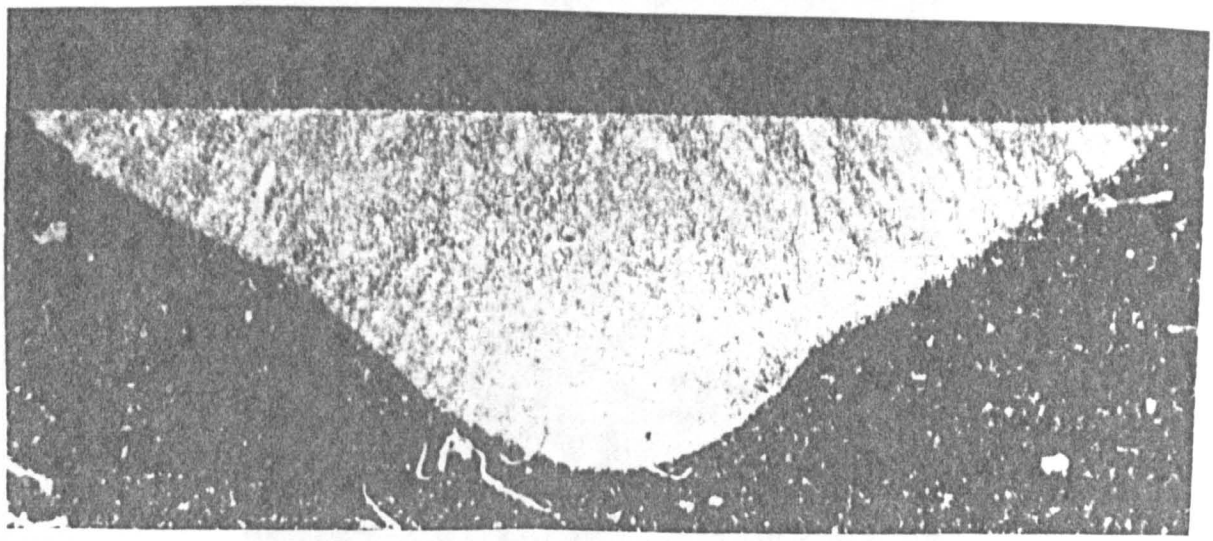

(a) P = 12.9 bars, I = 150A, V = 32 volts
arc length = 10mm, plasma flow setting = 3

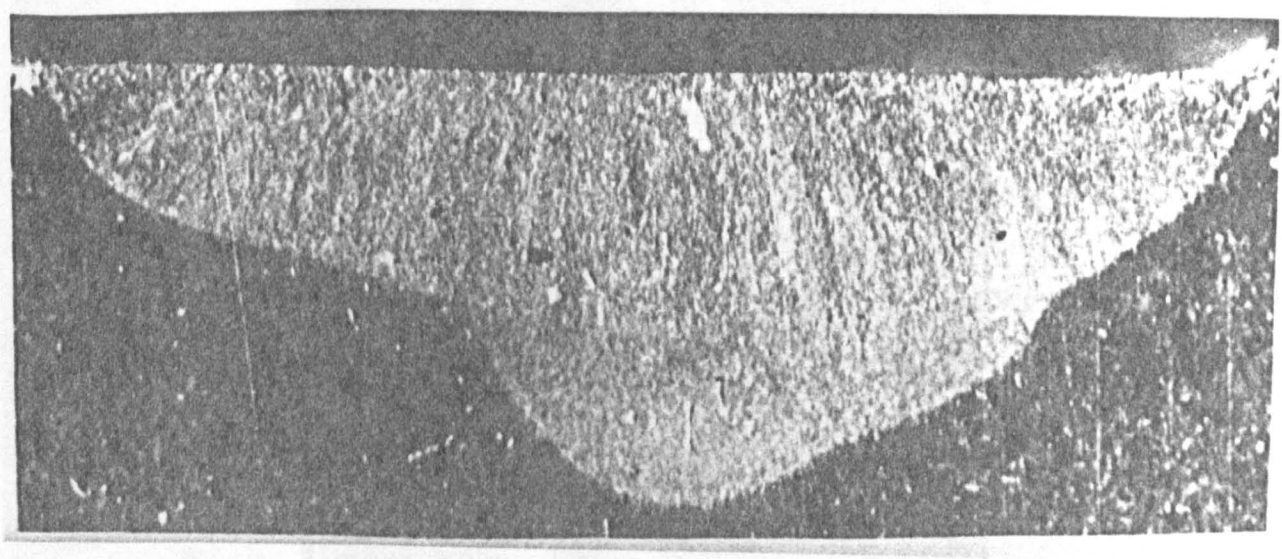

(b) P = 7.8 bars, I = 150A, V = 25V
arc length = 10mm, plasma flow setting = 1

Figure 101 Bead Appearance in Plasma Welding

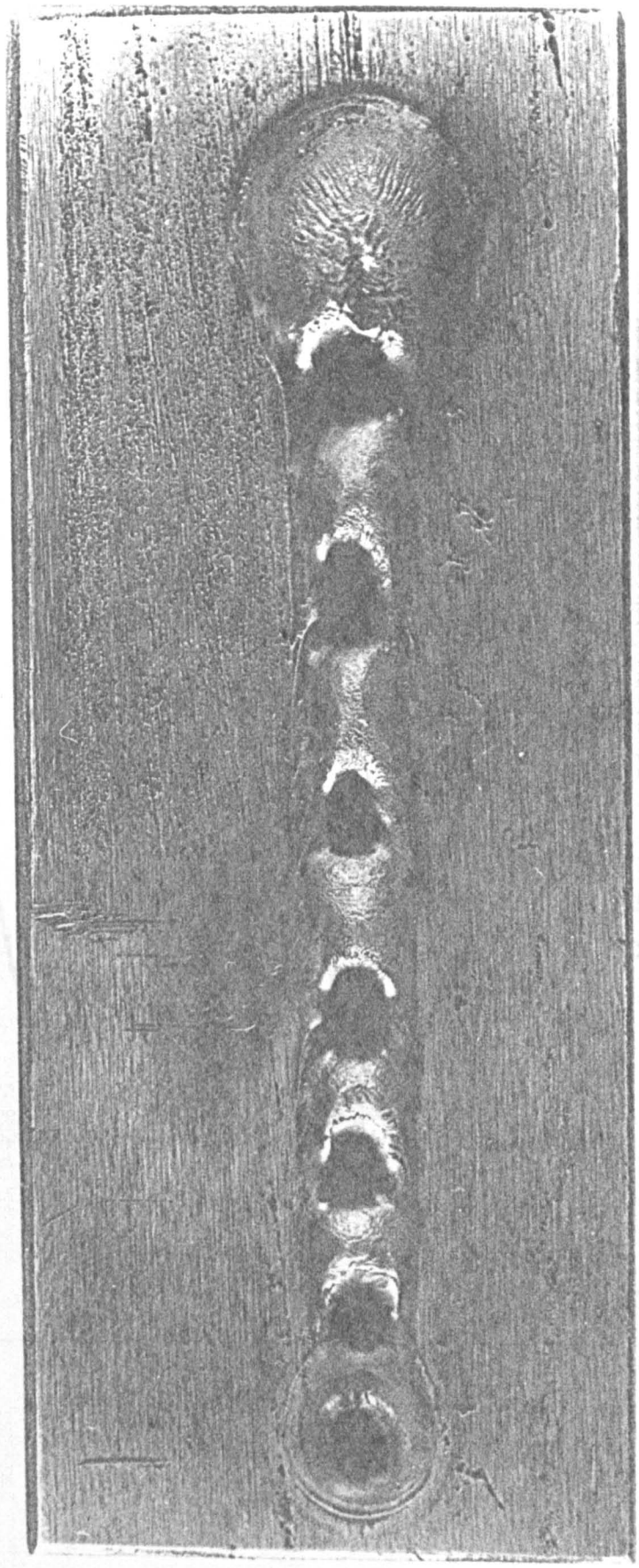

Figure 102 Typical Example of Weld Bead Humping

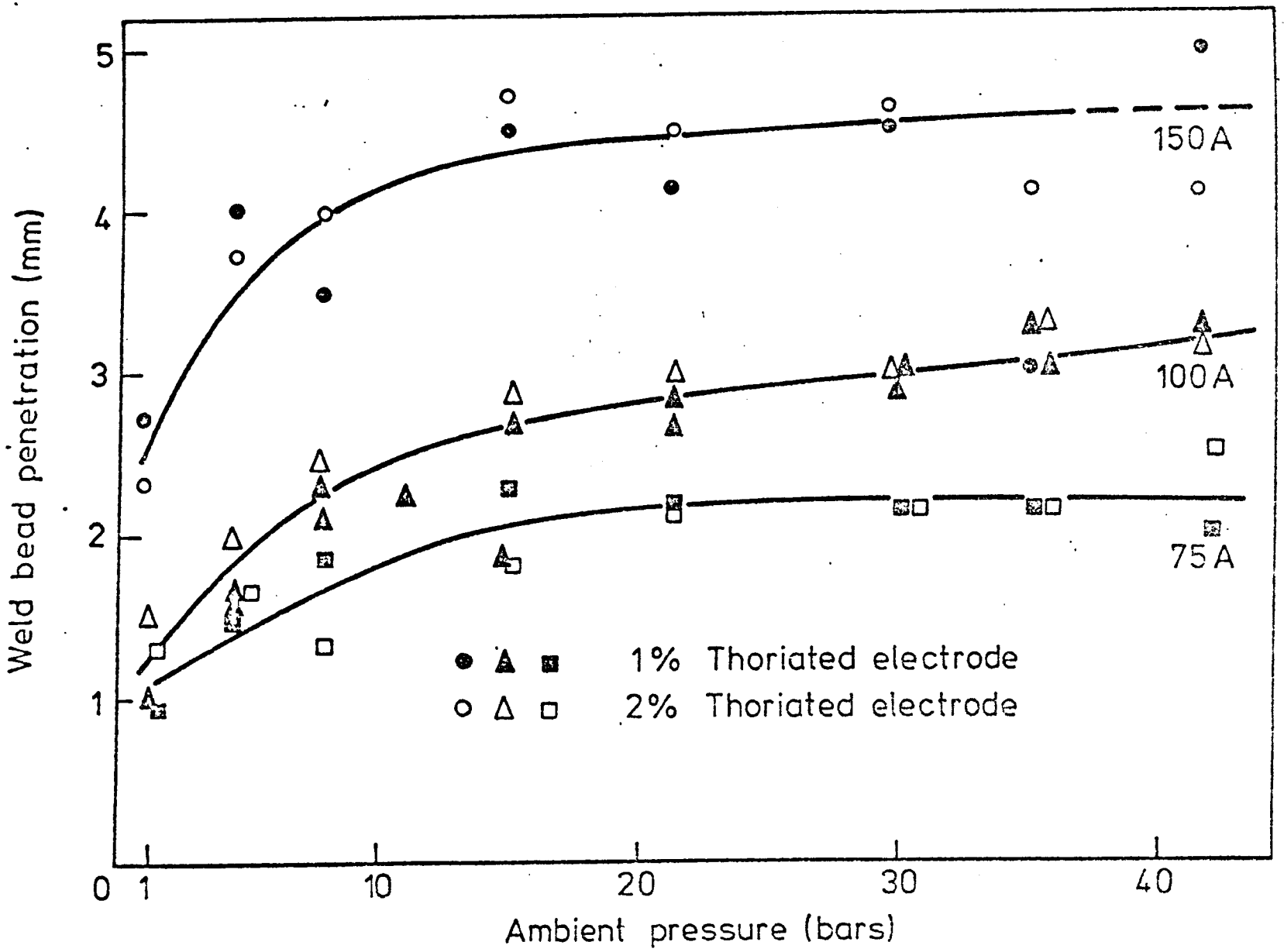

FIGURE 103. INFLUENCE OF PRESSURE AND CURRENT ON PENETRATION FOR A 2 mm ARGON TIG ARC.

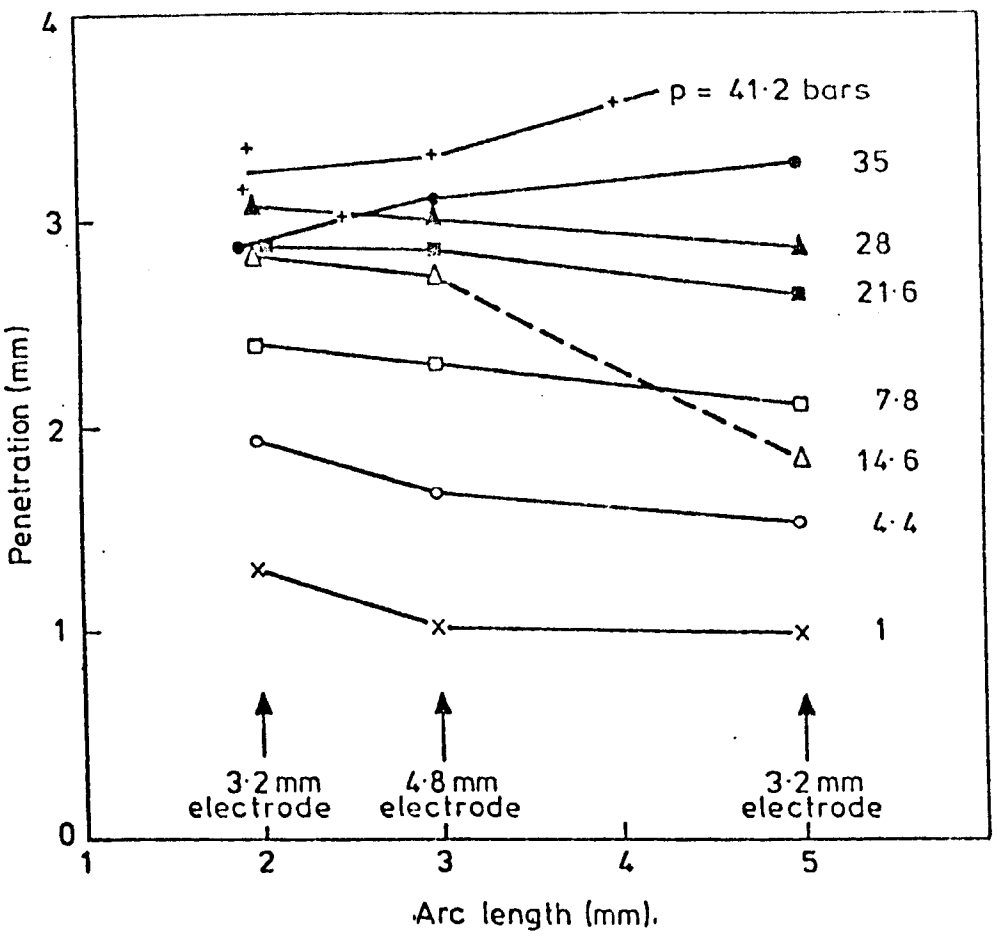

FIGURE 104 INFLUENCE OF ARC LENGTH ON WELD BEAD PENETRATION FOR A 100 AMP ARGON TIG ARC.

changes little above this pressure. This behaviour is seen for 75, 100 and 150 Amp arcs. Figures 103 and 104 show that penetration roughly doubles over the first 15 bars for all currents investigated. It may be deduced from figure 103.this behaviour is roughly linearly dependent on current at any pressure. Penetration is found (figure 104) to be only weakly influenced by arc length although at pressure below about 30 bars penetration decreases slightly with increasing arc length. Above this pressure there is a tendency for penetration to increase slightly with arc length. An increase in penetration is observed with increasing arc length when welding is performed in the presence of a magnetic field (see figure 105). This is presumably associated with a decrease in the influence of the magnetic field strength at the pool with increasing arc length.

Experiments made with arcs burning in gas flows give similar results to those found in stagnant atmospheres. This applies to welds made with and without an applied magnetic field (see table 9).

Table 9 Influence of Shielding Gas Flow on Weld Bead Geometry at 41.8 Bars (I=100A, travel speed 1.38mm/s)

With or Without Magnetic Field	Flow Setting S	Weld Bead Depth D (mm)	Weld Bead Width W (mm)	Weld Bead Area A (mm^2)	HAZ Depth D (mm)	HAZ Width W (mm)	HAZ Area A (mm^2)	Melting Efficiency Z (%)
With	0	1.43	5.86	6.6	3.71	9.57	26.00	5.28
field	2	1.43	6.57	7.2	4.11	9.71	30.20	5.38
l = 2mm	4	1.57	6.43	7.8	3.57	10.71	29.00	5.21
Without	0	3.00	4.79	10.6	4.36	9.93	29.40	7.26
field	2	2.79	6.57	13.2	4.21	10.57	30.80	8.68
l = 3mm	4	3.14	5.71	13.6	4.64	9.78	30.20	8.68

The application of a magnetic field causes a considerable reduction in the influence of pressure on penetration. Figure 106 shows that the influence of pressure is then confined mainly to the first 5 bars and increases only slowly over the range 5 to 42 bars. At one bar the application of the magnetic field affects a 25% reduction in penetration. This figure is over 50% at 40 bars. Indeed, penetration with a field at 42 bars is only slightly greater than without a field at one bar.

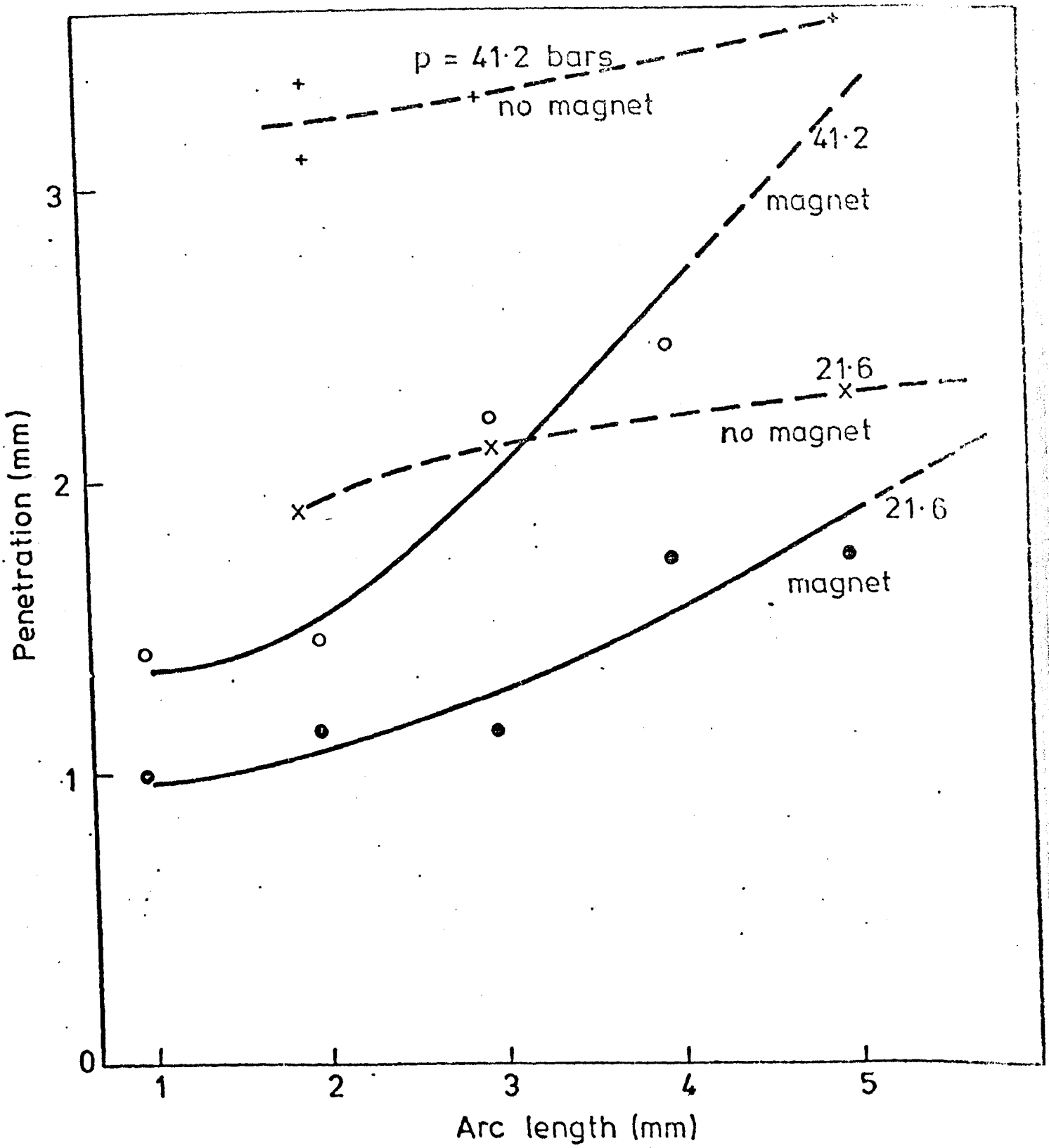

FIGURE 105. INFLUENCE OF ARC LENGTH ON BEAD PENETRATION
(100 A, ARGON TIG ARC)

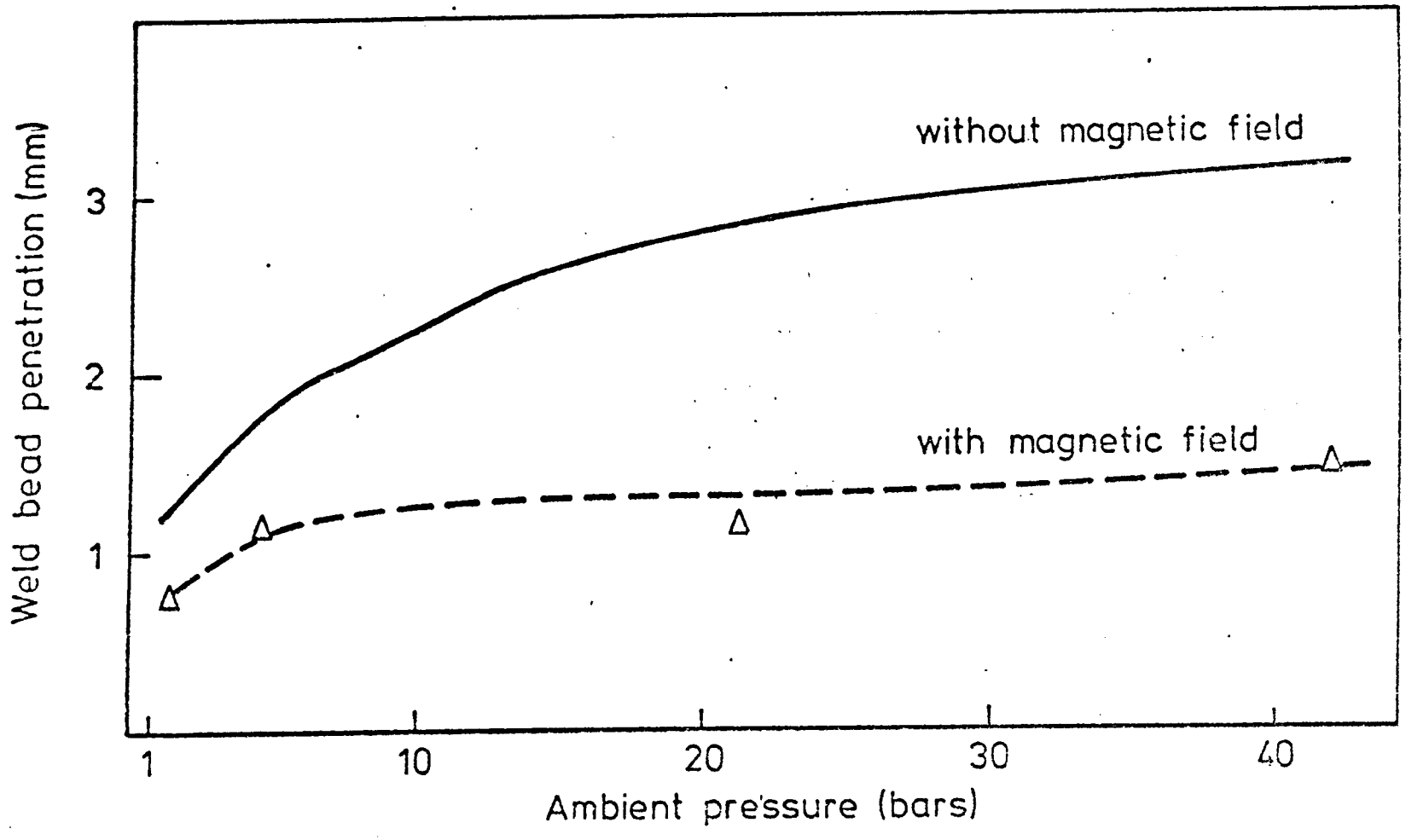

FIGURE 106. INFLUENCE OF MAGNETIC FIELD ON WELD BEAD PENETRATION FOR A 2 mm, 100 AMP ARGON TIG ARC.

4.4.2. Weld Bead Width

Weld bead width is not as strongly influenced by pressure as penetration. There is an indication that bead widths may even initially decrease (over the range 1 - 10 bars) particularly at high currents (see figure 107). Above 20 bars weld bead width is only slightly dependent on pressure for currents of 75 and 100 Amps but a significant pressure dependence exists at 150 Amps. This is associated with the onset of the bead instabilities reported in section 4.3.1. The strongest influence on bead width is due to arc current. This causes an increase in width at every pressure (see figure 107). Gas flow has only a small effect on bead width (see table 9). There is a slight tendency for the narrowest beads to result when no gas flow is applied. Bead width is also substantially unaffected by the application of a magnetic field although a slight increase is found at low pressures (see figure 109).

Arc length exerts a complicated influence on bead width as may be seen from figure 108. Bead width increases marginally with arc lengths at very low pressures (1 to 4.4 bars). For higher pressures the width sometimes decreased with arc length after an initial increase.

4.4.3. Weld Bead Aspect Ratio (Width/Depth)

It is convenient to express the pressure dependence of weld bead geometry in terms of the width (W) to depth (D) ratio. The pressure dependence of W/D for different current and arc lengths is shown in figures 110 and 111. Under normal atmospheric conditions W/D is generally between 3 and 5 for a 100 Amp arc depending on arc length. This ratio decreases with decreasing arc length indicating the existence of more hemispherical-like pools at low arc lengths. The initial change with pressure is sharp. This mirrors the separate behaviour of W and D already reported. It appears that for long arcs W/D may experience an increase between 8 and 15 bars before decreasing at higher pressures (see figure 110). This behaviour is associated with increasing bead width with pressure (see figure 108). At very high pressures W/D is substantially independent of arc length and then takes a value close to two (unless weld pool instabilities, exist in which case considerable pool broadening may occur). At one bar the influence of increasing

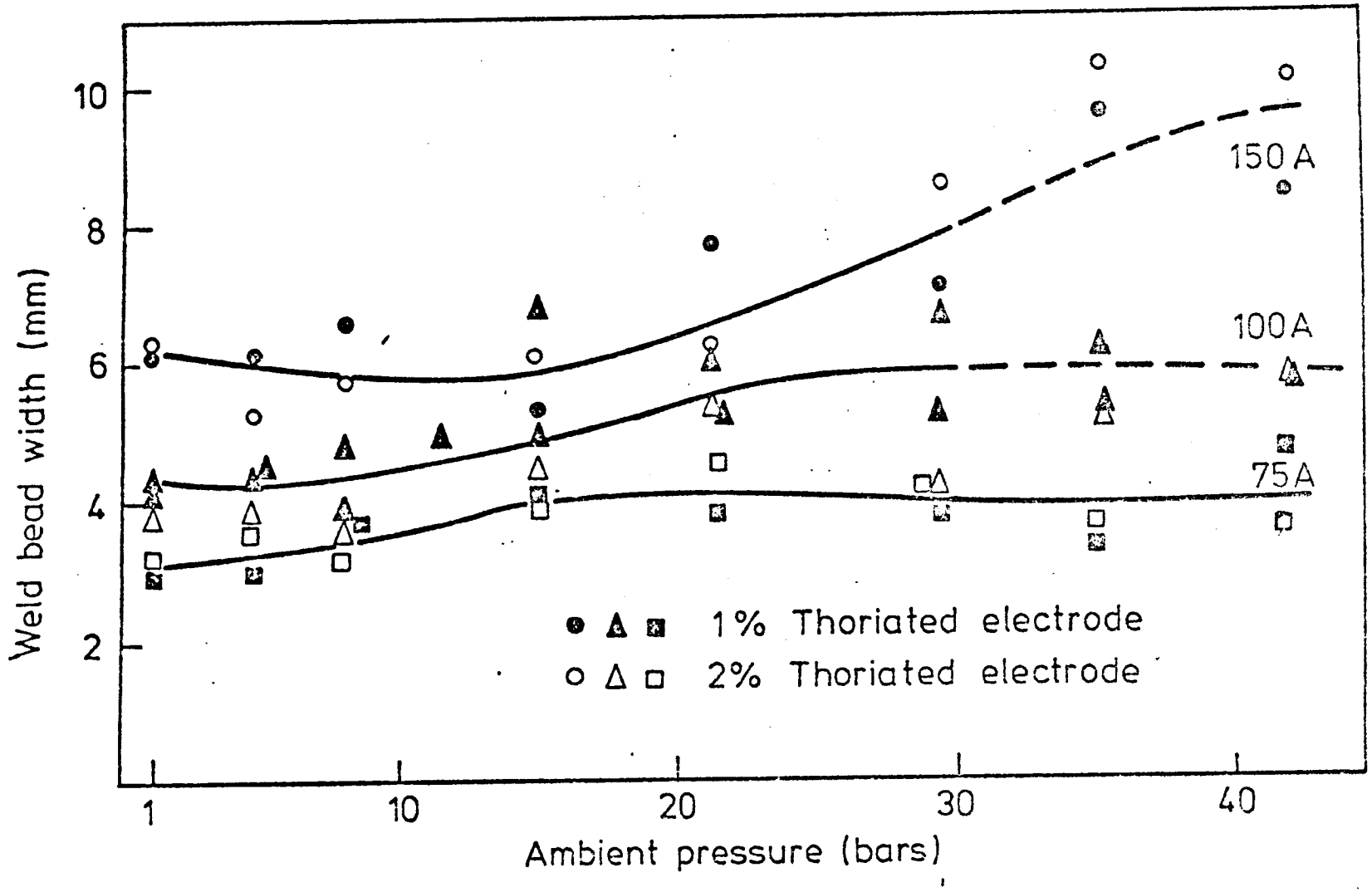

FIGURE 107. INFLUENCE OF PRESSURE AND CURRENT ON WELD BEAD WIDTH FOR A 2mm ARGON TIG ARC.

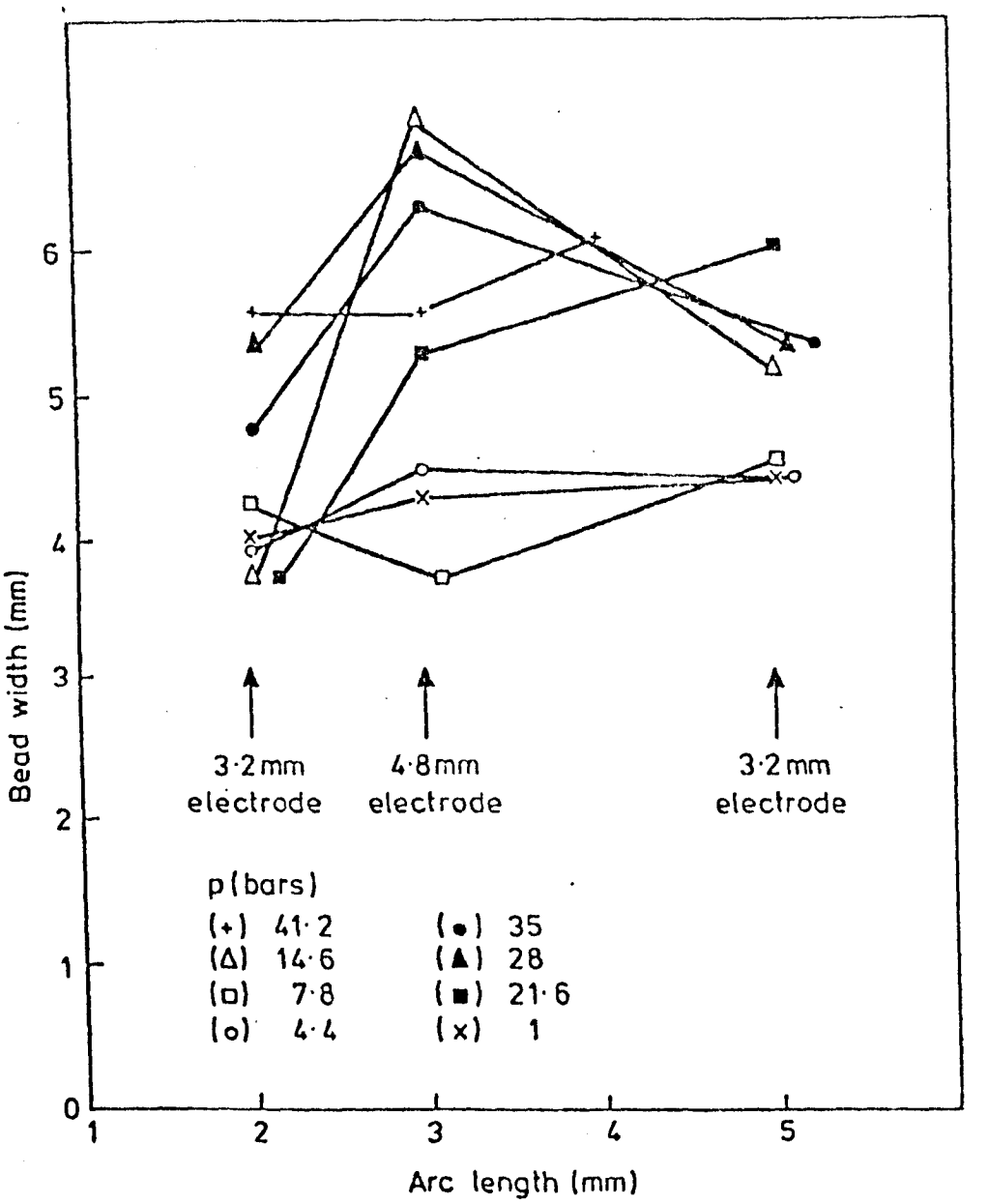

FIGURE 108. INFLUENCE OF ARC LENGTH ON WELD BEAD WIDTH FOR A 100 AMP ARGON TIG ARC.

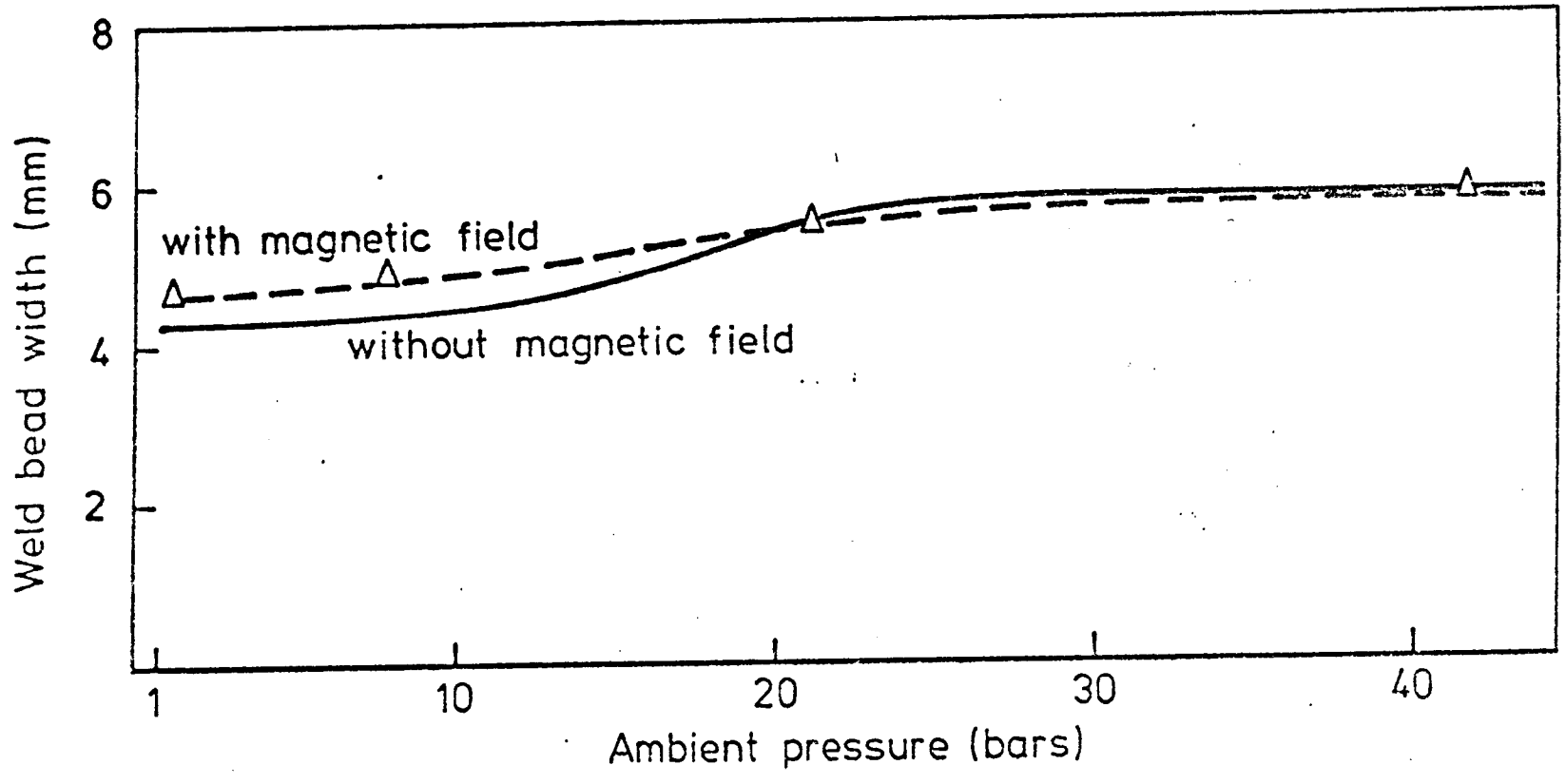

FIGURE 109. INFLUENCE OF PRESSURE AND MAGNETIC FIELD ON WELD BEAD WIDTH FOR A 100 AMP, 2 mm ARGON TIG ARC.

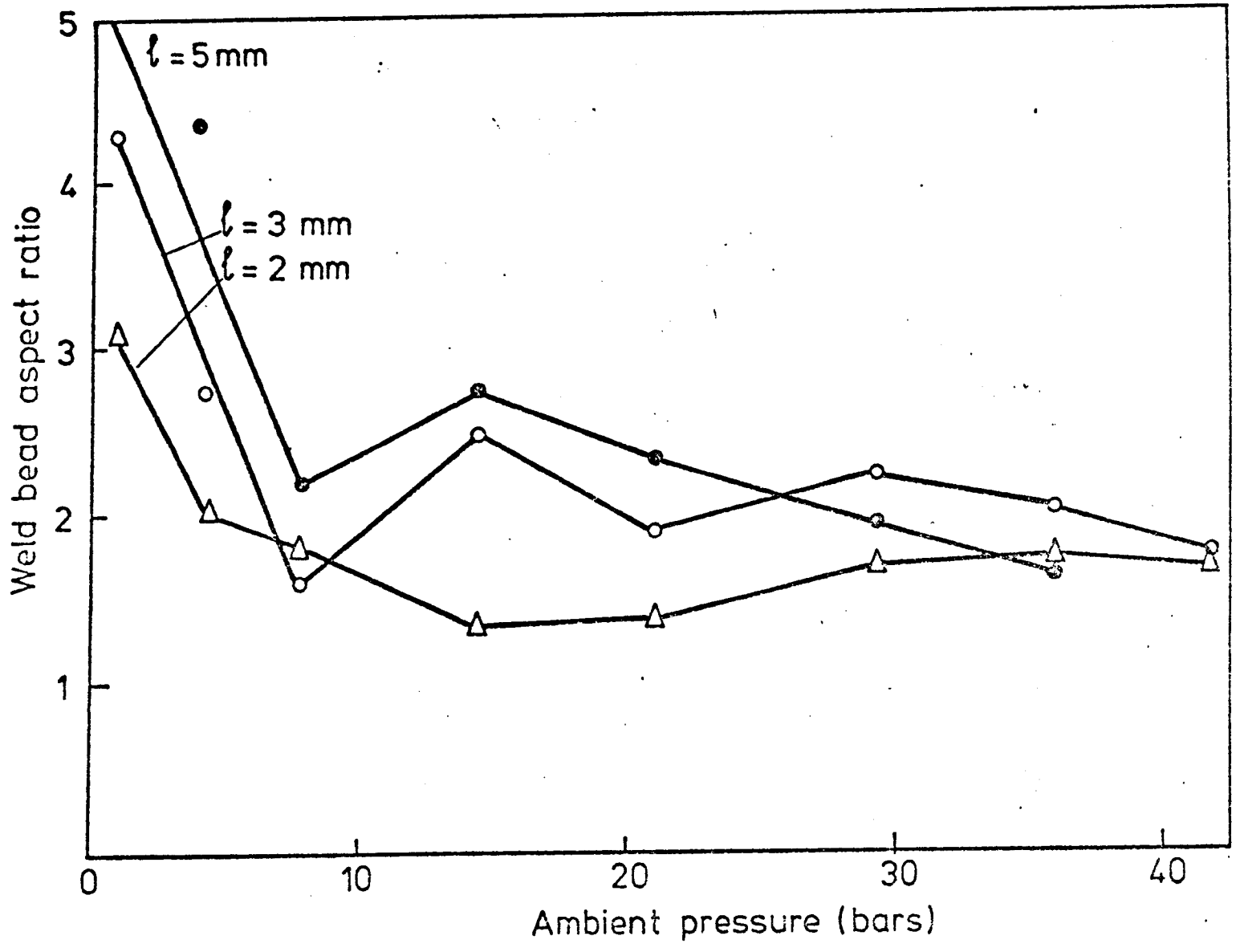

FIGURE 110. INFLUENCE OF PRESSURE AND ARC LENGTH (ℓ) ON WELD BEAD ASPECT RATIO (WIDTH / DEPTH) FOR THE 100 AMP ARGON TIG ARC.

current is generally to decrease W/D (figure 111). This behaviour becomes less pronounced with increasing pressure.

The aspect ratio with a magnetic field at one bar, 100 Amps and 2mm is 6 (figure 111). This is twice the value without a field. Under these conditions W/D falls quickly over the first few bars thereafter changing little up to 42 bars. W/D is then about 4 at 42 bars i.e. about twice that without a field.

4.4.4. Weld Bead Area (Cross Sectional)

Weld bead area is markedly affected by both pressure and arc current (see figure 112). At low currents (75A) the fusion area increases by a factor of 3 over the first 20 bars thereafter changing little. Indeed, the fusion effect of a high pressure 100 Amp arc is very similar to that of the atmospheric 150 Amp arc (see figure 112). Saturation behaviour is not strictly observed for currents of 100A or 150A within the pressure range investigated. These currents produce increases in fusion area by factors of 4 and 3 respectively over the range 1-42 bars.

The application of a magnetic field significantly reduces the fusion area at high pressures (figure 114). Under normal atmospheric conditions this effect is less marked than at higher pressures where a 50% reduction in melted volume may be produced by applying a field. It can be seen from figure 115 that arc length exerts only a weak influence on weld bead area over the range 2-5mm. At low pressures slight decreases are observed with increasing arc length. At high pressures an initial increase may be followed by a decrease. However, this behaviour is within the range of reproducibility and cannot be reliably interpreted as a trend.

A few experiments with shielding gas flows have been performed at 42 bars. These show that the fusion area may initially increase with gas flow (see table 9). This effect is less pronounced when a magnetic field is also applied.

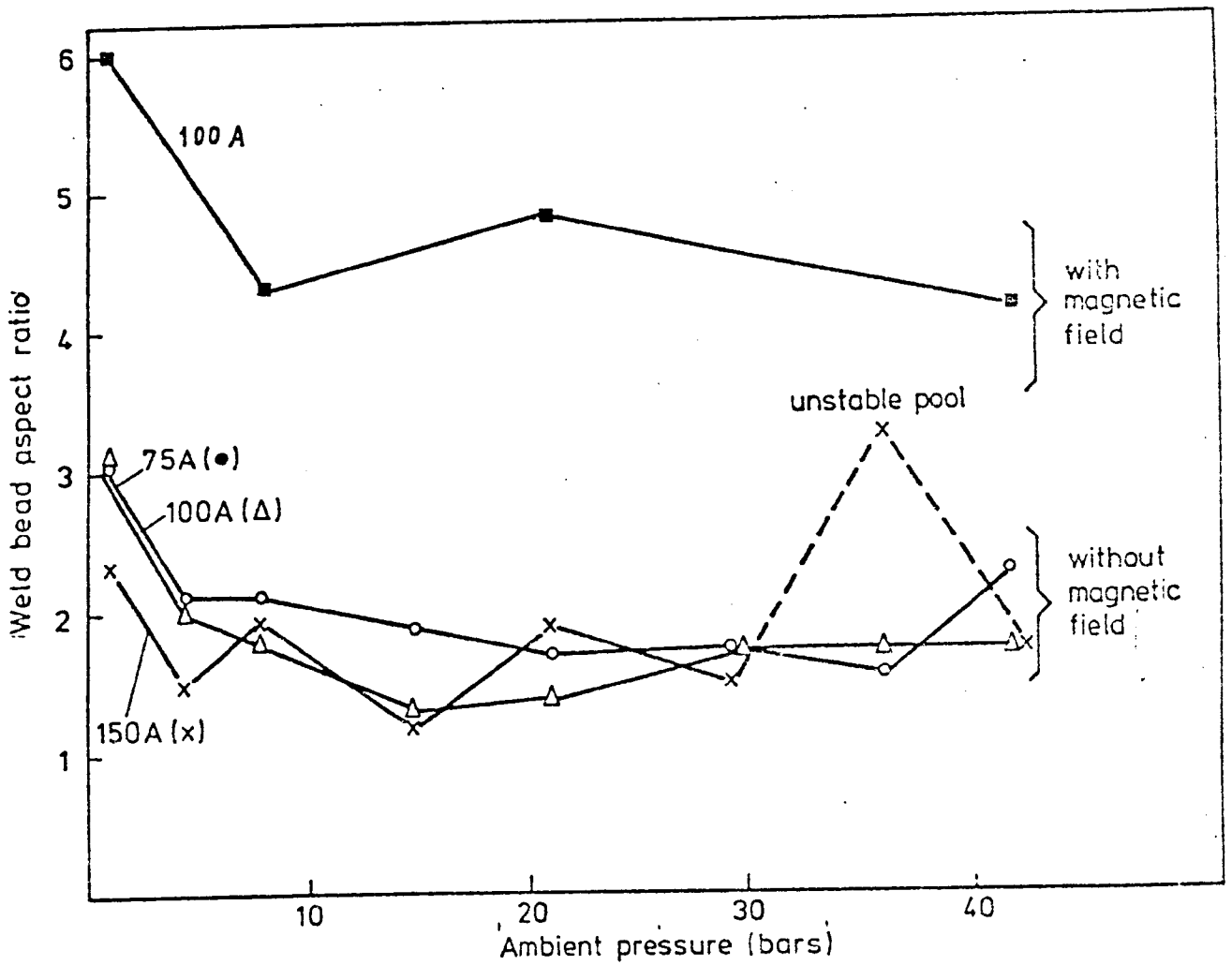

FIGURE 111. INFLUENCE OF PRESSURE ARC CURRENT AND MAGNETIC FIELD ON THE WELD BEAD ASPECT RATIO FOR A 2mm ARGON TIG ARC (1% Thoriated Tungsten electrode)

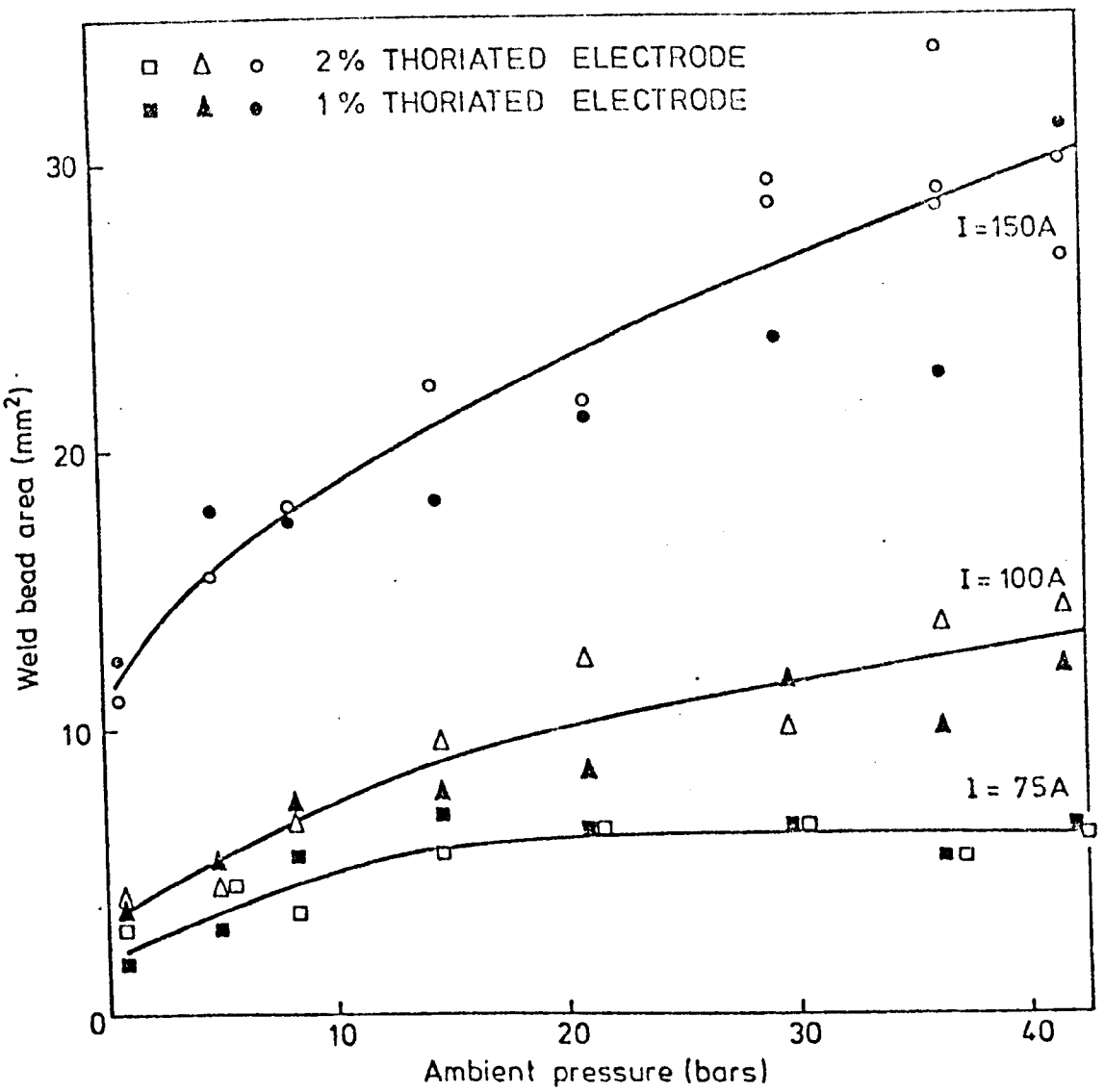

FIGURE 112. WELD BEAD AREA FOR A 2 mm ARGON TIG ARC.

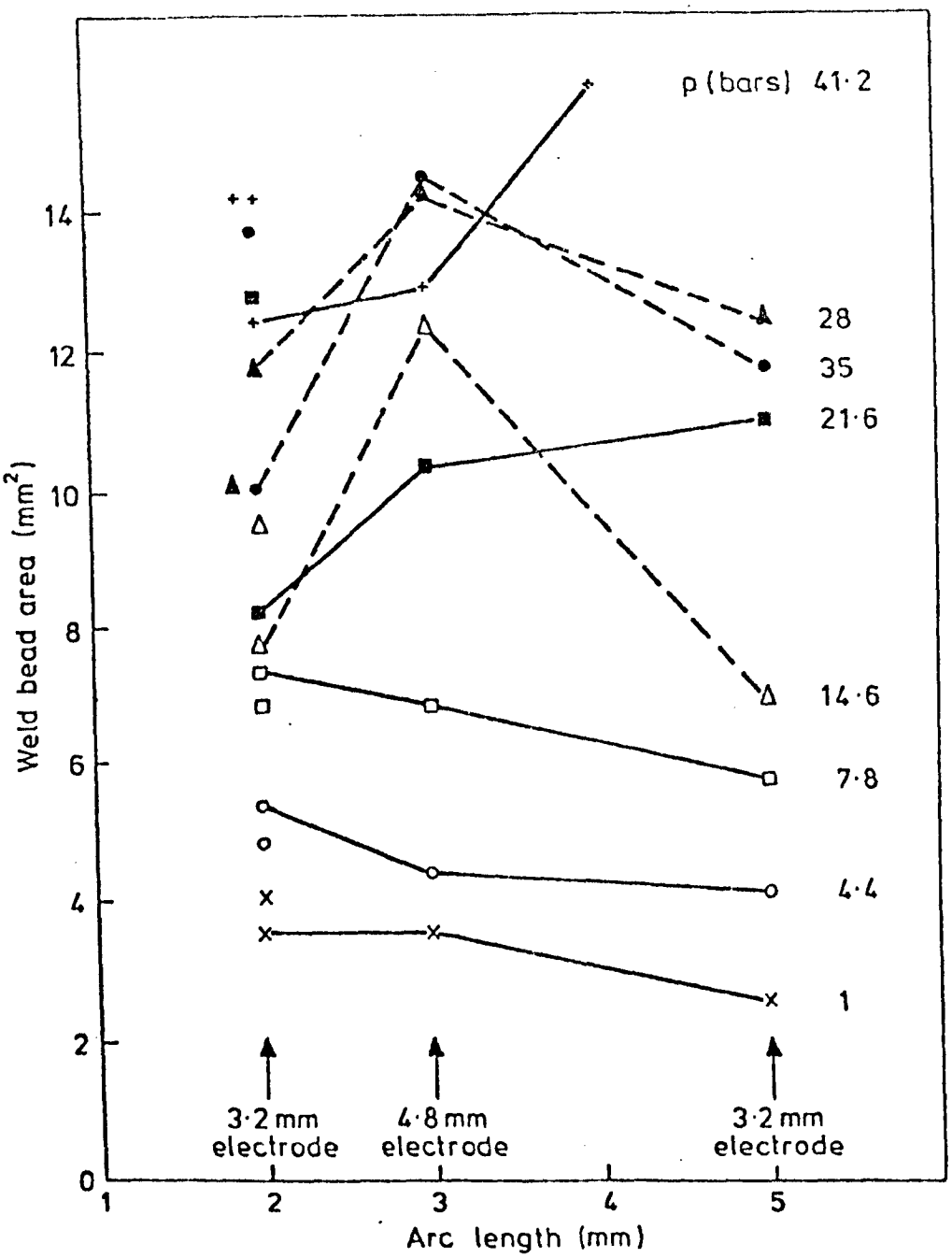

FIGURE 113. INFLUENCE OF ARC LENGTH ON WELD BEAD FUSION AREA FOR A 100 AMP ARGON TIG ARC.

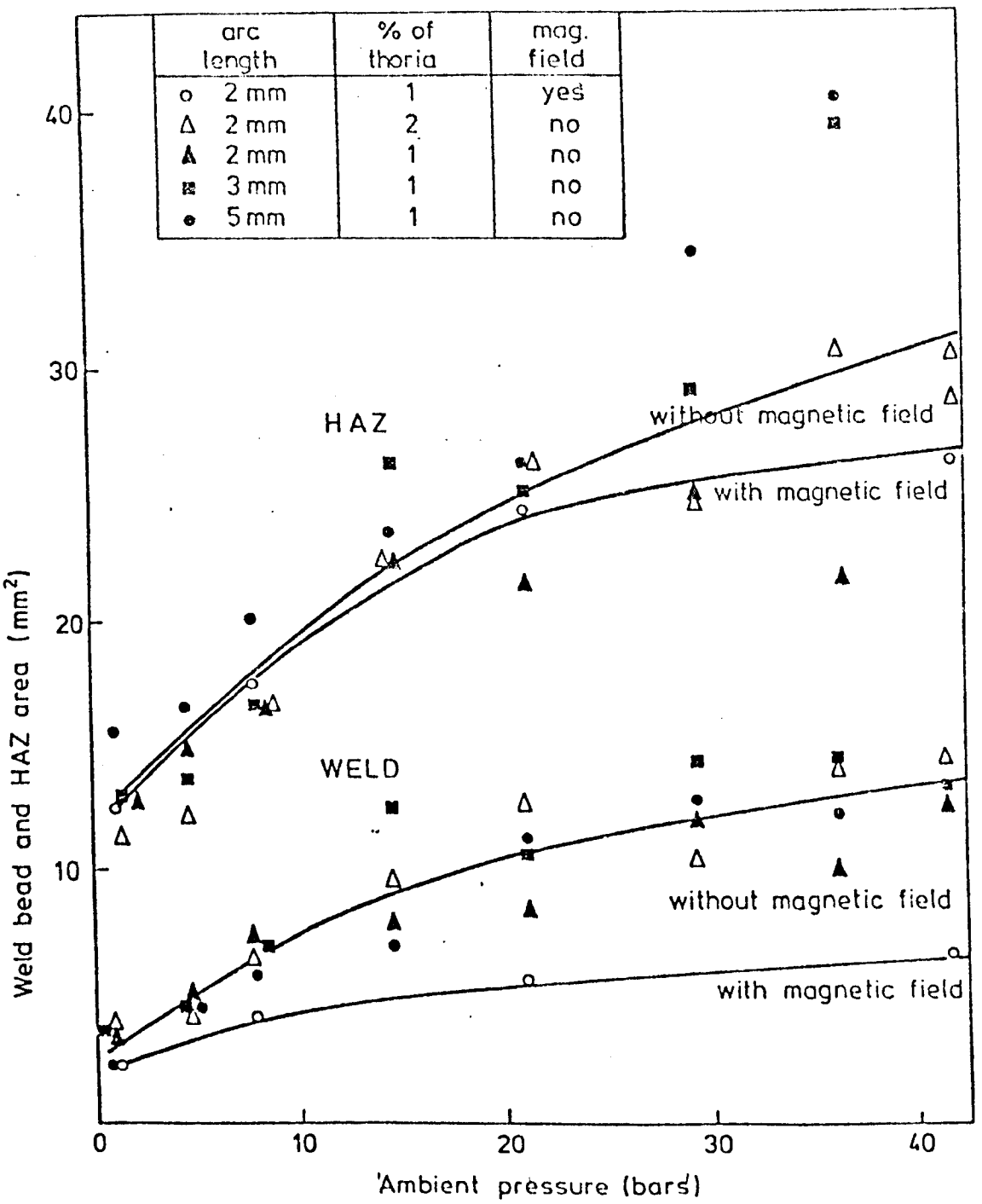

FIGURE 114. INFLUENCE OF PRESSURE, ARC LENGTH AND MAGNETIC FIELD ON WELD BEAD AND HAZ AREAS FOR A 100 AMP ARGON TIG ARC.

4.5. Argon TIG Arc HAZ Geometry

4.5.1. HAZ Penetration

HAZ penetration is strongly influenced by pressure and arc current (see figure 115). The pressure dependence is particularly strong over the first 20 bars. Thereafter saturation (or a slow increase) is observed to occur at the lower currents examined (i.e. 75A and 100 Amps). Arc length has only a slight effect on penetration (figure 116) at pressures below about 30 bars. Above this pressure there is a tendency for penetration to increase with arc length. Gas flow also has little influence on HAZ penetration (table 9). This result also applies to magnetically controlled arcs. Magnetic field was found to have a significant effect on fusion area. However, HAZ penetration suffers only a slight reduction (see table 9).

4.5.2. HAZ Width

The influence of pressure on HAZ width is very much dependent on the welding current adopted (figure 117). At the lowest current (75A) only a small increase (but a significant percentage increase) was found over the pressure range 1-42 bars. At higher currents HAZ width initially decreases with increasing pressure before increasing above about 10 bars (for 150 Amp arcs). This increases by nearly a factor of 2 between 8 and 42 bars. Arc length has the effect of increasing HAZ diameter (118). Magnetic field also has a similar effect although this is slight. No significant influence of gas flow is observed (see table 9).

4.5.3. HAZ Aspect Ratio

The influence of current, arc length and pressure on HAZ aspect ratios is shown in figures 119 and 120. The aspect ratio at 1 bar and 100 Amps is about 3 for all arc lengths investigated. This figure generally decreases with pressure to a value near 2 at 42 bars. It can also be seen from these figures that aspect ratios tend to increase with increasing arc length and decreasing current although the influence of these variables becomes less pronounced with increasing pressure. The application of a magnetic field produces less semi-circular HAZ cross-sections than obtained without the field. At one bar similar aspect

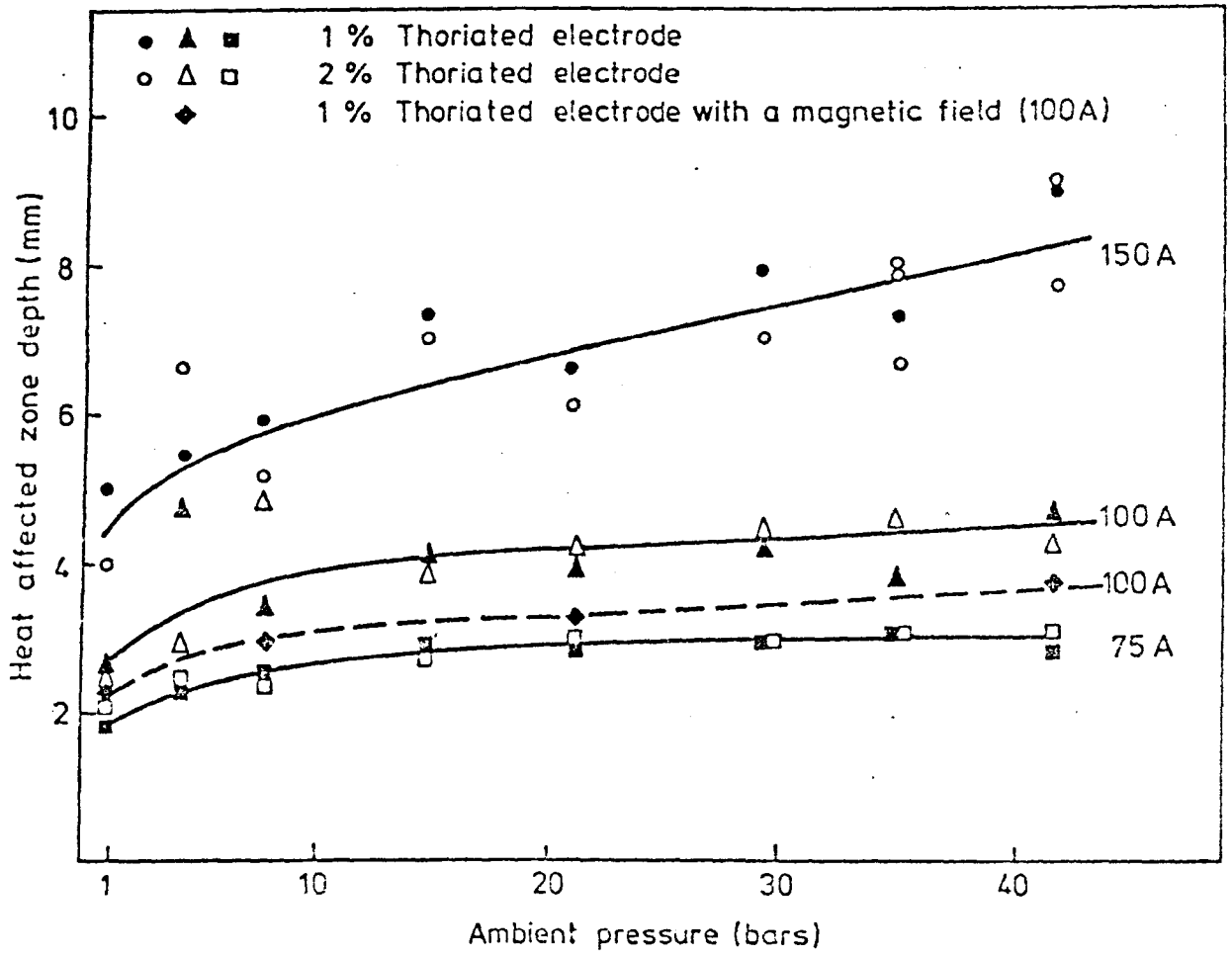

FIGURE 115. INFLUENCE OF PRESSURE AND ARC CURRENT ON HEAT AFFECTED ZONE DEPTH FOR A 2 mm ARGON TIG ARC

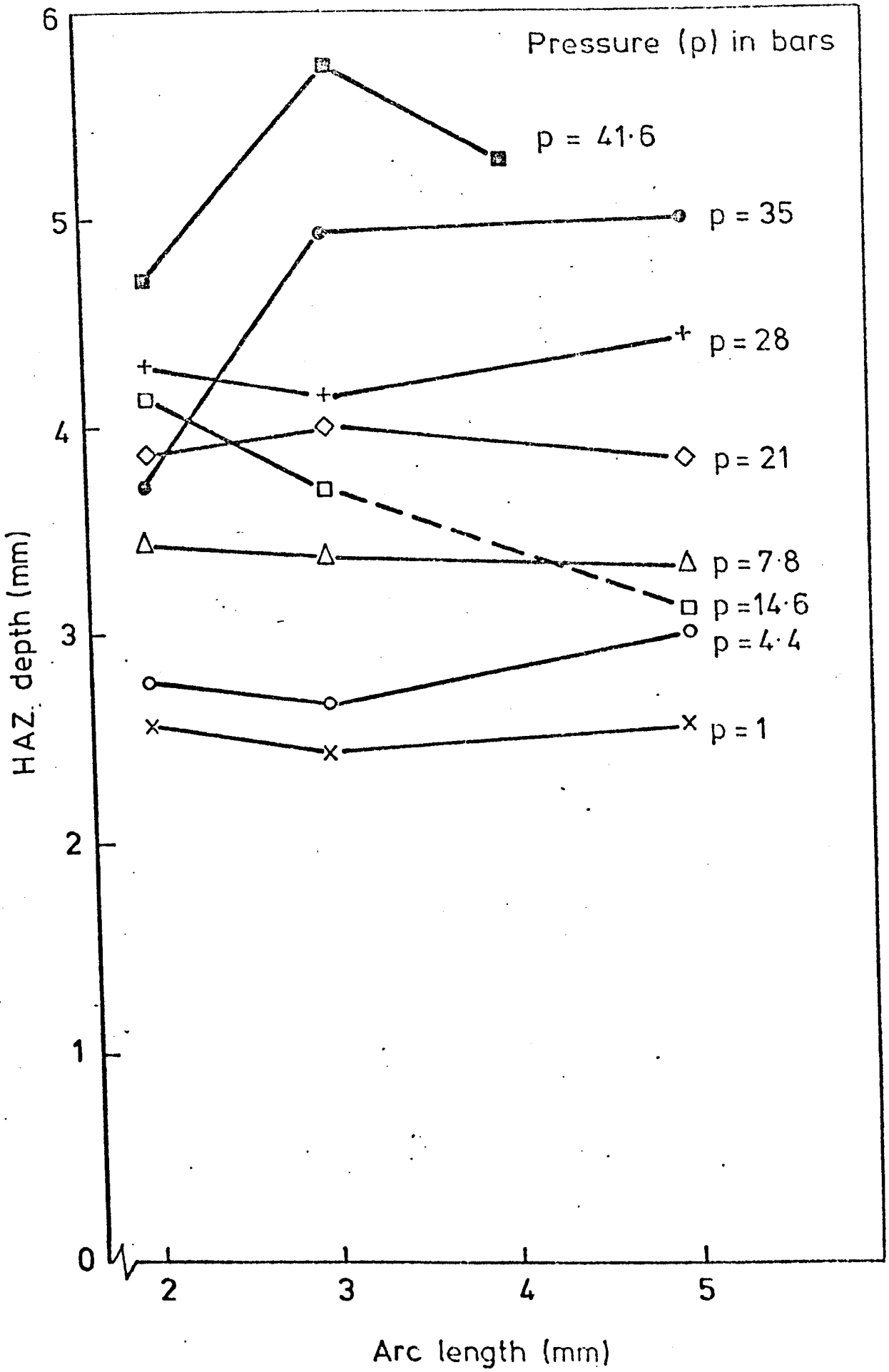

FIGURE 116. INFLUENCE OF ARC LENGTH ON HAZ PENETRATION FOR A 100 AMP ARGON TIG ARC.

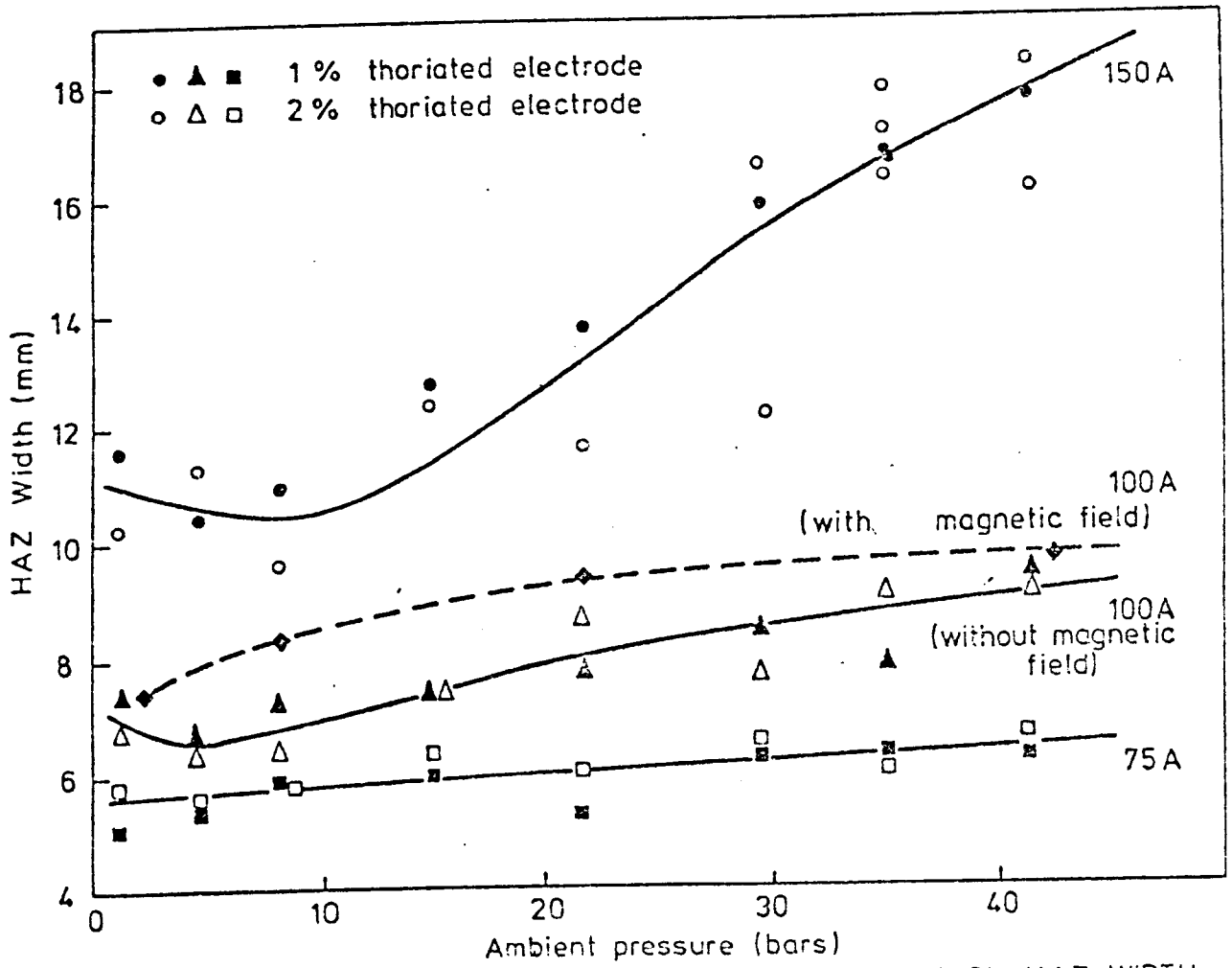

FIGURE 117. INFLUENCE OF AMBIENT PRESSURE AND ARC CURRENT ON HAZ WIDTH FOR 2 mm ARGON TIG ARC.

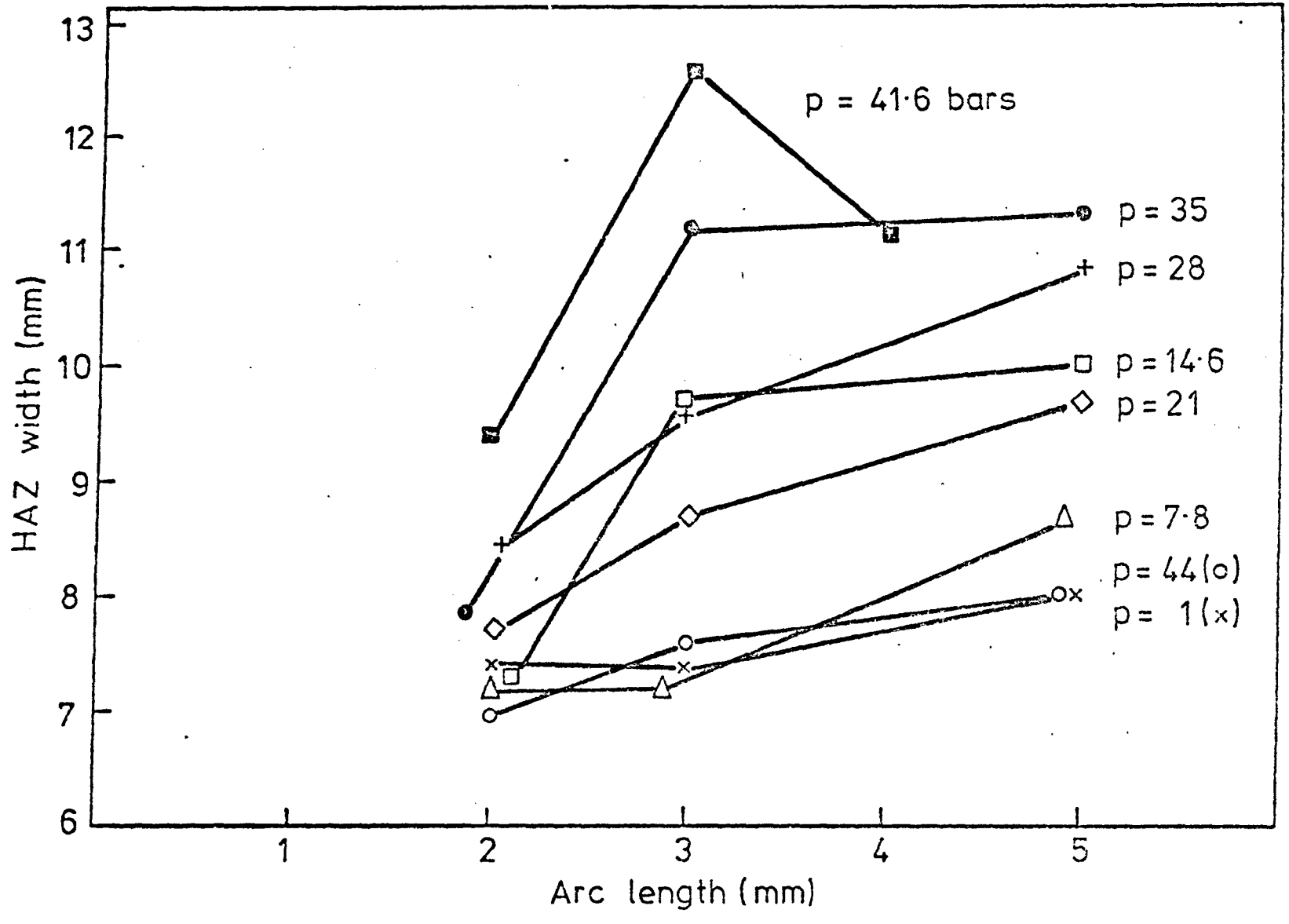

FIGURE 118. INFLUENCE OF ARC LENGTH AND PRESSURE ON HAZ WIDTH FOR A 100 AMP ARGON TIG ARC.

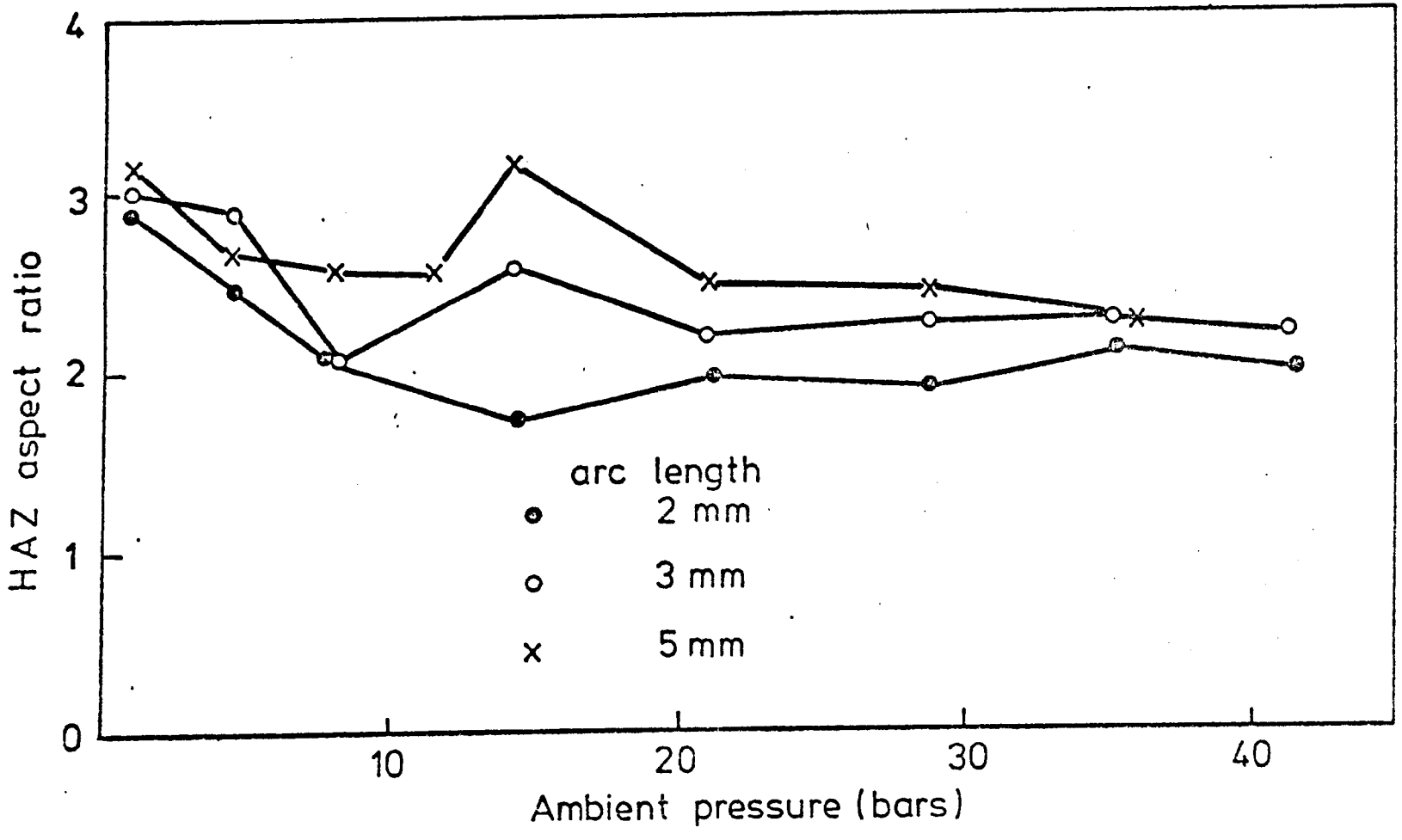

FIGURE 119 INFLUENCE OF AMBIENT PRESSURE AND ARC LENGTH ON HAZ ASPECT RATIO FOR A 100 AMP ARGON TIG ARC (1% Thoriated electrode)

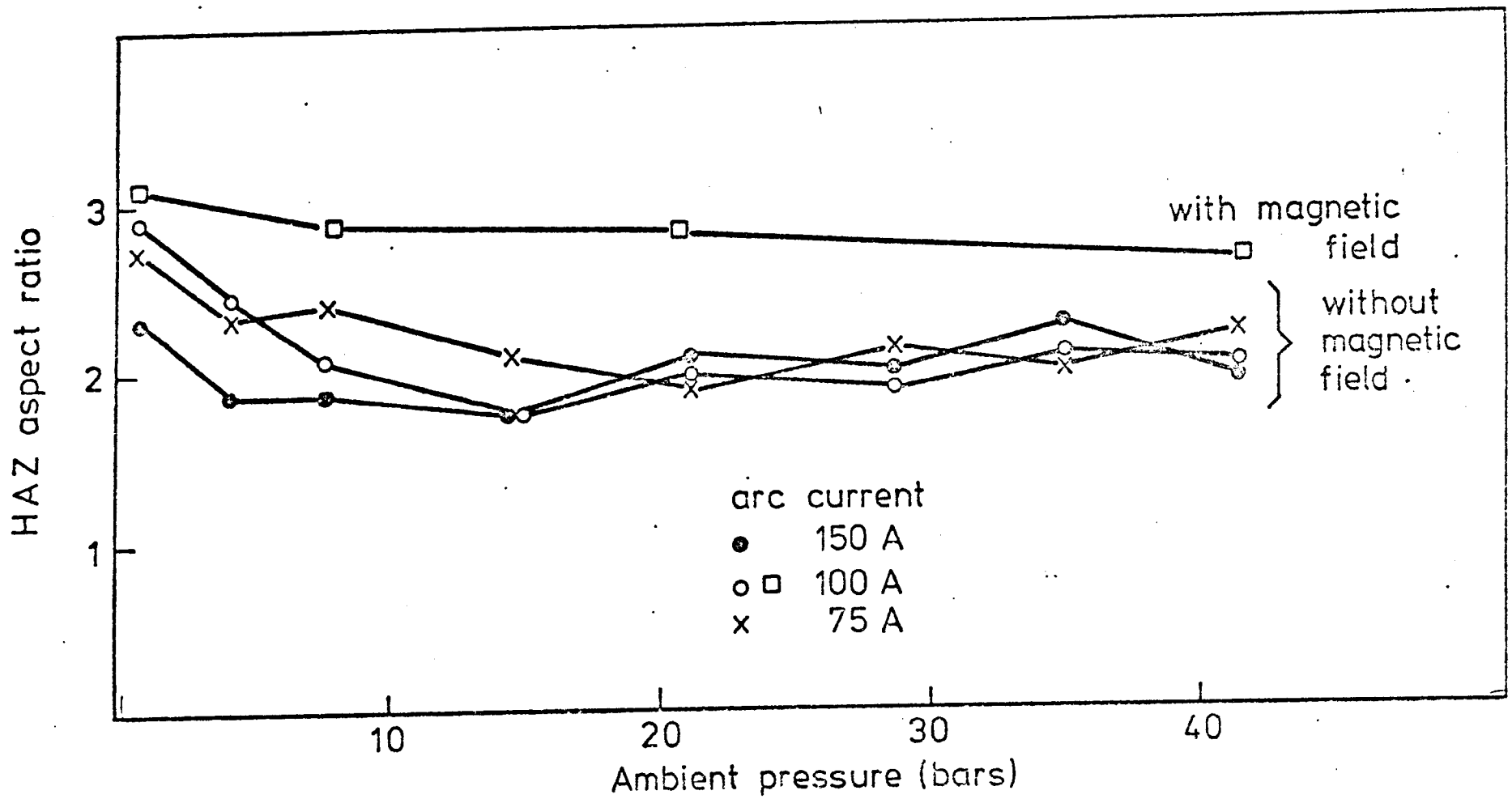

FIGURE 120. INFLUENCE OF AMBIENT PRESSURE AND ARC CURRENT ON HAZ ASPECT RATIO FOR A 2mm ARGON TIG ARC.

ratios (i.e. $\sim$3) are found with and without a field. However, at 42 bars the respective values are 2.6 and 2. The aspect ratio's of magnetically stirred pools are little influenced by pressure and generally have a value near the none stirred atmospheric value (figure 120).

4.5.4. HAZ Area (Cross Sectional)

HAZ area is strongly pressure dependent (figure 121). For 150 Amp arcs this increases by a factor of more than three over the pressure range investigated. At lower currents the corresponding rise is nearer a factor of 2 than 3. There is a trend, particularly at high pressure, for the HAZ area to increase with arc length. This is associated with HAZ broadening and not an increase in penetration (see section 4.5.2). Measurements made with magnetically controlled arcs give results that are not significantly different from those obtained for the corresponding none magnetically controlled arcs (see figure 114).

4.6. Relationships Between HAZ and Weld Pool Geometry for Argon TIG Arcs

It can be seen from figures 103 and 115 that HAZ and weld bead depth behave in a similar manner with increasing pressure. In both cases the initial dependence is strong followed by saturation at the lower currents. There is, however, a tendency for HAZ depth at I=150A to continue increasing after weld bead penetration has reached saturation. Weld bead and HAZ widths also behave in a similar manner. Both exhibit an initial tendency to decrease (particularly at I=150A) before increasing at pressures above about 10 bars. Areas enclosed by the respective isotherms also increase in a similar manner with pressure. In both cases the continued increase in area above about 20 bars is attributed to an increase in the width of the respective zones with pressure. The most significant difference between the behaviour of fusion and HAZ shapes is observed when a magnetic field is applied. Weld bead depth and area decrease quite markedly on the application of a field. No such effects are found on the corresponding HAZ dimensions. This result has many important implications for weldment heat transfer theories.

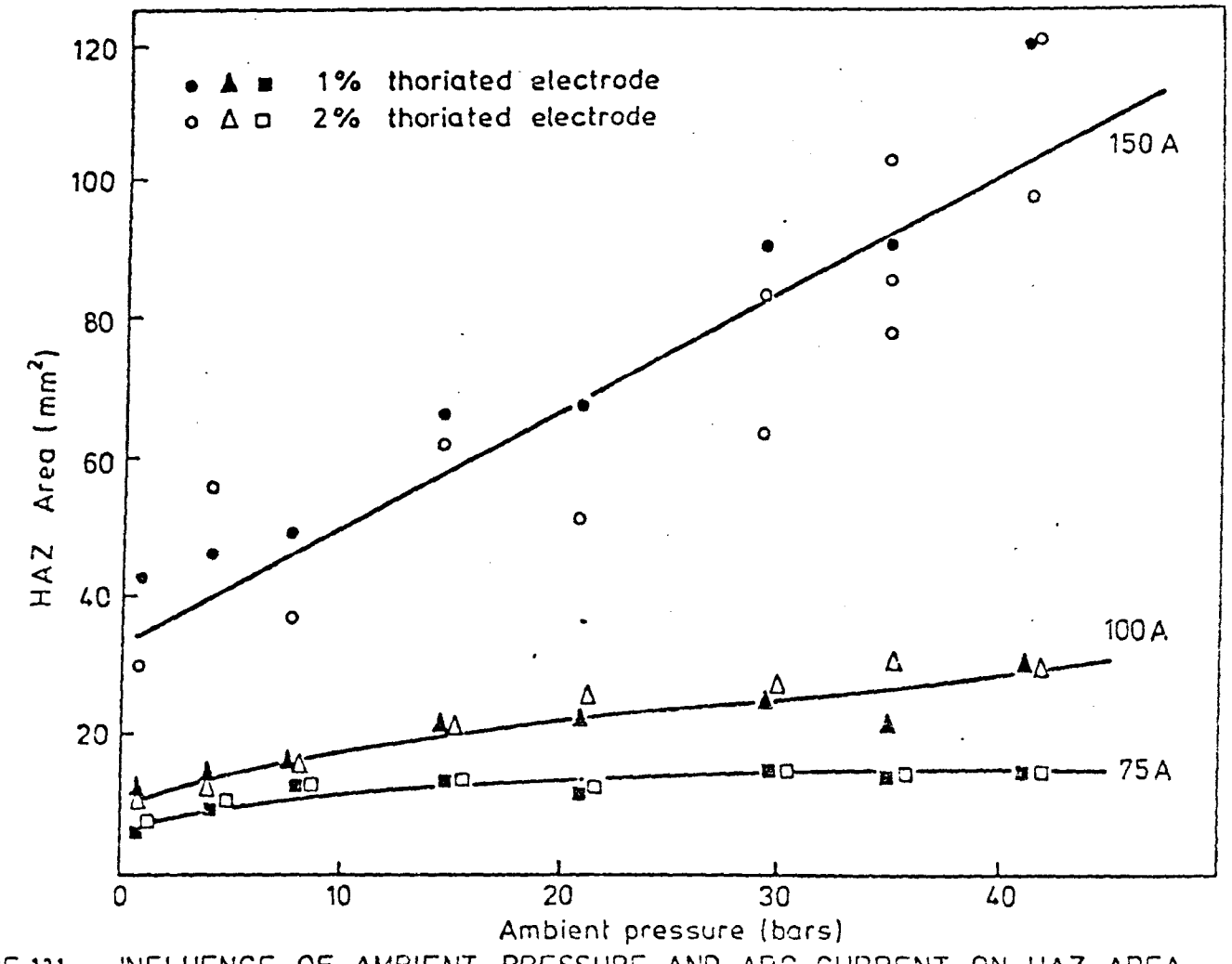

FIGURE 121. INFLUENCE OF AMBIENT PRESSURE AND ARC CURRENT ON HAZ AREA FOR A 2 mm ARGON TIG ARC.

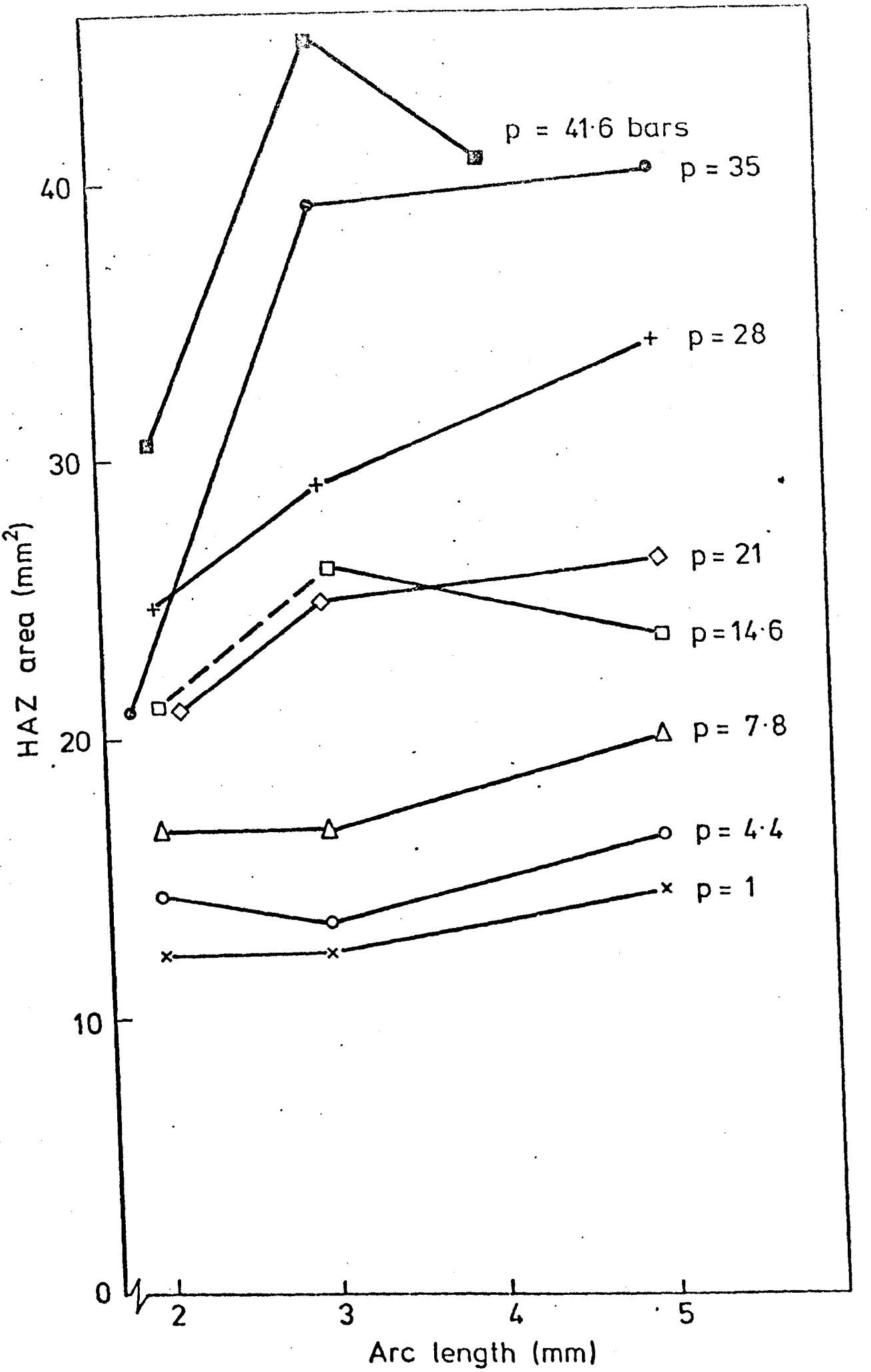

FIGURE 122. INFLUENCE OF ARC LENGTH ON HAZ AREA FOR A 100 AMP ARGON TIG ARC.

HAZ and weld bead dimensions can be combined to give the mean temperature gradient between fusion and HAZ boundaries. Results are shown in figures 123 and 124 where calculations are based on

$$\text{Temp. gradient} \equiv \frac{\Delta T}{\Delta \ell} \simeq \frac{750}{\Delta \ell} \quad (^{o}C/mm) \tag{97}$$

ΔT in equation 97 is the difference between temperatues at the fusion line and outer HAZ boundary. $\Delta \ell$ is the distance between these isotherms and has been found from surface and depth measurements. It can be seen that depth gradients are less than surface gradients. The difference between these measurements generally decreases with increasing current. Both gradients are only weakly influenced by pressure although there is a tendency to decrease slowly with pressure at high currents. Measurements for arc lengths of 2 and 5mm's show a similar dependence on pressure but significantly lower gradients exist for the longer arc length (figure 125). The most important variable influencing temperature gradients is arc current. It is found that the gradient increases by a factor of 2 when current is halved (reduced from 150A to 75A) at 1 bar. The corresponding factor is about 3 at 42 bars. The application of a magnetic field has the effect of reducing the depth gradient although the surface gradient is little affected.

4.7. Melting Efficiency for Argon TIG Arcs

Weld bead size is affected by many variables. These not only include plate characteristics but also arc characteristics and the relative motion of arc and plate. It is convenient to combine these parameters so as to define a melting efficiency (or ratio), Z. This is defined as the percentage or fraction of the total process power that is required to just melt the volume of weld metal produced per second. Z has been discussed in section 2 (see equation 33) but it is instructive to state this more explicitly here.

$$\text{i.e.} \quad Z = \frac{\rho . v . A.}{IV} \left(L_F + \int_{T_P}^{T_M} C_p . \, dT \right) \times 100\% \tag{98}$$

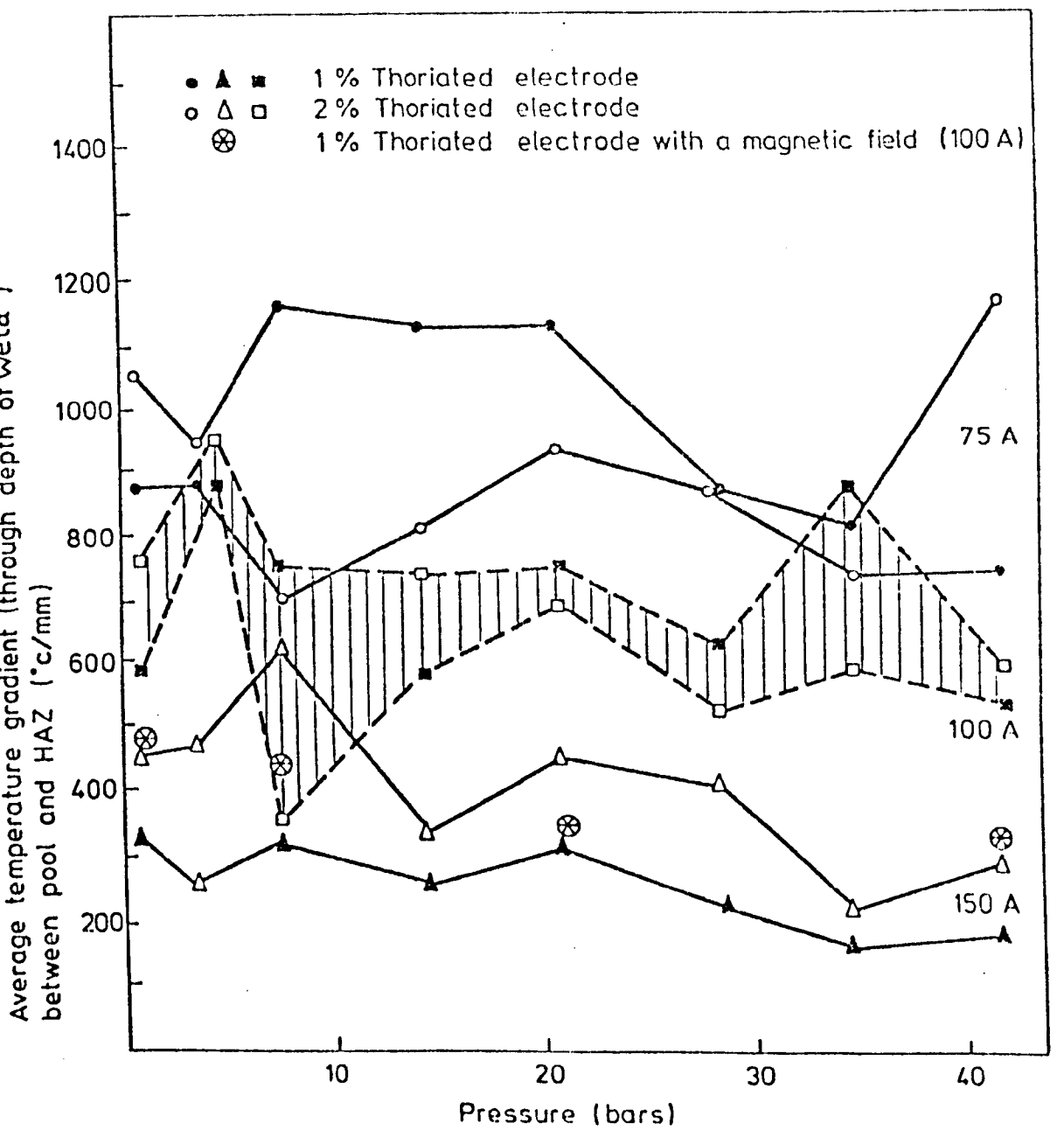

FIGURE 123. INFLUENCE OF PRESSURE AND ARC CURRENT ON THE AVERAGE TEMPERATURE GRADIENT THROUGH THE HAZ DEPTH FOR A 2 mm ARGON TIG ARC.

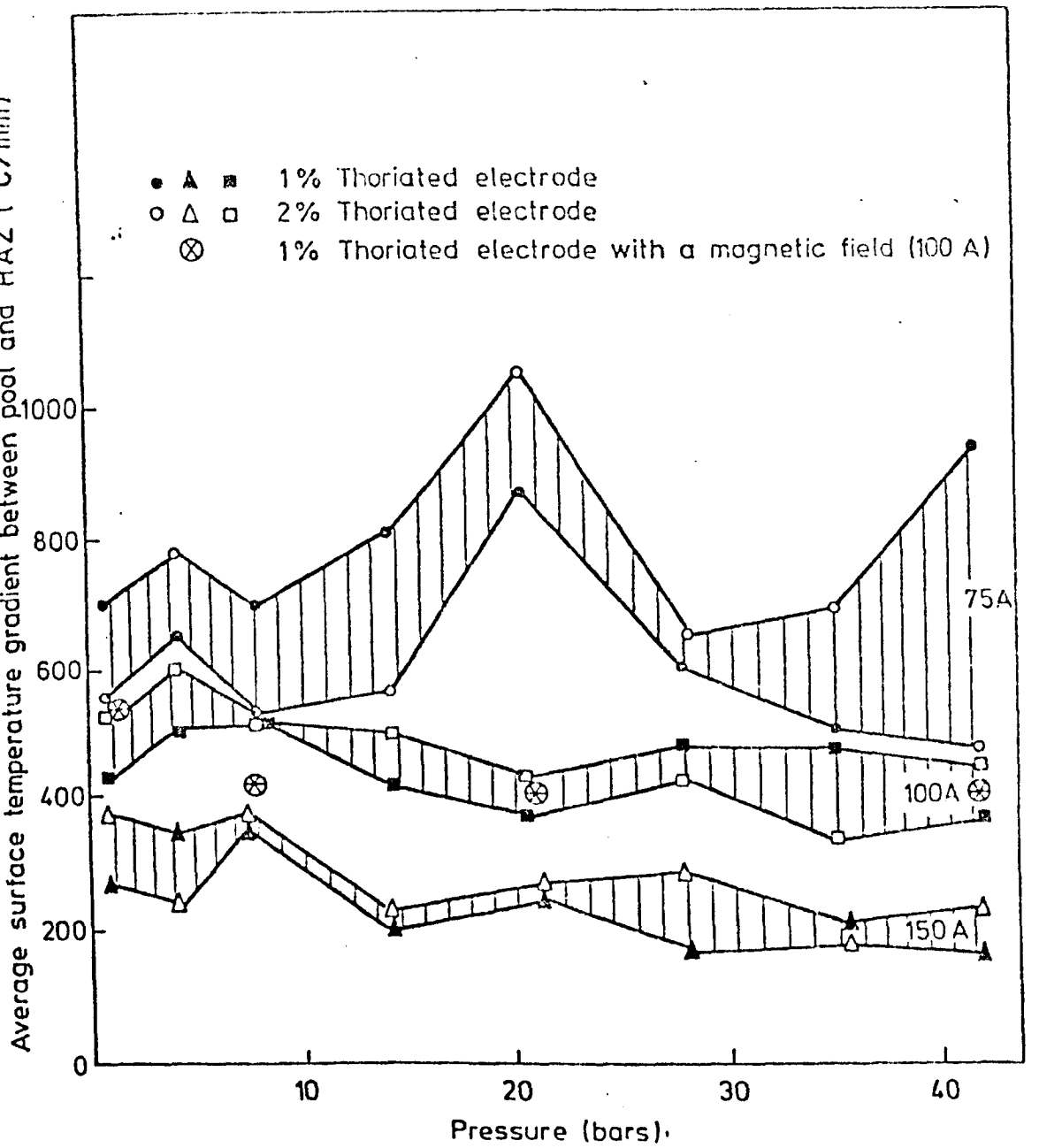

FIGURE 124. INFLUENCE OF PRESSURE AND ARC CURRENT ON THE AVERAGE TEMPERATURE GRADIENT ACCROSS THE PLATE SURFACE BETWEEN HAZ AND FUSION LINES FOR A 2mm ARGON TIG ARC.

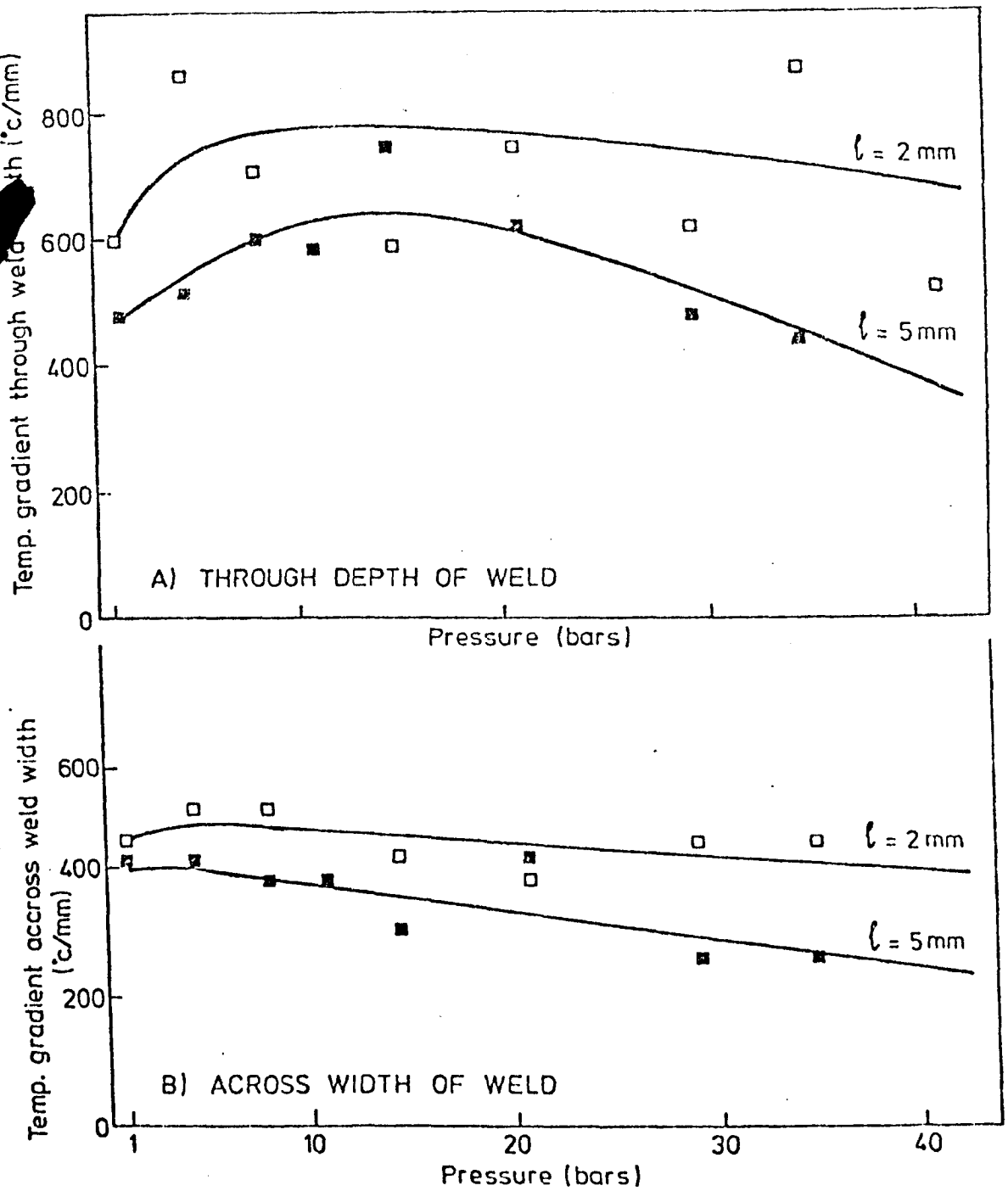

FIGURE 125. INFLUENCE OF PRESSURE AND ARC LENGTH ON THE AVERAGE TEMPERATURE GRADIENT BETWEEN THE FUSION AND HAZ ISOTHERMS (100 AMP ARGON TIG ARC)

where ρ is weld metal density (at plate temperature)

C_p is weld metal specific heat

L_F is the weld metal latent heat of fusion

T_M and T_p are melting and plate temperatures respectively

v is welding speed

A is bead cross sectional area

I and V are welding current and voltage respectively

Data (ref.159) suggest that

$$\rho \simeq 7.9 \times 10^3 \text{ kg/m}^3$$

and $$\left(L_F + \int_{T_p}^{T_M} C_p \, dT \right) \simeq 1.5 \text{ KW/kg}$$

Therefore equation 98 becomes

$$Z = 1.19 \frac{vA}{IV} \quad \% \tag{99}$$

Where I.V is in KW's, v in mm/s and A in mm^2. This expression has been used to calculate experimental melting efficiencies presented here. Melting efficiency is discussed in terms of the parameters listed below.

1) pressure
2) arc current
3) arc length
4) welding speed
5) gas flow
6) magnetic field
7) total process power
8) welding position (i.e. down hand or overhead)

The effect of each of these parameters on Z is calculated with all others being held constant.

4.7.1. Effect of Pressure on Z

The pressure dependence of Z is strongly influenced by welding current (see figure 126). At the lowest current examined Z initially increases with pressure before reaching a peak between 10 and 20 bars and then decreasing. At 100 Amps an initial increase with pressure is followed by saturation near 20 bars. For the largest current examined (150A) melting efficiency again initially increases before falling slowly with pressure. For the 100 Amp arc similar behaviour is also observed at different arc lengths (figure 127) and when a magnetic field is applied. However, melting efficiency is generally found at any pressure to decrease with decreasing current, increasing arc length or when a magnetic field is applied.

4.7.2. Effect of Process Power on Z

Melting efficiency measurements for a given current and arc length have also been plotted against total process power (see figure 128). This representation shows more clearly the tendency of Z to have a peak value (particularly at 75 Amps). The efficiency at any arc power decreases with increasing arc length (129). However, arcs with the same power but different currents (i.e. different arc lengths and/or pressure) can have similar melting efficiency. This last result can be found by superimposing figures 128 and 129. This result is shown in figure 130. Welds made without a magnetic field have efficiencies of roughly twice those made with a field (e.g. figures 131 and 127).

4.7.3. Effect of Arc Length on Z

At any pressure Z falls as arc length is increased (see figure 132). This effect is most marked at low pressures. At pressures above about 15 bars Z falls slowly with increasing arc length.

4.7.4. Effect of Arc Current on Z

Z increases with increasing arc current at any pressure. This effect is most pronounced at low pressures as may be seen from figure 126.

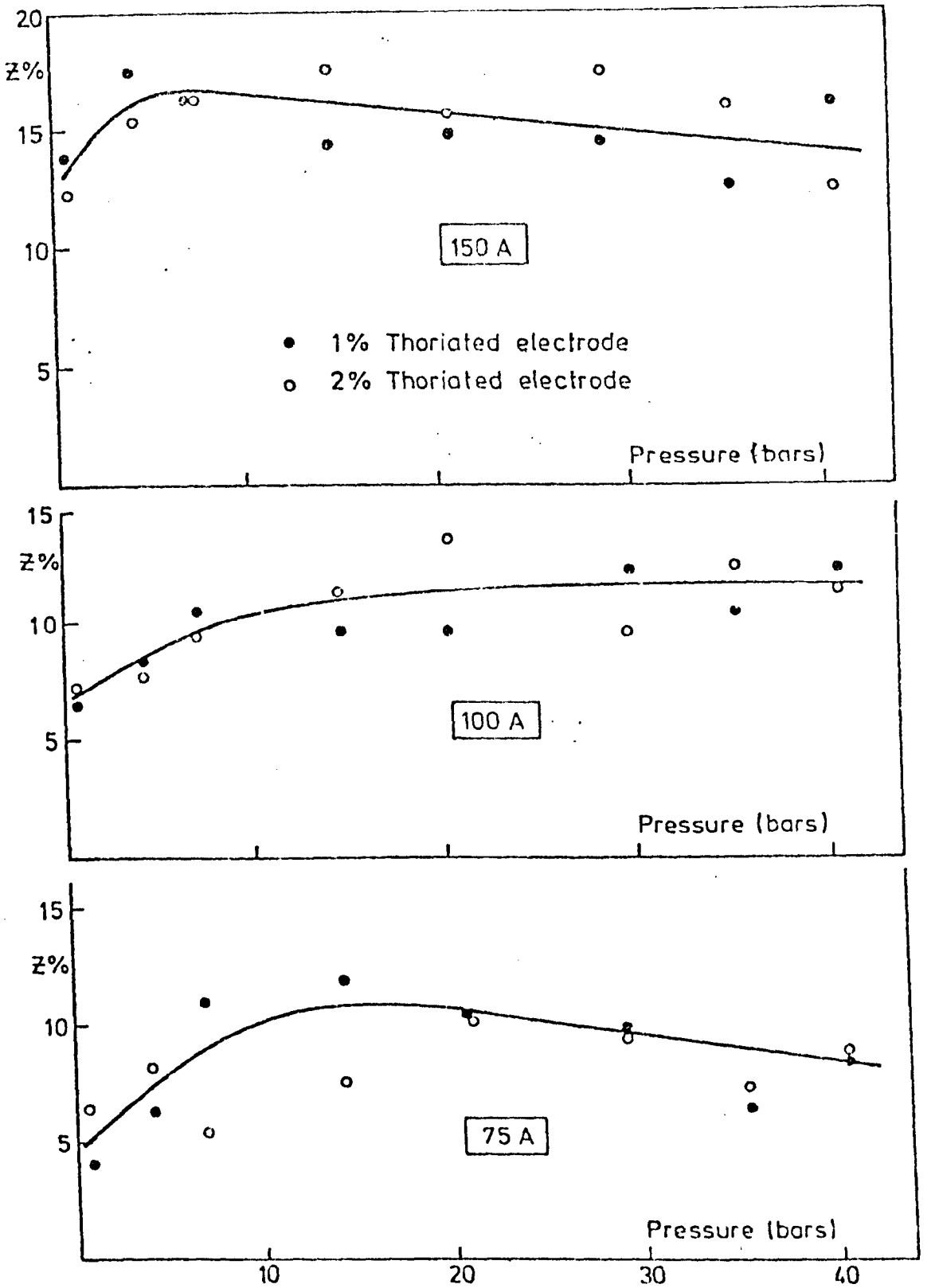

FIGURE 126. INFLUENCE OF PRESSURE ON WELD BEAD MELTING EFFICIENCY (Z) (2mm ARGON TIG ARC)

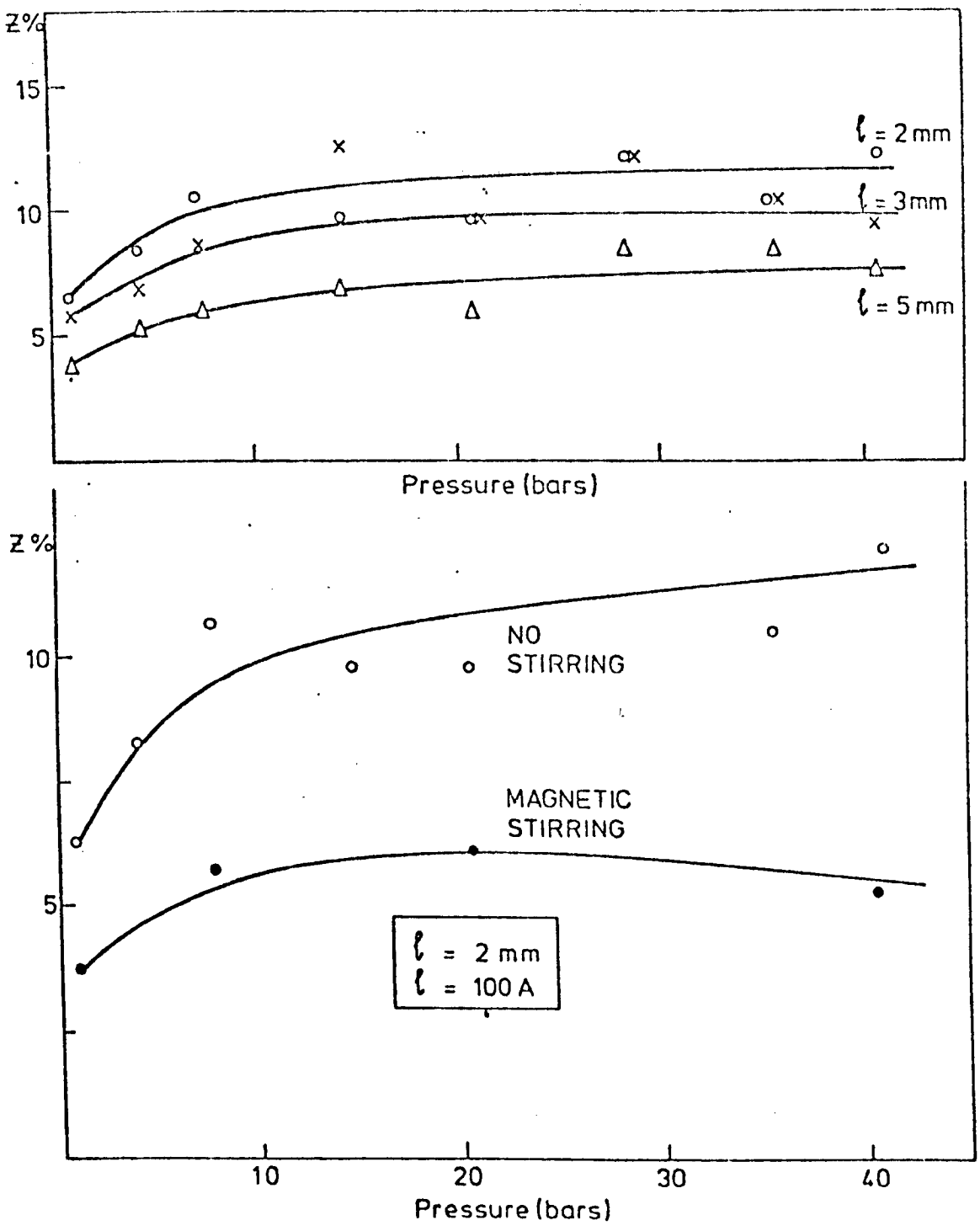

FIGURE 127. INFLUENCE OF ARC LENGTH AND MAGNETIC STIRRING ON MELTING EFFICIENCY (Z) (100 AMP, ARGON TIG ARC)

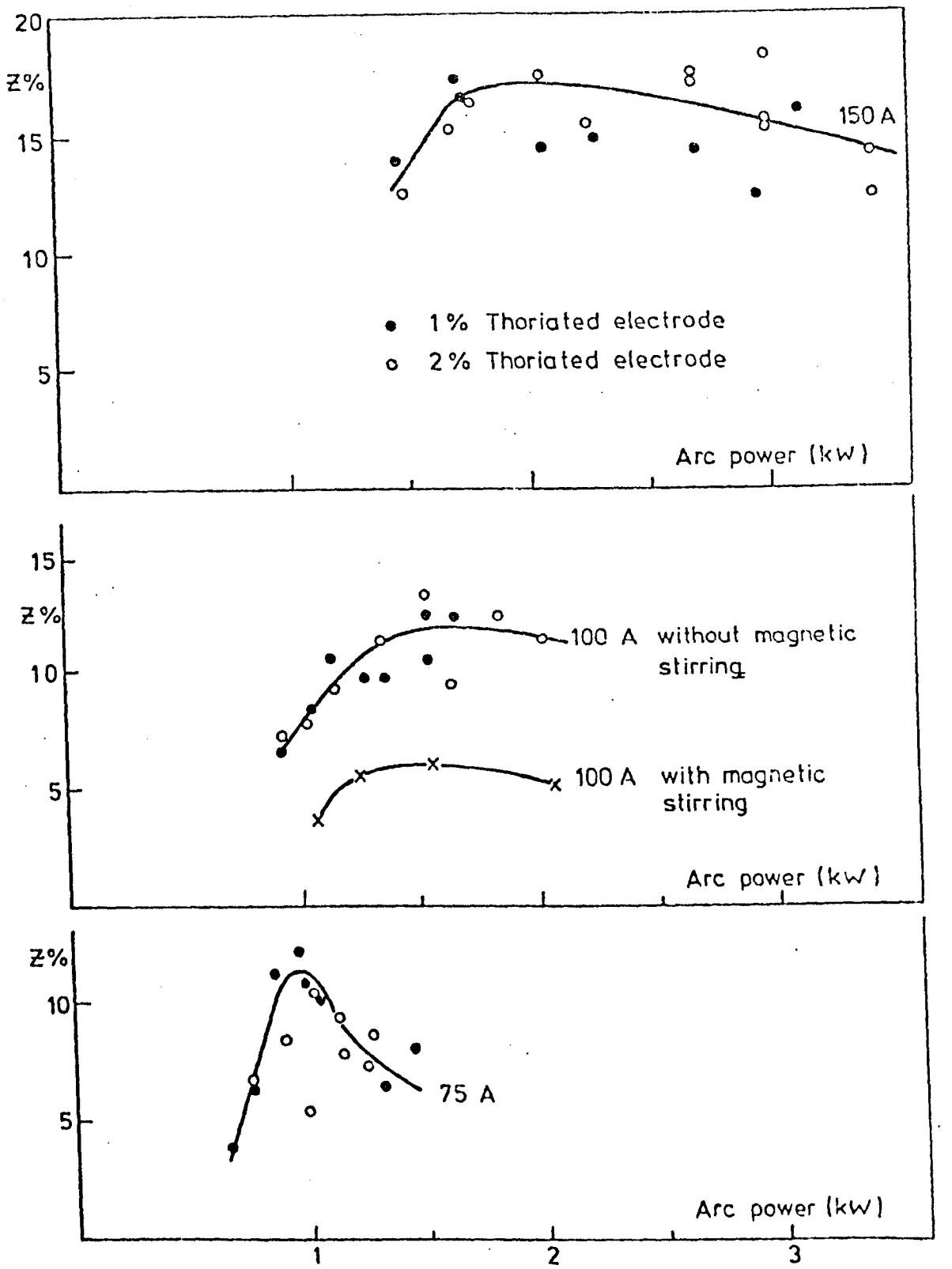

FIGURE 128. INFLUENCE OF ARC POWER ON WELD BEAD MELTING EFFICIENCY (Z) (2 mm ARGON TIG ARC)

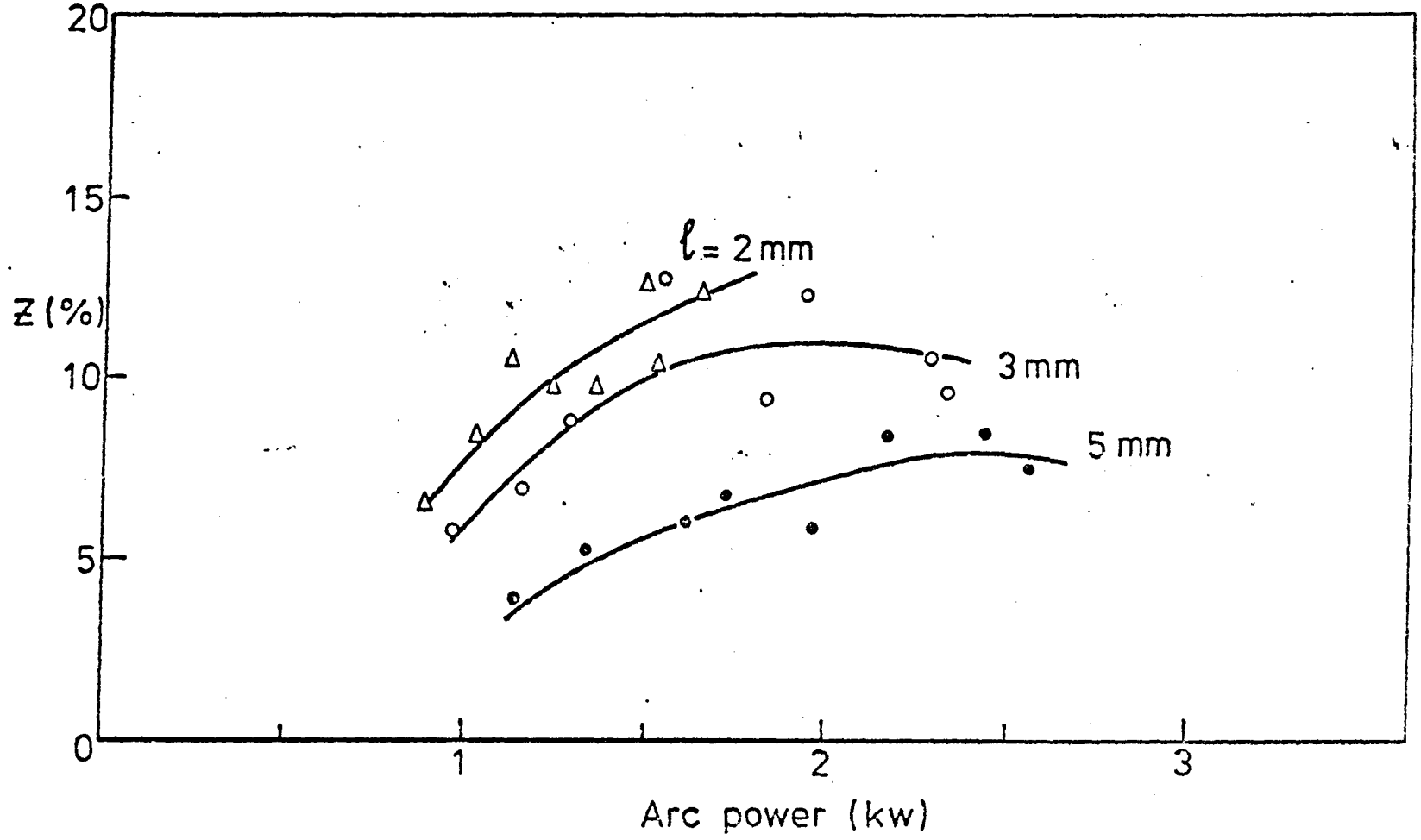

FIGURE 129. INFLUENCE OF ARC POWER AND LENGTH ON MELTING EFFICIENCY (Z) (100 A, ARGON TIG ARC)

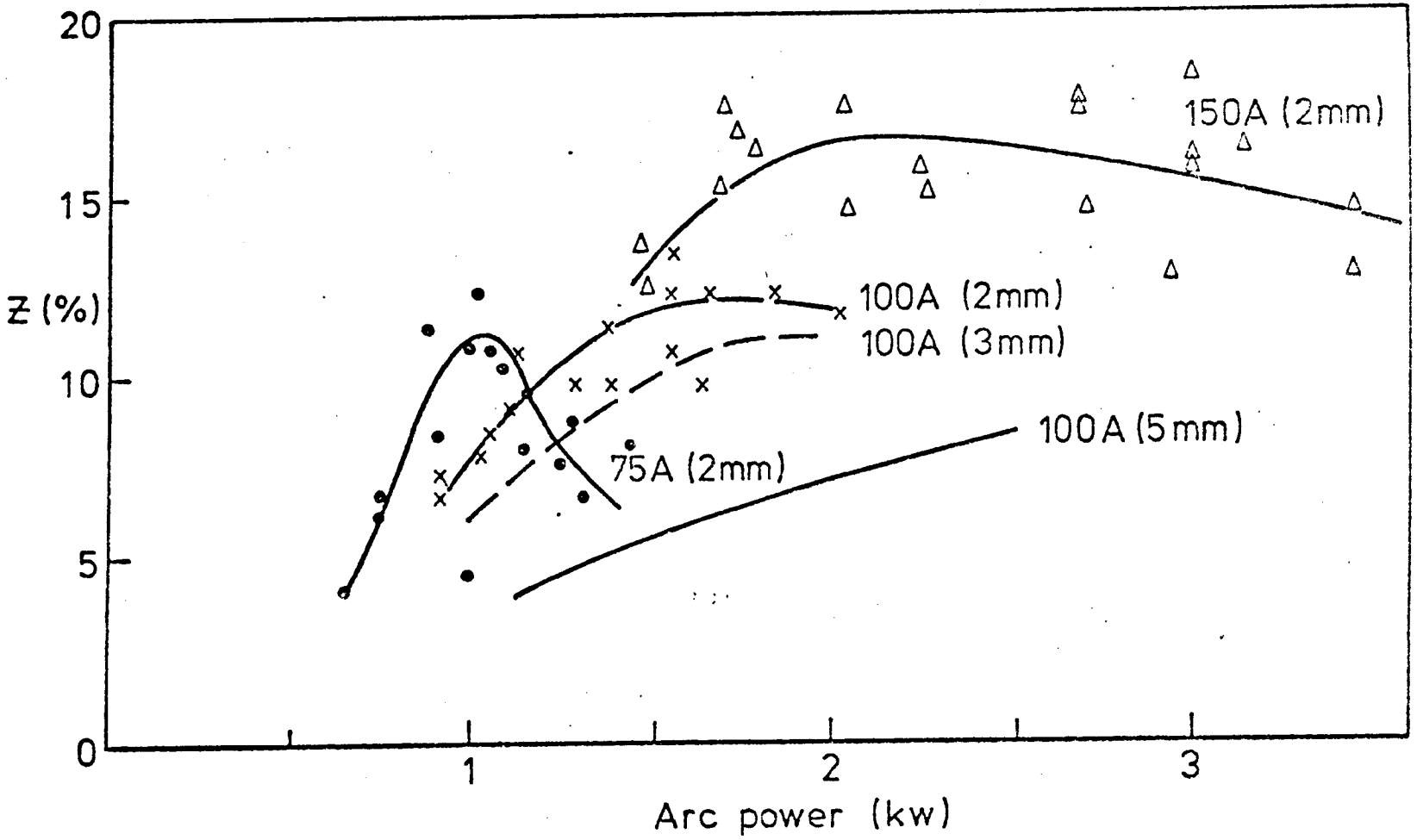

FIGURE 130. COMPARISON OF THE POWER DEPENDENCE OF MELTING EFFICIENCY (Ƶ) AT DIFFERENT CURRENTS AND ARC LENGTHS FOR AN ARGON TIG ARC.

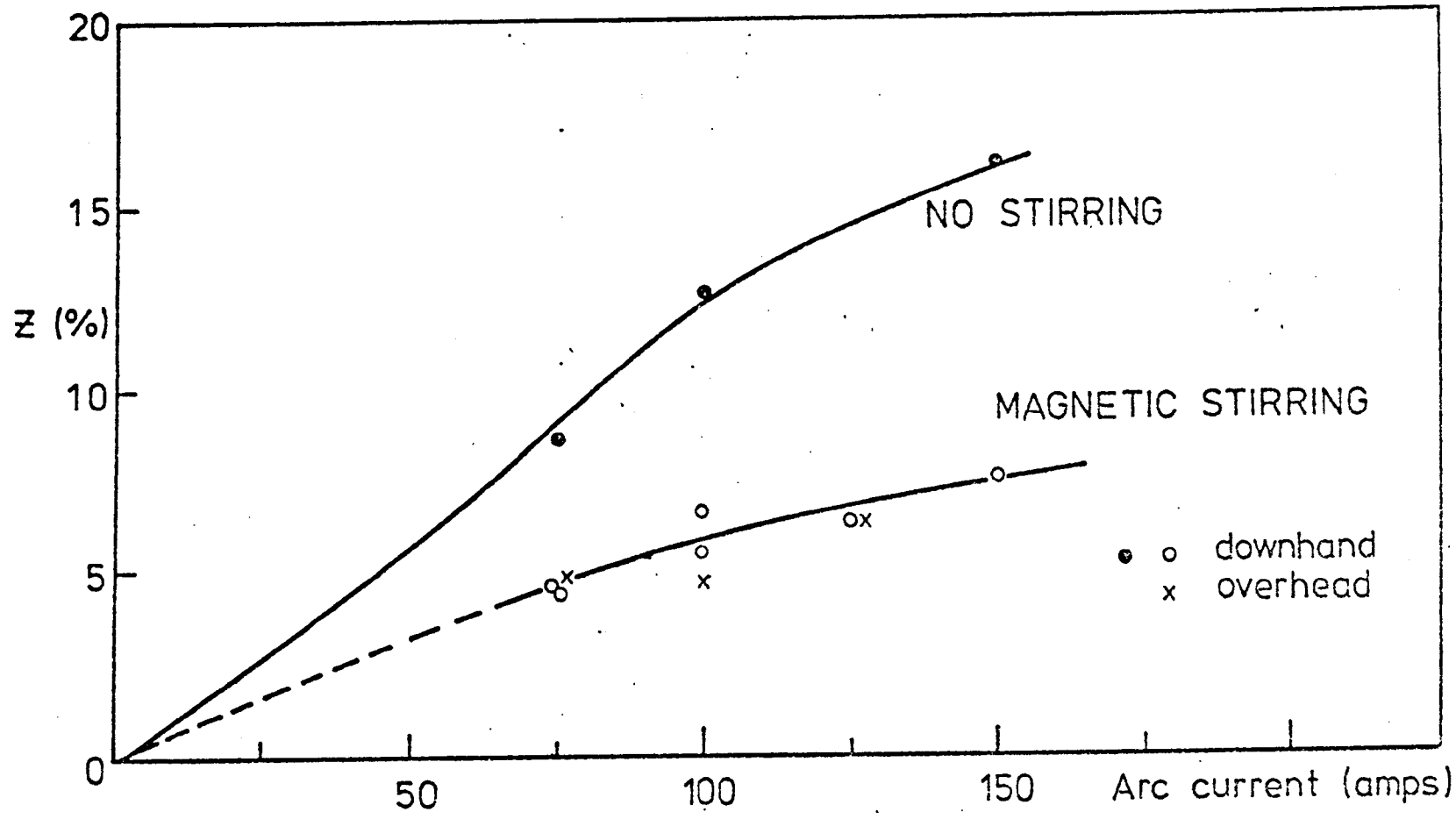

FIGURE 131. INFLUENCE OF MAGNETIC STIRRING , WELDING POSITION AND ARC CURRENT ON MELTING EFFICIENCY FOR A 2mm ARGON ARC AT 41·6 BARS

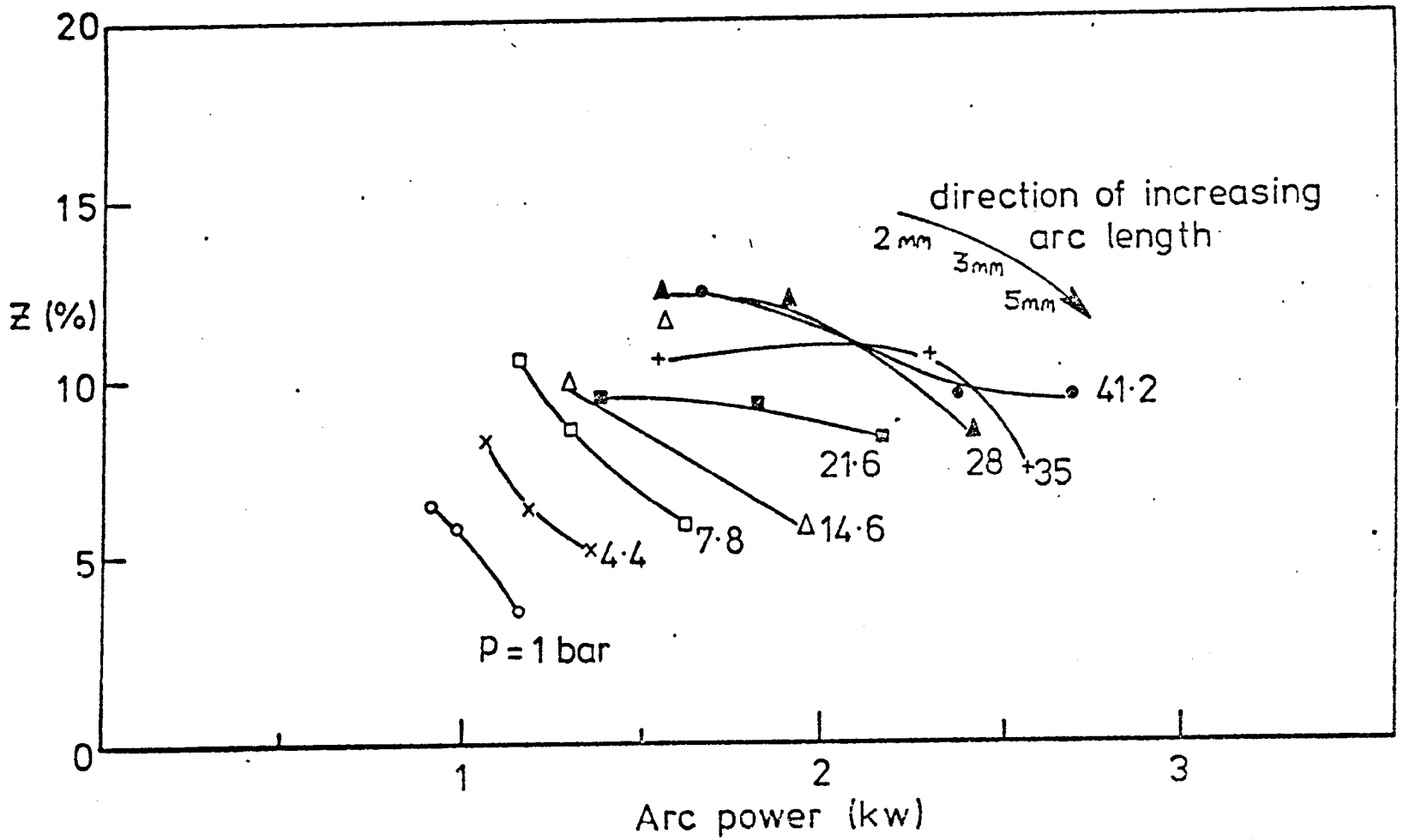

FIGURE 132. INFLUENCE OF ARC LENGTH AND PROCESS POWER ON MELTING EFFICIENCY FOR A 100 AMP ARGON TIG ARC.

4.7.5. Effect of Welding Speed on Z

A limited number of experiments were performed at speeds of other than that usually adopted (i.e. 1.38 mm/s). Results are shown in figure 133. It can be seen that Z increases considerably with increasing speed.

4.7.6. Effect of Magnetic Field on Z

Welds made in the presence of a magnetic field are generally found to have melting efficiencies of about half those without a field. This result applies to a wide range of pressures (see figure 127), arc currents and welding positions (see figure 131). It is known that process power is little influenced by the application of a field and so this result is attributed almost entirely to a decrease in fusion area. Z is fairly insensitive to arc length for welds made in the presence of a field.

4.7.7. Effect of Gas Flow on Z

Gas flow has no significant influence on Z for both the magnetic and non magnetic cases (see table 9).

4.8. Process Efficiency Measurements from HAZ Dimensions for Argon TIG Arcs

It is well known (e.g. ref. 105) that a moving point heat source in a semi-infinite plate generates a temperature distribution given by

$$T = T_p + \frac{q}{2\pi Kr} \exp\left(\frac{-v(r-x)}{2\alpha}\right) \qquad (100)$$

where T_p is plate ambient temperature

q is heat input

r distance from source

K thermal conductivity

α thermal diffusivity

x distance from source along direction of motion

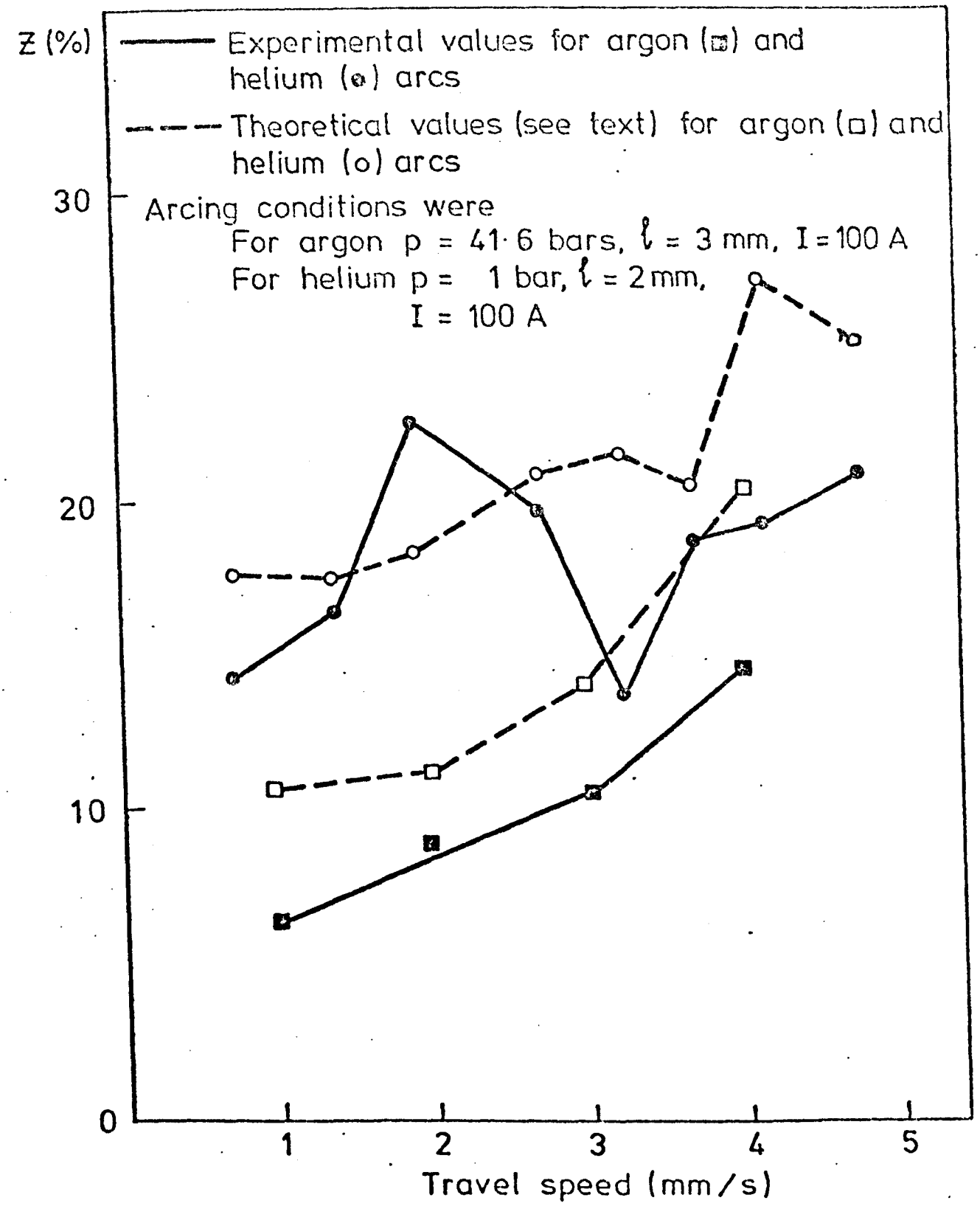

FIGURE 133. INFLUENCE OF TRAVEL SPEED ON MELTING EFFICIENCY (Ƶ)

Well's (ref.103), by finding the position x corresponding to the pool width, has shown that this may be approximated by

$$q \simeq \pi dK(T-T_p)\left(1 + \frac{vd}{5\alpha}\right) \text{ for } 0.1 \lesssim \frac{vd}{5\alpha} \text{ i.e. equation (31)}$$

where d is the diameter of the isotherm T. This expression is known to give a fair representation of behaviour away from the melting isotherm. However, the finite distribution of heating, latent heat effects, and convective contributions within the pool make point source - conductive model predictions near to the pool much less realistic. For this reason estimates of q are made here on the basis of HAZ dimensions.

The expression for q is only strictly valid for semi-circular isotherms since it is assumed that the HAZ aspect ratio is 2 (through the point source assumption). If this is not the case then the identification of d is difficult and theory doesn't strictly relate to the experimental situation. To obtain a comparison between theory and experiment a number of equivalent d's may then be identified. For example:-

(a) An average diameter is given by

$$d = \frac{W + 2D}{2} = W.\left(\frac{1}{2} + \frac{1}{\beta}\right)$$

where β is the aspect ratio (HAZ)

(b) An average diameter equivalent to HAZ area (A)

$$d = \sqrt{\frac{8A}{\pi}}$$

(c) An average diameter equivalent to the HAZ perimeter length (ℓ)

$$d = 2\frac{\ell}{\pi}$$

Results of these alternative identifications are shown in table 10 for a 100A, 2mm arc (1% thoriated electrode data has been used).

Pressure	Aspect Ratio	Width Experimental	2xDepth Experimental	Aspect Ratio Equivalent W	Area Equivalent W	Perimeter Equivalent
P(bar)	β	W(mm)	2xD(mm)	$W(\frac{1}{2}+\frac{1}{\beta})$ (mm)	$\sqrt{\frac{8A}{\pi}}$ (mm)	$\frac{2\ell}{\pi}$ (mm)
1	2.9	7.4	5.2	6.3	5.6	6.4
4.4	2.5	6.9	5.6	6.2	6.1	6.6
7.8	2.1	7.1	6.8	7.0	6.5	7.2
14.6	1.8	7.3	8.2	7.8	7.4	7.9
21.7	2.0	7.7	7.8	7.7	7.4	8.5
28.2	2.0	8.4	8.6	8.5	8.0	8.3
35	2.1	7.9	7.4	7.7	7.4	10.2

Table 10 Equivalent HAZ Widths Derived from Weld Bead Data for a 2mm 100 Amp Argon Arc (1% thoriated electrode)

It can be seen that measured values of W are generally a fair representation on any basis (i.e. any equivalent heat flow width) when $\beta=2$. In other cases W gives higher values that the heat flow equivalent widths. Because of the somewhat arbitrary choice of other length scales and the reasonably semicircular HAZ geometries found here (see section 4.7) calculations have been performed by identifying d with W.

The physical data for K and α are taken as average values between pool and HAZ boundary temperatures. For this purpose data presented by Swift-Hook and Gick (ref.159) is used. Values are then

$$K = 30 \text{ W/mk}$$
$$\alpha = 5.4 \text{ mm}^2/\text{s}$$

The relationship between q and d can now be computed from equation 31.. The result is shown in figure 134 and may be expressed as

$$q = 312.4 \{(1 + 0.11d)^2 - 1\} \qquad (101)$$

where q is in KW and d in mm.

Equation 101 allows the weldment heat input (q) to be estimated from HAZ dimensions (d). The process heat transfer efficiency η can then be estimated using the process power (I.V) required to create the HAZ diameter d i.e.

$$\eta = \frac{q}{I.V} \times 100\%$$

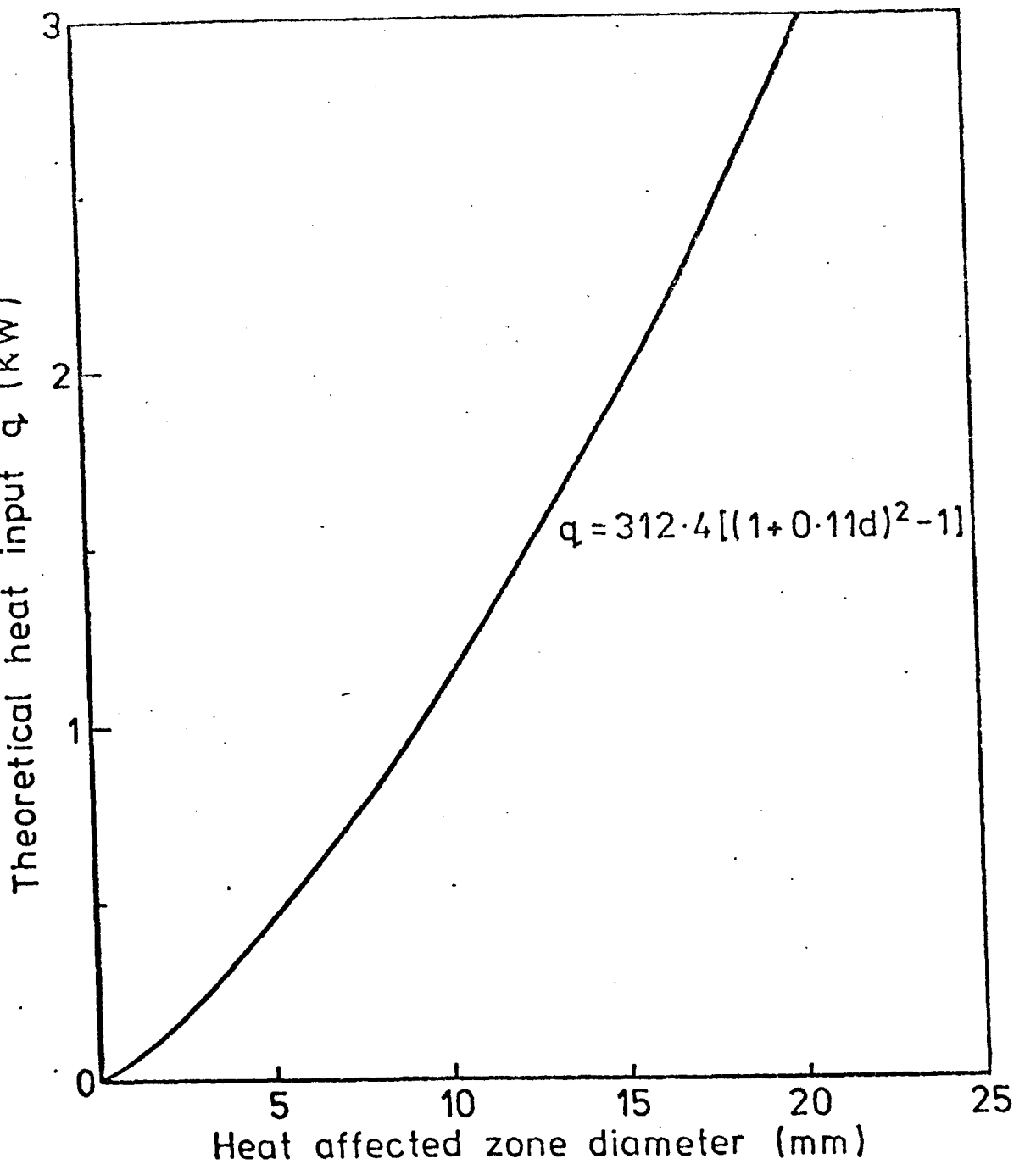

FIG. 134. RELATIONSHIP BETWEEN HAZ DIAMETER AND HEAT INPUT.

Process heat transfer efficiencies obtained in this manner are shown in figures 135a) and b). These show that process efficiency decreases with pressure despite a general increase in weld area and heat input. This behaviour is particularly noticeable at low currents. With I = 75 Amps efficiency falls from about 70% at 1 bar to about 45% at 42 bars. The corresponding falls for 100 and 150 Amps are 70% to 50% and 80% to 75% respectively. Arc length appears to have only a small effect on these estimates of process efficiency (see figure 135) with the longest arcs tending to have the lowest efficiencies. Values obtained in the presence of a magnetic field are generally similar to those without a magnetic field despite the significant difference in melted volumes (see figure 135).

4.9. Theoretical Melting Efficiencies for Argon TIG Arcs

In section 4.8 the process efficiency η was found from HAZ dimensions. This allows the heat input q to be estimated from process power (i.e. $q = \eta.I.V$). Conduction theory can then be used to estimate pool size. Equation 31 can be re-arranged to give the theoretical pool area A^T by calculating the pool diameter d. i.e.

$$A^T = \frac{\pi d^2}{8} = \frac{\pi}{4} \cdot \left(\frac{5\alpha}{2v}\right) \cdot (1 + \theta - \sqrt{1 + 2\theta}) \qquad (102)$$

where $\theta = \dfrac{2.v.q}{5\alpha\pi KT}$

T is taken as the difference between fusion isotherm and initial plate temperature. This theoretical pool size can now be substituted into the expression used to compute Z (see equation 99). The result is a theoretical melting efficiency (Z^T) defined by

$$Z^T = 0.744. \frac{\alpha}{KT} .\eta. \left(\frac{1 + \theta - \sqrt{1 + 2\theta}}{\theta}\right) \qquad (103)$$

For the present purposes a more suitable form of equation 103 is

$$I.V.Z^T = \bar{\alpha} \quad (1 + \bar{\theta}q - \sqrt{1 + 2\bar{\theta}q}) \qquad (104)$$

where

$$\bar{\alpha} = \frac{1.94.\pi d^2}{v}, \quad \bar{\theta} = \frac{2v}{5\alpha\pi KT}$$

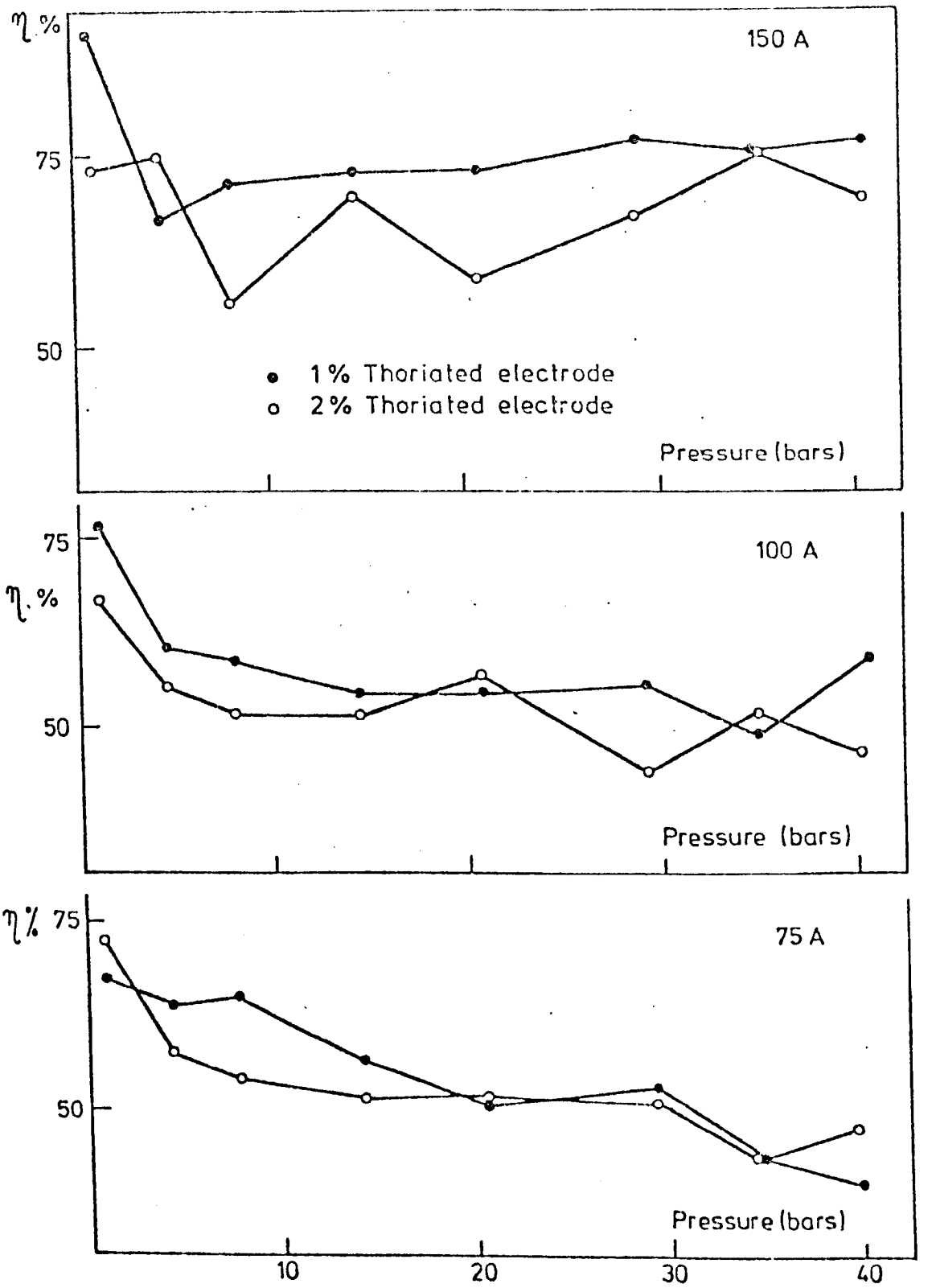

FIGURE 135a HEAT TRANSFER EFFICIENCY ($\bar{5}$) CALCULATED FROM HAZ WIDTH

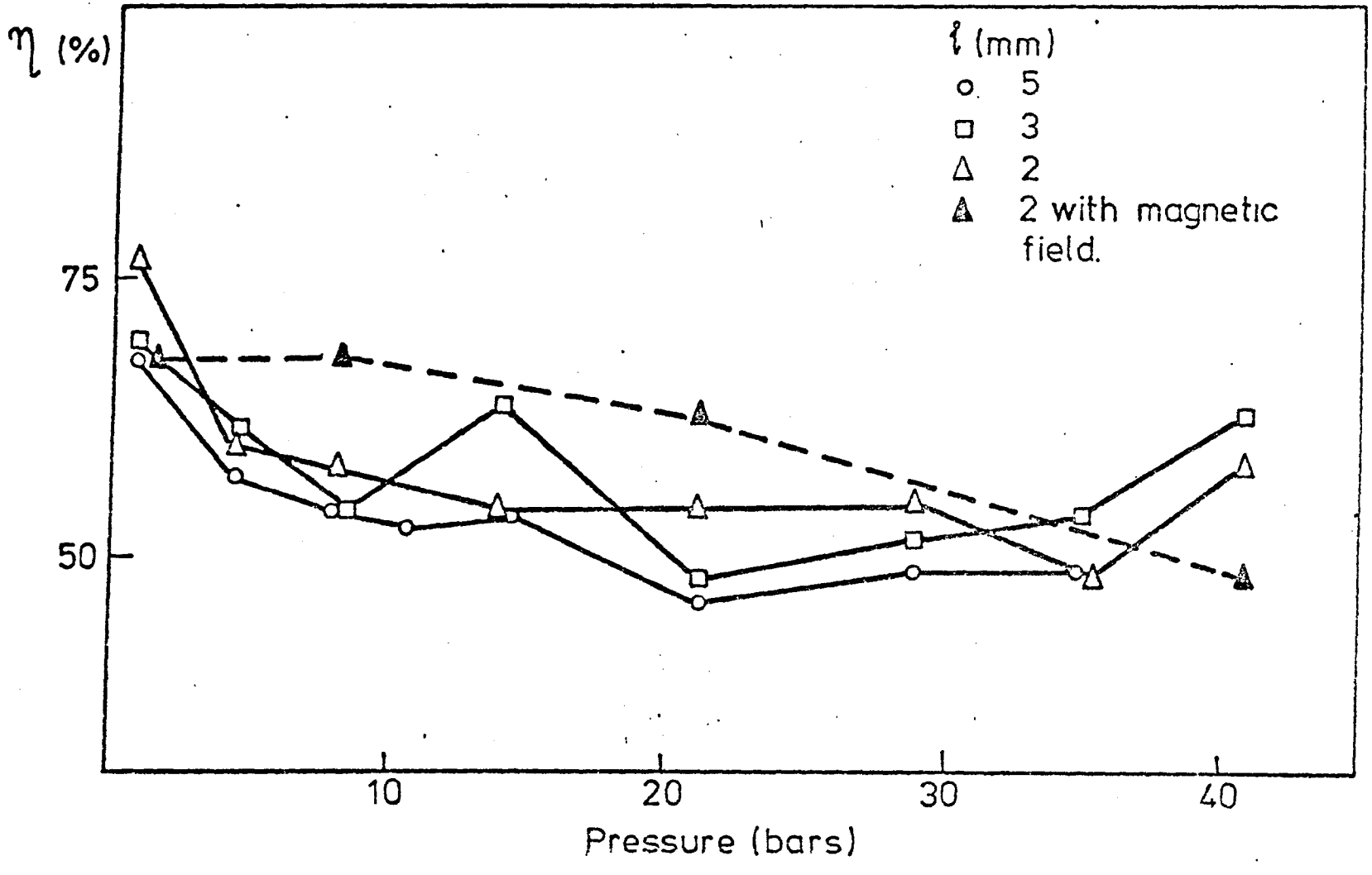

FIGURE135b. HEAT TRANSFER PROCESS EFFICIENCY (η) CALCULATED FROM HAZ WIDTH. THE INFLUENCE OF MAGNETIC STIRRING AND ARC LENGTH (100 AMP ARGON TIG ARC)

Process efficiency (η) and heat input (q) have already been found from HAZ dimensions. To obtain estimates of Z^T it is assumed that all of the heat entering the plate enters through the pool. This is a less stringent restatement of the point source assumption. However, it is important to restate this assumption as it implies that the heat flux through the HAZ isotherm is the same as the heat through the pool fusion boundary therefore allowing the same process efficiency to be applied in both regions. The expression for Z^T is sensitive to the choice of temperature at which thermal properties are evaluated or more generally, to values associated with these properties (this difference in interpretation is given further consideration in section 5.4). For the present purposes two situations are chosen with which to compare conductive theory. These are

(I) When properties are evaluated at the melting temperature i.e. this is not too unreasonable when applying the expression at and near the pool. Thus (ref.159)

$\alpha = 6mm^2/s$

$K = 35\ W/mK$

$C = 780\ J/kg^oC$

(II) When properties are evaluated at a suitable mean temperature between the pool and plate. Then (ref.159)

$\alpha = 5mm^2/s$

$K = 24\ W/mK$

$C = 620\ J/kg^oC$

Applying these values to $\bar{\alpha}$ and $\bar{\theta}$ in equation 104 enables plots of $Z^T.IV$ as a function of q to be obtained.

For case I

$$Z^T.IV = 140.73\ \{1 + 0.558q - \sqrt{1 + 1.116q}\} \qquad (105)$$

For case II

$$Z^T.IV = 101.20\ \{1 + 0.976q - \sqrt{1 + 1.952q}\} \qquad (106)$$

where travel speed has been taken as 1.38mm/s and both q and IV are in KW's. These relationships are shown in figure 136 and called the high 'K' (case I) and low 'K' (case II) conditions. Low 'K' theory can be seen to give a good representation of the relationship between melting rate and heat input for arc currents of 75A and 100A. However, when welding is performed in the presence of a field much lower melting

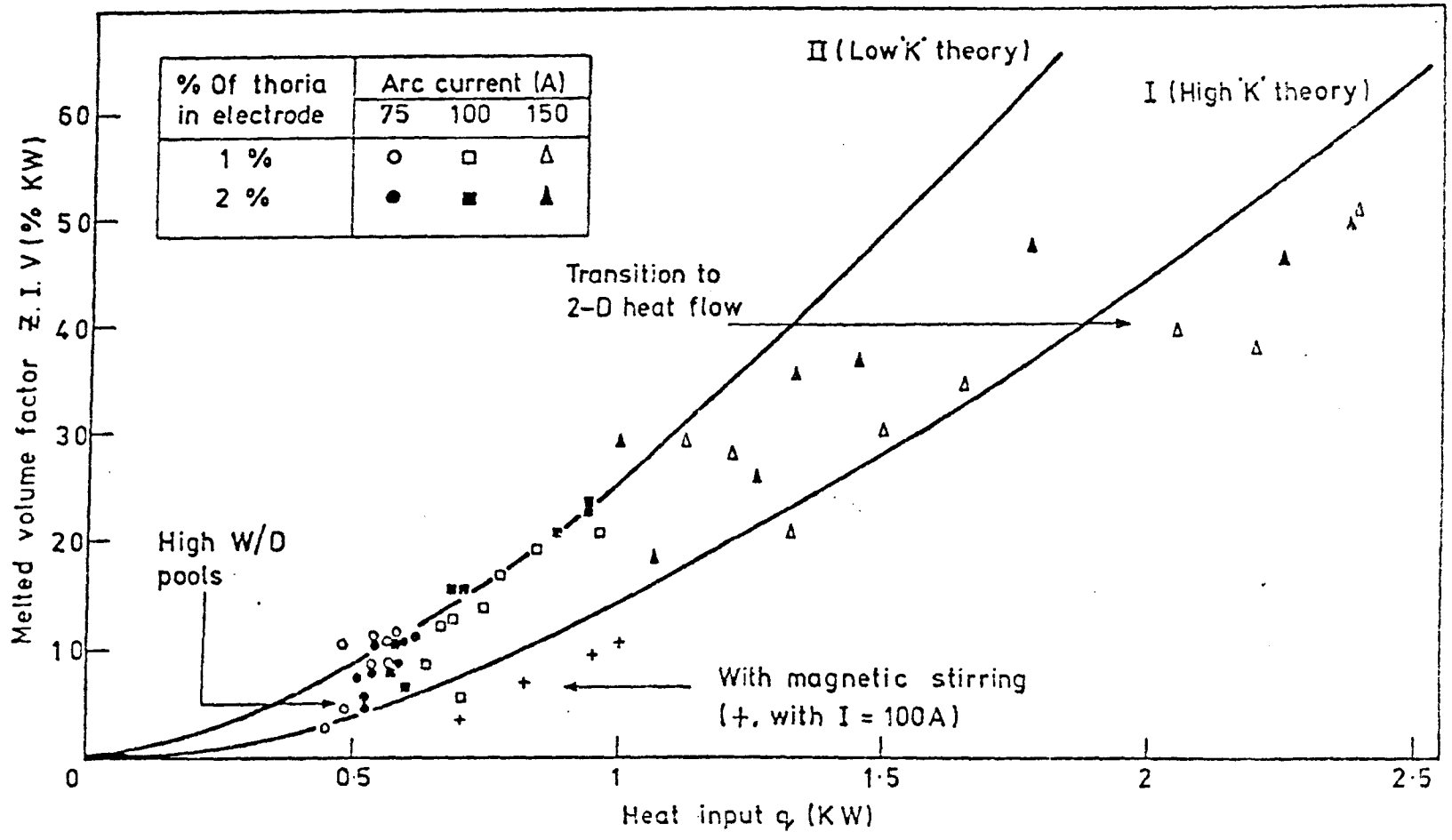

FIGURE 136. THE INFLUENCE OF WELDMENT HEAT INPUT (q) ON MELTING FOR ARGON TIG ARCS (2 mm ARC LENGTH).

rates are obtained and data is better represented by the high 'K' curve. Experiments with 150 Amp arcs also follow low 'K' conductive behaviour. However, at higher pressures (corresponding to higher heat inputs) behaviour moves from that of low 'K' to that of high 'K'. i.e. Melting rate for 150 Amp arcs is significantly less than that expected on the basis of conductive theory at high pressures. This is thought to be associated with the high values of process efficiency found for 150 Amp arcs from HAZ diameters. At 42 bars process efficiencies of about 75% were found from HAZ measurements with I=150A. At lower currents the corresponding efficiencies were roughly 50%. If the true high current efficiency was also near 50% then the power input q would be reduced by a factor of 50/75 i.e. 0.66. This would move such points to the left so as to correspond with predicted low 'K' behaviour.

Curves I and II in figure 136 can be used to predict melting efficiencies if IV and q are known. This has been done for low K values and results are shown in figures 138 to 140. These figures show that very good agreement is achieved between experiment and low 'K' curves at pressures above 4.4 bars for I=75A and 100 Amps. Relatively poor low 'K' agreement is found for atmospheric arcs, high current arcs and for arcs with magnetic stirring (see figure 132 and 136). The poor agreement, has in each case a different origin:

1) For atmospheric arcs aspect ratios are significantly larger than 2. Therefore heat input is over estimated from HAZ width. This gives larger theoretical melting efficiencies than observed in practice. At higher pressures, ratios of nearly 2 are invariably obtained and theory can then be readily compared with experiment.
2) For high current arcs the values of efficiency obtained from HAZ widths are probably too high. This is associated with a transition to three dimensional heat flow in the specimens used.
3) For cases involving magnetic fields conductive transfer is likely to be in competition with convection which will thereby increase the effective thermal conductivity. Under these circumstances low 'K' theory is not expected to agree with experimental findings. It is worth noting

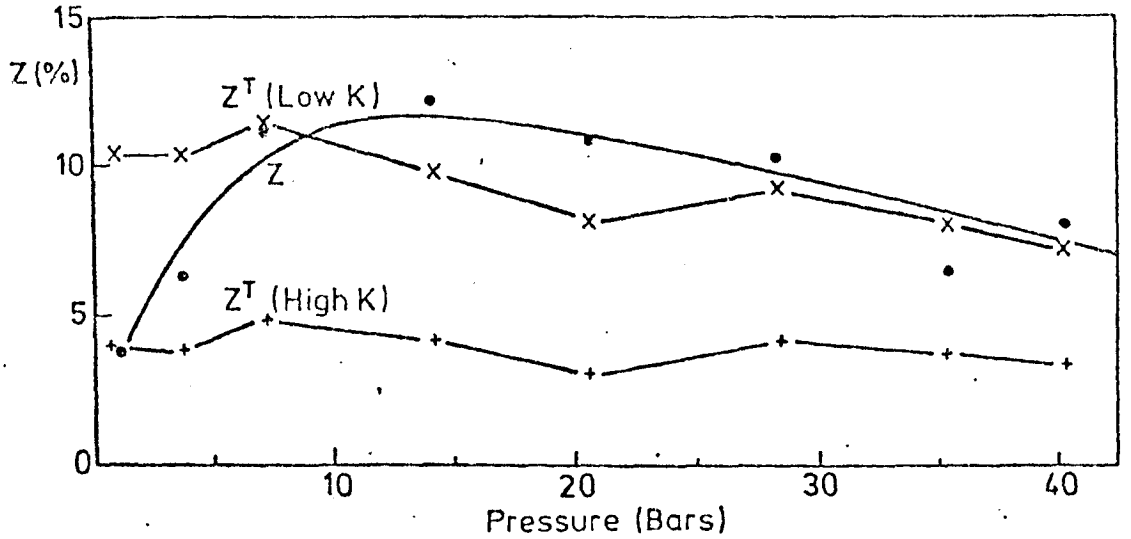

FIG. 137. PRESSURE DEPENDENCE OF EXPERIMENTAL (Z) AND PREDICTED (Z^T) MELTING EFFICIENCIES FOR ARGON TIG ARCS (75A, 2mm, 1% Thoriated data)

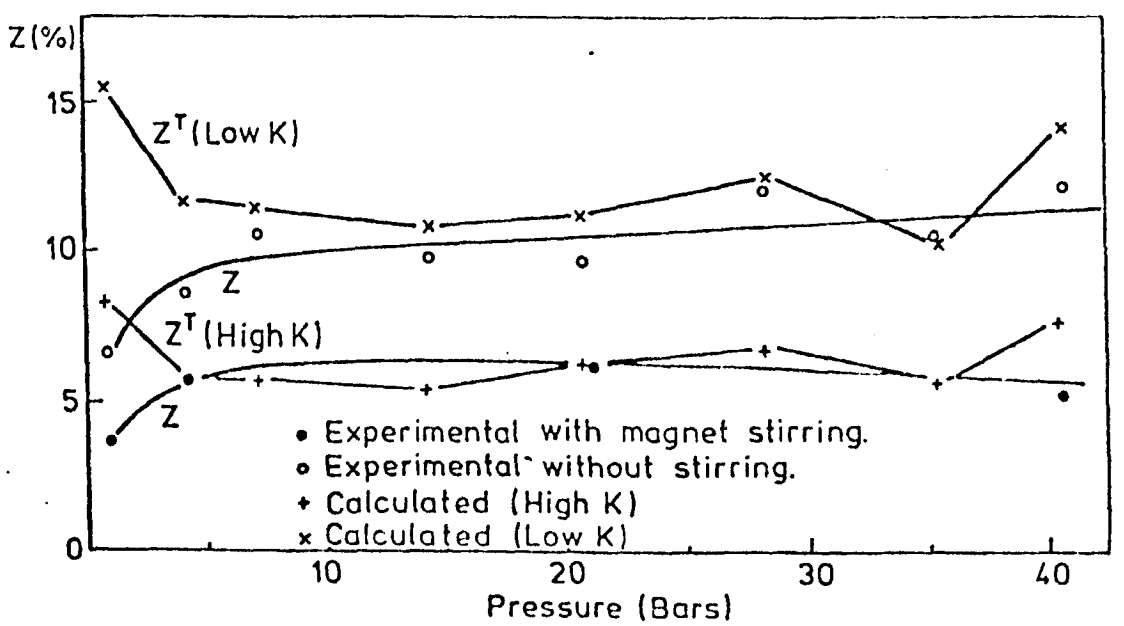

FIG. 138. PRESSURE DEPENDENCE OF EXPERIMENTAL (Z) AND THEORETICAL (Z^T) MELTING EFFICIENCIES FOR ARGON TIG ARCS (100A, 2mm, 1% Thoriated data)

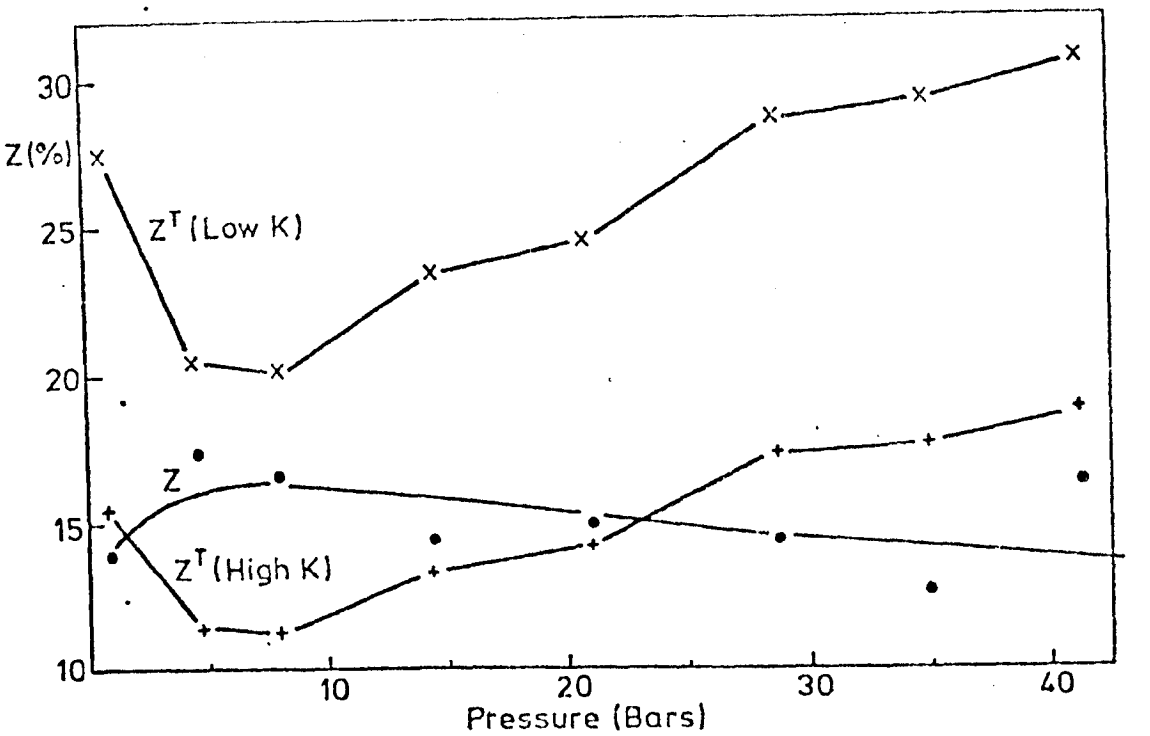

FIG. 139. PRESSURE DEPENDENCE OF EXPERIMENTAL (Z) AND PREDICTED (Z^T) MELTING EFFICIENCIES FOR ARGON TIG ARCS (150 A, 2mm, 1% Thoriated data)

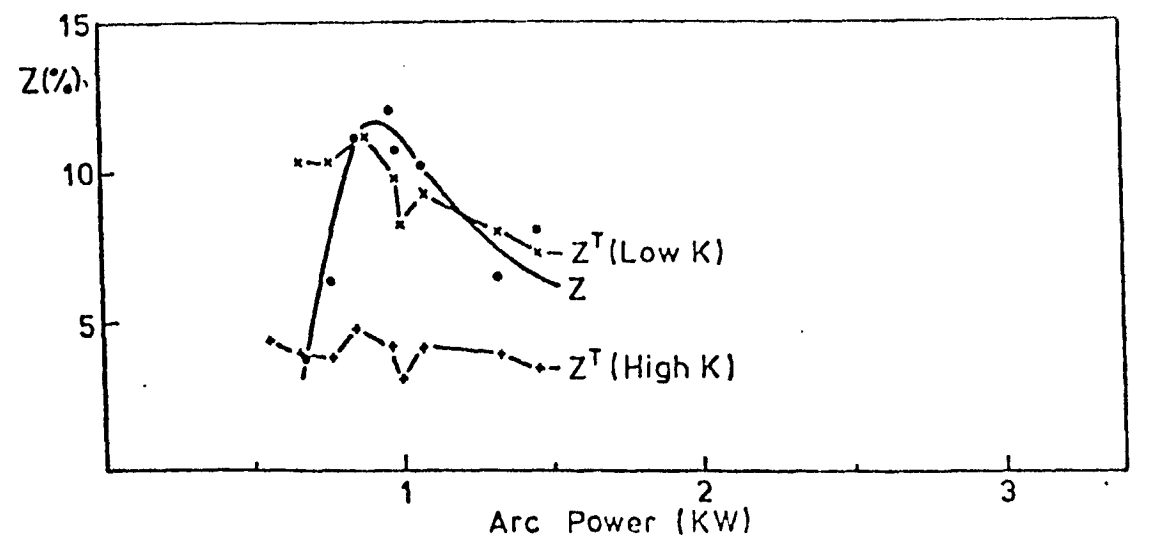

FIG. 140. INFLUENCE OF ARC POWER ON EXPERIMENTAL (Z) AND THEORETICAL (Z^T) MELTING EFFICIENCY FOR AN ARGON TIG ARC (75A, 2mm, 1% THORIATED DATA)

that explanations involving reduced q's or increased z's are not valid as is readily seen from weld geometry measurements i.e. HAZ dimensions are similar to those found when no field is applied. Therefore, similar heat input will exist and q values will not be greatly different from those used. Z values are expected to be about half those without a field because of the observed difference in weld bead area sizes.

If the above corrections are applied for estimations (1) and (2) then reasonable agreement with theory is obtained.

4.10. The Helium TIG Arc Weld Bead Geometry

4.10.1. Weld Bead Penetration

Penetration is found to increase markedly with pressure over the first 8 bars (see figure 141). Beads then become shallower until again increasing in depth between 11 and 15 bars. As in argon arcs weld bead penetration is reduced when a magnetic field is applied. The pressure dependence of penetration is similar both with and without a magnetic field. Penetration is largely insensitive to arc length at all pressures (see figure 142) although there is a tendency for penetration to increase for arc lengths of between 2 and 3mm's (thereafter remaining near the value at 3mm). Current (figure 143) exerts the largest influence on penetration although the effect is less pronounced when a magnetic field is applied. Indeed, the difference between results found with and without a magnetic field diverge as current increases. This is largely due to only a weak current dependence between 100 and 150 Amps for welds made in the presence of a magnetic field.

4.10.2. Weld Bead Width

Weld bead width is found to increase with pressure over the first 8 bars. Behaviour then becomes less predictable (see figure 144). This contrasts the behaviour of TIG arcs where bead width changes little with pressure. Again the influence of magnetic field is to produce wider weld beads. However, a decrease is observed between about 8 and 11 bars when magnetic stirring is applied.

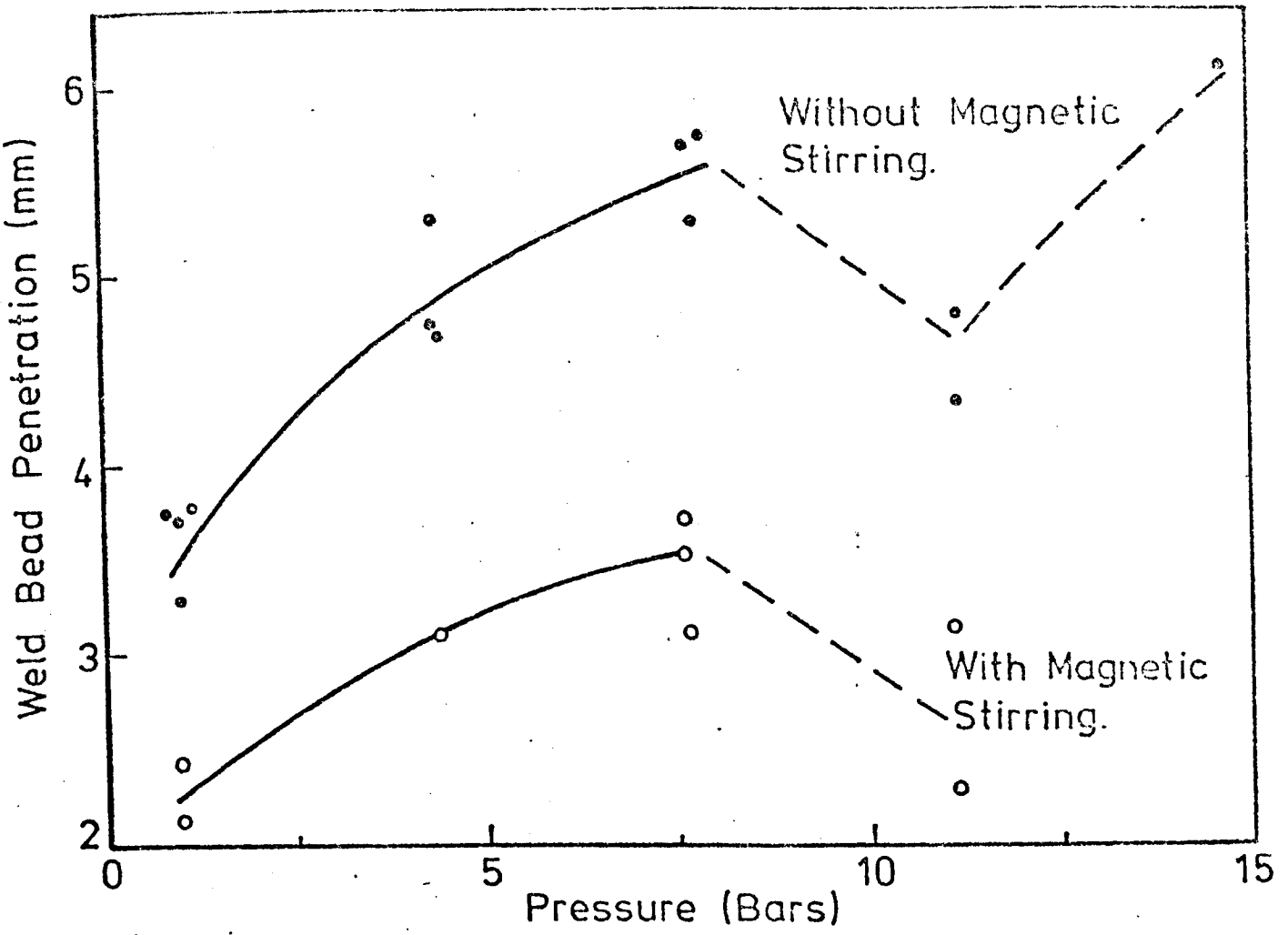

FIG. 141. THE INFLUENCE OF PRESSURE AND STIRRING ON WELD BEAD PENETRATION FOR A 100 AMP, 3mm HELIUM TIG ARC.

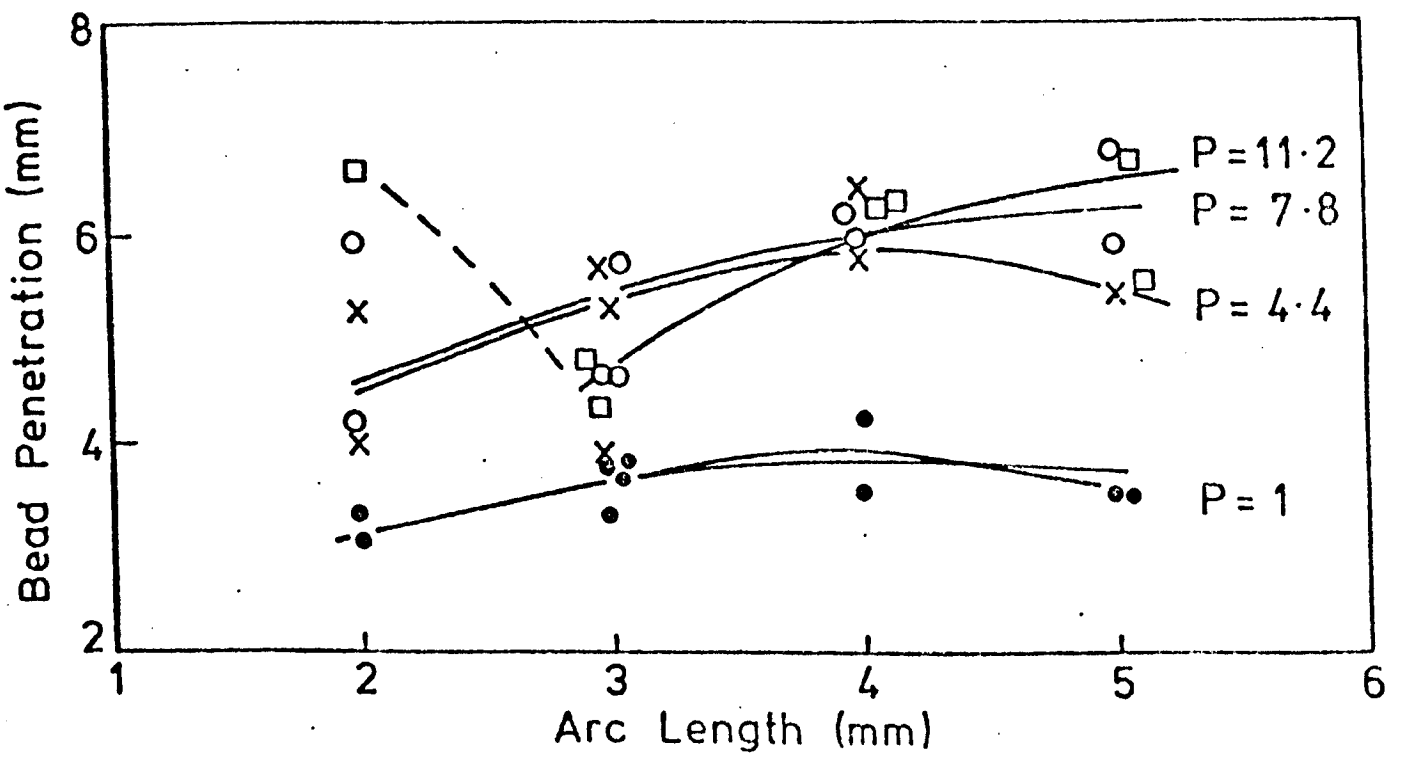

FIG. 142. INFLUENCE OF ARC LENGTH ON WELD BEAD PENETRATION FOR A 100 AMP, HELIUM TIG ARC.

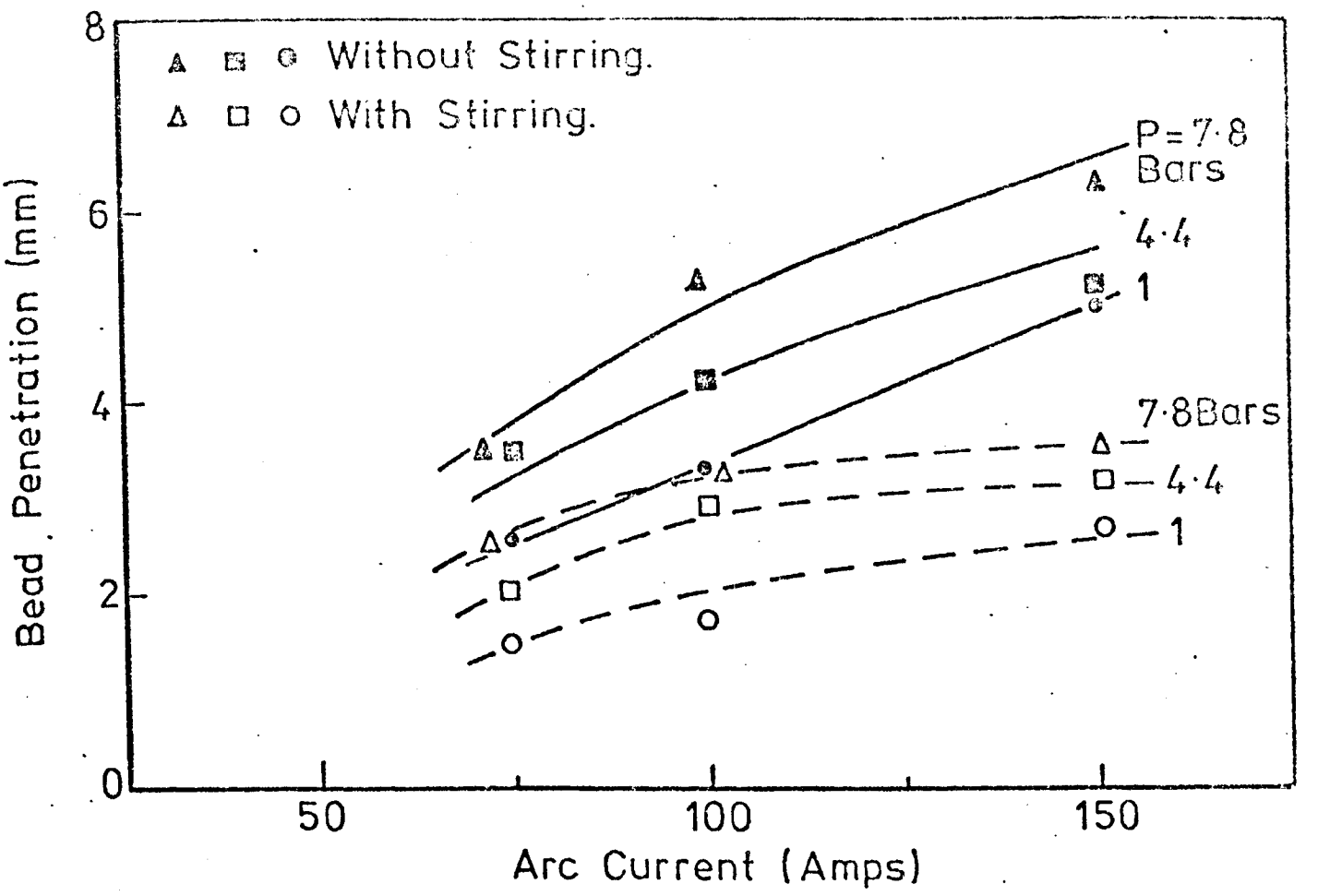

FIG. 143. THE INFLUENCE OF ARC CURRENT AND MAGNETIC STIRRING ON BEAD PENETRATION FOR A 2mm HELIUM ARC.

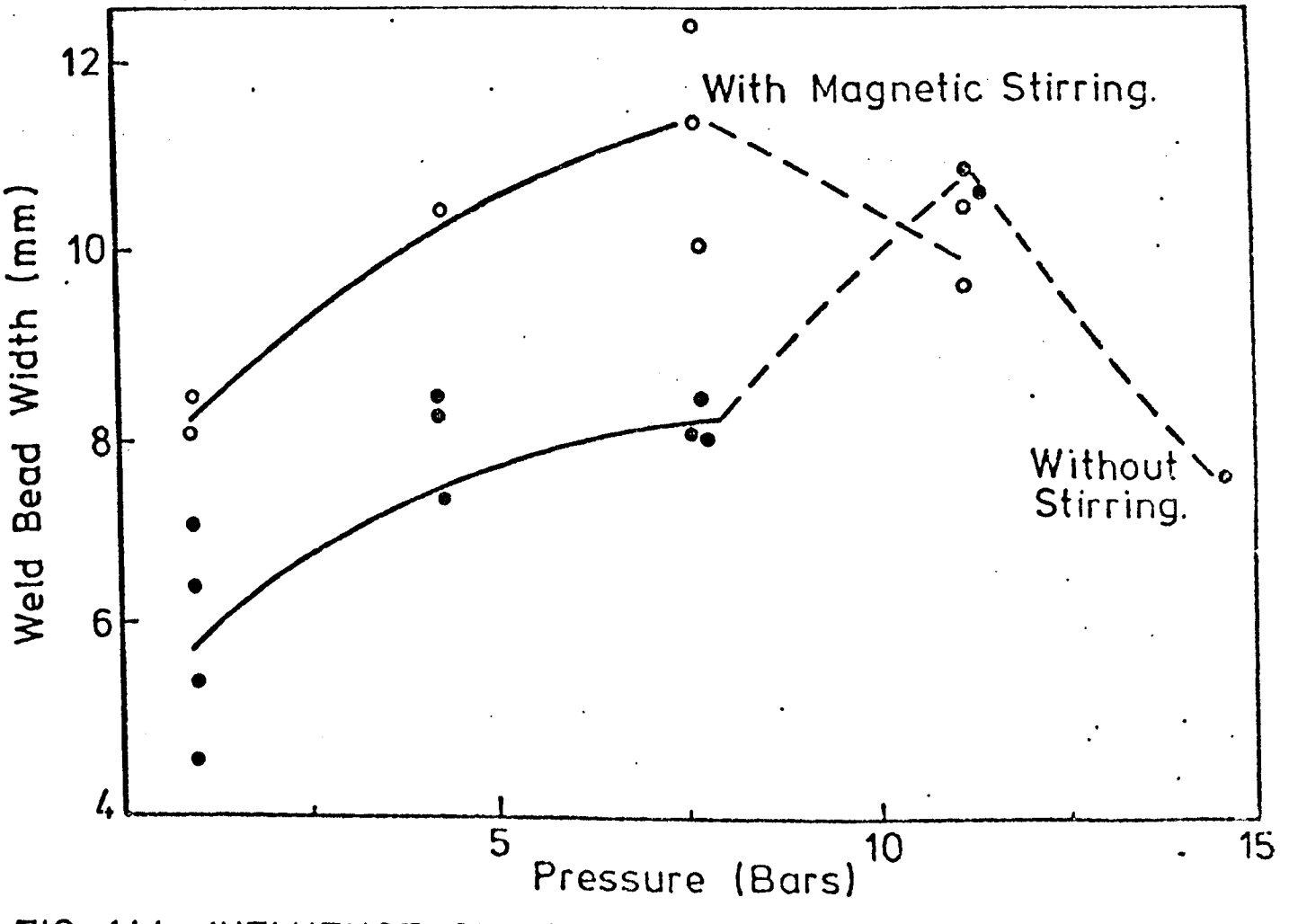

FIG. 144. INFLUENCE OF AMBIENT PRESSURE ON WELD BEAD WIDTH (WITH AND WITHOUT MAGNETIC STIRRING) FOR A 100 A, 3mm, HELIUM TIG ARC.

4.10.3. Weld Bead Aspect Ratio

Weld bead aspect ratios, even at 1 bar, are significantly below 2 (typically 1.7 at 1 bar). These decrease slowly (figure 145) with increasing pressure (with the exception of an increase at 11 bars). Aspect ratios as low as 0.9 have been found (e.g. at 14 bars for a 100 Amp, 3mm arc). Welds made in the presence of a magnetic field exhibit ratios of between about 3 and 4 over the range of pressures investigated (see figure 145). This is significantly lower than found for argon.

4.10.4. Weld Bead Area (Cross-Sectional)

Weld bead area increases by more than a factor of 2 over the first 8 bars and thereafter pressure has little effect. The influence of an applied magnetic field (figure 146) is small for helium arcs and only a small reduction in area is observed over the first 8 bars when such a field is applied. Bead area is strongly influenced by arc length at all pressures and this dependence increases with increasing pressure (see figure 147). The spread of results shown in figure 147 is expected in view of the observed electrode erosion experienced with helium arcs. Experiments made in the presence of a field (figure 148) show a similar dependence although experiments at short arc lengths for a pressure of 11.2 bars show smaller areas than those at 4.4 bars. This behaviour is in agreement with the high pressure decrease noted in figure 146. The dependence on arc length in the presence of a magnetic field is strong at long arc lengths. This is thought to result from a reduction in the influence of a field on the pool and arc i.e. due to decreasing field strength at the pool.

Bead area increases regularly with arc current, both with and without a magnetic field (see figure 149).

4.11. Helium TIG Arc HAZ Geometry

4.11.1. HAZ Penetration

Haz penetration (figure 150) increases markedly with pressure both with and without magnetic stirring. Values found in the presence of a field are marginally less than those without a field and the difference between these results changes little with pressure.

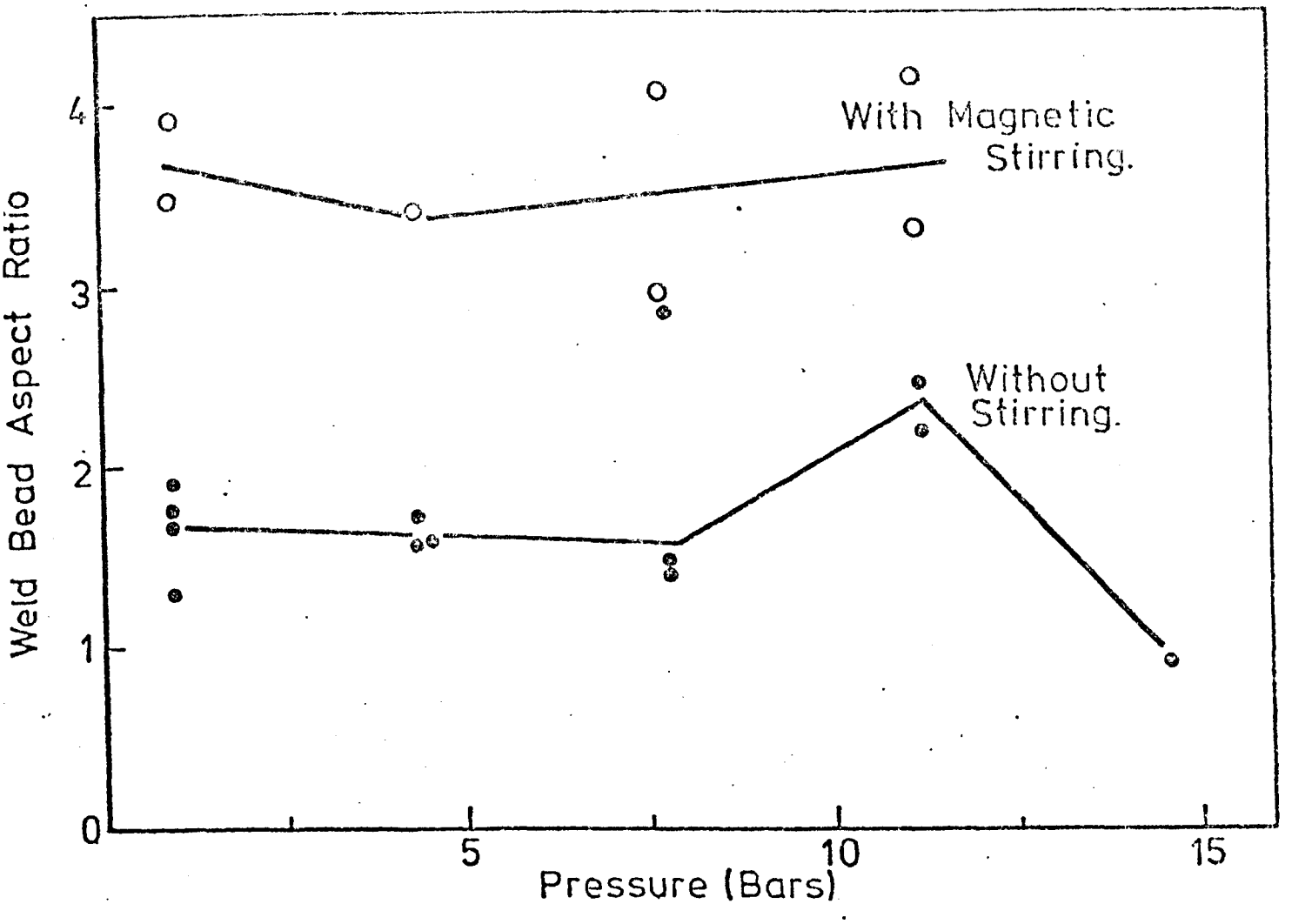

FIG. 145. INFLUENCE OF AMBIENT PRESSURE ON WELD BEAD ASPECT RATIO FOR A 100A, 3mm, HELIUM TIG ARC.

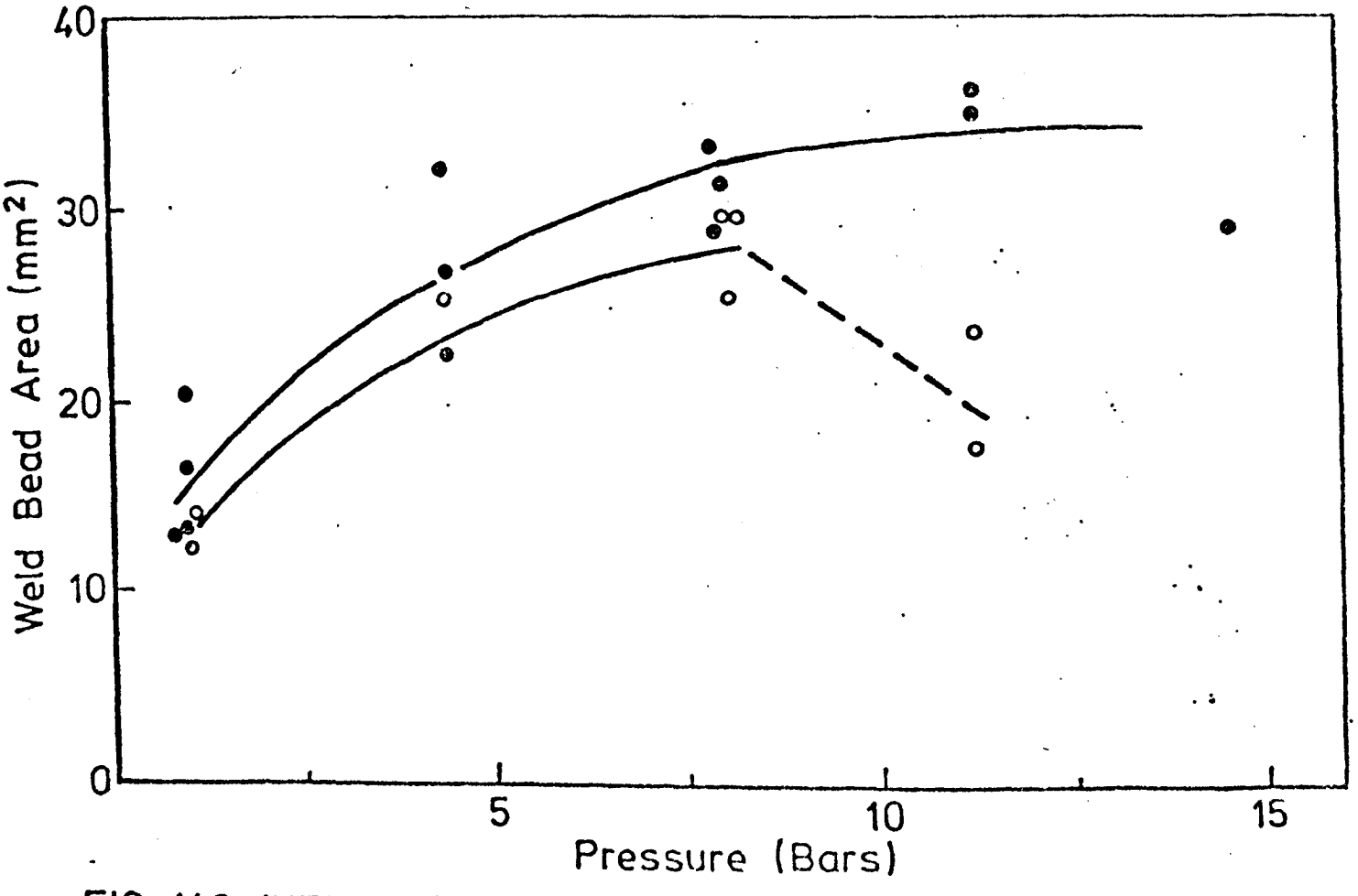

FIG. 146. INFLUENCE OF MAGNETIC STIRRING AND AMBIENT PRESSURE ON WELD BEAD AREA FOR A 100A, 3mm, HELIUM TIG ARC.

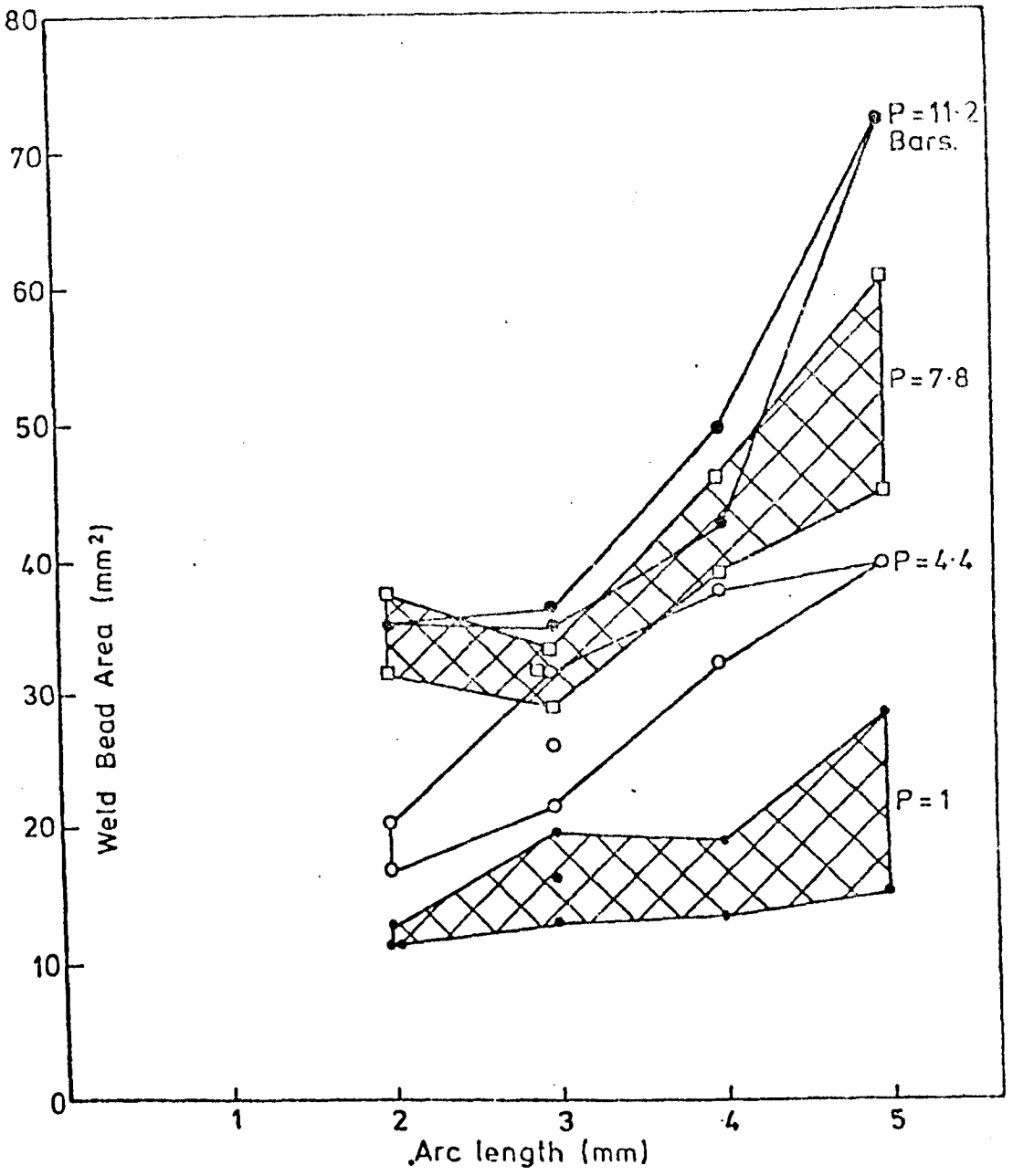

FIG. 147. INFLUENCE OF ARC LENGTH AND AMBIENT PRESSURE ON WELD BEAD AREA FOR A 100A, HELIUM TIG ARC.

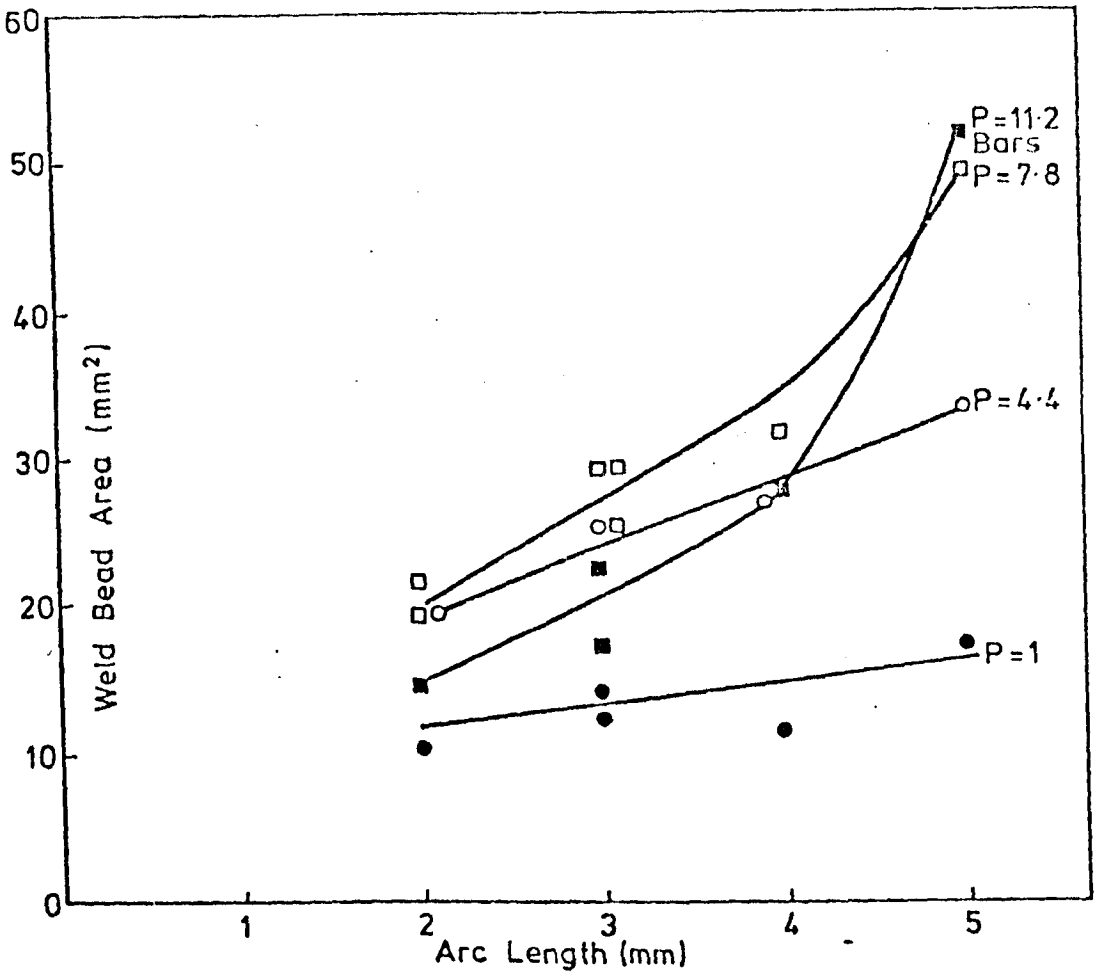

FIG. 148. INFLUENCE OF ARC LENGTH AND AMBIENT PRESSURE ON WELD BEAD AREA (WHEN MAGNETIC STIRRING IS APPLIED) 100 A, HELIUM TIG ARC.

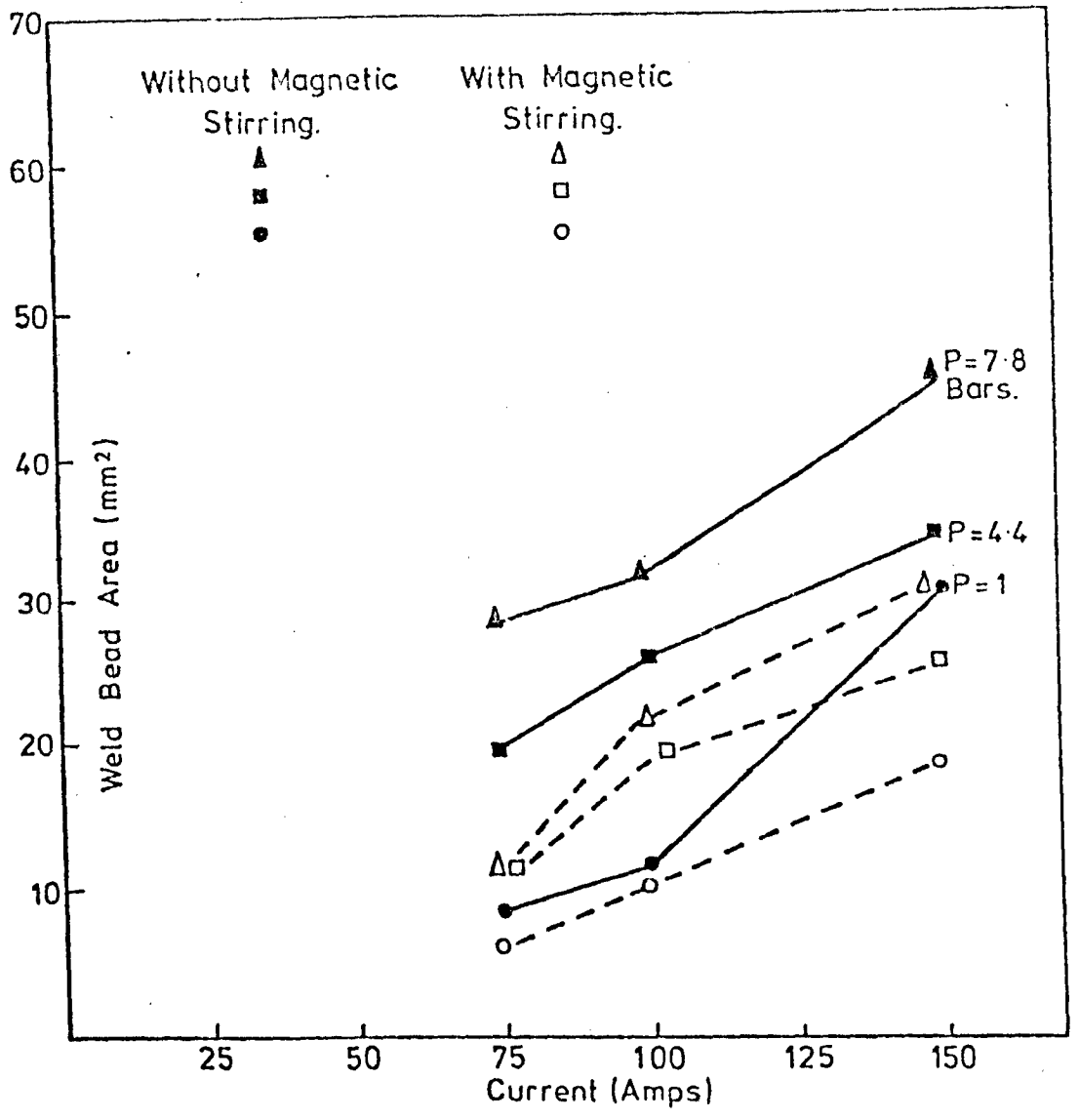

FIG. 149. INFLUENCE OF ARC CURRENT ON WELD BEAD PENETRATION FOR A 2mm HELIUM TIG ARC.

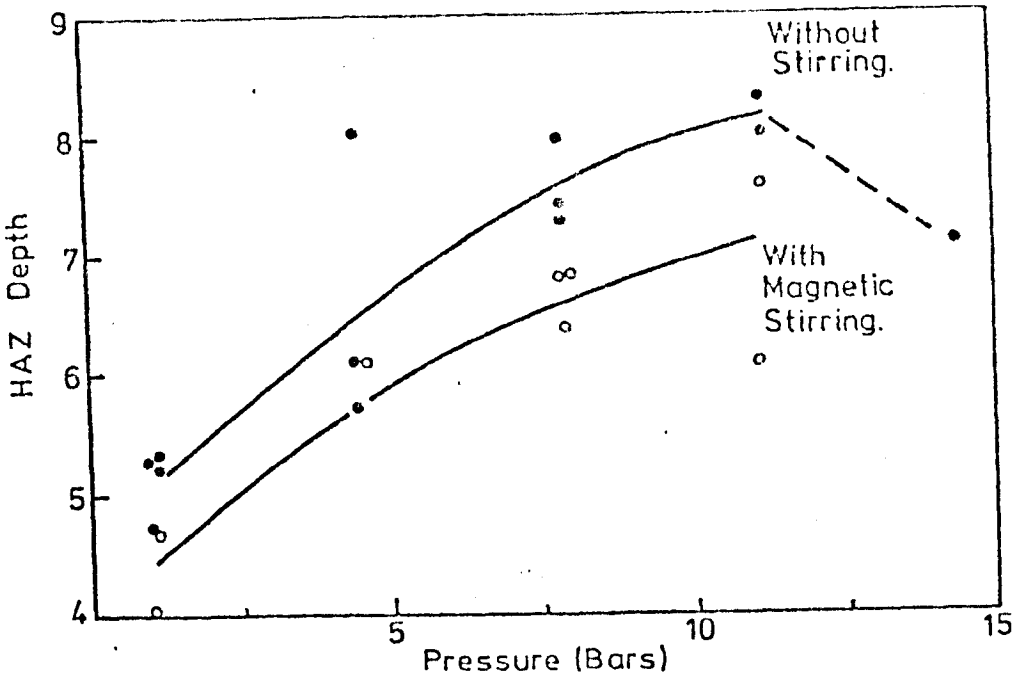

FIG. 150. INFLUENCE OF AMBIENT PRESSURE ON HEAT AFFECTED ZONE (HAZ) PENETRATION FOR THE 100A, 3mm, HELIUM TIG ARC.

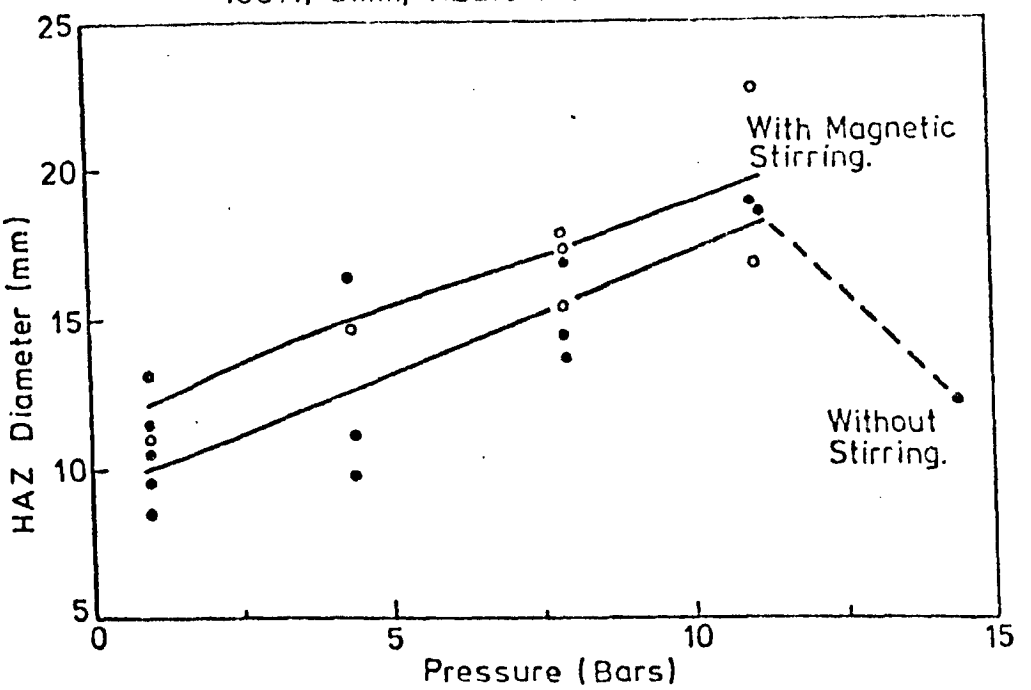

FIG. 151. INFLUENCE OF AMBIENT PRESSURE ON HAZ DIAMETER FOR THE 100A, 3mm, HELIUM TIG ARC.

4.11.2. HAZ Width

HAZ diameter (figure 151) increases strongly with pressure and values obtained in the presence of a magnetic field are marginally greater than those without a field.

4.11.3. HAZ Aspect Ratio

A result of behaviour noted in the two previous sections is to produce aspect ratios (figure 152) close to 2 at all pressures. This value is greater when magnetic stirring is applied i.e. between 2.4 and 3 over the range of pressure investigated.

4.11.4. HAZ Area

HAZ area (figure 153) is strongly pressure dependent increasing by a factor of about 4 over the pressure range 1-11 bars. No significant difference is observed between results obtained with and without a magnetic field.

4.12. Melting Efficiencies for Helium TIG Arcs

Melting efficiency (Z) has been measured for a range of pressures, arc lengths, currents and travel speeds. The influence of magnetic stirring has also been examined.

4.12.1. Influence of Pressure on Z

The influence of pressure (figure 154) is strongly dependent on arc current. At low currents (75A to 100A) the melting efficiency initially increases and falls after a pressure of about 8 bars. For the highest current (150A) examined efficiency is a decreasing function of pressure. This behaviour is more clearly understood in terms of process power (see section 4.12.2). Similar behaviour is observed when welding is performed in a magnetic field (figure 154) although melting efficiencies are then lower.

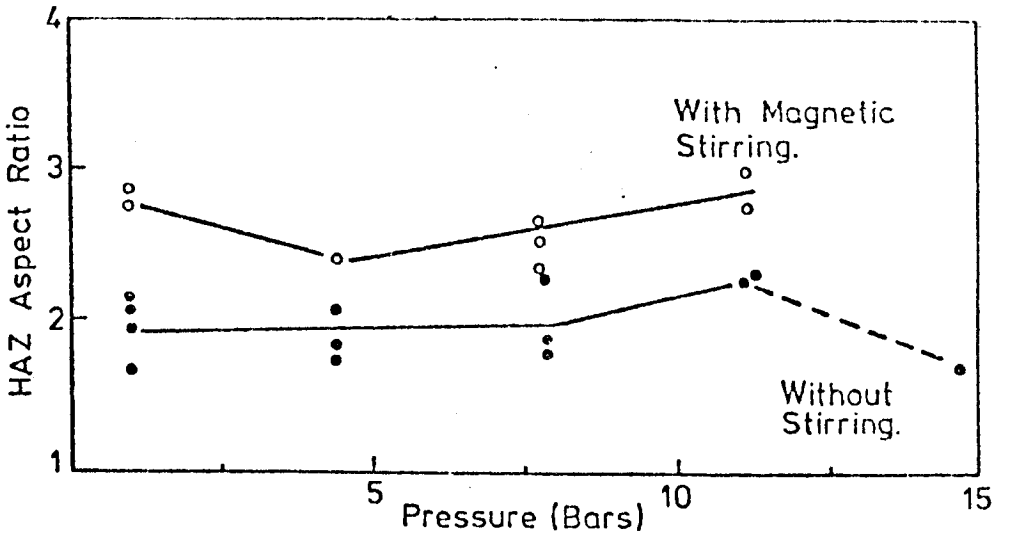

FIG. 152. INFLUENCE OF AMBIENT PRESSURE ON HAZ ASPECT RATIO FOR THE 100 A, 3mm, HELIUM TIG ARC.

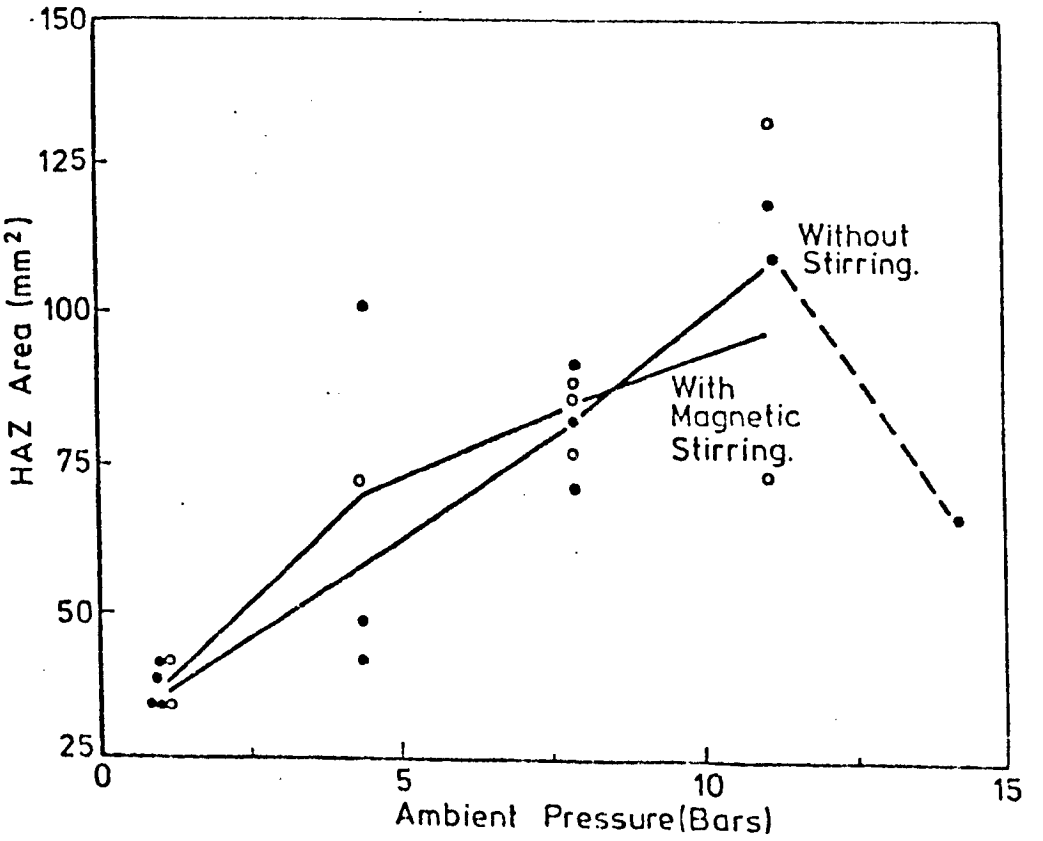

FIG. 153. INFLUENCE OF AMBIENT PRESSURE ON HAZ AREA FOR THE 100 A, 3mm, HELIUM TIG ARC.

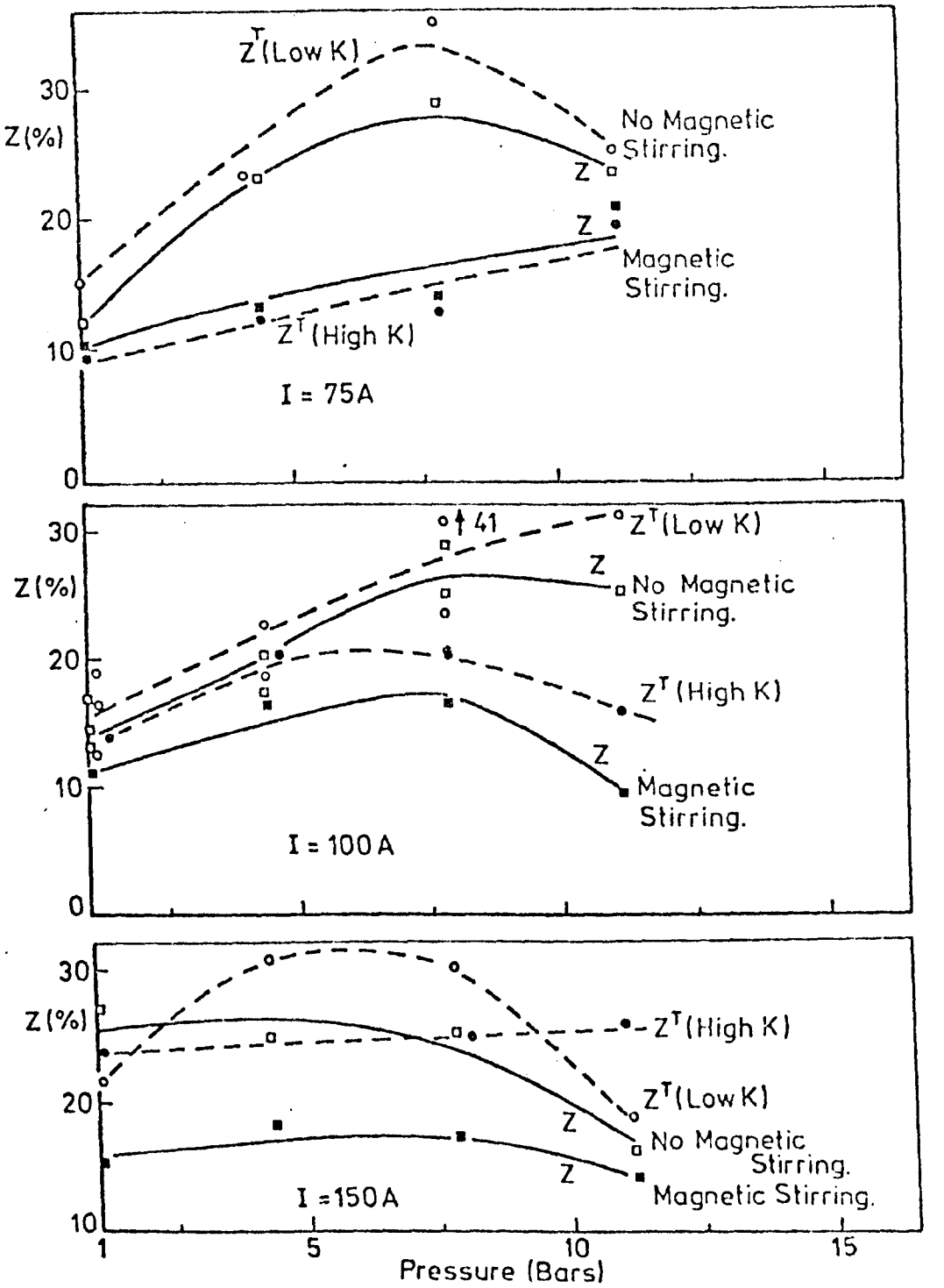

FIG. 154. INFLUENCE OF AMBIENT PRESSURE, ARC CURRENT AND MAGNETIC STIRRING ON EXPERIMENTAL (Z) AND THEORETICAL (Z^T) MELTING EFFICIENCIES FOR A 2mm HELIUM TIG ARC.

4.12.2. Influence of Process Power of Z

Melting efficiency has been plotted against process power for given values of arc current and length. Results are shown in figures 155 and 156. It can be seen that melting efficiency increases with arc power until a maximum is reached. This is followed by a decrease in melting efficiency. Such behaviour is quite general and has been observed both with and without magnetic stirring. At low powers the difference between these two cases is generally small. It is also observed that the process power at which peak efficiency occurs are the same both with and without a magnetic stirring. This power tends to increase with increasing current (see figure 156) and arc length (see figure 155) but generally lies near 2KW. A comparison is made in figure 157 between the behaviour of helium and argon arcs. It can be seen that Z increases more quickly with power in helium than in argon and that, for a given arc length and current, considerably higher efficiencies are obtained in helium.

4.12.3. Effect of Arc Length on Z

For low process powers (before the peak in Z is reached) Z is found to decrease with increasing arc length (see figure 157). This behaviour is similar to that of argon. However, after the process power corresponding to the peak in Z, long arcs become more efficient melting sources than short arcs (see figure 157).

4.12.4. Effect of Arc Current on Z

The phenomena of peaking is again observed with increasing current. Low current arcs are more efficient melting agents than high current arcs before peak power is reached. After this point high current arcs give the greatest melting efficiency (see figure 156). This behaviour also holds when a magnetic field is applied.

4.12.5. Effect of Welding Speed on Z

A limited number of runs (see figure 133) indicates that Z increases with travel speed. The increase follows a similar trend as found for argon but higher efficiencies are achieved.

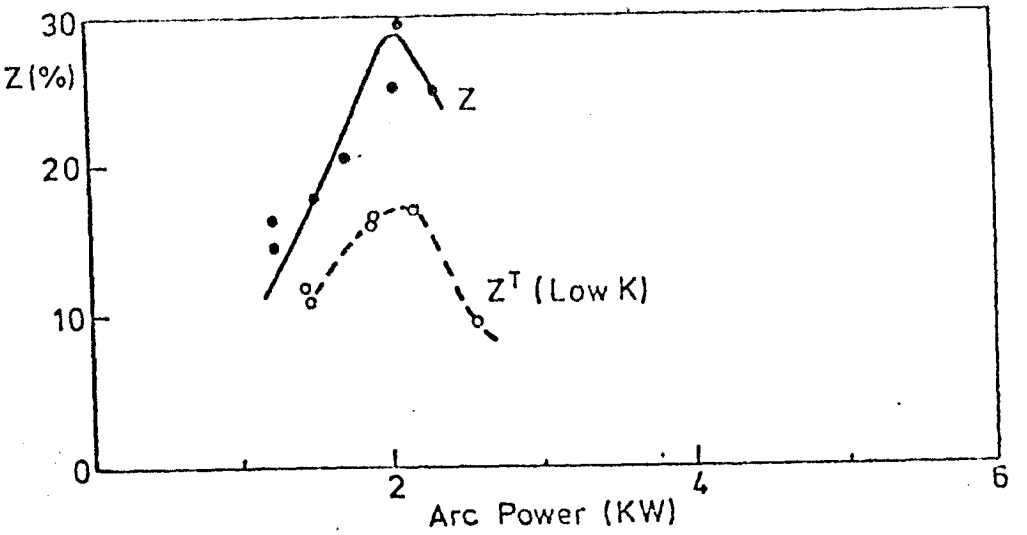

FIG. 155 (a) ℓ = 2mm.

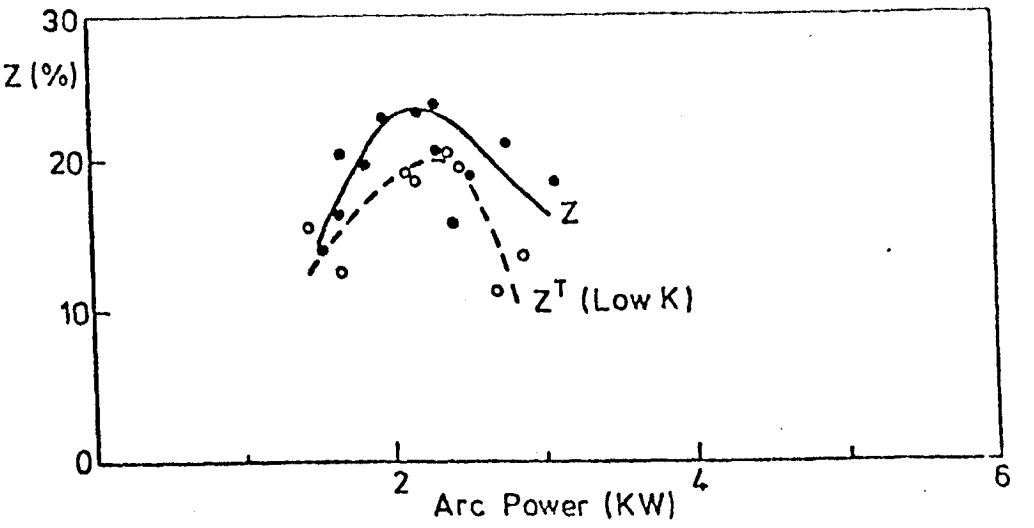

FIG. 155 (b) ℓ = 3mm.

FIG. 155. INFLUENCE OF PROCESS POWER AND ARC LENGTH ON EXPERIMENTAL (•) AND THEORETICAL (o) MELTING EFFICIENCIES FOR A 100 A, HELIUM TIG ARC.

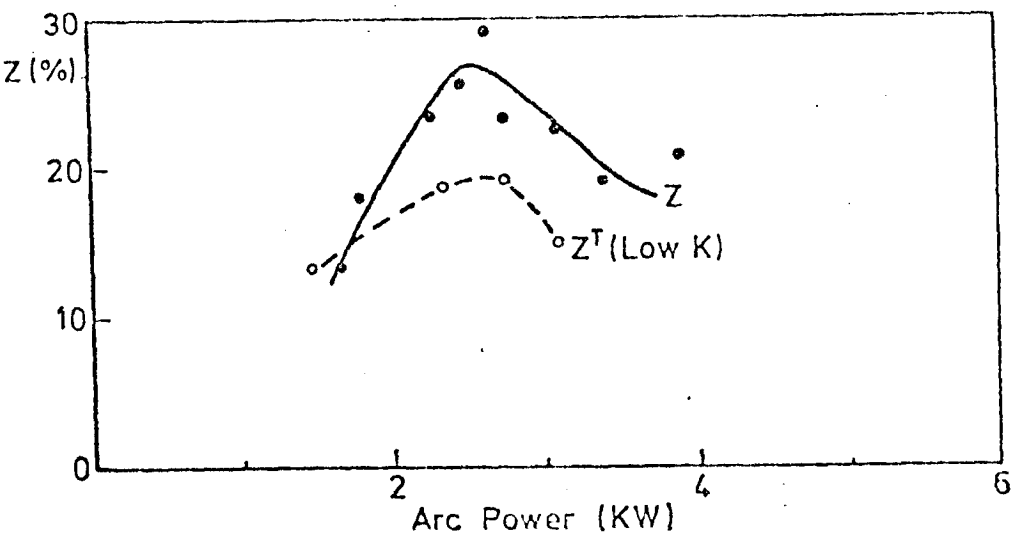

FIG. 155 (c) $\ell = 4$ mm

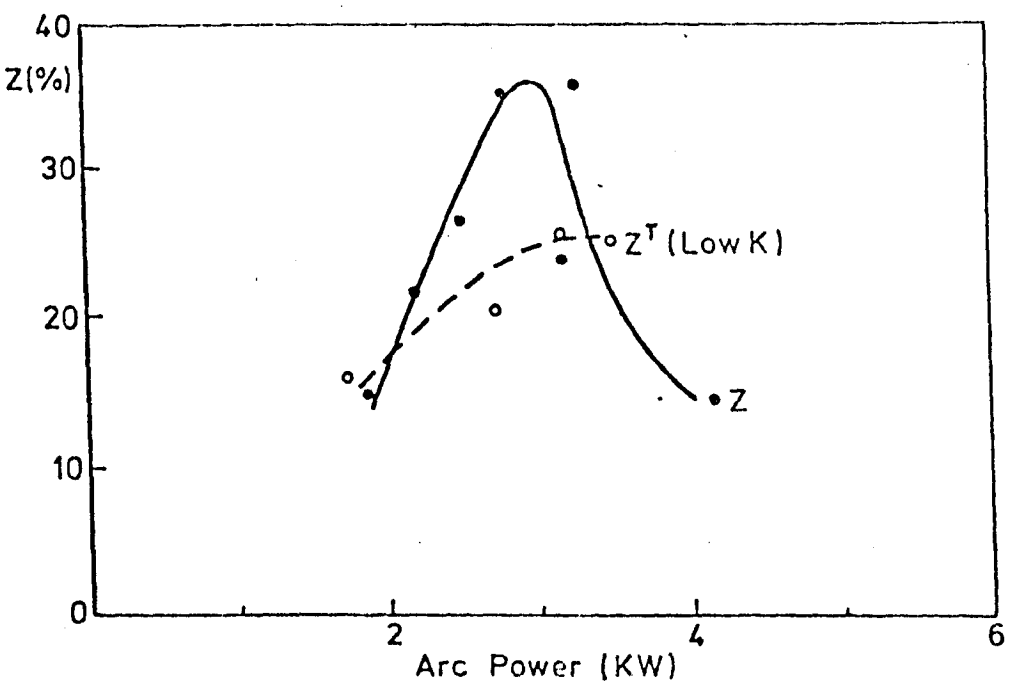

FIG. 155. (d) $\ell = 5$ mm

FIG. 155. INFLUENCE OF PROCESS POWER AND ARC LENGTH ON EXPERIMENTAL (•) AND THEORETICAL (o) MELTING EFFICIENCIES FOR A 100A, HELIUM TIG ARC.

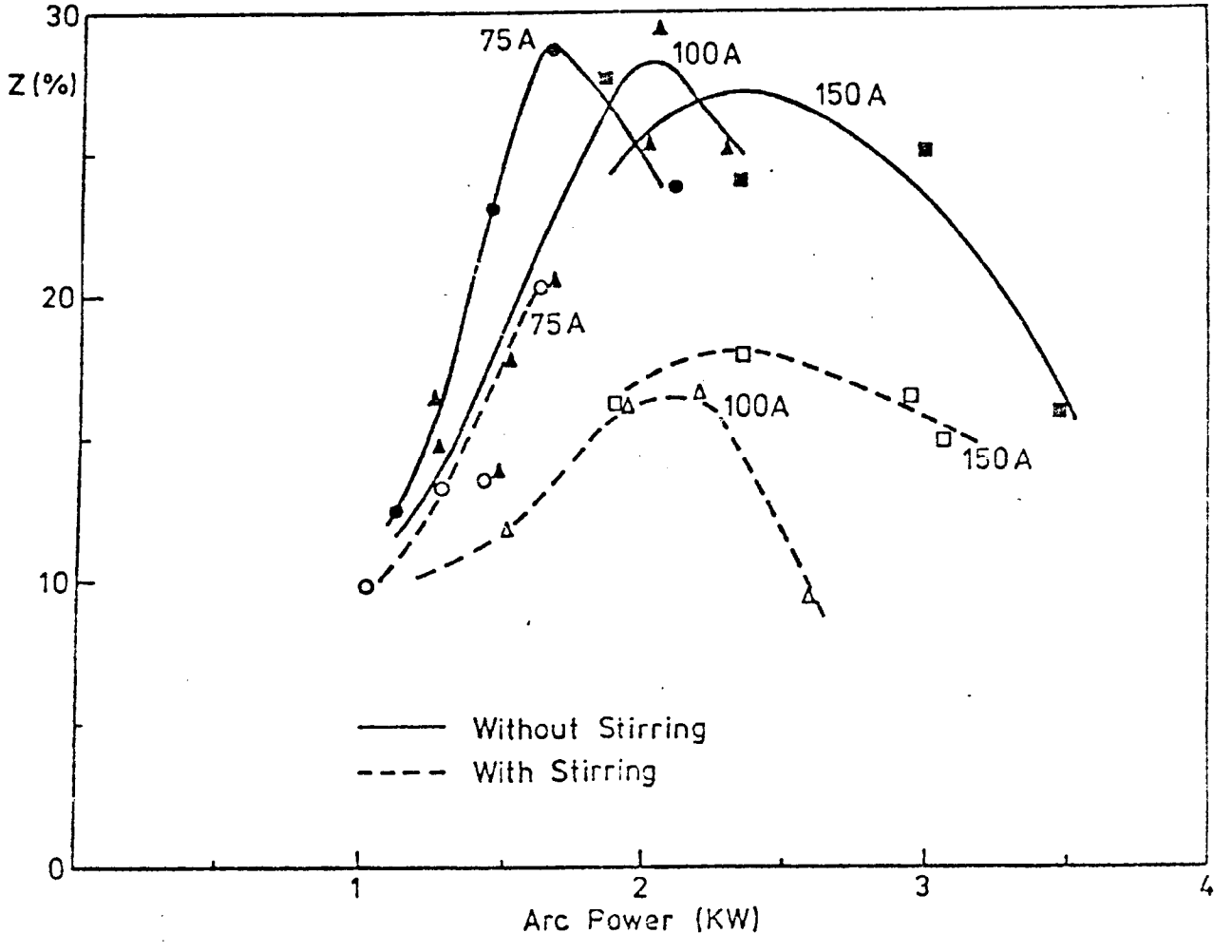

FIG. 156. INFLUENCE OF ARC POWER, ARC CURRENT AND MAGNETIC STIRRING ON THE MELTING EFFICIENCY OF 2mm, HELIUM TIG ARCS.

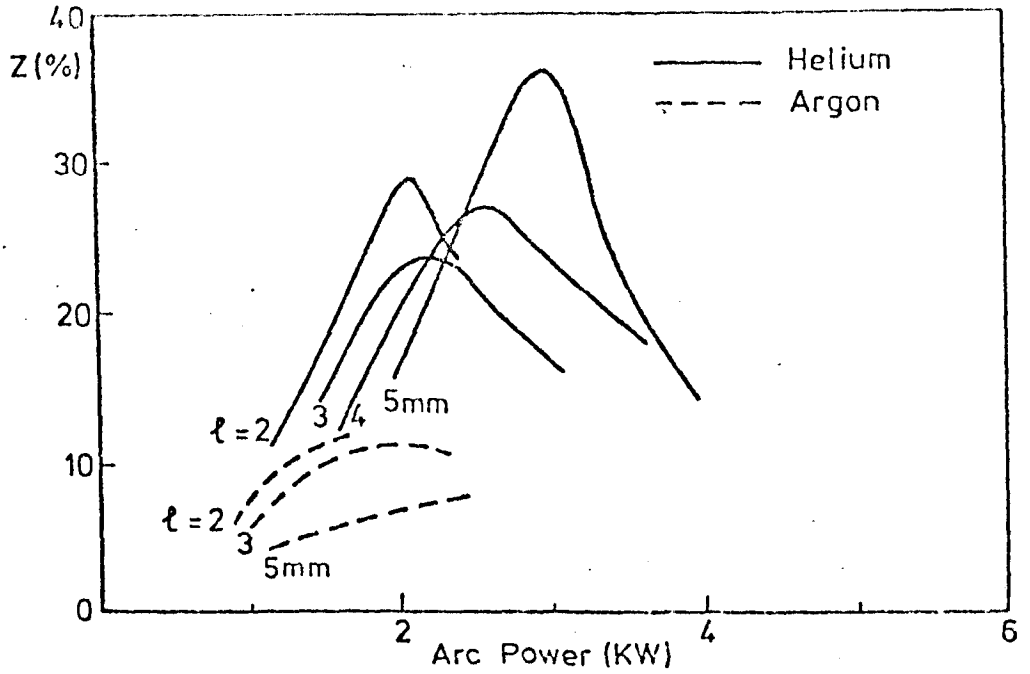

FIG. 157. INFLUENCE OF ARC POWER AND ARC LENGTH ON MELTING EFFICIENCIES FOR 100 A, ARGON AND HELIUM TIG ARCS.

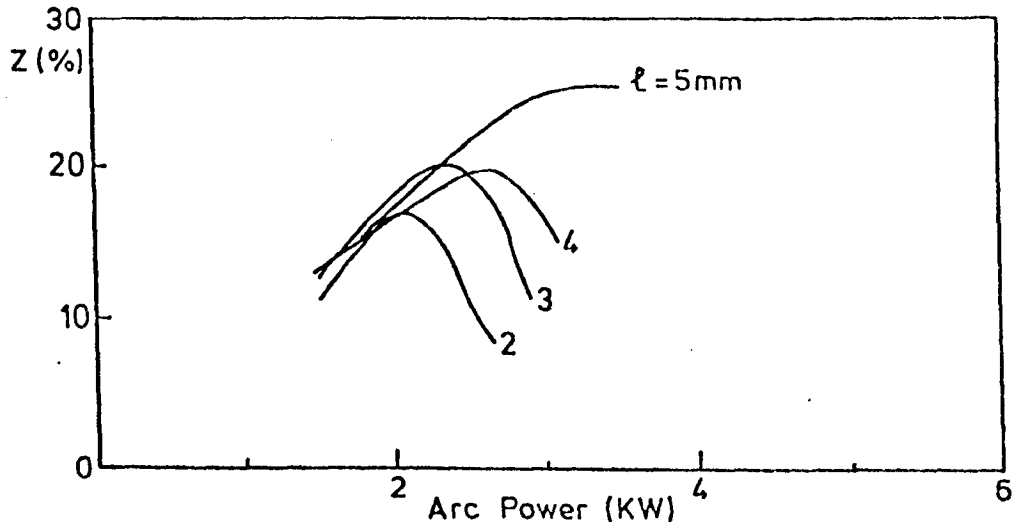

FIG. 158. INFLUENCE OF ARC POWER AND ARC LENGTH ON MELTING EFFICIENCY WHEN STIRRING IS APPLIED TO THE 100A, HELIUM TIG ARC.

4.12.6. Influence of a Magnetic Field on Z

The general characteristics with a field are similar to those without a field. However, there are a number of differences. The main difference is that melting efficiency is reduced by the application of magnetic stirring. It is also found that arc length has no influence (see figure 158) on Z for process powers lower than 2KW. At higher powers Z falls with increasing power depending on arc length. Indeed, above 2KW, Z increases with increasing arc length.

4.13. Process Efficiency Measurements from HAZ Dimensions for Helium TIG Arcs

Process efficiencies have again been estimated on the basis of HAZ widths. This procedure often lead to impossibly high process efficiencies (i.e. > 100%), especially when magnetic stirring was applied (see figure 159). Efficiencies of order 100% are thought to be the result of high aspect ratios leading to an over estimate of the effective isotherm width. However, despite this behaviour HAZ width has still been used to estimate Z^T. This is largely to maintain consistency with the analysis of argon TIG results. Further, such an analysis throws light on the suitability and consequences of using HAZ width for correlating bead characteristics.

Process efficiencies are generally found to be greater for helium arcs than argon arcs. Also, the tendency of efficiency to fall with pressure is less pronounced with helium than found for argon. Typical process efficiencies are roughly 80% and appear higher (for reasons already given) when a magnetic field is applied. The observed insensitivity of η to pressure is not unexpected on the basis of the observed strong increase in HAZ diameter with pressure. This was not found for argon.

4.14. Theoretical Melting Efficiencies (Z^T) for Helium TIG Arcs

Efficiencies obtained in the manner described above have been combined with process power to compute pool area on the basis of conductive heat transfer theory (see section 4.9). Theoretical melting efficiencies have been found and compared to experimental values and the results obtained are shown in figure 154. It can be seen that reasonable agreement is

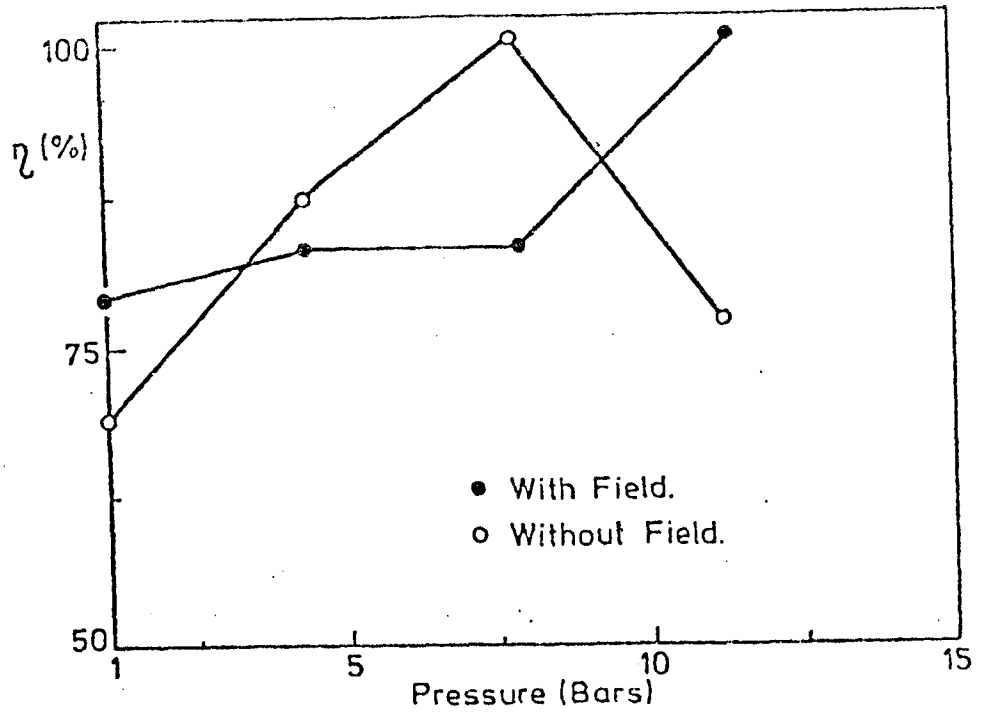

FIG. 159 (a) I = 75A

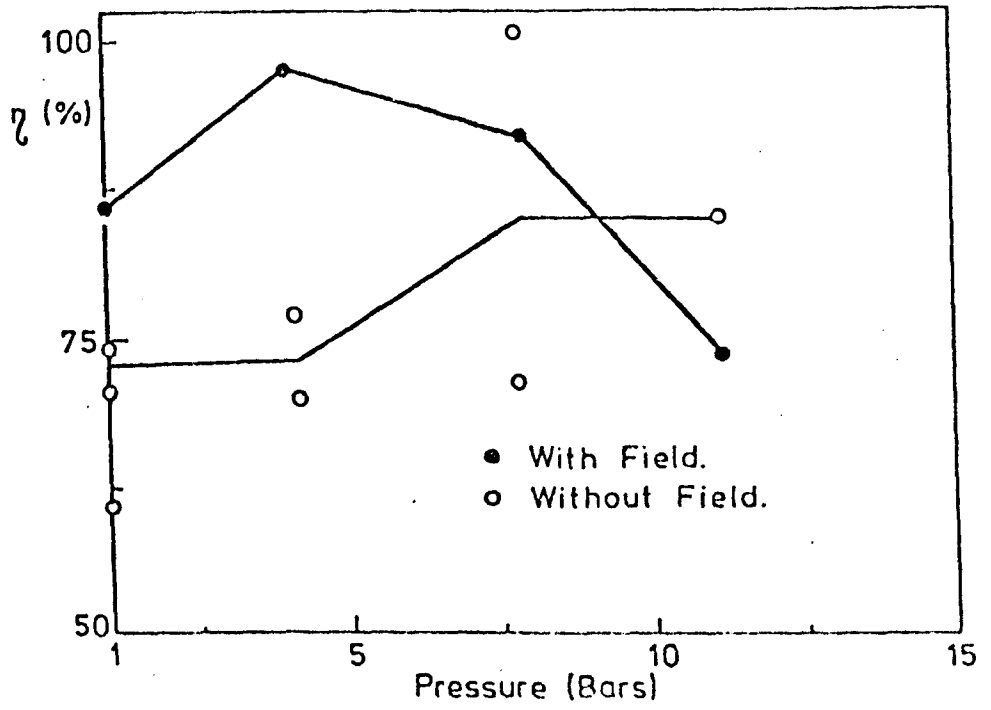

FIG. 159 (b) I = 100A

FIG. 159. INFLUENCE OF PRESSURE AND ARC CURRENT ON PROCESS EFFICIENCY * (η) FOR 2mm, HELIUM TIG ARCS. (* CALCULATED FROM HAZ DIAMETER)

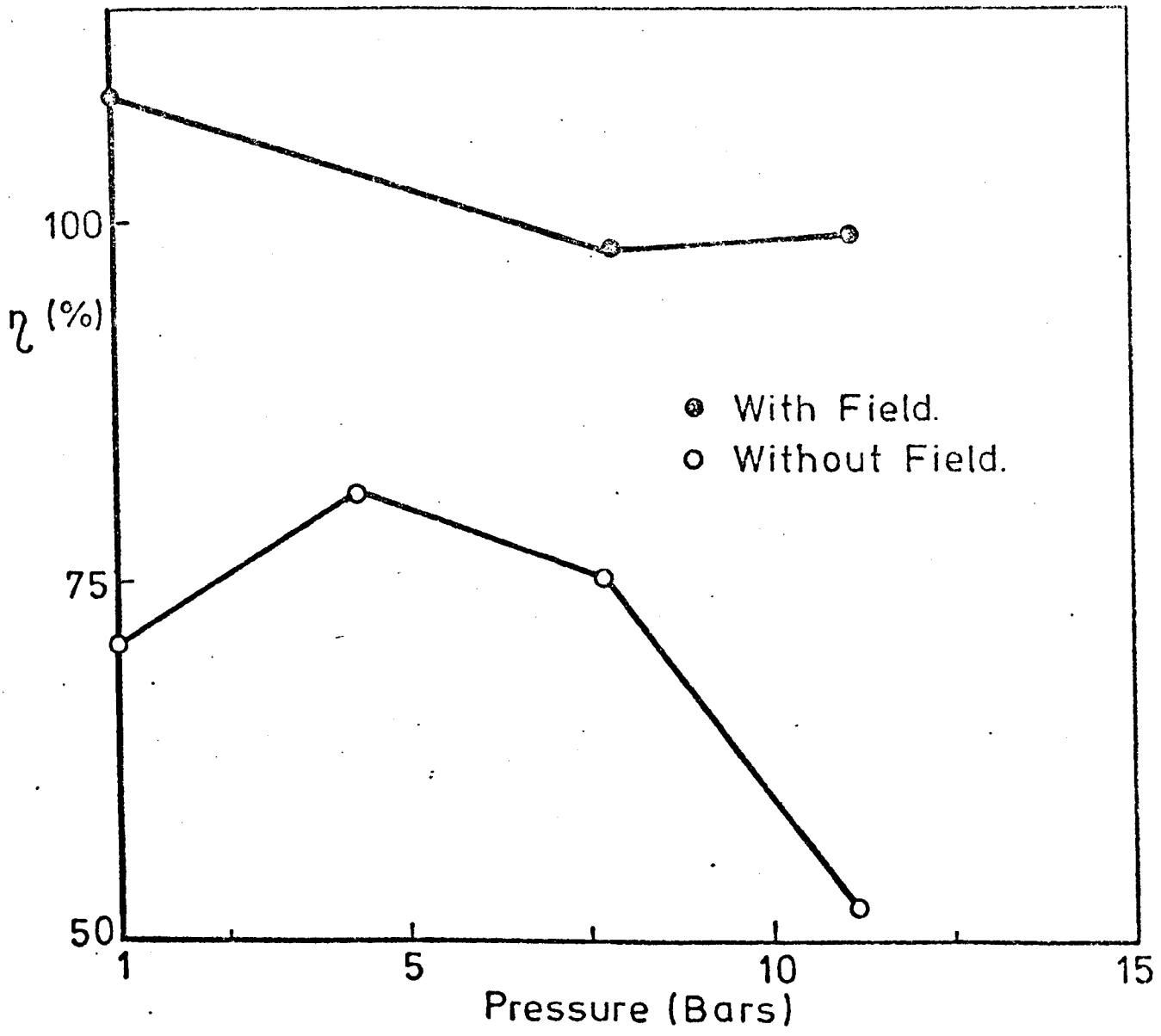

FIG. 159 (c) I = 150 A

FIG. 159. INFLUENCE OF PRESSURE AND ARC CURRENT ON PROCESS EFFICIENCY * (η) FOR 2mm, HELIUM TIG ARCS. (* CALCULATED FROM HAZ DIAMETER)

obtained despite the use of process efficiencies which are anticipated as being rather high i.e. high heat inputs. The general trends observed at each current are well represented by the theoretical predictions based on HAZ diameter measurements. Perhaps the worst agreement occurs for the 150 Amp arc with a magnet (see figure 154). However, it is more appropriate to compare these results to a high'K' model (the significance of which has yet to be discussed). If this is done then the general trend is well mirrored by the predictions. The difference in magnitude between Z and Z^T (typically about 5%) may be explained on the ground of high process efficiencies.

A more general comparison of theory and experiment is afforded by a plot of Z.I.V. versus q. Experimental values of Z.I.V. plotted against corresponding values of q (η.IV) found from HAZ dimensions are shown in figure 160. In the absence of a magnetic field fair agreement is obtained for low power arcs between experiment and theory (low 'K'). At high heat inputs points tend to fall between high 'K' and low 'K' theory. This behaviour was also found for argon TIG arcs. The application of a field has the effect of reducing Z for a given q and bringing points more into line with high 'K' theory.

4.15. The Constricted Argon - Tungsten Arc Weld Bead Geometry

Many more variables exist in the constricted arc situation than for free arcs. A full investigation of all such variables is not appropriate as the main emphasis has been on free arcs. Results presented here are for arcs on stainless steel plate moving at 3.8mm/s. This contrasts previous work, the bulk of which was on mild steel plate moving at 1.38mm/s. Heat affected zone measurements were found particularly difficult on stainless steel and are not reported. Attention is therefore confined to bead geometry.

4.15.1. Weld Bead Penetration

Weld bead penetration is found to increase with increasing pressure and arc current (see figure 161). It is also found that deeper welds were obtained using the smaller of the two constricting orifices used. The influence of gas flow on penetration is less straight forward

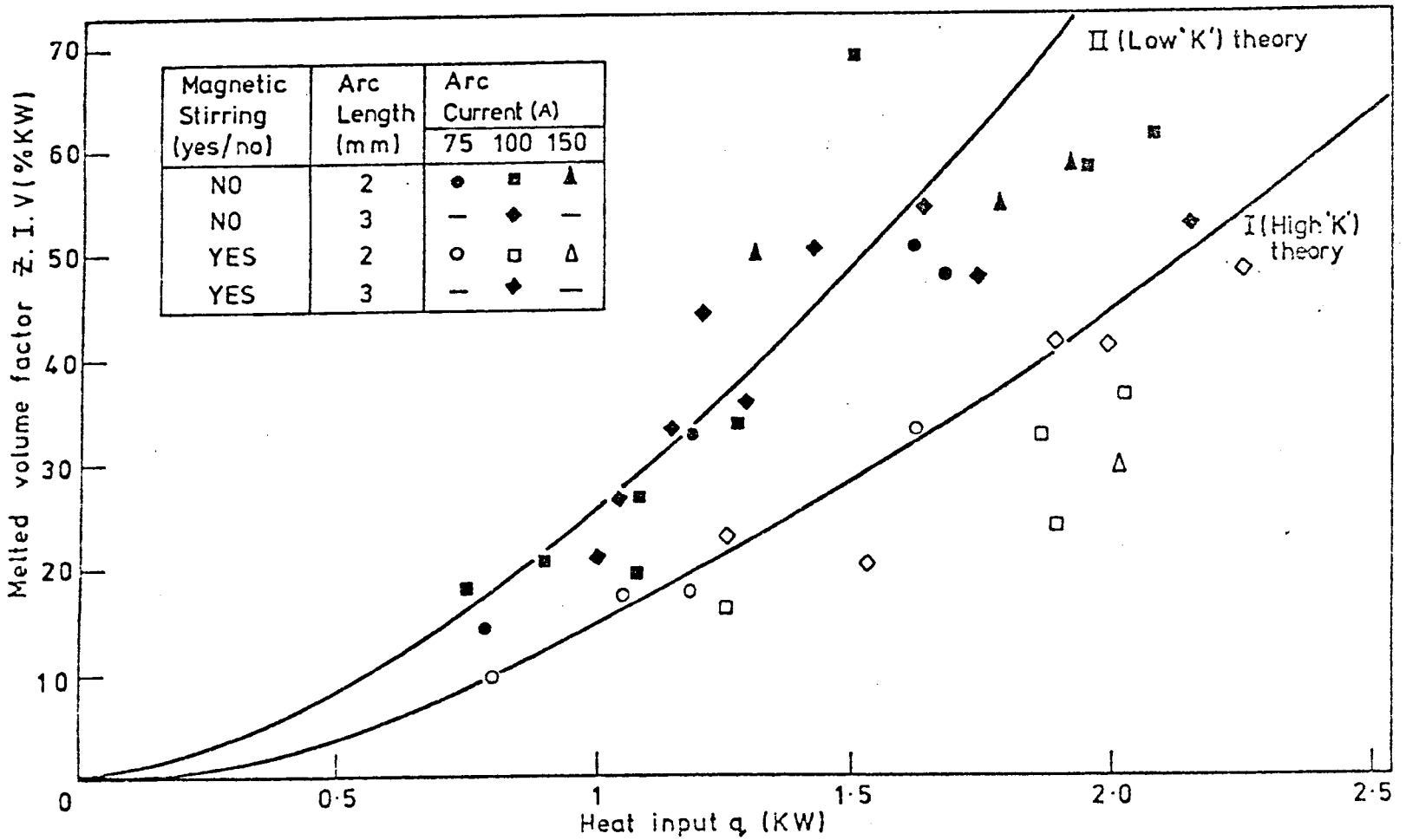

FIGURE 160. THE INFLUENCE OF WELDMENT HEAT INPUT (q) ON MELTING FOR HELIUM TIG ARCS

(see figure 162). Initially, increase in gas flow causes an increase in penetration. This behaviour is followed by a fall in penetration although further increases may occur.

4.15.2. Weld Bead Width

Weld bead width increases with both pressure and arc current (figure 162a). The major increase is found to occur over the first 8 bars with only small increases occurring thereafter. This behaviour is found for all currents examined. Also bead width is largest for the smallest orifice used (i.e. 3.2mm diameter). Increasing gas flow (figure 162b) has the effect of marginally decreasing weld bead width (behaviour at 4.4 bars is an exception to this rule).

4.15.3. Weld Bead Area

Weld bead area increases with pressure and current as shown in figures 163a) and 163b). Fusion area changes with plasma flow rate are less well defined. Generally speaking only small (pressure dependent) changes occurred with a tendency to increase at 1 bar and decrease at 14 bars.

4.15.4. Melting Efficiencies with Constricted Argon-Tungsten Arcs

Melting efficiency behaves in a manner similar to fusion area. This factor increases with both pressure (figure 164a) and current (figure 164b). Increasing gas flow (figure 164c) causes Z to fall with the exception of atmospheric values.

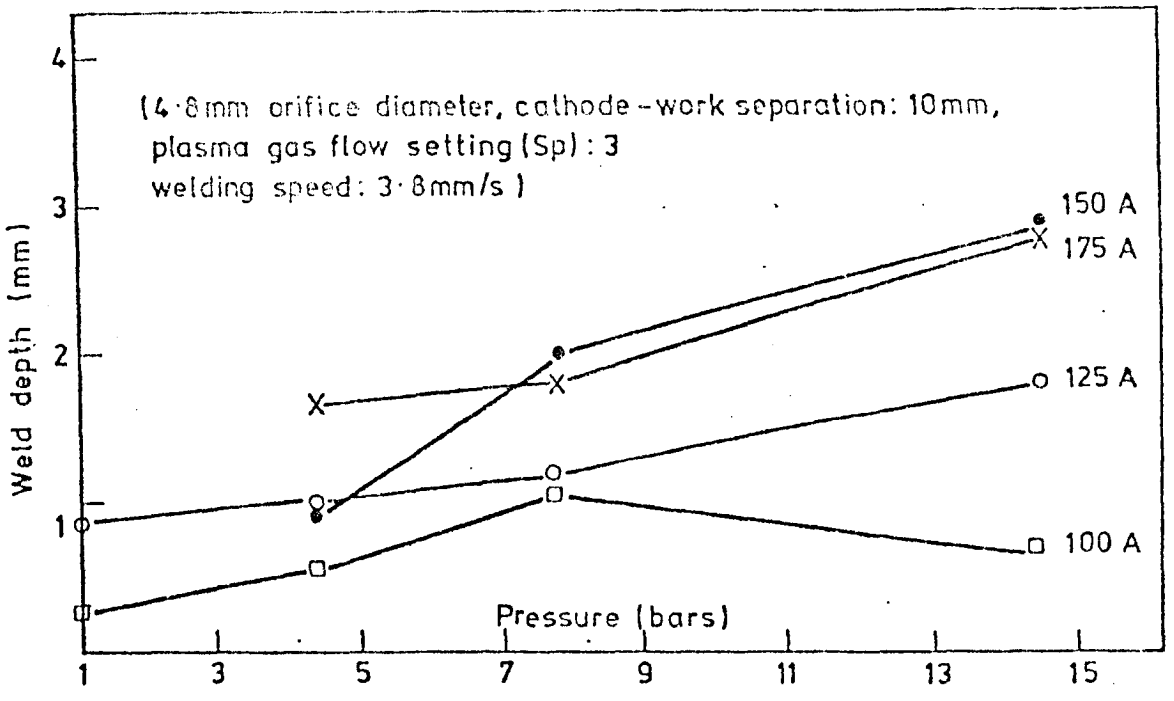

FIGURE 161a, INFLUENCE OF AMBIENT PRESSURE AND ARC CURRENT ON WELD BEAD PENETRATION IN PLASMA WELDING.

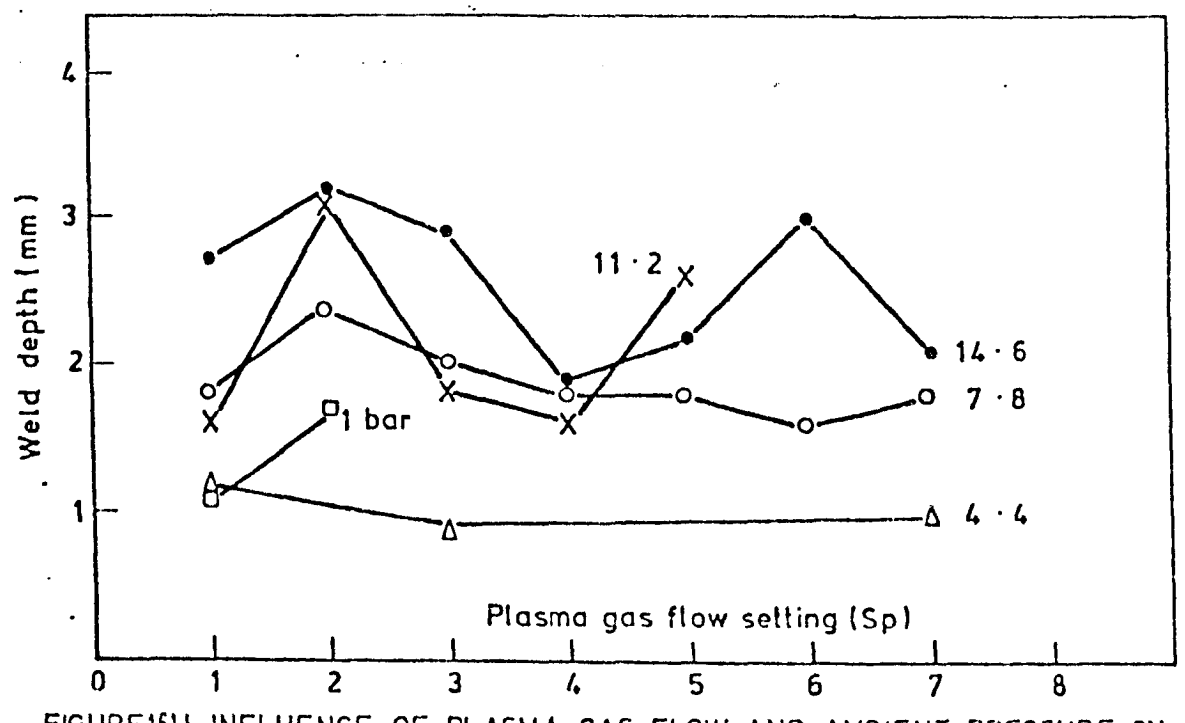

FIGURE 161b. INFLUENCE OF PLASMA GAS FLOW AND AMBIENT PRESSURE ON WELD BEAD PENETRATION IN PLASMA WELDING (I = 150 A) (OTHER CONDITION ARE AS FOR FIGURE 161a,).

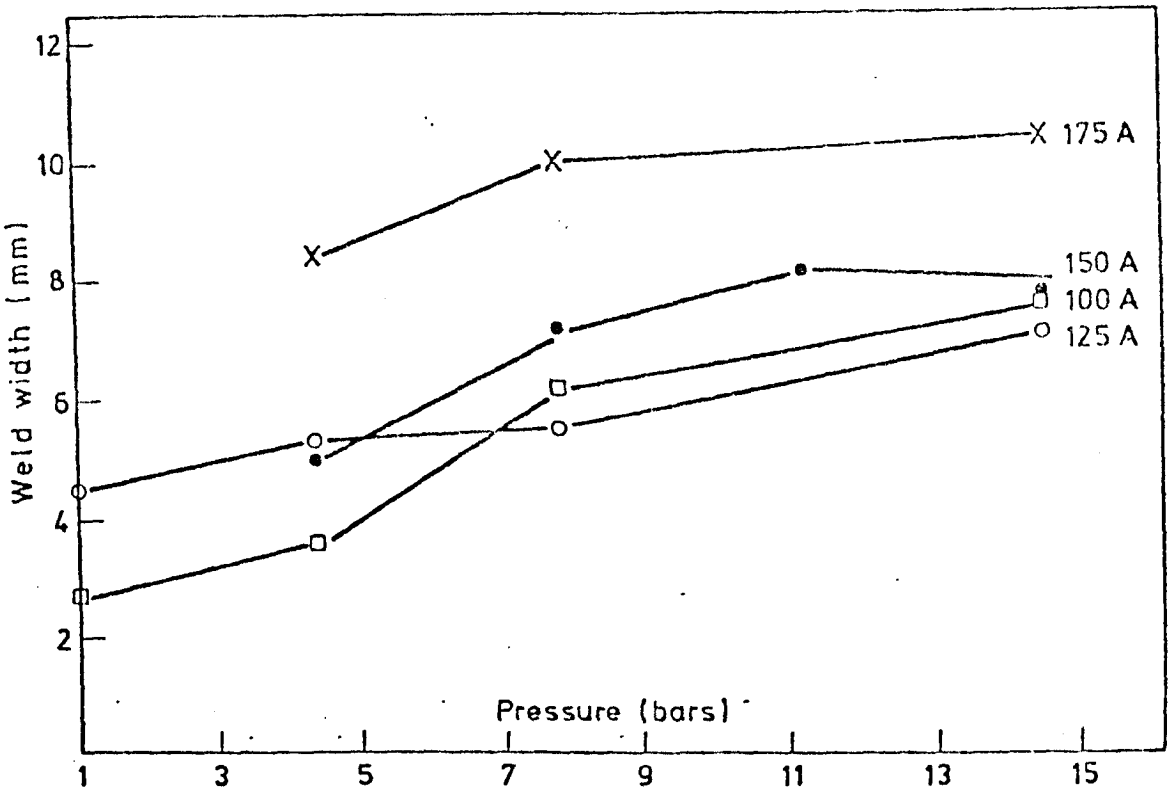

FIGURE 162a. INFLUENCE OF AMBIENT PRESSURE AND ARC CURRENT ON WELD BEAD WIDTH IN PLASMA WELDING. (SAME CONDITIONS AS IN FIGURE 161a).

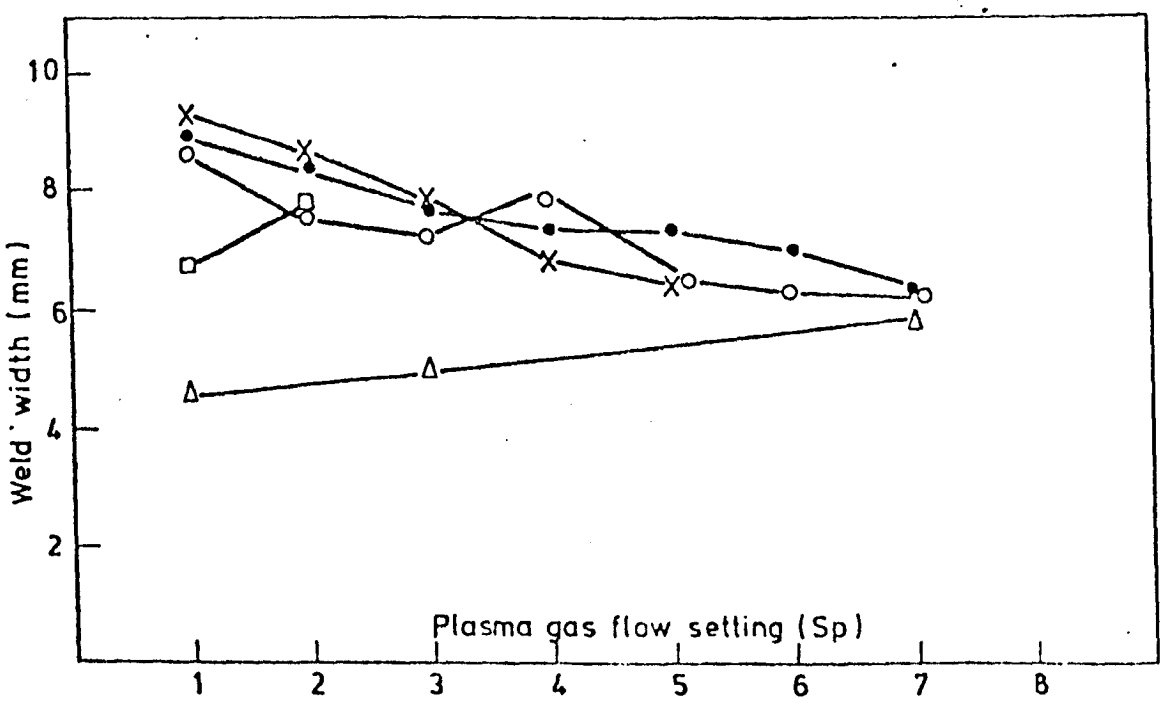

FIGURE 162b. INFLUENCE OF PLASMA GAS FLOW RATE AND AMBIENT PRESSURE ON WELD BEAD WIDTH IN PLASMA WELDING (I = 150A) (SAME CONDITIONS AND NOTATION AS USED IN FIGURE 161b).

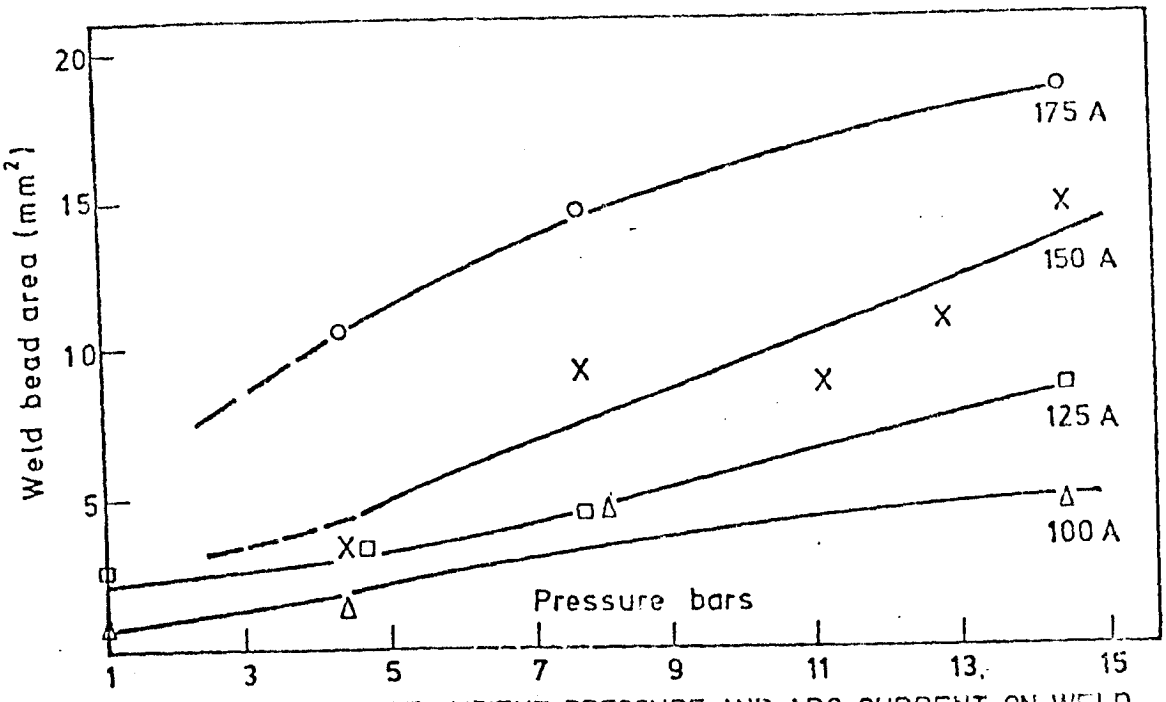

FIGURE 163a. INFLUENCE OF AMBIENT PRESSURE AND ARC CURRENT ON WELD BEAD AREA IN PLASMA WELDING. (CONDITIONS AS GIVEN IN FIGURE 161a)

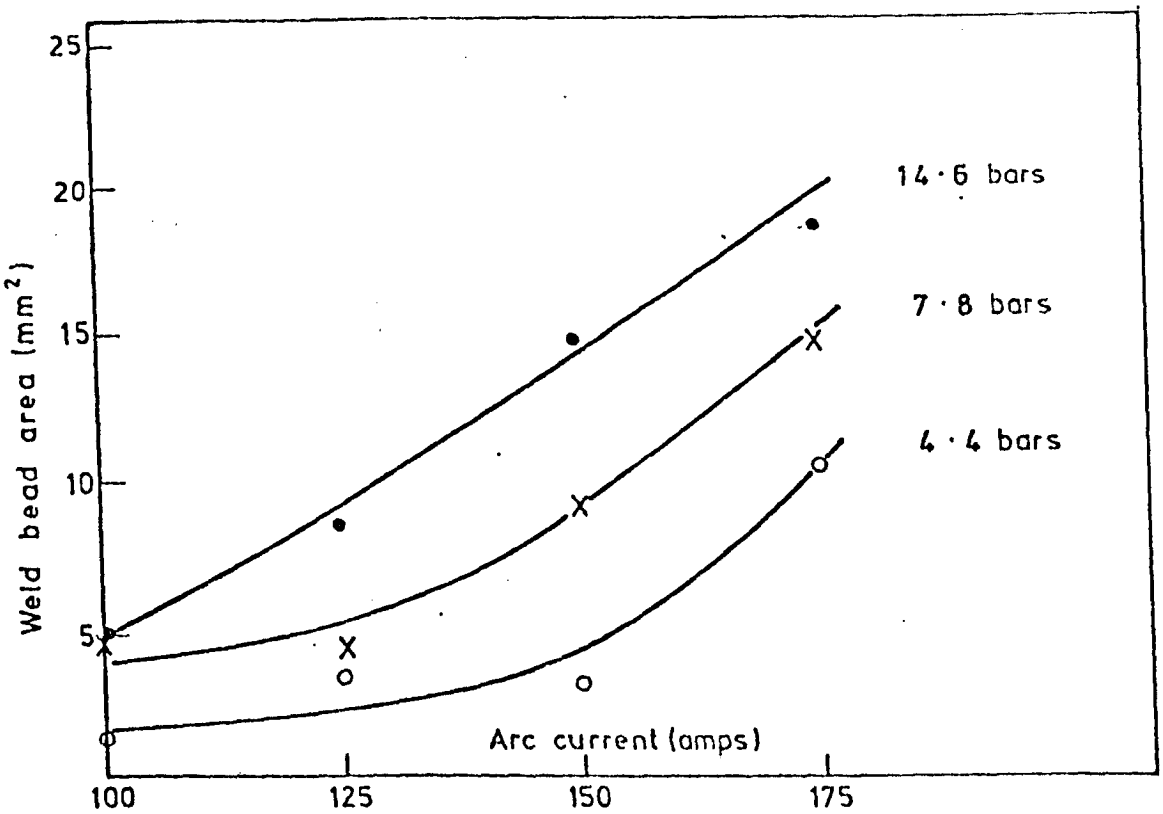

FIGURE 163b. INFLUENCE OF ARC CURRENT AND AMBIENT PRESSURE ON WELD BEAD AREA (CONDITIONS AS GIVEN IN FIGURE 161a).

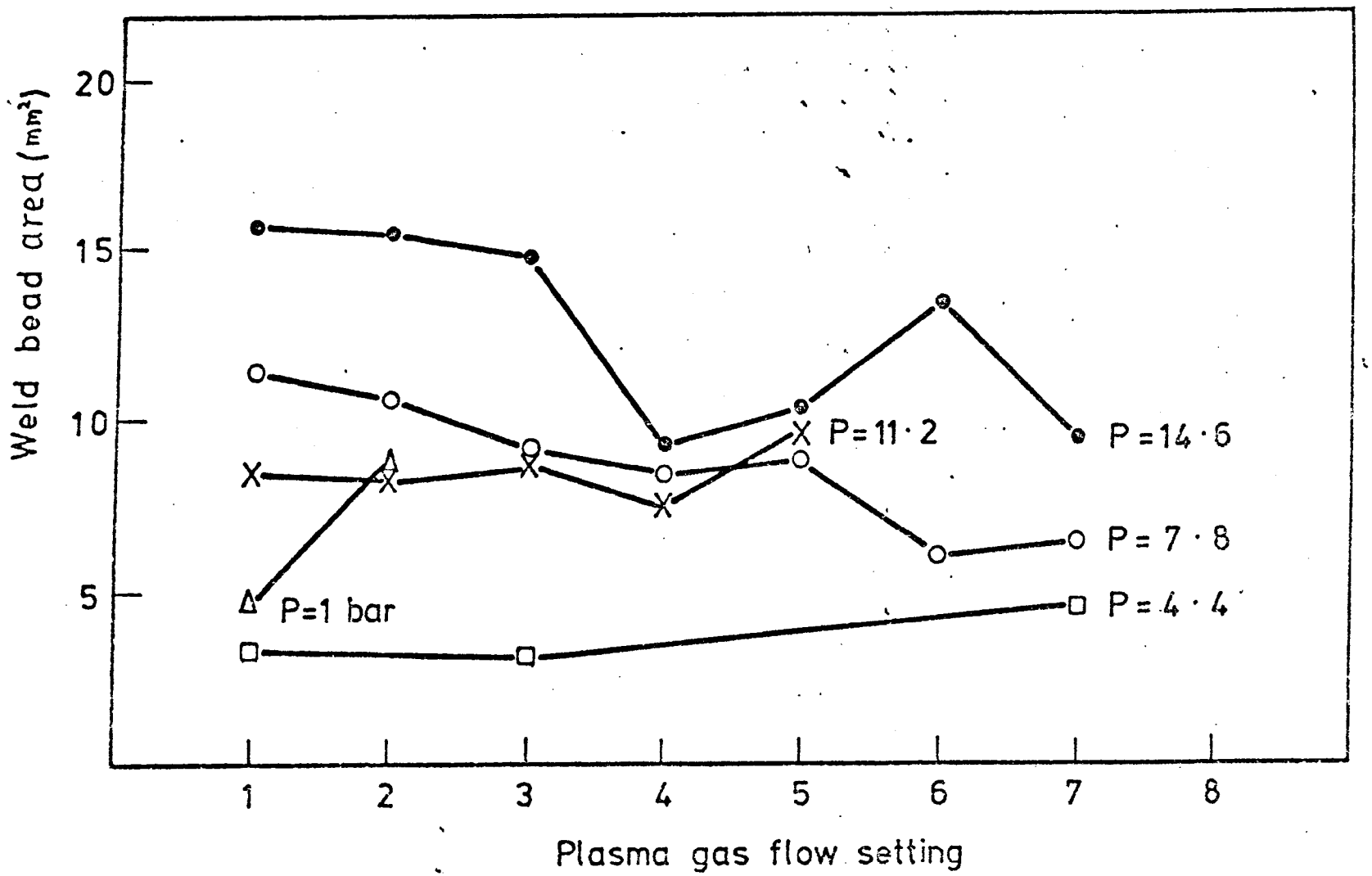

FIGURE 163c. INFLUENCE OF PLASMA GAS FLOW RATE AND AMBIENT PRESSURE ON WELD BEAD AREA IN PLASMA WELDING (I = 150A). (OTHER CONDITIONS AS GIVEN IN FIGURE 161a.).

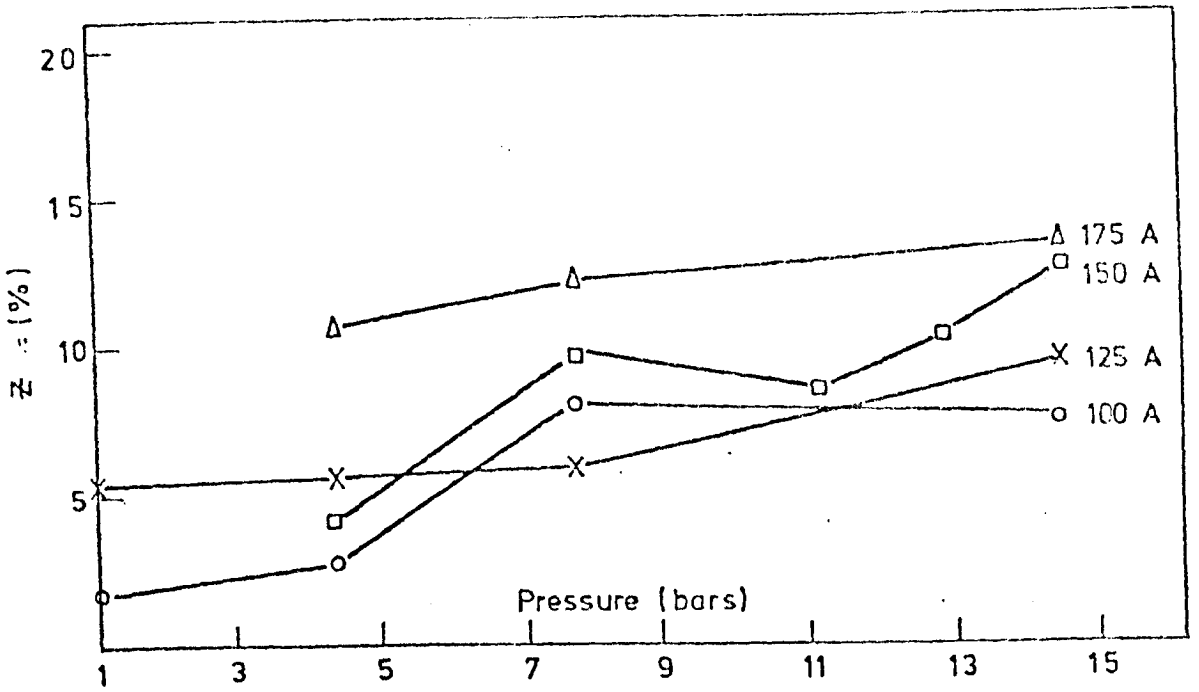

FIGURE 164a. INFLUENCE OF AMBIENT PRESSURE AND ARC CURRENT ON MELTING EFFICIENCY IN PLASMA WELDING. (CONDITIONS AS GIVEN IN FIGURE 161a.).

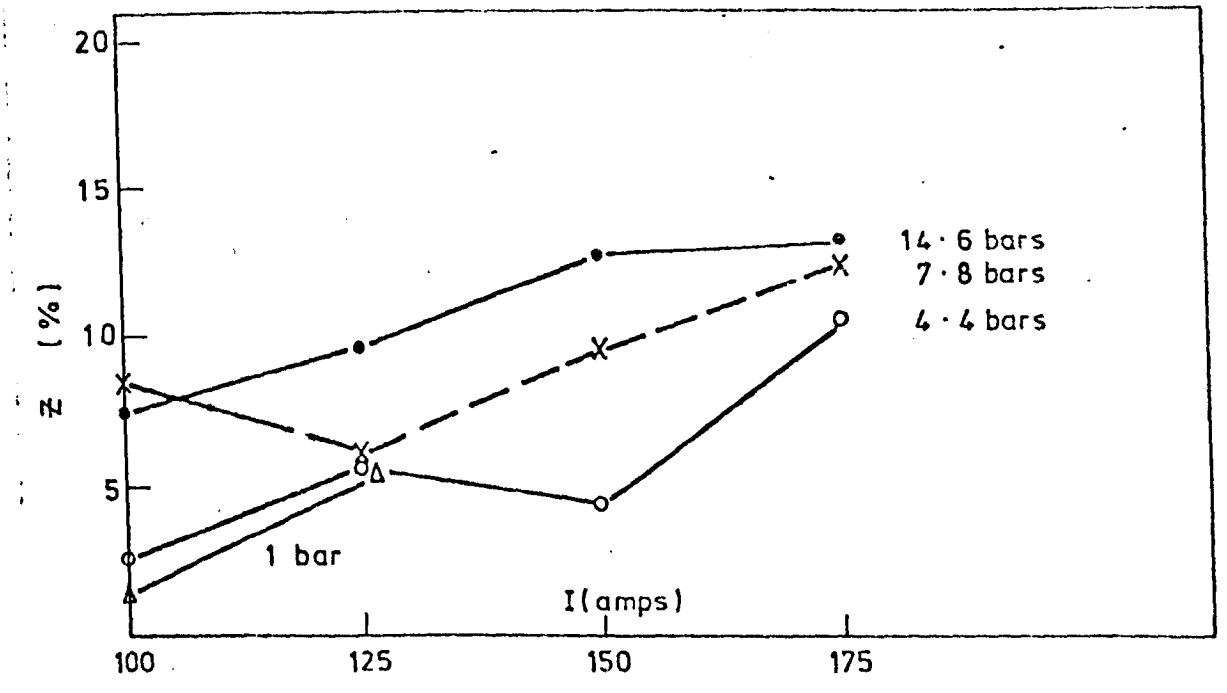

FIGURE 164b. INFLUENCE OF ARC CURRENT AND AMBIENT PRESSURE ON MELTING EFFICIENCY IN PLASMA WELDING. (CONDITIONS AS GIVEN IN FIGURE. 161a.).

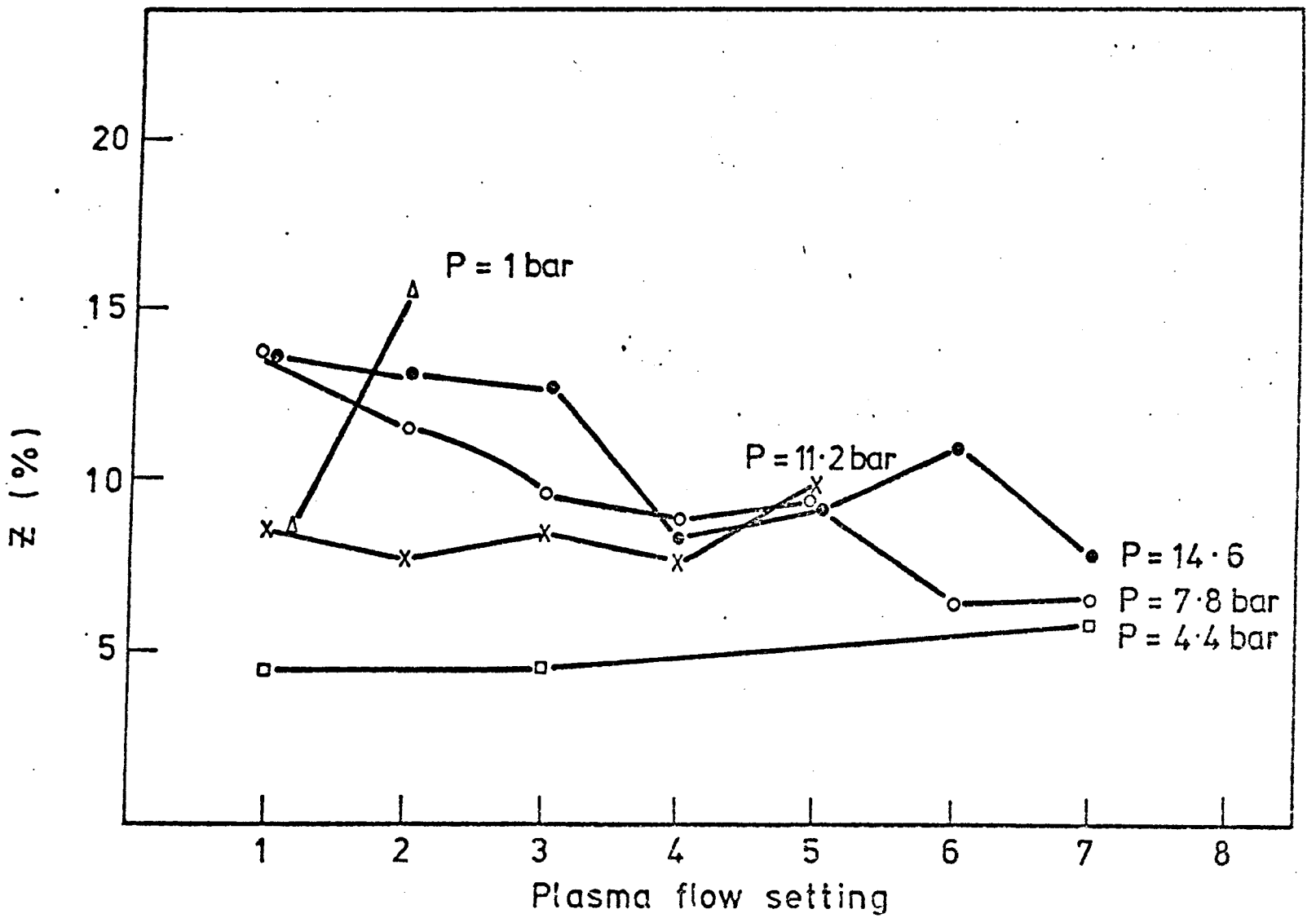

FIGURE 164c. INFLUENCE OF PLASMA FLOW RATE AND AMBIENT PRESSURE ON MELTING EFFICIENCY IN PLASMA WELDING (I = 150A) (OTHER CONDITIONS AS GIVEN IN FIGURE 161 b).

Cranfield Institute
of Technology

C.J.Allum

Characteristics and Structure of High Pressure (1-42Bars) Gas Tungsten Arcs

Volume 2

School of Industrial Science

Ph.d. Thesis

5. Discussion of Characteristics

5. DISCUSSION OF CHARACTERISTICS

5.1. Introduction

Many varied and complex phenomena compete to produce the observed arc and weld pool characteristics. To understand these, further experiments of a structural nature are required. Experiments of this type are reported in section 6 and discussed in sections 7 and 8. In this section a discussion of characteristics is given. The major aims of this discussion are:

i) To compare the results obtained using different arc forms.

ii) To emphasise the results considered to be of particular importance and to compare these, where possible, with previous investigations.

iii) Develop models capable of explaining results presented here.

iv) To identify regions where further experiments of a structural nature may prove useful.

Factors (i) to (iv) are considered roughly in this order but such a format is not strictly adhered to. Indeed, in places it is found more appropriate to include this material in sections on 'Discussion of Structure' and 'General Discussion'.

5.2. Arc Appearance and Arc Modes

It is generally observed that the effect of increasing pressure is to reduce arc cross-section; increase arc luminousity, promote instabilities and influence other factors such as arc rooting. These observations are not new and have been reported by a number of researchers (see literature survey). However, very little information (and usually of a qualitative nature) is generally given and no quantitative understanding of these observations presently exists. The extent to which a high pressure arc exhibits the above pressure dependence is strongly dependent on the arc form considered.

The atmospheric argon TIG arc is stable and jet like in appearance with an outer penumbra. It is known that at lower pressures (below atmospheric) the arc may appear ball shaped and diffuse. As pressure is increased the arc column contracts and the outer penumbra disappears

(at about 3 bars). Measurements made here indicate that column contraction obeys a $p^{-0.17}$ law for pressures below 15 bars. This behaviour is dependent on other factors such as shielding gas flow rate. The shielding gas flow may also generate arc column instabilities. At pressures above 30 bars column instabilities appear even in the absence of a shielding gas flow. Despite the reduction in arc cross-section the column appears 'flappy' and less directional. This suggests that the stabilising jet present under normal atmospheric conditions is less effective at higher pressures. It is interesting to compare this behaviour with that observed for helium TIG arcs. The atmospheric helium arc is diffuse and ball shaped appearing similar to the low pressure argon arc. A strong jet, similar to that of the atmospheric TIG arc, is formed as ambient pressure is increased above atmospheric. At pressures of order 10 bars 'self-pulsating' arcs were observed. These were associated with tungsten erosion at the cathode and the consequent reduction in arc ionization potential. In contrast to these arc forms, the constricted argon TIG arc remained stable over the range investigated (1-14 bars). Arc diameter changed in a complicated manner with pressure due to the influences of plasma gas flow, orifice diameter and arc current. For this arc form shielding gas flow had no noticeable influence on behaviour. Any general theory of the column must clearly explain the observed changes in arc dimensions and stability. An explanation must also be given as to why the constricted arc is more stable than the unconstricted.

Anode characteristics are affected by, and have an effect on, column behaviour. Argon arcs on copper anodes are found to be much less stable than the corresponding arcs on steel anodes. Clearly vapourization is influencing arc rooting. The influence of anode characteristics is most pronounced when considering discontinuous arc rooting movements over the anode surface. These have previously been reported under normal ambient conditions by a number of workers (see section 2). For low speed anodes ($\sim$mm's/sec) this mode is only observed at low currents. However, the same mode has been observed on high speed anodes (m/s) at currents of order 200 Amps (9). It is generally found that the threshold current above which this behaviour disappears increases with increasing arc length. This corresponds to

a weaker cathodic jet at the anode. Indeed highly constricted anode roots gives rise to anode jets that interact with the cathode jet to produce the observed arc form. Matsunawa and Nishiguchi (10) have previously observed that the threshold current increases with pressure for an argon arc on a copper anode. This observation is in agreement with that found here. A number of further observations have been made here. On copper anodes this behaviour disappears entirely near about 8 bars for all arc lengths investigated (up to 10mm). The most interesting result concerns the observed pressure dependence of this phenomena on mild steel anodes. For this material the pressure dependence is in the opposite direction to that found on copper. The threshold current for a given arc length decreases with increasing pressure. It is also found that this behaviour is absent when welding in the overhead position for pressures greater than atmospheric with argon arcs on steel. This indicates that buoyancy is influencing arc rooting. In contrast to the above behaviour the helium TIG arc always exhibited a continuous anode root even at very low currents (down to 15A). The helium root was in every case a highly constricted single anode spot while argon arcs often exhibited multiple spots.

On steel I_C decreases as:- pressure increases, arc length is reduced, and when buoyancy forces act with the arc jet. The last two effects produce a stronger arc jet. This promotes vapourization and keeps vapour in the vicinity of the anode. The corresponding value of I_C is lower on steel than on copper again indicating that the presence of vapour lowers I_C. On high speed anodes (say > 1 m/s) the arc passes over an anode region in about 1ms. This is roughly equal to heat conduction time scales and so much less vapourization is expected to occur. I_C is then expected to increase (as observed). The absence of this mode for helium arcs may be explained by postulating that the anode heating density is always high enough to produce sufficient ions for the effect not to occur. The above theory would suggest that I_C should always decrease with increasing pressure (due to increasing current density). However, it is observed to increase on copper. A possible explanation of this effect may be associated with a reduction in arc jet velocity with pressure, thereby allowing vapour to migrate more readily away from the anode region. This has previously been used to explain observations at 1 bar (82). Such a reduction in arc momentum is

expected due to a competing buoyancy generated jet acting away from the anode (see section 8). Further indications of the importance of the arc jet may be inferred from the fact that the discrete rooting behaviour always occurs on the negative arm of the V-I curve (i.e. before the current is high enough for a strong jet to develop).

A degree of melting was generally observed at the cathode. This resulted in gross erosion for small diameter electrodes in argon TIG welding. With larger diameter electrodes (≥3.2mm) only local melting at the electrode tip occurred. This was not usually accompanied by tungsten transfer. For helium arcs erosion was observed even with large electrodes. At pressures above about 10 bars this resulted in a 'self-pulsing' arc mode. The cathodic behaviour reported above may be explained if more heat enters the cathode, if the density of cathodic heating increases or if both these mechanisms come into play. A simple energy balance at the cathode indicates that the total cathode heating is relatively unaffected by pressure.

Consider a very short arc with negligible power appearing in the column. The power appearing at the cathode is then given by

$$\begin{aligned} Q \text{ (cathode)} &\simeq Q \text{ (zero arc length power)} - Q \text{ (anode)} \\ &\simeq I\,(V_C + V_a) - I\,(V_a + \phi + V_T) \end{aligned}$$

Where equation 25 has been used

$$\therefore Q \text{ (cathode)} \simeq I.(V_C - \phi - V_T) \qquad (107)$$

ϕ and V_C are the dominant terms in this expression. Therefore, cathode heating is expected to be little influenced by pressure since V_C is largely unaffected by pressure (see section 6.4). Melting of the cathode is therefore thought to be the result of a greater intensity of electrode heating. This is completely in line with the observed contraction of the arc root at the cathode.

Simple theoretical considerations may be used to indicate why contraction might be expected. The fact that electrode melting is observed at high pressures indicatesthe existence of higher tip temperatures than at 1 bar. Considerably higher temperatures might

actually exist due to the known increase in boiling point with pressure allowing higher maximum temperatures to be sustained. The Richardson-Dushmann expression (see equation 35) then indicates that the thermionic current density increases and hence contraction can be expected. Another approach is to consider the pressure dependence of behaviour described by the Child-Langmuir expression (see equation 22) or the Debye length (equation 2). From equation 22 the current density (J) is expected to behave very roughly as

$$J \propto V^{3/2} \cdot d^{-2}$$

Where V is the fall voltage and d the extent of the sheath. Experiments indicate that V is independent of pressure. Consideration of equation 2 - see section 5.3 - shows that d probably decreases as $P^{-\frac{1}{4}}$. On this basis the cathode spot radius (R_c) is expected to decrease as:

$$R_c \propto p^{-1/4}$$

This compares with the value

$$R_c \propto p^{-1/7}$$

found experimentally.

5.3. Electrical Characteristics

A detailed account of electrical characteristics was given in section 4.2. It was found that the pressure dependence of arc voltage is largely a result of changes in the column component. The sum of anode and cathode voltages remains substantially unaffected for all arc forms considered. The main variables influencing arc voltage are ambient pressure, gas composition, welding process, electrode separation, current and shielding gas flow rate. For short arcs the dependence on arc length (ℓ) is linear and may be presented by an expression of the form $E.\ell$ where E is the Electric field strength. It is found that E has a roughly square root dependence on pressure for a wide range of arcing conditions. The exact form of this dependence is influenced by factors such as shielding gas type and flow rate, arc current and anode composition. Detailed considerations indicate that E increases with arc current and shielding gas flow rate. However, E is

lower on vapourizing anodes than on non vapourizing anodes (i.e. cooled copper anodes). Voltage mirrors energy exchanges within the arc and so a detailed understanding of results presented in section 4.2 may only be gained by considering such exchanges. The approach adopted in this section is to develop simple energy balance equations and to compare the behaviour predicted by these, with that observed experimentally.

Before doing this some attention is given to the behaviour of the zero electrode separation voltage (V_o). This is substantially independent of pressure but shows a consistent trend for lower values on steel anodes than on copper anodes (i.e. by about 2V). Clearly no detailed comments can be made (on the basis of this data) concerning the influence of pressure on the components of V_o - the anode and cathode falls. However, electrostatic probe measurements reported in section 6.4 show that both V_c and V_a are substantially independent of pressure. It is also found that V_c is independent of arc length and so changes in V_o with pressure may be attributed to anodic behaviour. The pressure independence of V_c and V_a is not surprising in view of the nature of the anode and cathode falls. Both these regions are effectively collisionless (see below) and therefore only sense 'pressure' in terms of 'end effects' i.e. changes in boundary conditions at the column end of the anode and cathode falls.

A number of interesting conclusions may be drawn from this behaviour. The electric field strength increases in both regions with pressure. This indicates that the anode and cathode fall voltages are insensitive to changes in field strength. An estimate of the pressure dependence of the electric field strength, E, may be given by considering sheath thickness predicted by equations 2 and 22. An estimate based on equation 2 is

$$E \alpha n_+^{\frac{1}{3}} \alpha p^{\frac{1}{4}} \quad \text{(see appendix 4)}$$

If equation 22 is used then

$$E \alpha J^{\frac{1}{2}} \alpha p^{n}$$

where n has a value of 1/7 at the cathode and between 1/4 and 1/6 at the anode.

Coupled to this behaviour is a significant increase in current density in these regions. These results indicate that current density and field strength have little influence on fall voltages. The determining factor is therefore thought to be associated with material composition. Indeed, differences are observed between steel and copper anodes and between argon and helium arcs, V_a is larger on cooled copper anodes, where vapourization is more difficult than for steel anodes. Also, higher values of V_a are observed with helium. The last observation is attributed to the higher ionization potential of helium compared to that of argon. V_a has previously been reported (ref.1) to depend on arc length and current. This is reported to be due to a strong arc jet (at high current and low arc length) localizing vapour in the electrode region. Such an explanation is consistent with the present finding..

Energy exchange within the column may be used to interpret observed changes in the column voltage (V_c). In this section only the arc length dependence of V_c is discussed. Axial and radial variations are considered in sections 6.4 and 8. The total power appearing in the column is ($I.V_c$) where this is dissipated as conduction Q(K), convection Q(CV) and radiation Q(R) losses such that:

$$I.V_c = Q(CV) + Q(R) + Q(K) \qquad (108)$$

Each of these contributions to V_c will now be considered and estimated.

The convective contribution is a result of entrained gas being heated in the column and subsequently expelled to atmosphere near the anode. This may be written as

$$Q(CV) \simeq \dot{m}h \qquad (109)$$

where $\dot{m}$ is the mass passing through the arc per second and h the enthalpy change (between arc and atmosphere).

The mass flow flux may be expressed as

$$\dot{m} = \rho.\langle v \rangle.A \qquad (110)$$

Where $\langle v \rangle$ is the mean flow velocity through the arc cross-section of area A. ρ is the plasma density. It is convenient to link $\dot{m}$ to the

momentum flux (F) which may be used to define a root mean square velocity U_{rms} (see equations 14 and 15). i.e.

$$F = \rho . U_{rms}^2 . A \qquad (111)$$

In the present model it is assumed that

$$\langle v \rangle \simeq U_{rms}$$

Then combining this condition with equations 109, 110 and 111 gives

$$Q(CV) = h\sqrt{F.\rho.A} \qquad (112)$$

The behaviour of Q(CV) depends strongly on the mechanism of momentum generation. If the dominant mechanism is the current-self magnetic field interaction then F is known (F_M) and given by equation 14. However, at large currents, long arc lengths or high pressures, natural convection may dominate. F is then given by the bouyancy force (F_B). i.e.

$$F_M = \frac{\mu_o I^2}{4\pi} \cdot \ell n \frac{R}{R_o} \quad \text{(see equation 14)}$$

$$F_B = \rho_\infty . g . \tau \qquad (113)$$

Where ρ_∞ is the density of the cool chamber atmosphere, g the acceleration due to gravity and τ the arc volume. Substituting into equation 112 gives the respective expressions for Q(CV) when magnetic, $Q_M(CV)$, or buoyancy $Q_B(CV)$, forces dominate. These are:-

$$Q_M(CV) = \frac{h.I.R}{2} \sqrt{\rho . \mu_o . \ell n \frac{R}{R_o}} \qquad (114)$$

$$Q_B(CV) = h.\pi.R^2 \sqrt{\rho_\infty . \rho . g . \ell} \qquad (115)$$

If the buoyancy force is not negligible then

$$Q(CV) = Q_M(CV) \left(1 \mp \frac{F_B}{F_M}\right) \qquad (116)$$

Where the negative sign applies to down hand welding and the positive to overhead welding. Before returning to this expression the radiative and conductive components of Q will be considered.

It has been found (ref.31,32) possible to represent the power density (q_r) of radiation from an argon plasma as a thermodynamic function

$$q_r = q_r(T,P) \tag{117}$$

The total radiation leaving the plasma is then found (ref.31,32) to be given by

$$Q(R) = \int_{\text{arc volume}} q_r . d\tau \tag{118}$$

Bauder has also shown that equation 117 may be written as

$$q_r(T,P) = P.q_r(T) \tag{119}$$

The influence of pressure on radiation may then be written approximately as

$$Q(R) \simeq P.\tau. \langle q_r \rangle \tag{120}$$

where $\langle q_r \rangle = \frac{1}{\tau} \int_{\tau} q_r . d\tau$

and is defined as the average radiation source strength. It has been implicitly assumed in this approximation that temperature is little influenced by pressure (see section 7.3).

The conductive contribution is obtained by integrating the Fourier heat flux expression over the arc surface. i.e.

$$Q(K) = - \int_{\text{arc surface}} K.\frac{\partial T}{\partial n} \, dS_n \tag{121}$$

Where the co-ordinate n is normal to the surface S_n. K is the thermal conductivity. The evaluation of this integral depends on a great many factors: Flow conditions may modify the effective value of K-An increase by a factor of 20 (ref.36) may occur if fully turbulent conditions exist; vapourization may change composition - this will influence K, the

temperature field and temperature gradients; thermal equilibrium may not exist near the electrodes - K may then change by an order of magnitude (ref.35). Estimates of Q(K) made here are based on the major loss going to the atmosphere through the column (see later in this section). The column boundary (S_n) is taken as an isotherm and so K is approximately constant on this boundary. It is then readily shown that equation 121 becomes

$$Q(K) = 2\pi K.\ell.\alpha.\Delta T \qquad (122)$$

Where α is a combined shape factor for the temperature profile and column shape, ℓ is arc length, ΔT is the temperature difference between the arc axis (assumed to be slowly varying - see ref. 30) and column boundary. K is the effective thermal conductivity at the column boundary allowing for the (possiblity of turbulent effects). Values of α are tabulated below.

Temperature Profile	Column Shape	α
Linear	Cylindrical	1.0
Parabolic (ref.40)	Cylindrical	2.0
Bessel function (ref.40)	Cylindrical	2.8
Linear	Conic	0.33
Parabolic	Conic	0.66
Bessel function	Conic	0.93

Table 11 Influence of Arc Shape and Temperature Profile on α

Expressions 108, 116, 120 and 122 may now be combined to give V_c. The result is

$$V_c = \frac{h.R}{2}\sqrt{\frac{\rho.\mu_o.\ell n\frac{R}{R_o}}{}}\left(1 \mp \frac{F_B}{F_M}\right)^{\frac{1}{2}} + \frac{2\pi K\ell\alpha\Delta T}{I} + \frac{\pi.R^2.\ell\beta.P.\langle q_r\rangle}{I} \qquad (123)$$

The arc volume τ has been put equal $\pi.R^2.\ell\beta$ where β is a volumetric shape factor.

Equation 123 may be used to investigate the dependence of V_c on ambient pressure, arc length, arc current and gas properties. However, further information is required about the dependence of arc radius on these factors. It has been experimentally observed that

$$R = R_1.P^{-n} \quad (n > 0) \text{ see equation 82}$$

Where the behaviour of R_1 may be described from Ohms law i.e.

$$J = \sigma.E$$

Re-arranging gives

$$V_c = \frac{I.\ell}{\pi.\sigma.R^2}$$

$$V_c = \frac{I.\ell.P^{2n}}{\pi.\sigma.R_1^2} \qquad (124)$$

Combining 123, 82 and 124 gives

$$\frac{I.\ell.P^{2n}}{\pi.\sigma.R_1^2} = \left(1 \mp \frac{F_B}{F_M}\right)^{\frac{1}{2}} \cdot \frac{h.R_1.P^{\frac{1-2n}{2}}}{2} \cdot \sqrt{\rho_1.\mu_o.\ell n\frac{R}{R_o}}$$

$$+ \frac{2\pi K\alpha\ell\Delta T}{I}$$

$$+ \frac{\langle q_r \rangle \pi R_1^2.\ell.\beta\ P^{1-2n}}{I} \qquad (125)$$

Where the suffix '1' has been used to denote atmospheric properties. For the temperature range encountered in argon TIG arcs h and σ may be regarded as being independent of pressure (ref.35,160). Equation 125 may be regarded as a fourth order equation in R. However, this is unsuitable for the present discussion as analytical solutions for R do not exist. Models are therefore considered where one or other of the terms dominates. Under these conditions equation 125 gives:

i) for convectively dominated columns with $F_M >> F_B$

$$\left(\frac{I.\ell}{\pi\sigma R_1^2}\right) P^{2n} \simeq \left(\frac{h.R_1}{2}.\sqrt{\rho_1.\mu_o.\ell n\ \frac{R}{R_o}}\right) P^{\frac{1-2n}{2}}$$

Thus $n \simeq 1/6$

$R_1 \propto I^{1/3}$

and $R_1 \propto \ell^{1/3}$ for $R >> R_o$ (long arc)

i.e. for $R \gg R_o$ the logarithmic term changes slowly. Near the cathode the logarithmic term is strong and is associated with strong entrainment and hence enthalpy development. These expressions allow V_c (equation 124) to be written as

$$V_c \alpha\ I^{1/3}\ \ell^{1/3}.\ P^{1/3}$$

ii) for conduction dominated columns

$$\left(\frac{I.\ell}{\pi\sigma R_1^2}\right) P^{2n} \simeq \left(\frac{2\pi K\alpha\ell\Delta T}{I}\right)$$

Thus $n \simeq 0$

$R_1 \alpha\ I$

and R_1 is independent of ℓ

$\therefore V_c \alpha\ \ell/I$

iii) for radiation dominated columns

$$\left(\frac{I.\ell}{\pi\sigma R_1^2}\right) P^{2n} \simeq \left(\frac{\langle q_r \rangle\ P.\pi.R_1^2.\ell.\beta}{I}\right) P^{1-2n}$$

Thus $n \simeq \frac{1}{4}$

$R_1 \alpha\ I^{\frac{1}{2}}$

and R_1 is independent of ℓ

$\therefore V_c \alpha\ \ell\ P^{\frac{1}{2}}$

These functional relationships are shown in table 12.

Type of Arc	Quantity	Exponent of Variable		
		I	ℓ	P
Convective (magnetic)	V_c	+0.33	+0.33	+0.33
	R	+0.33	+0.33	+0.17
Conductive	V_c	-1.00	+1.00	0.00
	R	+1.00	0.00	0.00
Radiative	V_c	0.00	+1.00	+0.50
	R	+0.50	0.00	+0.25

Table 12 Arc Column Models

For arcs in which convection and radiation dominate the voltage increases with pressure such that the pressure dependence is between $p^{0.33}$ and $p^{0.50}$. Associated with this behaviour is a reduction in cross-section described by $p^{-0.17}$ to $p^{-0.25}$. This behaviour is in excellent agreement with that observed for argon TIG arcs where the voltage increases in accordance with $p^{0.43}$ to $p^{0.54}$ and radius decreases as $p^{-0.17}$. The theory also indicates a positive V-I slope with a dependence of less than $I^{0.33}$. The V-I curve is predicted to have a slope of between $\ell^{0.33}$ and $\ell^{1.00}$. In contrast, conductively dominated arcs show a negative V-I characteristic with a linear dependence on arc length. However, the voltage is predicted to be independent of pressure. The first two predictions are characteristic of the atmospheric helium TIG arc (see section 4.2.2). However, the voltage is observed to increase in contrast to the prediction. This may be explained by the emergence of a strong plasma jet at high pressures giving rise to conductive - convective behaviour. The influence of welding position may be taken into account by considering the ratio of buoyancy to magnetic forces. In the event of buoyancy forces being much greater than magnetic ($F_B >> F_M$) then reasoning similar to that given above gives

$$R \propto I^{\frac{1}{2}} \ell^{\frac{1}{2}} p^{-\frac{1}{4}}$$

$$V_c \propto \ell^{\frac{1}{2}} p^{\frac{1}{2}}$$

The pressure dependency of this behaviour is in line with that observed for radiation and magnetically dominated arcs. It may also be seen that the voltage characteristic is unaffected by current despite a broadening of the arc. However, considerations of section 8 show that although F_B/F_M increaseswith pressure this is generally less than 0.1 (nevertheless F_B may be very important in the outer arc reaches). On this basis positional changes are likely to influence V_c by a factor of

$$\sqrt{\frac{1 + 0.1}{1 - 0.1}} \simeq 1.1 \quad \text{or} \quad \sim 10\% \text{ of } Q(CV)$$

The situation considered experimentally was for an arc at about 20 bars (see figure 79) with an arc length of 4mm. The corresponding value of V_c is of order 15 volts. Hence 10% of Q(CV) will have an upper limit of about 1 volt. This explains why welding position has only a slight influence on arc voltage.

The first order model developed here also predicts the observed shift in the V-I characteristic turning point to lower currents with increasing pressure. This is shown schematically in figure 165. The influence of shielding gas flow on arc voltage may be incorporated into the model by allowing the effective value of the thermal conductivity (K) to increase due to the onset of turbulence. Calculations by Ramakrishman et al (36) indicate that K may be increased by this mechanism by a factor of 25 for high temperature argon arcs. It should also be noted that this effect is proportional to arc length as observed (see figure 76).

For the purpose of numerating the theory described above a 100 Amp, 3mm argon TIG arc is considered and the components of electric field strength are calculated. A more convenient form for V_c (see equation 108) is

$$E = \frac{V_c}{\ell} = E(CV) + E(K) + E(R) \qquad (126)$$

where E(CV), E(K) and E(R) are the convective, conductive and radiative electric field contributions respectively.

Equations 114 and 82 allow the convective contribution E(CV) to be written as

$$E(CV) = \frac{h}{2}\sqrt{\rho_1 . \mu_o . \ell n \frac{R}{R_o}} \cdot \left(\frac{R_1}{\ell}\right) p^{0.33}$$

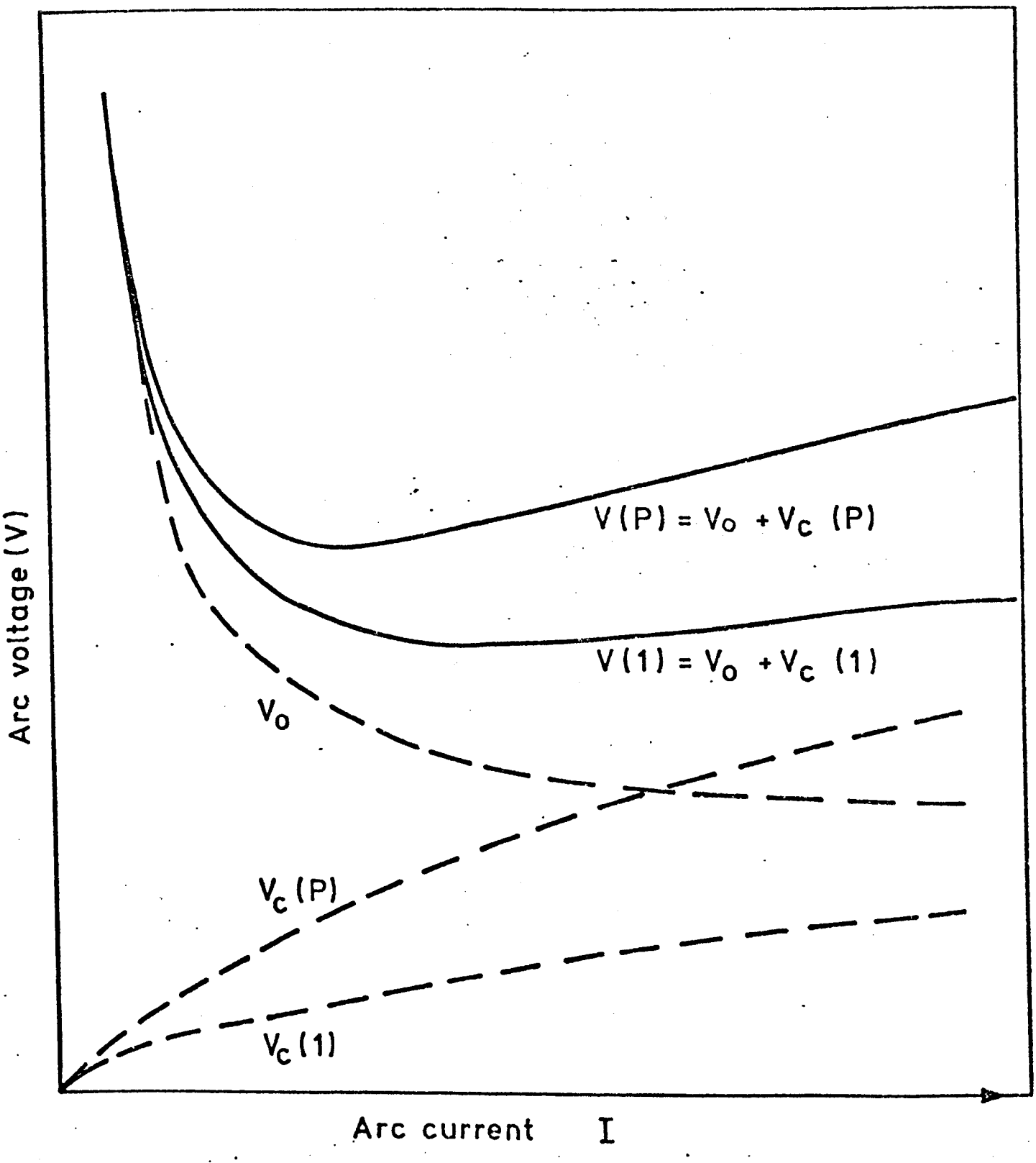

FIGURE165. SCHEMATIC REPRESENTATION OF THE INFLUENCE OF ARC CURRENT AND AMBIENT PRESSURE ON ARC VOLTAGE (SEE FIGURE 58)

This has been evaluated for the range of parameters $6 \geq R/R_o \geq 4$. $11{,}000K \geq T \geq 8{,}000K$; arc cone semi-angle of 45^o. These give

$$E(CV) = (0.45 \pm 0.13)\ P^{0.33}\ V/mm \qquad (127)$$

Where gas properties from ref.160 have been used. Clearly E(CV) is fairly insensitive to the choice of temperature or arc column divergence employed.

The radiative component of electric field strength (see equation 120) may be written as

$$E(R) \simeq \beta . \frac{\langle q_r \rangle}{J} . P^{0.66}$$

Where J is the average anodic current density at 1 bar. Experimental values (see section 6.2) are typically $2 \times 10^6 A/m^2$. For a cone: $\beta \sim 1/3$. However, $\langle q_r \rangle$ is strongly temperature dependent. (see table 13). Taking a value associated with the mean electrical conductivity temperature (see section 7.3) of about 11,500K gives

$\langle q_r \rangle \simeq 8 \times 10^8\ W/m^3$. Therefore:-

$$E(R) \simeq 0.15\ P^{0.66}\ V/mm \qquad (128)$$

The conductive contribution requires integrating over the surface of the column (see figure 166). This has been split into three regions designated S_1, S_2 and S_3 where these refer, respectively, to the outer arc surface, the anode surface and the cathode. The integral 121 now gives:-

$$E(K) = \frac{1}{\ell . I} \left\{ K_1 \int_{S_1} \frac{\partial T}{\partial n}\ ds + K_2 \left(\frac{\partial T}{\partial n}\right)_2 S_2 + K_3 \left(\frac{\partial T}{\partial n}\right)_3 S_3 \right\}$$

where K_1, K_2, K_3 are evaluated at the temperatures of the corresponding surfaces. The temperature gradient at the column surface is approximated to a linear fall off between the axis and surface with a temperature difference of 3,000K.

$$\text{i.e. } \left(\frac{\partial T}{\partial n}\right)_{S_1} = \frac{3000}{R(Z)}$$

T	H^d (MJ/kg)	ρ^a (g/cm^3)	K^a (W/mk)	μ^a (mg/ms)	C_p^a (kJ/kg K)	σ^b (mho/mm)	q^b (W/mm^3)
7000	3.651	69.50	0.36	193	0.540	1.10	0.008
8000	4.228	60.73	0.58	207	0.628	1.64	0.018
9000	4.965	53.72	0.91	218	0.892	2.39	0.045
10000	6.124	47.68	1.35	225	1.511	3.07	0.128
11000	8.184	41.98	1.95	218	2.721	3.90	0.370
12000	11.830	36.23	2.70	200	4.676	4.93	1.180
13000	17.780	30.39	3.60	175	7.242	5.81	2.850

Table 13 Properties of Atmospheric Argon

(a) Metcalfe & Quigley (CEGB lab note R/M/N738)

(b) Emmons, H. (Physics of Fluids, June 1967)

H enthalpy

ρ density

K thermal conductivity

μ viscosity

C_p specific heat

σ electrical conductivity

q radiative strength

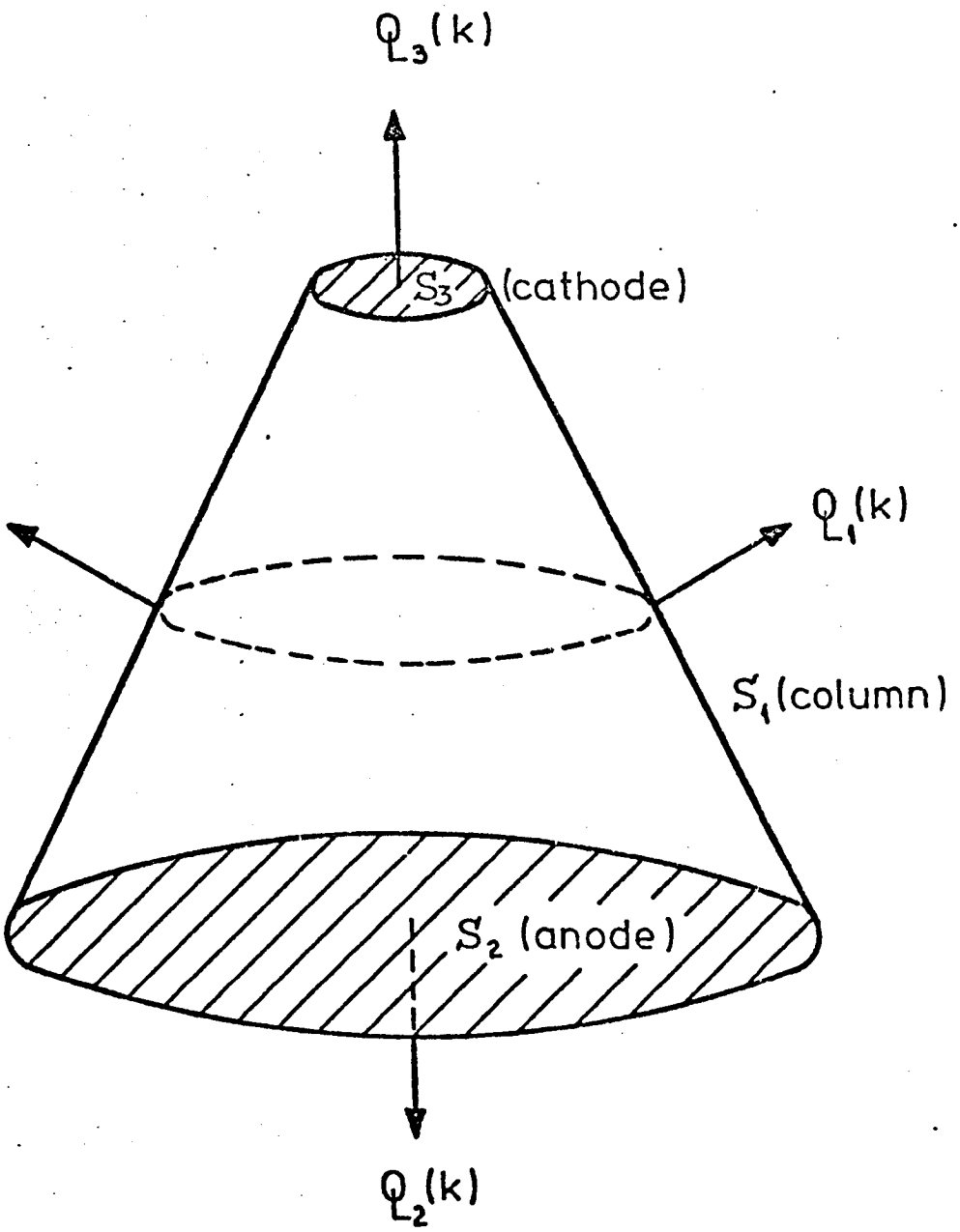

FIGURE 166. SCHEMATIC REPRESENTATION OF CONDUCTIVE LOSSES FROM ARC SURFACE (S)

Where R(Z) is the radius at a distance Z from the cathode. For consistency (with the convective estimate) R is taken as

$$R = Z/2 \quad \text{i.e. a cone semi-angle of } 45^{o}$$

$$\text{Thus} \int_{S_1} \frac{\partial T}{\partial n}\, ds \simeq \int_{o}^{\ell} \frac{6000}{Z} \cdot \frac{2\pi}{3} \cdot Z \cdot dZ \simeq 4000.\pi\ell$$

The axial gradients at the anode and cathode are taken with reference to the literature survey as

$$\left(\frac{\partial T}{\partial n}\right)_2 \simeq 10^6 \text{ K/m}, \quad \left(\frac{\partial T}{\partial n}\right)_3 \simeq 5.10^6 \text{ K/m}$$

with area factors of

$$S_2 = \pi\left(\frac{3.10^{-3}}{2}\right)^2 \text{ m}^2, \quad S_3 = \pi\left(\frac{1.0 \times 10^{-3}}{2}\right)^2 \text{ m}^2$$

i.e. effective conduction arc diameters at the anode and cathode of 3mm and 1mm respectively.

Combining this data gives

$$E(K) = (126K_1 + 24K_2 + 13K_3) \text{ V/m}$$

Suitable temperatures near the anode and cathode are 10,000K and 12,000K respectively (ref.30). The corresponding values of K are 1.35W/mK and 2.70W/mK (see table 13). Flow conditions at the arc boundary may significantly influence the value of K. However, taking a temperature 8000K and ignoring flow effects gives K_1 = 0.58W/mK. Therefore,

$$E(K) \simeq 73 + 32 + 35 = 140 \text{ (V/m)} \qquad (129)$$

Thus the major conductive loss is to the atmosphere.
Combining equations 126 to 129 gives

$$E \simeq 0.45P^{0.33} + 0.14 + 0.13P^{0.66} \text{ (V/mm)} \qquad (130)$$

The atmospheric value is

$$E \simeq 0.72 \text{ V/mm}$$

This compares favourably with experimental values of 0.7 - 0.8 V/mm. The convective contribution dominates and accounts for 60% of the calculated column voltage. Radiative and conductive contributions are estimated to account for approximately 20% each of the column power. The pressure dependence of E as given by equation 130 is compared with that found experimentally in figure 73. Again the agreement is good. It is interesting to note that the radiative term starts to dominate at about 22 bars.

The simple model developed here appears to be remarkably successful in explaining the observed characteristics of the arc column. However, great care should be taken in applying such a model as significant uncertainties do exist, particularly with the radiative and conductive terms. The real strength of such calculations is to be associated with correctly identifying trends on the basis of reasonable assumptions and not with the exact prediction of arc properties. More detailed experiments and theories are required for this latter task and these approaches are considered in latter sections. The mechanisms responsible for energy expenditure in the constricted arc are different than in the free arc.. These are not considered here.

The models developed for interpreting arc column voltage may also be used to indicate the pressure dependence of other physical quantities.

i) arc column power density ($\wp$)

$$\wp = J.E$$
$$= I.E/\pi R^2$$

Taking $R \propto P^{-0.17}$ (experimental) and $E \propto P^{0.5}$ (experimental) gives

$$\wp \propto P^{0.84}$$

ii) arc column mass flow rate ($\dot{M}$). From equation 112

$$\dot{M} \simeq F\rho A$$
$$\simeq \frac{IR}{2}\sqrt{\rho\mu_o \ell n \frac{R}{R_o}}$$

$$\therefore \dot{M} \propto P^{0.33}$$

iii) Average (RMS) velocity. From equation 111

$$v\ (\text{RMS}) \simeq \sqrt{F/\rho A}$$

$$\simeq \frac{I}{2\pi R}\sqrt{\frac{\mu_o}{\rho}\cdot \ell n\left(\frac{R}{R_o}\right)}$$

$$\therefore\ v\ (\text{RMS}) \propto P^{-0.33}$$

i.e. the arc column velocity falls despite a contraction in the arc column, and an increase in the mass flow rate.

iv) Axial velocity v_z. From equation 16

$$v_z \simeq \left(\frac{\mu_o I J_o}{2\pi\rho}\right)^{\frac{1}{2}}$$

$$\therefore\ v_z \propto P^{-0.36}$$

v) Stagnation pressure (as experienced at the anode) associated with the flow (ΔP). From equation 17

$$\Delta P \simeq \frac{1}{2}\rho v_z^2 \simeq \frac{\mu_o I J_o}{4\pi}$$

$$\therefore\ \Delta P \propto P^{0.28}$$

Thus the stagnation pressure increases with ambient pressure.

vi) Arc column momentum flux F. From equation 14

$$F = \frac{\mu_o I^2}{4\pi}\ \ell n\ \frac{R}{R_o}$$

i.e. F is independent of ambient pressure.

vii) Force (F_A) exerted by arc on anode

$$F_A \propto \rho v(\text{rms})^2 A$$

where A is impingement area $\simeq \pi R^2$.

Using equation 111 gives

$$F_A \propto F$$

Thus F_A is independent of ambient pressure.

viii) Electrical conductivity σ.

$$\sigma = J/E$$

Using data from (i) gives

$$\sigma \propto P^{0.16}$$

This may be used to investigate the independence of arc temperature on ambient pressure (see section 7.3).

ix) Arc column Reynolds number (R_e)

$$R_e = \frac{\rho . v . L}{\eta}$$

Where v is the plasma gas velocity (see iv), η is viscosity, ρ is density and L is a characteristic length scale taken as the cathode spot diameter.

i.e.

$$\frac{\pi L^2}{4} = I/J_o$$

Substituting from (iv) gives

$$R_e = \frac{I}{\pi\eta} \sqrt{2 \mu_o \rho}$$

$$\therefore \quad R_e \propto P^{0.5}$$

Considerations given in this section have been successful in accounting for many of the observed characteristics of electrical behaviour at high pressures. Further developments are made in section 6,7,8 where a more detailed account is given by considering arc structure.

5.4. Discussion of Weldment Characteristics

A detailed account of weldment characteristics is given in section 4.3. These results show that ambient pressure has a strong influence on the resulting bead geometry. This state of affairs is not surprising in view of gross changes in arc behaviour observed over the range of pressures investigated. Previous reports (see Literature Survey) of changes in weld bead structure with pressure have been largely confined to the observation that weld penetration increases with most observations being made between 1 and 20 bars. The present contribution has investigated a wide range of variables (including pressures of up to 45 bars) and

processes. Quantitative comparisons have been made with conductive heat transfer theory. Calculated melting and process efficiencies have been used to correlate weld dimensions, HAZ dimensions and process parameters.

The present state of knowledge of weld bead formation is such that it is not feasible to attempt an explanation of all observations made here. The main aims of this section are therefore directed at:-

i) Emphasising results considered to be of particular interest especially with respect to existing theories.
ii) Associating weld bead phenomena with process characteristics.
iii) Emphasising the pressure dependence of properties and effects of changing process details e.g. gas composition, the addition of magnetic stirring etc.

In conductive heat transfer models of weld bead formation the only arc/process property of any interest is the total heat entering the plate. This is taken to enter through a point and so the structure of the heat source is not accounted for. Such models have proved useful in predicting the characteristics of weldment heating away from the pool but of very limited value in predicting behaviour in and near the pool. Point source conductive models are clearly incapable of indicating the cause of weld bead turbulence experienced above about 30 bars with argon TIG arcs. This behaviour is often associated with uneven penetration and assymetrical bead profiles. Behaviour of this sort was observed for a wide range of arcing conditions (i.e. arc currents, arc lengths, electrode geometries and compositions). It was found possible to stabilise weld pool behaviour by the application of an external magnetic field. These results suggest that the observed behaviour is not directly attributable to the total or density of arc heating or to arc current. It was also found that no simple visual correlation could be made between the stability of the arc and that of the pool. The fact that arc current is not the dominant variable indicates that turbulence is not in itself the result of a breakdown in the 'current-self magnetic field' generated flow within the pool. Flow breakdowns of this type have previously been predicted (ref.44 to 49). However, the effect is clearly manifest in a change in weld pool motion and may be overcome with the imposition of a purely rotational motion (see section 4.3) by the

application of an external magnetic field. One possible explanation of this behaviour consistentwith the analysis given above is that minor elements in the base plate play an important role. This may be associated with changes in physical properties of the vapour with ambient pressure (i.e. vapour pressure, boiling point). These in turn may produce changes in arc rooting and hence lead to changes in weld pool motion. It is also possible that such changes in pool motion modify the distribution of minor elements directly under the arc and hence lead to further changes in pool motion (i.e. modified EM force). The vapourization of minor elements has previously been put forward as a mechanism for changes in bead structure observed under normal atmospheric conditions. However, no conclusive evidence has yet been found.

Significant changes in the structure of helium TIG arc weld beads have also been found. It is found possible to produce a keyhole action. This behaviour appears to be directly related to the onset of plasma streaming in the high pressure helium arc. At pressures above about 5 bars very strong convective forces are observed and these are often associated with a reflected jet from the anode plate. This effect coupled to the high thermal conductivity of helium, gives rise to a significant increase in heat transfer and penetration.

The two effects described above are extreme manifestations of the influence of pressure on bead geometry and are immediately apparent by visual inspection. However, many changes in bead geometry are not apparent from surface inspection. In argon the weld width is observed to change only marginally across the range of pressures investigated (1-42 bars). The main influence of pressure is then to increase weld bead penetration. This is particularly noticeable over the first 10 bars.

Such behaviour may be understood in terms of enhanced weld pool convection and a more point like conductive heat source due to a highly constricted arc root. An increase in penetration is also observed in helium. However, in this case the bead width also increases. At pressures of above 4 bars weld bead penetration may be estimated from

bead width. For argon it is then found that penetration is approximately equal to half the weld width for a wide range of arc lengths and currents i.e. $W/D \simeq 2$. In helium atmospheres the penetration may be even greater than the width and aspect ratios as small as 0.93 have been observed.

Evidence of the influence of weld pool motion is afforded by a comparison of HAZ and weld bead dimensions. On the basis of purely conductive heat transfer both dimensions simply represent known isotherms and are related in a well defined manner to heat input and other process variables. However, HAZ diameter increases with pressure despite the weak pressure dependence of bead width. This is a strong indication that heat input increases with ambient pressure and that mechanisms other than pure conduction are influencing the position of the pool boundary (which should otherwise also broaden). In an attempt to quantify this behaviour the positions of the HAZ isotherms have been used to compute process heat transfer efficiency. This has been done on the basis of purely conductive heat transfer which will certainly apply away from the pool edge. Results show an increase in heat input but at a rate slower than the increase in process power (i.e. process efficiency falls with increasing pressure). Further experiments to examine this finding are given in section 6. The justification of this method of estimating heat input is strongly dependent on the HAZ having a nearly semi-circular cross-section (as required by theory). In practice values of between 2 and 3 are observed for the HAZ aspect ratio with the small deviation from theory presumably resulting from the structure of the arc heat source (i.e. this becomes more point-like with increasing pressure). Predictions of heat input have then been applied to calculating the fusion area expected if only conductive heat transfer exists. These calculations are generally in remarkably good agreement with observed fusion areas. However, the poorest agreement is obtained for atmospheric arcs. This is attributed to significant deviations from hemispherical pool geometry at 1 bar. These results indicate that conductive heat transfer can explain the observed melted volume but not the shape of the melted region. This implies that convection significantly influences weld bead shape but plays little part as a heat transfer mechanism in the pool (i.e. apart from transferring heat to different regions of the pool, convection doesn't influence the efficiency of melting).

It is found convenient to express the relationship between bead characteristics and process parameters in terms of melting efficiency (Z). Detailed changes in the observed melting efficiency have been predicted in terms heat input calculated from HAZ diameters. This is a strong validification of the approach adopted. For experiments performed at a given pressure, Z, is observed to increase with process power and travel speed. Higher values are also found in helium than for argon. This behaviour has previously been observed (ref.116) under normal atmospheric conditions. However, if process power is increased by raising the ambient pressure Z may initially increase before going through a maximum and then decreasing, despite an increase in heat input. This effect has been shown to be a direct result of the predicted fall in process heat transfer efficiency with increasing pressure. It therefore appears that for a given arc length, current, travel speed and gas type, a process power (associated with a pressure) exists at which the most efficient melting may be achieved (details have been given in section 4.3).

Weld bead experiments were also performed under the influence of magnetic stirring. Apart from stabilizing the pool at high pressures a number of other interesting observations were made. The main effect of such a force was to significantly reduce weld bead penetration while leaving bead width substantially unaffected. It was found that weld bead characteristics were less sensitive to changes in ambient pressure than without a field. Despite this, the structure of the HAZ was very similar to that found when no field was applied. This indicates that the heat input and process efficiency are little affected (see section 6) by the application of a field. However, substantially less melting occurs. Results and correlations presented in section 4.3 show that convection due to magnetic stirring influences weld shape and heat transfer. This last factor may be crudely understood in terms of conductive heat transfer theory with an 'effective thermal conductivity' (K eff) that takes convection into account i.e. For a given heat input the melting isotherm moves towards the origin of heating with increasing K. In the present case K is expected to increase due to a convective contribution. It is found possible to predict the melted volume (or Z) by using a value of K associated with the melting point of steel (i.e. a factor of 2 greater than that existing between HAZ and fusion boundary).

It therefore appears that although the indigenous field is too weak to influence the 'effective k', the applied field isn't. An estimate of the maximum indigenous field (B_I) is given by Amperes law applied at the current conducting boundary (R) of the pool surface i.e.

$$B_I = \frac{\mu . I}{2\pi R}$$

Current density measurements (see section 6) indicate R≃2mm. For a 100A

$$B_I \sim 100 \text{ Gauss}$$

This may be regarded as significantly greater than the effective indigenous field because it occurs at the pool boundary where there is no significant flow. This value must also decrease in a direction perpendicular to the plate surface due to current divergence. It is reported by Wilgoss (ref.111) that an effective value of B_I is of order 10 Gauss. This is significantly less than the field applied i.e. ~50 Gauss and hence an influence of the applied field, especially on penetration, is expected.

6. Experimental Results (Structural)

6. EXPERIMENTAL RESULTS (STRUCTURAL)

6.1. Anode Heating

Calorimetric experiments have been performed for a range of conditions (see section 3.6.1). In this section results are presented and analysed. Owing to the large number of results to be represented it has been found appropriate in many situations to represent results in tabular form. Graphical representation is reserved to indicate typical behaviour or for the more important results.

6.1.1. The Argon TIG Arc on a Copper Anode

6.1.1.1. Total Power Collected by the Anode (Q)

Results are presented in tables 14 to 20 and typical behaviour is shown graphically.

(A) Influence of Arc Length (ℓ) on Q

Zero arc length 'heat inputs' Q_o have been estimated by plotting graphs of Q against ℓ. Results obtained in this manner are shown in tables 14 to 20. Only 1 bar and 41.2 bar results have been represented in graphical form (see figures 167 and 168). It can be seen that at 1 bar Q is generally linearly dependent on arc length with a gradient that increases with arc current. At 41.2 bars Q is found to increase with arc length in a manner that is slightly less sensitive to arc length. The dependence on arc length has been quantified and is represented by $Q_c/I\ell$ (see tables 14 to 20) where Q_c is the column power contribution ($Q_c=Q-Q_o$). It may be seen that there is significant anode heating even at zero arc length (Q_o). This component is shown graphically in figure 169. Also shown in the same figure is the zero arc length power that does not enter the anode. This is denoted by $P_L(\ell=0)$ and obtained graphically from

$$P_L\ (\ell=0) = I.V_o - Q_o$$

$P_L(\ell=0)$ is interpreted physically as the heat input to the cathode.

It can be seen that pressure has only a small influence on Q_o and that Q_o increases in direct proportion to arc current (I). The behaviour at 1 bar is well represented by

$$Q_o\ (1\ \text{bar}) = 8.I$$

Results at higher pressures are generally written $\pm$100W of this behaviour.

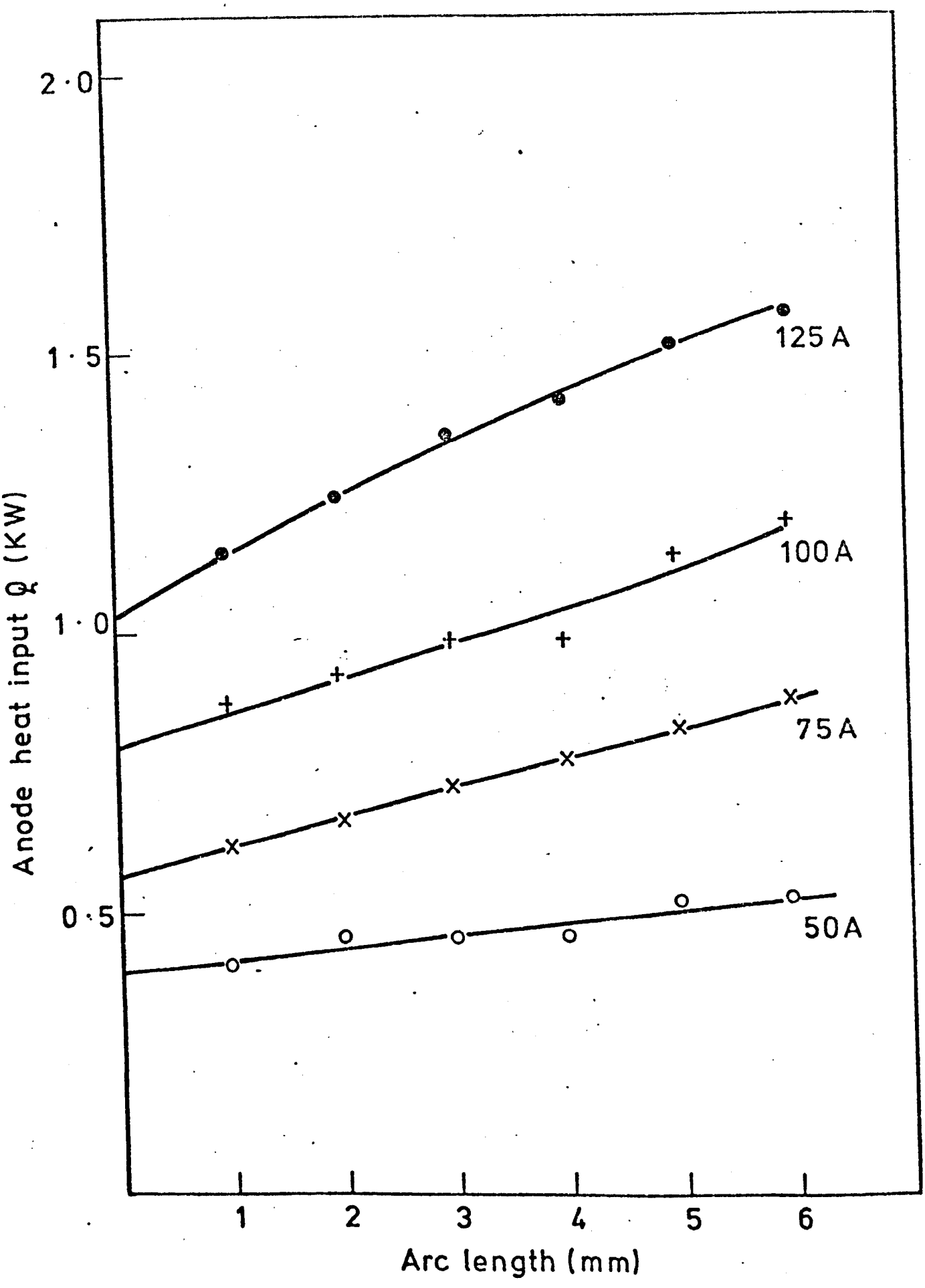

FIGURE 167. INFLUENCE OF ARC LENGTH AND CURRENT ON ANODE HEATING WITH AN ARGON TIG ARC ABOVE A WATER COOLED COPPER ANODE (P = 1 BAR)

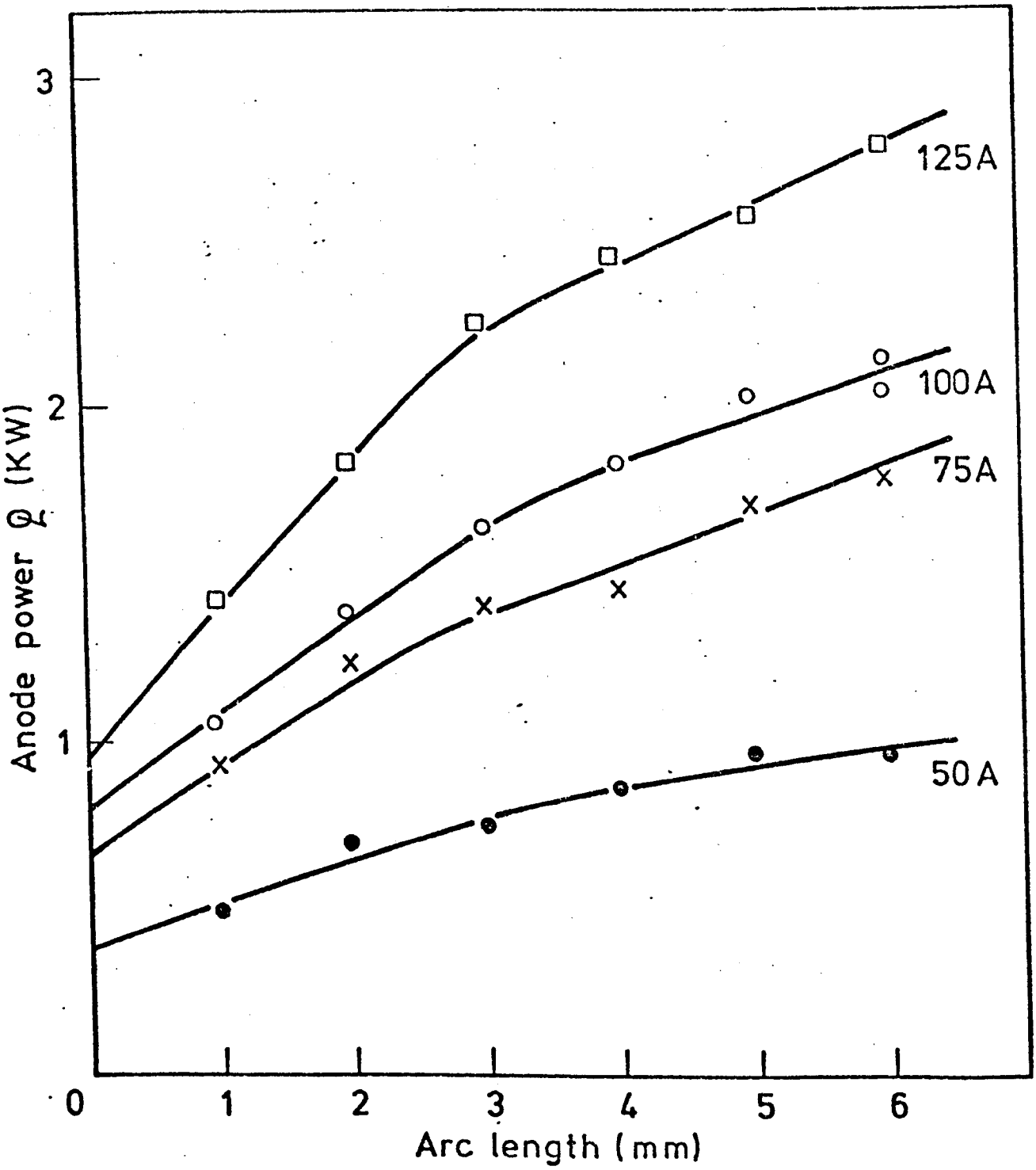

FIGURE 168. INFLUENCE OF ARC LENGTH AND CURRENT ON ANODE HEATING WITH AN ARGON TIG ARC ABOVE A WATER COOLED COPPER ANODE (P = 41·6 BARS)

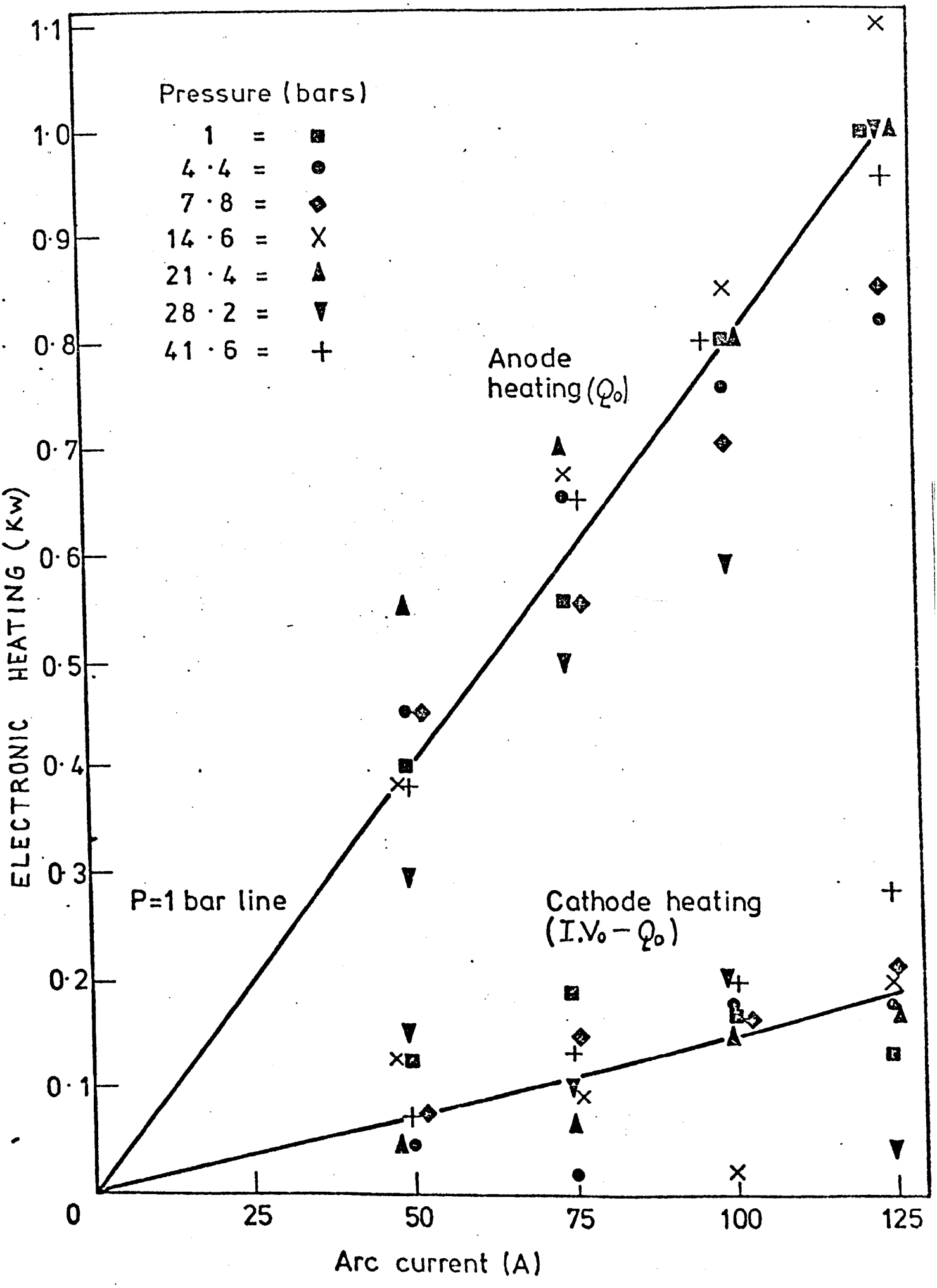

FIGURE 169. INFLUENCE OF ARC CURRENT AND AMBIENT PRESSURE ON ELECTRONIC HEATING AT THE ANODE AND CATHODIC FOR ARGON TIG ARCS ON A COPPER ANODE.

Definition and Interpretation of Parameters Numerated in Tables 14 to 27

ℓ electrode separation

V arc voltage

P arc power (I.V)

Q power collected by anode

η process heat transfer efficiency

i.e. $\eta = \frac{Q}{P} \times 100\%$

P_L process power not entering anode

i.e. $P_L = P - Q$

ΔP_L process power not entering electrodes

i.e. $\Delta P_L = P_L - P_L \ (\ell=0)$

where $P_L \ (\ell=0)$ is power to the cathode

P_c power appearing in the column

i.e. $P_c = P - P \ (\ell=0)$

Q_c power developed in the column that contributes to anode heating

i.e. $Q_c = Q - Q \ (\ell=0)$

η_c efficiency of transferring power developed in the column to the anode

i.e. $\eta_c = \frac{Q_c}{P_c} \times 100\%$

TABLE 14 Analysis of Heat Transfer Data for Argon TIG Arcs on a Copper Anode. Ambient Pressure = 1.Bar

Arc Current 50A

ℓ (mm)	V (Volts)	P (W)	Q (W)	η (%)	P_L (W)	$\frac{\Delta P_L}{I\ell}$ (V/mm)	P_C (W)	$\frac{P_C}{I\ell}$ (V/mm)	Q_C (W)	$\frac{Q_C}{I\ell}$ (V/mm)	η_C (%)
0	10.6	530	400	75	130						
1	11.6	580	416	72	164	0.66	50	1.00	16	0.32	32
2	12.5	625	468	75	157	0.27	95	1.95	68	0.68	72
3	13.1	655	468	71	187	0.38	125	0.83	68	0.45	54
4	14.0	700	468	67	232	0.51	170	0.85	68	0.34	40
5	14.8	740	520	70	220	0.35	210	0.84	120	0.48	57
6	15.9	795	520	65	275	0.48	265	0.88	120	0.40	45
Average	-	-	-	71	-	0.44	-	0.89	-	0.45	50
Arc Current 75A											
0	10.1	758	560	74	198	-	-	-	-	-	-
1	11.1	833	624	75	209	0.15	75	1.00	64	0.85	85
2	11.9	893	676	76	217	0.13	135	0.90	116	0.77	86
3	12.6	945	728	77	217	0.08	188	0.84	168	0.75	89
4	13.3	998	780	78	218	0.07	240	0.80	220	0.73	92
5	14.0	1050	832	79	218	0.05	293	0.78	272	0.73	93
6	15.0	1125	884	79	366	0.37	368	0.82	324	0.72	88
Average	-	-	-	77	-	0.14	-	0.86	-	0.76	89
Arc Current 100A											
0	9.7	970	800	82	170	-	-	-	-	-	-
1	10.7	1070	884	83	186	0.16	100	1.00	84	0.84	84
2	11.6	1160	936	81	224	0.27	190	0.95	136	0.68	92
3	12.6	1260	988	78	272	0.34	290	0.97	188	0.63	65
4	13.3	1330	988	74	342	0.43	360	0.90	188	0.47	52
5	14.0	1400	1144	82	256	0.17	430	0.86	344	0.69	80
6	14.8	1480	1196	81	284	0.19	510	0.85	396	0.66	78
Average	-	-	-	80	-	0.26	-	0.92	-	0.66	75
Arc Current 125A											
0	9.3	1106	1030	89	133	-	-	-	-	-	-
1	10.5	1313	1144	87	169	0.29	150	1.20	141	1.13	94
2	11.6	1450	1248	86	202	0.28	288	1.15	245	0.98	85
3	12.7	1588	1352	85	236	0.27	425	1.13	349	0.93	82
4	13.6	1700	1404	83	296	0.33	538	1.08	401	0.80	75
5	14.5	1813	1508	83	305	0.28	650	1.04	505	0.81	78
6	15.4	1925	1560	81	365	0.31	763	1.02	557	0.74	73
Average	-	-	-	85	-	0.29	-	1.10	-	0.90	81

TABLE 15 Analysis of Heat Transfer Data for Argon TIG Arcs on a Copper Anode. Ambient Pressure = 4.4 Bars

ℓ (mm)	V (Volts)	P (W)	Q (W)	η (%)	P_L (W)	$\frac{\Delta P_L}{\Delta \ell}$ (V/mm)	P_C (W)	$\frac{P_C}{\Delta \ell}$ (V/mm)	Q_C (W)	$\frac{Q_C}{\Delta \ell}$ (V/mm)	η_C (%)
Arc Current 50A											
0	9.6	480	440	92	40	-	-	-	-	-	-
1	12.0	600	485	81	115	1.50	120	2.4	45	0.9	38
2	14.2	710	555	78	155	1.15	230	2.3	115	1.15	50
3	15.7	785	624	79	161	0.81	305	2.03	184	1.23	60
4	17.0	850	624	73	226	0.93	370	1.85	184	0.92	50
5	17.5	875	659	75	216	0.70	395	1.58	219	0.88	55
6	18.3	915	693	76	222	0.61	435	1.45	253	0.84	58
Average	-	-	-	79	-	0.95	-	1.94	-	0.99	52
Arc Current 75A											
0	9.0	675	660	98	15	-	-	-	-	-	-
1	11.5	863	763	88	100	1.13	188	2.51	103	1.37	55
2	14.0	1050	832	79	218	1.35	375	2.50	172	1.15	46
3	16.0	1200	900	75	300	1.27	525	2.33	240	1.07	46
4	17.3	1298	970	75	328	1.04	623	2.08	310	1.03	50
5	18.5	1388	1040	75	348	0.89	713	1.90	380	1.01	53
6	19.7	1478	1040	70	438	0.94	803	1.78	380	0.84	47
Average	-	-	-	80	-	1.10	-	2.18	-	1.08	50
Arc Current 100A											
0	9.4	940	760	81	180	-	-	-	-	-	-
1	11.8	1180	900	76	280	1.00	240	2.40	140	1.40	58
2	14.0	1400	1040	74	360	0.90	460	2.30	280	1.40	61
3	15.7	1570	1110	71	460	0.93	630	2.10	350	1.17	56
4	17.2	1720	1258	73	462	0.71	780	1.95	498	1.25	64
5	18.5	1850	1316	71	534	0.71	910	1.82	556	1.11	61
6	19.5	1950	1385	71	565	0.64	1010	1.68	625	1.04	62
Average	-	-	-	74	-	0.82	-	2.04	-	1.23	59
Arc Current 125A											
0	8.0	1000	320	82	180	-	-	-	-	-	-
1	10.4	1300	900	69	400	1.76	300	2.40	80	0.64	27
2	14.0	1750	1316	75	434	1.02	750	3.00	496	1.98	66
3	16.8	2100	1525	73	575	1.05	1100	2.93	705	1.88	64
4	18.6	2325	1732	74	593	0.83	1325	2.65	912	1.82	69
5	20.0	2500	1800	72	700	0.83	1500	2.40	980	1.57	65
6	21.5	2688	1870	70	818	0.85	1688	2.25	1050	1.40	62
Average	-	-	-	74	-	1.06	-	2.61	-	1.55	59

TABLE 16 Analysis of Heat Transfer Data for Argon TIG Arcs on a Copper Anode. Ambient Pressure = 7.8 Bars

ℓ (mm)	V (Volts)	P (W)	Q (W)	η (%)	P_L (W)	$\frac{\Delta P_L}{\Delta \ell}$ (V/mm)	P_C (W)	$\frac{P_C}{\ell}$ (V/mm)	Q_C (W)	$\frac{Q_C}{\ell}$ (V/mm)	η_C (%)
Arc Current 50A											
0	10.0	510	440	86	70	-	-	-	-	-	-
1	13.3	665	485	73	180	2.20	155	3.10	45	0.9	29
2	16.1	805	555	69	250	1.80	295	2.95	115	1.15	39
3	18.1	905	589	65	316	1.64	395	2.63	149	0.99	38
4	19.5	975	624	64	351	1.41	465	2.33	184	0.92	40
5	20.5	1025	693	68	332	1.05	575	2.06	253	1.01	49
6	21.7	1085	693	64	392	1.07	575	1.92	253	0.84	44
Average	-	-	-	70	-	1.52	-	2.50	-	0.97	40
Arc Current 75A											
0	9.5	713	560	79	153	-	-	-	-	-	-
1	12.6	945	693	74	252	1.32	232	3.09	133	1.77	57
2	15.5	1163	901	78	262	0.73	450	3.00	341	2.27	76
3	17.5	1313	971	74	342	0.84	600	2.67	411	1.83	69
4	19.0	1425	1040	73	385	0.77	712	2.37	480	1.60	67
5	20.3	1523	1109	73	414	0.70	810	2.16	549	1.46	68
6	21.6	1620	1144	71	476	0.72	907	2.02	584	1.30	64
Average	-	-	-	75	-	0.85	-	2.55	-	1.71	67
Arc Current 100A											
0	8.8	880	710	81	170	-	-	-	-	-	-
1	11.8	1180	901	76	279	1.09	300	3.00	191	1.91	64
2	14.9	1490	1109	74	381	1.06	610	3.05	399	2.00	65
3	17.7	1770	1248	71	522	1.17	890	2.97	538	1.79	60
4	20.1	2010	1387	69	623	1.13	1130	2.83	677	1.72	60
5	22.0	2200	1525	69	675	1.01	1320	2.64	815	1.63	62
6	23.5	2350	1629	69	721	0.92	1470	2.45	919	1.53	63
Average	-	-	-	73	-	1.06	-	2.82	-		62
Arc Current 125A											
0	8.5	1063	850	80	213	-	-	-	-	-	-
1	11.3	1413	1109	79	304	0.73	350	2.80	259	2.07	74
2	15.0	1875	1387	74	488	1.10	812	3.25	537	2.15	66
3	17.5	2188	1525	70	663	1.20	1125	3.00	675	1.80	60
4	20.0	2500	1803	72	697	0.97	1437	2.87	953	1.91	66
5	21.7	2713	1941	72	772	0.89	1650	2.64	1091	1.74	66
6	23.3	2913	2045	70	868	0.87	1850	2.47	1195	1.59	65
Average	-	-	-	74	-	0.96	-	2.84	-	1.88	66

TABLE 17 Analysis of Heat Transfer Data for Argon TIG Arcs on a Copper Anode. Ambient Pressure = 14.6 Bars

l (mm)	V (Volts)	P (W)	Q (W)	η (%)	P_L (W)	$\frac{\Delta P_L}{\Delta l}$ (V/mm)	P_C (W)	$\frac{P_C}{l}$ (V/mm)	Q_C (W)	$\frac{Q_C}{l}$ (V/mm)	η_C (%)
Arc Current 50A											
0	10.3	515	380	74	135	-	-	-	-	-	-
1	14.6	730	416	57	314	3.58	215	4.30	36	0.72	17
2	18.4	920	555	60	365	2.30	405	4.05	175	1.75	43
3	20.6	1030	624	61	406	1.81	515	3.43	244	1.63	47
4	22.3	1115	693	62	422	1.44	600	3.00	313	1.57	52
5	23.5	1175	693	59	482	1.39	660	2.64	313	1.25	47
6	25.0	1250	693	56	557	1.41	735	2.45	313	1.04	43
Average	-	-	-	61	-	1.99	-	3.31	-	1.33	42
Arc Current 75A											
0	10.3	773	680	88	93	-	-	-	-	-	-
1	14.7	1103	832	76	271	2.37	330	4.40	152	2.03	46
2	18.4	1380	901	65	479	2.57	607	4.05	221	1.47	36
3	20.5	1538	971	63	567	2.11	765	3.40	291	1.29	38
4	22.5	1688	1075	64	613	1.73	915	3.05	395	1.32	43
5	24.5	1838	1179	64	659	1.51	1065	2.84	499	1.33	47
6	26.5	1988	1248	63	740	1.44	1215	2.70	568	1.26	47
Average	-	-	-	69	-	1.95	-	3.41	-	1.45	43
Arc Current 100A											
0	8.6	860	850	99	10	-	-	-	-	-	-
1	12.6	1260	901	72	359	3.49	400	4.00	51	0.51	13
2	17.5	1750	1248	71	502	2.46	890	4.45	398	1.99	45
3	21.0	2100	1456	69	644	2.11	1240	4.13	606	2.02	49
4	23.7	2370	1595	67	775	1.91	1510	3.78	745	1.86	49
5	25.5	2550	1664	65	886	1.75	1690	3.38	814	1.63	48
6	27.5	2750	1664	61	1086	1.79	1890	3.15	814	1.36	43
Average	-	-	-	72	-	2.25	-	3.82	-	1.56	42
Arc Current 125A											
0	10.4	1300	1100	85	200	-	-	-	-	-	-
1	14.6	1825	1317	72	525	2.60	525	4.20	217	1.74	41
2	18.5	2313	1733	75	1013	3.25	1013	4.05	633	2.53	62
3	22.0	2750	2011	73	1450	3.33	1450	3.87	911	2.43	63
4'	-	-	2288	-	-	-	-	-	-	-	-
5	26.5	3313	2427	73	2013	2.90	2013	3.22	1327	2.12	66
6	28.5	3563	2600	73	2263	2.75	2263	3.02	1500	2.00	66
Average	-	-	-	75	-	2.97	-	3.67	-	2.16	60

TABLE 18 Analysis of Heat Transfer Data for Argon TIG Arcs on a Copper Anode. Ambient Pressure = 21.4 Bars

l (mm)	V (Volts)	P (W)	Q (W)	η (%)	P_L (W)	$\frac{\Delta P_L}{\Delta l}$ (V/mm)	P_C (W)	$\frac{P_C}{\Delta l}$ (V/mm)	Q_C (W)	$\frac{Q_C}{\Delta l}$ (V/mm)	η_C (%)
Arc Current 50A											
0	12.0	600	550	92	50	-	-	-	-	-	-
1.7	17.4	870	763	88	107	0.67	270	3.18	213	2.5	79
2.7	20.5	1025	832	81	193	1.06	425	3.15	282	2.1	66
3.7	23.0	1150	901	78	249	1.08	550	2.97	351	1.9	64
4.7	24.8	1240	971	78	269	0.93	640	2.72	421	1.8	66
5.7	26.3	1315	971	74	344	1.03	775	2.51	421	1.5	59
6.7	28.5	1425	971	68	454	1.21	825	2.46	421	1.3	51
Average	-	-	-	80	-	1.00	-	2.83	-	1.85	64
Arc Current 75A											
0	10.2	765	700	92	65	-	-	-	-	-	-
1	15.0	1125	971	86	154	1.19	360	4.8	271	3.6	75
2	19.0	1425	1040	73	385	2.13	660	4.4	340	2.27	52
3	22.0	1650	1248	76	402	1.50	885	3.9	548	2.44	62
4	24.3	1823	1317	72	506	1.47	1058	3.5	618	2.06	58
5	26.5	1988	1387	70	601	1.43	1223	3.3	687	1.83	56
6	28.5	2138	1526	71	612	1.22	1373	3.1	826	1.84	60
Average	-	-	-	77	-	1.49	-	3.8	-	2.34	61
Arc Current 100A											
0	9.0	900	800	89	100	-	-	-	-	-	-
1	13.5	1350	971	72	379	2.79	450	4.5	171	1.71	38
2	18.4	1840	1317	72	523	2.12	940	4.7	517	2.59	55
3	22.1	2210	1595	72	615	1.72	1310	4.37	795	2.65	61
4	24.8	2480	1803	73	677	1.44	1580	3.95	1030	2.51	65
5	27.4	2740	1941	71	799	1.40	1840	3.68	1141	2.28	62
6	29.8	2980	2066	69	914	1.36	2080	3.47	1266	2.11	61
Average	-	-	-	74	-	1.81	-	4.11	-	2.31	57
Arc Current 125A											
0	9.0	1125	1000	89	125	-	-	-	-	-	-
1	13.6	1700	1387	82	313	1.50	575	4.6	387	3.1	67
2	19.5	2440	1733	71	707	2.33	1315	5.26	733	3.06	56
3	23.0	2875	2080	72	795	1.79	1750	4.67	1080	2.88	62
4	25.8	3225	2288	71	937	1.62	2100	4.20	1288	2.58	61
5	28.5	3563	2565	72	998	1.40	2438	3.90	1565	2.50	64
6	31.5	3938	2704	69	1234	1.48	2813	3.75	1704	2.27	61
Average	-	-	-	75	-	1.69	-	4.40	-	2.73	62

TABLE 19 Analysis of Heat Transfer Data for Argon TIG Arcs on a Copper Anode. Ambient Pressure = 28.2 Bars

l (mm)	V (Volts)	P (W)	Q (W)	η (%)	P_L (W)	$\frac{\Delta P_L}{\Delta l}$ (V/mm)	P_C (W)	$\frac{P_C}{l}$ (V/mm)	Q_C (W)	$\frac{Q_C}{l}$ (V/mm)	η_C (%)
Arc Current 50A											
0	8.9	445	290	65	155	-	-	-	-	-	-
1	13.1	655	453	70	202	0.94	210	4.20	163	3.26	78
2.	18.0	900	654	73	246	0.91	445	4.45	364	3.64	82
3	21.4	1070	755	71	315	1.07	625	4.17	465	3.10	74
4	23.5	1175	805	69	370	1.08	730	3.65	515	2.58	71
5	25.3	1265	855	68	410	1.02	820	3.28	565	2.26	69
6	27.4	1370	906	66	464	1.03	925	3.08	616	2.05	66
Average	-	-	-	69	-	1.01	-	3.81	-	2.82	73
Arc Current 75A											
0	8.0	600	500	83	100	-	-	-	-	-	-
1	12.1	908	755	83	153	0.71	308	4.11	255	3.4	83
2	17.5	1313	956	74	357	1.71	713	4.75	456	3.04	64
3	21.6	1620	1157	71	463	1.61	1020	4.53	657	2.92	64
4	24.2	1815	1258	69	557	1.52	1215	4.05	758	2.53	62
5	27.0	2025	1359	67	666	1.51	1425	3.80	859	2.29	60
6	29.5	2213	1459	66	754	1.45	1613	3.58	959	2.13	59
Average	-	-	-	73	-	1.42	-	4.14	-	2.77	65
Arc Current 100A											
0	8.0	800	590	74	210	-	-	-	-	-	-
1	12.5	1250	884	71	366	1.56	450	4.50	294	2.94	65
2	18.5	1850	1144	62	706	2.48	850	4.25	554	2.77	65
3	21.5	2150	1352	63	798	1.96	1350	4.50	762	2.54	56
4	25.2	2520	1664	66	856	1.62	1720	4.30	1074	2.69	62
5	28.2	2820	1768	63	1052	1.68	2020	4.04	1178	2.36	58
6	31.0	3100	1924	62	1176	1.61	2300	3.83	1334	2.22	58
Average	-	-	-	66	-	1.82	-	4.24	-	2.59	61
Arc Current 125A											
0	8.3	1038	1000	96	38	-	-	-	-	-	-
1	13.7	1713	1352	79	361	2.58	675	5.40	352	2.82	52
2	19.3	2413	1612	67	801	3.05	1375	5.50	612	2.45	45
3	23.8	2975	1924	65	1050	2.70	1937	5.17	924	2.46	48
4	27.2	3400	2132	63	1268	2.46	2362	4.72	1132	2.26	48
5	30.0	3750	2340	62	1410	2.20	2712	4.34	1340	2.14	49
6	33.1	4138	2444	59	1694	2.21	3100	4.13	1444	1.93	47
Average	-	-	-	70	-	2.53	-	4.88	-	2.34	48

TABLE 20 Analysis of Heat Transfer Data for Argon TIG Arcs on a Copper Anode Ambient Pressure = 41.6 Bars

l (mm)	V (Volts)	P (W)	Q (W)	η (%)	P_L (W)	$\frac{\Delta P_L}{\Delta l}$ (V/mm)	P_C (W)	$\frac{P_C}{\Delta l}$ (V/mm)	Q_C (W)	$\frac{Q_C}{\Delta l}$ (V/mm)	η_C (%)
Arc Current 50A											
0	9.0	450	380	84	70	-	-	-	-	-	-
1	13.0	650	484	74	166	1.92	200	4.00	104	2.08	52
2	19.7	985	699	71	286	2.16	535	5.35	319	3.19	60
3	24.0	1200	753	63	447	2.51	750	5.00	373	2.49	50
4	27.5	1375	861	63	514	2.22	925	4.63	481	2.41	52
5	30.0	1500	968	65	532	1.85	1050	4.20	588	2.35	56
6	33.0	1650	968	59	682	2.04	1200	4.00	588	1.96	49
Average	-	-	-	68	-	2.12	-	4.53	-	2.41	53
Arc Current 75A											
0	10.5	788	650	82	138	-	-	-	-	-	-
1	16.5	1238	914	74	324	2.48	450	6.00	264	3.52	59
2	22.7	1703	1237	73	466	2.19	915	6.10	587	3.91	64
3	26.3	1973	1399	71	574	1.94	1485	5.27	799	3.33	63
4	29.3	2220	1452	65	768	2.10	1432	4.77	802	2.67	56
5	32.5	2438	1721	71	717	1.54	1650	4.40	1071	2.86	65
6	35.5	2663	1775	67	888	1.67	1875	4.17	1125	2.50	60
Average	-	-	-	72	-	1.99	-	5.12	-	3.13	61
Arc Current 100A											
0	10.0	1000	800	80	200	-	-	-	-	-	-
1	14.5	1450	1056	73	394	1.94	450	4.50	292	2.92	65
2	21.5	2150	1392	65	758	2.79	1150	5.75	628	3.14	55
3	26.5	2650	1632	62	1018	2.73	1650	5.50	868	2.89	53
4	30.0	3000	1824	61	1176	2.44	2000	5.00	1060	2.65	53
5	33.7	3370	2016	60	1354	2.31	2370	4.74	1252	2.50	53
6	36.8	3680	2016	55	1664	2.44	2680	4.47	1252	2.09	47
Average	-	-	-	65	-	2.44	-	4.99	-	2.71	55
Arc Current 125A											
0	10.0	1250	960	77	290	-	-	-	-	-	-
1	16.5	2063	1410	69	653	2.90	813	6.50	450	3.60	55
2	22.4	2800	1824	65	976	2.74	1550	6.20	864	3.46	56
3	28.5	3563	2256	63	1307	2.71	2313	6.17	1296	3.46	56
4	32.5	4063	2448	60	1615	2.65	2813	5.63	1488	2.98	53
5	35.5	4438	2592	58	1846	2.49	3188	5.10	1632	2.61	51
6	39.0	4875	2784	57	2091	2.40	3625	4.83	1824	2.43	50
Average	-	-	-	64	-	2.65	-	5.74	-	3.09	54

TABLE 21 Analysis of Heat Transfer Date for Helium TIG Arcs on a Copper Anode. Arc Current = 100A

ℓ (mm)	V (Volts)	P (W)	Q (W)	η (%)	P_L (W)	$\frac{\Delta P_L}{\Delta \ell}$ (V/mm)	P_C (W)	$\frac{P_C}{\Delta \ell}$ (V/mm)	Q_C (W)	$\frac{Q_C}{\Delta \ell}$ (V/mm)	η_C (%)
Pressure = 1 Bar											
0	15.0	1500	1290	86	210	-	-	-	-	-	-
1	17.5	1750	1500	86	250	0.40	250	2.5	210	2.10	84
2	19.0	1900	1670	88	230	0.10	400	2.0	380	1.90	95
3	21.5	2150	1890	88	260	0.17	650	2.17	600	2.0	92
4	23.5	2350	2060	88	290	0.20	850	2.13	770	1.93	91
5	25.2	2520	2230	89	290	0.16	1020	2.04	940	1.88	92
Average	-	-	-	88	-	0.21	-	2.17	-	1.96	91
Pressure = 4.4 Bars											
0	15.0	1500	1300	87	200	-	-	-	-	-	-
1	18.7	1870	1620	86	250	0.50	370	3.70	320	3.20	86
2	22.5	2250	1950	85	300	0.50	750	3.75	650	3.25	87
3	26.5	2650	2140	83	510	1.03	1150	3.83	840	2.80	73
4	29.0	2900	2340	84	560	0.90	1400	3.50	1040	2.60	74
5	32.0	3200	2510	78	690	0.98	1700	3.40	1210	2.42	71
Average	-	-	-	84	-	0.78	-	3.64	-	2.85	78
Pressure = 7.8 Bars											
0	14.5	1450	1280	88	170	-	-	-	-	-	-
1	18.5	1850	1560	84	290	1.20	400	4.00	280	2.80	70
2	23.5	2350	1890	81	460	1.45	900	4.50	610	3.05	68
3	27.1	2710	2280	84	470	0.87	1260	4.20	1000	3.33	79
4	31.0	3100	2450	79	650	1.20	1650	4.13	1170	2.93	71
5	34.0	3400	2560	75	840	1.34	1950	3.90	1280	2.56	66
Average	-	-	-	82	-	1.21	-	4.15	-	2.93	71
Pressure = 11.2 Bars											
0	15.0	1500	1330	89	170	-	-	-	-	-	-
1	20.0	2000	1670	84	330	1.60	500	5.00	340	3.40	68
2	24.5	2450	2010	84	390	1.10	900	4.50	680	3.40	76
3	25.5	2550	2340	92	210	0.13	1050	3.50	1010	3.37	96
4	30.0	3000	2510	83	490	0.80	1500	3.75	1180	2.95	79
5	36.0	3600	2900	81	700	1.06	2100	4.20	1570	3.14	75
Average	-	-	-	86	-	0.94	-	4.19	-	3.25	79

TABLE 22 Analysis of Heat Transfer Data for Argon TIG Arcs on a Mild Steel Anode. Ambient Pressure = 1 Bar

ℓ (mm)	V (Volts)	P (W)	Q (W)	η (%)	P_L (W)	$\frac{\Delta P_L}{\Delta \ell}$ (V/mm)	P_C (W)	$\frac{P_C}{\ell}$ (V/mm)	Q_C (W)	$\frac{Q_C}{\ell}$ (V/mm)	η_C (%)
Arc Current 50A											
0	8.0	400	240	60	160	-	-	-	-	-	-
2	10.4	520	334	64	186	0.26	120	1.20	94	0.94	78
3	11.7	585	390	67	195	0.23	185	1.23	150	1.00	81
4	12.5	625	446	71	179	0.10	225	1.13	206	1.03	92
5	12.9	645	446	69	199	0.17	245	0.98	206	0.83	84
Average	-	-	-	66	-	0.19	-	1.14	-	0.95	84
Arc Current 75A											
0	8.5	638	530	83	108	-	-	-	-	-	-
2	10.4	780	624	80	156	0.32	142	0.95	94	0.63	66
3	11.2	840	652	78	188	0.36	202	0.90	122	0.54	60
4	12.0	900	680	76	220	0.37	262	0.87	150	0.50	57
5	12.6	945	737	78	208	0.27	307	0.82	207	0.55	67
Average	-	-	-	79	-	0.33	-	0.89	-	0.56	63
Arc Current 100A											
0	7.7	770	620	81	150	-	-	-	-	-	-
2	9.5	950	694	73	256	0.53	180	0.90	74	0.37	41
3	10.4	1040	809	78	231	0.27	270	0.90	189	0.63	70
4	11.5	1150	867	75	283	0.33	380	0.95	247	0.62	65
5	12.4	1240	924	75	316	0.33	470	0.94	304	0.61	65
Average	-	-	-	76	-	0.37	-	0.92	-	0.56	60
Arc Current 125A											
0	7.9	988	880	89	108	-	-	-	-	-	-
2	10.4	1300	1021	79	279	0.68	312	1.25	141	0.56	45
3	11.5	1438	1078	75	360	0.67	450	1.20	198	0.53	44
4	12.2	1525	1138	73	412	0.61	537	1.07	233	0.47	43
5	13.0	1625	1191	74	434	0.52	637	1.03	311	0.50	49
Average	-	-	-	78	-	0.62	-	1.14	-	0.52	45

TABLE 23 Analysis of Heat Transfer Data for Argon TIG Arcs on a Mild Steel Anode. Ambient Pressure = 7.8 Bars

ℓ (mm)	V (Volts)	P (W)	Q (W)	η (%)	P_L (W)	$\frac{\Delta P_L}{\Delta l}$ (V/mm)	P_C (W)	$\frac{P_C}{\Delta l}$ (V/mm)	Q_C (W)	$\frac{Q_C}{\Delta l}$ (V/mm)	η_C (%)
Arc Current 50A											
0	8.5	425	300	71	125	-	-	-	-	-	-
2	11.9	595	397	67	198	0.73	170	1.70	97	0.97	57
3	14.0	700	454	65	246	0.81	275	1.83	154	1.03	56
4	15.5	775	454	59	321	0.98	350	1.75	154	0.77	44
5	16.5	825	454	55	371	0.98	400	1.60	154	0.62	39
Average	-	-	-	63	-	0.88	-	1.72	-	0.85	49
Arc Current 75A											
0	7.9	593	475	80	118	-	-	-	-	-	-
2	11.8	885	557	63	328	1.40	292	1.95	82	0.55	28
3	13.5	1013	613	61	400	1.25	420	1.87	138	0.61	33
4	15.6	1170	668	57	502	1.28	577	1.92	193	0.64	33
5	17.0	1275	724	57	551	1.15	682	1.82	249	0.66	37
Average	-	-	-	64	-	1.27	-	1.89	-	0.62	33
Arc Current 100A											
0	7.6	760	680	89	80	-	-	-	-	-	-
2	11.0	1100	780	70	320	1.20	340	1.70	100	0.50	29
3	14.2	1420	836	59	584	1.68	660	2.20	156	0.52	24
4	16.0	1600	891	56	709	1.57	840	2.80	211	0.53	25
5	16.9	1690	947	56	743	1.33	930	1.86	267	0.53	29
Average	-	-	-	66	-	1.45	-	2.14	-	0.52	27
Arc Current 125A											
0	8.2	1025	860	84	165	-	-	-	-	-	-
2	12.2	1525	983	64	543	1.51	500	2.00	123	0.49	25
3	14.2	1775	1040	59	735	1.52	750	2.00	180	0.48	24
4	16.0	2000	1098	55	902	1.47	975	1.95	238	0.48	24
5	17.6	2200	1156	53	1044	1.41	1175	1.88	296	0.47	25
Average	-	-	-	63	-	1.48	-	1.96	-	0.48	25

TABLE 24 Analysis of Heat Transfer Data for Argon TIG Arcs on a Mild Steel Anode. Ambient Pressure = 21.4

ℓ (mm)	V (Volts)	P (W)	Q (W)	η (%)	P_L (W)	$\frac{\Delta P_L}{\Delta \ell}$ (V/mm)	P_C (W)	$\frac{P_C}{\ell}$ (V/mm)	Q_C (W)	$\frac{Q_C}{\ell}$ (V/mm)	η_C (%)
Arc Current 50A											
0	8.4	420	240	57	180	-	-	-	-	-	-
2	13.2	660	340	52	320	1.40	240	2.4	100	1.00	42
3	15.2	760	397	52	363	1.22	340	2.27	157	1.05	46
4	17.9	895	454	51	441	1.31	475	2.38	214	1.07	45
5	20.5	1025	510	50	515	1.34	605	2.42	270	1.08	45
Average	-	-	-	52	-	1.32	-	2.37	-	1.05	45
Arc Current 75A											
0	8.5	638	450	71	188	-	-	-	-	-	-
2	13.6	1020	567	56	453	1.77	382	2.55	117	0.78	31
3	16.2	1215	624	51	591	1.79	577	2.56	174	0.77	30
4	19.0	1425	680	48	745	1.86	787	2.62	230	0.77	29
5	21.5	1613	737	46	876	1.83	975	2.60	287	0.77	29
Average	-	-	-	54	-	1.81	-	2.58	-	0.77	30
Arc Current 100A											
0	8.4	840	630	75	210	-	-	-	-	-	-
2	12.4	1240	780	63	460	1.25	400	2.00	150	0.75	38
3	18.5	1850	891	48	959	2.50	1010	3.37	261	0.87	26
4	20.5	2050	947	46	1103	2.23	1210	3.03	317	0.79	26
5	22.4	2240	947	43	1293	2.17	1400	2.8	317	0.63	23
Average	-	-	-	55	-	2.04	-	2.8	-	0.76	28
Arc Current 125A											
0	8.5	1063	770	72	293	-	-	-	-	-	-
2	13.8	1725	985	58	740	1.79	662	2.65	215	0.86	32
3	19.0	2375	1121	47	1254	2.56	1312	3.50	351	0.94	27
4	20.0	2500	1149	46	1351	2.12	1437	2.87	379	0.76	26
5	22.8	2850	1203	42	1647	2.17	1787	2.86	433	0.70	24
Average	-	-	-	53	-	2.16	-	2.97	-	0.82	27

TABLE 25 Analysis of Heat Transfer Data for Argon TIG Arcs on a Mild Steel Anode. Ambient Pressure = 41.8 Bars

ℓ (mm)	V (Volts)	P (W)	Q (W)	η (%)	P_L (W)	$\frac{\Delta P_L}{\Delta \ell}$ (V/mm)	P_C (W)	$\frac{P_C}{\ell}$ (V/mm)	Q_C (W)	$\frac{Q_C}{\ell}$ (V/mm)	η_C (%)
Arc Current 50A											
0	8.4	420	240	57	180	-	-	-	-	-	-
2	13.9	695	334	48	361	1.81	275	2.75	94	0.94	34
3	17.5	875	390	45	485	2.03	455	3.03	150	1.00	33
4	21.0	1050	446	42	604	2.12	630	3.15	206	1.03	33
5	23.7	1185	446	38	739	2.24	765	3.06	206	0.82	27
Average	-	-	-	46	-	2.05	-	3.00	-	0.95	32
Arc Current 75A											
0	9.0	675	310	46	365	-	-	-	-	-	-
2	15.5	1163	476	41	687	2.15	488	3.25	166	1.4	34
3	19.1	1433	635	44	798	1.92	758	3.37	325	1.44	43
4	22.0	1650	635	38	1015	2.17	975	3.25	325	1.08	33
5	25.2	1890	635	34	1255	2.37	1215	3.24	325	0.87	27
Average	-	-	-	41	-	2.15	-	3.28	-	1.13	34
Arc Current 100A											
0	10.5	1050	500	48	550	-	-	-	-	-	-
2	21.0	2100	846	40	1254	3.52	1050	5.25	346	1.73	33
3	23.0	2300	846	37	1454	3.01	1250	4.17	346	1.15	28
4	26.0	2600	925	36	1675	2.81	1550	3.88	425	1.06	27
5	30.0	3000	1005	33	1995	2.89	1950	3.90	505	1.01	26
Average	-	-	-	39	-	3.06	-	4.30	-	1.24	29
Arc Current 125A											
0	10.5	1313	800	61	513	-	-	-	-	-	-
2	20.0	2500	1149	46	1351	3.35	1187	4.75	349	1.40	29
3	24.0	3000	1259	42	1741	3.27	1687	4.50	459	1.22	27
4	28.5	3563	1313	37	2250	3.47	2250	4.50	513	1.03	23
5	31.0	3875	1313	34	2562	3.28	2562	4.10	513	0.82	20
Average	-	-	-	44	-	3.34	-	4.50	-	1.12	25

TABLE 26A Analysis of Heat Transfer Data for Argon TIG Arcs on Mild Steel Anodes in the Presence of an Axial* Magnetic Field. (*Details are given in text).
Arc Current 100A

South Pole Pointing at Pool

ℓ (mm)	V (Volts)	P (W)	Q (W)	η (%)	P_L (W)	$\frac{\Delta P_L}{I\ell}$ (V/mm)	P_C (W)	$\frac{P_C}{I\ell}$ (V/mm)	Q_C (W)	$\frac{Q_C}{I\ell}$ (V/mm)	η_C (%)
0	9.5	950	675	71	275	-	-	-	-	-	-
2	11.0	1100	809	74	291	0.08	150	0.75	134	0.67	89
3	11.8	1180	867	73	313	0.19	230	0.77	192	0.64	83
4	12.5	1250	925	74	325	0.13	300	0.75	250	0.63	83
5	13.2	1320	925	70	395	0.24	370	0.74	250	0.50	68
Average	-	-	-	72	-	0.16	-	0.75	-	0.61	81
Pressure = 7.8 Bars											
0	10.2	1020	610	60	410	-	-	-	-	-	-
2	13.1	1310	724	55	586	0.88	290	1.45	114	0.57	39
3	14.6	1460	836	57	624	0.71	440	1.47	226	0.75	51
4	16.3	1630	891	55	739	0.82	610	1.53	281	0.70	46
5	17.5	1750	947	54	803	0.79	730	1.46	337	0.67	46
Average	-	-	-	56	-	0.80	-	1.48	-	0.67	46
Pressure = 21.4 Bars											
0	11.5	1150	700	61	450	-	-	-	-	-	-
2	16.0	1600	808	51	792	1.71	450	2.25	108	0.54	24
3	18.0	1800	836	46	964	1.71	650	2.17	136	0.45	21
4	20.0	2000	891	45	1109	1.65	850	2.13	191	0.48	22
5	22.5	2250	947	42	1303	1.71	1100	2.2	247	0.49	22
Average	-	-	-	49	-	1.70	-	2.19	-	0.49	22
Pressure = 41.2 Bars											
0	11.5	1150	770	62	440	-	-	-	-	-	-
2	19.4	1940	834	43	1106	3.33	790	3.95	124	0.62	16
3	23.0	2300	861	37	1439	3.33	1150	3.83	151	0.50	13
4	26.0	2600	915	35	1685	3.11	1450	3.63	205	0.51	14
5	28.5	2850	968	34	1882	2.88	1700	3.40	258	0.52	15
Average	-	-	-	42	-	3.16	-	3.70	-	0.54	15
South Pole Pointing away from Pool Pressure = 41.2 Bars											
0	11.5	1150	655	57	495	-	-	-	-	-	-
2	20.3	2030	793	39	1237	3.71	880	4.40	138	0.69	16
3	24.0	2400	875	36	1525	3.43	1250	4.17	220	0.73	18
4	27.5	2750	875	32	1875	3.45	1600	4.00	220	0.55	14
5	29.5	2950	985	33	1965	2.94	1800	3.6	335	0.67	19
Average	-	-	-	39	-	3.38	-	4.04	-	0.66	17

TABLE 26B Analysis of Heat Transfer Date for Helium TIG Arcs on Steel Anodes in the Presence of an Axial Magnetic*Field is Applied. (*Details of field are given in text). Arc Current 100A

(A) Southpole Pointing towards Pool

Pressure = 1 Bar

l (mm)	V (Volts)	P (W)	Q (W)	η (%)	P_L (W)	$\frac{\Delta P_L}{\Delta l}$ (V/mm)	P_C (W)	$\frac{P_C}{\Delta l}$ (V/mm)	Q_C (W)	$\frac{Q_C}{\Delta l}$ (V/mm)	η_C (%)
0	10.0	1000	640	64	360	-	-	-	-	-	-
2	14.0	1400	907	69	493	0.67	400	2.00	267	1.34	66
3	15.7	1570	1077	69	493	0.44	570	1.90	437	1.46	77
4	17.7	1770	1134	64	636	0.69	770	1.93	494	1.24	64
5	19.7	1970	1247	63	723	0.73	970	1.94	607	1.21	63
Average	-	-	-	66	-	0.63	-	1.94	-	1.31	68
Pressure = 11.2 Bars											
0	10.5	1050	760	72	290	-	-	-	-	-	-
2	20.0	2000	1219	61	781	2.46	950	4.25	459	2.30	48
3	24.5	2450	1418	58	1032	2.47	1400	4.67	658	2.19	47
4	27.0	2700	1701	63	999	1.77	1050	4.13	941	2.35	57
5	29.5	2950	1871	63	1079	1.58	1900	3.8	1111	2.22	58
Average	-	-	-	63	-	2.07	-	4.21	-	2.27	53

(B) Southpole Pointing away from Pool

Pressure = 1 Bar

0	9.5	950	600	63	350	-	-	-	-	-	-
2	13.3	1330	851	64	479	0.66	380	1.90	251	1.26	66
3	14.6	1460	964	66	496	0.49	510	1.70	364	1.21	71
4	16.5	1650	1077	65	573	0.56	700	1.75	477	1.19	68
5	17.5	1750	1247	71	503	0.31	800	1.60	647	1.29	81
Average	-	-	-	66	-	0.51	-	1.74	-	1.24	72
Pressure = 11.2 Bars											
0	12.5	1250	950	76	300	-	-	-	-	-	-
2	23.0	2300	1474	64	826	2.63	1050	5.25	524	2.62	50
3	26.5	2650	1644	62	1006	2.35	1400	4.67	694	2.31	49
4	28.5	2850	1814	64	1036	1.84	1600	4.00	864	2.16	54
5	31.0	3100	1985	64	1115	1.63	1850	3.70	1035	2.07	56
Average	-	-	-	66	-	2.11	-	4.41	-	2.29	52

TABLE 27 Analysis of Heat Transfer Data for Helium TIG Arcs on a Mild Steel Anode. Arc Current 100A

ℓ (mm)	V (Volts)	P (W)	Q (W)	η (%)	P_L (W)	$\frac{\Delta P_L}{\Delta \ell}$ (V/mm)	P_C (W)	$\frac{P_C}{\ell}$ (V/mm)	Q_C (W)	$\frac{Q_C}{\ell}$ (V/mm)	η_C (%)
Ambient Pressure 1 Bar											
0	8.8	880	660	95	220	-	-	-	-	-	-
2	12.9	1290	967	75	323	0.52	410	2.1	307	1.54	75
3	14.6	1460	1138	78	322	0.34	580	1.9	478	1.59	82
4	16.3	1630	1195	73	435	0.54	750	1.9	535	1.34	71
5	17.5	1750	1252	72	498	0.56	870	1.7	592	1.18	68
Average	-	-	-	75	-	0.49	-	1.9	-	1.41	74
Ambient Pressure 4.4 Bars											
0	8.4	840	700	83	140	-	-	-	-	-	-
2	15.0	1500	1081	72	419	1.40	660	3.30	381	1.91	58
3	19.5	1950	1252	64	698	1.86	1110	3.7	552	1.84	50
4	22.0	2200	1423	65	777	1.95	1360	3.4	723	1.81	53
5	25.0	2500	1707	68	793	1.31	1660	3.3	1070	2.14	64
Average	-	-	-	70	-	1.54	-	3.4	-	1.93	56
Ambient Pressure = 7.8 Bars											
0	9.0	900	700	78	200	-	-	-	-	-	-
2	16.7	1670	1081	65	589	1.95	770	3.85	381	1.91	49
3	20.0	2000	1280	64	720	1.73	1100	3.67	580	1.93	53
4	24.0	2400	1593	66	807	1.52	1500	3.75	893	2.23	60
5	26.0	2600	1707	66	893	1.39	1700	3.40	1007	2.01	59
Average	-	-	-	68	-	1.65	-	3.67	-	2.02	55
Ambient Pressure = 11.2 Bars											
0	11.0	1100	800	73	300	-	-	-	-	-	-
2	21.0	2100	1252	60	848	2.74	1000	5.00	452	2.24	46
3	25.5	2550	1479	58	1071	2.34	1450	4.84	699	2.30	47
4	30.5	3050	1650	54	1400	2.75	1950	4.88	850	2.13	44
5	33.5	3350	1763	53	1587	2.57	2250	4.50	963	1.93	43
Average	-	-	-	60	-	2.60	-	4.81	-	2.15	45

Heat input to the cathode also has a weak pressure dependence. Averaging values of $P_L(\ell=0)$ across all pressures gives a current dependent of

$$P_L\ (\ell=0) \simeq 1.5I$$

The behaviour of Q_o and P_L indicates that the zero length arc voltage is substantially independent of pressure with a value of 9.5 volts. This is in fair agreement with the observed behaviour of V_o (see figures 66 and 67).

(B) Influence of Arc Current on Q

Results obtained at 1 bar and 41.2 bars are shown in figures 170 and 171. These illustrate that Q is linearly dependent on arc current with a slope that increases with arc length. Similar behaviour is observed at other pressures as may be seen from tables 14 to 20.

(C) Influence of Pressure on Q

The general results are again given in tabular form with only a typical result being shown graphically (3mm arc length, see figure 172). It may be seen from figure 172.that pressure has a modest influence on the 50 Amp arc examined. However, the sensitivity of Q to pressure increases with current although the increase with pressure is largely confined to the first 15 bars for all currents.

Results shown in tabular form indicate that the influence of pressure increases with arc length for a given current. This effect becomes negligible in the limit as arc length tends to zero.

6.1.1.2. Efficiency of Heat Transfer (η)

It is convenient to express Q as a fraction (η) of the total process power p. Results for η may be found in tables 14 to 20. Results show that efficiency is primarily influenced by arc length and pressure i.e. Arc current exerts only a weak influence on η. At zero arc length efficiency is found to be independent of pressure (within the range of experimental accuracy) and is generally of order 80 ($\pm$5)%. The

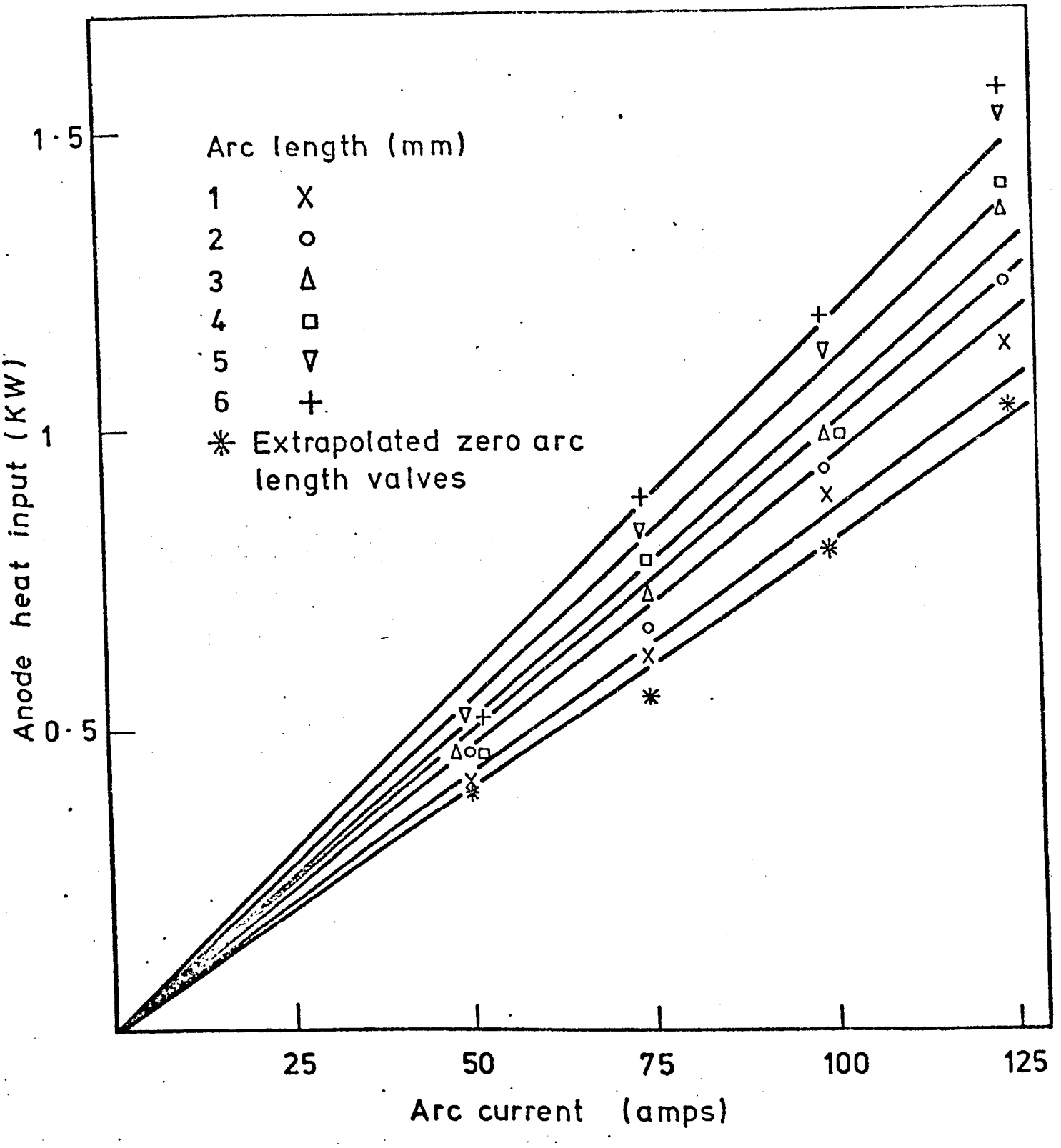

FIGURE 170. INFLUENCE OF ARC CURRENT ON ANODE HEATING FOR AN ARGON TIG ARC ON A COPPER ANODE (P = 1 BAR)

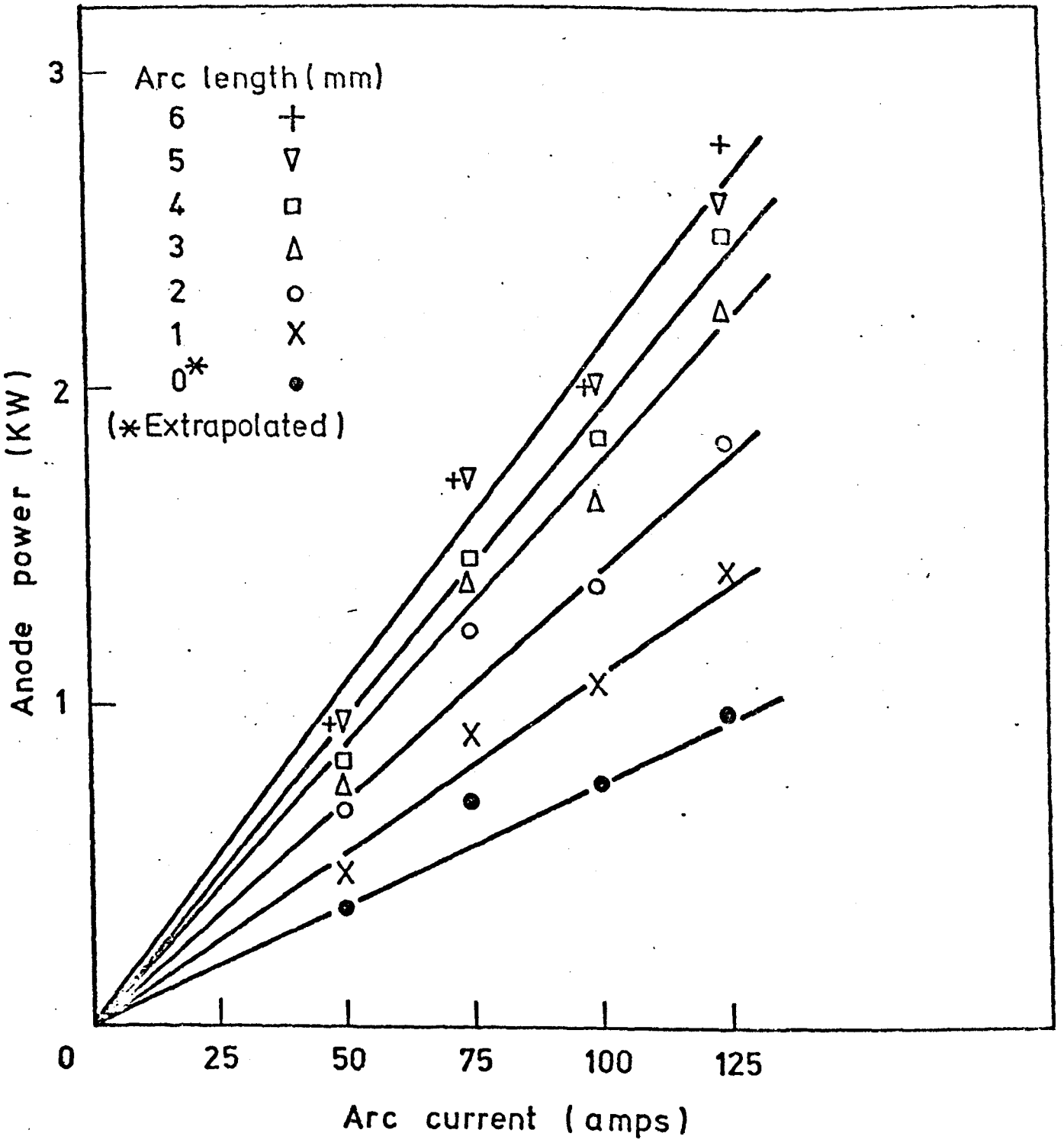

FIGURE 171. INFLUENCE OF ARC CURRENT AND LENGTH ON ANODE HEATING FOR ARGON ARCS ON A COPPER ANODE (P = 41·6 BARS)

dependence of η on pressure becomes pronounced with increasing arc length. Values measured at 1 bar are substantially independent of arc length (to within $\pm 5\%$) while values at 41.6 bars vary for a 100 Amp arc from 80% at ℓ=0 to 55% at ℓ=6mm. This behaviour is also found for other currents at 41.6 bars. The dependence of η on arc length is shown graphically in figure 173 for I = 100 Amps. Figure 173 shows that the pressure dependence of efficiency is strongly dependent on arc length. For this reason the average behaviour (averaged over arc length and current) has been used to represent the pressure dependence of efficiency (see figure 174). This shows a fall of 9% between 1 and 14.6 bars. Average efficiency then increases between 14.6 bars and 21.4 bars thereafter decreasing to 41.2 bars. The largest change occurs over the first 14.6 bars with only a further fall of 2.5% between 14.6 bars and 41.6 bars.

6.1.1.3. Process Power (PL) not Entering the Anode

The power not entering the anode (P_L) is defined by $P_L = P - Q$. This factor is shown in tables 14 to 20. The value at ℓ=0 (i.e. $P_L(\ell=0)$) represents power appearing at the cathode. This has already been discussed. It is also of interest to investigate that fraction of the power appearing in the column that does not appear at the anode. This is given by

$$\Delta P_L = P_L - P_L(\ell=0)$$

A more suitable form of ΔP_L is to express this per unit length and current. i.e. $\Delta P_L/I.\ell$. These results are also shown in tables 14 to 20. The behaviour of this ratio is generally, only weakly dependent on arc length at any pressure or current. This suggests that losses from the arc column are directly proportional to arc length and current. It is therefore reasonable to compute the average (over arc length) of this ratio. This has been done and results are shown in figure 175 as a function of pressure for different currents. It can be seen that the arc column loss per amp per mm increases quickly over the first 14.6 bars. This falls to 21.2 bars before again rising. The fall corresponds to the pressure at which the average process efficiency abruptly increased (see figure 174). Above 14.6 bars the fractional loss increases with arc current indicating that ΔP_L is increasing more quickly than arc current at

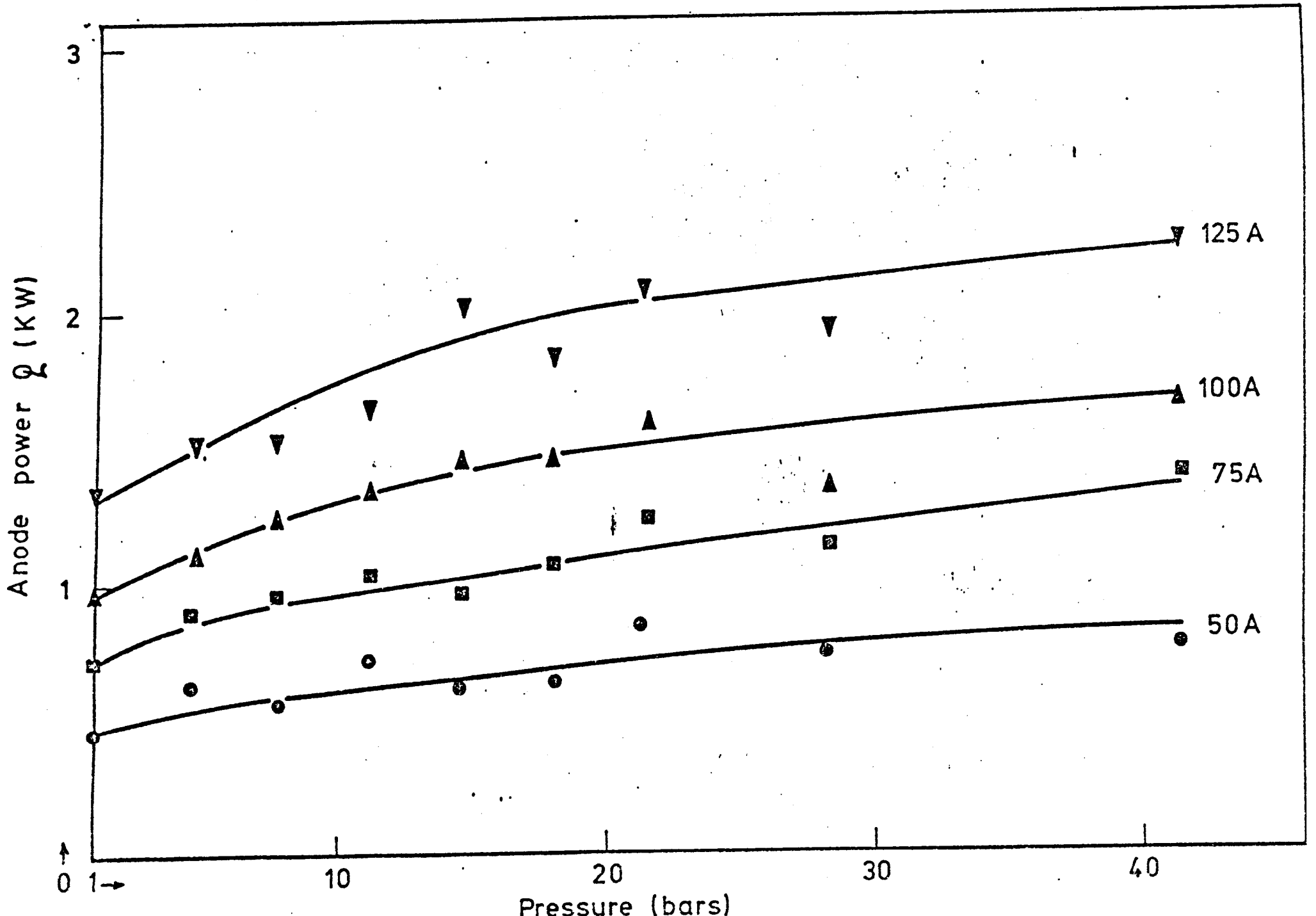

FIGURE 172 INFLUENCE OF AMBIENT PRESSURE AND ARC CURRENT ON ANODE HEATING (COPPER)

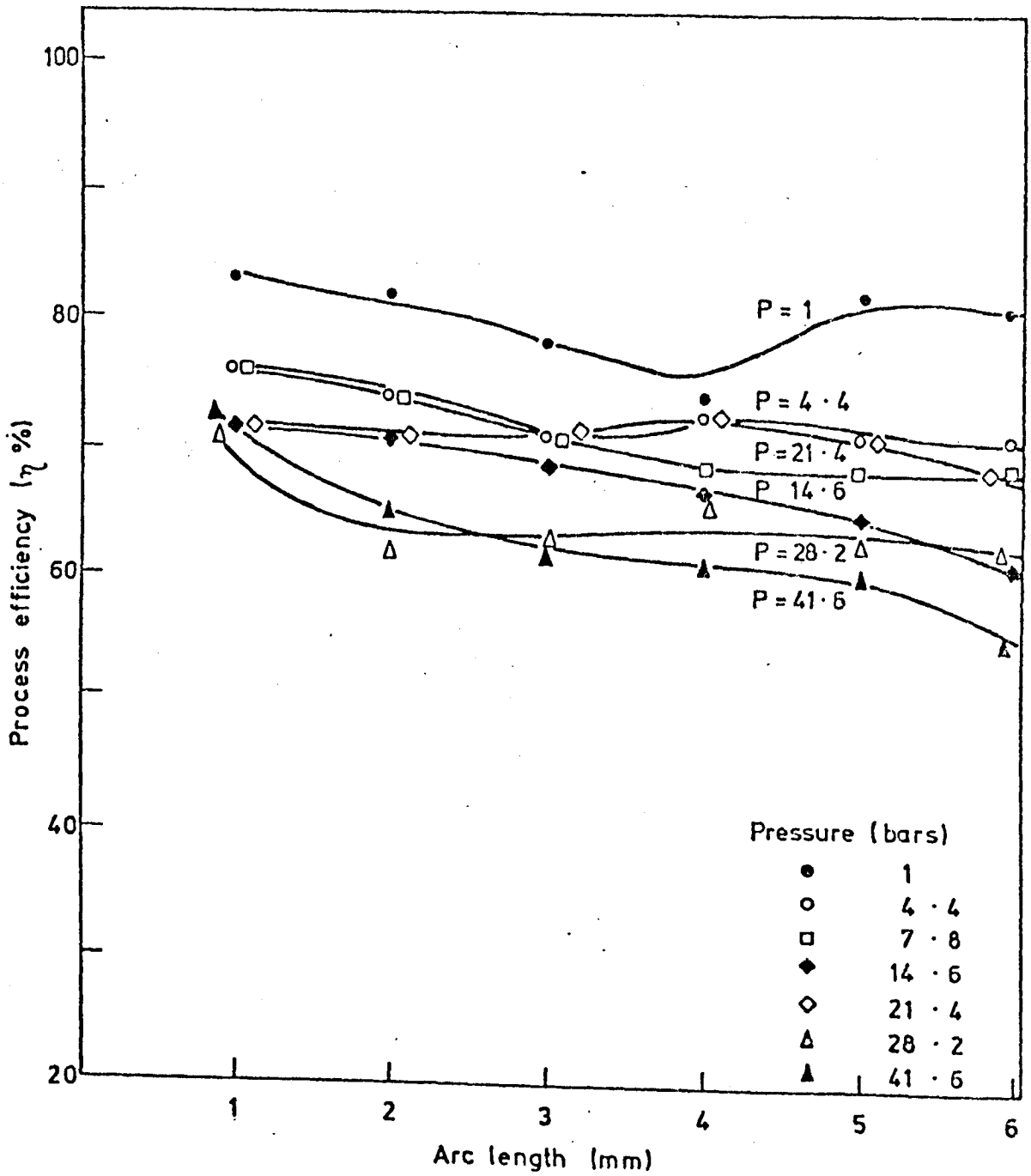

FIGURE 173. INFLUENCE OF ARC LENGTH ON HEAT TRANSFER EFFICIENCY FROM AN 100 A ARGON TIG ARC TO A COPPER ANODE.

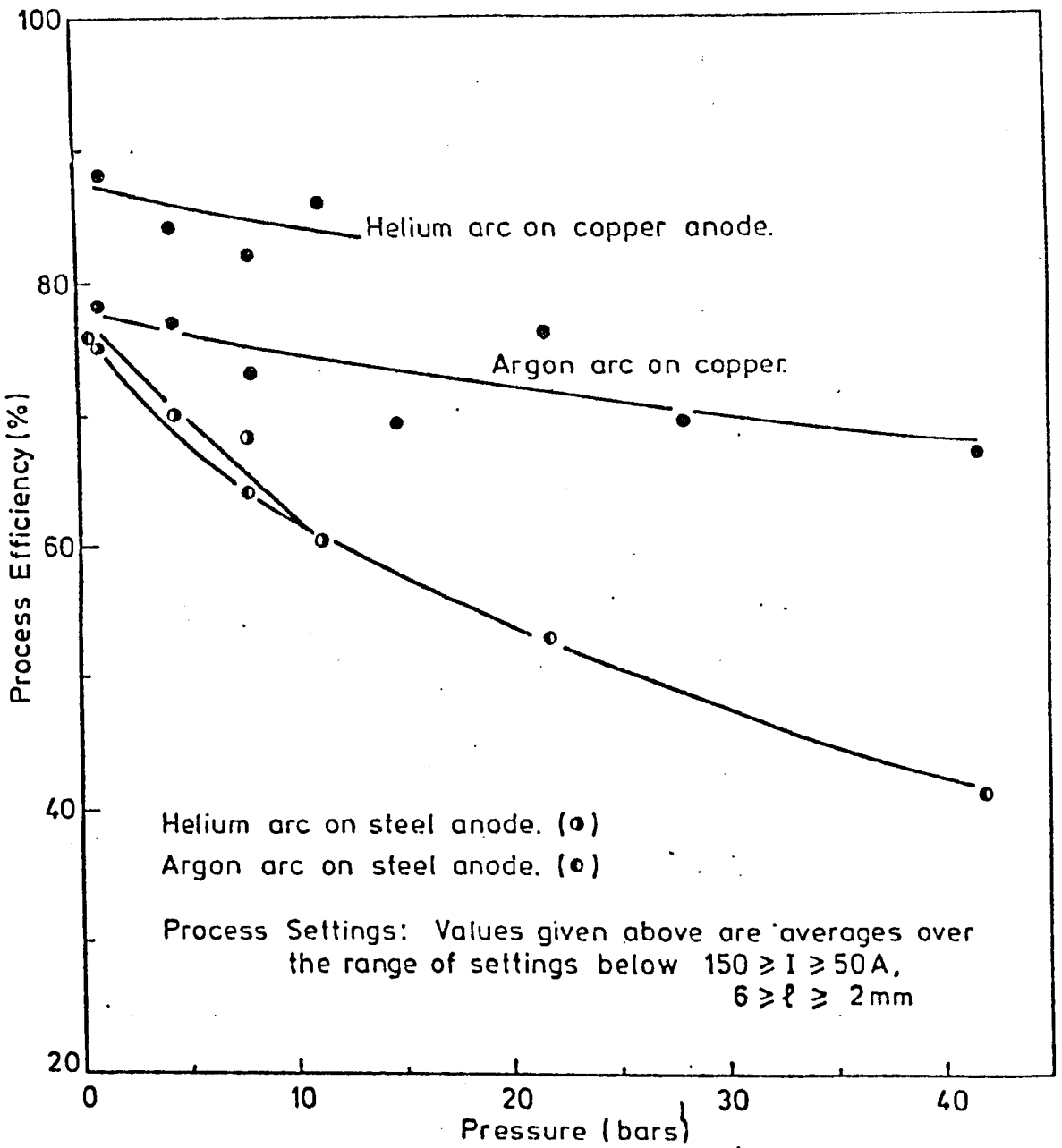

FIG. 174. PRESSURE DEPENDENCE OF PROCESS EFFICIENCY FOR DIFFERENT ARCING SITUATIONS.

high pressures. Below this pressure $\Delta P_L/I.\ell$ is substantially independent of arc current indicating that arc column losses are directly proportional to current.

Behaviour reported above has a pressure dependence that is very roughly represented by a square root law (see figure 175). This indicates that power losses from the column (that enter the anode) are roughly in proportion to the power appearing in the column.

6.1.1.4. The Influence of Arc Heating on Q

Results for Q have been obtained for a range of arc lengths. These results may be used to estimate the contribution (Q_c) that arc column power makes to anode heating. Q_c is given by

$$Q_c = Q - Q(\ell=0)$$

The fundamental assumption involved in this identification is that the zero arc length heating (Q_o), obtained by extrapolating results from a number of arc lengths, is independent of arc length. This is considered further in later sections. Q_c has been calculated and is shown in tables 14 to 20. It can be clearly seen that Q_c increases with arc length, arc current and pressure. A more useful expression of the behaviour of Q_c is in terms of $Q_c/I.\ell$. This is also shown in tabular form. Results are also shown graphically in figure 176. These figures show that $Q_c/I.\ell$ is only weakly influenced by arc length at low pressures. At high pressures $Q_c/I.\ell$ decreases slowly with arc length. However, the behaviour is again slow enough to make it reasonable to examine the average value (averaged over arc length). These comments show that Q_c increases with arc length slightly less strongly than ℓ. Results obtained at 50 Amps indicate that $Q_c/I.\ell$ may increase slightly for arc lengths between 1 and 2mm's. This behaviour is also occasionally found at higher currents.

The average value of $Q_c/I.\ell$ is shown in figure 177 as a function of arc current. At low pressures the fractional increase with arc current is quite significant e.g. 0.45 to 0.9 W/A.mm at 1 bar. However at higher pressures the fractional change is small (although the absolute change is generally similar to that at all pressures e.g. 2.4 to 3.1 W/A.mm at

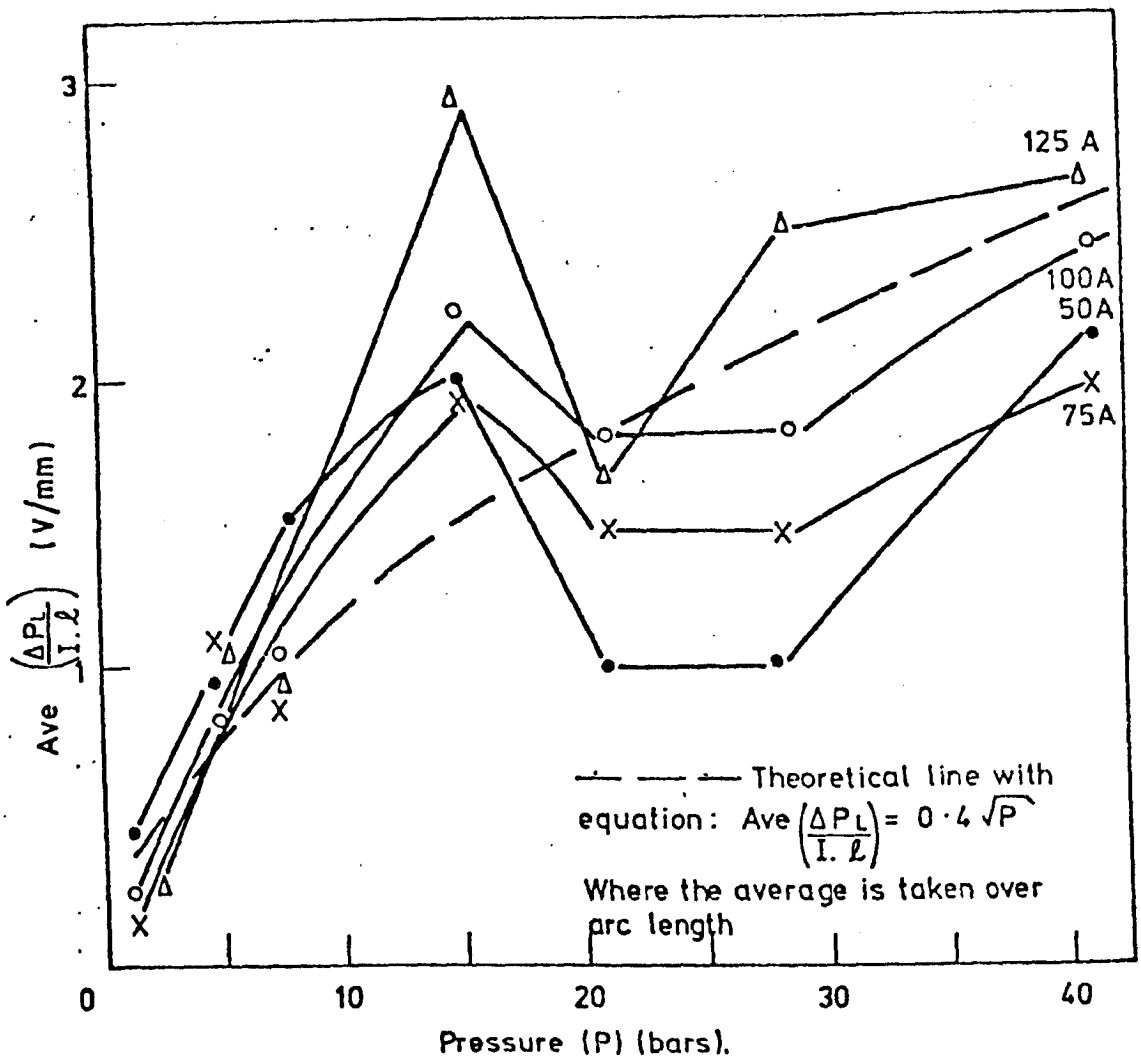

FIGURE 175 INFLUENCE OF AMBIENT PRESSURE AND ARC CURRENT ON POWER APPEARING IN THE COLUMN BUT NOT AT THE ANODE (ΔP_L) FOR ARGON TIG ARCS ON A COPPER ANODE.

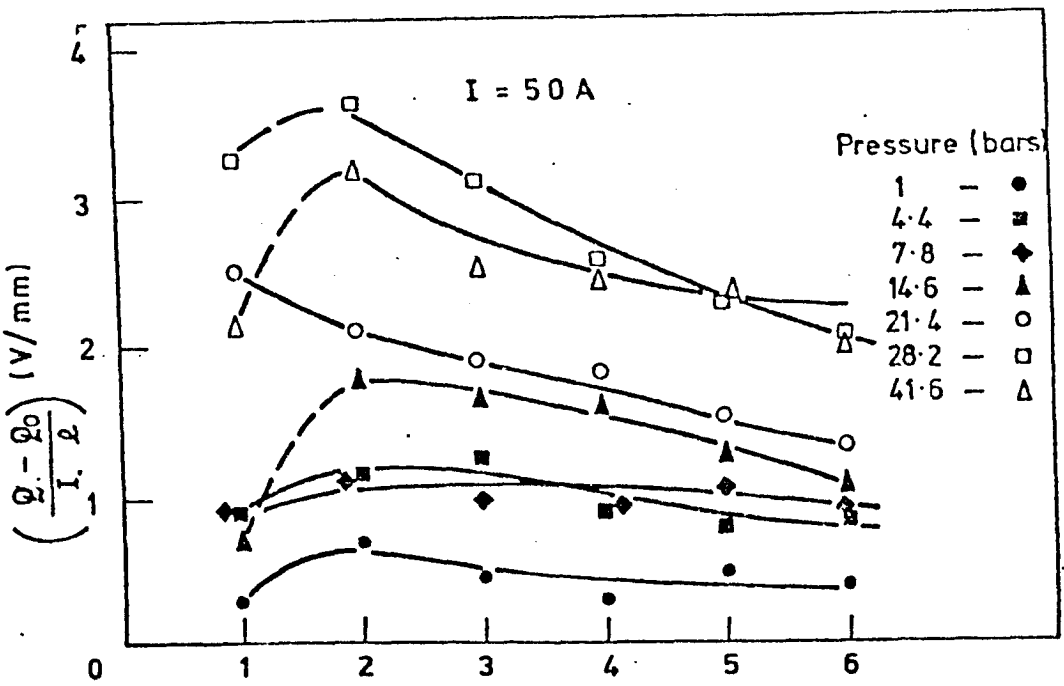

FIGURE 176 a.

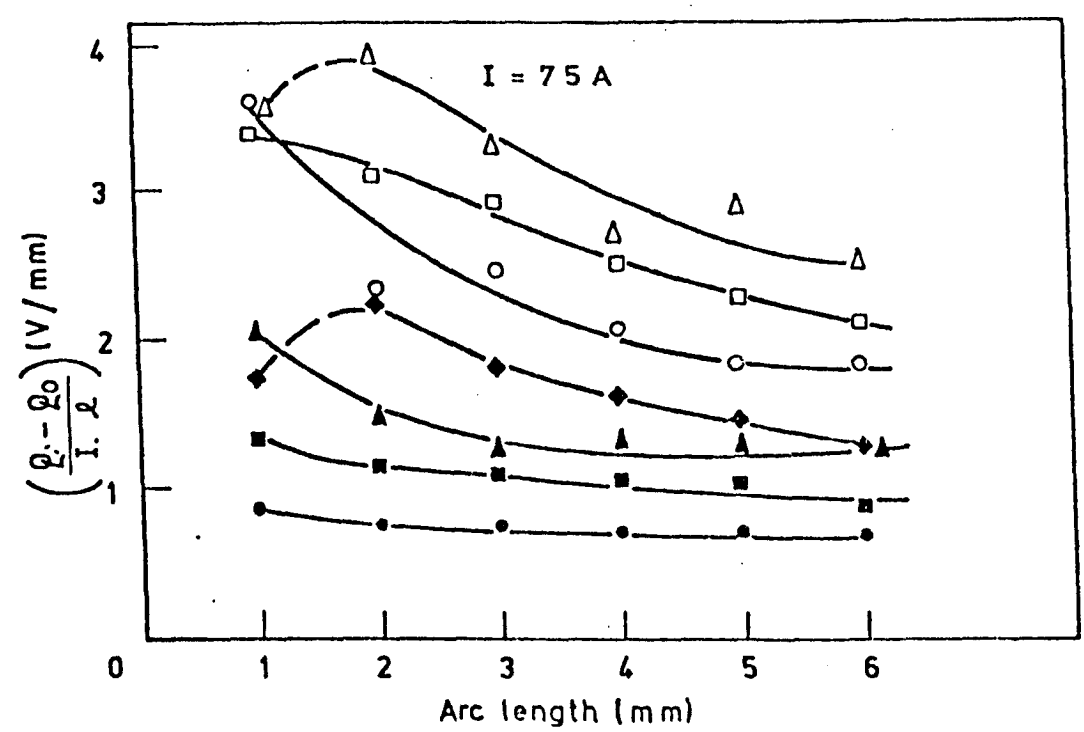

FIGURE 176 b INFLUENCE OF ARC LENGTH AMBIENT PRESSURE AND ARC CURRENT ON THE CONTRIBUTION TO ANODE HEATING MADE BY POWER DEVELOPED IN THE COLUMN ($Q_i - Q_0$) FOR ARGON TIG ARCS ON A COPPER ANODE

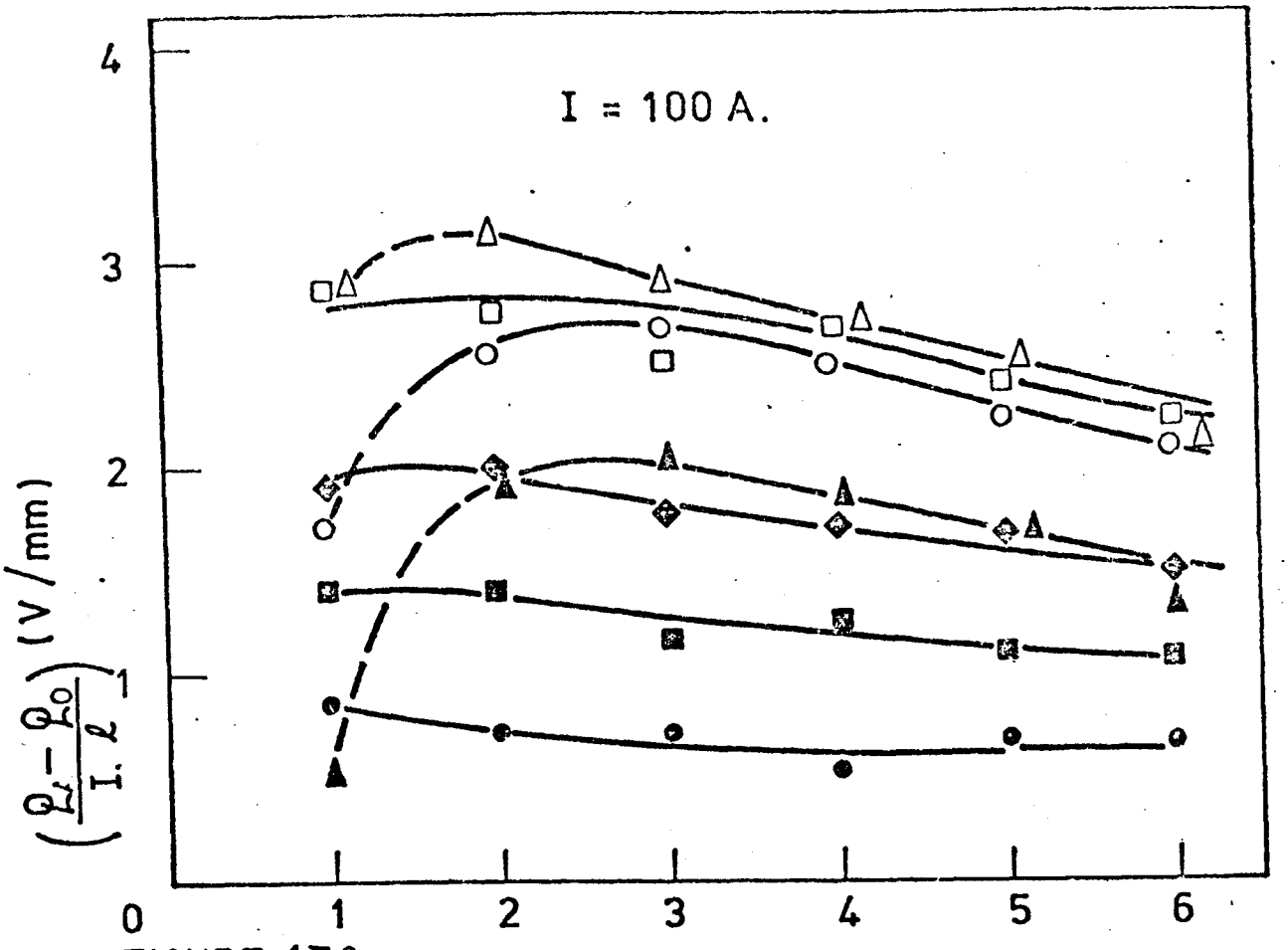

FIGURE 176 c.

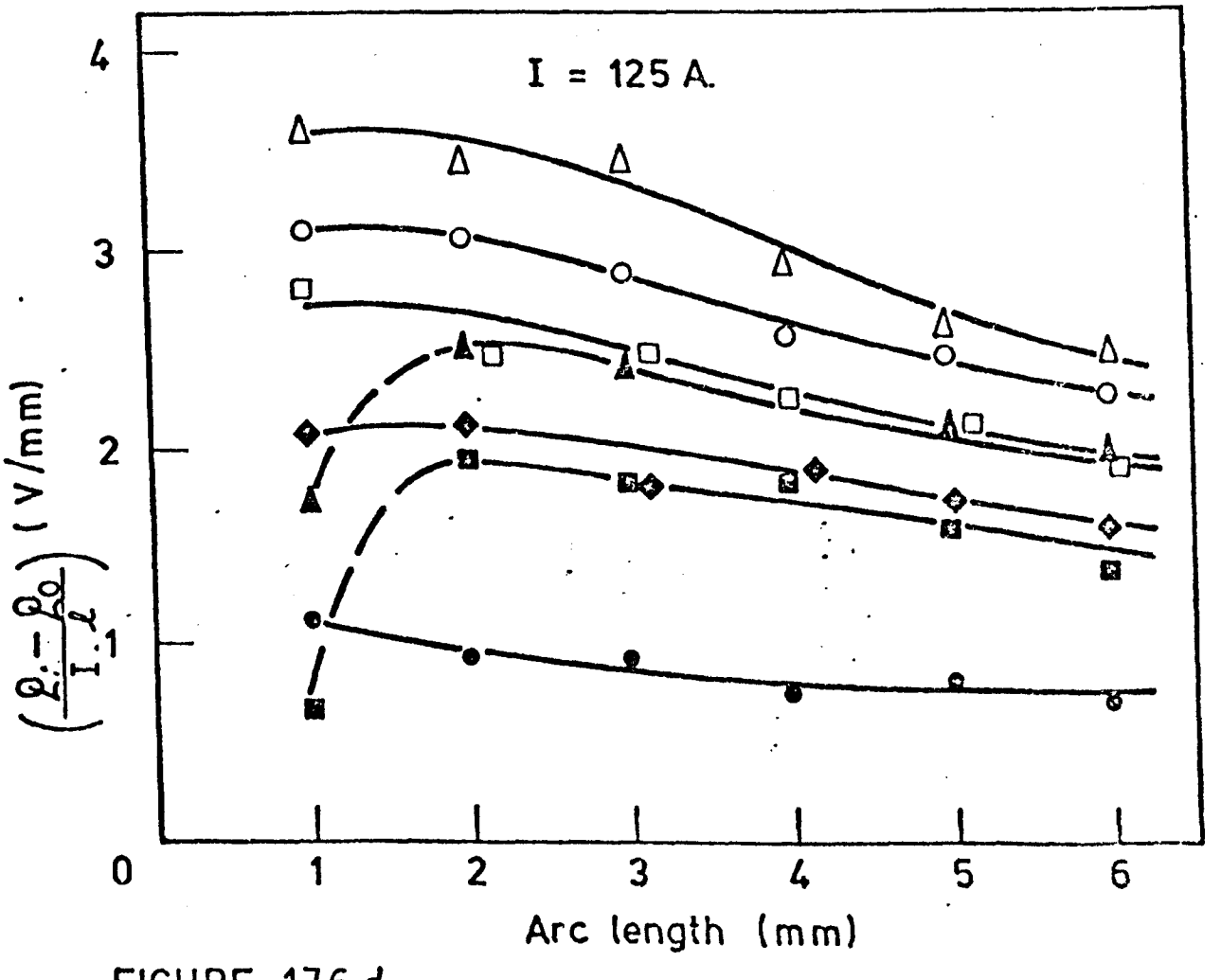

FIGURE 176 d.

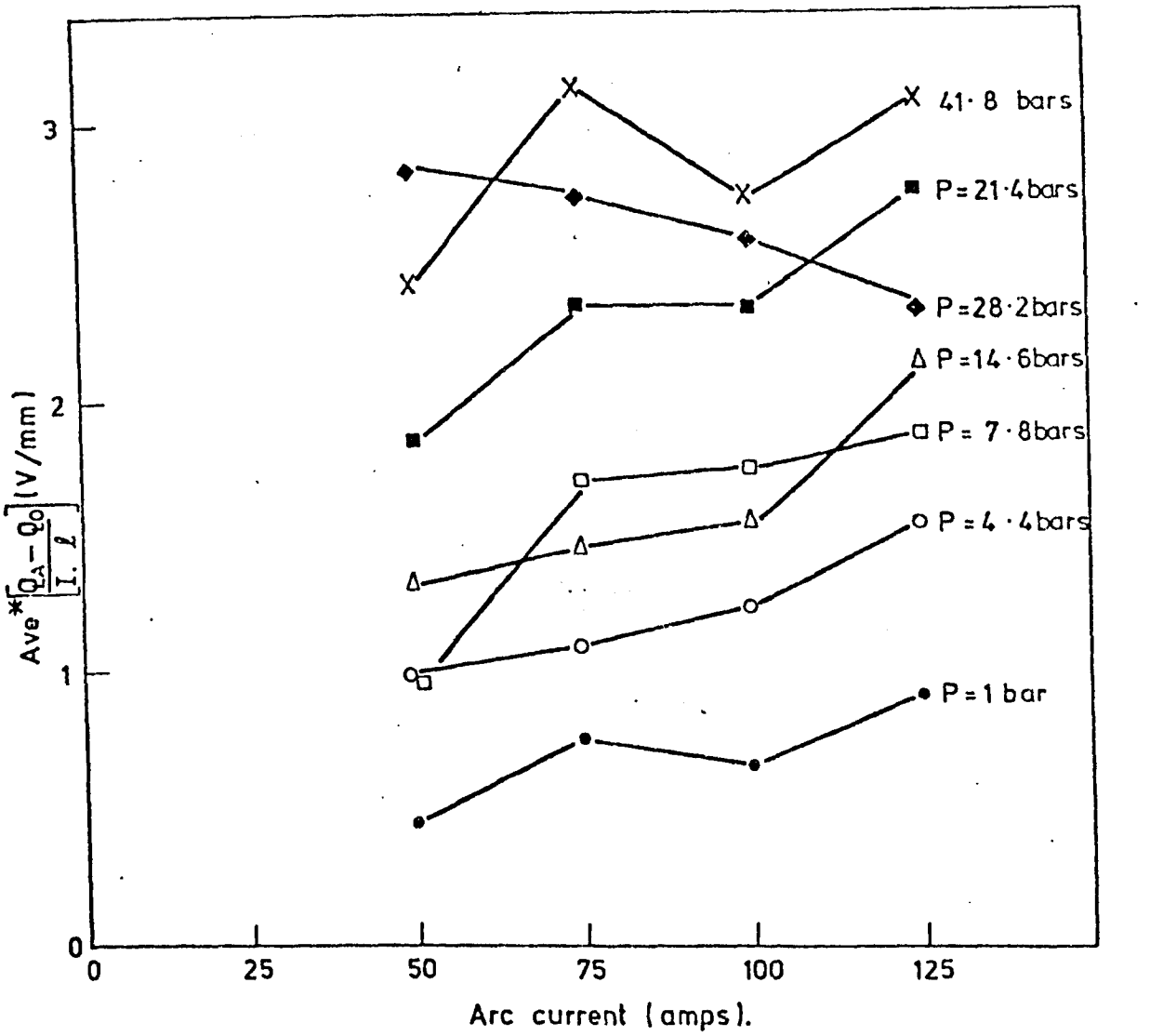

FIGURE 177. INFLUENCE OF ARC CURRENT AND AMBIENT PRESSURE ON THE CONTRIBUTION TO ANODE HEATING MADE BY POWER DEVELOPED IN THE COLUMN ($Q_A - Q_0$) (ARGON TIG ARC ON A COPPER ANODE)
*THE AVERAGE IS TAKEN OVER ARC LENGTH

41.2 bars). These results show clearly that Q_c increases more quickly than I i.e. anodic heating by gas heating increases more strongly than I.

The pressure dependence of the average value of $Q_c/I.\ell$ is shown in figure 178. This increases by about a factor of five over the pressure range investigated. At low pressures (up to 21.6 bars) $Q_c/I.\ell$ increases with current but at higher pressures the dependence on current is weak. The pressure sensitivity is also less strong above this pressure than at lower pressures with a saturation effect being observed between 30 and 40 bars. A deeper physical insight can be gained into the role of arc column heating on anode heating by expressing the contribution (Q_c) as a percentage of the total power appearing in the column i.e. that part of the column power that subsequently contributes to anode heating. This is denoted by η_c and defined as the 'column-anode heating efficiency' where

$$\eta_c = \left(\frac{Q - Q_o}{P - P_o}\right) \times 100\%$$

$$\text{i.e.} \quad \eta_c = \frac{Q_c}{P_c} \times 100\%$$

may be related to the process efficiency (η) by

$$\eta_c = \eta \cdot \frac{Q_c}{Q} \cdot \frac{P}{P_c}$$

η_c has been calculated as a function of arc length, current and pressure (see tables 14 to 20). η_c is generally only weakly influenced by arc length and so the average value has again been used to display the behaviour of η_c as a function of pressure and arc current (see figure 179).

The pressure dependence of η_c is generally different for the high current arcs (75A,100A,125A) than for I=50A. Only small differences exist between in arc behaviour at 75A, 100A and 125A's. The efficiency of 50 Amp arcs is less than that of high current arcs for pressures below 21.2 bars. Above this pressure all currents have efficiencies in the range 50 $\pm$10%. Only a weak pressure dependence is observed for the 50 Amp arc. However, high current arcs are significantly influenced by pressure over about the first 15 bars. In this pressure range the

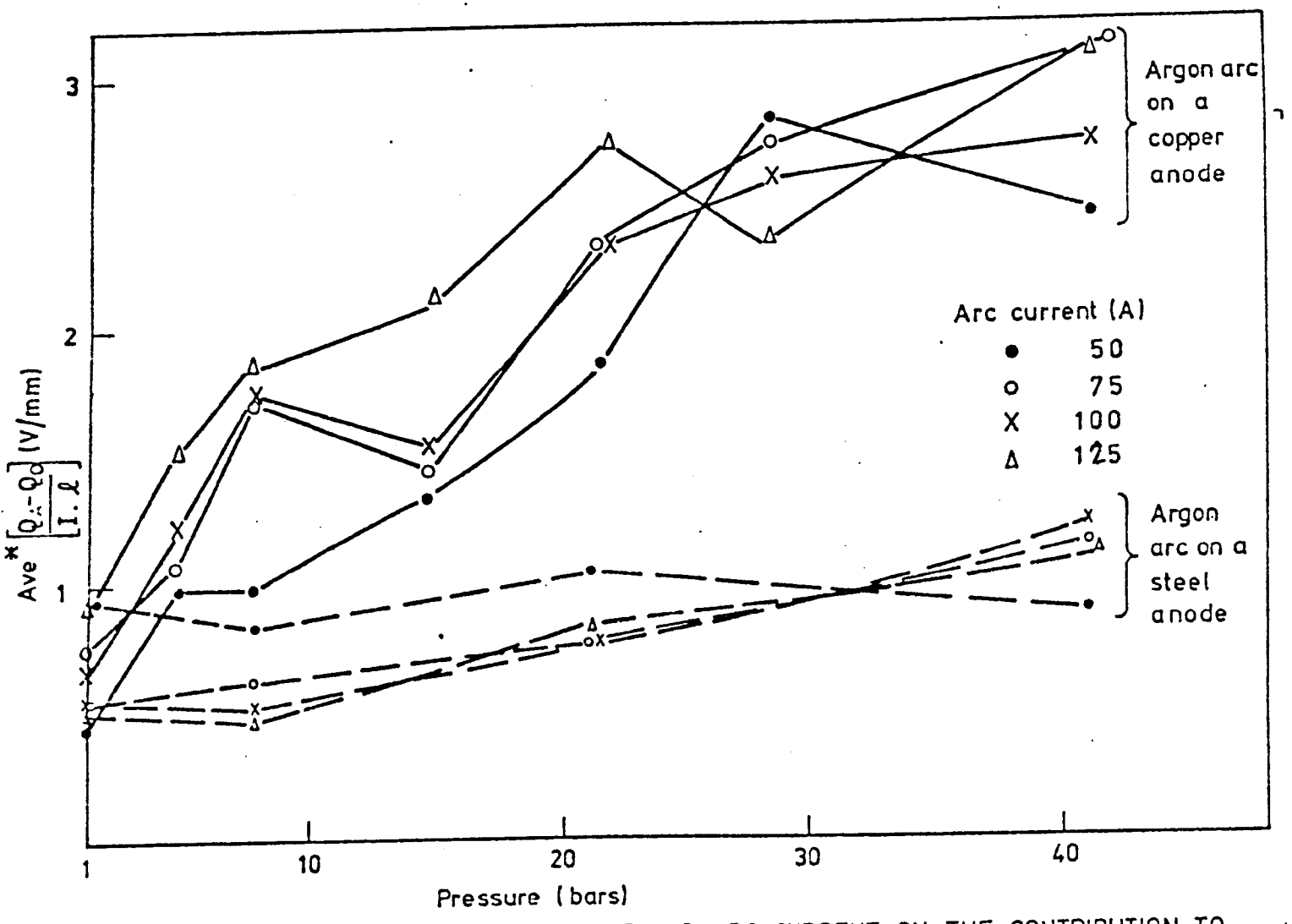

FIGURE178. INFLUENCE OF AMBIENT PRESSURE AND ARC CURRENT ON THE CONTRIBUTION TO ANODE HEATING MADE BY POWER DEVELOPED IN THE COLUMN ($Q_{.} - Q_0$) FOR ARGON TIG ARCS ON COPPER AND STEEL ANODES. (* THE AVERAGE IS TAKEN OVER ARC LENGTHS)

efficiency falls from between 75-89% at 1 bar to 42-60% at 14.6 bars. Thereafter only small changes occur. This behaviour reflects the fact that high pressure arc columns are less efficient anode heating sources than at low pressures.

6.1.1.5. Anode and Cathode Fall Voltages

The zero electrode separation heat input is associated with purely electronic heating. At the anode this may be represented by

$$Q_o = I(V_a + \phi + V_T) \quad \text{(see equation 25)}$$

where V_a is the anode fall voltage, $I.V_T$ the thermal power carried by electrons to the anode and ϕ the work function. The sum $V_a + V_T$ can be found from

$$V_a + V_T = \frac{Q_o}{I} - 4.4$$

where ϕ has been taken as 4.4V.

Values of $V_a + V_T$ obtained in this manner are shown in table 29. At 1 bar values range from 3.1 to 3.8V for currents between 50 and 125 Amps.

Current Amps	Pressure (Bars)						
	1	4.4	7.8	14.6	21.8	28	41.8
50	3.6	4.4	4.4	3.2	6.6	1.4	3.2
75	3.1	4.4	3.1	4.7	4.9	2.3	4.3
100	3.6	3.2	2.7	4.1	3.6	1.5	3.6
125	3.8	3.2	2.4	4.4	3.6	3.6	3.3
Average	3.5	3.6	3.2	4.1	4.7	2.2	3.6

Table 29 $V_a + V_T$ for Argon TIG Arcs on a Copper Anode

Variations with arc current are generally within the range of experimental accuracy as are changes with ambient pressure. The average value (averaged over current) for all pressures may be represented by 3.4 ± 1.2V. The average value at 1 bar is 3.5V compared to a corresponding value of 3.6V at 41.8 bars.

Thermal contributions to this sum may be found with reference to equation 27

$$V_T = \frac{5k.T}{2e}$$

For cooled copper anodes where little vapourization occurs, T may be taken as in the region of 10^4K. V_T then becomes 2.2V. This indicates anode fall voltages of 1.4 ± 1.2V for the range of conditions considered here.

Cathode fall voltages (V_C) may be estimated, using this information, from the sum of the fall voltages. This has been done and results are shown in table 30.

Current (Amps)	Pressure (Bars)						
	1	4.4	7.8	14.6	21.8	28	41.8
50	7.0	5.2	5.8	7.1	5.4	7.5	5.8
75	7.0	4.6	6.4	5.6	5.3	5.7	6.2
100	6.1	6.2	6.1	4.5	5.4	6.5	6.4
125	5.5	5.8	6.1	6.0	5.4	4.7	6.7
Average	6.4	5.5	6.1	5.8	5.4	6.1	6.3

Table 30 $V_C - V_T$ (anode) for Argon TIG Arcs on a Copper Anode

i.e. $V_C = V_o - V_a$

$$V_C - V_T \text{ (anode)} = V_o - (V_a + V_T)$$

Values of $V_C - V_T$ (anode) change little with current and pressure and may be represented by 5.9 ± 0.5V over the range investigated. Using the value of V_T previously obtained gives

$$V_C = (8.1 \pm 0.5)\ V$$

6.1.2. Helium TIG Arcs on a Copper Anode

Experiments with helium arcs were restricted to the range of pressures over which it was previously found possible to weld (1 - 11.2 bars). Results are shown in table 21.

6.1.2.1. Total Power (Q) Collected by the Anode

The total power collected at the anode is found to increase in a linear manner with arc length. Results shown in table 21 have been displayed graphically (although not shown here). In this manner zero arc length values have been obtained. The zero arc length anode heat input (Q_o) is found to be independent of pressure having a value of 1.3KW for a 100 Amp arc. This compares with a value of 0.8KW for the corresponding argon arc. The remainder of the process power (P_L (ℓ=0)) must appear at the cathode. Again, this contribution is only weakly influenced by pressure falling from 0.21KW at 1 bar to 0.17KW at 11.2 bars. The average value is 0.188KW. This compares with a value of 0.150KW for the corresponding argon arc. As with argon arcs it is observed that the influence of pressure increases with arc length.

6.1.2.2. Efficiency of Heat Transfer (η)

Efficiency is little affected by ambient pressure over the range 1 to 11.2 bars. This contrasts behaviour in argon where η is most sensitive to pressure over this range. Only small changes are generally observed with increasing arc length. For all conditions (pressures and arc lengths) examined η may be represented by 84 $\pm$ 9% with the mean value at 11.2 bars (86%) being only 2% less than the mean value at 1 bar (88%).

6.1.2.3. Process Power (P_L) not Entering the Anode

The zero arc length value of P_L has been identified as the cathode heating. At longer arc lengths P_L is also associated with arc column energy not entering the anode. Results indicate that $\Delta P_L/I.\ell$ is only weakly influenced by arc length. Arc column losses are therefore approximately proportional to arc length.

Arc column losses increase with pressure. At 1 bar arc column losses are equivalent to 0.21V/mm while at 11.2 bars the corresponding number is 0.94V/mm. However, a value of 1.21V/mm was obtained at 7.8 bars indicating that saturation may have been reached in helium at fairly low pressures.

6.1.2.4. Influence of Arc Heating on Q

Power appearing in the column increases in almost direct proportion to arc length (see table 21). The part of this power (Q_c) contributing to anode heating also increases more or less linearly with arc length. This behaviour gives rise to column transfer efficiencies (η_c) that are little affected by arc length. The average value of η_c changes relatively little with pressure from 91% at 1 bar to 79% at 11.2 bars. Values of η_c are significantly larger in helium than in argon.

6.1.2.5. Anode and Cathode Fall Voltages

Results have been used in a manner previously described (see section 6.1.1.5) to obtain $V_a + V_T$ and $V_C - V_T$ for helium TIG arcs on copper anodes. These results are shown in tables 31 and 32. Only the 100 Amp arc was investigated and little variation occurred over the pressure range 1 to 11.2 bars (8.4 to 8.9V for $V_a + V_T$ and 6.1 to 6.5V for $V_C - V_T$).

Thus $V_a + V_T = 8.7 \pm 0.3V$

$V_C - V_T = 6.3 \pm 0.2V$

The thermal contribution is more difficult to separate in this instance as very little information is available for helium. However, if ΔT is taken as

$$\Delta T = 591.E_I.\ I^{0.087} \quad \text{(ref.64)}$$

where E_I is the ionization potential and I the arc current, then

$$\Delta T = 22{,}000K$$

$$\therefore \quad V_T = 4.7V$$

This gives $V_a = (4.0 \pm 0.3)V$

and $V_C = (11.0 \pm 0.2)V$

These values are considerably higher than the corresponding argon figures.

Arc Current Amps	Pressure (Bars)			
	1	4.4	7.8	11.2
100	8.5	8.6	8.4	8.9

Table 31 Behaviour of $V_a + V_T$ for Helium TIG Arcs on a Copper Anode

Arc Current Amps	Pressure (Bars)			
	1	4.4	7.8	11.2
100	6.5	6.4	6.1	6.1

Table 32 Behaviour of $V_C - V_T$ for Helium TIG Arcs on a Copper Anode

6.1.3. Argon TIG Arcs on a Steel Anode (Conduction Limited Pool)

Experiments similar to those discussed for copper anodes have also been performed for mild steel anodes. Results are given and analysed in tables 22 to 25.

6.1.3.1. Total Power Collected by the Anode

At zero electrode separation all of the arc power appears at the electrodes. The zero arc length contribution at the anode (Q_o) is shown in figure 180. It can be seen that Q_o is generally independent of pressure and linearly dependent on current such that

$$Q_o = 6.4I$$

This compares with a value of 8I found for copper anodes. The difference between these values is associated in section 7.2 with a change in the anode fall and thermal contributions.

Power appearing at the cathode is given by P_L (ℓ=0). The behaviour of this quantity at 1 bar is generally similar to that obtained for the copper anode. However, significant differences exist at pressures above 21.4 bars. At 41.8 bars it appears that nearly as much power enters the cathode as the anode.

The total power to the anode increases with arc length. It is found that $Q_c/I.\ell$ is largely independent of both I and ℓ for arcs other than those at 50 Amps (see figure 178). This shows that Q is linearly dependent on both I and ℓ for high current arcs ($I \geq 75$ Amps). At lower currents (50A) $Q_c/I.\ell$ is significantly greater than for higher currents (with the exception of results found at 42.1 bars).

Anode heating is far less pressure dependent for steel anodes than previously reported for copper anodes. No influence of pressure is observed for the 50 Amp arc over the pressure range 1 to 42.8 bars ($Q_c/I.\ell$ = 0.95V/mm). However, for the 125 Amp arc $Q_c/I.\ell$ increases from 0.52V/mm at 1 bar to 1.12V/mm at 41.8 bars. Associated with this is an increase in heat input (for a 5mm arc) from 1191W to 1313W. Such an increase is still small compared to the corresponding copper arc (i.e. 1508W to 2592W).

6.1.3.2. Efficiency of Heat Transfer

Heat transfer efficiencies at 1 bar are generally similar but slightly lower to those found for copper anodes. Efficiency is only weakly dependent on arc length and current for high current arcs at one bar. At higher pressures efficiency becomes increasingly sensitive to arc length but still has only a weak dependence on arc current.

The zero arc length anode power is little affected by pressure over the range 1-21.4 bars. However, at 41.8 bars a significant fall is experienced and this is associated with an increase in cathode heating. (See section 6.1.3). The strong dependence on arc length at high pressures causes the average efficiency (averaged over current and arc length) to fall much more quickly than with a copper anode i.e. at 41 bars the average efficiency is about 42% for steel anodes compared to 67% for copper. The difference between these materials may be considered further by examining arc column losses and the efficiency of column power transfer.

6.1.3.3. Process Power (P_L) not Entering the Anode

Significantly more power appears in the column of the copper arc than in the steel arc (see tables 14 to 25). This has been discussed in section 4. It may also be seen from these tables that marginally more column power fails to appear at the anode for steel arcs than for copper arcs i.e. more power goes to environment and cathode.

$\Delta P_L/I.\ell$ is linearly dependent on arc length for all pressures and currents but increases strongly with arc current. This shows that ΔP_L is linearly dependent on arc length and has a stronger than linear dependence on arc current. Similar behaviour was also reported for copper arcs.

6.1.3.4. Influence of Arc Heating on Q

The contribution to anode heating made by power appearing in the column is given by Q_c. This behaviour has already been discussed. It is interesting to examine the percentage of the column power (η_c) that contributes to anode heating. Typical values at 1 bar are of order 50% compared to 80% for copper arcs (see figure 179). This difference has only a slight effect on process efficiency because only a small part of the process power appears in the column at 1 bar. At higher pressures η_c quickly falls to about 30% (between 1 and 7.8 bars) and maintains this level until 41.8 bars. Similar pressure dependent behaviour was observed for copper arcs. However, for copper arcs saturation occurred at $\eta_c \approx 50\%$. The lower transfer efficiencies observed for steel can now be explained in terms of

i) lower column powers
ii) a smaller fraction of this power entering the anode
iii) a smaller electronic contribution to anode heating

6.1.3.5. Anode and Cathode Fall Voltages

These have been obtained in a manner previously described and results are shown in tables 33 and 34. The behaviour of low current arcs appears significantly different from that of high current arcs.

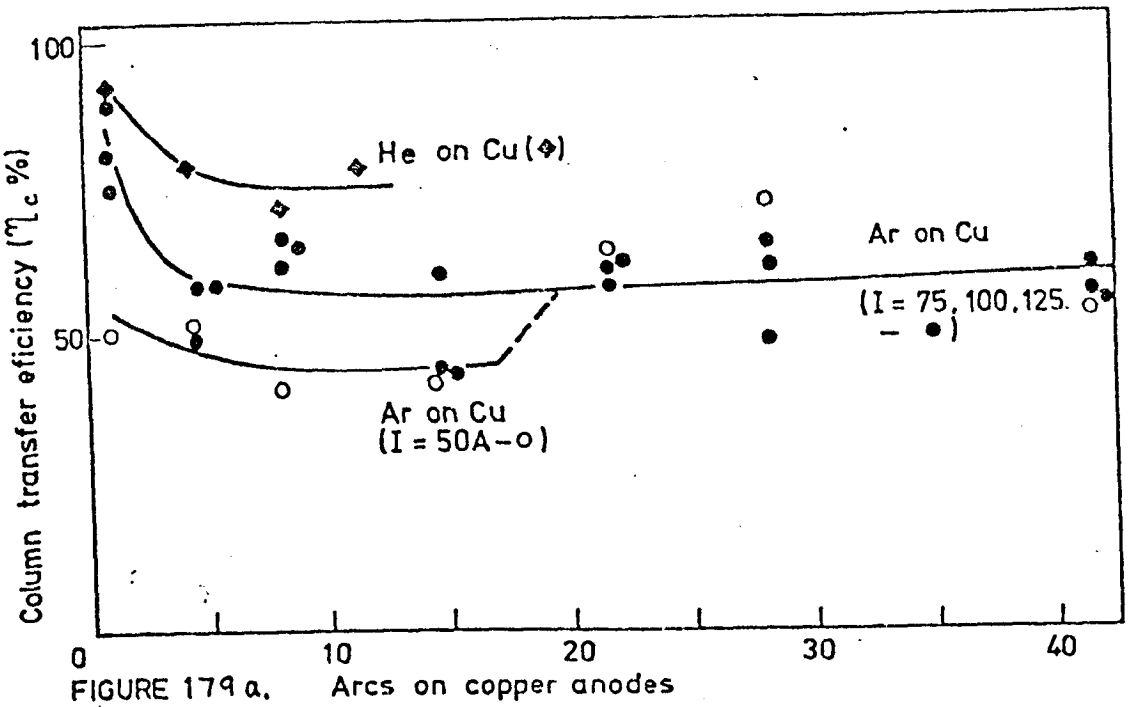

FIGURE 179 a. Arcs on copper anodes

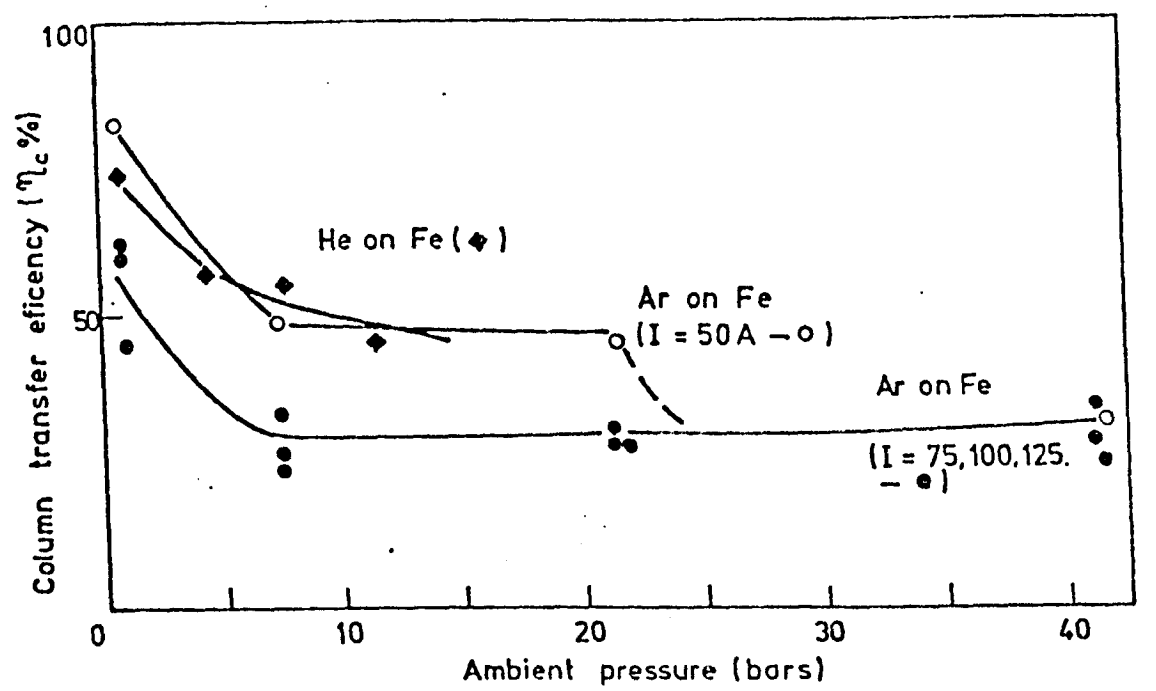

FIGURE 179 b. Tig arcs on steel anodes

FIG. 179. INFLUENCE OF AMBIENT PRESSURE ON THE PERCENTAGE OF THE COLUMN POWER (η_c) CONTRIBUTING TO HEATING

Arc Current (Amps)	Pressure (Bars)			
	1	7.8	21.8	41.8
50	0.4	1.6	0.4	0.4
75	2.7	1.9	1.6	-0.3
100	1.8	2.4	1.9	0.6
125	2.6	2.5	1.8	2.0
Average *	2.4	2.3	1.8	0.8

Table 33 Behaviour of $V_a + V_T$ for Argon Arcs on Steel Anodes

Arc Current (Amps)	Pressure (Bars)			
	1	7.8	21.8	41.8
50	7.6	6.9	8.0	8.0
75	5.8	6.0	6.9	9.1
100	5.9	5.7	6.5	9.9
125	5.3	5.7	6.7	8.5
Average *	5.7	5.6	6.7	9.2

Table 34 Behaviour of $V_C - V_T$ for Argon Arcs on Steel Anodes

(* only 75, 100 and 125 Amp arcs included)

Within the pressure range 1-21.8 bars $V_a + V_T$ is between 1.6V and 2.7V for $I \geq 75A$. For I=50A, values as low as 0.4 regularly occur. Behaviour at 41.8 bars is anomolous but within the range of experimental accuracy. Generally a value of

$$V_a + V_T = 1.6 \pm 0.8V$$

represents the pressure range of $I \geq 75A$. This must be compared with $3.4 \pm 1.2V$ for copper arcs. However, for short steel arcs the change in thermal energy is expected to be small due to an increase in anode temperature and a decrease in arc temperature near the anode. An increase in boiling point with pressure would allow a further increase in pool temperature. Taking a pool temperature between boiling and melting points and a metal arc temperature ($\sim$ 6000K) immediately adjacent to the anode gives $\Delta T \simeq 4000K$. This gives $V_T \sim 0.7V$.

Thus $V_a \simeq 0.9 \pm 0.8V$.

This compares with a value of 1.4 ± 1.2V for a copper arc.
The corresponding cathode fall is $V_C - V_T = 7.4 \pm 1.8$V.

$$\text{or } V_C = 8.1 \pm 1.8\text{V}$$

This is in good agreement with the range 8.1 ± 0.5V found for the copper arcs. It therefore appears that the anode fall is probably slightly less for steel than copper. The cathode fall is almost unaffected. These results may also be used to explain the difference observed in Q_o, i.e. 8.0I for copper compared to 6.5I for steel. Considering equation 25 gives

$$(V_a + V_T + \phi)\ \text{copper} - (V_a + V_T + \phi)\ \text{steel} \approx 2 \pm 2\text{V}$$

This figure (2 ± 2V) compares well with the observed difference of 1.5V.

6.1.3.6. Influence of Magnetic Field Strength on Anode Heating

The total heat input to the anode is little affected by the application of a magnetic field of either polarity (see table 26A). However, the sum of the fall voltages appears to increase with the application of a field. Associated with this is an increase in Q_o.

Behaviour described above results in a reduction in the column contribution to anode heating. The associated 'column efficiency' is therefore also lower. Despite this the total process efficiency is little affected by the application of a field.

6.1.4. Helium TIG Arcs on a Mild Steel Anode

Helium TIG arcs have been operated on mild steel anodes with conduction limited pools. As for helium experiments with copper anodes only 100 Amp arcs were investigated. Results are shown in table 27.

6.1.4.1. Total Power Collected by the Anode

The anode power (Q_o) at zero electrode separation is only slightly influenced by ambient pressure and increase from 0.66KW to 0.80KW over the range 1 to 11.2 bars. The average value (0.725KW) is considerably less than that found using a copper anode (1.30KW) and between the values obtained using argon with a copper anode (0.8KW) and a steel anode

(0.65KW). The remainder of the process power appears at the cathode. The average value of P_L (ℓ=0) is 0.215KW. This compares favourably with behaviour on a copper cathode (0.188KW). At any pressure the anode power is linearly dependent on arc length and increases with current. The pressure sensitivity of $Q/I.\ell$ is markedly stronger than found for argon arcs on steel anodes but still less than observed for helium arcs on copper anodes.

6.1.4.2. Efficiency of Heat Transfer (η)

At one bar efficiency is little influenced by arc length. An arc length dependence develops with increasing pressure leading to a decrease in η with increasing arc length. The zero arc length efficiency is little influenced by pressure (73-83%) but lower than observed for copper anodes (82-88%). The average value at any pressure decreases from 75% at 1 bar to 60% at 11.2 bars. This compares with corresponding figures of 88% and 86% for arcs on copper anodes. Such behaviour is very similar to that found for argon and a comparison is given in figure 174.

6.1.4.3. Process Power not Entering the Anode

The power not entering the anode can be seen to have a linear dependence on arc length (see $\Delta P_L/I.\ell$ in table 27). Behaviour was such that generally about twice as much column power failed to contribute to anode heating than in copper anode experiments.

6.1.4.4. Influence of Arc Heating on Q

The contribution to anode heating by power generated in the column was in all cases less than for copper anodes. The efficiency of column power transfer (η_c) is generally 20-30% less than for a copper anode. η_c is found to have pressure dependence similar to that observed for other arc forms i.e. η_c initially decreases quickly with pressure before changing only slowly with pressure.

6.1.4.5. Anode and Cathode Fall Voltages

Values have been obtained in a manner previously described and results are shown in tables 35 and 36. $V_a + V_T$ is substantially less than previously found for copper and may be generally represented by 2.8 $\pm$ 0.8V over the range of present interest. The contribution of V_T may be quite significant on copper (4.7V). However, if a metal vapour region exists over the region of current transport then V_T may well be as low as estimated for steel anodes (0.7V).

Current Amps	Magnetic Field Arrangement	Pressure (Bars) 1	4.4	7.8	11.2
100	No field	2.0	2.6	2.6	3.6
100	South pole towards pool	2.0	-	-	3.2
100	South pole away from pool	1.6	-	-	4.1
Average		2.1	2.6	2.6	3.6

Table 35 Behaviour of $V_a + V_T$ for Helium Arcs on a Steel Anode

Current Amps	Magnetic Field Arrangement	Pressure (Bars) 1	4.4	7.8	11.2
100	No field	6.0	5.4	6.4	7.4
100	South pole towards pool	8.0	-	-	7.3
100	South pole away from pool	7.9	-	-	8.4
Average		7.3	5.4	6.4	7.7

Table 36 Behaviour of $V_C - V_T$ for Helium Arcs on a Steel Anode

The significantly lower values of $V_a + V_T$ (and similar in size to those for argon) suggest the anode fall to be dominated by metal vapour for gas-steel-tungsten arcs. For the present purposes V_T is taken between these estimates i.e. $V_T \approx 2.7 \pm 2V$. This gives

$$V_a = 0.1 \pm 2.8V$$

This figure is well within the range found for argon TIG arcs (i.e. $0.9 \pm 0.8V$) but much less than for helium-copper arcs.

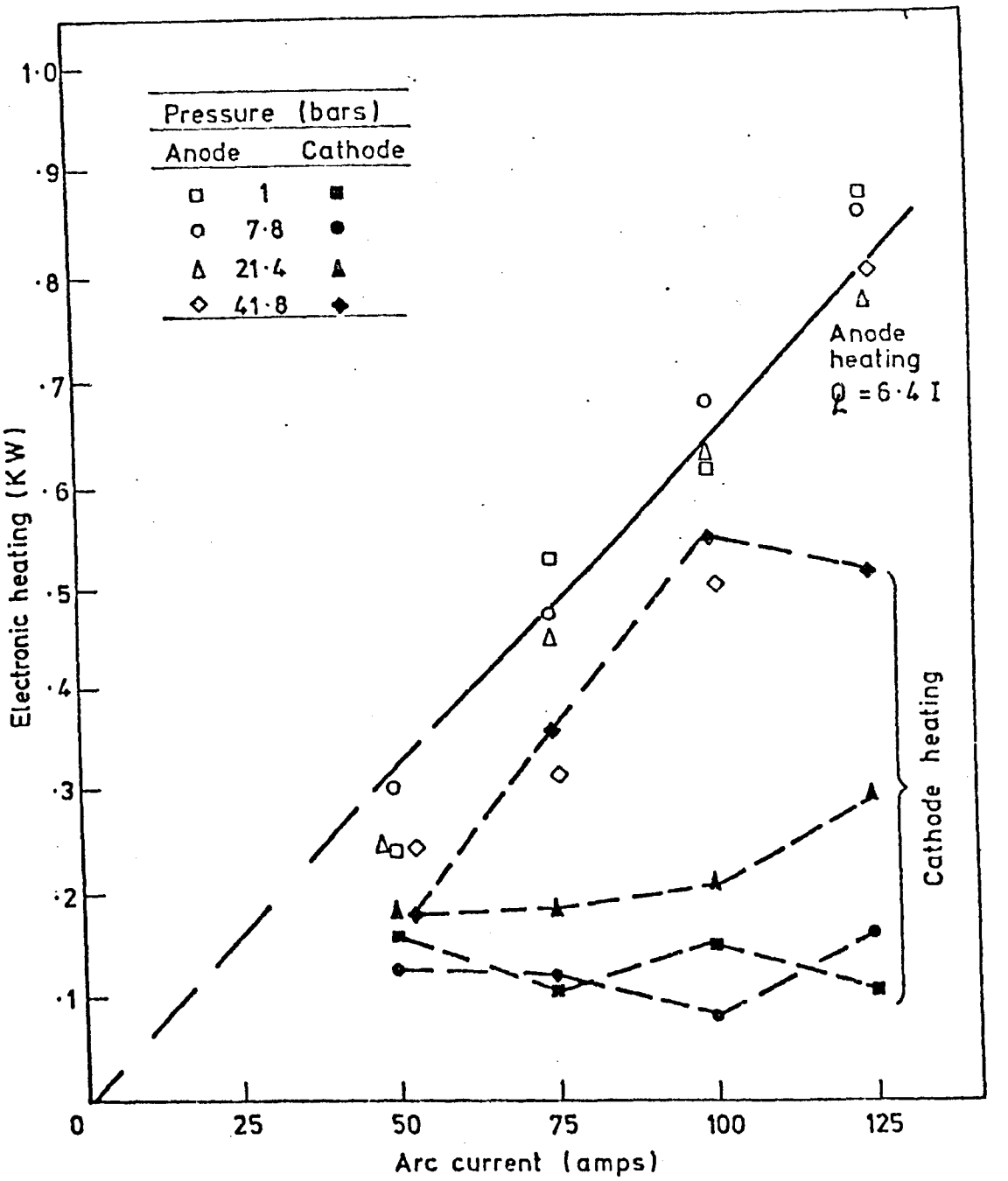

FIGURE 180. INFLUENCE OF ARC CURRENT AND AMBIENT PRESSURE ON ELECTRONIC HEATING AT THE ANODE AND CATHODE FOR ARGON TIG ARCS ON STEEL ANODES.

Using this value of V_T gives

$$V_C - V_T = 6.6 \pm 1.2V$$

$$V_C = 9.3 \pm 3.2V$$

This compares with a value of $11 \pm 0.2V$ for helium arcs on copper.

6.1.4.6. Influence of Magnetic Field Strength on Anode Heating

Calorimetric measurements have also been performed for arcs in axial magnetic fields. Experiments were made for situations in which the south pole of the magnet was directed to and away from the pool. Results are given in tables 35 and 36. No significant difference was found between behaviour with the poles in either direction. Also the total heat input was little affected by the application of a field. However, a lower process efficiency was found at one bar with a field than without. This is associated with a slightly higher voltage. Behaviour previously observed for P_L, Q_C and η_c was again found. Comparable anode and cathode fall voltages are also found. The cathode heat input (P_L (ℓ=0)) is observed to be higher (0.355KW) with a magnet than without (0.220KW) at 1 bar. This difference is within the range of reproducibility. At higher pressures very similar results are found.

6.1.5. Constricted Argon TIG Arcs on a Copper Anode

Experiments were performed to examine the influence of a constriction at the cathode on heat transfer to the anode. For this purpose orifice diameters of 3.2mm and 4.8mm were examined. The same electrode - orifice geometry reported in section three was used.

6.1.5.1. Anode Heating

Anode heating generally increases with ambient pressure (see figure 181). As with TIG arcs, the increase in anode heating is most noticeable for long arc lengths. For such arcs anode heating may double between 1 and 14.6 atmospheres. Figure 181 also shows that changes in anode heating with pressure are particularly noticeable over the pressure ranges 1-4 bars and 11-15 bars. This result appears to be confined to an arc current of 150 Amps but may also occur for the smaller orifice examined (figure 182). At higher or lower currents the sensitivity to ambient

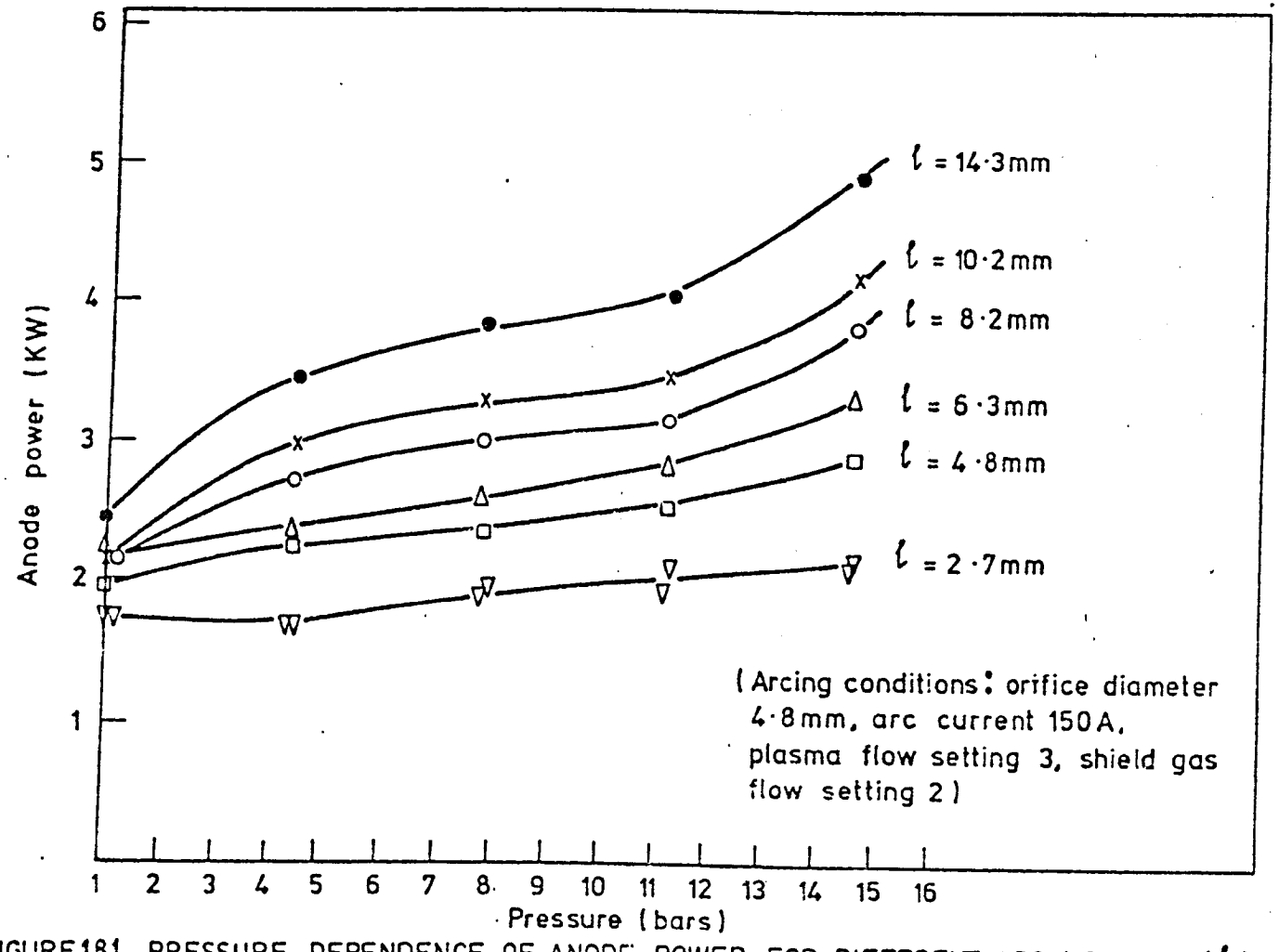

FIGURE 181. PRESSURE DEPENDENCE OF ANODE POWER FOR DIFFERENT ARC LENGTHS (l) WITH A PLASMA ARC ABOVE A COPPER ANODE.

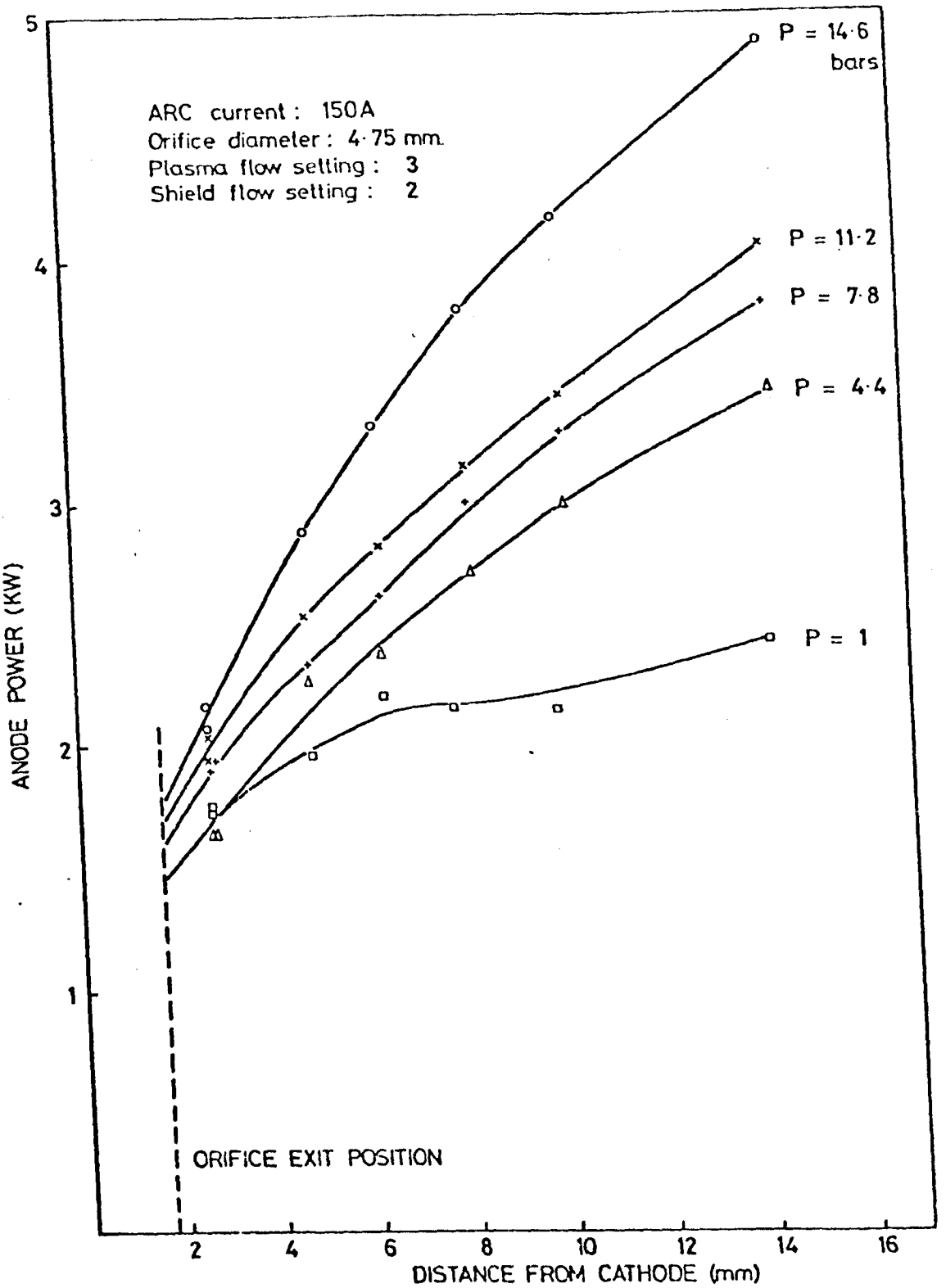

FIG.181. PRESSURE DEPENDENCE OF ARC PLASMA ANODE POWER.

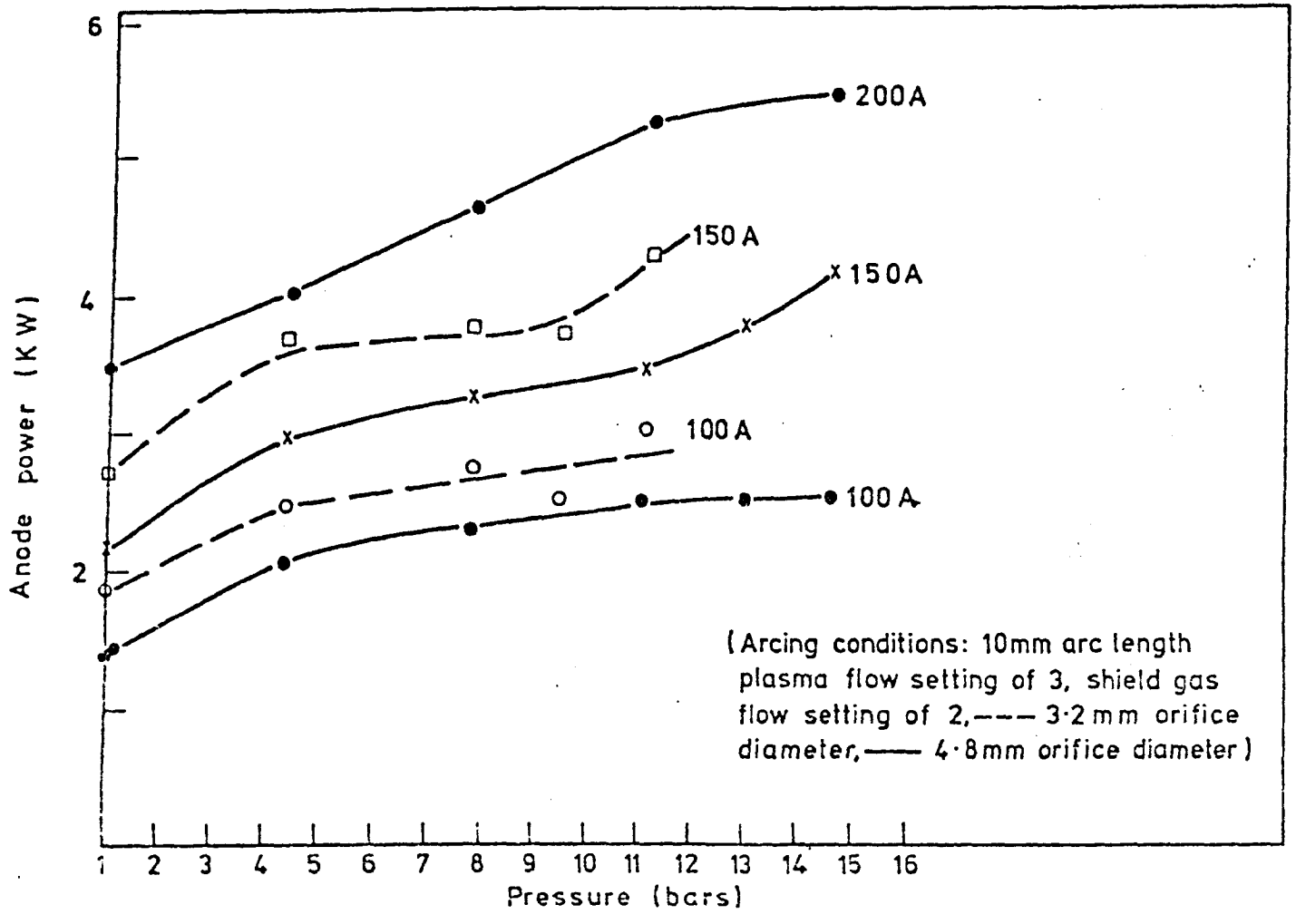

FIGURE 182. EFFECT OF PRESSURE ON ANODE POWER AT DIFFERENT ARC CURRENTS AND ORIFICE SIZES FOR A PLASMA ARC ON A COPPER ANODE.

pressure between 11 and 15 bars is not observed.

It can be seen from figure 182 that greater heat transfer occurs using the smaller orifice diameter. However, pressure appears to have little influence on the difference between these orifices. Results shown in figure 182 may also be used to deduce that anode heating increases in an approximately linear manner with arc current.

6.1.5.2. Efficiency of Heat Transfer to the Anode

The calorimetric results shown in figure 181 correspond to process power measurements given in figure 89. This information has been combined to obtain process heat transfer efficiencies (figure 183). Under normal atmospheric conditions efficiencies of 77 - 88% are observed. These may fall, depending on arc length, to values as low as 60% at 11 bars. It appears from figure 183 that the lowest efficiencies occur at the longest arc lengths. There is also a noticeable trend for efficiency to increase between 11 and 15 bars. This is associated with the corresponding increase in process power shown in figure 181.

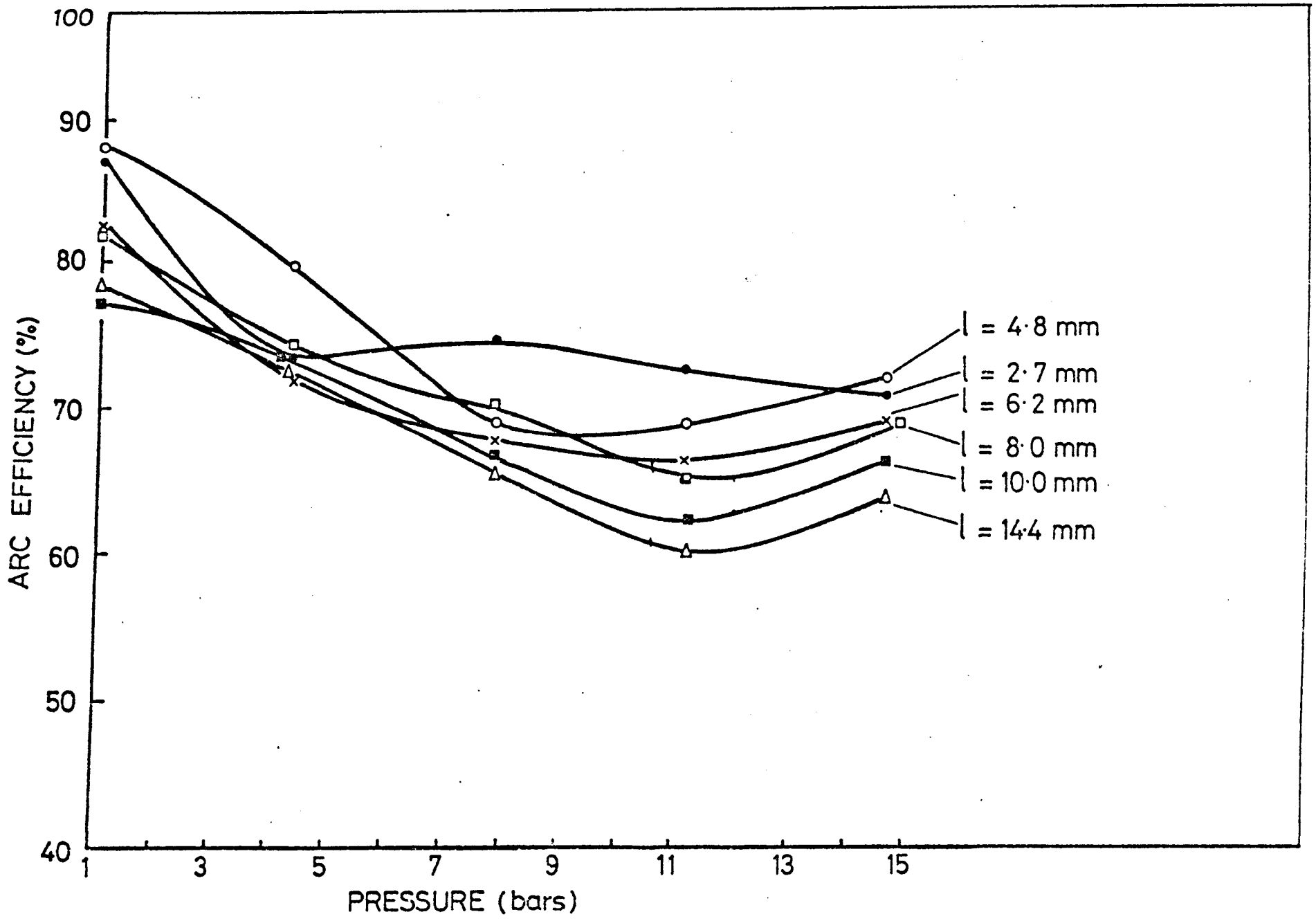

FIG.183. EFFICIENCY OF THE ARC PLASMA PROCESS. (I = 150A, l = 3·2 mm, Orifice diameter : 4·75 mm)

6.2. Distribution of Current at the Anode

Current density has been measured using the split copper anode arrangement described in section 3.6.2.

6.2.1. Argon TIG Arcs

6.2.1.1. Electrical Boundary

UVO traces give a direct measure of the extent of the region carrying current at the anode. Measurements of the radius of this region are shown in figure 184 (see also figure 46). The relationship between electrical radius and shielding gas flow at any pressure is of a complicated nature. At low pressures there is a tendency for the radius to initially increase the flow. Further increases in flow cause a decrease in radius. The influence of pressure is much clearer than that of flow. Generally it can be seen that the radius falls with pressure. Average electrical radii (averaged over flow) are shown as a function of pressure in figure 46 where this data is compared with corresponding photographic measurements. An approximate representation of this data is given by a power law in the form

$$R = R_1 p^{-n} \quad \text{(see equation 82)}$$

n is 0.17 for the anode and column regions although a stronger pressure dependence is obtained when the flow rate is high. Photographic estimates of the arc boundary at the cathode give a weaker dependence than 0.17 (i.e. $\sim$ 0.11).

6.2.1.2. Current Density

Current density distributions have been obtained from UVO traces using procedures reported in section 3.6.2. Results obtained by Abel transforming the experimental data are shown in figure 185. It can be seen that shielding gas flow exerts no systematic influence on the maximum current density. This result is to be expected in view of the complicated behaviour of the electrical boundary with flow. Results for different pressures (with a flow setting of 2) are shown in figure 186. This figure indicates that axial current density increases with pressure by about a factor of four between 1 to 14 bars.

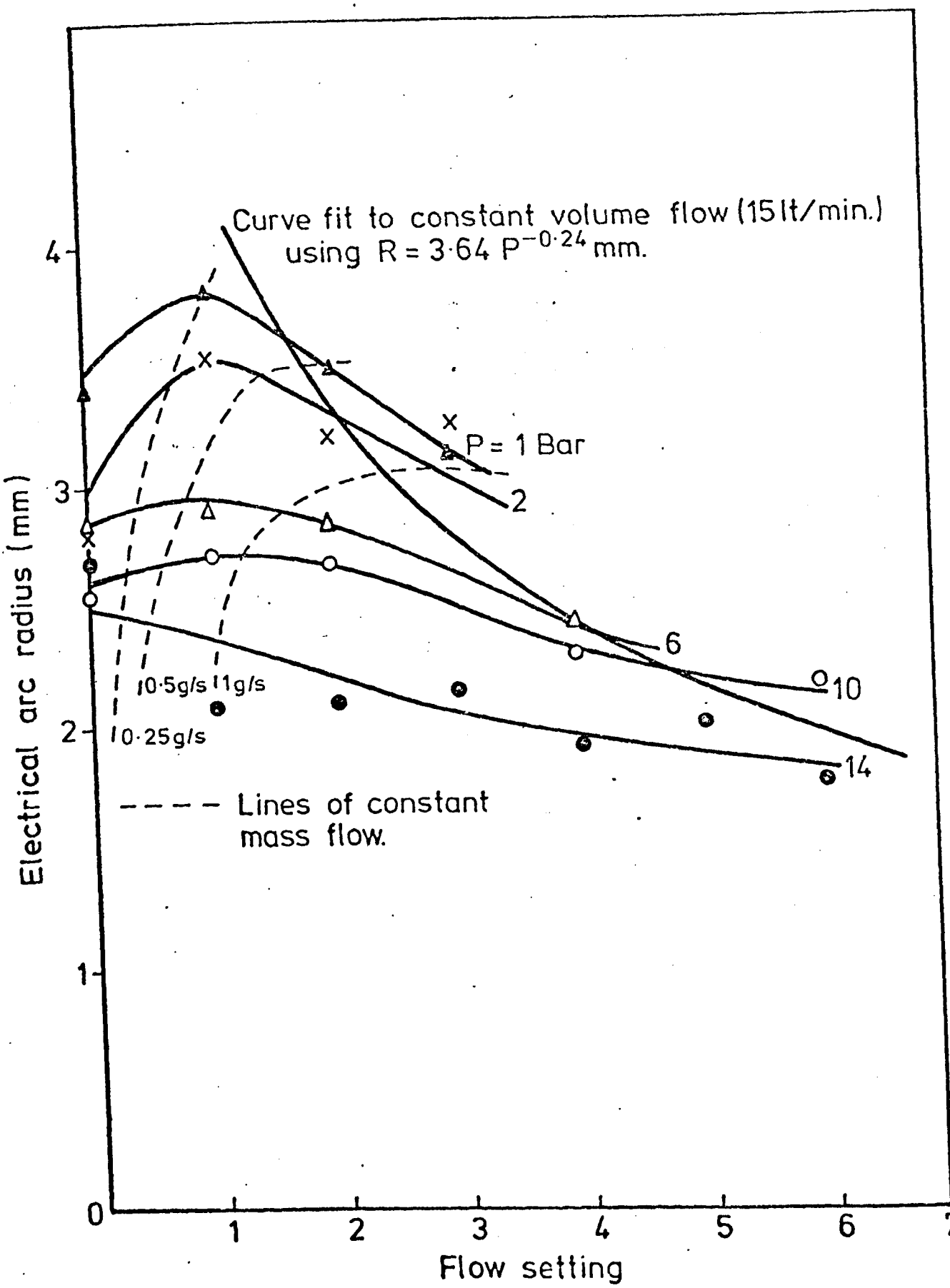

FIG.184. VARIATION OF THE ELECTRICAL RADIUS AT THE ANODE WITH FLOW SETTING FOR VARIOUS PRESSURES.

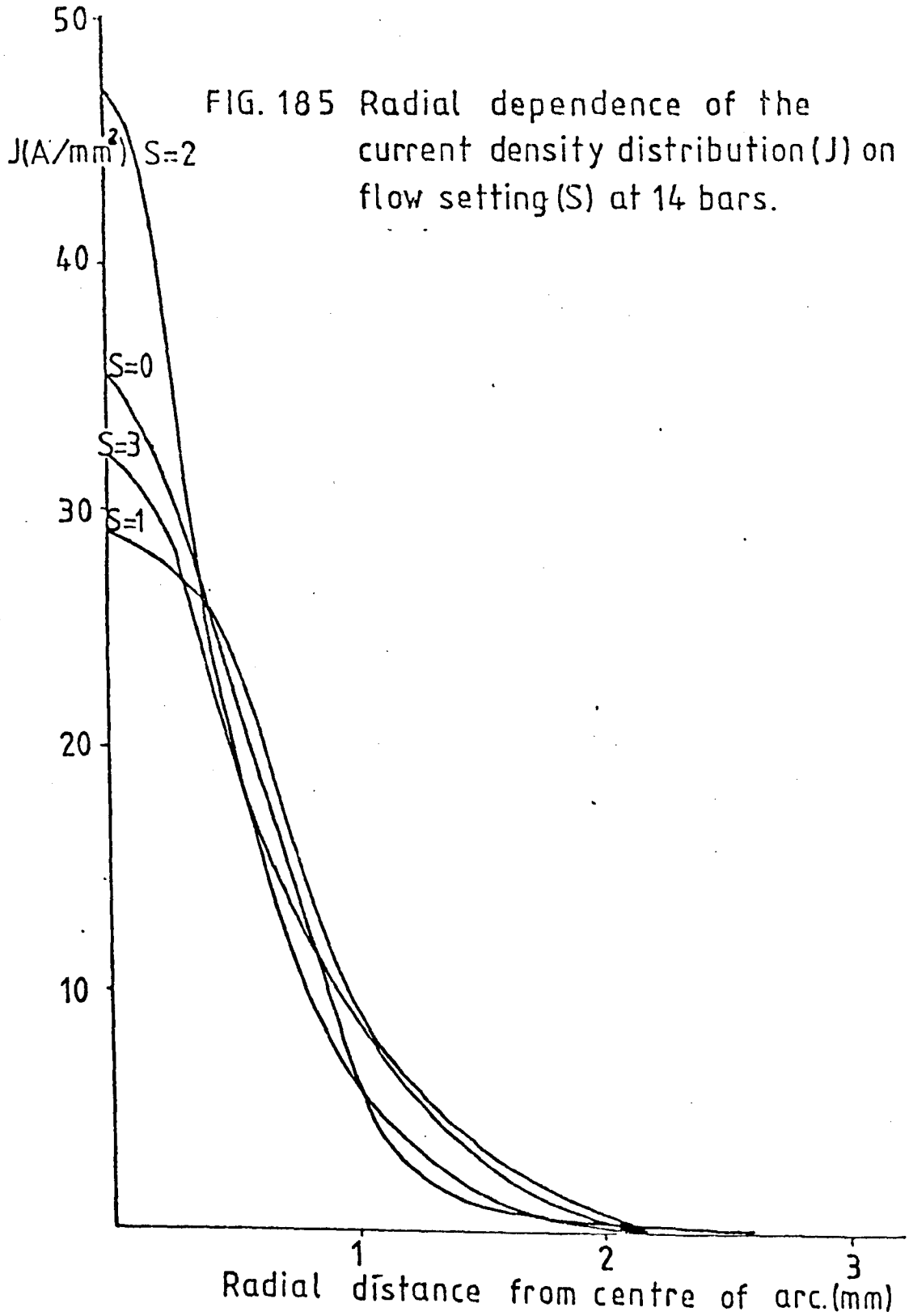

FIG. 185 Radial dependence of the current density distribution (J) on flow setting (S) at 14 bars.

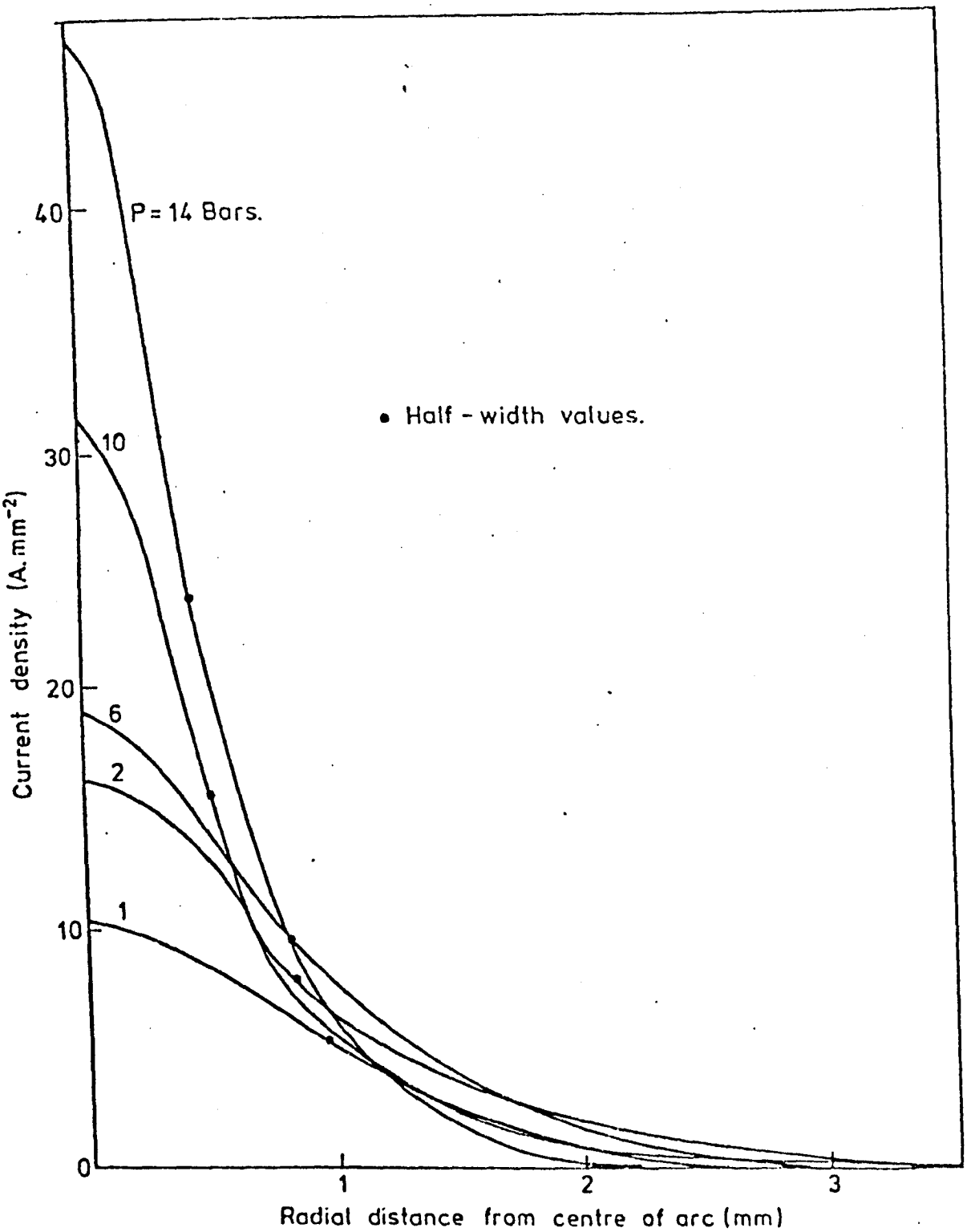

FIG.186. PRESSURE DEPENDENCE OF THE CURRENT DENSITY DISTRIBUTION. (FLOW SETTING OF 2)

The general form of the current density distribution is of a Gaussian nature. This suggests that the simpler analysis based on the slope of a UVO trace at the cross-over point is also appropriate (see section 3.6.2). Results have also been analysed using this technique. These are compared with those obtained using the Abel method in table 37. Fairly good agreement is obtained between these measurements indicating that distributions are of a Gaussian nature and that the computational techniques are reasonably accurate. These methods can only be considered as very approximate techniques at high shielding gas flow rates because considerable fluctuations occur in arc position i.e. the accuracy with which the mean gradient can be plotted is then limited.

Current densities at 1 bar are typically of order $10A/mm^2$ compared to about $35A/mm^2$ at 14 bars. The maximum current density at any pressure is between 3.8 and 5.0 times greater than the mean value where mean values have been calculated on the basis of the electrical radius (see table 37). The electrical radius was found (section 6.2.1.1) to have a pressure dependence of $p^{-0.17}$. The mean current density therefore increases as $p^{0.34}$.

Results reported above are for an arc current of 100A and arc length of 3.2mm. However, a few experiments have been performed at other currents and arc lengths. These results are shown in table 38. It can be seen that the axial current density falls with increasing arc length for all flows and currents examined. At short arc lengths J_o was also observed to fall with increasing current. Similar values were obtained for both 100 Amp and 150 Amp arcs at the longer arc length examined (i.e. 4.8mm). The anomolous result at 150 Amps for a 4.8mm arc and flow of 6 is due to an Abel transform error (uncertainty in input data at high flow).. The peak value is found to occur off axis (at 0.7mm) and is $30A/mm^2$. If a mean line is plotted through these points then an axial value of about $25A/mm^2$ is appropriate. This is similar to the Gaussian value of $22A/mm^2$.

Pressure (bars)	Flow Setting (S)	J_o Abel A/mm^2	J_o Gaussian A/mm^2	$\bar{J}$ ** A/mm^2	$\frac{J_o(\text{Abel})}{\bar{J}}$	$\frac{J_o(\text{Gaussian})}{\bar{J}}$
1	0	8.0	14.5	2.77		
1	1	10.3	8.8	2.19		
1	2	10.0	8.4	2.61		
1	3	10.0	9.1	2.38		
* Average over flow values		9.6	10.2	2.50	3.8	4.1
2	0	18	14.1	4.09		
2	1	9	11.7	2.51		
2	2	16	12.2	3.15		
2	3	16	11.1	3.03		
* Average		14.8	12.3	3.2	4.6	3.8
6	0	23	19.9	3.89		
6	1	18	18.3	3.73		
6	2	19	18.0	3.89		
6	3	30	22.4	5.48		
* Average		22.5	19.7	4.3	5.2	4.6
10	0	26	15.3	4.93		
10	1	24	24.0	4.36		
10	2	31	27.7	4.46		
10	4	25	26.4	6.07		
10	6	-	32.0	6.82		
* Average		26.5	25.1	5.3	5	4.7
14	0	35	28.1	4.27		
14	1	29	23.8	7.2		
14	2	47	32.8	7.2		
14	3	32	33.3	6.64		
14	4	-	35.2	8.73		
14	5	-	42.6	7.96		
14	6	-	54.4	10.39		
* Average		35.8	35.7	7.5	4.8	4.8

* Averaged overflow

** $\bar{J} = \frac{I}{\pi R^2}$ where R is the electrical boundary

Table 37 Influence of Pressure and Gas Flow on Current Density (3.2mm, Argon TIG Arc on a Copper Anode).

Arc Length (mm)	3.2				4.8			
Flow Setting	3		6		3		6	
Current	100	150	100	150	100	150	100	150
J_o (Gaussian)	35	21	59	45	14	16	29	22
J_o (Abel)	38	32	71†	46	20	32	33	11*

† Poor data due to flow conditions disturbing arc

* This is the result of an off - axis peak in current density. The peak value occurs at 0.7mm from the axis and has a value of 30A/mm^2.

Table 38 Influence of Arc Length and Current on Anode Current Density

The reproducibility of measurements was investigated by a series of tests with a given arc condition (100A, 3.2mm, 14 bars, flow setting of 3). These were made on different occasions and results are shown in table 39. The reproducibility of arc disturbances in the presence of a shielding gas flow are also included in this table. It can be seen that deviations of ± 18% occurred in axial current density values obtained for nominally identical arcing conditions. Such variations are not unexpected at high pressures since arcing conditions are time dependent (i.e. fluctuations occur). It should also be noted that the standard deviation in measured electrical boundaries (8%) would indicate a deviation of 16% in current densities. This is close to the above value.

Experiment Number	J_o (Gaussian) A/mm^2	R mm	F Hz	$\bar{x}$ (mm)	x_m (mm)	σ (mm)
1	33.3	2.2	46	.0.17	0.54	0.09
2	34.9	2.5	58	0.12	0.35	0.08
3	38.9	2.5	56	0.13	0.41	0.09
4	22.6	2.3	53	0.11	0.32	0.07
Ave. Value	32.4	2.4	53	0.13	0.41	0.08
Deviation (standard)	±6	±.2	±5	±0.02	±0.1	±0.01
Percentage deviation	18	8	10	14	25	13

Table 39 Reproducibility of Arcing Conditions for Current Density Measurements at 14 Bars (cooled copper anode, 100 Amp, 3.2mm Argon Tungsten Arc in a Gas Flow of Setting 3).

6.3. Arc Stability

6.3.1. Argon TIG Arcs

6.3.1.1. Nature of Oscillations

Oscillation characteristics on cooled copper anodes have been measured for a range of pressures and shielding gas flows. It is generally found that very few small or large oscillations occur and that the most frequent amplitude has an intermediate value. This behaviour is represented in bar chart form (see figure 187), where the number of oscillations occurring within a given range of amplitudes is shown (for convenience of trace analysis, interval sizes are in multiples of 0.064mm). It can be seen from figure 187 that the total number of oscillations occurring at any pressure decreases with flow setting. The same figures show that the mean and maximum amplitudes also increase with flow at a given pressure. A statistical analysis of this data has been made to obtain:- the total number of oscillations (N), the mean oscillation amplitude ($\bar{x}$), the maximum amplitude (x_m) and the standard deviation (σ) of the data from the mean. This data is given on the respective bar charts. Also included on the bar charts is a comparison with the Poisson distribution calculated on the basis of observed mean values. The Poisson probability ($P_N(\bar{X},n)$) of occurrence of an oscillation with amplitude (normalised) between n and n-1 is (ref.161).

$$P_N(\bar{X},n) = \exp(-\bar{X}).\ \bar{X}^n/n! \quad (n = 1,2,3....) \qquad (131)$$

where N is the total number of oscillations and $\bar{X}$ the mean oscillation amplitude (normalised). The normalised mean ($\bar{X}$) is related to the true mean ($\bar{x}$) by

$$\bar{x} = \Delta.\bar{X}$$

where Δ is the division size (i.e. 0.064mm). Thus the normalised amplitude n is x/Δ where x is the real amplitude in multiples of Δ. The number of oscillations expected on the basis of Poissons law with amplitudes between x and $x-\Delta$ can now be obtained from equation 131:

$$N.\ \exp(-\bar{x}/\Delta)\ .\ (\bar{x}/\Delta)^{(x/\Delta)}/(x/\Delta)!$$

where x/Δ is integer by definition.

n = number of oscillations in a given interval of x
x = oscillation amplitude
$\bar{x}$ = mean oscillation amplitude
x_m = maximum oscillation amplitude
N = total number of oscillations
σ_N = standard deviation of x from $\bar{x}$
------ Poisson distribution

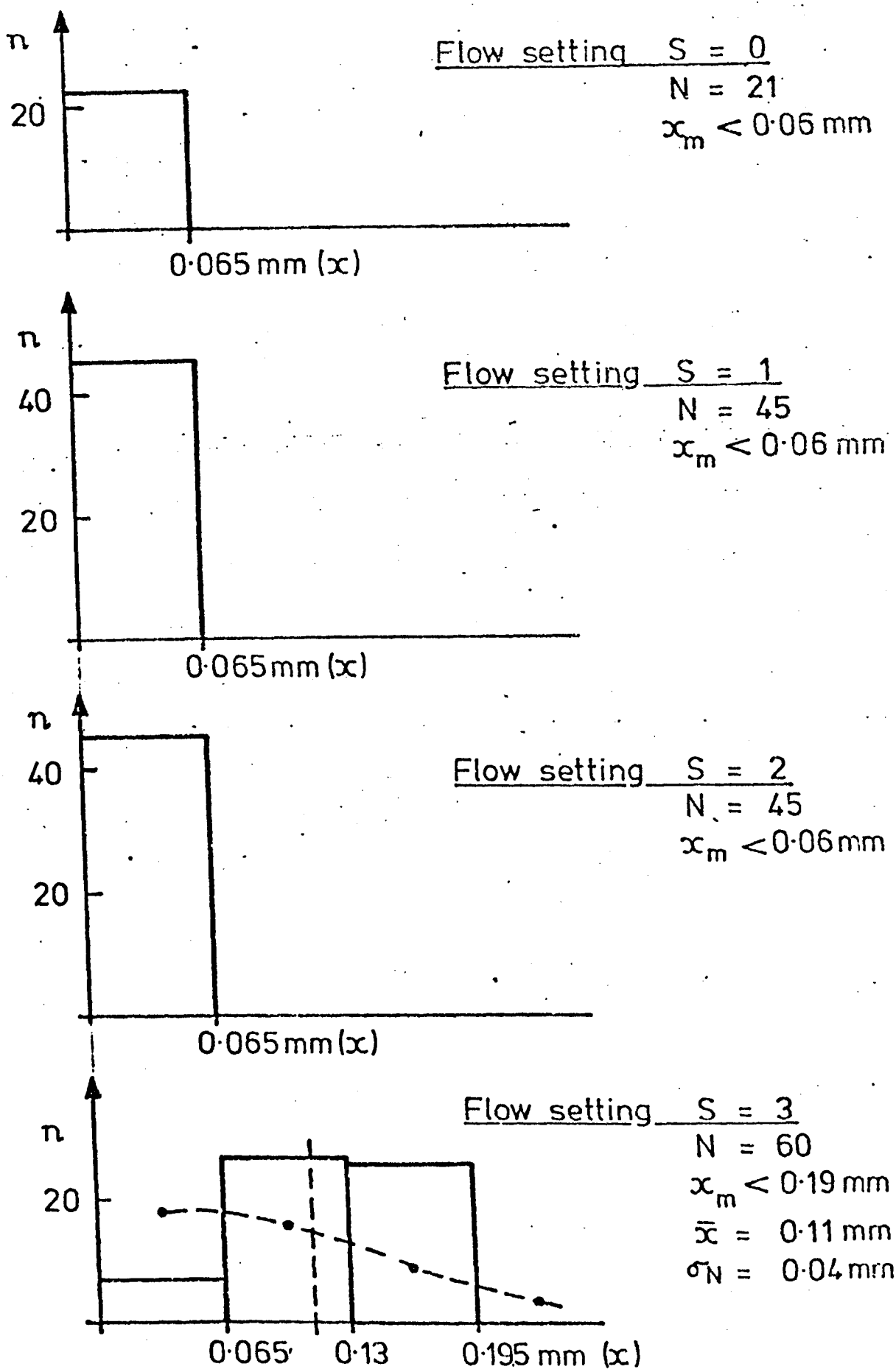

FIGURE 187.A DISTRIBUTION OF OSCILLATION AMPLITUDES FOR AN ARGON TIG ARC (100A, 3·2 mm) PASSING OVER THE SPLITTING PLANE OF A SEGMENTED COPPER

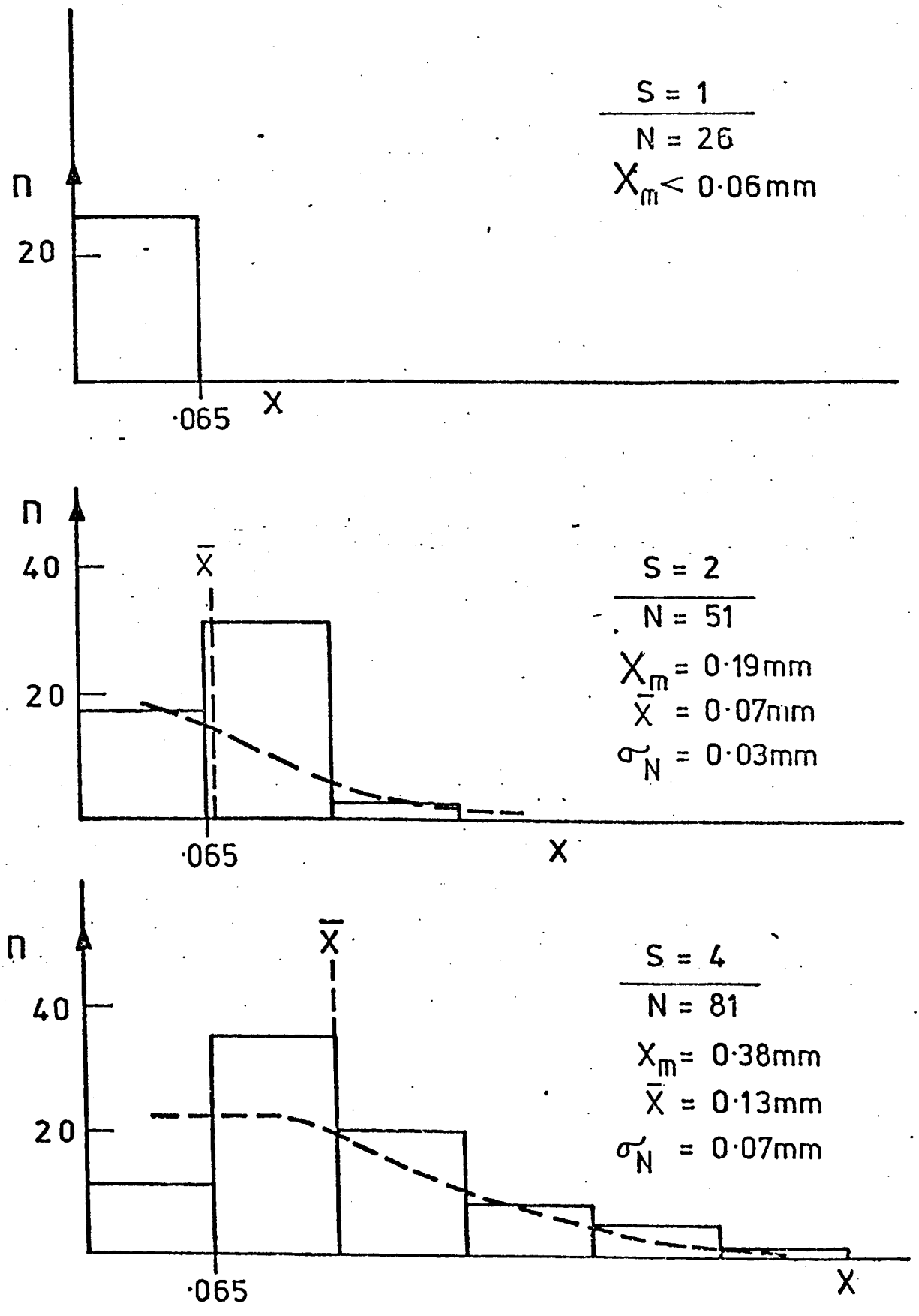

P = 6 bars

FIGURE 187 B

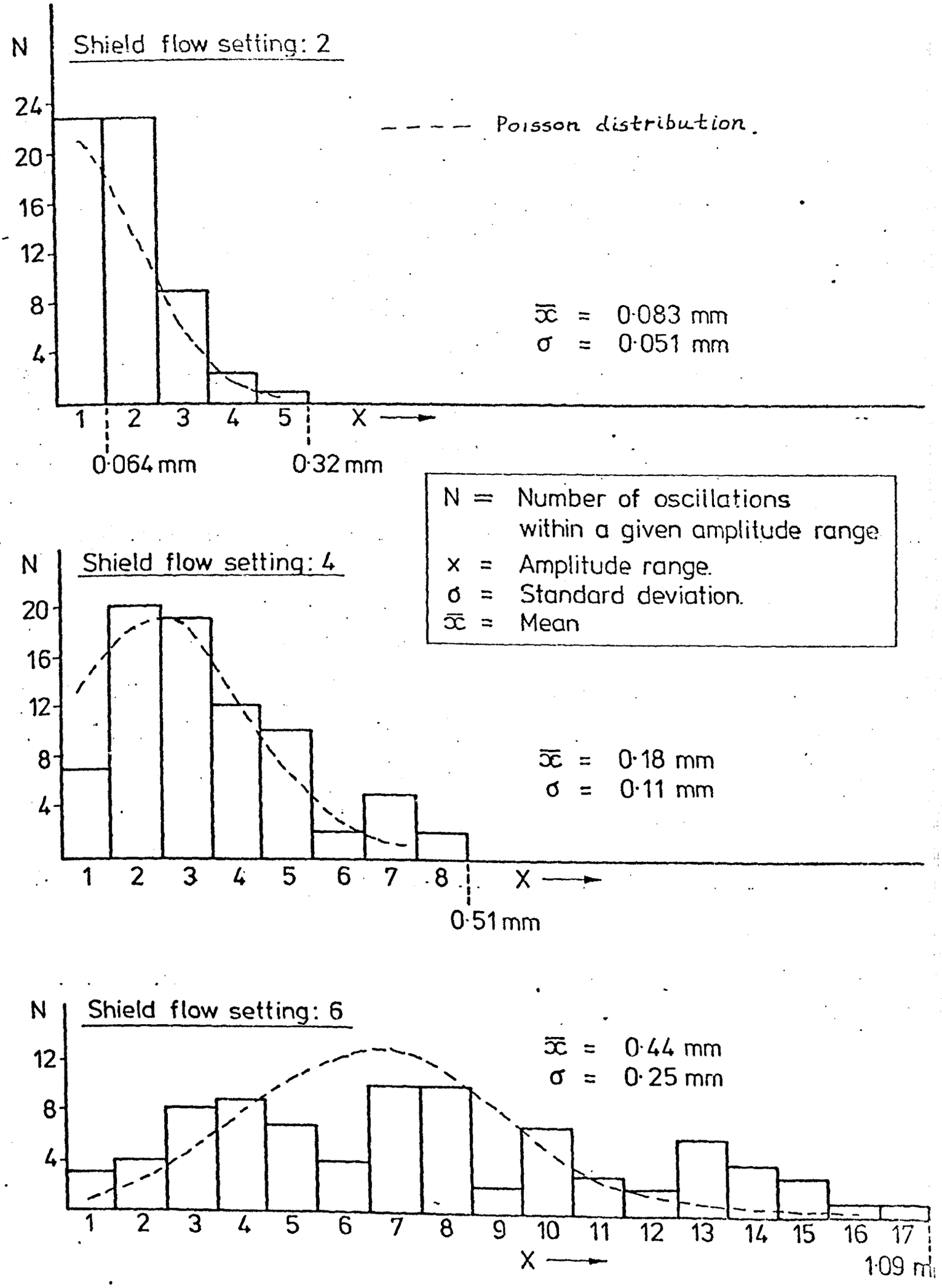

FIG.187C DISTRIBUTION OF OSCILLATION AMPLITUDES AT 10 BARS (Abs.)

P = 14

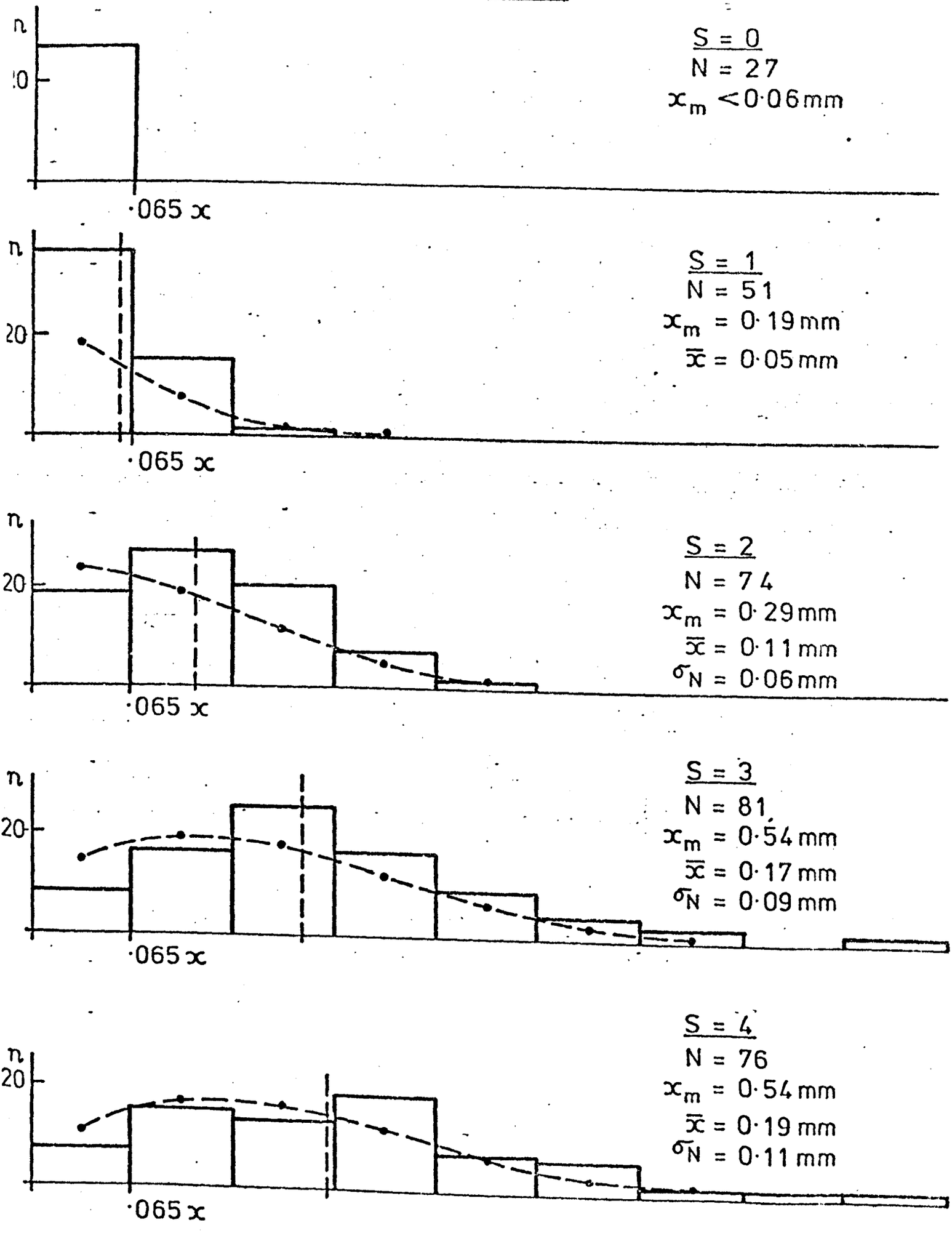
n
10
·065 x
S = 0
N = 27
x_m < 0·06 mm
n
20
·065 x
S = 1
N = 51
x_m = 0·19 mm
$\bar{x}$ = 0·05 mm
n
20
·065 x
S = 2
N = 74
x_m = 0·29 mm
$\bar{x}$ = 0·11 mm
σ_N = 0·06 mm
n
20
·065 x
S = 3
N = 81
x_m = 0·54 mm
$\bar{x}$ = 0·17 mm
σ_N = 0·09 mm
n
20
·065 x
S = 4
N = 76
x_m = 0·54 mm
$\bar{x}$ = 0·19 mm
σ_N = 0·11 mm

FIG. 187D

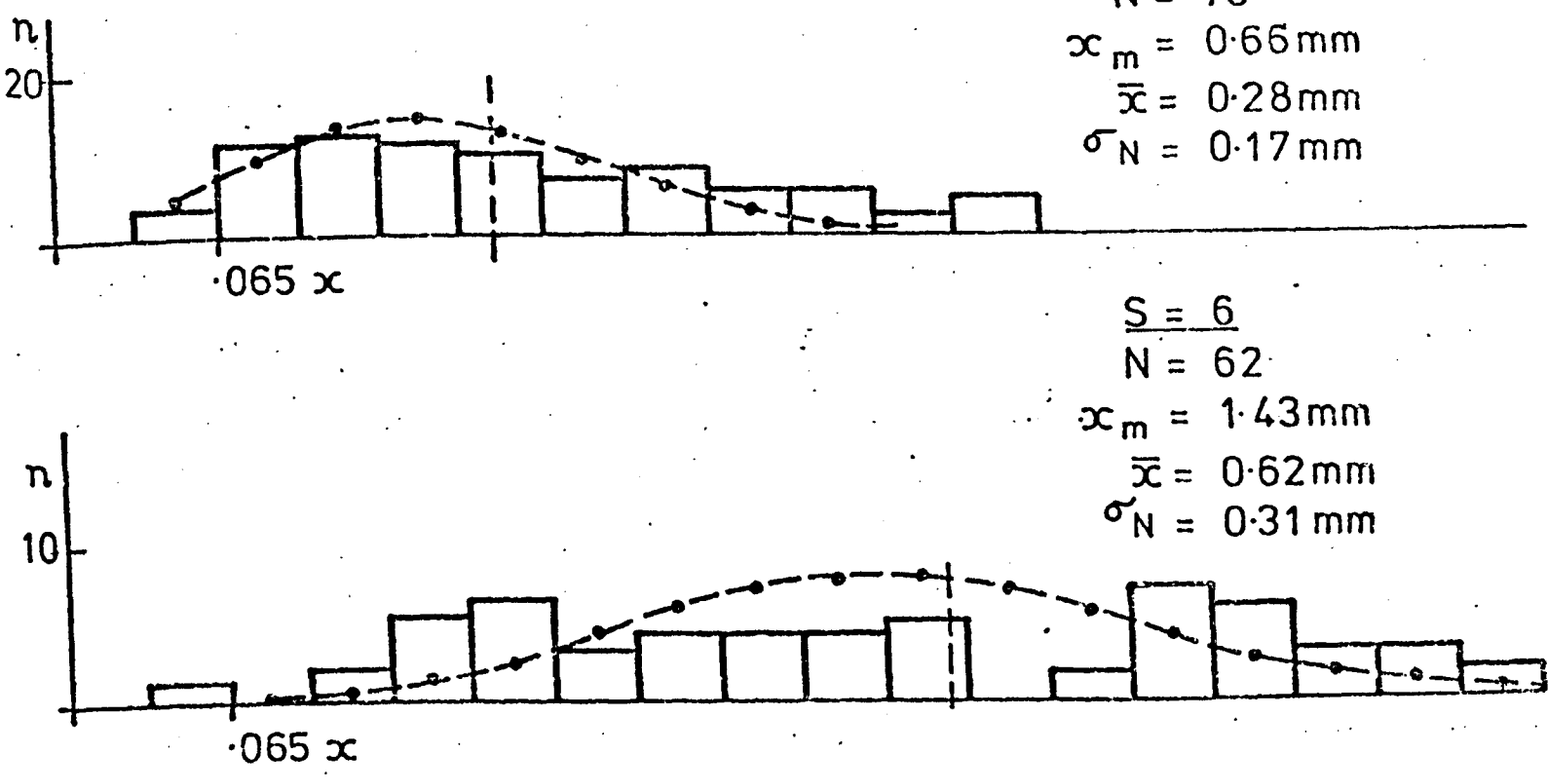

FIG.187. D(Continued)

It can be seen that the data is fairly well represented by this type of distribution. This implies that oscillation amplitudes are of an approximately Gaussian form for large samples and therefore random in nature.

6.3.1.2. Oscillation Amplitude

The mean oscillation amplitude is shown as a function of pressure and flow meter setting in figure 188. It can be seen that the amplitude increases with pressure for a given flow setting. Oscillations at 1 bar were insignificant over the range of flow settings shown and therefore do not appear in figure 188. Measurements of the maximum amplitude have also been made. These have been expressed as a percentage of the corresponding electrical arc radius at the anode (see figure 189). This ratio gives a measure of the maximum spatial perturbation and behaves in a similar manner to that observed for mean amplitude. It is instructive to transform these results out of laboratory co-ordinates and into a mass flow representation. This may be achieved using equations 84 and 86.

The result of this transformation is shown in figure 190. It can be seen that below a Reynolds number of 2,500 oscillations are small and independent of both pressure and flow. The small oscillations found at 1 bar correspond to this region. Above this Reynolds number oscillation amplitudes are dependent only on shielding gas mass flow rate .. i.e. independent of ambient pressure. For Reynolds numbers greater than 2,500 the sensitivity of the mean oscillation amplitude to flow is well represented by 0.16mm per g/s. At very high Reynolds numbers (20,000>) an even stronger sensitivity is observed. However, very little data is available for this region.

The transition region at 0.5g/s corresponds to a Reynolds number of about 2,260. This is precisely the region where pipe flows (ref.162) become turbulent. It would therefore appear that arc oscillations are coupled to the onset of turbulence in the shield. This is further substantiated by the random nature of observed column oscillations (section 6.3.1.1).

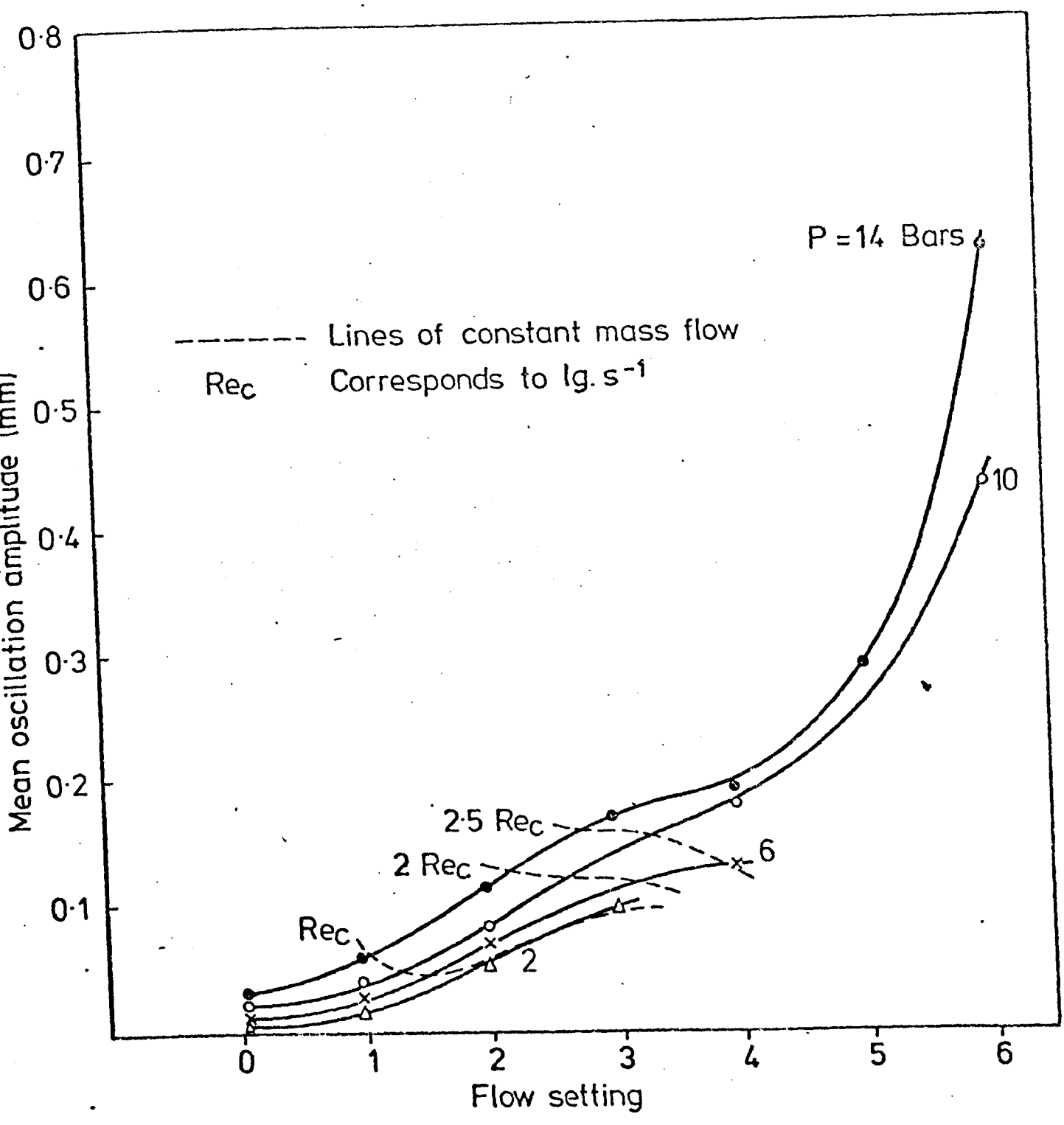

FIG.188. EFFECTS OF PRESSURE AND FLOW SETTING ON THE MEAN OSCILLATION AMPLITUDE.

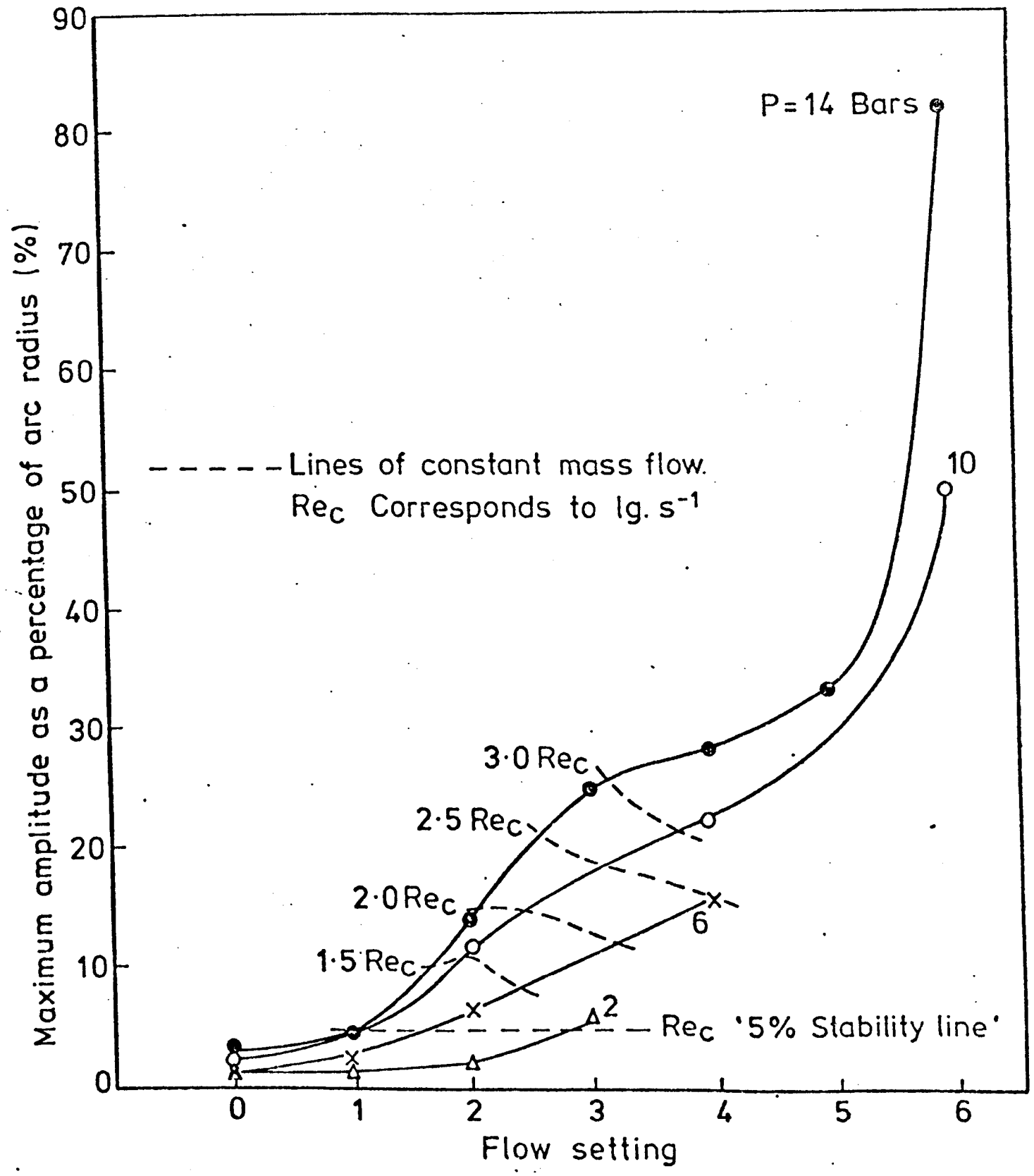

FIG.189. EFFECTS OF PRESSURE AND FLOW SETTING ON THE MAXIMUM OSCILLATION AMPLITUDE EXPRESSED AS A PERCENTAGE OF THE ARC RADIUS.

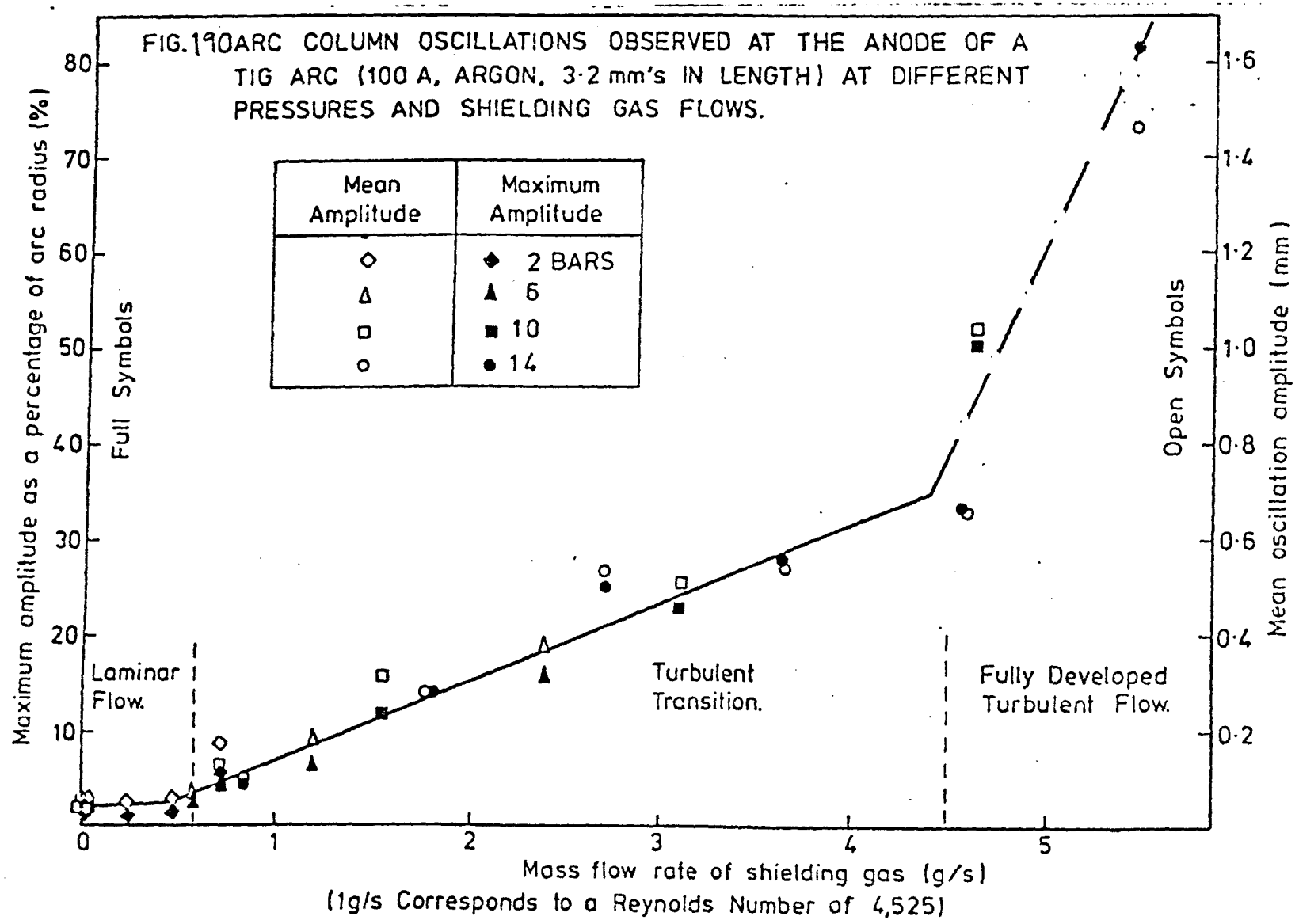
FIG.19 ARC COLUMN OSCILLATIONS OBSERVED AT THE ANODE OF A TIG ARC (100 A, ARGON, 3·2 mm's IN LENGTH) AT DIFFERENT PRESSURES AND SHIELDING GAS FLOWS.
Mean Amplitude
Maximum Amplitude
2 BARS
6
10
14
Full Symbols
Open Symbols
Maximum amplitude as a percentage of arc radius (%)
Mean oscillation amplitude (mm)
Laminar Flow.
Turbulent Transition.
Fully Developed Turbulent Flow.
Mass flow rate of shielding gas (g/s)
(1g/s Corresponds to a Reynolds Number of 4,525)

A measure of variance in arcing conditions (during a single run) is afforded by the standard deviation of oscillation aplitude from the mean. This is shown as a function of mass flow in figure 191. Again it can be clearly seen that behaviour similar to that described for oscillation amplitude is obtained. Results reported above were found for a 100 Amp arc of length 3.2mm. A limited number of experiments were also conducted at different currents and arc lengths (see table 40). Results indicate that the 150A arc behaves in a similar manner to the 100A arc at low flows. However, at high flows the 150A arc appears to be significantly more stable (see table 40). It is also found that 4.8mm arcs are similar in behaviour to 3.2mm arcs for low flows but significantly less stable at high flows. These trends are to be expected as arc 'stiffness' decreases with increasing arc length and decreasing current.

Flow Setting	Arc Length (mm)	Arc Current (Amp)	Current Density A/mm^2	Electrical Radius (mm)	F H_Z	$\bar{X}$ (mm)	X_m (mm)	σ (mm)
3	3.2	100	35	2.5	58	0.12	0.35	0.08
3	3.2	150	21	2.7	75	0.13	0.44	0.09
3	4.8	100	14	2.8	71	0.15	0.38	0.10
3	4.8	150	16	3.0	79	0.11	0.32	0.07
6	3.2	100	59	2.0	58	0.17	0.45	0.12
6	3.2	150	45	2.7	102	0.12	0.33	0.07
6	4.8	100	29	2.9	64	0.36	1.27	0.29
6	4.8	150	22	2.9	49	0.29	0.78	0.20

F = Oscillation Frequency

$\bar{X}$ = Mean Oscillation Amplitude

X_m = Maximum Oscillation Amplitude

σ = Standard Deviation of Amplitudes

Table 40 Influence of Arc Length and Current on Oscillation Characteristics at 14.6 Bars

6.3.1.2. Oscillation Frequency

No attempt has been made to analyse the distribution of frequencies occurring during a given experiment. Frequency has been defined here simply as the total number of oscillations over the time of occurrence. Result obtained using this definition are shown in figures 192 and 193.

FIG. 191 Standard deviation of oscillation amplitude as a function of shield mass flow rate (3·2mm, 100A, argon arc)

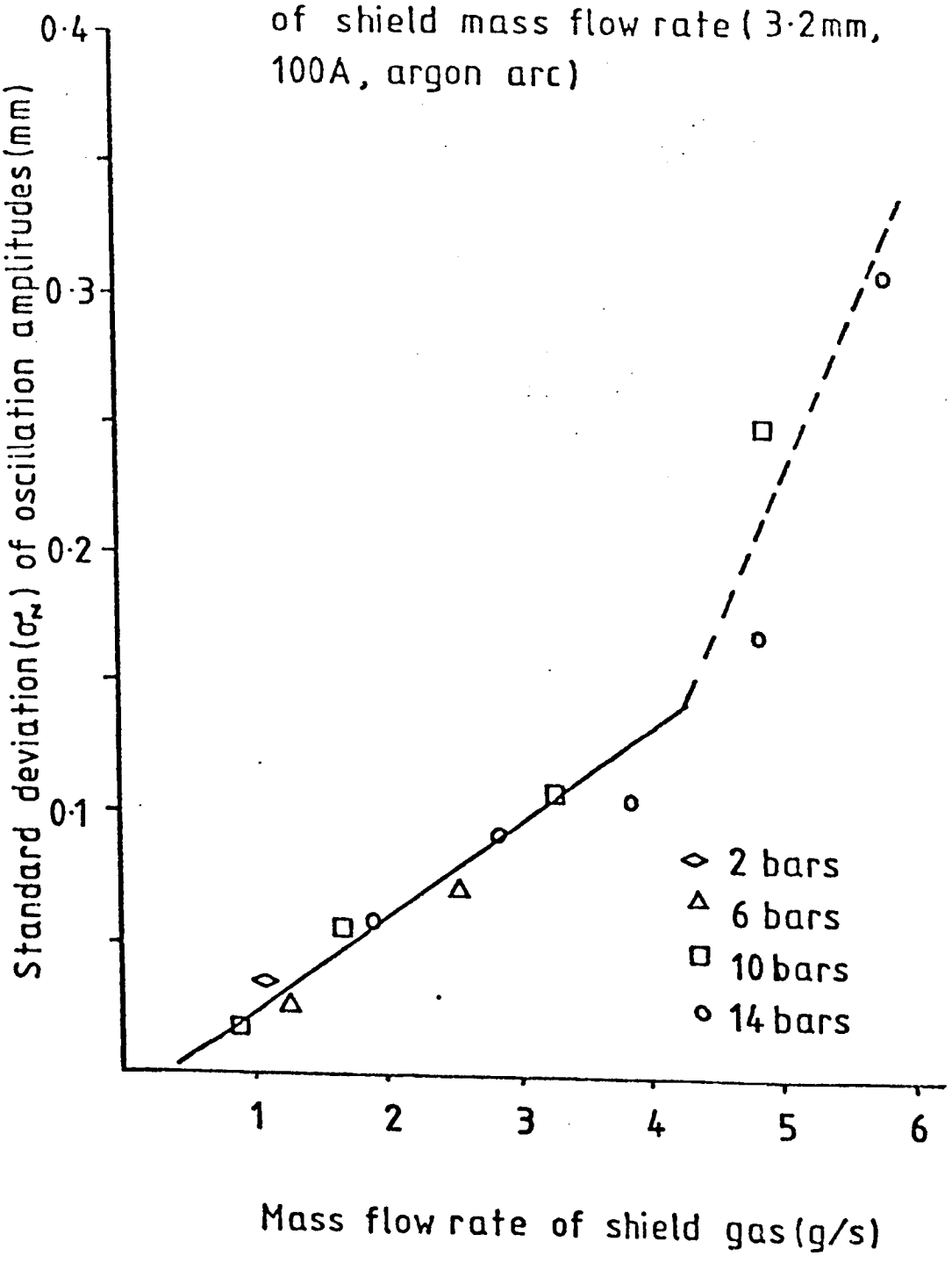

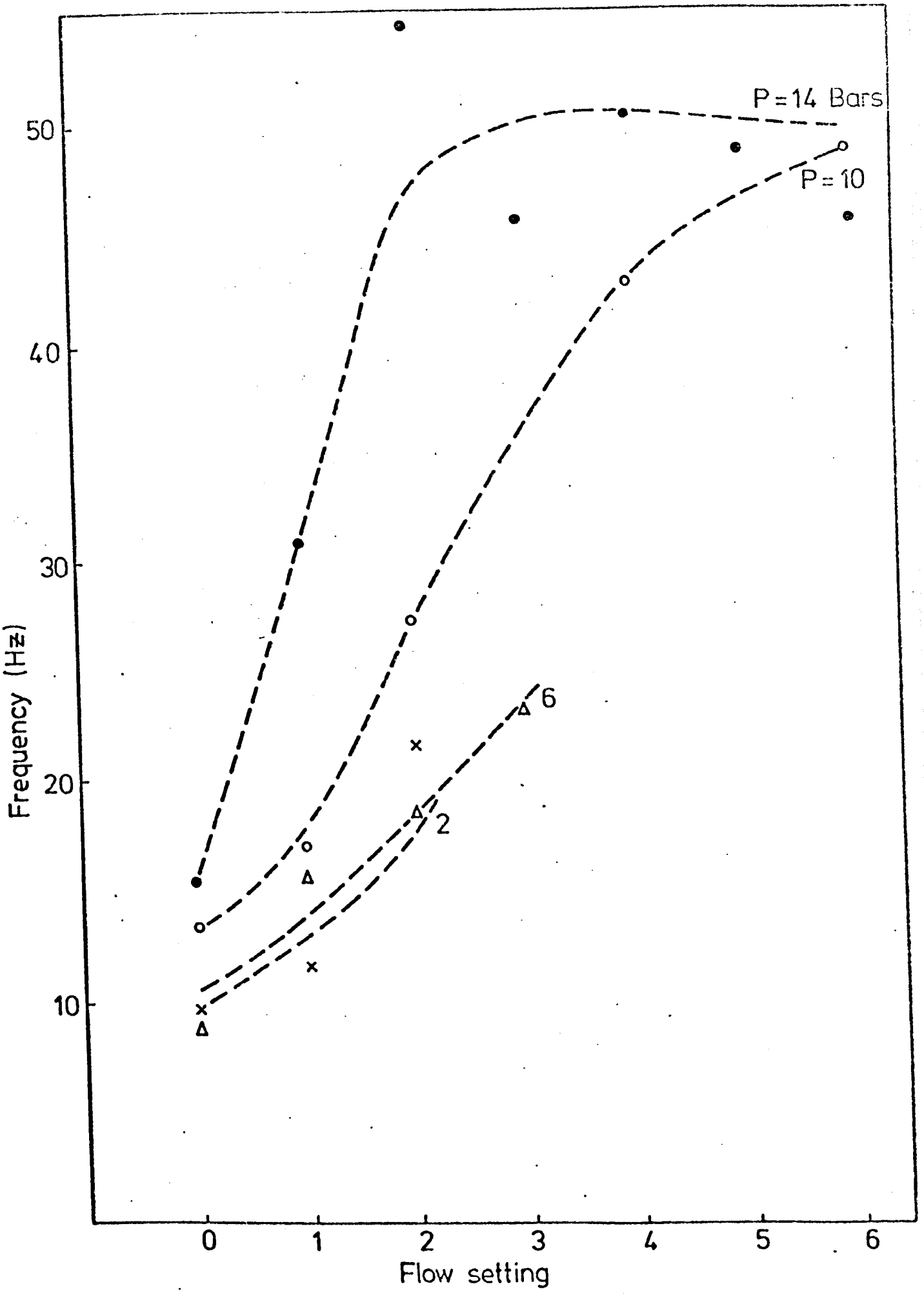

FIG.192. DEPENDENCE OF OSCILLATION FREQUENCY ON PRESSURE AND FLOW.

FIG. 193. Influence of shield gas flow rate on arc column oscillation frequency. (3·2 mm, 100A, argon arc)

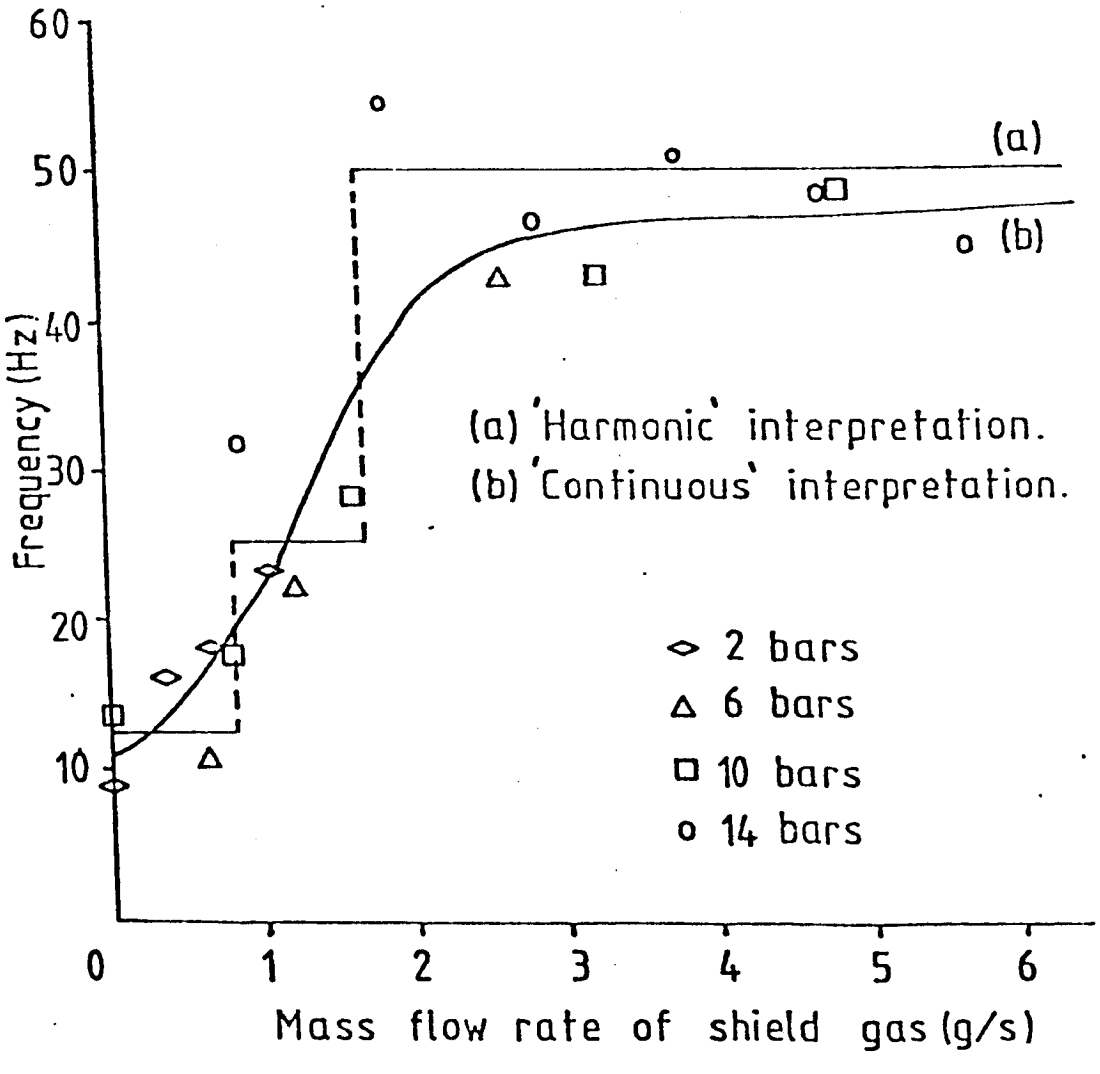

These have been plotted against flow meter setting and mass flow rate. It can be seen that frequency generally increases with flow meter setting at a given pressure. However, at 14 bars saturation is observed at a frequency near 50Hz. This behaviour is shown more clearly when results are displayed on a mass flow basis. It is possible to interpret this behaviour in terms of sub-divisions of the three phase supply frequency to the power supply. The arc is then regarded as 'beating' in tune with the supply frequency i.e. The large gap between 50Hz results and those between 20 and 30 lends itself to an interpretation in terms of 50Hz, 25Hz, 12.5Hz etc. oscillations. However, more points would be required to substantiate this interpretation.

Measurements of frequency (f) coupled to those of mean amplitude ($\bar{x}$) may be used to estimate the mean transverse velocity ($\bar{v}$) of the arc across the anode

$$\text{i.e. } \bar{v} \simeq 4.\bar{x}.f$$

$\bar{v}$ is generally less than 0.1m/s. This is much less than the plasma streaming velocity and hence a plasma element will see the arc as stationary but in some position displaced from equilibrium.

6.3.2. Constricted Argon Tungsten Arcs

Experiments with constricted tungsten arcs showed no sign of instabilities over the pressure range examined for TIG. This was true for a wide range of shielding and plasma gas conditions (see figure 194).

6.4. Electrostatic Probe Results

The application of electrostatic probes to the situation presently being considered was discussed in 3.6.4. Methods described in section 3.6.4 were used to investigate the structure of column voltage for 100 Amp argon arcs operating above steel anodes. Results are shown in figures 195 to 200. For the purpose of clarity and comparison the smoothed out data lines are shown in figures 201 to 205. These have been used to investigate the nature of voltage drops. Of particular interest are anode and cathode fall behaviour and the axial dependence of the electric field strength.

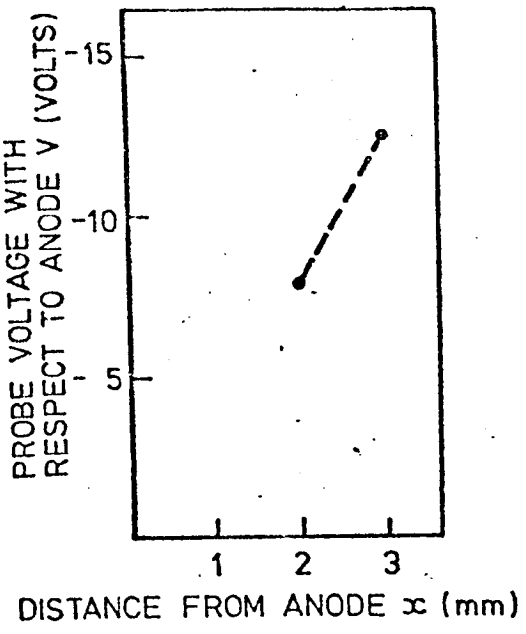

FIGURE 195a. ARC LENGTH (ℓ) = 3mm
PRESSURE (p) = 1 bar (abs)

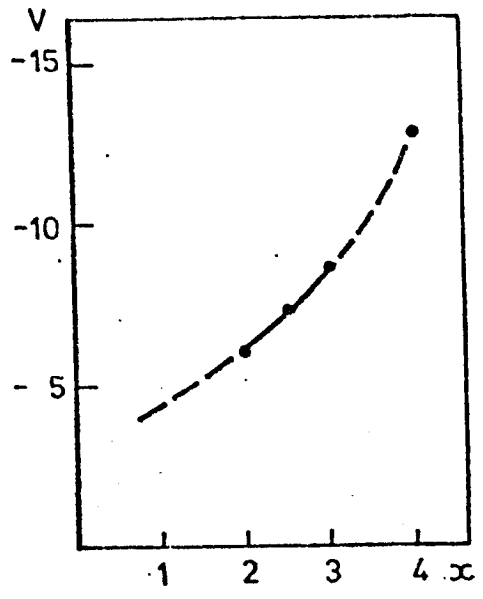

FIGURE 195b. ℓ = 4
p = 1

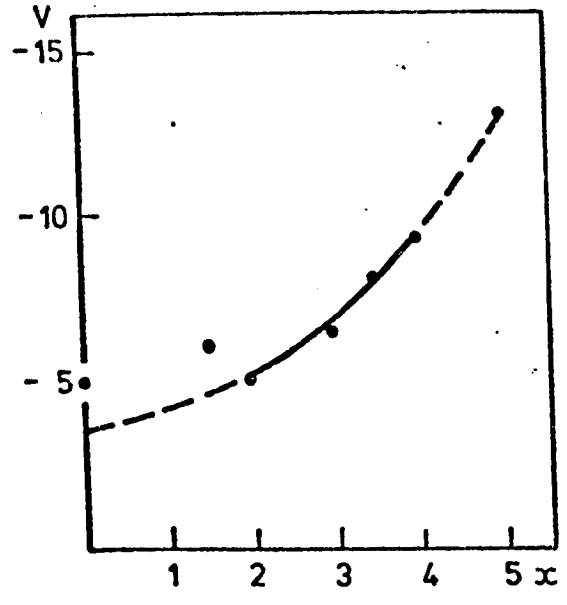

FIGURE 195c. ℓ = 5
p = 1

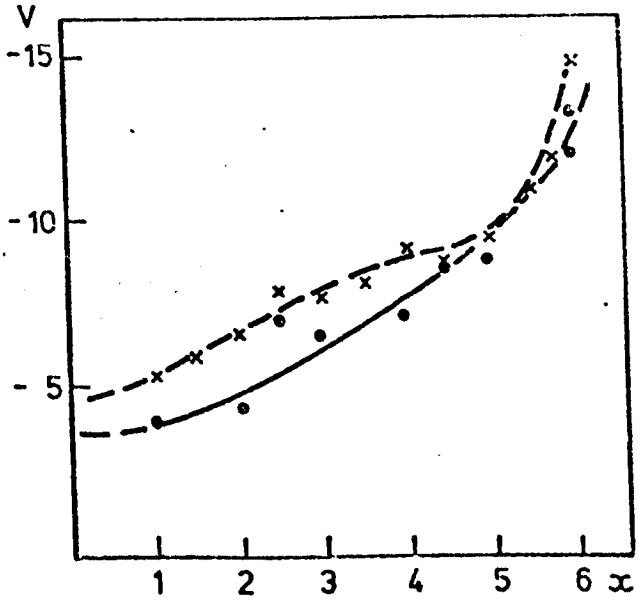

FIGURE 195d. ℓ = 6
p = 1

—x—x— COPPER ANODE
—•—•— STEEL ANODE

AXIAL DEPENDENCE OF PROBE VOLTAGE (DATA POINTS)
[EXPERIMENTAL CONDITIONS FOR PROBE TRACES; 100 AMPS, ARGON ARC IN STILL ATMOSPHERE ABOVE A MOVING STEEL ANODE]

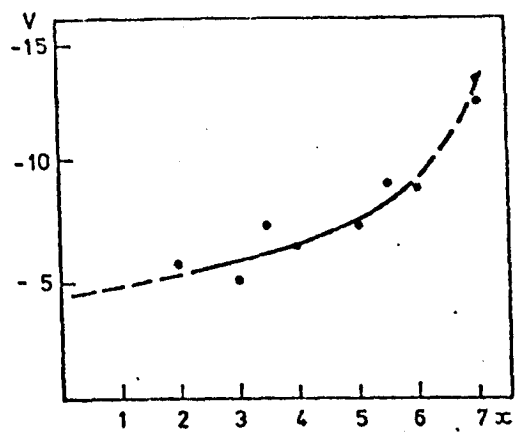

FIGURE 195 e. $\ell = 7$, $p = 1$

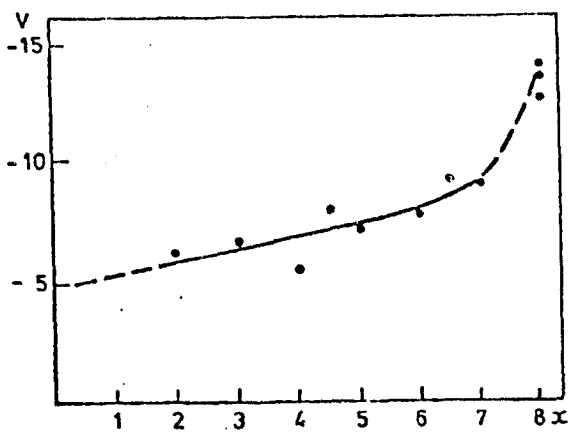

FIGURE 195 f. $\ell = 8$, $p = 1$

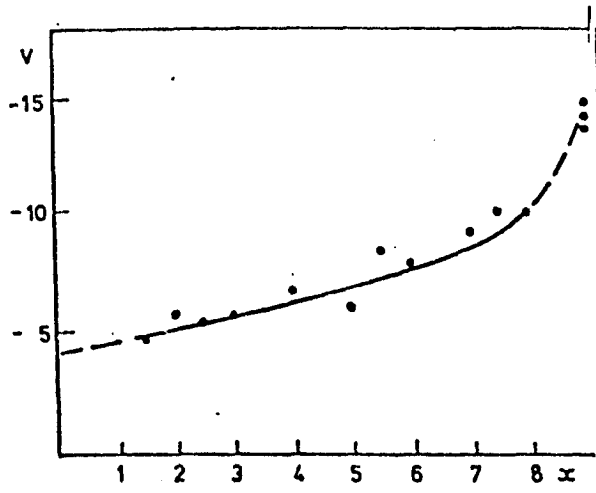

FIGURE 195 g. $\ell = 9$, $p = 1$

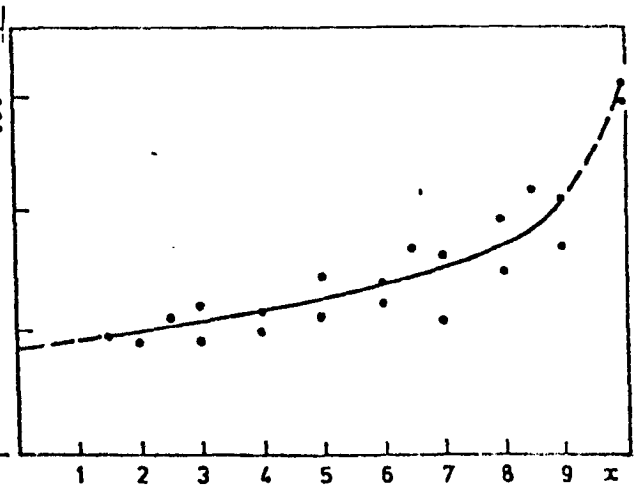

FIGURE 195 h. $\ell = 10$, $p = 1$

AXIAL DEPENDENCE OF PROBE VOLTAGE (DATA POINTS)

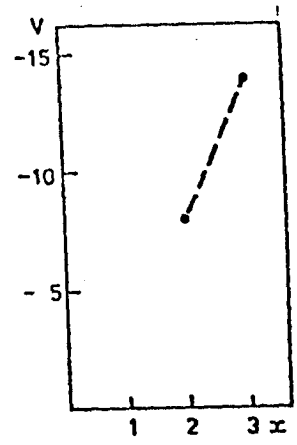

FIGURE 196 a. $\ell = 3$
$p = 4 \cdot 4$

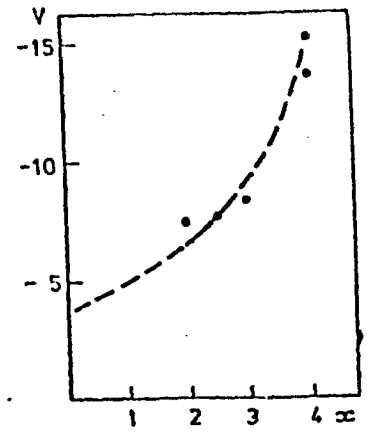

FIGURE 196 b. $\ell = 3$
$p = 4 \cdot 4$

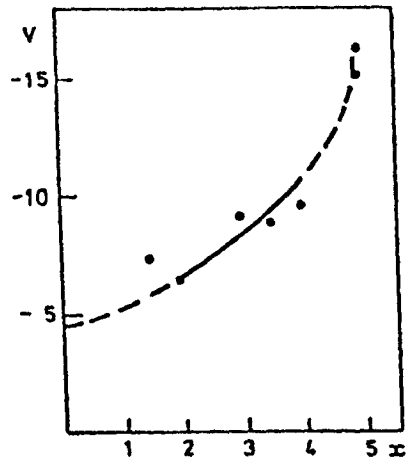

FIGURE 196 c. $\ell = 5$
$p = 4 \cdot 4$

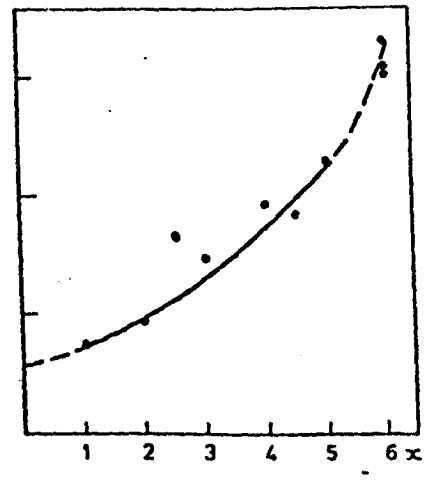

FIGURE 196 d. $\ell = 6$
$p = 4 \cdot 4$

AXIAL DEPENDENCE OF PROBE VOLTAGE (DATA POINTS)

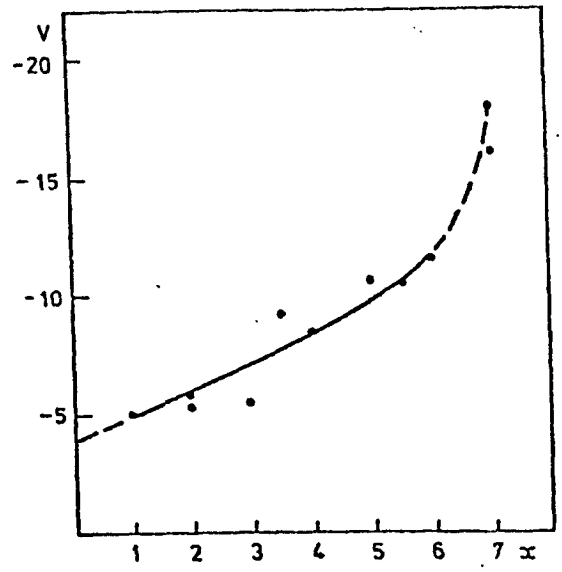

FIGURE 196 e . $\ell = 7$
$p = 4{\cdot}4$

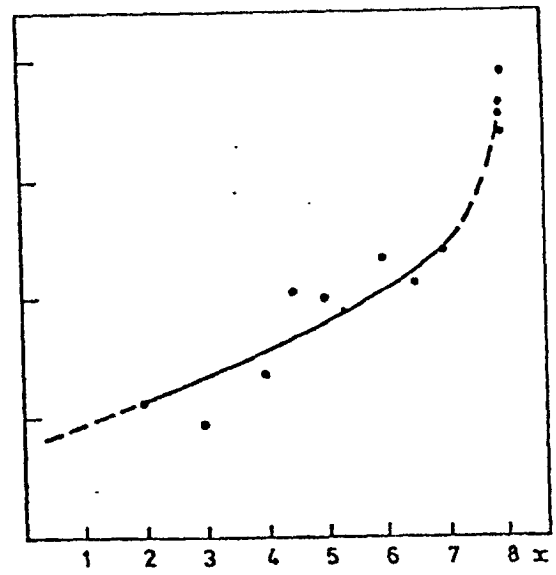

FIGURE 196 f. $\ell = 8$
$p = 4{\cdot}4$

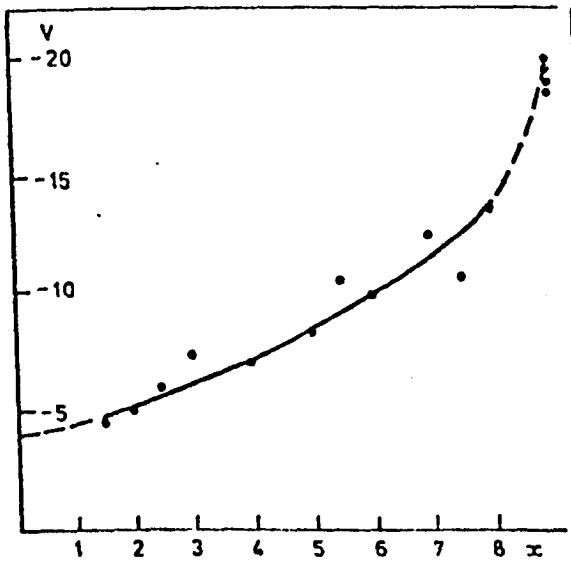

FIGURE 196 g. $\ell = 9$
$p = 4{\cdot}4$

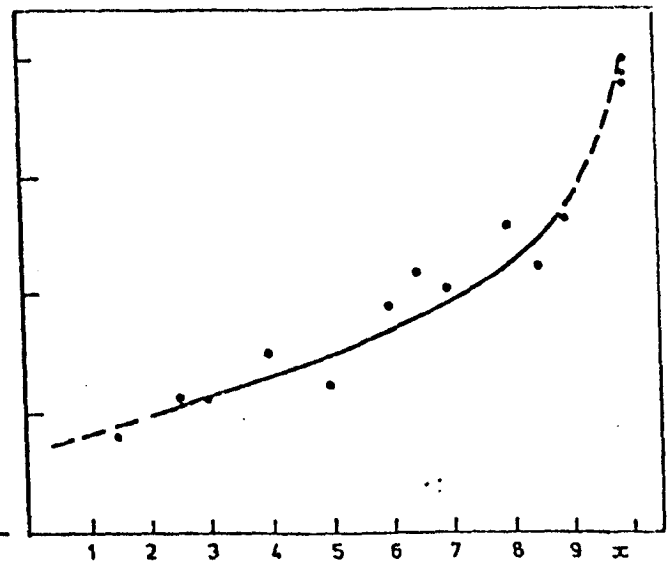

FIGURE 196 h. $\ell = 10$
$p = 4{\cdot}4$

AXIAL DEPENDENCE OF PROBE VOLTAGE (DATA POINTS)

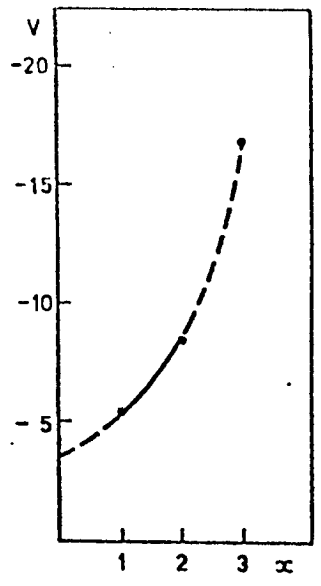

FIGURE 197a $\ell = 3$
$p = 7{\cdot}8$

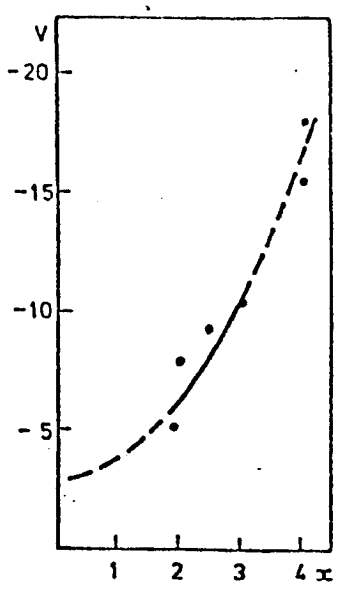

FIGURE 197b $\ell = 4$
$p = 7{\cdot}8$

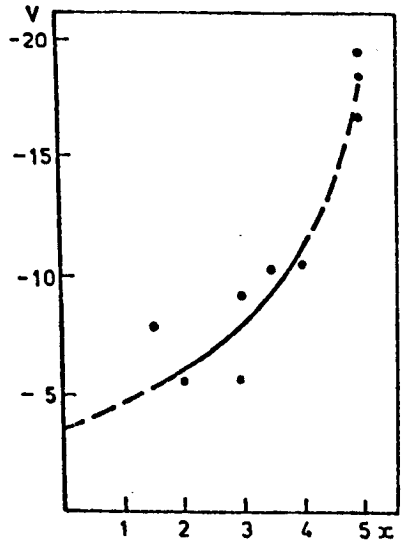

FIGURE 197c $\ell = 5$
$p = 7{\cdot}8$

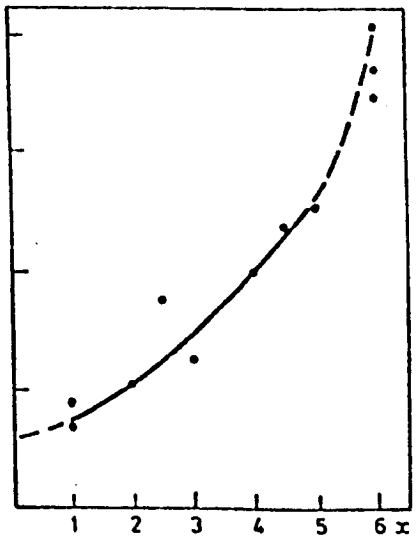

FIGURE 197d $\ell = 6$
$p = 7{\cdot}8$

AXIAL DEPENDENCE OF PROBE VOLTAGE (DATA POINTS)

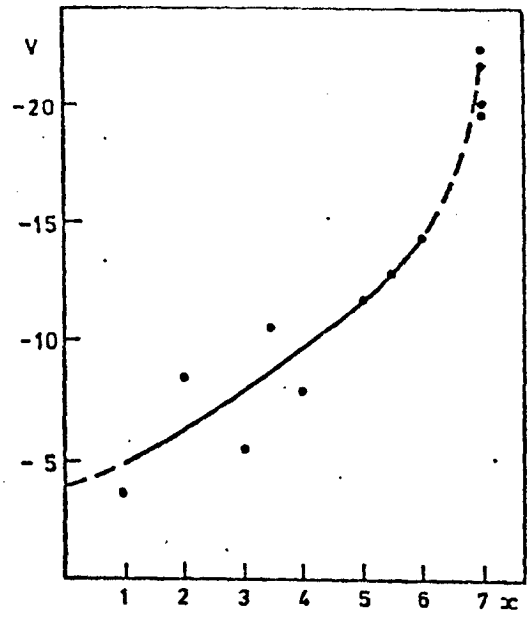

FIGURE 197e. $\ell = 7$
$p = 7 \cdot 8$

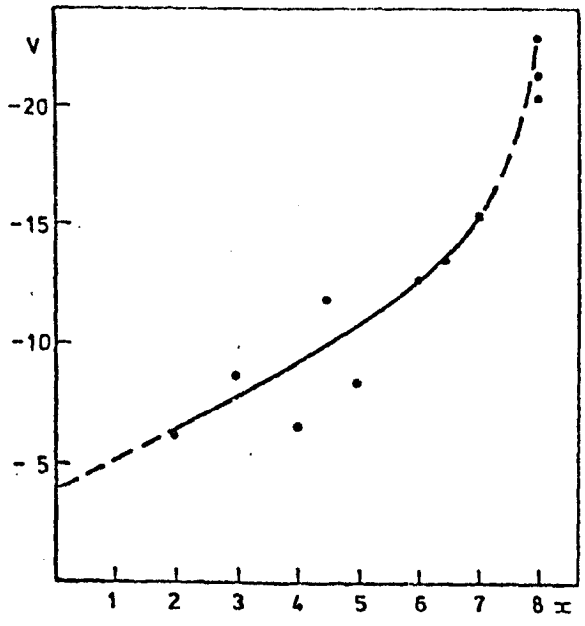

FIGURE 197f. $\ell = 8$
$p = 7 \cdot 8$

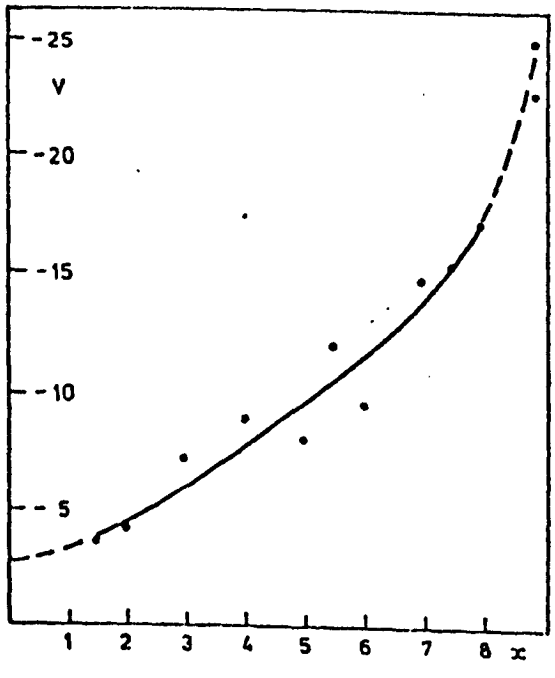

FIGURE 197g $\ell = 9$
$p = 7 \cdot 8$

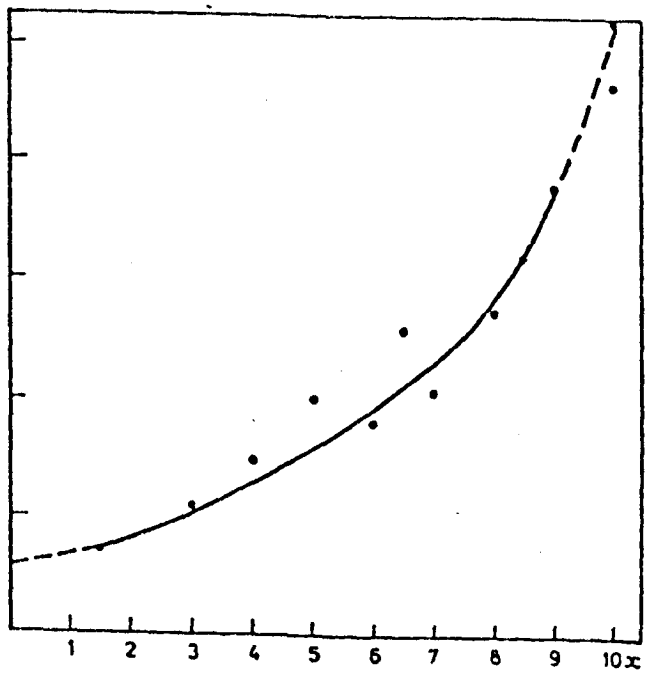

FIGURE 197h. $\ell = 10$
$p = 7 \cdot 8$

AXIAL DEPENDENCE OF PROBE VOLTAGE (DATA POINTS)

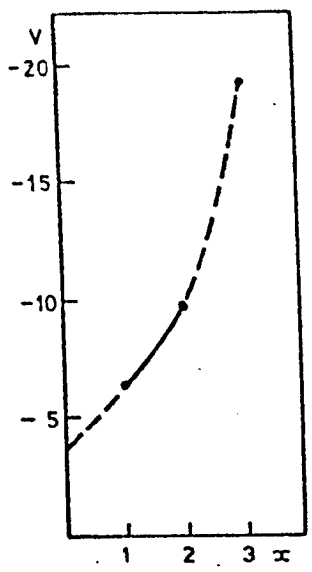

FIGURE 198 a. $\ell = 3$
$p = 14{\cdot}6$

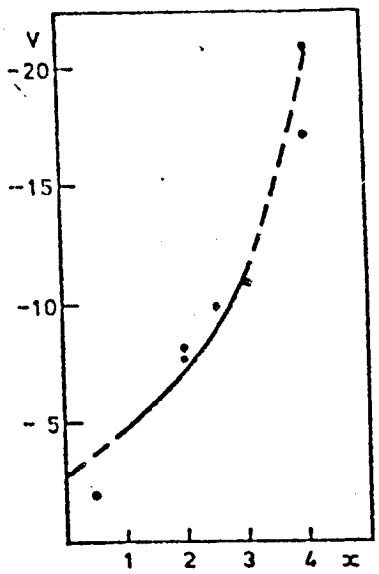

FIGURE 198 b. $\ell = 4$
$p = 14{\cdot}6$

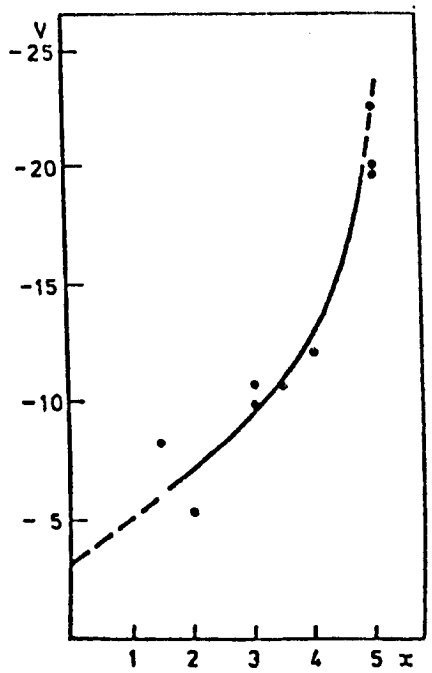

FIGURE 198c. $\ell = 5$
$p = 14{\cdot}6$

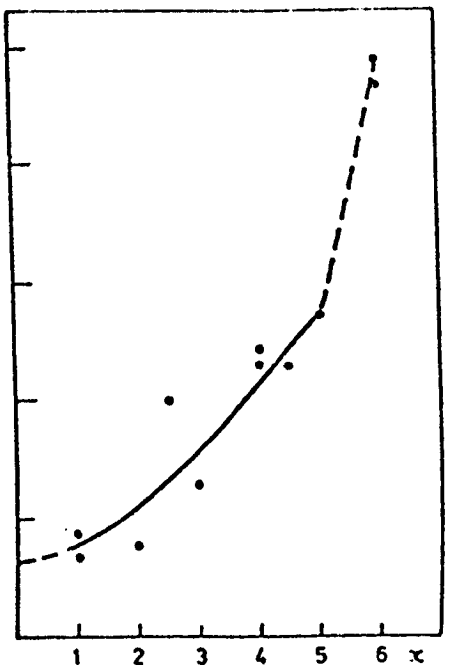

FIGURE 198 d. $\ell = 6$
$p = 14{\cdot}6$

AXIAL DEPENDENCE OF PROBE VOLTAGE (DATA POINTS)

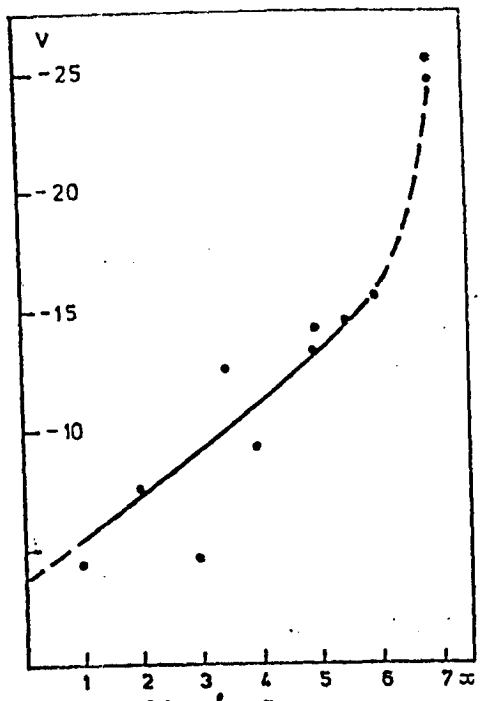

FIGURE 198e $\ell = 7$, $p = 14.6$

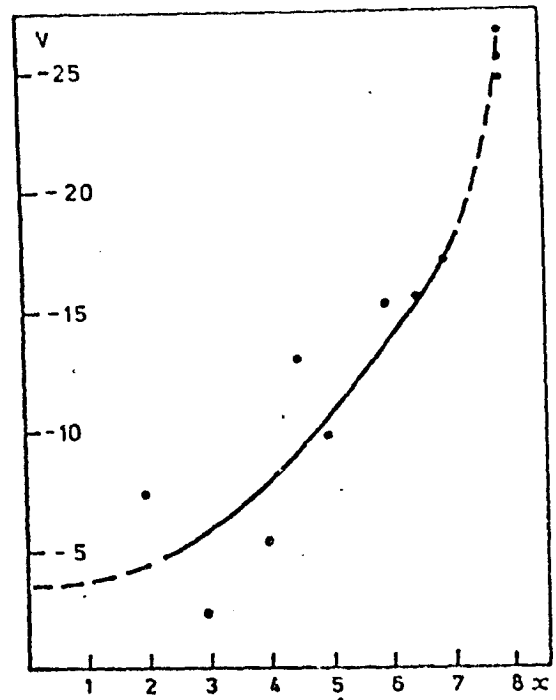

FIGURE 198 f. $\ell = 8$, $p = 14.7$

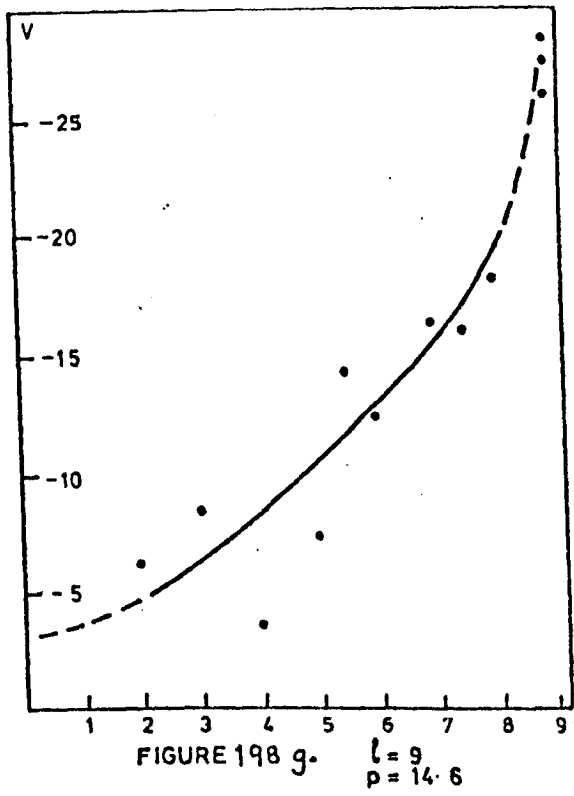

FIGURE 198 g. $\ell = 9$, $p = 14.6$

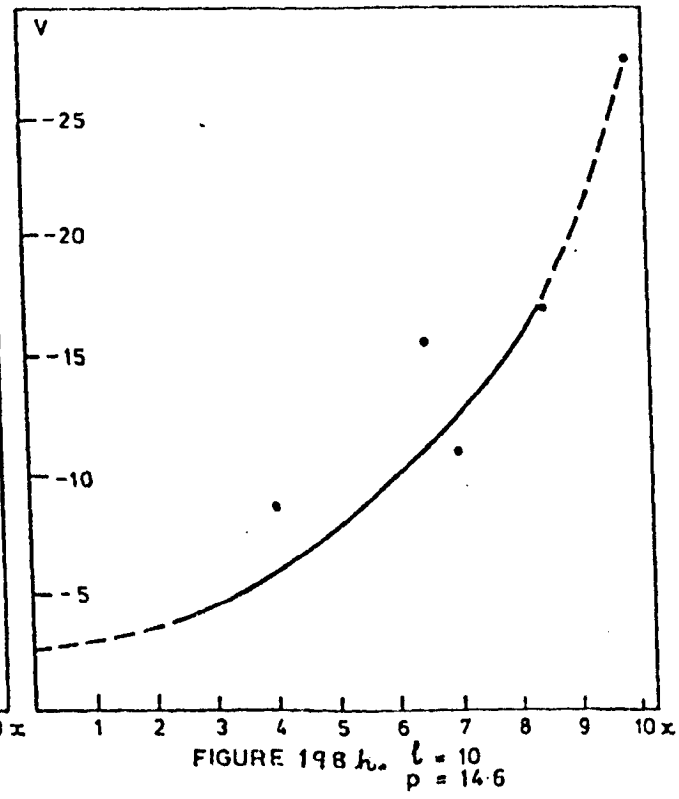

FIGURE 198 h. $\ell = 10$, $p = 14.6$

AXIAL DEPENDENCE OF PROBE VOLTAGE (DATA POINTS)

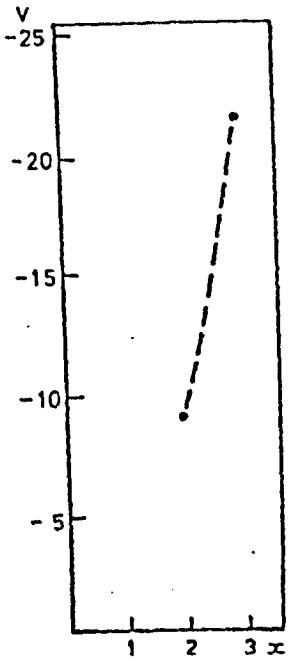

FIGURE 199a. $l = 3$, $p = 21.4$

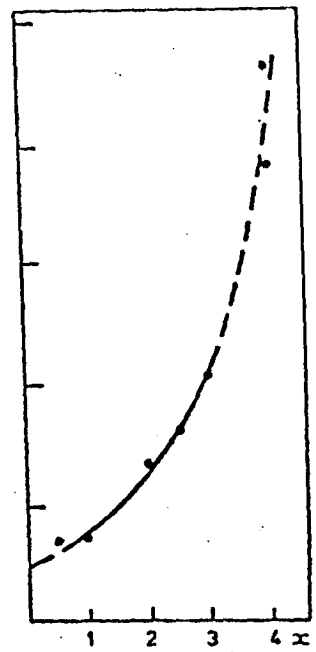

FIGURE 199b. $l = 4$, $p = 21.4$

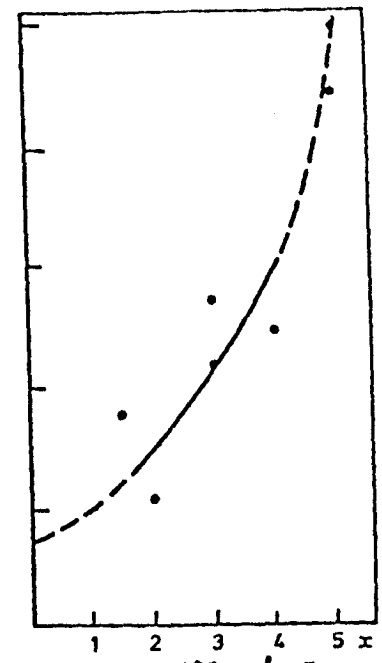

FIGURE 199c. $l = 5$, $p = 21.4$

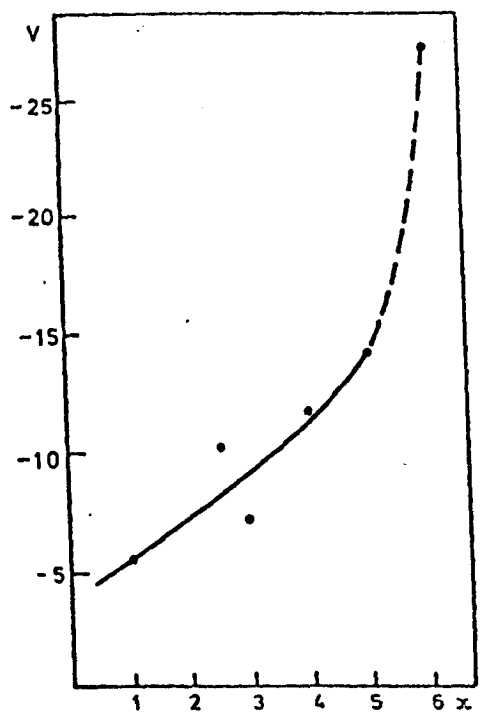

FIGURE 199d. $l = 6$, $p = 21.4$

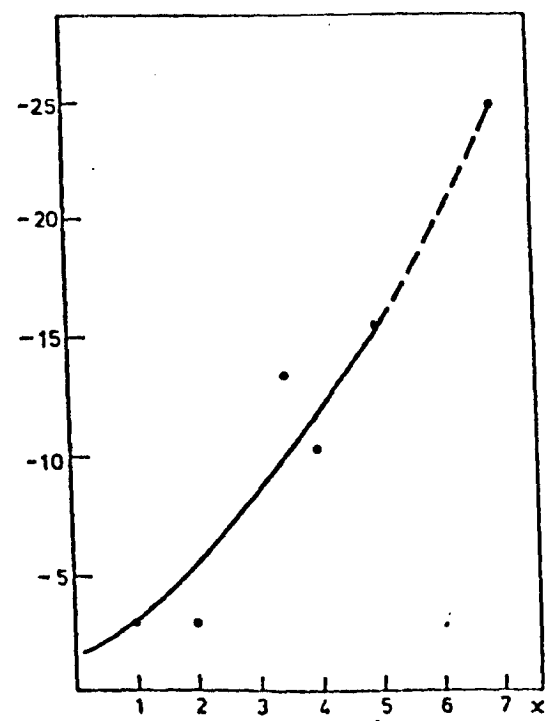

FIGURE 199e. $l = 7$, $p = 21.4$

AXIAL DEPENDENCE OF PROBE VOLTAGE (DATA POINTS)

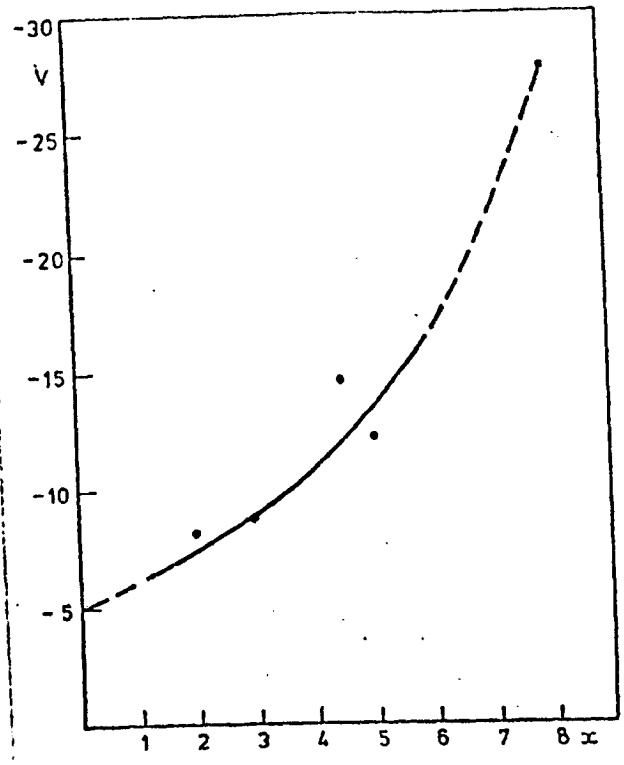

FIGURE 199f. $l = 8$
$p = 21{\cdot}4$

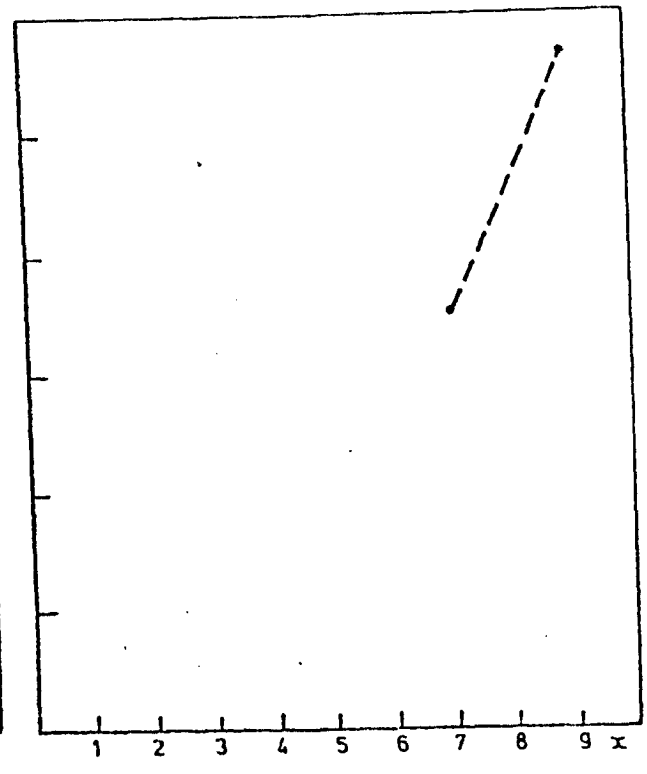

FIGURE 199g. $l = 9$
$p = 21{\cdot}4$

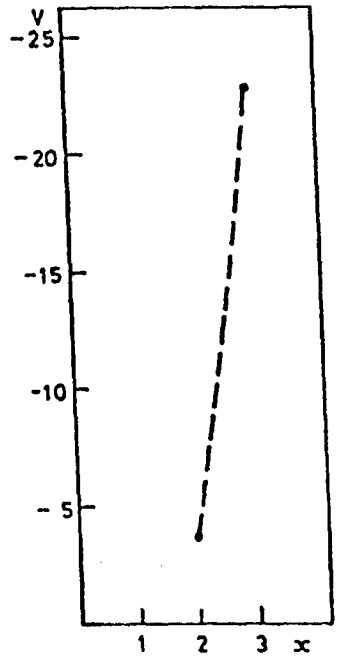

FIGURE 200a. $l = 3$
$p = 28{\cdot}2$

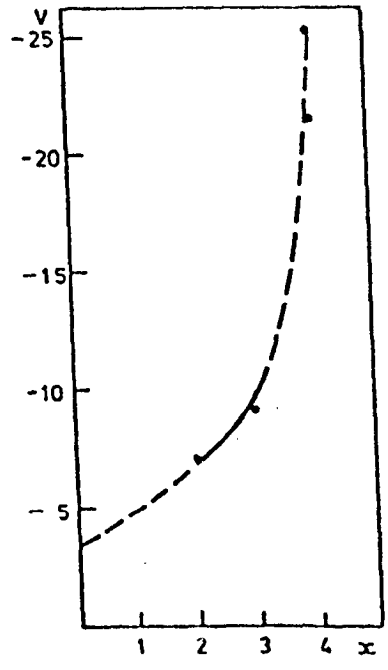

FIGURE 200b. $l = 4$
$p = 28{\cdot}2$

AXIAL DEPENDENCE OF PROBE VOLTAGE (DATA POINTS)

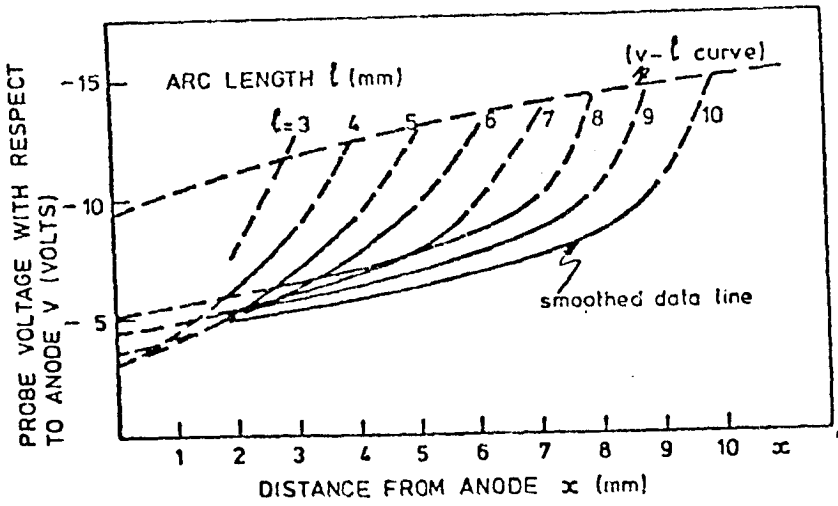

FIGURE 201. PRESSURE (p) = 1 bar (abs)

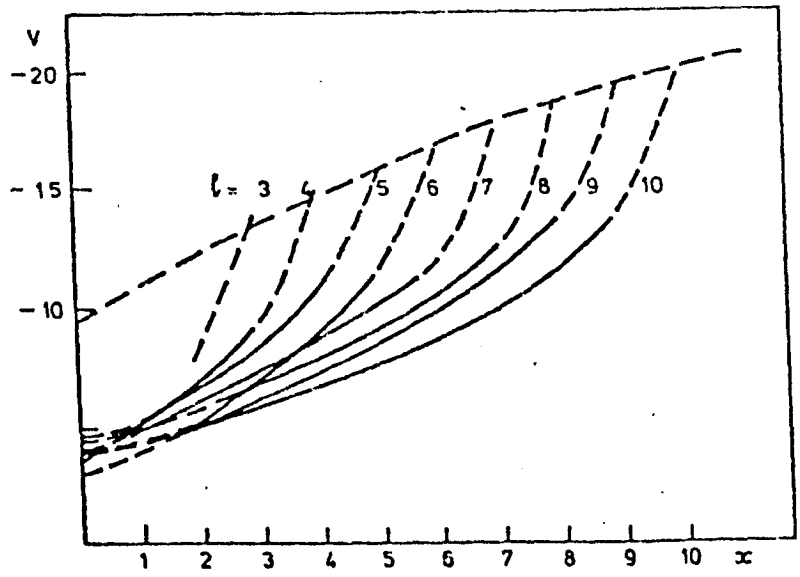

FIGURE 202. p = 4·4

AXIAL DEPENDENCE OF THE MEASURED PROBE VOLTAGE (SMOOTHED DATA LINES)

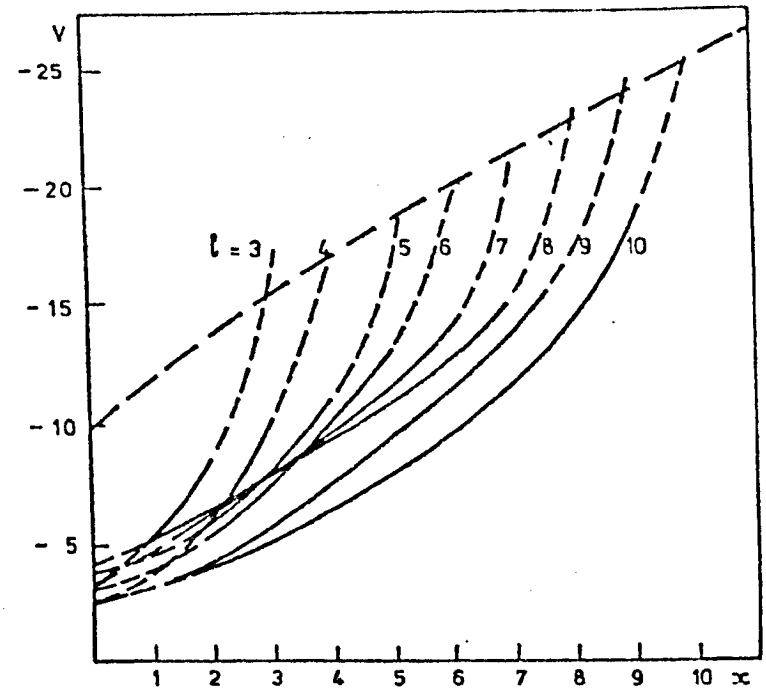

FIGURE 203. p = 7·8

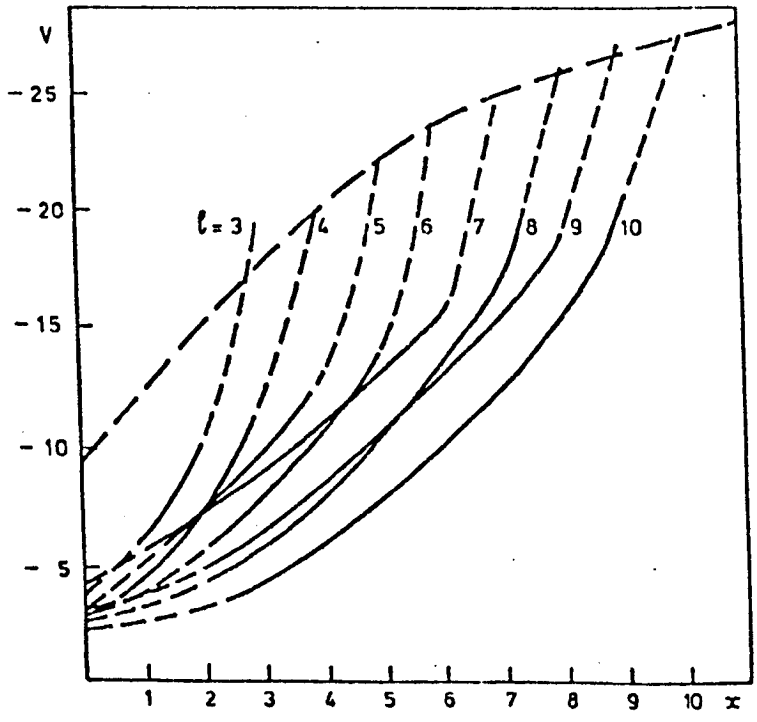

FIGURE 204. p = 14·6

AXIAL DEPENDENCE OF THE MEASURED PROBE VOLTAGE (SMOOTHED DATA LINES)

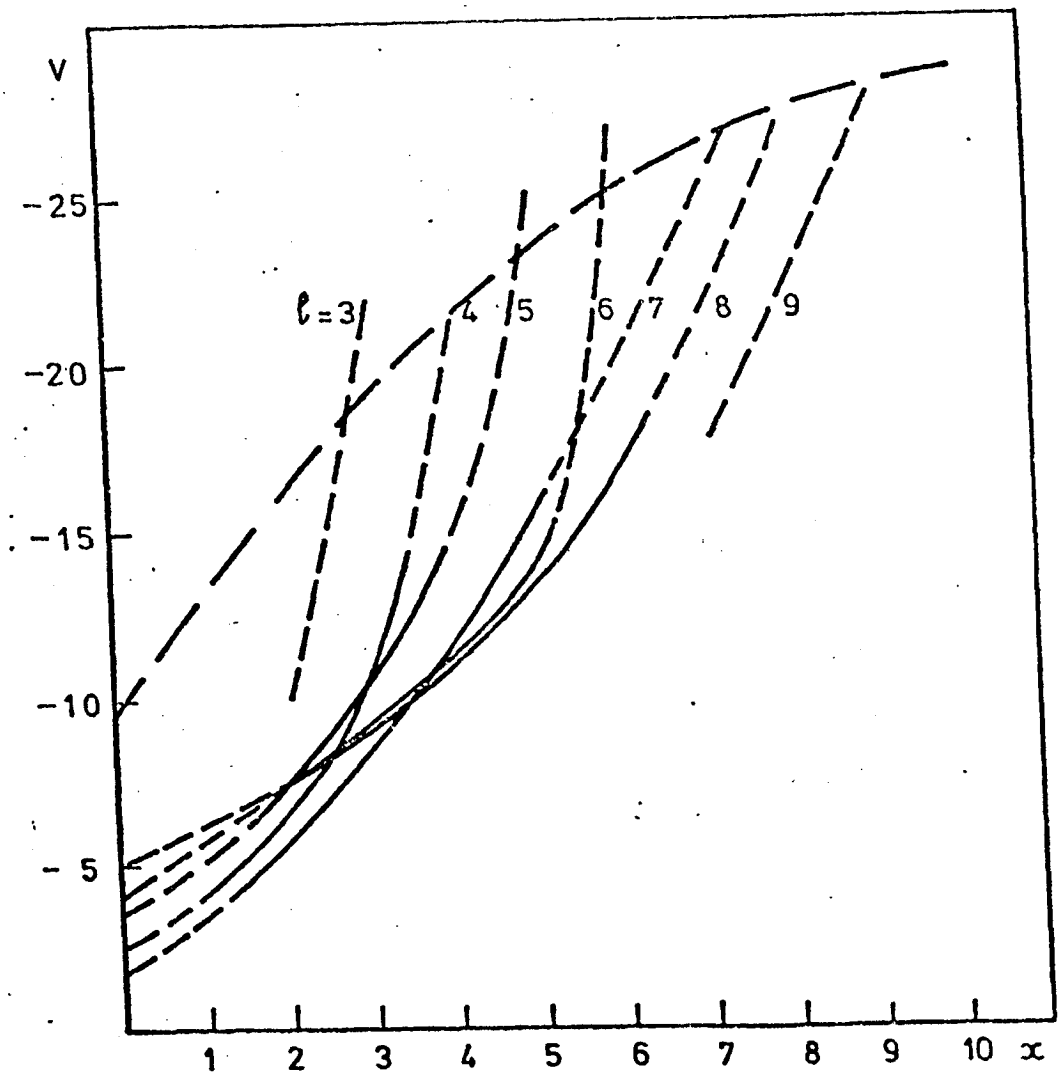

FIGURE 205. p = 21·4

AXIAL DEPENDENCE OF THE MEASURED PROBE VOLTAGE (SMOOTHED DATA LINES)

It may be seen from figures 195 - 200 that the scatter of experimental points increases with pressure. This is largely associated with an increase in column field strength producing larger errors in column potential ($\Delta\phi$) for a given error in probe position (Δx).

$$\text{i.e. } \Delta\phi \simeq E.\Delta x$$
$$\simeq 0.8.\sqrt{p}.\Delta x$$

Taking $\Delta x \simeq \pm 0.5$mm gives $\Delta\phi \simeq \pm 0.4\sqrt{p}$ volts. At the highest pressures investigated errors of order $\pm$ 2V are to be expected. This behaviour has been taken into account.in constructing mean lines through the data.

6.4.1. Voltage Drops at the Electrodes

It may be seen from figures 201 to 205 that the probe potential at the anode is substantially independent of arc length and ambient pressure. Extrapolated probe potentials at the anode are shown in figure 207. This figure shows that there is no correlation with ambient pressure although a weak correlation with arc length exists. The average anode probe potential increases by about 0.5V between 3 and 10mm arc lengths. However, this dependence is only pronounced for atmospheric arcs. Figure 207 also shows that the extrapolated probe potential at the anode is (3 ± 0.5)V for short arcs and (3.3 ± 0.8)V for long arcs. The true anode fall voltage (V_a) is obtained with reference to section 3.6.4 by subtracting between 1 and 2 volts from these figures (1.5 ± 0.5 volt). V_a may now be written as

$$V_a \simeq 1.5 \pm 1.5 \text{ volts}$$

This compares with the corresponding figure 0.9 ± 0.8 volts found calorimetrically.

Both techniques are therefore in agreement. The best agreement is obtained when a 'contact potential' of 2 volts is taken. This indicates the electron number density falls by less than an order of mangitude between the arc and probe surface. However, the main strength of the electrostatic probe findings lies in showing that both the anode and cathode falls are insensitive to pressure and substantially unaffected by arc length. A more direct measure of the influence of arc length on cathodic conditions was obtained by directly measuring the column

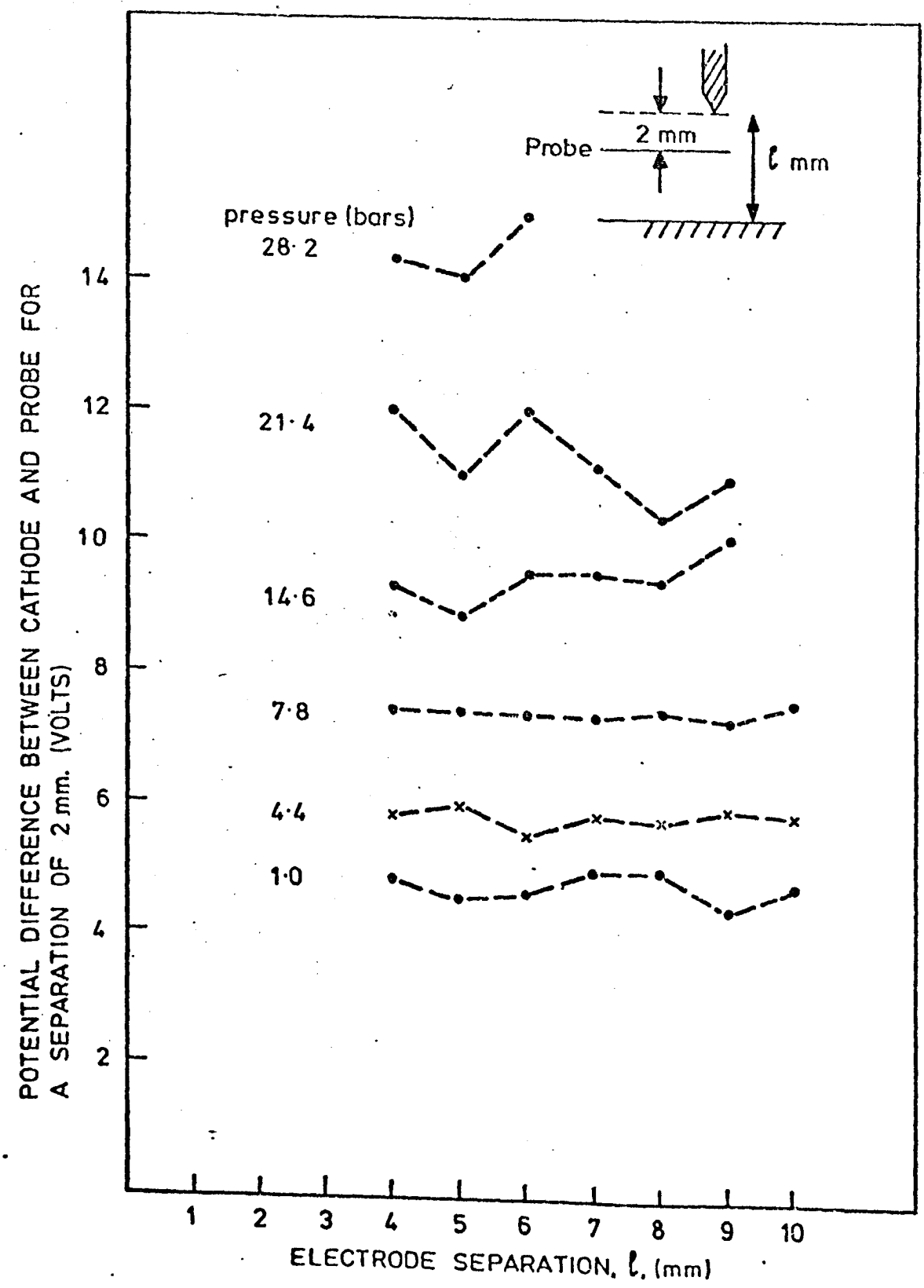

FIGURE 206. EFFECT OF ARC LENGTH ON THE POTENTIAL DIFFERENCE BETWEEN PROBE AND CATHODE FOR A SEPARATION OF 2 mm.

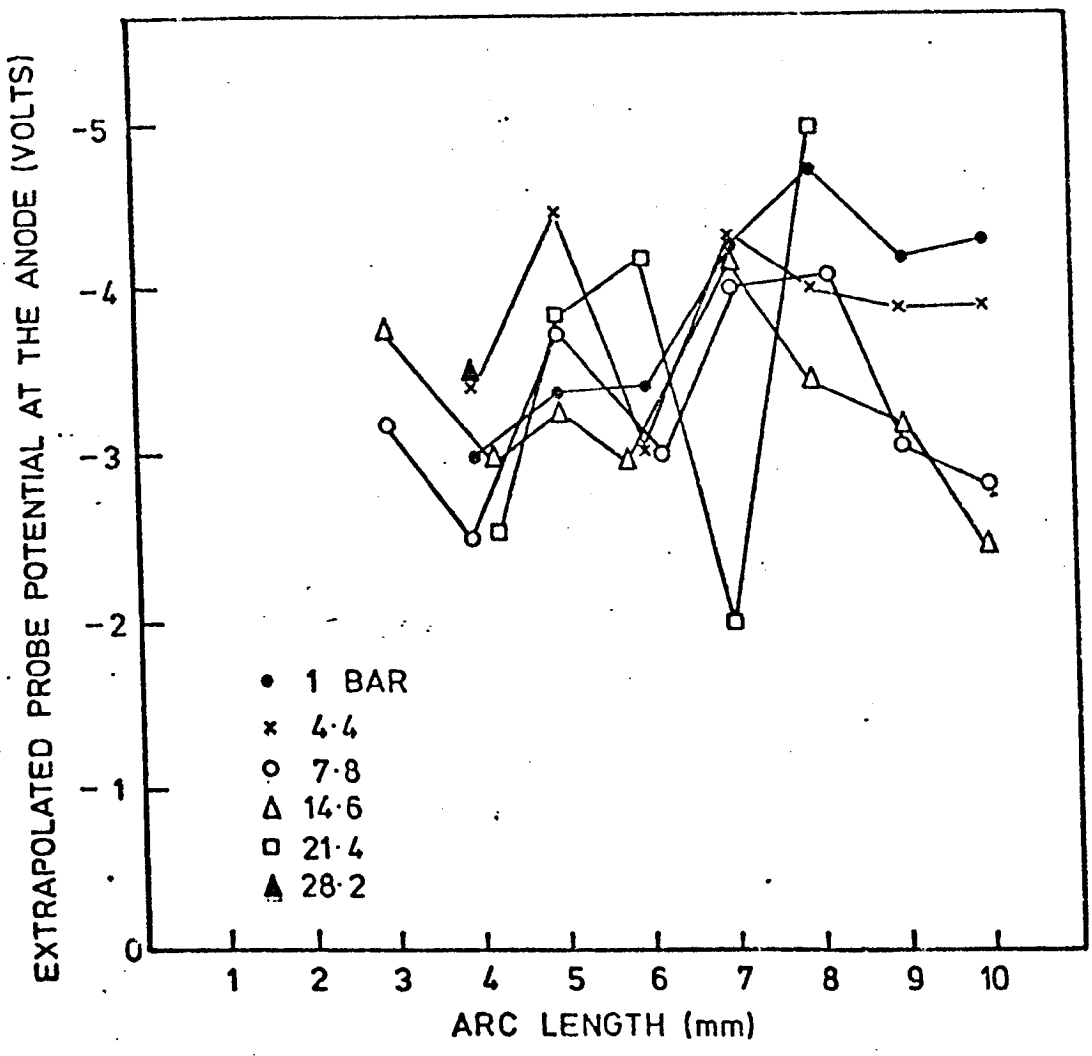

FIGURE 207. EFFECT OF PRESSURE AND ARC LENGTH ON THE PROBE POTENTIAL AT THE ANODE.

Note;
The true anode fall voltage is obtained by adding the contact potential obtained in the text.

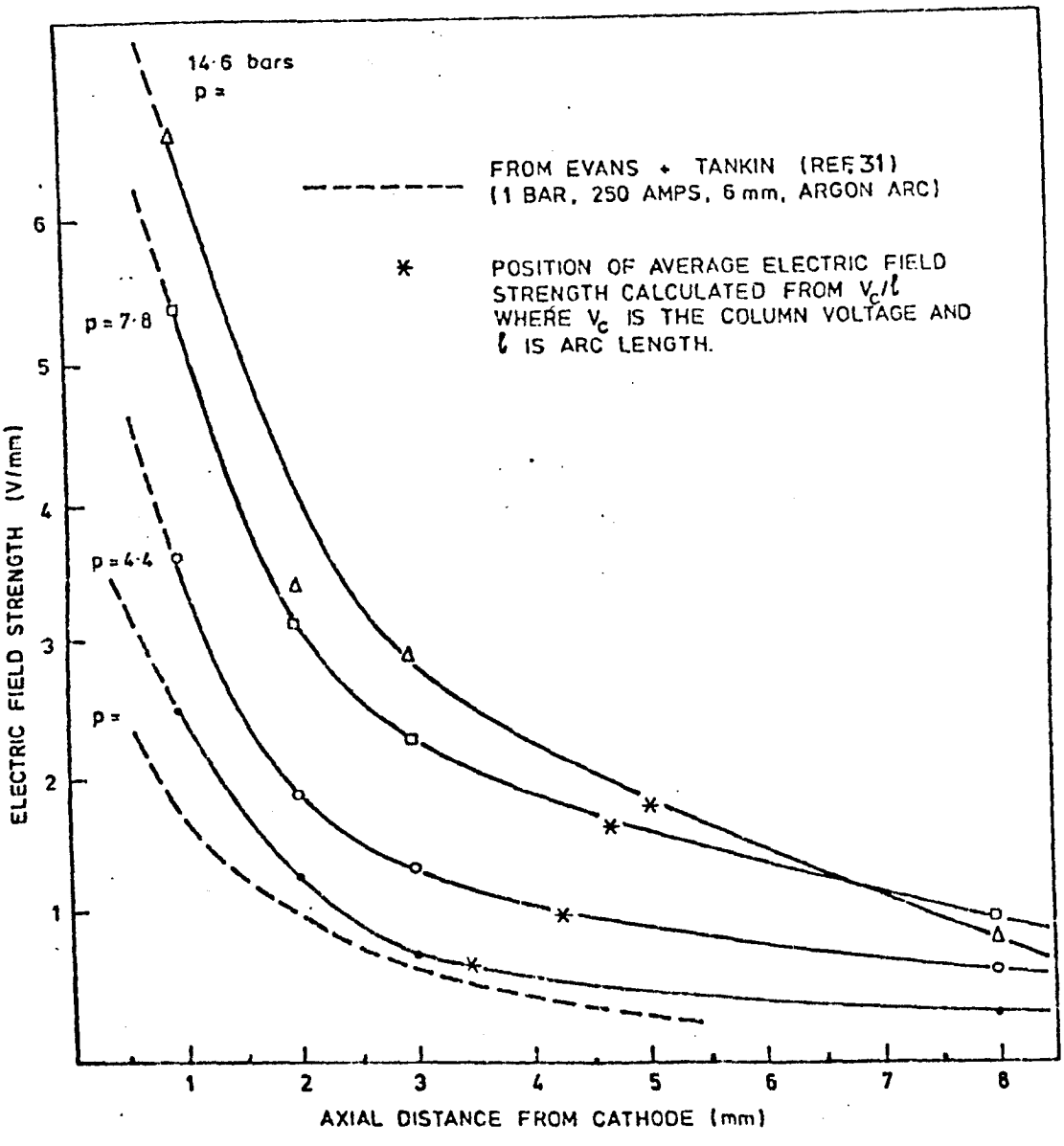

FIGURE 208. AXIAL DEPENDENCE OF ELECTRIC FIELD STRENGTH AT DIFFERENT PRESSURES FOR A 100 AMP, 10 mm, ARGON ARC.

potential with respect to the cathode for different arc lengths (see figure 206). These measurements could be performed very systematically and it can be seen that the potential 2mm's below the cathode is little influenced by arc length at all pressures examined. This implies that conditions near the cathode are independent of those at the anode.

6.4.2. Axial Dependence of Electric Field Strength

Figures 201 to 205 have been used to compute the axial dependence of electric field (E) strength. In previous sections E has been taken as the gradient of the V-ℓ characteristic. Here E is defined by

$$E = - \frac{\partial \phi}{\partial x}$$

Where x is the distance from the cathode and ϕ the local column potential. Values of E obtained in this manner are shown in figure 208 for an arc length of 10mm's. It can be seen that E has a strong axial dependence generally decreasing by about a factor of 6 between cathode and anode. Measurements of the average column field strength $\overline{E}$ have been obtained from

$$\overline{E} = \frac{1}{\ell} \int_0^{\ell} E.dx = \frac{\phi_c}{\ell}$$

Where ϕ_c is the column voltage. This expression suggests two methods for finding $\overline{E}$ i.e. by integrating E and by calculating ϕ_c directly from the column voltage. These estimates are in fair agreement and indicate that the position associated with the average column strength occurs near the cathode and moves towards the anode with increasing pressures (see figure 208). The agreement between these estimates also serves as an indication of the accuracy in obtaining the E curves of figure 208.

6.5. Radiation Measurements

Arc column radiation measurements have been made in the manner described in section 3.6.5. This investigation examined the influence of arc current, arc length, ambient pressure and gas composition on arc column radiation. These results are shown graphically in figures 209 to 217. Results show that radiation is an increasing function of arc length, arc current and ambient pressure. The strongest dependence is on arc

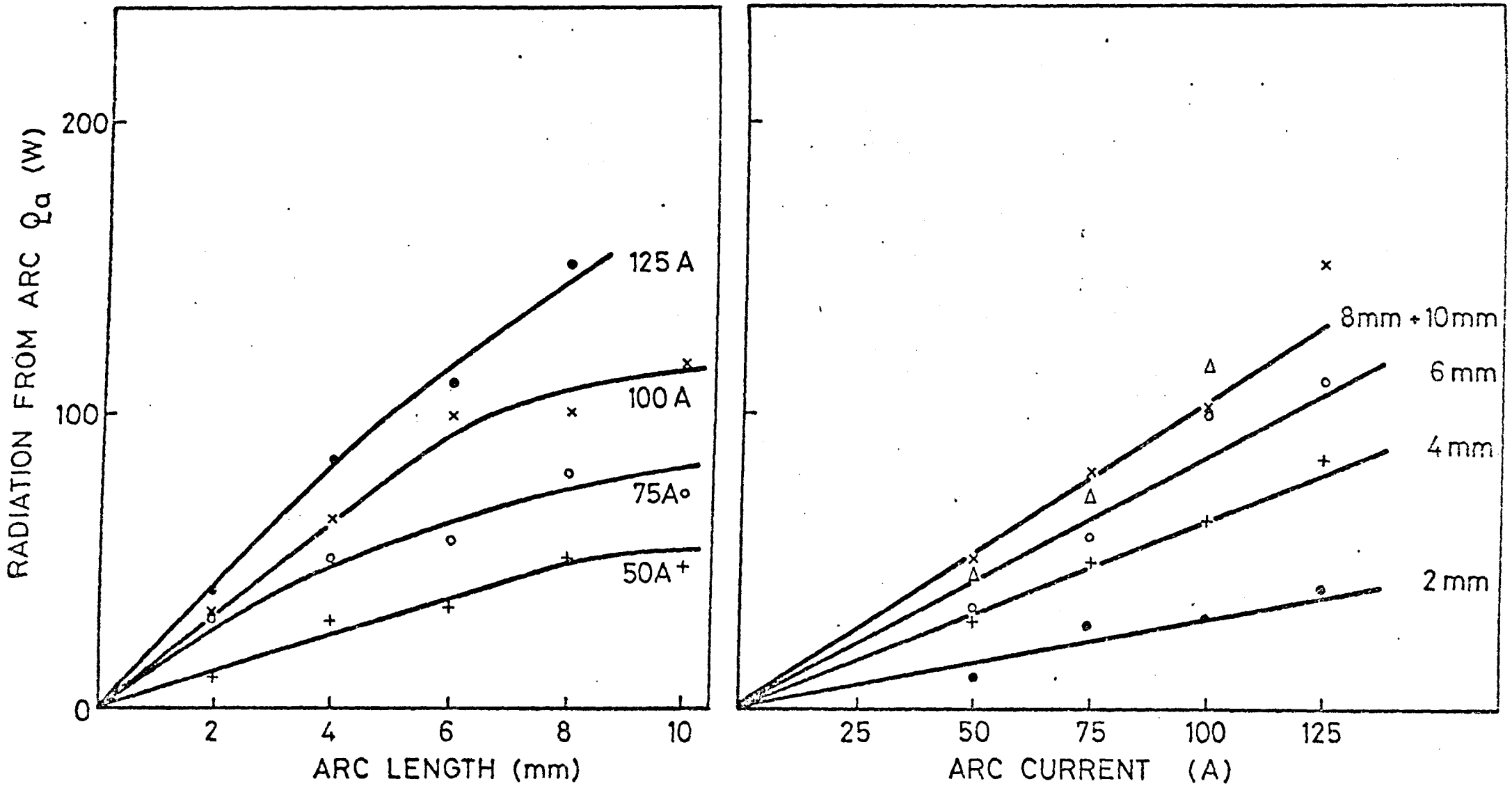

FIGURE 209. RADIATION FROM THE ARC (1 BAR, ARGON)
(OBTAINED BY CORRECTING THE TOTAL RADIATION MEASUREMENTS)

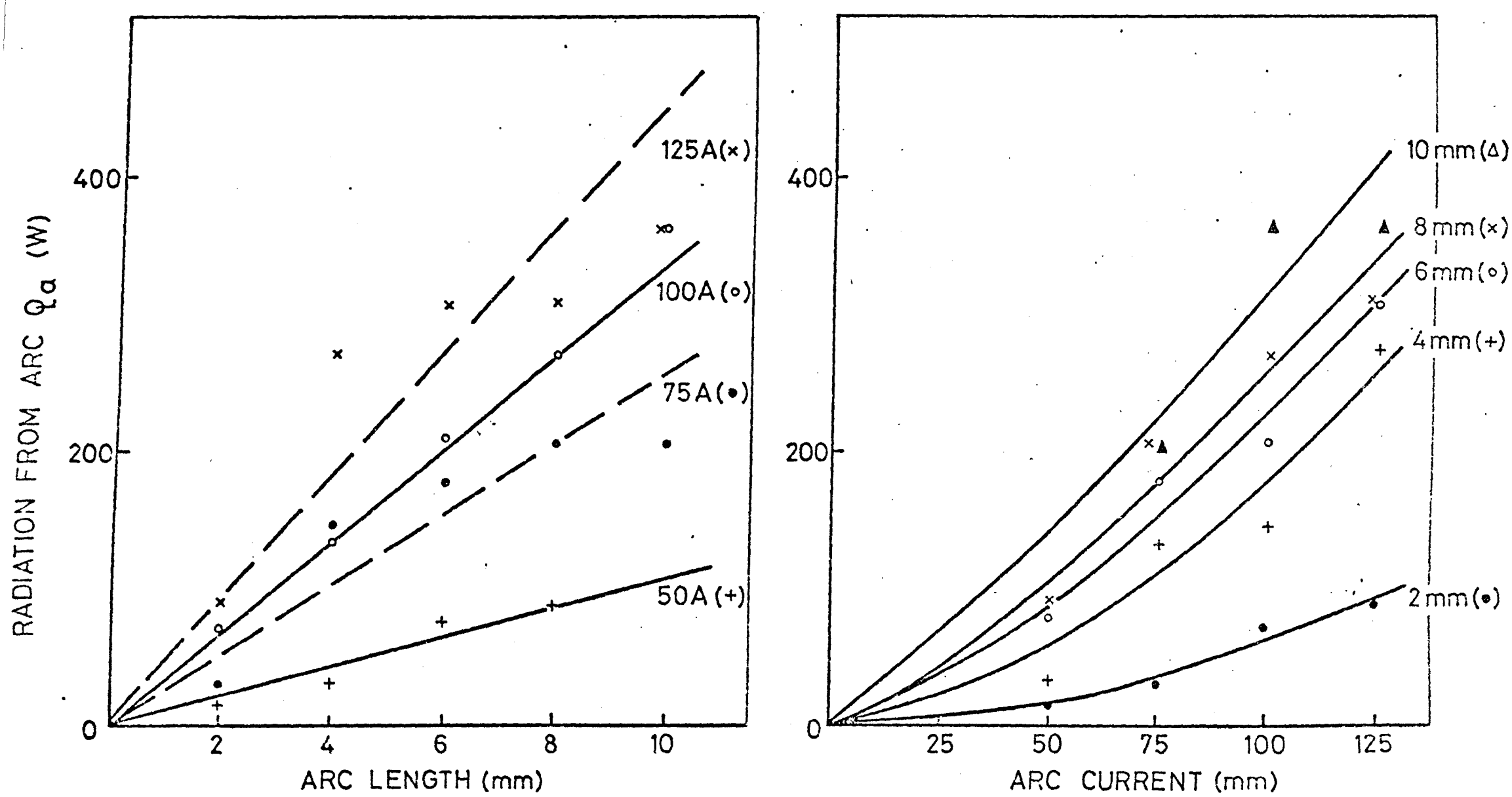

FIGURE 210 RADIATION FROM THE ARC (17·8 BARS, ARGON)
(OBTAINED BY CORRECTING THE TOTAL RADIATION MEASUREMENTS)

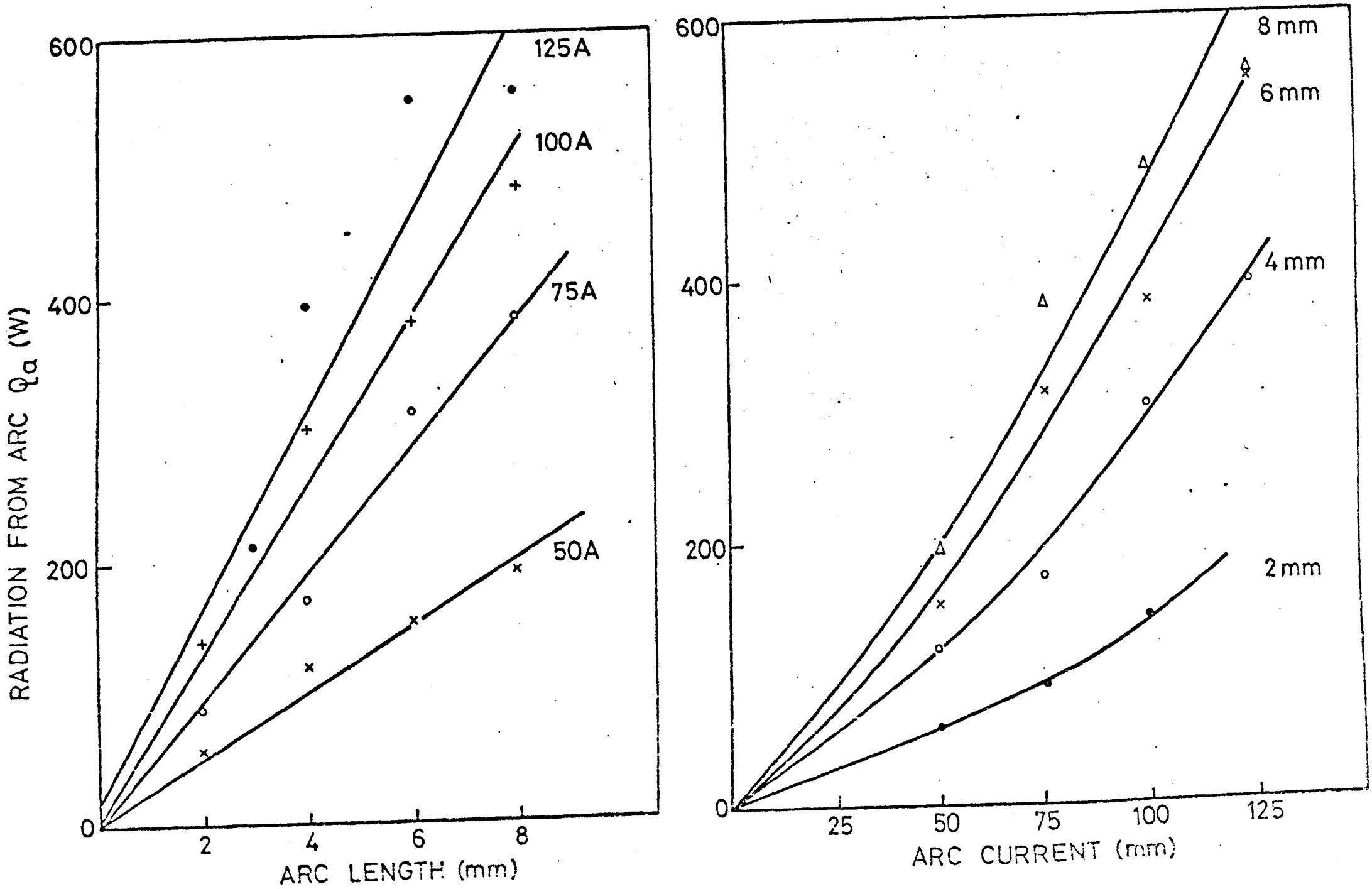

RADIATION FROM THE ARC (CATHODE) ARGON

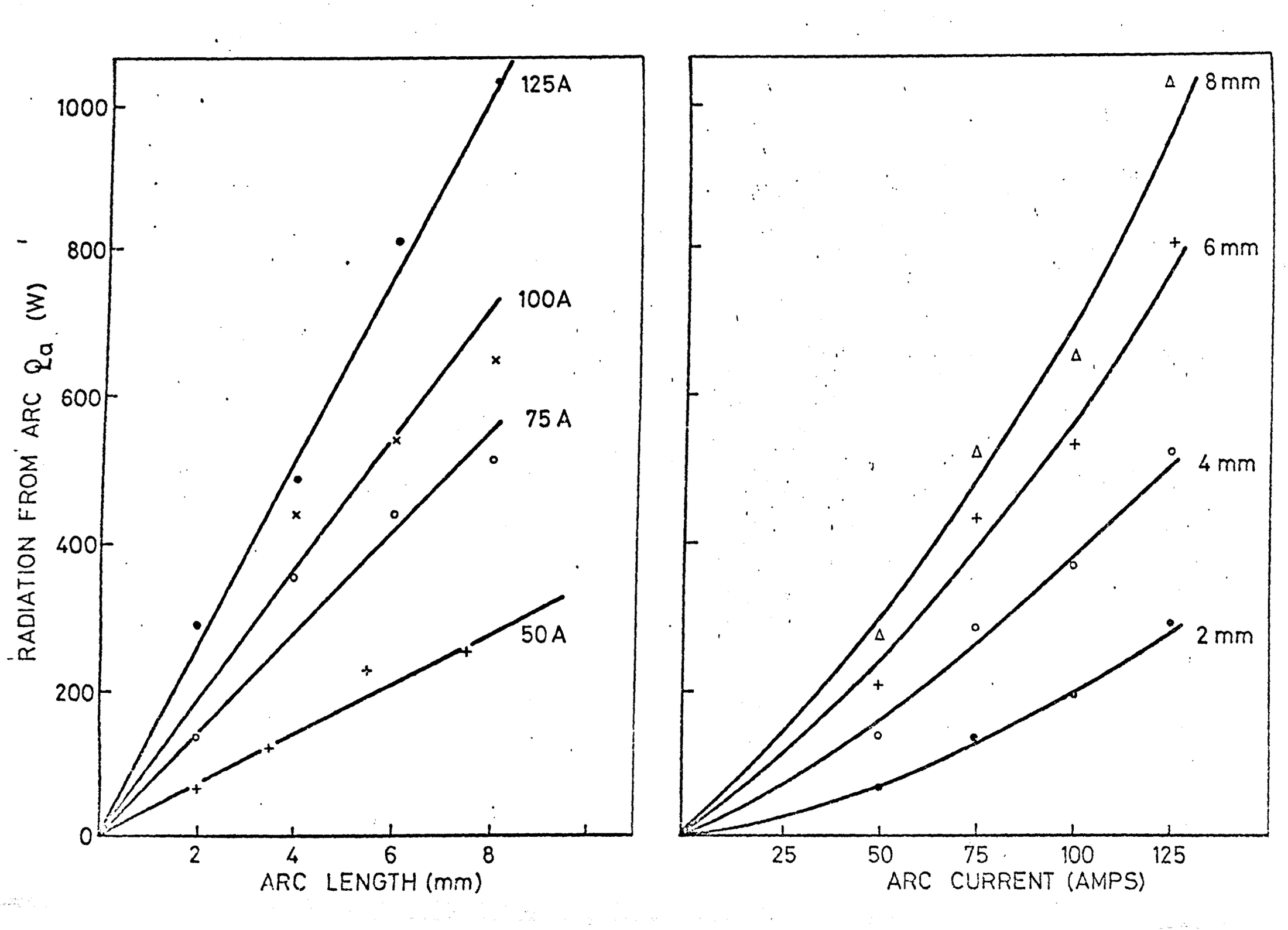
RADIATION FROM ARC Q_a (W)
1000
800
600
400
200
0
2
4
6
8
ARC LENGTH (mm)
125A
100A
75 A
50 A
8 mm
6 mm
4 mm
2 mm
25
50
75
100
125
ARC CURRENT (AMPS)

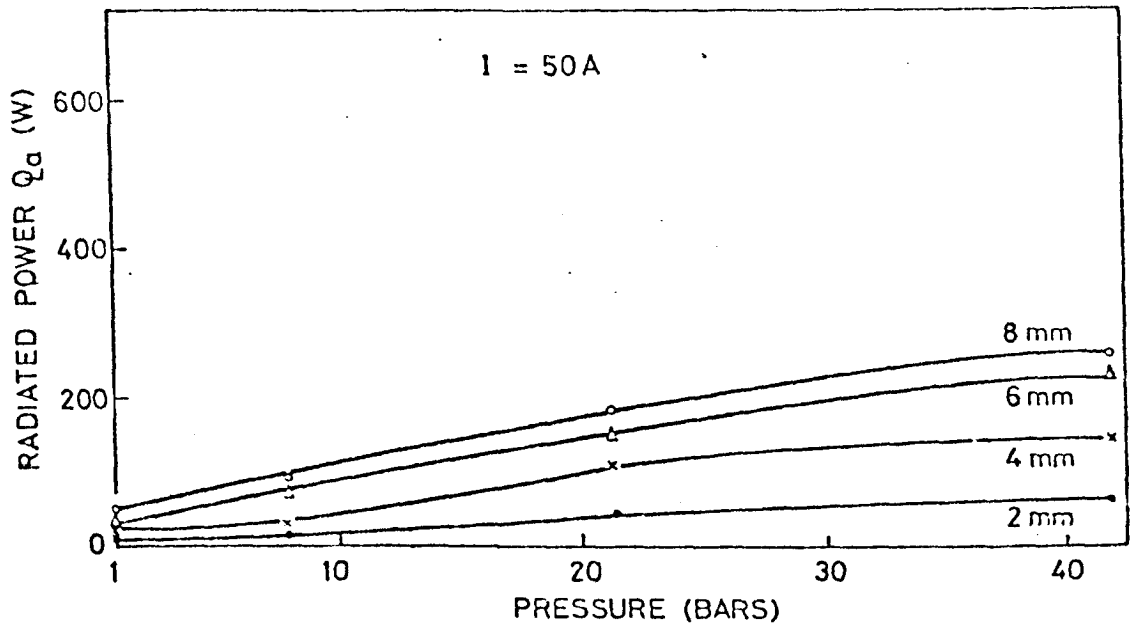

FIG. 213.

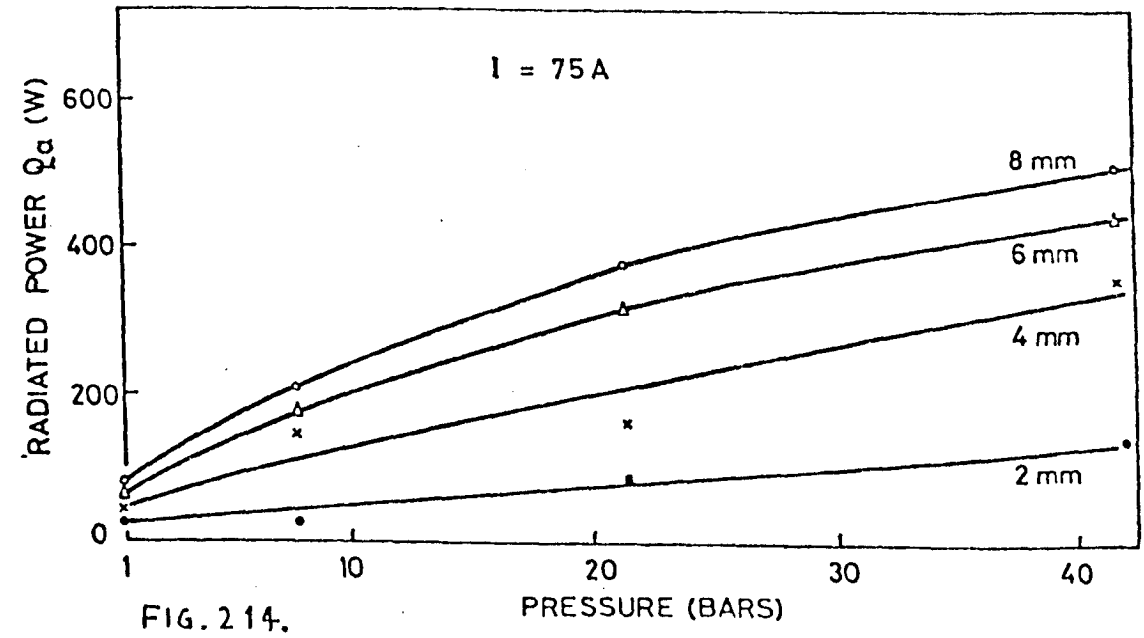

FIG. 214.

INFLUENCE OF PRESSURE AND CURRENT ON POWER RADIATED FROM ARC COLUMN. (FIGS. 213 to 216)

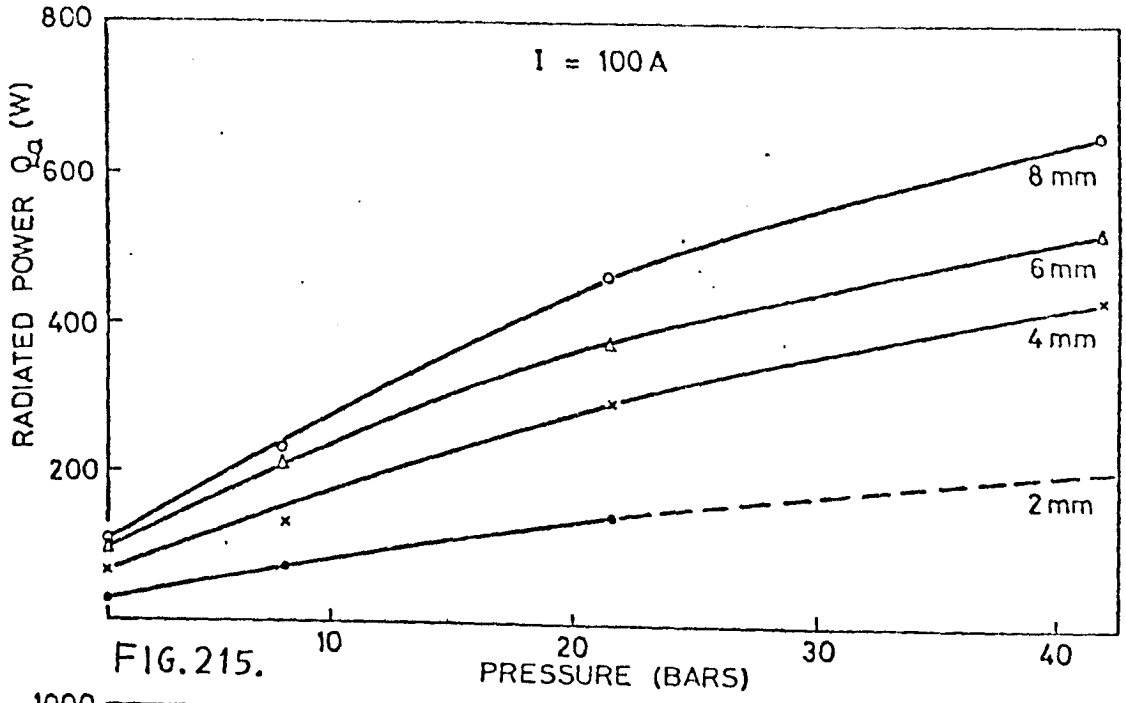

FIG. 215.

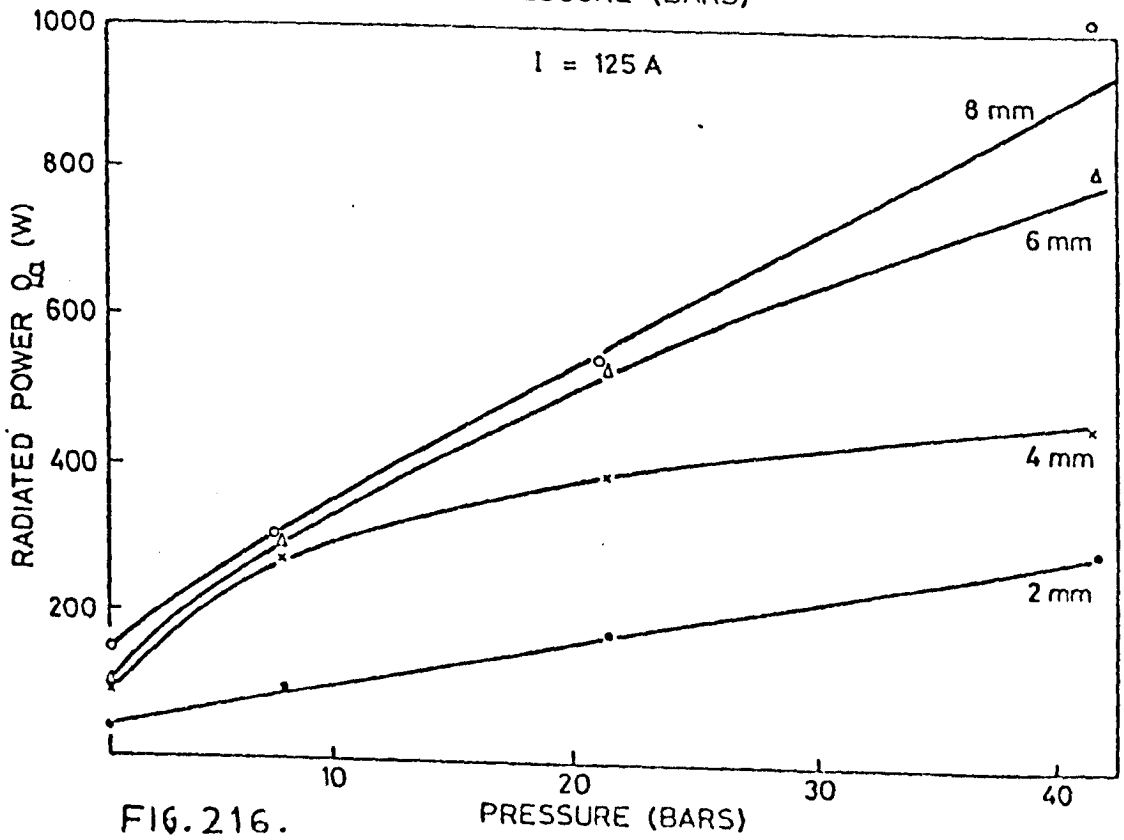

FIG. 216.

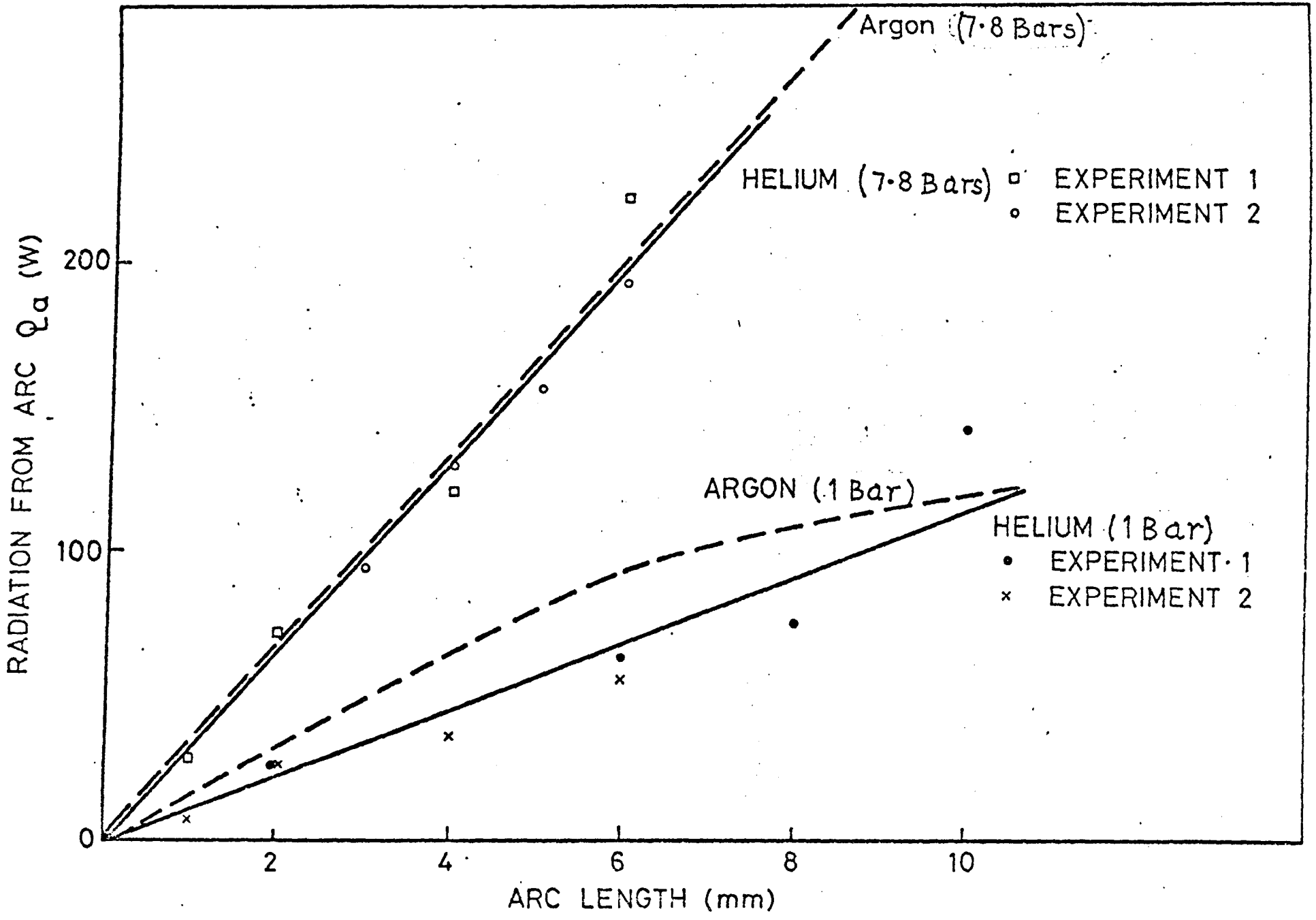

FIGURE 217. RADIATION FROM THE ARC (100 AMP, HELIUM ARC)

current. At one bar the current dependence is of a linear form for all arc lengths. For higher pressures a stronger dependence is noticed. At one bar the arc length dependence is of a linear form for 125 Amp arcs. For lower currents and for arc lengths greater than 6mm a weaker dependence is observed. Above one bar, substantially linear relationships are observed for all arc lengths and currents. In general it can therefore be seen that radiation is linearly dependent on arc length for short arcs ($\ell \leq 6$mm). A strong linear dependence on arc length was also obtained for helium arcs (figure 217). The pressure dependence of column radiation is shown for each current and arc length examined in figures 213 to 216.

On physical grounds it is considered important to understand the relationship between total power radiated from the column and total power appearing in the column ($I.V_c$). At a less physically meaningful level it is also important to relate the radiant energy to the total process power ($I.V$). Both of these dependencies have been evaluated and expressed in tabular form (see tables 41,42 and 43). It can be seen that the total radiant power leaving the column is only a small percentage of the process power. For a typical atmospheric welding arc (100 Amps, 3mm) a figure of 5% seems suitable. This figure can be seen to increase with arc length and ambient pressure. For a given arc length and pressure the current has no noticeable influence on 'radiation efficiency' between 75 and 125 Amps although significantly lower values are obtained for the 50 Amp arc. The radiative behaviour of high current ($I \geq 75A$) and low current arcs ($50A \geq I$) is significantly different. In view of the small effect of arc current compared to that of arc length average percentages have been formed at each arc length over the current range employed (see table 41). These figures show a clear trend of radiation efficiency increasing with arc length over the pressure range investigated. At one bar the average percentage varies from 3.4% at 2mm to 8.1% at 8mm. Corresponding values at 41.2 bars are 10.2% to 17.5%. Helium arcs give considerably lower radiant efficiencies, i.e. at 1 bar the percentage is 2% at 2mm and 3.1% at 8mm.

A physically more realistic measurement is the efficiency with which column power appears as radiation. Values given in table 43 show that

this efficiency is remarkably insensitive to arc current, arc length and ambient pressure. The total change from a 2mm, 50 Amp atmospheric arc to a 8mm, 125 Amp, 41.5 atmosphere arc is little more than a factor of two (i.e. 11.9% to 26.2%). If only high current arcs ($I \gtrsim 75A$) are included, the corresponding comparison is 19% to 26.2%. An examination of the data shows again that the low current arc (50 Amps) has a significantly lower radiative efficiency than high current arcs (by more than 5%). It is therefore reasonable to treat these as separate arc forms. Averages over arc length and current (see table 43) show that generally no significant effect of arc length or current is experienced by this radiation efficiency. There is however, a tendency to increase over the first 21 bars (from an average of 18.3 at 1 bar to 26.3 at 21 bars). The above considerations indicate that

$$Q_a = f(p).I.V_c$$

where for $I \geq 75$ Amps $f(p)$ has the values shown below:

P (bars)	1	7.8	21	41.5
f(p)	0.18	0.20	0.26	0.25

V_c has been determined as a function of arc length and pressure for high current argon arcs (see section 4.2). It was found that

$$V_c \simeq E_1.\ell.\sqrt{p} \qquad \text{where } E_1 \simeq 0.75 \text{ V/mm}$$

Therefore

$$Q_a = f(p).E_1.I.\ell.\sqrt{p} \tag{132}$$

This is in broad agreement with the qualitative expression inferred from the graphical form of Q_a. However, the current dependence is weaker than might be expected. This is explained by the fact that low current arcs have been neglected. Equation 132 shows that radiation increases slightly more strongly than $P^{0.5}$ and that broadly speaking 20% of the column power appears as radiation. This is in excellent agreement with the analysis given in section 5.3 (see equation 130). For helium arcs an expression similar in form to equation 132 may be applied (see table 44). The function $f(p)$ is then much smaller having a value (0.07) of about one third that in argon.

7. Discussion of Arc Structure

7. DISCUSSION OF ARC STRUCTURE

7.1. Introduction

The investigation of arc characteristics indicated a number of regions where further considerations of a structural nature could be of value. These mainly concerned arc stability and energy exchanges. In this section results from these investigations are discussed and compared where possible with comparable values previously found by other workers. Emphasis is placed on discussing these results with particular reference to explaining observed arc 'characteristics'. Theoretical considerations of structure are given in section 8. Further to this a general discussion of both characteristics and structure is included in section 9. The approach adopted here is to discuss separately each aspect of arc structure investigated.

7.2. Anode Heating

Anode heating experiments have implications for weld bead formation and can give data concerning arc column structure and behaviour in the fall regions. Experiments performed here systematically explored the influences of arc length, current and ambient pressure for a range of anode and arc atmosphere combinations (Argon and helium arcs on steel and copper anodes). It was generally found possible to express the heat input (Q) as

$$Q = Q_o + Q_c$$

Where Q_o is the extrapolated zero arc length heat input and Q_c the component due to arc column heat. A detailed analysis of the data revealed that factors such as cathodic heating and the fraction of column power contributing to anodic heating, could also be determined. These points have been extensively reported in section 6.1 and so only the most notable results are discussed here.

The zero arc length heat input is due to electronic effects and is directly proportional to arc current and independent of ambient pressure. However, anode and shielding gas compositions exert a strong influence (see table 45).

$Ar-Cu$	$Ar-Fe$	$He-Cu$	$He-Fe$
8 ± 1	6.4	13.0	7.3 ± 0.7

Table 45 Average Values of Q_o/I for Different Anode and Gas Compositions

This behaviour has been explained in the text by considering the electronic energy balance:

$$Q_o/I = \phi + V_a + V_T$$

In helium arcs on copper anodes V_T and ϕ are dominant. However, V_T is relatively small when significant quantities of metal vapour are generated at the anode as the local arc temperature is then lowered. Calculations of V_T and ϕ also yield values of V_a. These are shown below

$Ar-Cu$	$Ar-Fe$	$He-Cu$	$He-Fe$
1.4 ± 1.2	0.9 ± 0.8	4.0 ± 0.3	0.1 ± 2.8

Table 46 Anode Fall Voltage (V_a)

Again it should be noted that these values are substantially independent of pressure, current and arc length. The independence of pressure and arc length is also borne out by electrostatic probe measurements of V_a (see section 6.4). Probe measurements of V_a (A_r-F_e) give a value of 1.3 ± 0.8 for a plasma-probe contact potential of 2 volts. This is in good agreement with the calorimetric results shown in table 46. It is notable that V_a appears to increase as the effective ionization potential of plasma near the anode increases. This is in keeping with a view that regards V_a as necessary for charge generation in the anode sheath. The influence of anodic composition on arc behaviour has previously been noted where arc rooting was observed to be affected. Cathode fall voltages can likewise be estimated and are given below:

$Ar-Cu$	$Ar-Fe$	$He-Cu$	$He-Fe$
8.1 ± 0.5	8.1 ± 1.8	11.0 ± 0.2	9.3 ± 3.2

Table 47 Cathode Fall Voltage (V_c)

The higher values observed for helium may be explained by the higher ionization potential requiring more power for charge generation. This simple view is complicated by the probable appearance of tungsten vapour in the column. It can be seen from table 47 that anodic composition has very little influence on behaviour at the cathode.

The results for V_c and V_a confirm that not only is the sum of the fall voltages independent of pressure but so too are the components. Arc heating of the electrode regions is therefore expected to be little influenced by pressure at very short arc lengths. The observed pressure dependence of weld bead melting is therefore due to an increase in gas heating from the column i.e. Q_c. Results indicate that Q_c is roughly proportional to $I.V_c$ where the constant of proportionality is interpreted as the efficiency η_c of column transfer to the plate. η_c is found to be weakly dependent on current and arc length but strongly influenced by pressure. Most of the pressure dependence is exhibited over the first 10-20 bars, e.g. η_c and has a similar value at 42 bars. For argon arcs on steel η_c falls from about 60% at 1 bar to 30% at 10 bars (see figure 179). It is also found that higher column transfer efficiencies are observed for argon arcs on copper than on steel. A detailed understanding of this behaviour requires an investigation of not only energy generation in the column but also of heat transfer mechanisms at the anode. A full understanding of this behaviour is not feasible at the present time due to uncertainties discussed in section 2.4.1.4. However, a number of comments can be made on the basis of known column behaviour (see section 5).

The fall of η_c with pressure may be partly explained in terms of the increasing importance of arc column radiation (see sections 5 and 6.5). This may account for up to 25% of the power developed in the column. Radiative transfer is an inefficient heat transfer mechanism as about half this power is lost by upward radiation away from the plate. A fall in η_c is therefore expected. It is also notable that η_c decreases only slowly with arc length. In some situations an initial increase is even observed (figure 176). The last observation may be associated with the developmental stages of a plasma jet at short arc lengths as described in section 8.

Temperature gradients near the pool surface are expected to be lower for steel pools (due to vapourization) than on cooled copper. This should significantly reduce the effectiveness of the convective contribution brought to the anode surface by the jet and subsequently conducted into the work. In this manner vapourization is expected to lower column heat transfer efficiencies and be the cause of significantly lower values on steel than on copper. A detailed account of this mechanism is thought to be presently unobtainable due to the short comings of conventional heat transfer techniques which have already received attention. These short comings are amplified by the present results.

Despite this situation it is of some interest to understand the influence of arc current on gas heating. Arc current has been reported to have only a small effect on gas thermal properties (see section 2) and so a number of simple relationships may be deduced (see below). The conventional heat transfer expression (see equation 29 and 30) predicts that the convective contribution to anode heating increases in proportion to $A.R_e^{\frac{1}{2}}$ where R_e is the plasma jet Reynolds number and A is the impingement area.

Theoretical considerations show that $R_e \alpha I$ (see section 5.3) and experiments indicate (section 6.2) that the cross-sectional area of the jet is roughly such that current density is independent of current i.e. $A \alpha I$. In view of the weak influence of current on thermodynamic aspects of behaviour a convective contribution proportional to $I^{3/2}$ is therefore expected. This is in fair agreement with the observed behaviour (see figure 177).

The total process efficiency (η) has been discussed in some detail in section 6.1. The observed fall in this quantity with pressure is clearly related to an increase in column power and the decrease in column transfer efficiency i.e.

$$\eta = \frac{(V_a + V_T + \phi) + \eta_c . V_c}{V_o + V_c} \qquad (133)$$

(V_c is used here to represent the column component of arc voltage).

Where only η_c and V_c are sensitive to pressure such that V_c increases and η_c decreases. Process efficiencies obtained on copper anodes are considerably higher than those on steel. The only comparable results previously obtained are by Matsunawa and Nishiguchi (ref.10). These workers also found a significant difference between heat input measurements on copper and steel anodes for otherwise similar conditions. However, the maximum pressure investigated was 7 bars. The difference in behaviour between Cu and F_e is associated with a number of factors appearing in equation 133. Electronic contributions are higher on copper due to larger anode fall voltages and higher electron temperatures. Also, much more of the column power contributes to heating. i.e. η_c is larger as already discussed in this section. It is also clear from results presented here that copper anodes give a poor representation of heat transfer in welding arcs at high pressures although no great discrepancy is observed under normal atmospheric conditions. This is largely due to the small amount of power appearing in such arc columns i.e. 70 - 80 W per mm for a 100 amp agron arc. At 40 bars the corresponding figure is 400-500 W per mm. Indeed at high pressures electronic heating is no longer the dominant mechanism as Q often exceeds $2Q_o$ on copper anodes. Experiments with constricted TIG arcs on copper anodes show similar trends to those observed with the corresponding TIG arcs. In both cases efficiency generally decreases at low pressures with a possible increase near 15 bars. Despite these similarities the mechanisms of energy transfer are quite different.

Perhaps the most important heat transfer factor from a purely operational view point is process efficiency. Results show that heat input cannot be estimated from the usual expression combining arc power and welding speed unless the pressure dependence of process efficiency is taken into account. A suitable numerical factor may be obtained by substituting into equation 133. For argon arcs on steel it has been found that

$$V_a + V_T + \phi = 6.4V$$

$$\eta_c \simeq \begin{cases} 0.5 & P = 1 \text{ bar} \\ 0.3 & P > 1 \text{ bar} \end{cases}$$

$$V_o \simeq 8.5V$$

$$V_c \simeq 0.75.\ell.\sqrt{P} \quad \text{for } \ell \text{ in mm's}$$

For a typical short (∿2mm) welding arc equation 133 then gives

$$\text{and} \quad \eta = \begin{cases} \dfrac{64 + 4.5\sqrt{P}}{85 + 15\sqrt{P}} & \text{for } P > 1 \text{ bar} \\ 0.71 \text{ for } P = 1 \text{ bar} \end{cases}$$

The behaviour predicted by this expression is in reasonable agreement with estimates based on weld HAZ dimensions (see figure 134) i.e. η (1 bar) ∿ 70%, η (10 bar) ∿ 60%, η (40 bar) ∿ 50%. Calorimetric measurements of η are generally in fair agreement with HAZ estimates for currents below about 100 Amps. Above this current HAZ measurements over estimate process efficiency. This has been associated with departures from semi-infinite heat flow theory (see section 5.4) in the weldment at high currents.

Calorimetric heat transfer efficiencies for helium arcs on steel anodes show similar trends as those found for argon arcs. The agreement with corresponding HAZ estimates (see figure 159) is poor. This is tentatively attributed to the conduction limited nature of pools in calorimetric experiments and the wide scatter in results obtained from weld bead studies. In conduction limited pools vapourization is expected to play a larger role and hence influence the electronic thermal contribution.

Calorimetric measurements have shown that magnetic stirring has little effect on process efficiency or weldment heat input. This result confirms that inferred from weld bead HAZ dimenions. The substantial decrease in pool fusion area is therefore attributed to heat transfer mechanisms within the pool and not to a reduction in process heat input.

Finally, results also enabled cathodic heating to be estimated. This is calculated from the difference between extrapolated zero arc length process power and anodic heat input. No great accuracy is claimed for this estimate as a number of error terms appear in the final value. However, with a few exceptions it is found that this varies over a wide range of pressures as 1.5I for argon arcs. Increased cathodic melting at high pressures must therefore be primarily associated with a higher density of heating and not specifically with more heat transfer. Higher values are found for helium and for argon arcs in a magnetic field. The

higher helium values are associated with enhanced conduction (high thermal conductivity), higher cathode fall voltages and larger recombination energies (higher ionization potentials). The behaviour in a magnetic field is associated principly with strong plasma swirl at the cathode thereby increasing conduction to the electrode. However, this may be due to an error in locating the true zero arc length position due to weld pool lifting as a result of magnetic stirring. Such a possible source of error is suggested by the unusually high zero arc length voltages associated with those measurements.

7.3. Distribution of Current at the Anode

In this section the distribution of current at the anode (copper) of an argon TIG arc is discussed. This has direct consequences for the distribution of electronic heating and hence supplements data discussed in section 7.2 on the total heat transferred to the anode. Unfortunately, it was considered unfeasible to investigate the practical welding situation where gross melting occurs. Experiments were therefore confined to cooled copper anodes. A further restriction was placed on the technique employed by the requirement of reasonably stable arcing conditions. This limited the investigation to pressures below about 14 bars.

The distribution of current was found to be of an approximately Gaussian nature with a peak current density between 4 to 5 times the average current density. At one bar axial current densities of about 10 A/mm^2 were observed. These compare favourably with those reported in section 2. The corresponding value at 14 bars was about 36 A/mm^2. However, this was strongly dependent on flow conditions. The intensity of anode heating may be obtained by combining this data with values of anode fall voltage, work function and thermal energy. For argon arcs on copper the equivalent voltage is found to be $8 \pm 1V$ and substantially independent of pressure. The corresponding intensities of arc electronic heating are therefore 80 ± 10 W/mm^2 and 288 ± 36 W/mm^2 respectively. i.e. an increase by about a factor of four between 1 and 14 bars. These figures refer to a 100 Amp, 3.2mm arc. Similar values are expected (see table 38) for 150 Amp arcs. However, a significant decrease occurs when the arc length

is increased to 4.8mm. Measurements of arc radius at the anode indicate that the contraction obeys an $P^{-0.17}$ law at low flows and $P^{-0.25}$ for high shielding gas flows. The mean current density is then expected to increase with pressure in a manner described by $p^{0.34}$ to $p^{0.50}$. Similar behaviour is also expected for the peak (i.e. $J_o \propto \bar{J}$). This behaviour is in reasonable agreement with that reported earlier. Theoretical considerations given in section 5.3 indicated that this is precisely the behaviour to be expected. These considerations also explain the observed dependence on shielding gas flow where for purely conductive arcs, a decrease in accordance with $K^{-\frac{1}{2}}$ is expected (here K is the effective thermal conductivity of the shield which increases with turbulence in the shield).

Many of the experiments reported here have shown that significant differences exist between behaviour on copper anodes and on steel anodes. It is therefore difficult to extrapolate these current densities to the practical situation. However, vapourization should increase due to an increase in J_o with pressure. This is likely to give rise to further increases in J_o. Axial current densities obtained on copper anodes are therefore lower bound values for practical situations. The argument given above may be applied in a converse manner to explain the sensitivity to anode composition at high pressures. It is then argued that the increased current density generates more metallic vapour and thereby causes significant differences between behaviour on copper anodes and steel anodes. Significant differences may even exist between behaviour on stationary and moving vapourizing anodes.

The contraction of the heat source also has implications for the application of conductive heat transfer theory which assumes a point source.. It has been noted that weld bead and HAZ structure is of a more hemispherical shape at high pressures. This is thought to be due to the constricted nature of the anode root. Conduction theory is then likely to be a better representation of weldment heating (as observed). However, it may also be argued that the constricted root gives rise to stronger weld pool convection and hence a change in pool geometry. This is almost undoubtedly true for helium arcs where aspect ratios as low as 0.9 have been observed. For argon arcs these effects are difficult to separate

but it is worth noting that purely conductive theory gives a good representation of pool shape at high pressures. This indicates that convective effects are of secondary importance in heat transfer.

Electrical measurements of arc column diameter may be coupled to other observations to obtain an estimate of the pressure dependence of arc column temperature i.e. Using Ohms law gives

$$\sigma = \bar{J}/E \quad \text{(see equation 6)}$$

$$\text{where } \sigma = \sigma(T_\sigma, P)$$

$$\text{and } \bar{J} = I/\pi R^2$$

$$\therefore \bar{J} \simeq \bar{J}_1 . P^{0.34} \quad \text{(for low flows)}$$

$$\text{with } \bar{J}_1 = I/\pi R_1^2$$

$$\text{and } E \simeq E_1 P^{0.5}$$

$$\therefore \sigma = (\bar{J}_1/E_1) . P^{-0.16}$$

For high flows σ is effectively independent of pressure.

Using values given in fig.47 allows $\bar{J}_1$ to be identified as 3.2 A/mm^2. Values of E_1 found in section 5.3 for short arcs on copper give $E_1 \simeq 0.8$ V/mm. Therefore

$$\sigma = 4 . P^{-0.16} \text{ mho/mm}$$

Estimates of arc column temperature may be obtained from the thermodynamic behaviour of σ. Data given by Kannappan and Bose (ref.35) has been used to evaluate T_σ at a number of pressures (see table 47).

P (bars)	1	2	4	16	32
σ (mho/mm)	4	3.6	3.2	2.6	2.3
T_σ(K)	11,000	10,500	10,300	9,600	9,300

Table 47 Influence of Pressure on the Electrical Conductivity Temperature (T_σ)

Table 47 shows that T_σ is only weakly influenced by temperature - largely due to the behaviour of σ in the region $T \sim 10^4$K. The modest decrease in temperature is in good agreement with that previously reported by Bauder (ref.151) for wall stabilised arcs. This rather crude calculation lends weight to the approach adopted on many occasions

in this thesis of regarding pressure to have little influence on the temperature at which arc properties are evaluated.

7.4. Arc Stability

Arc stability is a particularly difficult behavioural feature to quantify. Indeed, this is a many sided aspect of behaviour with no single definition.. The approach adopted here was to observe fluctuations in the arc current carrying boundary as a function of shielding gas flow rate and ambient pressure. It is found that such oscillations are random in nature and are mainly determined by the shielding gas mass flow rate i.e. not volumetric flow or ambient pressure. The physical interpretation of such a result is associated with turbulence in the shield and is in keeping (as shown here) with many previously observed aspects of arc behaviour.

If the same volumetric flow of shielding gas is used at all pressures then the mass flow of shield increases directly as pressure. This leads to an increase in mass flow rate such that the Reynolds number corresponding to the onset of turbulence is reached at quite modest pressures. The observed behaviour is then explained in terms of turbulent heat transfer at the arc boundary. The mechanism for this behaviour is associated with a random temperature field, due to turbulence, creating a time dependent body force $\underline{J} \wedge \underline{B}$ - where both $\underline{J}$ and $\underline{B}$ are time dependent. Random column oscillations are then expected to occur. This is in keeping with the observed distribution of column oscillations. This interpretation has a number of consequences. Enhanced heat losses are expected from the column due to an increase in the effective thermal conductivity. These are reflected in the voltage sensitivity to shielding gas flow (see section 4.2). Arc shielding becomes progressively more difficult as volumetric and not mass flow rate is thought to be the dominant mechanism in shielding. In principle, it then follows that shielding and stability are incompatible above some ill defined pressure (see ref.163). Although such behaviour has been identified for argon arcs on copper anodes it appears that the presence of a weld pool exerts a stabilizing influence i.e. this counteracts the effect of flow by prohibiting arc movement at the anode.

The most important implication of the above finding is that many arc instabilities should be capable of stabilization by advantageously influencing behaviour in outer arc reaches. In plasma welding gas flow at the arc column boundary is imposed by pressure at the gas bottle and is therefore not as dependent on entrainment and turbulence. More stable conditions are then expected. This is indeed found to apply i.e. Experiments similar to those described above then show no sign of instability. A theoretical discussion of this is given in section 8.

Instabilities in arc columns have implications for pool behaviour. The most immediate effect is a lowering of the mean intensity of heating due to available heat being distributed over a larger anode area. In particular, the axial intensity may be significantly reduced. Also unstable pool conditions may be produced. Such behaviour has been observed at very high pressures (30 bars) although no correlation with arc behaviour could be discerned.

Finally, it is interesting to note that power supply characteristics may play some part in the observed mode of instability. Experiments performed here show that there is a possible correlation between the frequency of arc column oscillation instabilities and mains frequency to the power supply. This is possibly explained by the arc 'beating' at harmonics of the power supply frequency. Therefore even in constant current welding with very little current ripple the possibility of arc - power supply interactions exists.

7.5. Electrostatic Probe Results

Electrostatic probes have been used to investigate the distribution of arc voltage and hence the distribution of arc column power generation. Using this technique it has been possible to show that both anode and cathode fall voltages are substantially unaffected by ambient pressure. It is also found that the cathode fall voltage is independent of arc length and that the anode fall increases (but only slightly) with arc length on a steel anode. This last finding is in contrast to behaviour previously reported (ref.1) for arcs on copper anodes. It would therefore appear that vapourization at the anode has a significant influence on anode fall behaviour. This is also indicated by calorimetric

investigations. The magnitude of the anode fall voltage has been found by applying a correction factor accounting for the probe - plasma contact potential.

Values for V_a found in this manner are in good agreement with those obtained calorimetrically. Probe experiments have revealed that only small radial voltage gradients exist across the column. This is in good agreement with the observed axial nature of current flow i.e. the radial component of current density J_r is much smaller than the axial and by Ohms law it then follows that $E_z >> E_r$.

One particularly interesting result concerns the width of the radial distance over which significant probe voltages are measured. These are much wider than the current carrying region and are interpreted in terms of the existence of an arc heat affected zone capable of sustaining low levels of ionization. The basis for this association is related to the radial extent obtained when probes are used to collect current in an ion-saturation mode. The author therefore believes that a previous report (ref.164) associating this region with current transport is wrong. No great sophistication is claimed by the approach used to calculate the plasma - probe contact potential. However, the approach is not inappropriate in view of the logarithmic dependence of contact potential on the change in charge density across the sheath (see equation 60).

A number of interesting conclusions may then be arrived at concerning the use of electrostatic probes in high pressure plasma's. Experimental results indicate (see figure 207) that the maximum possible change in electron charge density across the sheath is (see equation 60)

$$e^3 \gtrsim \frac{n_{e\infty}}{n_{ep}}$$

This assumes the anode fall voltage to be zero. If calorimetric values are used to specify V_a then the maximum value is

$$e^2 \gtrsim \frac{n_{e\infty}}{n_{ep}}$$

These estimates suggest that electron density changes by at most a factor of 20 and probably a factor of 7. Previous reports (ref.51) of a factor of 100 are therefore quite unrealistic. The sharp rise in number density with temperature (ref.28) would then indicate that such errors give relatively small corresponding errors in temperature (10 - 20%). This would explain why temperature measurements obtained using probes (with $n_{e\infty} \simeq n_{ep}$) (ref.28) are of a very similar magnitude to those found by other methods (ref.30). However, the problem of a Langmuir probe in a high pressure plasma drawing current under ion-saturation conditions remains to be solved.

Voltage gradients taken from the axial distribution of arc potential have shown that electric field strength varies considerably between the electrodes. It is found that the axial position associated with the mean electric field ($\sim V_c/\ell$ for short arcs) lies nearer to the cathode than the anode and that this position shifts towards the anode with increasing pressure. Such a shift indicates that energy generation mechanisms are moving away from the cathode with increasing pressure. Behaviour of this type is to be expected in view of the gradual increase in the role played by radiation (see section 7.6). Experimental results and theoretical models presented here indicate that convection, which is predominantly localised near the cathode, becomes of slightly less relative importance with increasing pressure. Hence other less localised energy exchanges (e.g. radiation) influence the electric field strength. Despite this behaviour, the field strength near the cathode at high pressures is about five times that observed near the anode. The corresponding difference between power density ($\sigma.E^2$) at the anode and cathode is therefore a factor of order 25. Significantly larger factors are observed at 1 bar. Behaviour of this type is associated with the localised nature of convection and a disproportionate radiative contribution from this, the hottest arc region.

The observed behaviour of column potential (ϕ) and electric field strength E may be explained theoretically with the aid of equation 9. Results may also be used to estimate the axial dependence of a number of other quantities e.g. plasma flow velocity.

Consider the behaviour of equation 9 when convective and radiative mechanisms dominate.

$$\text{i.e.} \quad \underline{E}.\underline{J} = \rho Cp \ (\underline{U}.\underline{\nabla})T + W \qquad 9(a)$$

This may be considerably simplified by introducing a new variable (h), the enthalpy, such that

$$dh = Cp.dT$$

The convective term now becomes

$$\rho Cp(\underline{U}.\underline{\nabla})T = \rho(\underline{U}.\underline{\nabla})h = \rho h \ (\nabla.\underline{U})$$

Where the continuity of mass condition has also been used. Combining these equations allows 9(a) to be written as

$$\underline{E}.\underline{J} = \rho h \ (\nabla.\underline{U}) + W \qquad 9(b)$$

A useful expression may be found by integrating this equation radially across the arc:

$$E \int_0^\infty J_Z \ 2\pi r dr \simeq \int_0^\infty \rho h(\nabla.\underline{U}) 2\pi r dr + \int_0^\infty W.2\pi r dr \qquad 9(c)$$

Consider the convection term. Thermodynamic data (Table 13) shows that $\rho.h$ is substantially unaffected by temperature for temperatures of up to about 10^4K in argon. It is then reasonable to write

$$\int_0^\infty \rho.h \ (\nabla.\underline{U}) 2\pi r dr \simeq \rho.h \int_0^\infty \left\{ \frac{1}{r} \frac{\partial (r u_r)}{\partial r} + \frac{\partial u_z}{\partial z} \right\} . \ 2\pi r dr$$

$$\simeq \rho.h \left[2\pi U_r.r \right]_0^\infty + \rho.h \int_0^\infty \frac{\partial U_z}{\partial z} .2\pi r dr$$

$$\simeq \rho.h \frac{\partial}{\partial z} \int_0^\infty U_z.2\pi r dr$$

i.e. $U_r \to 0$ as $r \to \infty$ and $r \to 0$.

Using this last equation allows 9(c) to be written as:

$$E.I \simeq \rho.h \frac{\partial}{\partial z} \{\overline{U}.\pi.R^2\} + W^1 \qquad 9(d)$$

where

$$I = \int_0^\infty J_Z . 2\pi r dr$$

$$\bar{U} . \pi R^2 = \int_0^\infty U_Z . 2\pi r dr$$

$$W^1 = \int_0^\infty W . 2\pi r dr$$

$\bar{U}$ is defined as the mean flow velocity (radially averaged) and R is the radial extent of the region over which significant flow occurs. W^1 is the radiation per unit arc length. Experimental results presented here (see section 6.5) indicate that a reasonable approximation is to regard W^1 as independent of Z. An expression for the average velocity may now be obtained by noting that

$$E = \frac{\partial \phi}{\partial Z}$$

and integrating 9(d) along the axis (ϕ is the potential measured from the cathode end of the column). The result is

$$\bar{U} = \frac{\phi . I - W^1 . Z}{\rho . h . \pi . R^2} \qquad (134)$$

Both ϕ and W^1 are known from experimental results. R may be specified with regard to arc radius and current density results presented in previous sections. R has the following properties

i) Finite when Z = 0
   i.e. $R = R_o$
ii) $R \propto p^{-0.17}$
iii) $R \propto I^{0.5}$ (current density is little influenced by I)
iv) The column radius initially changes quickly with axial distance. However, at long arc lengths R changes slowly. This behaviour is roughly parabolic.

For a 100 Amp atmosphere arc it is then possible to write

$$R = R_o + K\sqrt{Z}$$

Where K is a constant. Experimental results indicate that

$$R_o = 0.5\text{mm}$$

For an arc length of 5mm's R is typically 3mm's. Hence

$$K \simeq \frac{3 - 0.5}{\sqrt{5}} \simeq \frac{\sqrt{5}}{2}$$

$$\therefore \quad R \simeq 0.5\ (1 + \sqrt{5Z})$$

Where Z is in mm's.

At other currents and arc lengths, (ii) and (iii) allow this to be written as

$$R \simeq 0.5\ (1 + \sqrt{5Z}).P^{-0.17}.(I/100)^{0.5}\ \text{mm} \qquad (135)$$

Combining equations (134) and (135) with experimental data for ϕ and W^1 allows $\bar{u}$ to be determined as a function of axial distance from the cathode and ambient pressure. Experimental data (see section 6.5) shows that

$$W^1 \simeq 0.2\ \bar{E}.I \simeq 0.2\ .\left(0.75\ .\ P^{0.5}\right).\ I\ \text{(W/mm)}$$

Where $\bar{E}$ is the average field strength.

i.e.

$$W^1 \simeq 15\ .\ P^{0.5}\ \text{(W/mm)}\ \text{for a 100A arc}$$

Direct measurements of ϕ are difficult to make because of difficulties in locating the column edge at the cathode (- the cathode fall must be excluded from ϕ). For this reason ϕ has been determined by integrating the field strength given in figure 208.

$$\text{i.e.} \quad \phi(Z) = \int_0^Z E.dZ$$

Values obtained in this manner are shown in table 49. The calculated values of $\bar{u}$ are shown in table 52 where gas properties (see table 13) have been evaluated at 12,000K. It should be noted that $\bar{u}$ increases by a factor of 1.25 if properties are evaluated at 11,000K. However, the axial form and pressure dependence are left unaffected. This data is also shown graphically in figure 218. It may be seen that axial velocity initially increases very steeply before passing through a maximum and then decreasing relatively slowly with axial distance from the cathode. This behaviour is in contrast to that predicted by Maeckers model which indicates that $\bar{u}$ should continually increase with increasing arc length. An explanation of the observed behaviour is

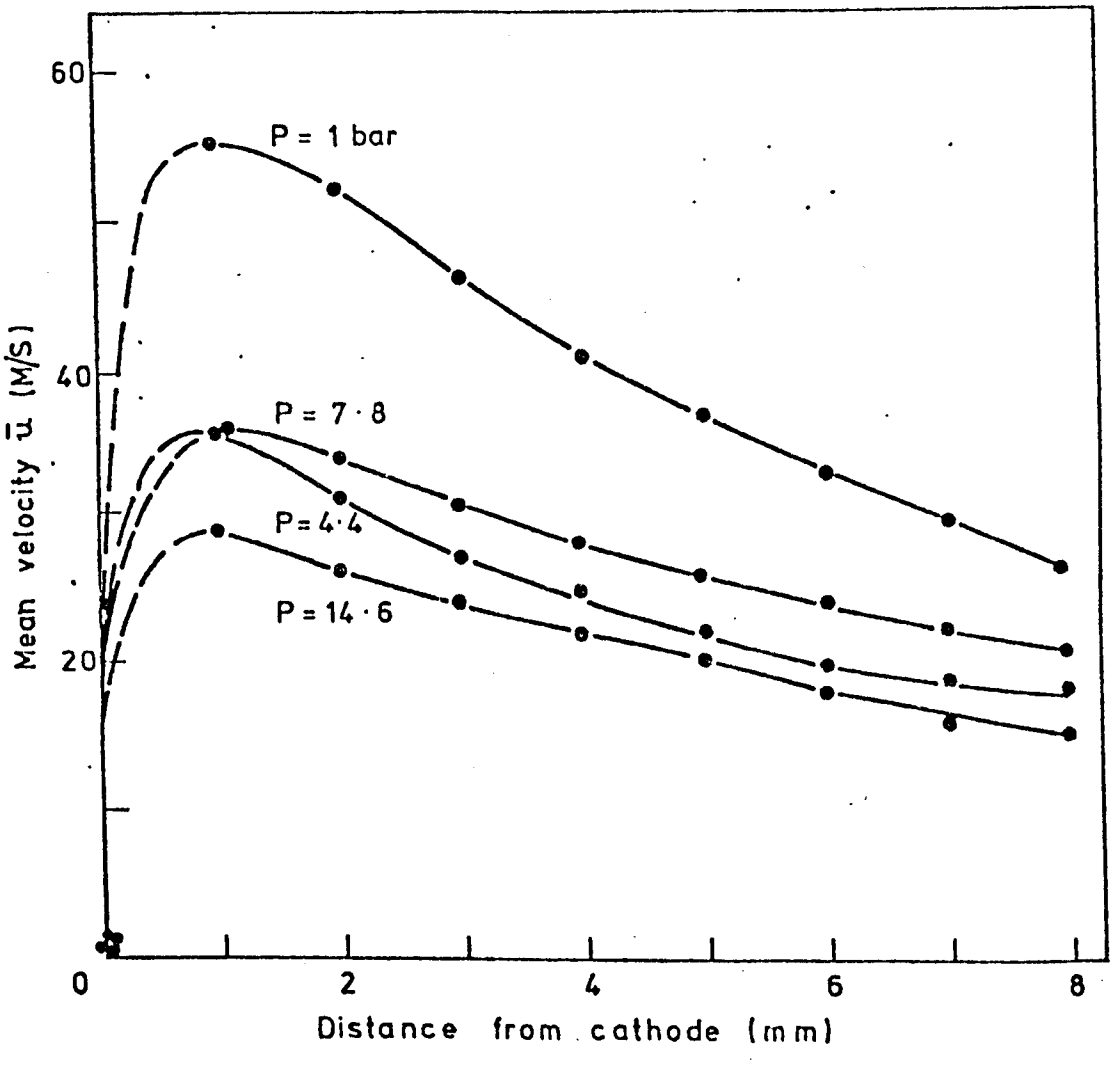

FIGURE 218. AVERAGE * PLASMA VELOCITY ($\bar{u}$) AS A FUNCTION OF DISTANCE FROM CATHODE AND AMBIENT PRESSURE (I=100A, ARGON TIG ARC OF LENGTH 10mm).
* AVERAGE ACROSS ARC.

given in section 8 in terms of the action of viscosity. It may also be seen that $\bar{u}$ generally decreases with increasing ambient pressure (as expected - see section 6). Typical values of $\bar{u}$ are 20m/s at 14.6 bars compared to 40m/s at 1 bar. An estimate of gas flow velocity on the arc axis may be obtained by considering a Gaussian distribution (see section 8) such that

$$V_z(r,Z) = U_o(Z).\ \exp\ (-a.r^2) \tag{136}$$

Where $U_o(Z)$ is the axial velocity and $a = a(Z)$ is a parameter yet to be identified. $a(Z)$ may be identified with the aid of the momentum flux (F) expression given by equation 14:

$$F = \int_o^\infty \rho V_z^2\ .2\pi r dr = \frac{\mu_o I^2}{4\pi} \cdot \ell n \left(\frac{R}{R_o}\right)$$

$$\therefore\ F \simeq \frac{U_o^2 .\rho.\pi}{2.a} \quad \text{i.e.} \quad a = \frac{U_o^2 .\rho.\pi}{2.F} \tag{137}$$

However, from equation (136) it can also be shown that

$$\bar{U}.\pi R^2 = U_o.\pi/a \tag{138}$$

Eliminating 'a' between expressions (137) and (138) gives

$$U_o = \frac{2F}{\rho\pi R^2 \bar{U}}$$

Substituting for $\bar{U}$ from equation (134) finally gives

$$U_o = \frac{2.F.h}{\phi.I\ -W^1.Z} \tag{139}$$

It is interesting to note that this expression is only marginally influenced by the axial dependence of arc radius. Experimental data has been used to calculate U_o and the results are shown in table 53 and figure 219. It is again found that velocity decreases slowly with axial distance and increasing pressure. Typical values at 1 bar are 100m/s and 30m/s at 14.6 bars. It is also interesting to note that the axial velocity is typically 2.5 times the mean at 1 bar but only 1.5 times the mean at 14.6 bars. This indicates that the high pressure velocity profile is not only lower and narrower, but also flatter than at 1 bar.

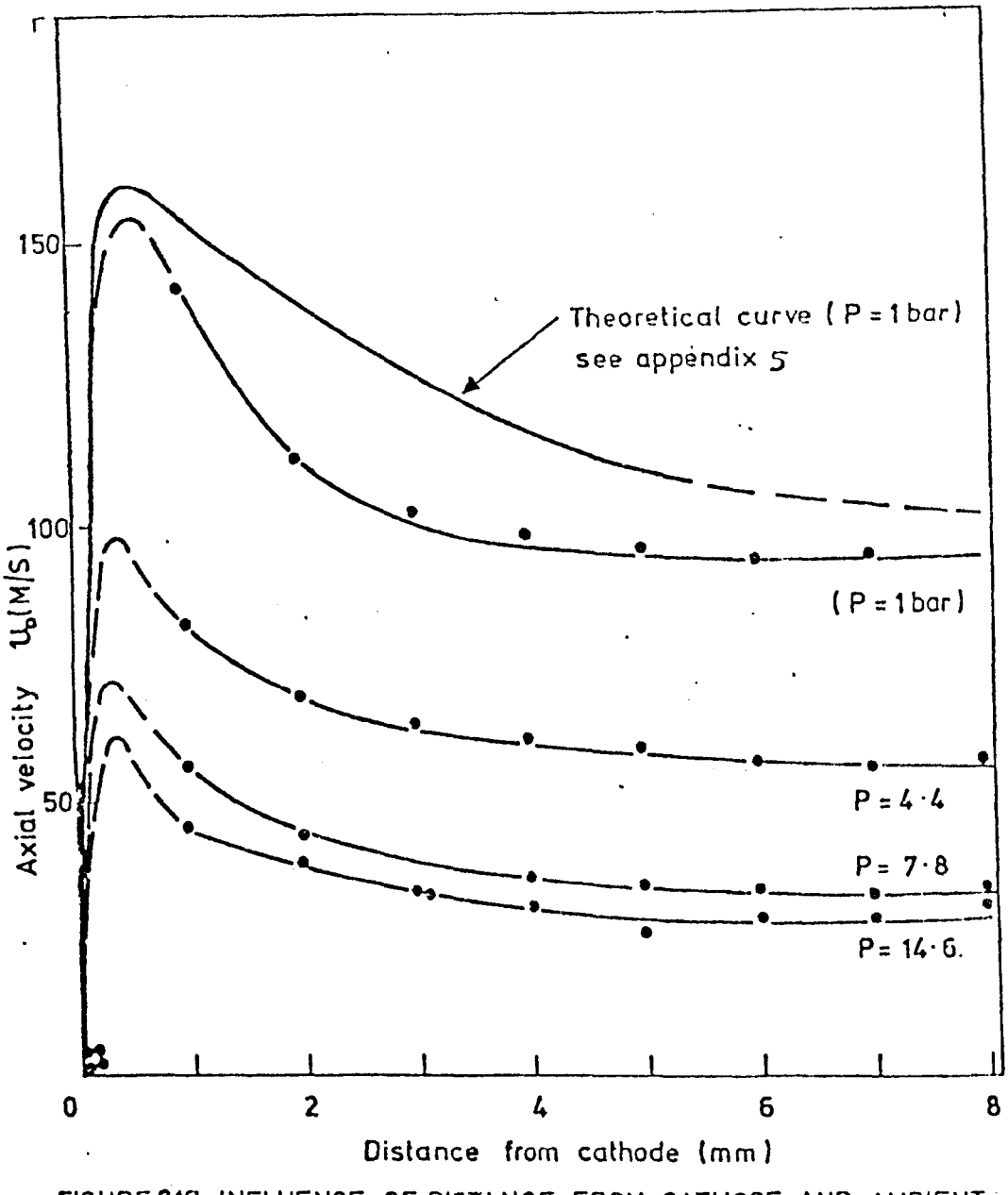

FIGURE 219. INFLUENCE OF DISTANCE FROM CATHODE AND AMBIENT PRESSURE ON THE AXIAL VELOCITY (100 A, 10 mm ARGON TIG ARC)

Axial velocity has been plotted against pressure in figure 220 for a number of arc lengths. This figure shows that the main influence of pressure is over the first 7 bars and that the sensitivity of U_o to arc length decreases with increasing pressure (see appendix 6).

Experimental data has also been used to estimate the enthalpy ($\dot{m}h$) and mass ($\dot{m}$) flux's (see tables 50 and 51 and figure 221 and 22) where $\dot{m}h$ has been calculated from

$$\dot{m}.h = \phi.I - W^{1}.Z$$

These results show that very strong entrainment occurs over the first millimeter. Indeed, typically 40% of the entrained mass flow occurs in this region for all pressures. Typical mass fluxes at 1 bar are 40mg/s compared to 130mg/s at 14.6 bars. The atmospheric figure is in line with values given in section 2. It should also be noted that the increase with pressure is slightly stronger than that predicted in section 6 i.e. $P^{0.33}$.

ϕ in Volts

P	Axial distance from cathode (mm)								
(Bars)	0	1	2	3	4	5	6	7	8
1	0	2.1	3.4	4.1	4.7	5.2	5.6	5.9	6.1
4.4	0	3.7	5.5	6.8	7.9	8.8	9.6	10.4	11.2
7.8	0	5.4	8.5	10.8	12.7	14.3	15.7	16.9	18.0
14.6	0	6.6	9.9	12.8	15.0	18.4	19.6	20.5	21.0

Table 49 Influence of Axial Distance from the Cathode on the Potential ϕ Developed in the Column (arc length 10mm, argon 100A arc)

$\dot{m}h$ in Watts

P	Axial distance from cathode (mm)								
(Bars)	0	1	2	3	4	5	6	7	8
1	0	195	305	365	410	445	470	485	490
4.4	0	339	487	586	664	723	771	820	868
7.8	0	493	761	949	1097	1221	1319	1377	1465
14.6	0	603	875	1108	1271	1549	1419	1554	1592

Table 50 Enthalpy Flux as a Function of Axial Distance from the Cathode and Ambient Pressure (arc length 10mm, argon 100A arc)

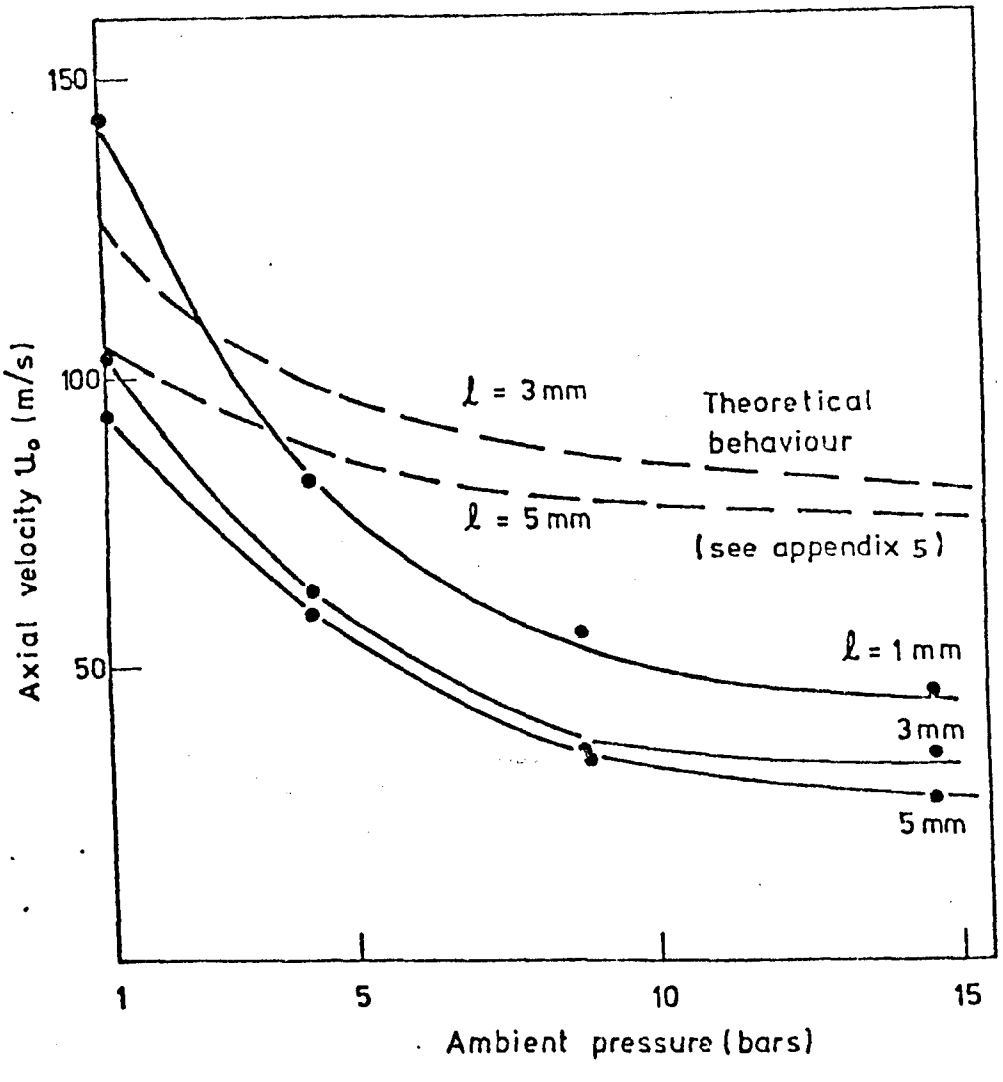

FIGURE 220. INFLUENCE OF AMBIENT PRESSURE AND DISTANCE FROM THE CATHODE ON THE AXIAL VELOCITY OF AN ARGON TIG ARC (I = 100A, 10 mm ARC LENGTH).

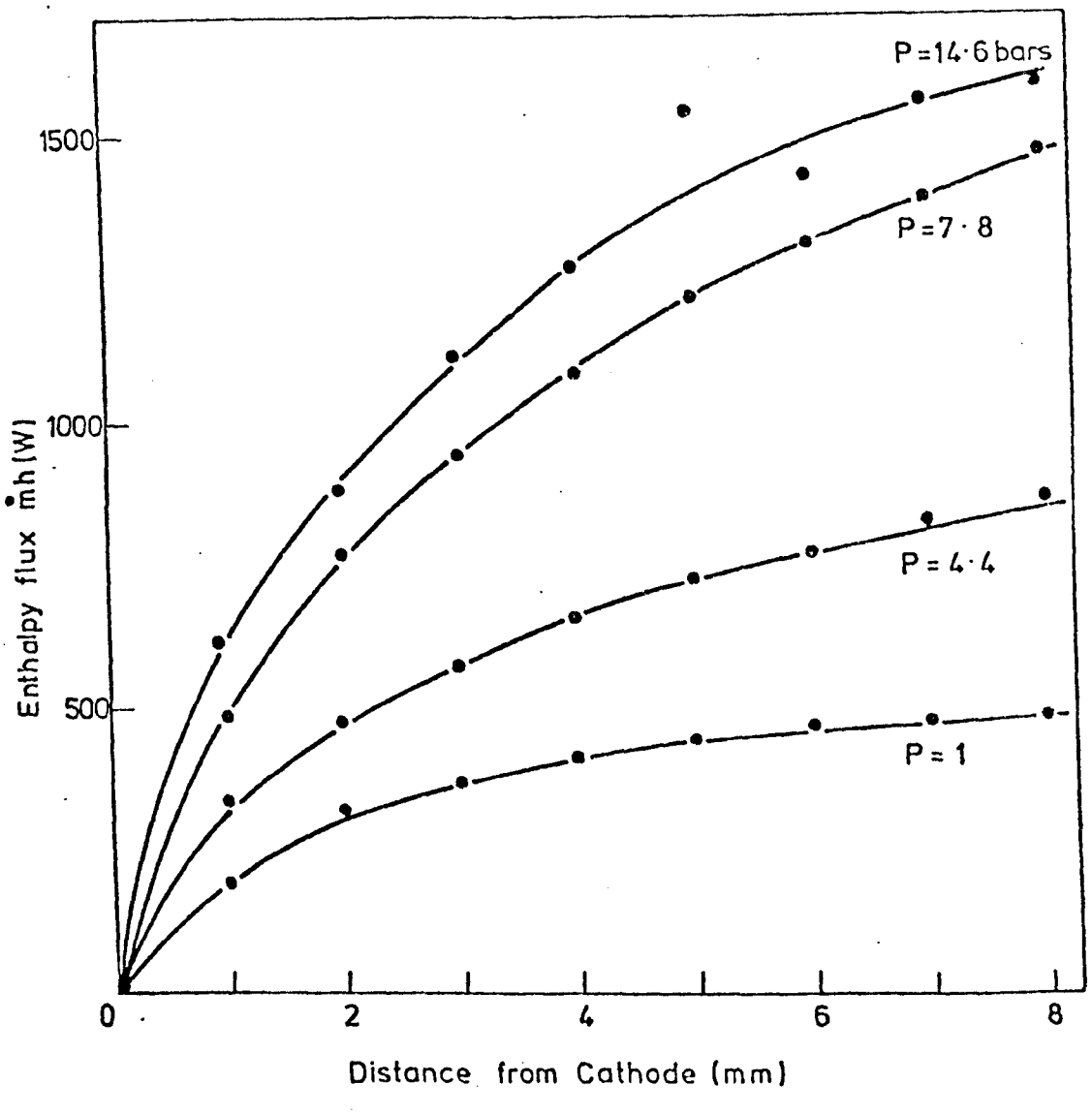

FIGURE 221. AXIAL DEPENDENCE OF THE ENTHALPY FLUX IN A 100A, 10mm ARGON TIG ARC AT VARIOUS PRESSURES.

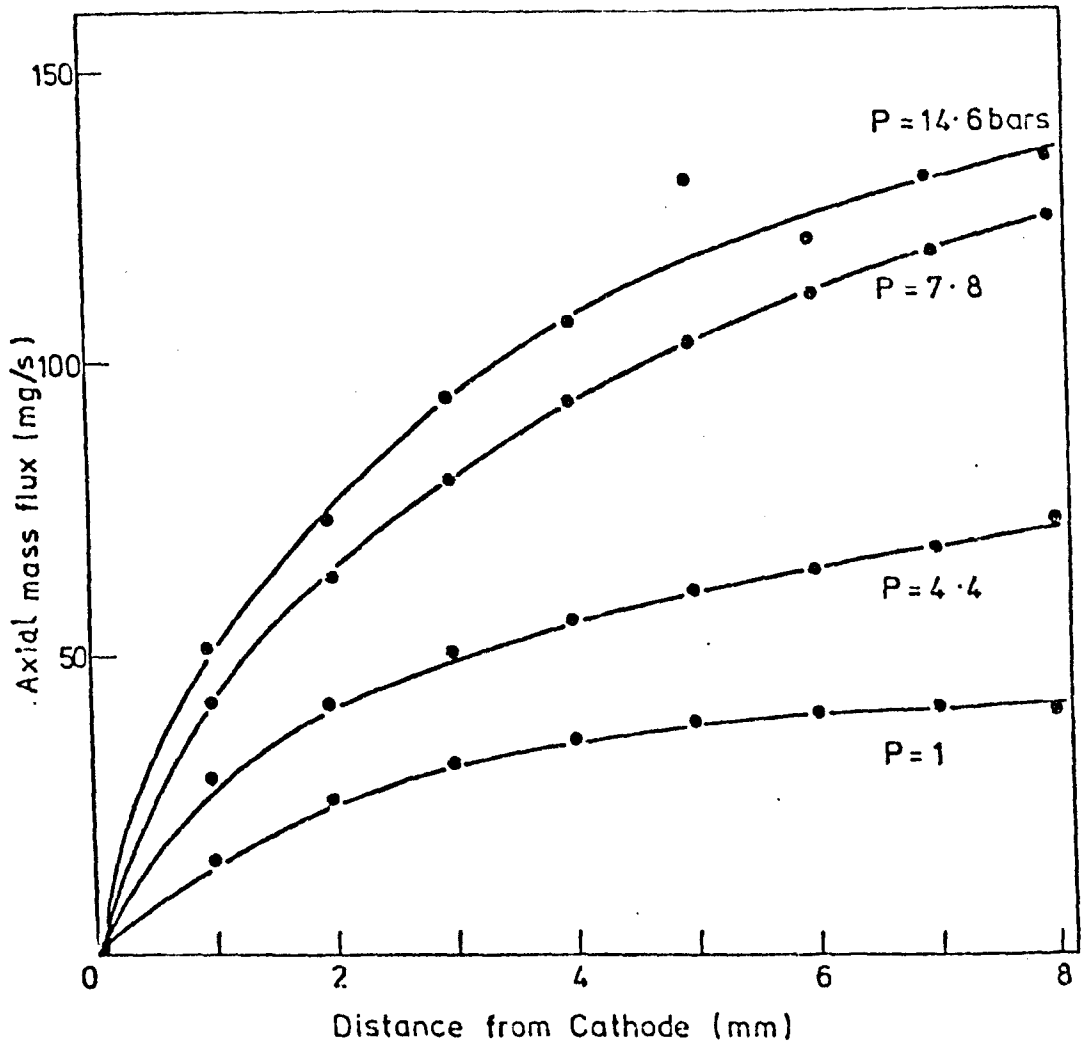

FIGURE 222. AXIAL DEPENDENCE OF THE AXIAL MASS FLUX IN A 100 A, 10 mm ARGON TIG ARC AT VARIOUS PRESSURES.

$\dot{m}^*$ in mg/s

P	Axial distance from cathode (mm)								
(Bars)	0	1	2	3	4	5	6	7	8
1	0	16	26	31	35	38	40	41	41
4.4	0	29	41	50	56	61	65	69	73
7.8	0	42	64	80	93	103	111	118	124
14.6	0	51	74	94	107	131	120	131	135

Table 51 Axial Mass Flow Rate as a Function of Axial Distance from the Cathode and Ambient Pressure (arc length 10mm, argon 100A arc).

* enthalpy evaluated at 12,000K.

$\bar{u}^*$ in m/s

P	Axial distance from cathode (mm)								
(Bars)	0	1	2	3	4	5	6	7	8
1	0	55	52	46	41	37	33	30	27
4.4	0	36	31	27	25	22	20	19	18
7.8	0	36	34	31	28	26	24	22	21
14.6	0	29	26	24	22	20	18	16	15

Table 52 Mean Velocity ($\bar{u}$, radially averaged) as a Function of Axial Position from the Cathode and Ambient Pressure (10mm, 100A argon arc)

* arc temperature taken as 12,000K. If 11,000K is used then $\bar{u}$ is greater by a factor of 1.25.

u_o^* in m/s

P	Axial distance from cathode (mm)								
(Bars)	0	1	2	3	4	5	6	7	8
1	0	142	111	103	98	95	94	94	101
4.4	0	82	69	64	61	59	57	56	57
7.8	0	56	44	34	37	35	34	33	34
14.6	0	46	39	34	32	27	29	29	31

Table 53 Axial Velocity as a Function of Axial Position from the Cathode and Ambient Pressure (10mm, 100A argon arc)

* arc temperature taken as 12,000K. If 11,000K is used then u_o is smaller by a factor of 0.7.

7.6. Radiation Measurements

Radiation from argon and helium TIG arcs has been investigated by measuring the radiative power collected by a blackened copper disc. The method employed allowed background effects to be accounted for and hence radiation eminating from the column could be found. Results show that the total radiated power increases with arc power such that

$$Q.(\text{Radiation}) = f(P).E.I.\ell$$
$$\simeq f(P).0.75.I.\ell.P^{0.5}$$

Where f(P) is a slowly increasing function of pressure having a value of 0.18 at 1 bar in argon and a corresponding value at 41.6 bars of 0.25 ($f(P) \simeq 0.21 \pm 0.04$). This figure shows that radiation accounts for about 20% of arc column power dissipation and is therefore an important column heat transfer mechanism. It may also be seen that the relative role of radiation increases with pressure from about 18% at 1 bar to 25% at 41.6 bars. This represents a 40% increase (i.e. 7/18) in the radiative contribution. The expression given above is based on data for arc currents of 75,100 and 125 Amps. Lower fractions of column power appear as radiation for 50A arcs. It would therefore appear that significant differences exist in the behaviour of low current (75A >I) and high current ($I \geqslant 75A$) arcs. This is not unexpected in view of changes in plasma flow velocity, arc rooting, V-I characteristic and other characteristics at low currents. Helium arcs were found to radiate a much smaller fraction ($\sim$ 6%) of the column power generated despite being at much higher temperatures. This result, coupled to the ball like shape (i.e. little convection), indicates that conduction is the major mechanism of heat arcs from such columns.

It has been pointed out (see section 6) that an error of up to $\pm$25% may be associated with measurements given here. This is largely associated with geometric factors that systematically affect all measurements in a similar manner. Hence the dependence on I, ℓ and P is much more accurately known. The error therefore primarily concerns f(P) which has a representative error of $\pm$0.05. Even with this possible error margin the present results are much lower than those cited in the literature survey. Indeed one of the few available reports (ref.67)

apparently gives impossibly high radiation levels. In view of the lack of information generally given this could be due to a failure to account for background effects and hence an over estimate of the column contribution. However, it is worth noting that an expression given by Stracham and Barrault (ref.68) gives good agreement with results presented here. There also seems to be some agreement in the literature on the relative insignificance (see section 2) of radiation as a heat transfer mechanism in helium arcs.. Experimental results presented here are in reasonable agreement with the rather rough analysis given in section 6. There it was found that radiation increased as $P^{0.66}$. This is in good agreement with the $f(P).P^{0.5}$ behaviour given above. It was also predicted that about 20% of the column power appears as radiation. The reasonable agreement with this simple model implies that radiation changes are a direct result of arc shape and density factors i.e. arc temperature and the relative importance of radiative mechanisms remain unaffected by pressure.

Despite the importance of radiation in the column this is unlikely to directly influence melting characteristics at the anode. This is because of the poor heat transfer efficiency of radiation which is probably responsible for the reduction in column heat transfer efficiency with increasing pressure (see section 6). i.e. about half of the radiated power is expected to radiate away from the plate anode. A significant fraction of the half impinging on the plate will be reflected from the shiny, pool surface and plate region. Even then only a small quantity will impinge direction on the pool, the remainder contributing to plate heating some distance from the pool. The effect of radiation on pool structure is almost entirely restricted to modifying the current density in the arc by flattening the temperature profile and hence indirectly affecting the density of electronic heating.

8. Arc Column Structure: A Theoretical Discussion

8. ARC COLUMN STRUCTURE: A THEORETICAL DISCUSSION

8.1. Introduction

Results presented here have shown that the most significant influence of ambient pressure is on processes occurring within the column. It is therefore appropriate to consider this region in more detail. Many of these processes may be described by considering the column as a whole and representing an arc property in terms of average behaviour. This approach has been applied with some success in section 6. However, there are aspects of arc behaviour which are not particularly amenable to this approach e.g. arc stability. A detailed understanding of this type of behaviour requires a knowledge of how conditions vary within the column. Unfortunately, a general approach to this problem involves the simultaneous solution of energy equations, momentum equations and Maxwells equations. No such solution presently exists for the convectively dominated column of a welding arc. Existing models have been discussed in section 2 and these have been shown to incorporate many unrealistic features. The aim of the present work is to develop a more realistic model capable of being applied to the problem of arc stability. This problem is central to the influence of pressure on arcs and is therefore considered to be of great importance in the present context. The approach adopted is to consider the momentum equations and obtain solutions for axial and radial plasma flows. These solutions are then used to estimate the relative importance of various forces acting in different regions of the column. From such considerations a model of arc stability is formulated. It is also possible to use these solutions to investigate aspects of energy transfer within the column (see section 7.5). No attempt is made to produce the full analysis in this section. These details of the analysis are given in appendix 5. The major emphasis is placed on describing the analytic foundations and discussing relevant results.

8.2. Formulation of Problem

Gas flow in the arc column may be described quite generally in terms of the Navier-Stokes equations (see equations 10 and 11).

Bodyforces in these equations may be specified if the current density is known i.e. Maxwells equations (see equ.4) may then be used to specify

the magnetic field. These equations must also be coupled to the relevant continuity expressions (see equs.12). To obtain solutions for $\underline{u}$ the arc is considered to be a highly directed flow with radial symmetry. Both of these conditions are well founded in experience. Azimuthal variations are then negligible and the axial velocity $u_z(r,z)$ is much greater than the radial component $u_r(r,z)$. The complete set of equations (in cylindrical co-ordinates r,z) then become

$$\rho(\underline{u}.\underline{\nabla})\ u_z = -\frac{\delta p}{\delta z} + \eta\nabla^2 u_z + J_r B + (\rho_\infty - \rho_a)g$$

$$0 = -\frac{\delta p}{\delta r} - J_z.B$$

with $$\frac{1}{r}\ \frac{\delta(rB)}{\delta r} = \mu_o\ J_z$$

$$\frac{\delta}{\delta r}\ (r\rho u_r) = -\frac{\delta}{\delta z}\ (r\rho u_z)$$

$$\frac{\delta r}{\delta r}\ (r.J_r) = -\frac{\delta}{\delta z}\ (r\ J_z)$$

These equations form the basis of the present theory where the co-ordinate system is described more fully in appendix 5.

The method of solving this set of equations is to:-

(a) Assume an axial form of current density, $J_z(r,z)$, consistent with the thermodynamic state of the column. This is often taken as uniform across the arc. However, experimental results (see Gvodetskii - ref.72) indicate a Gaussian distribution to be more appropriate. This is the form taken here i.e.

$$J = J_o \exp(-b.r^2)$$

where $J_o = J_o(Z)$ and $b = b(Z)$, both being determined by theoretical consideration (see appendix 6).

(b) Maxwells equations are then used to calculate the magnetic field strength. The magnetic components of the body force are then readily identified.

(c) The pressure distribution is then obtained by integrating the radial component of the momentum equation. This expression can then be inserted into the axial momentum equation.

(d) Steps (a) - (c) allow the axial momentum equation to be expressed in terms of just v_r and v_z. One of the variables may then be eliminated using the conservation of mass condition.

(e) At a number of stages in the above formulation it is required to make assumptions concerning the temperature field. These are:

(1) Viscosity is assumed to be independent of position in the arc. This assumption is a very good approximation for temperatures within the range 8,000K to 12,000K (i.e. argon TIG arcs) where a variation of only 10% is observed (see table 13).

(2) Density is assumed to vary little over the flow. This assumption may be in error by two orders of magnitude if momentum flow extends to the cold gas flow outside the arc. However, considerations given in appendix 5 show that the momentum flow is almost entirely restricted to the hot column and so an error of only about ±10% is associated with this assumption if density is evaluated at say 10^4K (see table 13).

(f) The final step taken in obtaining a solution is to assume a Gaussian type axial flow i.e.

$$u_z = u_o \exp(-ar^2)$$

where $u_o = u_o(Z)$ and $a = a(Z)$ are obtained in a self consistent manner from theoretical considerations. The axial dependence allowed for in specifying u_o and 'a' makes this assumption less restrictive than might at first appear. This type of radial dependence has been obtained experimentally by Laser-Doppler ananometry experiments (see ref.60) and so is quite reasonable. The consequences of this radial distribution are investigated more fully in appendix 6 and found to be in good agreement with such separate considerations as energy dissipation.

8.3. General Aspects of Solutions

Analytical solutions have been obtained for situations where one or other of magnetic or viscous body forces dominate. In the former case velocity is found to increase monotomically with axial distance from

the cathode and to be similar in form, although larger, than solutions previously found by Maecker. When viscous forces dominate the velocity falls steeply with axial distance from the cathode. In situations where both forces are significant numerical solutions have been obtained that show features of both solutions (see appendix 5 figure 1). The velocity then initially increases in a manner similar to that predicted by inviscid considerations. A peak value is then reached followed by a slow fall-off in axial velocity. This behaviour is slower than that given by the inviscid solution due to the continuing, although decaying, existence of an axial momentum source i.e. the magnetic field. Results obtained have been compared with experiments performed here which measured the pressure exerted on a small hole placed in the surface of a copper anode. Excellent agreement is found (see appendix 5). Results may also be compared with the axial dependence of flow velocity found from energy balance considerations and electrostatic probe measurements (see section 7.5). The agreement is again good.

Of particular interest is the pressure dependence of arc velocity. This falls with increasing pressure although not quite as strongly as previously predicted by the essentially one dimensional model used in section 6. The model also shows the flow boundary to contract with increasing pressure. Indeed the degree of contraction with pressure is stronger than that observed for the electrical boundary and so the arc jet becomes progressively confined to an inner core of the current conducting region with increasing pressure. This aspect is discussed more fully in the next section concerned with arc stability.

The model also considers the conditions under which buoyancy becomes important. This force is found to be generally negligible at 1 bar but to increase in importance with pressure. Although the force is negligible when 'averaged across the arc' at 1 bar it may still exert a significant influence at the outer arc boundary and hence have an influence on arc behaviour - especially at low currents where the magnetically generated momentum flux is low.

8.4. Arc Stability

The model developed has shown that

(a) The gas flow field is confined within the current conducting boundary and contracts at quicker rate than the current boundary with increasing pressure.

(b) Buoyancy forces became increasingly important with pressure

i.e. $\frac{F_B}{F_M} \alpha P$ (see section 5)

The combined effect of these predictions may be used to infer that high pressure arcs become progressively less stable. As pressure increases a larger region is created that is hot enough to conduct current but in which flow is negligible. This region is therefore susceptible to instabilities which may then influence the bulk behaviour of the column. For example, buoyancy forces may produce a flow in this region counter to that of the inner arc jet (as in down hand welding, although both flows will act in the same direction when welding overhead). The unsteady nature of buoyancy generated flows will then give rise to time dependent temperature effects in the outer current carrying zone. Clearly this behaviour will generate a time dependent body force and hence possibly gross column instabilities i.e. the current paths will be modified and hence both $\underline{J}$ and $\underline{B}$ will be affected. As pressure is increased conditions become all the more favourable for this type of behaviour due to increasing buoyancy and decreasing jet dimensions. Behaviour of this form has been observed experimentally (see section 5) where arcs in the over head position are found to be more stable than in the down hand position and less constricted at the anode. In down hand welding this last effect gives rise to an anode spot mode which has also been observed by Matsunawa and Nishiguchi (ref.10). Conditions become all the more favourable for this type of behaviour with increasing arc length as the arc force becomes more diffuse and buoyancy then has a stronger influence on flow and hence arc rooting at the anode.

Arc instabilities associated with effect (a) but independent of (b) may also be expected. Turbulent conditions may be created by high shielding gas flows. This effect has been observed and quantified by experiments

reported in section 6. Here turbulent exchanges again lead to a time dependent body force and arc column oscillations may be expected. Energy exchanges should also be influenced i.e. enhanced heat extraction due to turbulent heat transfer. This explains the increase in arc voltage with increasing gas flow rate at high pressures (see section 5).

Results and theory presented above point to a model of arc stability that depends on conditions existing in the outer arc reaches (see figure 223). It should therefore be possible to stabilize arcs by manipulating these conditions. A good deal of evidence exists to suggest that this is indeed the case. For instance, it is found here that constricted TIG arcs are reasonably stable. This is associated with the imposition of an external flow. The current conducting 'arc' region is then entirely confined within the flow and hence conditions in the outer arc reaches are stabilized. Freely burning TIG type arcs may be stabilized by changing conditions in this region. Such an effect may be brought about by the imposition of high frequency power or magnetic fields. In the former case the arc becomes an induction plasma at high frequencies with current being confined to an outer arc 'skin'. This will clearly modify arc conditions. Experiments performed at 1 bar indicate that this does indeed give rise to 'stiffer' arcs (ref.165). However, much more work is required in this field. Axial magnetic fields have the effect of introducing a component of swirl to the gas flow. This in turn acts as a stabilizing mechanism.

9. General Discussion

9.0. GENERAL DISCUSSION

An attempt has been made in this thesis to examine in a systematic manner the physical effects of pressure on gas-tungsten arcs. Experiments have been performed to determine the characteristics and structure of such arcs and models have been developed to explain many of the observations. The method employed has involved three distinct but overlapping and related phases. Initial studies concerned bulk characteristics of the column and weld pool. This work indicated a number of further areas of experimental study concerned with more detailed and specific (structural) questions. During the course of this work arc models were developed with a view to understanding the relationships between characteristics and structure. These aspects have already been discussed separately in sections 5, 7 and 8.

The main purpose of this section is to relate the previous discussions and thereby give a more general view of behaviour.

The present investigation has dealt solely with physical aspects of TIG welding arc behaviour with special reference to the influence of ambient pressure. Process characteristics have been observed to change significantly with pressure and it has been found possible to explain many of these changes by structural factors. Many of these results have been explained by theoretical models developed here, but areas do exist that have yet to be successfully modelled or fully explained.

Characteristics were investigated with particular reference to arc appearance, arc mode, electrical characteristics and weld bead studies. Perhaps the most singly striking characteristic to emerge with increasing pressure is the transition from an arc system dominated by energy generation at the electrodes to one where most power appears in the column. This was evidenced by arc voltage increasing almost entirely due to column phenomena (i.e. sum of fall voltages is independent of pressure). Detailed investigations revealed that E increases with the square root of ambient pressure. This behaviour has a great many implications, some of which are discussed below. Electrostatic probe measurements investigated the axial distribution of arc voltage. This showed that not only is V_o independent of pressure but

so too are the components of V_o. It is observed that the voltage gradient within the column has a highly non uniform form despite a reasonably uniform V-ℓ characteristic. A satisfactory physical interpretation of this dependence has been attributed to enthalpy generation near the cathode. Indeed models have been developed that predict many of the findings from investigations of electrical characteristics. For instance the observed decrease in arc column diameter with increasing pressure is predicted and theoretical results give a reasonable description of the pressure dependence of E. E is the result of convective, conductive and radiative energy transfer within the column. Measurements of radiative output show that this is an important factor accounting for 18% of E at 1 bar and 25% at 40 bars. Thus radiation increases with pressure. This is entirely in line with predicted behaviour if the 'column temperature' is little influenced by pressure. Electrical conductivity changes would indicate that this is the case. To compensate for the increasing importance of radiation the nett convective-conductive effects become of less relative importance. Detailed theoretical calculations show that enthalpy is expected to increase less quickly with pressure than E and hence make an increasingly less important contribution to E.at very high pressures. Such behaviour is understood in terms of plasma jet velocity falling with pressure. At the root of this effect is the finding that momentum generation is largely independent of pressure despite a strong increase in plasma density. Detailed theoretical models have been very successful in describing this behaviour i.e. good agreement with experimental measurements of arc velocity. The same theoretical considerations have also allowed a model of arc stability to be developed. This shows turbulent exchanges at the arc boundary to be responsible for many instabilities. The influence of such exchanges may also be used to explain the observed voltage dependence on shielding gas flow. Turbulent shielding gas flows exist at high pressures for quite moderate volumetric flow rates. The effective thermal conductivity is then significantly enhanced near the arc boundary. Hence an increase in conductive heat transfer and arc voltage. Quantitative information about the disturbing influence of turbulence was obtained from experiments monitoring the motion of the electrical arc boundary at the anode. These experiments showed that behaviour was indeed random and

and related to the Reynolds number of the shielding gas flow. Turbulence may also be created at high pressure by buoyancy forces which becomes increasingly important in the outer reaches of the high current arcs. The above comments serve to show that many of the observed changes in arc shape, stability and electrical characteristics have been successfully explained on the basis of structural investigation and theoretical considerations. These considerations also indicate ways in which arc behaviour may be advantageously manipulated. For example, arc instabilities may be overcome by changing conditions in the outer arc reaches. One method employed for doing just this was to constrict the arc near the cathode. The arc then burnt in an imposed, highly directed gas flow. Stabilization was then observed. Other possibilities include the use of high frequency power to shunt current to the outer arc regions (the arc is then of an inductive nature).

From the energy stand point it is also apparent that more power is available for weldment heating at high pressures. This is particuarly true in helium arcs. However, strong cathodic erosion must then also be contended with. It is known that small additions of argon to helium arcs may drastically effect arc behaviour. It is thought that by such an addition it may be possible to substantially increase heat input while minimising erosion. However, this work must await further investigations.

Although the electrical characteristics of the electrode regions are largely unaffected by pressure other changes do occur. These are associated with vapourization, enhanced heat transfer from the column and pool stability. It is in these regions that theoretical understandings have proved most difficult. The influence of anodic vapour on arc behaviour is seen in many results. Arcs on copper anodes are much less stable than those on steel anodes. Here vapour aids arc rooting stability. At very low currents arc rooting 'heel and step' motion is often observed.such that above some critical current (I_c) the arc returns to a fairly diffuse and continuous mode. However, for steel anodes I_c decreases with increasing pressure while for copper anodes I_c increases with pressure. This behaviour is again understood in qualitative terms by vapour stabilizing arc rooting. It has also

been proposed that such behaviour is influenced by buoyancy forces on copper anodes as experiments in over head welding show no sign of this mode. With this arrangement the plasma jet and buoyancy act in the same direction and hence produce a stronger directed gas flow at the anode. Vapour also has the expected effects of slightly lowering arc column voltage and anode fall voltage. This last factor is strongly influenced by vapour, being much smaller on steel anodes than on copper. Coupled to this is a significant reduction in heat transferred to steel anodes compared to copper anodes. It is found that not only does the electronic heating contribution fall but so also does that from the plasma jet to the plate. In this last case an explanation is given in terms of vapour, decreasing temperature gradients near the plate and hence heat convected from the plasma jet. Conventional heat transfer calculations therefore fail to account for the true nature of heat transfer at the anode. Such results also show that copper anode heat transfer calorimetry is a poor representation of the welding situation at high pressure. Indeed, reasonable agreement at 1 bar is due to the dominance of electronic heating terms and the relatively minor contribution made by conduction for the plasma jet.

Changes in the nature of the heat source give rise to pressure dependent weld bead characteristics. Generally, the pool depth increases while bead width is little influenced. The nett result is an increase in bead cross-sectional area and a decrease in bead aspect ratio. Both tendencies are easily understood in terms of results from structural investigations. Current density measurements show that the intensity of electronic heating is expected to rise by more than a factor of four over the first 14 bars. This result was obtained on a copper anode and may well be higher in the presence of significant metal vapour but it appears difficult to obtain reliable current density data for welding anodes. The effect of this is to create a more localised - point like - heat source giving, on the basis of conductive heat transfer theories, more hemispherical pools. This is in keeping with the observed bead aspect ratios of nearly 2. Further to this convection from the indigenous $\underline{J} \wedge \underline{B}$ interaction is expected to transfer heat more efficiently to the bottom of the pool than the sides. The increase in bead area is clearly due to enhanced convective heat transfer due to more heat

generation in the column. It is interesting to observe that despite the fall in process efficiency a higher efficiency of melting is usually observed at pressure. This has been explained using conductive heat transfer theories which are in good agreement with observation at high pressures. Using this theory it has been found possible to predict bead characteristics (over a wide range of conditions) from arc characteristics, plate composition and welding speed. However, at very high pressures pool instabilities occur. These remain as yet unexplained, but it has been speculated that these are due to an interaction between arc rooting, weld pool motion and vapour. This behaviour is possibly an extreme form of that occasionally found under normal ambient conditions. Stabilization may be brought about by the application of an axial magnetic field which imposes rotational motion on the pool. The application of such a field also reduces penetration and melted area. Such observations have been explained in terms of an increased effective thermal conductivity of the pool and a decrease in the downwards $\underline{J} \wedge \underline{B}$ force due to the imposition of rotational motion about the arc axis.

It is also interesting to note that process heat transfer efficiencies estimated from HAZ dimensions during bead studies are in fair agreement with those found by direct calorimetric measurements on steel anodes. In both cases a fall with pressure was observed and these values were substantially lower than those for copper anodes. Clearly in an underwater operational environment voltage must be reinterpreted in the context of heat input to take account of decreasing efficiencies i.e. (Amps x volts)/welding speed, will give a very poor representation of heat input TIG welding. A large number of other 'operational implications' are implicitly contained in results given above. However, it is considered inappropriate to discuss these here.

10. Conclusions

10. Conclusions

Work presented in this thesis has been aimed mainly at gaining an understanding of the influence of pressure on gas tungsten arcs. These results have implications in a number of other areas e.g. more general aspects of arc phenomena and submarine repair and maintenance techniques.

Such aspects are dealt with briefly in the section on 'General Conclusions'. More specific conclusions are now given under sub-headings describing the general nature of the conclusions. No attempt is made at exhaustively listing such conclusions. Emphasis has been placed on giving those conclusions reflecting the influence of pressure on behaviour.

10.1. Arc Appearance and Modes

1. The outer penumbra surrounding the argon tungsten arc disappears near 2 bars and the column contracts according to a $P^{-0.17}$ law. Stronger contractions may be observed at high shielding gas flow rates ($P^{-0.25}$). Contraction at the anode obeys a similar law although cathode spot diameters decrease as $P^{-0.14}$. Cathode spot contraction has been explained in terms of thermionic emission phenomena.
2. The appearance of helium tungsten arcs changes from being diffuse and ball shaped at 1 bar to exhibiting a strong plasma jet with a bright central core at 15 bars.
3. The appearance of constricted argon tungsten arcs is strongly dependent on plasma - forming gas flow considerations (i.e. flow rate and orifice size) as well as ambient pressure.
4. Arc column luminosity generally increases with pressure. This has been associated with an increase in the total radiative power from the column. For argon tungsten arcs the fraction of column power radiated is 18% at 1 bar and 24% at 42 bars. However, the fraction of the total process power appearing as radiation is significantly less being typically 5% at 1 bar and 10-15% at 42 bars. For helium tungsten arcs a much smaller fraction of the column power appears as radiation i.e. typically 6%.

5. Cathodic melting and erosion often occurs at high pressures. This is restricted to localized tip melting in argon arcs if electrode diameters of 3.2mm and greater are employed (for arc currents of less than 150 amps). A small ball is then formed at the electrode tip. If pure helium shielding gas flows are used then severe erosion occurs at quite low pressures (∿5 bars). Under some conditions this may lead to a 'self-pulsing' arc form due to the emission of tungsten vapour.

   The total heat to the cathode is little influenced by pressure. Cathodic erosion is therefore thought to be the result of an increase in the intensity of heating i.e. contraction of cathode spot.

6. Low current arc rooting phenomena is strongly influenced by ambient pressure, anode composition, arc orientation, arc length, shielding gas composition and arc current. It is found that arc root motion on a continuously moving anode is discontinuous below some critical current (all other factors being constant). The critical current increases with pressure for argon arcs on copper anodes and decreases for argon arcs on steel anodes. No discontinuous motion was observed for helium arcs on steel or copper anodes. The critical current for argon arcs was observed to increase with arc length and decrease when the arc orientation was such that buoyancy forces had the same direction as plasma streaming motion. It was also observed that the critical current always appeared on the negative arm of the V-I characteristic. i.e. At currents such that the contribution of enthalpy to the arc voltage was small.

7. At currents below the critical level, one or more highly constricted and mobile arc roots existed. However, for helium arcs only one arc root was ever observed ($I \geq 15A$).

8. It has been proposed that the behaviour reported in 6 and 7 is associated with the availability of a suitable supply of low ionization elements. This is determined by the intensity of anode heating, plasma gas flow near the anode, and anode composition.

9. Column stability visibly deteriorates with increasing pressure. This is adversely affected by the application of high shielding gas mass flow rates and favourably influenced by orientating the arc in the direction of the buoyancy force.

10.2. Physical Properties of High Pressure Gas Tungsten Arcs

Arc models have been developed to investigate many aspects of column behaviour. The conclusions presented in this section concern general aspects of these models. It is thought inappropriate to restate here mathematical expressions developed in the text.

1. Plasma streaming velocity decreases with increasing pressure (for argon tungsten arcs). This is attributed to the pressure independence of the magnetically generated momentum flux and the strong pressure dependence of plasma density.

2. A theoretical model of arc column plasma flow has been developed. This shows that viscous forces are important and must be accounted for. It is found that the axial flow velocity initially increases with distance from the cathode. Viscous forces then become significant at larger distances causing velocity to fall. Plasma flow is found to be confined to the current carrying region and the existence of a hot low velocity shear layer at the arc boundary has been identified. Behaviour in this region is thought to determine column stability.

. The model also predicts a decrease in the 'flow diameter' of a free arc with increasing pressure. Excellent agreement has been found between predictions and axial velocities measured manometrically and from energy structure.

3. The characteristic arc column temperature (T_σ) decreases slightly with increasing pressure. However, this may be represented by $10{,}500 \pm 1{,}000$K for $15 \geqslant P \geqslant 1$ bar.

4. Buoyancy forces increase in importance with pressure (i.e. both in absolute terms and with respect to magnetically generated momentum). Buoyancy is particularly significant in the outer arc reaches where gas flow velocity is low.

5. The average power density generated in the column of an argon tungsten arc increases as $P^{0.84}$.

6. The Reynold's number for plasma flow in the column increases as $P^{0.5}$. However, values were always below 1000 and so laminar flow conditions are expected to exist near the arc axis.

7. Flow conditions near the column boundary are dominated by shielding gas flow considerations, i.e. principally the mass flow rate of the shield. The associated shield Reynolds number may exceed 20,000 and turbulence is therefore expected. This has significant implications for arc stability.

8. The stagnation pressure exerted by the arc jet at the weld pool surface increases with pressure. However, the total force on the pool is little influenced by pressure.

9. The electrical conductivity of an argon TIG column is little influenced by pressure.

10.3. Electrical Properties

1. The total arc voltage is significantly influenced by ambient pressure. This is associated primarily with a change in the column component. Measurements with electrostatic probes have found that both the anode and cathode fall voltages are largely independent of pressure. The total voltage of an argon-tungsten arc may be represented by

$$V = V_o + E_1.p^n.\ (1 + \theta).\ell$$

where θ is a factor accounting for the influence of shielding gas flow on arc voltage E_1, n, θ and V_o depend on material properties and values are given in the text.

2. The distribution of arc column voltage is non linear and gives rise to a highly non linear electric field strength. The position of the average value of field strength moves away from the cathode with increasing pressure. This is associated with changes in the distribution of arc power generation with increasing pressure.

3. The V-I characteristic of argon tungsten arcs exhibits a negative gradient at low currents and a positive gradient at high currents. The position of the turning point tends to lower currents with increasing pressure and the gradient of the positive V-I arm increasing with pressure. Both effects have been associated with an increase in the role of convective heat transfer with pressure.

4. The V-I characteristics of helium tungsten arcs exhibits a negative gradient for all pressures and currents investigated here. This is explained in terms of the dominance of conduction in the column even when strong plasma flow exists (i.e. relatively low enthalpy flows still occur due to the low density of helium).

5. Theoretical models have been developed that account for many of observed characteristics of arc voltage.

6. Electric field strength at the electrodes increases with pressure despite the independence of fall voltages on pressure i.e. fall voltage is independent of electric field strength.

10.4. Arc Stability

1. Turbulent shielding gas flow conditions have a pronounced influence on arc stability particularly on copper anodes. Random oscillations of the arc root are then observed. This behaviour has been associated with the creation of a turbulent shear layer with non steady current density and magnetic field conditions. A time dependent $\underline{J} \wedge \underline{B}$ body force then exists which causes the column position to fluctuate.

2. The constricted argon tungsten arc is stable for a wide range of arcing conditions. This is attributed to such arcs burning in an imposed gas flow.

3. Buoyancy forces may have a stabilizing or disruptive influence depending on arc orientation.

4. Instabilities examined here originate in the outer arc HAZ region or shear layer. Stability may be restored by manipulating conditions in this region e.g. by the creation of an induction plasma.

10.5. Power Development and Dissipation in the Column

1. The distribution of power dissipation shifts from electrode regions to the column with increasing pressure. More than half of the power generated appears in the column when the arc length is such

that

$$\ell \geq \frac{10}{\sqrt{P}} \text{ mm} \quad \text{argon arcs}$$

$$\ell \geq \frac{5}{\sqrt{P}} \text{ mm} \quad \text{helium arcs}$$

2. The total power appearing in the column increases approximately as the square root of pressure.

3. Power dissipation in the column of an argon tungsten arc is dominated by convection (∿60% at 1 bar). Conduction and radiative contributions are approximately equal and account for about 20% at 1 bar. The effect of pressure is to slightly decrease the convective contribution and correspondingly increase the radiative contribution. However, a significant increase in conductive transfer may also occur when arcs burn in highly turbulent shielding gas flows.

4. Theoretical models have been developed to describe the energy structure of the column. These are in fair agreement with experimental findings.

5. The distribution of convective power dissipation is strongly non linear being largely concentrated near the cathode.

6. Helium arcs are conductively dominated at atmospheric pressure. This behaviour becomes conductive - convective at higher pressures with radiation playing only a very small role.

10.6. Power Transfer to the Electrodes

1. The total power transferred to the cathode is little influenced by pressure for argon tungsten arcs and is approximately given by 1.5I (Watts) where I is arc current in amps. This has been explained in terms of cathode fall voltage and contributions to anode heating.

2. Power transferred to the anode has two components: Electronic and gas heating. The electronic component is little influenced by pressure while the gas contribution increases with pressure. The behaviour of both these components is strongly influenced by anode composition in a manner indicated below.

3. The electronic component of anode heating has been expressed as

$$Q_e = I\ (V_a + \phi + \frac{5}{2} \cdot \frac{KT}{e})$$

where the notation is explained in the text. Although V_a and T are little influenced by pressure it is found that both are substantially greater on copper anodes than on steel. This is attributed to the influence of anode vapourization. For steel anodes $Q_e \approx 6.5I$ (Watts) and the corresponding value on copper anodes is 8.I (Watts) for argon arcs.

4. The efficiency of column power transfer to the anode decreases with pressure (strongly over the first 10 bars and thereafter remains constant). It is found that the efficiency is significantly less on steel anodes than on copper.

5. As a result of conclusions 3 and 4 it is observed that the efficiency of transferring the total process power to the anode, decreases with pressure and is less on steel than on copper. Significant differences exist between materials and experiments performed on cooled copper anodes are poor representations of real welding situations.

6. The application of a magnetic field has little effect on process heat transfer efficiency or on the total power transferred. This behaviour is also reflected by the insensitivity of HAZ dimensions to magnetic stirring (despite the decrease in fusion area - see 10.7).

7. The intensity of heat transfer to both electrodes increases with pressure: e.g. the intensity of electronic heating on a copper anode increases by a factor of 4 over the pressure range 1 to 14 bars. It is also found that at every pressure the maximum intensity is between 4 and 5 times the mean.

10.7. Fusion Characteristics

1. Pressure has a significant influence on fusion characteristics for TIG arcs in argon. The major effects are largely confined to the first 20 bars. Over this pressure range bead penetration is observed to approximately double. However, fusion width is little influenced by pressure. For argon arcs, arc length has little influence on

fusion characteristics and the dominant process variable is arc current. Associated with behaviour described above is a reduction in bead aspect ratio with increasing pressure. In the absence of bead instabilities this has a value close to 2 for pressures greater than 10 bars. It is also found that, for a given arc length and current, bead area increases by about a factor of 3 over the pressure range 1 to 40 bars.

2. Pressure is also observed to have a significant effect on fusion characteristics for TIG arcs in helium shields. Penetration increases markedly over the first 8 bars although behaviour is less well defined at higher pressures. Arc current is the dominant process variable in determining penetration with arc length playing a very minor role. Unlike argon arcs it is found that bead width increases significantly with pressure and arc length. Behaviour described above gives rise to fusion area increasing by about a factor of 3 over the first 10 bars with bead aspect ratios generally remaining independent of pressure and having a value near 1.7. Arc length exerts a strong influence on bead area i.e. this may double between 2mm and 5mm arcs for all pressures examined.

3. High pressure helium arcs may have extremely penetrating characteristics giving rise to 'keyhole' behaviour under some conditions.

4. Bead instabilities have been observed for high pressure (> 30 bars) argon TIG arcs. The cause of these is not presently known. However, stabilization may be brought about by the application of an axial magnetic field.

5. The application of a magnetic field has a significant influence on fusion characteristics. For argon arcs it is observed that penetration is significantly reduced when a field is applied. However, bead width is little influenced (slight increase). For helium arcs the fusion depth is again reduced by the application of a field but significant bead dilation also occurs. In both argon and helium smaller melted volumes are created when a field is applied than would otherwise occur. This effect is most pronounced in argon where the application of a field may reduce fusion area by a factor of 2 at high pressures.

Despite significant changes in fusion characteristics, the application of a field has very little influence on HAZ structure.

6. In many situations it is found possible to reliably predict heat transfer efficiencies on the basis of HAZ widths. This approach is particularly suitable for hyperbaric argon TIG arcs at currents of 100 Amps and less.

7. Melting efficiencies (Z) have been predicted on the basis of conductive heat transfer theory. Z has also been found directly from experimental weldment measurements.

   It is found that Z increases as welding speed increases. Also, Z is significantly larger in helium shields than in argon shields (values of over 30% have been achieved).

   The application of a magnetic field causes Z to fall by roughly a factor of 2. However, more complicated dependencies exist for the influence on Z of arc length, arc current, process power and ambient pressure.

   For argon TIG arcs Z generally decreases with increasing arc length. This behaviour is also observed for low power helium TIG arcs. At high process powers, long helium arcs become more efficient melting sources than short arcs. This is particularly noticeable when a permanent magnet is fixed to the torch and used for magnetic stirring. The influences of ambient pressure on Z is very sensitive to arc current. At the lowest currents examined (i.e. 75A) Z was observed to peak. This occurred for argon and helium arcs and for pools with magnetic stirring.

   Melting efficiency estimates based on conduction heat transfer models are generally in fair agreement with measured values. In particular, the tendency for peak values of Z is often correctly predicted. It is found possible to account for behaviour in a magnetic field by using the concept of an 'effective thermal conductivity'.

8. Results presented indicate that the effect of indigenous weld pool motions is mainly confined to influencing weld pool shape. The total melted volume appears to be adequately described by conduction based theories and is therefore little influenced by convection. Convection is important when a strong applied field is used and may be accounted for by the concept of an effective thermal conductivity. This explains why the same process power and heat input then produces less melting.

10.8. General Conclusions

1. Ambient pressure exerts a significant effect on the nature of gas-tungsten arcs and on resulting fusion characteristics. Details have been given here.

2. The influence of ambient pressure on arc characteristics has been used to gain a deeper understanding of the behaviour of atmospheric arcs.

3. The application of GTA to submarine repair and maintenance tasks is feasible to water depths of at least 450m. However, weld pool stabilization may be required beyond 300m e.g. by the application of magnetic stirring.

4. A re-evaluation of the significance of GTA process parameters is required in operational situations e.g. especially arc voltage and shielding gas flow rate and composition.

5. Automatic welding techniques will be required if fusion welding techniques are to be applied beyond the saturation diving limit (300-400m), Under these conditions a detailed knowledge of process characteristics (as given here) is considered essential for adequate process control and reliability.

REFERENCES

REFERENCES

1. FINKELNBURG, W. MAECKER, H. — Electric arcs and thermal plasma. Handbuch Der Physik. Vol.XXLL pp254-444. ARL translation. Published by Springer-Verlag of Heidelberg 1962.

2. ECKER, G. — Theory of the electrode components of the arc discharge. Welding Institute Conference, London 'Physics of Welding Arc Symposium' 1962.

3. GUILE, A. E. — Arc electrode Phenomena. IIW DOC.212-170-69, 1969.

4. MAECKER, H. — Z. Physik. 141 pp198-216, 1955.

5. JACKSON, C. E. — The science of arc welding. Welding Journal, 39, Research Supplement, 1960.

6. GOLDMAN, K. — Electric arcs in argon. Welding Institute Conference, London. 'Physics of Welding Arc Symposium', 1962.

7. OLSEN, H. N. — Temperature measurements in high pressure arc plasmas. Paper presented at the 11th Gaseous Electronics Conference, New York, 1957.

8. WILKINSON, J. B. and MILNER, D. R. — Heat transfer from arcs. Br.Weld J. pp115-128 Feb.1960.

9. REEVES-SAUNDERS, R. — The evaluation of high current.DC arcs on rotating anodes. Vol.1, PhD Thesis. The Australian National University, Canberra, 1972.

10. MATSUNAWA, A. and NISHIGUCHI, K. — Arc characteristics in high pressure argon atmospheres. Welding Institute Conference, London. Arc Physics and Weld Pool Behaviour, 1979.

11. METCALFE, J. C. QUIGLEY, M. B. C. — Arc and pool instability in GTA welding. A.W.J. (Research Supplement) May 1977.

12. SINGH, B. P. — Influence of electrode vertex angle on TIG arc characteristics. MSc Thesis, Material Dept. Cranfield Institute of Technology, 1979.

13. ANDREWS, J. G. CRAINE, R. E. — Fluid flow in a hemisphere induced by a distributed source of current. J.Fluid Mech. Vol.84, Part 2, pp281-290, 1978.

14. COBINE, J. D. — Gaseous conductors. p295, Publ. Dover, New York, 1958.

15. GOLDMAN, K. — Electric arcs in argon: Heat distribution. British Welding Journal. July 1963.

16. LANCASTER, J. F. Energy distribution in argon shielded welding arcs. British Welding Journal, 1, pp412-426, Sept.1954.

17. GLICKSTEIN, S. S. Arc modelling for welding analysis. Welding Institute Conference, London. Arc Physics and Weld Pool Behaviour, 1979.

18. GUILE, A. E. The electric field in the column of high-pressure argon arcs. Proc.2nd.Int.Cont. on Gas Discharges IEE London, 1972.

19. SAVAGE, W. F. STRUNK, S. S. and ISHIKAWA, Y. The effect of electrode geometry in gas tungsten-arc welding. American Welding Journal. Research Supplement. pp489-S to 496-S, 1965.

20. OKADA, M. MARUO, H. Studies on the plasma jet. Welding Institute Conference, London. Arc Physics and Weld Pool Behaviour, 1963.

21. ECKERT, E. R. G. and PFENDER, E. Advances in plasma heat transfer. From the book: Advances in Heat Transfer. pp229-316, 1967.

22. SHERCLIFF, J. A. A text book of magnetohydrodynamics. Pergamon Press Ltd. Oxford, 1965.

23. SAVAGE, W. F. NIPPES, E. F. and ZANUER, F. J. Determination of GTA weld puddle configurations by impulse decounting. American Welding Journal. Research Supplement pp201-S to 210-S. July 1978.

24. DEVOTO, R. S. Transport coefficients of ionized argon. The Physics of Fluids. Vol.16, No.5, May 1973.

25. QUIGLEY, M. B. C. Physics of the welding arc. Welding and Metal Fabrication. pp619-626, December 1977.

26. COWLEY, M. Integral methods of analysing electric arcs, I and II. J.Appl.Phys: J.Phys.D. Vol.7, 1974.

27. BAUDER, U. IEE Gas Discharge Conference. Bucharest, page 310. 1969.

28. GICK, A. E. F. QUIGLEY, M. B. C. and RICHARDS, P. H. The use of electrostatic probes to measure the temperature profiles of welding arcs. J.Phys.D: Appl.Phys, 6 (16), pp1941-9, 1973.

29. LOWKE, J. J. Calculated properties of vertical arcs stabilized by natural convection. J.Appl.Phys. 50 (1), pp147-157, Jan.1979.

30. GLICKSTEIN, S. S. Temperature measurements in a free burning arc. American Welding Journal. 55 (8), pp2225-2295, 1976.

31. EVANS, D. L.
TANKIN, R. S.
Measurement of emission and absorption radiation by an argon plasma..
Phys. of Fluids, Vol.10, No.6, pp1137-44, 1967.

32. BAUDER, U.
Radiation from high-pressure plasmas.
J. of Appl. Physics. Vol.39, No.1. Jan. 1968.

33. EMMONS, H. W.
Arc measurement of high temperature gas transport properties.
Phys. of Fluids. Vol.10, No.6. June 1967.

34. ASINOVSKY, E. I.
PAKHOMOV, E. P.
YARTSEV, I. M.
Argon plasma viscosity measurements.
Proc. of IEE Conf. on Gas Discharges.
pp376-378, 1978.

35. KANNAPPAN, D. and
BOSE, T. K.
Transport properties of a two temperature argon plasma.
Phys. of Fluids, Vol.20, No.10, Pt.1,
October 1977.

36. RAMAKRISHNAN, S.
STOKES, A. D.
LOWKE, J. J.
An approximate model of high current free burning arcs.
J.Phys.D: Appl.Phys. Vol.11, 1978.

37. BOWMAN, B.
Measurements of plasma velocity distributions in free burning DC arcs up to 2160A.
J.Phys.D: Appl.Phys 5, pp1422, 1972.

38. HILL, R. J.
JONES, G. R.
The influence of laminar and turbulent flows upon the electrical characteristics of wall-stabilised arcs.
J.Phys.D: Appl.Phys. Vol.12. 1979.

39. HOWATSON, A. M. and
TOPHAM, D. R.
The instability of electric arcs burning axially in accelerated flow.
J.Phys.D: Appl.Phys. Vol.9, 1976.

40. LOWKE, J. J.
Simple theory of free burning arcs.
J.Phys.D: Appl.Phys. Vol.12, pp1873-86, 1979.

41. LANCASTER, J. F.
The dynamics of the plasma jet in a free burning arc.
IIW DOC 212-87-66, 1966.

42. CHANG, C. W.,
EAGER, T. W.
SZEKELY, J.
Modelling the velocity fields in welding arcs.
Welding Institute Conference, London.
Arc Physics and Weld Pool Behaviour, Paper 31.
May 1979.

43. SHERCLIFF, J. A.
Fluid motions due to an electric current source.
J.Fluid Mech. Vol.40, Pt.2, pp241-250, 1970.

44. SOZOU, C.
J. Fluid Mech. 46, pp241. 1971.

45. SOZOU, C.
J.Fluid Mech. 63, pp665. 1974.

46. SOZOU, C.
Proc. Roy, Soc. A 329, pp71. 1972.

47. SOZOU, C.
PICKERING, W. M.
J. Fluid Mech. 70, pp509. 1975.

48. SOZOU, C.
PICKERING, W. M.
J. Fluid Mech. Vol.73, Pt.4, pp641-650. 1976.

49. ATTHEY, D. — A mathematical model of fluid flow in a weld pool at high currents. J. Fluid Mechs. 98, pp787-801. 1980.

50. MOTT-SMITH, H. LANGMUIR, I. — The theory of collectors of gaseous discharges. Phys.Rev.28, p727. 1926.

51. CLEMENTS and SMY — J.Phys.D: Appl.Phys. L135. 1975.

52. ALLUM, C. J. GICK, A. E. F. RICHARDS, P. H. QUIGLEY. — J.Phys.D: Appl.Phys. L135. 1975.

53. ALLUM, C. J. METCALFE, J. C. QUIGLEY, M. B. C. — A modified low pressure probe theory applied to measurement of temperature profiles in plasma welding. CEGB R/M/N925. 1977.

54. MECHEV, V. S. EROSHENKO, L. E. — Radial distribution of the temperature of the electric argon arc. Avt. Svarka No.3. pp6-9. 1975.

55. SHAW, C. D. Jn. — Diagnostic studies of the GTAW arc Pt.1. - Observational studies. American Welding Journal. pp33-S to 44-S. February 1975.

56. MILLS, G. S. — Use of emission spectroscopy for welding arc analysis. American Welding Journal. Research Supplement pp93-S to 96-S. March 1977.

57. MECHEV, V. S. EROSHENKO, L. E. — Determining the temperature of the plasma in an arc discharge in argon. Avt. Swarka. No.8, pp1-6, 1970.

58. PETRIE, T. W. PFENDER, E. — The influence of cathode tip on temperature and velocity fields in a gas-tungsten arc. American Welding Journal. Research Supplement pp588-S to 596-S. December 1970.

59. KOBAYASHI, M. and SUGA, T. — A method for the spectral temperature measurement of a welding arc. Welding Institute Conference, London. Arc Physics and Weld Pool Behaviour. May 1979.

60. SEEGER, G. TILLER, W. — Laser diagnostics on the TIG arc. Welding Institute Conference, London. Arc Physics and Weld Pool Behaviour. May 1979.

61. EDELS, H. HEARNE, K. YOUNG, A. — J. Maths and Phys. XL1.1,62. 1962.

62. TSAO, K. C. and PAVELIC, V. — Spectroscopic studies of a constricted argon plasma arc. Welding Institute Conference, London. Arc Physics and Weld Pool Behaviour. May 1979.

63. SHAW, C. B. — Effect of Orifice geometry in plasma-arc welding of Ti-6Al-4V. American Welding Journal. Research Supplement pp121-S to 125-S. April 1980.

64. SIMONIK, A. G. PANGILSKAYA, L. H. — Approximation of the temperature of the arc column in terms of the effective ionization potential and the welding current. Svar. Proiz. No.2, pp5-7. 1974.

65. QUIGLEY, M. B. C. RICHARDS, P. H. SWIFT-HOOK, D. T. GICK, A. E. F. — Heat flow to the work piece from a TIG welding arc. J.Phys.D: Appl.Phys. 6, pp2250-2259. 1973.

66. WIENECKE, — Z.Physik 143, p118. 1955.

67. SCHOEK, P. A. — An investigation of the anode energy balance of high intensity arcs on argon. Book: Modern Developments in Heat Transfer. Ed. by Ibele and published by Academic Press, New-York - London. pp353-400. 1963.

68. STRACHAN, D. C. BARRAULT, M. R. — Axial velocity variations in high-current gas flow free-burning arcs. J.Phys.D: Appl.Phys. Vol.9, pp435-446. 1976.

69. OKADA, T. YAMAMOTO, H. HARADA, S. — Observation of the shielding gas flow pattern during arcing by the use of a laser light source. Welding Institute Conference, London. Arc Physics and Weld Pool Behaviour. May 1979.

70. METCALFE, J. C. QUIGLEY, M. B. C. — Heat transfer in plasma arc welding. American Welding Journal. Research Supplement March 1975.

71. DENNERY, F. — Electric field distribution in welding arcs. Welding Institute Conference, London. Arc Physics. 1962.

72. GVOZDETSKII, V. S. — Distribution of current density in the column of the welding arc. Avt. Svarka. No.11, pp1-8. 1974.

73. LUDWIG, H. C. — Plasma-energy transfer in gas shielded welding arcs. American Welding Journal. Research Supplement pp276-S to 300-S. July 1959.

74. LUDWIG, H. C. — Welding Handbook, Pt.1, p322. American Welding Soc. 1968.

75. NESTOR, O. H. — Heat intensity and current density distribution at the anode of high current, inert gas arcs. J.Appl.Phys. No.5, Vol.33. 1962.

76. BENNETT, A. P. and HARLEN, F. — Measuring the UV radiation hazards to welders. Welding and Metal Fabrication. October 1980.

77. LUDWIG, H. C. — Current density and anode spot size in the gas tungsten arc. American Welding Journal. Research Supplement pp234-S to 240-S. May 1968.

78. BUSZ-PEUCKERT, G..T. FINKELNBURG. W. The anode mechanism of the thermal argon arc. Z.Physik 144, pp244-251. 1954.

79. APPS, R. L. MILNER, D. R. Heat flow in argon arc welding. British Welding Journal. October 1955.

80. MILNER, D. R. SALTER, G. R. WILKINSON, J. B. Arc characteristics and their significant in welding. British Welding Journal. Feburary 1960.

81. ECKER, G. The electrode components of the arc discharge. Ergebn.d.exakt. Naturw, 33, ppl-104. 1961.

82. GUILE, A. E. HAMILTON, M. A. McLELLAND, I. A. REEVES-SAUNDERS, R. Arc current distribution in 'continuous high-speed' anode tracks. J.Phys.D.Appl.Phys. Vol.8 pp964-970. 1975.

83. GVODETSKII, V. S. The function of distribution of the current density in the anode spot. Auto. Weld. No.12, pp20-24. 1973.

84. SAVITSKII M. M.et al The current density in the anode spot during the welding of standard refined steels. Avt. Svarka. No.7. ppl7-20. 1979.

85. MECHEV, V. S. ZAMKOV, V. N. PRILUTSKII, V. L. Radial distribution of the current density in the anode spot of an argon-shielded arc. Avt. Svarka. No.8, pp7-10. 1971.

86. EROKHIN, A. A. BURKAROV, V. A. ISCHENKO, Yu-S. Influence of tungsten cathode geometry on some welding arc characteristics and weld penetration. Scar. Proiz. No.12. ppl7-19. 1971.

87. EROKHIN. A. A. The force exerted by the arc on the metal being melted. Avt. Svarka. No.7. ppl21-126. 1979.

88. KOTOV, G. N. CHERKESO, V. S. E. MENSHOVA, O. V. Distribution of the gas kinetic component of the arc pressure along its radius. Avt. Svarka. No.10, pp72-73. 1974.

89. STEPANOV, V. V.et al Distribution of pressure in the plasma arc and the effect of the rate of plasma-forming gas on weld quality. Avt. Svarka. No.6. pp5-7. 1977.

90. SELYANENKOV, V. V. N. STUPACHENKO, M. G. Measurement of pressure of a welding arc. Svar. Proiz. No.9, ppl2-14. 1973.

91. RUSSO, V. L. SUZDALE, I. V. YAVINO, E. I. The effect of arc voltage and the geometry of sharpening of a non-consumable electrode on the force effect of the arc. Svar. Proiz. No.7. pp6-8. 1977.

92. SAVAGE, W. F. NIPPES, E. F. AGUSA, K. Effect of arc force on defect formation in GTA welding. American Welding Journal. Research Supplement p212-S. July 1979.

93. HELMOY, E. On the pressure distribution in a welding arc. IIW DOC. 212-400-77. 1977.

94. CAYLESS, M. A. Average kinetic energy of diffusing particles in discharge and electron tubes. Br.J. of Appl.Phys. Vol.12, pp523-524. September 1961.

95. RYKALIN, N. N. et al Calculating the heat transfer when a body is heated by plasma jet. IIW DOC. 212-93-66. 1966.

96. RYKALIN, N. W. Thermal characteristics for interaction between a plasma jet and a heated body. IIW DOC. 212-92-66. 1966.

97. SIBULKIN, M. J. J. Aeronaut. Sci. 19, p570. 1952.

98. QUIGLEY, et al The use of electrostatic probes in welding arcs. IEE Gas Discharge Conference. 1976.

99. GHENT, H. W. et al Welding Institute Conference, London. Arc Physics and Weld Pool Behaviour. Paper 4. May 1979.

100. MALMUTH, N. D.
HALL, W. F.
DAVIS, B. I.
ROSEN, C. D.
Transient thermal phenomena and weld geometry in GTAW. American Welding Journal. Research Supplement pp388-S to 400-S, September 1974.

101. COLLINGS, N.
WONG, K. Y.
GUILE, A. E.
Efficiency of tungsten-inert-gas arcs in very-high-speed welding. Proc.IEE. Vol.126, No.3 March 1979.

102. GHENT, H. W.
HERMANCE, C..E.
KERR, H. W.
STRONG, A. B.
Heat conduction modelling of two-dimensional TIG weld pools. Welding Institute Conference, Arc Physics and Weld Pool Behaviour. May 1979.

103. WELLS, A. A. Heat flow in welding. American Welding Journal. Research Supplement pp263-S to 267-S. May 1952.

104. ROSENTHAL, D. The theory of moving sources of heat and its application to metal treatments. Trans. of ASME, 68 (11), pp849-866, 1946.

105. CARSLAW, H. S. and
JAEGGER, J. C.
Conduction of heat in solids. 2nd Ed. Clarendon Press, Oxford. 1959.

106. PEARSON, J. R. A. On convection cells induced by surface tension. J. Fluid Mech. 4, pp489-500. 1958.

107. ISHNIZAKII, K.
MURAI, K.
KANKE, Y.
Penetration in arc welding and convection in molten metal. IWW W.G 212 DOC-77-66. April 1966.

108. MORGAN-WARREN E. J. Weld metal solidification and its control by stirring. Weld Pool Physics Conference. Welding Institute Conference, London. Arc Physics and Weld Pool Behaviour. 1979.

109. WILGOSS, R. A. — Electromagnetic control of fluid motion in TIG weld pools. Welding Institute Conference, London. Arc Physics and Weld Pool Behaviour. 1979.

110. MATSUDA, F. USHIO, M. NAKAGAWA, H. NAKATA, K. — Effects of electromagnetic stirring on the weld solidification structure of aluminium alloys. Welding Institute Conference, London. Arc Physics and Weld Pool Behaviour. May 1979.

111. WILGOSS, R.A . — CEGB, Report RD/M/R305. May 1980.

112. ANDERSON, D. — Streaming due to a surface tension gradient. IIW DOC. 212-71-09.

113. WOODS, R. A. MILNER, D. R. — Motion in the weld pool in arc welding. American Welding Journal. Research Supplement pp163-S to 173-S. April 1971.

114. BUKAROV, V. A. ISHCHENKO, Yu.S. LOSHAKOVA, V.G. — The effect of the convection of metal in the weld pool on penetration. Svar. Proiz. No.11, pp4-7, 1978.

115. THORN, K. et al — The interaction of process variables - their influences on weld dimensions in a GMA welds on steel plate. Metal construction. pp128-133, March 1982.

116. NILES, R. W. and JACKSON, C. E. — Weld thermal efficiency of the GTAW process. American Welding Journal. Research Supplement. pp25-S to 32-S. January 1975.

117. SPILLER, K. R. MacGREGOR, G. J. — Effect of electrode vertex angle on fused weld geometry in TIG-welding. Welding Institute Conference; Advances in Welding Processes. April 1970.

118. CHIHOSKI, R. A. — The effect of varying electrode shape on arc, operations, and quality of welds in 2014-T6AL. American Welding Journal. Research Supplement. pp210-S,212-S. May 1968.

119. CHASE, T. F. SAVAGE, W. F. — Effect of anode composition on tungsten arc characteristics. American Welding Journal. Research Supplement pp467-S, 473-S. November 1971.

120. BENNET, W. S. MILLS, G. S. — GTA weldability studies on high manganese stainless steels. American Welding Journal. Research Supplement pp548-S to 553-S. November 1974.

121. GLICKSTEIN, S. S. YENISCAVICH, W. — A review of minor element effect on the welding arc and weld penetration. WRC Bull. No.266. pp18. May 1977.

122. MILLS, G. A. — Arc/weld pool interactions and their effects on GTA weld penetration. Welding Institute Conference, London. Arc Physics and Weld Pool Behaviour. May 1979.

123. BRADSTREET, B. J. Effect of surface tension and metal flow on weld bead formation. American Welding Journal. Research Supplement pp314-S to 322-S. 1968.

124. TAGUCHI, H.
HANEDA, M.
MANAGA, S. Dropping transfer of filler wire for vertical plasma welding. Welding Institute Conference, London. Arc Physics and Weld Pool Behaviour. May 1979.

125. GUILE, A. E. Processes at arc cathode roots on non refractory metals having films of their own oxide. Welding Institute Conference, London. Arc Physics and Weld Pool Behaviour. May 1979.

126. ALLUM, C. J.
APPS, R. L. Underwater welding for construction and repair. Conference organised by the Society for Underwater Technology, London. 1981.

127. DYNACHENKO, V. V.
OLSHANSKII, A. N. Effect of controlled atmosphere pressure on welding process variables. Scar. Proiz. No.11. pp6-8. 1968.

128. WALDIE, B. Underwater cutting. Conference organised by the Society for Underwater Technology. January 1982.

129. BACH, F. Hanover Technical Institute. Verbal Presentation to IIW 212 Group at Hanover Meeting in 1979.

130. NISHIGUCHI, K.
MATSUNAWA, A. Arc characteristics and cathode by phenomena in low pressure atmospheres. Technology Reports of the Osaka University. Japan. Vol.19. No.897. 1969.

131. LEVIN, M. L. Some observations of the effect of pressure the tungsten inert gas arc. Proceedings of IEE Conference on Gas Discharge p300. Bucharest. 1969.

132. STALKER, A. W. and
SALTER, G. R. A preliminary study of the effect of increased pressure on the welding arc. Welding Institute Report no.RR-SMT-R-7504. April 1975.

133. HAMILTON, D. J.
GUILE, A. E. Br.J.App.Phys. (Series 2), 1, (3) pp335-42 1968.

134. PETRENKO, V. I. et al High current pulsed arc in hydrogen at pressures up to 400 atm. Proceedings of IEE. Bucharest Conference. 1969.

135. BOROVIK, E. S. et al Long high-pressure arcs. Sov.Phys. - Tech.Phys. Vol.6. No.11. May 1962.

136. MITIN, R. V. et al — A long high-press arc in argon. Sov.Phys. - Tech.Phys. Vol.9. No.2. Aug. 1964.

137. MITIN, R. V. et al — Pulsed heating of a high-pressure arc in argon I and II. Sov.Phys. - Tech.Phys. Vol.10. No.7. Jan.1966.

138. KNYAZEV, Yu.R.et al — Pulse high-pressure arc in helium and hydrogen. Sov.Phys. - Tech.Phys. Vol.12. No.3. September 1967.

139. BOROVIK, E.S. et al — Pulsed arc in argon at pressures up to $10^8 N/m^2$ (1000 Atm). Sov.Phys. - Tech.Phys. Vol.12. No.4. 1967.

140. BURRILL, E. L. and LEVIN, M. L. — The effect of pressure on the MIG welding arc Proc.IEE Conf. on gas discharges. pp.595-599, 1970.

141. WEIZEL, W. and ROMPE, R. — The theory of electric arcs and sparks. Leipzig, 1949.

142. PETERS, Th. — Z. Physik, 135, 573, 1953.

143. PINFOLD, B. E. — Private communication.

144. EDMONDS, T. G. ALLUM, C. J. PINFOLD, B. E. and NIXON, J. H. — The effect of pressure on the tungsten argon welding arc. Proc. of W.I International Conf. 'Arc physics and weld pool behaviour'. London, May 1979.

145. GROVES, D. — Current status of underwater welding for off shore pipelines and associated equipment. Proc. of W.I.Int. Conf. 'Pipeline Welding'. London, Feb. 1977.

146. ALLUM, C. J. PINFOLD, B. E. and NIXON, J. H. — High pressure inert gas shielded arcs (1-19 bars). IIW DOC XII - B - 286 - 80. 1980.

147. FRIND, G. and DAMSKY, B. L. — Electric arcs in turbulent flows IV US Airforce, Aerospace Research Labs. A.R.L. 70-0001. Jan. 1970.

148. KHAGENHJELM, H. O. — Hyperbaric welding at 320 MSW. Development of welding procedures. IIW DOC. CReAu 34-80.

149. CHRISTIENSEN — IWW DOC.

150. WALDIE, B. — Effects of increasing ambient pressure on cutting characteristics and heat transfer in plasma cutting. Proc. of IEE Conf. 'Gas Discharges and their Applications' paper 189. Edinburgh. 1980.

151. BAUDER, U. H. — A.R.L. Report. Steady state arc discharges at pressures up to 1000 bars. Wright-Patterson Air Force Base, Ohio, USA. 1969.

152. INGLIS, M. R. and NORTH, T. H. — Underwater welding: A realistic assessment. Welding and Metal Fabrication. April 1979.

153. PINFOLD, B. E. CLIFTON, T. and MOFITT, B. — Cranfield, internal report, 1973.

154. ZEMANSKY, — Heat and thermodyhamics. McGraw-Hill 5th Edition. 1968.

155. CLEMENTS, R. M. and SMY, P. R. — The floating potential of a Langmuir probe in a high-pressure plasma. J.PhysD: Appl.Phys. Vol.7, 1974.

156. CLEMENTS, R. M. and SMY, P. R. — Langmuir probe measurement of electron temperature in high pressure plasmas. J.Appls.Phys. Vol.44, No.8, August 1973.

157. — Handbook of thermophysical properties of solid materials. Vol.II, Pergamon Press. 1962.

158. JEANS, Sir J. — Kinetic theory of gases.. Cambridge Univ. Press.

159. SWIFT-HOOK, D. T. and GICK, A. E. F. — Penetration welding with lasers. CEGB report. R/M/N637 June 1972.

160. DRELLISHEK, K. S. KNOPP, C. F. and CAMBEL, A. B. — North Western University. Illinois, Report no.NU-GDL A.3.62. 1962.

161. ALLUM, C. J. PINFOLD, B. E. and NIXON, J. H. — Some effects of shielding gas flow on argon-tungsten arcs operating in high pressure (1 to 14 bars) environments. American Welding Journal. Research Supplement. July 1980.

162. HILTUNEN, V. and PIETIKAINEN, J. — Investigations and observations on material transfer in metal-inert-gas welding. Proc. of WI Int. Conf. 'Arc Physics and Weld Pool Behaviour'. London May 1979.

163. SHIMADA, W. and GOTOH, T. — Characteristics of high frequency pulsed DC TIG welding process. IIW DOC. 212-388-77.

164. MILLS, G. S. — Fundamental mechanisms of penetration in GTA welding. American Welding Journal. pp.21-S to 24-S. Jan. 1979.

165. WASZINK, J. H.
Van Den Heuvel, G.J.M. Heat generation and heat flow in the filler wire in GMA welding.
Philips Research Lab..report, Eindhoven, The Netherlands (MS.11.827) 1982.

Appendix 1

Calibration of Flow Meter for Use at Pressures Above 1 Bar

The device used here for measuring flow rates employed a float and tapered tube. In equilibrium the float's weight is balanced by a pressure gradient generated across the float. This arises from momentum dissipation across the float and may be represented by a drag coefficient (C_D).

$$\text{i.e. } \frac{1}{2}\rho . v^2 C_D = m.g/a$$

Where v is the free stream flow velocity hear the float and ρ is the gas density. m is the float mass and g the acceleration due to gravity. 'a' is an area factor related to the float diameter. The volumetric flow rate (W) is given by

$$W = v.A$$

(A is the tube cross-sectional area at the point with velocity v). Where it can now be seen that

$$W = A\sqrt{\frac{2m.g}{\rho C_D.a}}$$

For parabolic tapered tube profiles the float position (on a linear scale) is then proportional to the volumetric flow rate. To a first approximation C_D is expected to be independent of pressure since viscosity changes little with pressure (ref.166). It is then possible to write

$$W = K\frac{.S}{\sqrt{p}}$$

Where K is an instrument constant, p the absolute pressure in bars and S is a scale setting number. (for the flow meter used K = 10 ℓ/min). The pressure dependence inferred above was tested experimentally using the following procedure:-

1) The chamber was pressurised in a continuous manner using gas from only the flow meter.
2) Throughout the pressurization process the flow meter value was adjusted to regulate the float position to a setting(s) of four.

3) Measurements of chamber pressure were taken as a function of time at regular intervals.

These results are shown in table A1. This procedure allowed gas flow into the chamber to be quantified. i.e. Chamber pressure is given by

$$P = \frac{N k T}{V}$$

Where V is the chamber volume, T the temperature, k is Boltzmann's constant and N is the number of particles in the chamber.

The rate of change of pressure in the chamber ($\dot{P}$) may be written as

$$\dot{P} = \frac{\dot{N} k T}{V}$$

After a little manipulation this becomes

$$\dot{P} = \frac{P.W}{V}$$

$$\text{or} \quad W = \frac{\dot{P}}{P}.V$$

The right hand side of this expression was determined from data given in table A1 (Chamber Volume = 73 ℓ). The result is shown in figure A2 and compared with predicted values. It can be seen that good agreement exists.

Flow meters with this type of calibration curve give rise to decreasing (as $1/\sqrt{P}$) volumetric flow rates at constant setting (s) and increasing mass flow rates (as $\sqrt{P}$).

Figure A1 Calibration of flowmeter

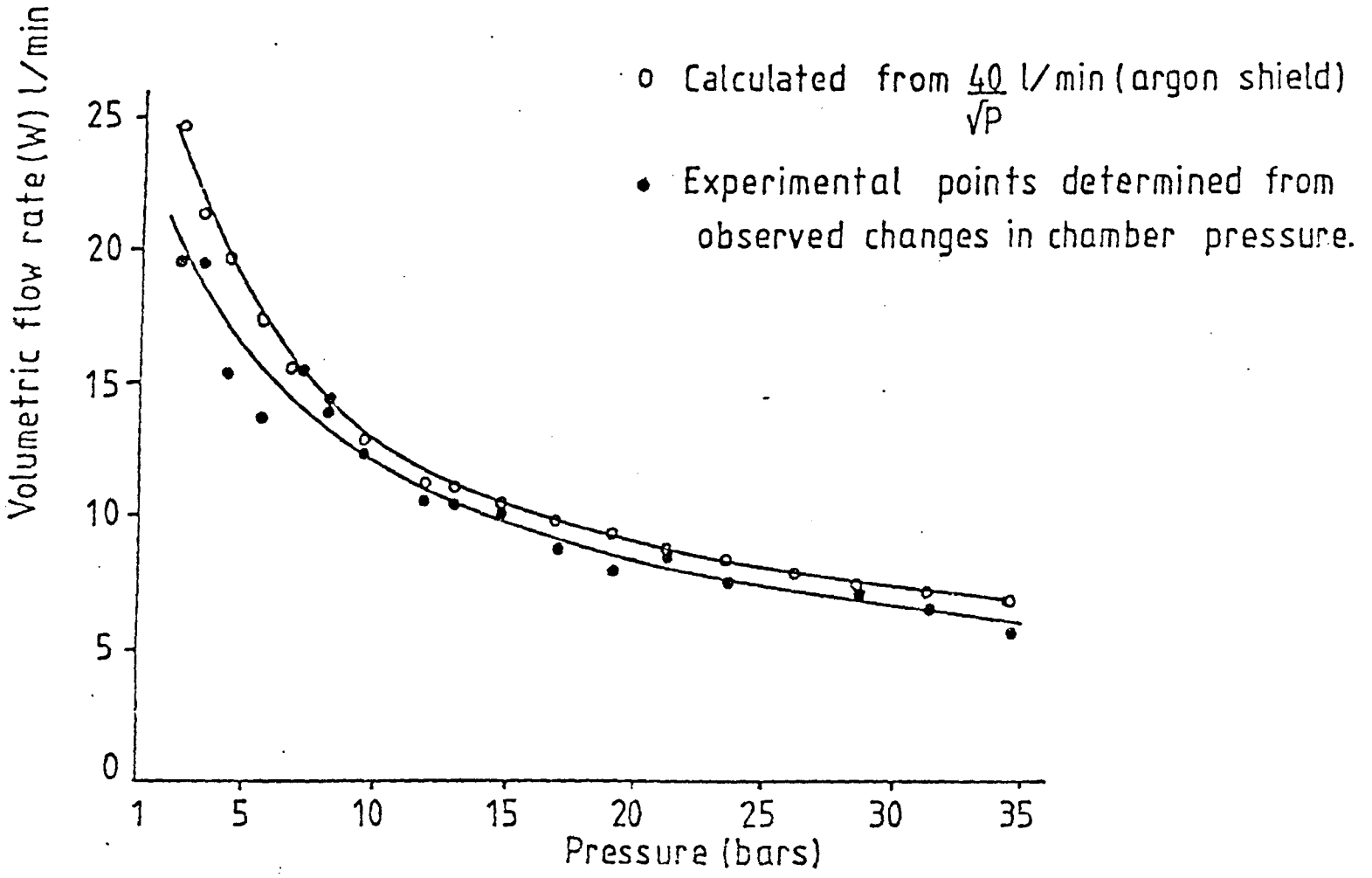

Time (mins,secs)	Chamber Pressure (PSI gauge)	Rate of Change of Chamber Pressure $\dot{P}$ (bar/min)	Experimental Flow Rate $\left(\frac{\dot{P} \cdot V}{P}\right)$ (ℓ/min)	Theoretical Flow Rate $40/\sqrt{P}$ (ℓ/min)
0,40	20			
1	23	0.71	19.9	24.8
1,20	27			
1,40	30			
2	35	0.92	19.8	21.7
2,20	39			
2,40	45			
3	49	0.92	15.6	19.3
3,20	54			
3,40	60			
4	65	1.02	13.8	17.2
4,20	70			
4,40	76			
5	85	1.43	15.4	15.3
5,20	90			
5,40	96			
6	104	1.53	13.8	14.1
6,20	111			
6,40	119			
7	126	1.63	12.4	12.9
7,20	135			
7,40	142			
8	150	1.63	10.6	12.0
8,20	158			
8,40	167			
9	176	1.84	10.3	11.1
9,20	185			
9,40	194			
10	204	2.04	10.0	10.4
10,20	214			
10,40	224			
11	234	2.04	8.8	9.7
11,20	244			
11,40	255			

Continued . . . .

12	265	2.04	7.8	9.2
12,20	275			
12,40	286			
13	297	2.45	8.5	8.7
13,20	310			
13,40	321			
14	333	2.45	7.5	8.2
14,20	345			
14,40	356			
15	370	2.76	7.7	7.8
15,20	383			
15,40	395			
16	410	2.86	7.2	7.4
16,20	423			
16,40	436			
17	450	2.86	6.6	7.1
17,20	464			
17,40	480			
18	495	2.65	5.6	6.8

Table A1. Chamber Pressure as a Function of Time. (Pressurized with Argon through a Flow Meter Maintained at a Constant Setting of S=4).

Appendix 2

Abel Transform Matrices

The area element (Aij) shown in figure 13 have been evaluated for a circle of unit radius. Calculations have been performed for unit circles divided into 5, 6 and 7 segments. Results are given below in matrix form where

$$A(N) = \begin{pmatrix} A11 & 0 & \cdots & & \\ A21 & A22 & \cdots & & \\ \vdots & \vdots & & & \\ AN1 & AN2 & \cdots & & ANN \end{pmatrix}$$

The area of the corresponding segment in a circle of radius R is then found by multiplying by R^2. Area elements Aij given below may be used to obtain the matrix elements required to convert current measurements to current densities

$$A(5) = 10^{-2} \times \begin{pmatrix} 3.142 & 0 & 0 & 0 & 0 \\ 4.511 & 4.913 & 0 & 0 & 0 \\ 4.121 & 5.392 & 6.195 & 0 & 0 \\ 4.058 & 4.474 & 6.206 & 7.253 & 0 \\ 4.034 & 4.260 & 4.868 & 6.937 & 8.175 \end{pmatrix}$$

$$A(6) = 10^{-2} \times \begin{pmatrix} 2.182 & 0 & 0 & 0 & 0 & 0 \\ 3.132 & 3.412 & 0 & 0 & 0 & 0 \\ 2.862 & 3.744 & 4.302 & 0 & 0 & 0 \\ 2.818 & 3.107 & 4.310 & 5.037 & 0 & 0 \\ 2.801 & 2.958 & 3.381 & 4.817 & 5.677 & 0 \\ 2.793 & 2.894 & 3.133 & 3.647 & 5.279 & 6.252 \end{pmatrix}$$

$$A(7) = 10^{-2} \times \begin{pmatrix} 1.603 & 0 & 0 & 0 & 0 & 0 & 0 \\ 2.302 & 2.507 & 0 & 0 & 0 & 0 & 0 \\ 2.103 & 2.751 & 3.161 & 0 & 0 & 0 & 0 \\ 2.070 & 2.283 & 3.166 & 3.701 & 0 & 0 & 0 \\ 2.058 & 2.173 & 2.484 & 3.539 & 4.171 & 0 & 0 \\ 2.052 & 2.127 & 2.302 & 2.679 & 3.879 & 4.593 & 0 \\ 2.049 & 2.101 & 2.216 & 2.434 & 2.866 & 4.191 & 4.980 \end{pmatrix}$$

Appendix 3
(see section 3.6.5.3)

Radiative Characteristics of a Point Source Arc

The conditions under which an arc may be regarded as a point source of radiation may be obtained by considering figure 40. It is assumed that no self absorption occurs within the arc and that the arc radiates isotropically above a reflecting surface. An elemental arc region (δV) may then be regarded as a real (Q) and imaginary (Q') source such that the radiative flux from δV through an area A at a distance $\underline{\ell} + \underline{a}$ from Q and $\underline{\ell} - \underline{a}$ from Q' is

$$\delta q = \frac{A.\varepsilon}{4\pi} \left(\frac{Q}{|\underline{\ell}+\underline{a}|^2} + \frac{Q'}{|\underline{\ell}-\underline{a}|^2} \right)$$

i.e. see equation 77. $\underline{\ell}$ is a vector from the point of intersection of Q and Q' with the pool and disc centre. $\pm \underline{a}$ is a vector from the pool centre to Q and Q' respectively.

writing $Q' = \alpha Q$

and $e = |\underline{a}|/|\underline{\ell}|$

gives

$$\delta q = \frac{Q.A.\varepsilon}{4\pi\ell^2} \left(\frac{1}{1 + e^2 + 2e.\cos\beta} + \frac{\alpha}{1 + e^2 - 2e.\cos\beta} \right)$$

where β is defined by the direction cosine between $\underline{\ell}$ and $\underline{a}$

i.e. $(\hat{\underline{\ell}}.\hat{\underline{a}}) = \cos\beta$

$$\text{i.e.} \quad \delta q = \frac{Q.A.\varepsilon}{4\pi\ell^2} \left(\frac{(1+e^2).(1+\alpha) - 2e\cos\beta.(1-\alpha)}{(1+e^2)^2 - (2e.\cos\beta)^2} \right)$$

The most difficult characteristics to account for are encountered by a strongly radiating imaginary source ($\alpha \approx 1$) with the real source near the electrode ('a' becomes equal to arc length). Then

$$\delta q \approx \frac{Q.A\varepsilon}{4\pi\ell^2} \left(\frac{1+e^2}{(1+e^2)^2 - (2e\cos\beta)^2} \right)$$

$$\simeq \frac{Q \cdot A\varepsilon}{4\pi \ell^2} \left[1-e^2(1-4\cos^2\beta) + O(e^4)\right]$$

The arc therefore appears a point source to within 1% when

$$0.01 \simeq e^2 \left|(1-4\cos^2\beta)\right|$$

The most unfavourable case is for $\cos\beta = 1$. Then

$$\ell > 10\sqrt{3}\, L$$

Where L is the arc length. Taking L $\sim$ 10mm (as used in some radiation tests) gives

$$\ell > 18\text{cm}$$

Experiments performed here used 'disc-arc' separations of 20cm and so point source characteristics are expected to be obeyed.

Appendix 4

Anode Fall Field Strength

An estimate of the field strength (E) in the anode fall may be obtained from

$$E = \frac{V_a}{\lambda_D}$$

Where λ_D is the extent (see equation 2) of the region over which the anode fall voltage (V_a) exists. It must be emphasised that this estimate is only very approximate as λ_D assumes the existence of collision dominated conditions. From equation 2

$$\lambda_D \propto \frac{1}{\sqrt{n_+}}$$

Where n_+ is the number of positive ions per unit volume. Under equilibrium conditions this is given by Saha's equation and may be expressed as

$$\frac{n_- . n_+}{n_o} = F(M, V_I, T)$$

i.e. for single ionization processes

$$e^- + A^+ \rightleftharpoons A^o + \text{energy}$$

Where F is a function of ionic mass (M), ionization potential (V_I) and temperature (T). n_o is the number density of neutral particles at pressure P and n_- is the number density of electrons. For a plasma

$$n_- = n_+$$

hence

$$n_+^2 = n_o . F(M, V_I, T)$$

Under the temperature conditions encountered in argon TIG arcs only relatively low degrees of ionization occur (typically less than 10%). Hence

$$n_o \propto P$$

and therefore

$$n_+ \alpha P^{1/2}$$

$$\text{and} \quad \lambda_D \alpha P^{-1/4}$$

$$\text{i.e.} \quad E \alpha P^{1/4}$$

This argument assumes that temperature is unaffected by pressure. It has been observed that temperatures associated with changes in electrical conductivity are little affected by pressure and so this assumption has some basis. However, the strong temperature dependence of F means that the above argument has only a qualitative significance.

Appendix 5

J. Phys. D: Appl. Phys., 14 (1981) 1041–59. Printed in Great Britain

Gas flow in the column of a TIG welding arc

CJ Allum
Department of Materials, Cranfield Institute of Technology, Cranfield, Bedford MK43 0AL, UK

Received 12 June 1980, in final form 9 October 1980

Abstract. Gas motion in the column of a TIG welding arc is described by assuming a gaussian form for the radial dependence of the axial velocity. Momentum equations are then solved with magnetic, viscous and gravitational body forces. The predicted dependence of axial velocity on arc length and current is in good agreement with experimentally measured values which have been obtained by manometrically observing the pressure distribution at the anode of a TIG arc. Particular attention is given to the effect of electrode characteristics and ambient pressure on gas flow.

1. Introduction

Welding arcs have many peculiarities not to be found in other types of arc. These arise from the short arc lengths ($< 10^{-2}$ m) normally employed and the moderate range of currents (50–500 A) necessary for weld pool control. Such arcs are transitional in nature having properties common to high current (e.g. 10 kA circuit breakers) and low current (> 30 A) buoyancy dominated arcs. Electrode characteristics may have a considerable influence on arc behaviour. For example, many welding processes employ a consumable electrode of continuously changing geometry. The characteristics of such arc columns are dominated by metal vapour and vaporisation may play a significant role in gas flow behaviour. Nonconsumable arcs are simpler to consider. The most widely used nonconsumable arc welding process is Tungsten Inert Gas (TIG) where an arc is commonly struck between a pointed rod electrode and a plate anode. This is the situation investigated here. However, the 'equivalent cathode' approach adopted here may be extended to other electrode geometries.

Gas flow is an important and poorly understood factor in welding and may influence the integrity of welds in a variety of ways. Atmospheric contaminants entrained by the arc may effect arc and electrode characteristics and consequently weld metallurgical properties. Weld geometry is in part determined by convective heat transferred from the hot neutral arc gas to the liquid metal. Further effects may be involved if the stagnation pressure of the gas flow causes a pool depression, e.g. modified heat transfer geometry and possibly a change in metal flow within the pool.

Models of gas flow in TIG arc columns must account for the interaction of arc current with the associated magnetic field. Maecker (1955) first showed that velocities predicted by such a mechanism are of the same order as those found experimentally (Wienecke 1955). However Maecker's model neglects viscosity and is consequently limited in application. Other models (e.g. Lancaster 1966, Chang *et al* 1979) have regarded the arc as being essentially similar to a free jet with a magnetic source of momentum. It is shown

0022-3727/81/061041 + 19 $01.50

here that such an approach has a large number of unsatisfactory features. In the present model viscous, magnetic and buoyancy forces are considered and account is taken of the inherently short arc lengths used in welding.

2. Model of a TIG arc column

Before formulating a mathematical model of a TIG arc column, some attention is given to the principle features of such a column. The conditions under which welding is performed correspond to a convectively stabilised arc with a strong cathodic contraction giving rise to a bell shaped arc envelope. The anodic contraction is generally weak although at current–arc length combinations outside the scope used for welding, an anode spot mode may occur. Such arcs are generally asymmetrical and difficult to model (see§2.1). Under normal atmospheric welding conditions TIG arcs exhibit a high degree of stability. Turbulent shielding gas flows and other disruptive effects may influence arc behaviour at higher pressures (Allum 1980). However at atmospheric pressure shielding gas flows are generally of Reynolds numbers lower than 2000 and typically velocities are of order 1 m s^{-1}. TIG arcs may therefore reasonably be regarded as operating in stagnant atmospheres. The stability of TIG arcs is reflected in a highly directed, jet-like, flow away from the cathode with a good degree of radial symmetry. Arc column Reynolds numbers are found to be well within the laminar regime (see §5) and so turbulent effects are negligible. These considerations allow a reduction in the general form of equations governing flow behaviour. The relevant Maxwell, momentum and continuity equations are given by equations (1)–(5). Viscous, magnetic and buoyancy forces are included in the momentum equations discussed here. To solve these equations for the axial velocity, a form of current density consistent with the thermodynamic properties of the arc column is required. This allows the magnetic and pressure terms to be evaluated. Many previous investigations have taken the current density to be uniform across the arc. This is unlikely to be realistic in the presence of large radial temperature gradients. The behaviour of the electrical conductivity with temperature suggests that arcs have sharp electrical boundaries. However the appearance in the column of material vaporised from the anode may lead to a peaked distribution. In keeping with results found by Gvozdetskii (1974) the axial current density is taken as having a gaussian form.

The treatment given here makes the energy equation redundant by postulating a gaussian form for the axial velocity. A detailed discussion of the consequences of this restriction is delayed until solutions have been obtained for the axial velocity.

2.1. Mathematical formulation

The model described allows the relevant momentum, Maxwell and continuity equations to be written in cylindrical polar coordinates (r, z) as:

$$\rho U\cdot\nabla U_z=-\frac{\partial p}{\partial z}+J_rB+\frac{1}{r}\frac{\partial}{\partial r}\left(\eta r\frac{\partial}{\partial r}U_z\right)+(\rho-\rho_\infty)g_z \tag{1}$$

$$0=-\frac{\partial p}{\partial r}-J_zB \tag{2}$$

$$\frac{1}{r}\frac{\partial}{\partial r}(rB)=\mu_0J_z \tag{3}$$

$$\frac{\partial B}{\partial z} = -\mu_0 J_r \tag{4}$$

$$\frac{\partial}{\partial r}(\rho r u_r) = -\frac{\partial}{\partial z}(\rho r u_z). \tag{5}$$

u and J are vectors representing velocity and current density respectively. The suffixes r and z, when applied to the components of these vectors, represent radial and axial components respectively; p is the excess pressure with respect to the ambient pressure; B is the azimuthal magnetic field and g_z is the component of gravitational acceleration seen by the arc ($g_z = g\cos\theta$). θ is an angle between the action of g ($g = 9.81$ m s^{-2}) and the axis of arc symmetry z. The material properties are ρ, density of arc gas; ρ_∞, density of ambient gas; η, viscosity of arc gas. μ_0 is the permeability of free space. The region of contact between arc and cathode (cathode spot) is ill defined and an unsuitable origin for the coordinate system (r, z). Instead, the origin is taken at the centre of an 'equivalent cathode', disc shaped in geometry, and situated a distance δ downstream of the electrode tip. The physical situation at the cathode can then be treated by prescribing boundary conditions at a suitably chosen equivalent cathode.

An expression for the axial momentum flux F may be obtained by considering equations (1), (4) and (5). Substituting equations (4) and (5) into the axial momentum equation gives:

$$\frac{\partial}{\partial z}[\rho U_z^2 + P + (B^2/2\mu_0)] + (\rho_\infty - \rho)g_z = \frac{1}{r}\frac{\partial}{\partial r} r\left(\eta\frac{\partial}{\partial r}U_z - \rho U_r U_z\right).$$

Using the symmetry and still atmosphere conditions and integrating across the flow gives

$$\frac{\partial F}{\partial z} = -2\pi\int_0^\infty \{(\partial/\partial z)[P + (B^2/2\mu_0)] + (\rho_\infty - \rho)g_z\}\, r\, dr \tag{6}$$

with

$$F = 2\pi\int_0^\infty r\rho U_z^2\, dr. \tag{7}$$

A further useful relation may be obtained by looking at the axial value of equation (1). When $r = 0$ this becomes

$$\rho U_z(0,z)\frac{d}{dz}U_z(0,z) = -\frac{dP}{dz}(0,z) + \left[\eta\frac{1}{r}\frac{\partial}{\partial r}\left(r\frac{\partial}{\partial r}U_z\right)\right]_{(r=0)} + (\rho - \rho_\infty)g_z. \tag{8}$$

By symmetry, the axial magnetic field is zero so the $J \wedge B$ body force does not appear in equation (8). This expression shows that the magnetic force affects axial motion by creating an axial pressure gradient. It then follows that free jet type solutions are obtained if the pressure term in the axial momentum equation is neglected—even with the retention of the $J \wedge B$ term. This explains why Lancaster's solution (1966) obtained by including the magnetic force ($J_r B$) in equation (1), but neglecting the associated pressure, differed only in detail from that found for a free jet. Equations (6) and (8) form the basis of the present study.

The axial dependence of the viscous term in (8) may be found from the gaussian assumption, i.e.

$$U_z(r,z) = U_z(0,z)\exp(-ar^2)$$

where $a(z)$ is related to the momentum flux by equation (7). Integrating equation (7)

gives

$$a(z)=\pi\rho U^2{}_z(0,z)/2F. \tag{9}$$

This allows the viscous term in equation (8) to be identified. Therefore

$$\rho U_z(0,z)\frac{\mathrm{d}}{\mathrm{d}z}U_z(0,z)=-\frac{\mathrm{d}P}{\mathrm{d}z}(0,z)-\frac{2\pi\eta\rho U_z{}^3(0,z)}{F}-(\rho_\infty-\rho)g_z. \tag{10}$$

Identification of $a(z)$ by equation (9) has involved the additional assumption that density changes little over the region of flow. If momentum diffused as far as the cold atmosphere then an error of two orders of magnitude may be involved with this assumption. However, for the above distribution of velocity it may be shown that the integration is justified provided the inequality below holds:

$$[U_z(0,z)/U_z(R,z)]^2\gg\langle\rho\rangle/\langle\rho_\infty\rangle.$$

where R is the electrical arc boundary, $\langle\rho\rangle$ the mean density within this boundary and $\langle\rho_\infty\rangle$ the mean density from R, across the heat affected zone, to some region where negligible flow occurs. It is later found (§6) that even for unfavourable circumstances:

$$(\sim 20)^2\gg(\sim 10).$$

The inequality is clearly satisfied and the effect of neglecting momentum flow in the heat affected zone is negligible.

The axial pressure gradient in equation (10) may be evaluated by introducing a gaussian distribution of current density into Maxwell's equations and integrating the radial momentum equation.

Accordingly, current density is written as

$$J_z(r,z)=J_z(0,z)\exp(-br^2)$$

where $b=b(z)$. For convenience the maximum values of current density, $J_z(0,z)$, and velocity, $U_z(0,z)$, will be written as J_0 and U_0 respectively. The parameters J_0 and b are readily related by the conservation of current condition.

$$I=\pi(J_0/b). \tag{11}$$

It is convenient to introduce an arc boundary, $R(z)$, by considering the mean current density J where

$$J=I/\pi R^2. \tag{12}$$

Further, if C is the fraction of current outside R then

$$J=J_0\frac{(C-1)}{\ln C}. \tag{13}$$

In subsequent calculations a value of 0.05 is assigned to C although this value is not critical. Equation (13) allows b and J_0 to be related to $R(z)$. However $R(z)$ cannot be found from the equations forming the basis of the present model. A suitable form is given to $R(z)$ in §5.

The distribution of magnetic field may now be obtained by integrating one of Maxwell's equations. The result is

$$B=\frac{\mu_0 I[1-\exp(-br^2)]}{2\pi r}. \tag{14}$$

Integrating the radial momentum equation with this value of B, yields:

$$P(r, z)=(\mu_0 I J_0/4\pi)G(\infty, br^2) \tag{15}$$

where G is defined by the integral

$$G(a, b)=\int_b^a \frac{\exp(-x)\,[1-\exp(-x)]}{x}\,dx. \tag{16}$$

Relevant properties of $G(a, b)$ are given in the appendix and used when required.

Of particular interest is the axial value of the excess pressure $P(0, z)=P_0$. From the above expressions

$$P_0=(\mu_0 I J_0/4\pi)G(\infty, 0)$$

therefore

$$P_0=(\mu_0 I J_0/4\pi)\ln 2. \tag{17}$$

Maecker (1955) obtained a similar expression for the axial pressure for a uniform current density across the column. In Maecker's expression J replaces $J_0 \ln 2$ above. Therefore, equation (17) predicts a maximum pressure that is larger by a factor of 2.16 than that given by Maecker. Substituting for $P(0, z)$ from equation (17) allows equation (10) to be written as

$$\rho U_0 \frac{dU_0}{dz}=\frac{\mu_0 I \ln 2}{4\pi}\frac{dJ_0}{dz}-\frac{2\pi\eta\rho U_0^3}{F}-(\rho_\infty-\rho)g_z. \tag{18}$$

F may be evaluated by considering the magnetic and pressure terms in equation (6) which becomes

$$\frac{\partial F}{\partial z}=-2\pi\int_0^\infty \varphi\, r\, dr-2\pi\int_0^\infty g_z(\rho_\infty-\rho)\, r\, dr \tag{19}$$

where

$$\varphi=\frac{\partial}{\partial z}[P+(B^2/2\mu_0)].$$

Equations (11), (14) and (15) may be used to show that

$$\varphi=\frac{\mu_0 I}{4\pi}\frac{dJ_0}{dz}G(\infty, br^2) \tag{20}$$

therefore

$$\frac{\partial F}{\partial z}=-\frac{\mu_0 I}{4}\frac{dJ_0}{\partial z}\int_0^\infty G(\infty, br^2)\,dr^2-2\pi g_z\int_0^\infty(\rho_\infty-\rho)\, r\, dr. \tag{21}$$

The first integral in this expression may be evaluated (see Appendix). F is then readily shown to be

$$F(z)=F(0)+\frac{\mu_0 I^2}{8\pi}\ln\frac{J_0(0)}{J_0(z)}-2\pi z g_z\int_0^\infty(\rho_\infty-\rho)\, r\, dr. \tag{22}$$

$F(0)$ is a constant of integration identified as the momentum flux at an equivalent cathode situated close to the tip of the electrode. It is in this region of strong entrainment that enthalpy flow is developed. An initial momentum flux may be created, independently of magnetic effects, by rapid expansion of entrained gas and the associated pressure exerted at the electrode surface and magnetic arc wall.

The second term in equation (22) is a magnetically generated component of the axial momentum flux. This reduces to an expression first found by Maecker (1955) when J_0 is related to the arc boundary, i.e.

$$(\mu_0 I^2/4\pi) \ln [R(z)/R(0)]. \tag{23}$$

It is interesting to note (from equation (22)) that a significant increase in $J_0(z)$, by for example anodic vaporisation, causes F to decrease. This may be interpreted in terms of an arc jet competing with an anode jet and thereby reducing the net flux. Such a picture is consistent with the bell shape of a TIG arc. Observation indicates that the arc boundary increases rapidly from the cathode spot. Most of the arc column momentum generation should therefore come from this region as the logarithmic term in equation (22) changes slowly. These considerations show that it is not unreasonable as a first approximation, to represent the momentum flux of an arc column as being generated by a point source situated at the cathode spot. Equations developed here will be shown to incorporate features of such solutions (see §4).

The buoyancy term in equation (22) may be evaluated if the arc composition and temperature field are known. Such detailed information is generally not available. An estimate of the importance of this term may be obtained by introducing an effective radius R_H of the heat distribution such that

$$2\pi z g_z \int_0^\infty (\rho_\infty - \rho)\, r\, dr \simeq \pi R_H^2 z g_z \rho_\infty. \tag{24}$$

This is consistent with the 'top-hat' distribution given by

$$\rho/\rho_\infty = \begin{cases} \ll 1 & R_H \geqslant r \\ = 1 & R_H < r. \end{cases}$$

The arc column density falls sufficiently slowly with temperature for R_H to correspond to an isotherm beyond that of the luminous arc boundary (corresponding to about 7000 K for an argon arc). Experimental results (Allum 1980) indicate that R_H increases with pressure despite a decrease in the electrical and luminous boundaries with increasing pressure. R_H is not proportional to other types of arc boundary introduced here and is therefore a difficult factor to account for. Despite this, it is clear from equation (24) that the buoyancy term increases with both arc length and environmental pressure; (R_H also increases with both these factors). This may be interpreted by supposing that a momentum jet generated by buoyancy forces opposes that generated magnetically by the arc current. There is experimental evidence suggesting that a change in arc mode may occur as a result of this action (Allum 1980). With increasing buoyancy, an anode spot mode is developed which is associated with a decrease in stability, i.e. TIG arcs are convectively stabilised. Equations (23) and (24) may be used to quantify these ideas by estimating the importance of buoyancy with respect to magnetic momentum flux. From these equations the buoyancy force is negligible when

$$I^2 \gg \frac{4\pi^2 |g_z| \rho_\infty z R_H^2}{\mu_0 \ln [R(z)/R(0)]}.$$

Suppose that the buoyancy force becomes important when it is, say, 10% or more of the magnetic term. The critical current I_c at which this occurs is

$$I_c = \left(\frac{40\pi^2 |g_z| \rho_\infty z R_H^2}{\mu_0 \ln [R(z)/R(0)]} \right)^{1/2}.$$

For a typical 100 A argon TIG arc the following values are assigned

$$\rho_\infty = 2 \text{ kg m}^{-3}$$

$$z = 5 \times 10^{-3} \text{ m}$$

$$|g_z| = 9.8 \text{ m s}^{-2} \text{ (i.e. } \Theta = 0)$$

$$R(z)/R(0) \simeq 5$$

$$R_H \simeq 5 \times 10^{-3} \text{ m}.$$

The expression is insensitive to the ratio of cathode to anode spot diameters. No great error is made by taking this value as 5. Experiments (Nestor 1966, Allum 1980) have shown that the distribution of heat at the anode is much broader than that of current. A reasonable estimate of R_H for the arc considered here is taken with reference to Nestor's work (Nestor 1966) as 5 mm.

Substituting into the last expression gives

$$I_c \simeq 22 \sqrt{p} \text{ A}$$

where p is the ambient pressure in bar. This result suggests that it is realistic to neglect buoyancy in the short TIG arcs used for welding at 1 atm. However, this is not necessarily true at higher pressures. According to this expression, the pressure at which buoyancy should influence a 100 A argon TIG arc of 5 mm length is about 20 bars or 200 m of sea water in underwater welding applications. Marked differences in the positional capability of the process should be noticed near this depth. The above considerations show the buoyancy term in equation (18) to be negligible although buoyancy should be accounted for in the expression for F at high pressures. This indicates that buoyancy is negligible on the axis, where the arc jet is strongest, but of some relative consequence when averaged across the arc. However, the buoyancy force falls with radial distance indicating that the jet velocity is falling correspondingly more quickly in the radial direction. This is in keeping with a result of §6 showing axial momentum to be confined within the arc boundary. Buoyancy then has little competition in the heat-affected arc zone. In situations where buoyancy is important the arc is expected to be asymmetrical (as in the anode spot mode) and probably unstable. Equations obtained here will not then apply. Consequently buoyancy will be neglected in the solutions of following sections.

3. Inviscid solution

When viscous dissipation is negligible the solution of equation (18) may be written as

$$U_0^2(z) = U_0^2(0) + \frac{\mu_0 I J_0(0) \ln 2}{2\pi\rho} \left(1 - \frac{J_0(z)}{J_0(0)}\right).$$

To compare this expression with that previously found by Maecker (1955) the initial velocity is put equal to zero. This then gives

$$U_0(\infty) = 1.48 \, V_M$$

where V_M is the 'Maecker velocity' as given by

$$V_M=\left(\frac{\mu_0 I J(0)}{2\pi\rho}\right)^{1/2}.$$

The magnitude of V_M is too large to account for experimental results (§7).

4. Point momentum source model

The inviscid model regards momentum as being provided by an extended source along the arc axis. Velocity at the cathode was taken as zero and viscosity was neglected. In this model the opposite approach is adopted. Arc column momentum is regarded as being generated entirely at the cathode, i.e. by a point source of momentum. This is essentially equivalent to neglecting current in the arc column. Placing $I=0$ in equation (18) gives

$$\rho U_0 \frac{\mathrm{d}}{\mathrm{d}z} U_0 \simeq -2\pi\eta\rho U_0^3/F$$

with

$$F=F(0)=\text{constant.}$$

therefore

$$U_0=F(0)/2\pi\eta z. \tag{25}$$

This solution shows a singularity at the cathode, as might be expected from a point momentum source model. It is also very similar to that obtained for a free jet in which case the factor of 2 is replaced by 8/3. The inclusion of viscosity allows for the radial diffusion of momentum and the accompanying reduction in axial velocity. However this axial drop-off in velocity is quicker than might be expected from experimental results (see §7). The physical justification of this approach is based on the behaviour of the rotational part of the $J\wedge B$ body force, i.e. that part of the force which cannot be balanced by a pressure term and is in turn responsible for fluid motion. Using expressions from §2, it can be shown that

$$\text{curl}\,(J\wedge B)=\frac{\partial\varphi}{\partial r}\theta$$

where θ is a unit vector in the azimuthal direction. φ is proportional to the rate of change of the axial current density (see equation (20)). The rotational part of the $J\wedge B$ force therefore has a strong axial dependence in a diverging arc column. It follows that momentum creation is mostly concentrated near the electrode.

The magnetic force is introduced into $U(0)$ through $F(0)$. Close estimates of $F(0)$ appear difficult to make and so dimensional analysis is used to give the form of $F(0)$. If the functional form of $F(0)$ is given by

$$F(0)=\text{function}\,(\mu_0, I, \text{length scale, geometry of current distribution})$$

then

$$F(0)=\kappa\mu_0 I^2$$

where κ is an empirical dimensionless parameter depending on the geometry of the current distribution. Experimental results presented here (see §7) suggest that

$$\frac{1}{2\pi}\gtrsim\kappa\gtrsim\frac{1}{8\pi}.$$

For present purposes, the lower bound value is adopted. The axial velocity now becomes

$$U_0=\frac{\mu_0}{(4\pi)^2}\frac{I^2}{\eta z}. \tag{26}$$

This result is in broad agreement with the more general treatments of Lancaster (1966) and Chang *et al* (1979). Taking η (10 000 K) $=2.25\times10^{-4}$ kg m s^{-1} (Metcalfe and Quigley 1975) and considering a 100 A, 5 mm-long argon arc gives $U_0\simeq72$ m s^{-1}. This is substantially lower than the value of 303 m s^{-1} predicted by the inviscid solution. To obtain this last value the density and current density have been taken as 4.8×10^{-2} kg m^{-3} (Metcalfe and Quigley 1975) and about 10^8 A m^{-2} (Guile 1969) respectively.

However, this comparison is strongly dependent on values of current and arc length used, i.e. with $I=300$ A and $z=2$ mm the viscous value is 1446 m s^{-1} and the inviscid value 530 m s^{-1}. The real situation is likely to be between these extremes. A model accounting for both factors is therefore required.

Solutions of the free jet problem (Loityanskii 1960) show that the jet 'diameter' falls with increasing Reynolds number, i.e. increasing current in the present case. Further, it is found that the total axial mass flow is $8\pi\eta z$ with half of this being nearly parallel to the axis and within the jet diameter. Clearly incompressibility is not an acceptable assumption in such a model. These results contrast solutions accounting for both magnetic and viscous forces (§6) where gas flow is confined to the arc and arc diameters are found to increase with increasing current. Despite these differences there are many features of the more general solutions (see §§5, 6 and 7) that can only be understood in terms of the action of viscosity. The behaviour of this model is particularly important in interpreting the effect of initial conditions (i.e. $W(0)$) on flow behaviour.

5. Numerical solutions

For the purpose of numerical computation it is convenient to normalise equations (18) and (22). Velocity is normalised with respect to the inviscid solution $U_0(\infty)$. Arc radius and axial distances are normalised with respect to the equivalent cathode spot radius. Equation (18) now becomes

$$\frac{\mathrm{d}}{\mathrm{d}x}\left(W^2+\frac{1}{r^2}\right)=-\frac{16\times\ln 2\times\ln 20}{0.95}\frac{W^3}{Ref} \tag{27}$$

and

$$f=f(0)+\ln r \tag{28}$$

where

$$W=U_0/U_0(\infty)$$

$$r=R/R(0)$$

$$x=z/R(0)$$

$$f(z)=F(z)/(\mu_0 I^2/4\pi)$$

$$Re=2R(0)\,U_0(\infty)\rho/\eta.$$

The relation $r=r(x)$ is required for closure of these equations. Optical and electrical boundaries away from the anode may be approximately represented by $r\simeq1+Ax^n$ where A is a constant and $1\geqslant n>0$. Calculations were performed for parabolic and conic

forms of r, both of which are found to exhibit the same qualitative behaviour. When the effective cathode is centred near the electrode tip ($\delta \simeq 0$), a reasonable representation of axial changes in the current density is given by $r \simeq 1 + \sqrt{x}$. Calculations presented here are based on this expression although recourse to energy considerations is strictly required. The Reynolds number defined above is based on the cathode spot diameter and inviscid velocity at a large distance from the cathode. Substituting for $U_0(\infty)$ gives

$$Re = \frac{I}{\eta \pi}\left(\frac{2\mu_0 \rho \ln 2 \times \ln 20}{0.95}\right)^{1/2}.$$

Re does not depend on a length scale and is proportional to arc current and the square root of ambient pressure. For a 100 A argon TIG arc $Re \simeq 72\sqrt{p}$. On this basis flow within a TIG arc is laminar at 1 atm. Reynolds numbers based on inviscid solutions are not unique. If the point momentum solution is used then a Reynolds number $Re(V)$ based on this is

$$Re(V) = \frac{1}{8}\frac{\rho \mu_0 I^2}{\eta^2 \pi^2}\frac{R(0)}{L}$$

where L is the arc length. Relating this to the magnetic value gives

$$Re = 11.85\,(x\,Re(V))^{1/2}.$$

This confirms that the flow is laminar, with the possible exception of very short arcs ($L \simeq R(0)$), i.e. considering the least favourable case of $x = 1$, shows that $150 \leqslant Re(V) \leqslant 3732$ for $100 \leqslant I \leqslant 500$ A. It now remains to specify the initial momentum flux $f(0)$. This may be accomplished in a number of ways, e.g.

(i) An experimentally determined function, f, may be substituted into equation (27) and the calculated velocities compared to experimental values.

(ii) Calculations may be performed which account for arc structure near the cathode. This is in general a very difficult task and will involve energy balance considerations.

(iii) An arbitrary normalised initial velocity may be specified, i.e. using equation (9) $f(0)$ may be expressed in terms of $W(0)$ and related to the initial mass flux (see §6).

Here, $f(0)$ is equated to $W(0)^2$ and solutions are sought for the range $1 \geqslant W(0) \geqslant 0.1$. To avoid singularities computation is started at $x = 0.1$. Equations (27) and (28) may now be written as

$$\frac{\mathrm{d}}{\mathrm{d}x}\left(W^2 + \frac{1}{r^2}\right) = -\frac{17.49}{Re}\frac{W^3}{[W(0)^2 + \ln r]} \tag{29}$$

where

$$f = W(0)^2 + \ln r$$

$$r = (1 + \sqrt{x}) \qquad x \geqslant 0.1.$$

Numerical solutions for W have been obtained (figure 1). Solutions have the same axial dependence for $W(0) = 0.1$ and 1. It can be seen that arc velocity initially increases under the action of the magnetic force. Viscous forces then become dominant and the velocity falls. This behaviour is readily understood in terms of the approximate solutions previously obtained. The existence of an axial momentum source ensures that the velocity falls much less slowly than in free jet solutions. It is interesting to note that the maximum

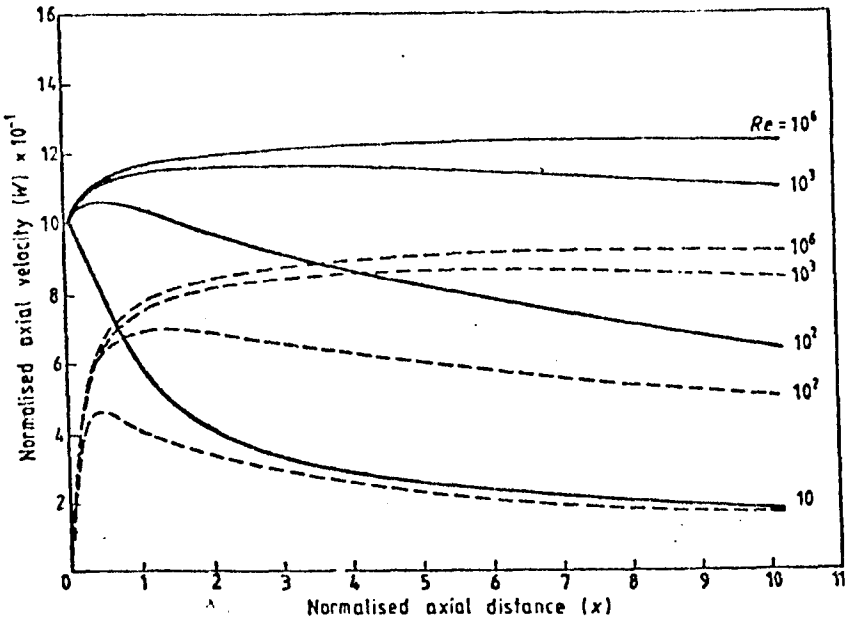

Figure 1. The effect of Reynolds number on the axial velocity for a parabolic arc profile with $W(0.1)=0.1$ (broken curve) and 1.0 (full curve).

pressure at the anode may be the same for a very short arc as for a much longer one. By placing $dW/dx=0$ in equation (29) it can be shown that the position of the maximum velocity moves away from the cathode with increasing Reynolds number in accordance with $Re^{1/3}$. This implies that the position of the maximum moves downstream with increasing pressure in a manner described by $P^{1/6}$. However, it is noticed that the position at which viscous forces become important moves closer to the cathode with increasing initial momentum flux.

Cathodic conditions, as represented by $W(0)$, clearly effect the flow. This initial effect is not preserved with increasing arc length. For example, the initial difference of a factor of ten between $W(0.1)=1$ and $W(0.1)=0.1$ for $Re=100$ is reduced to 1.5 at a normalised axial distance of 10. A similar comparison (not shown graphically) between $W(0.1)=0.5$ and $W(0.1)=0.1$ gives a much smaller difference (~ 1.1). To compute effects of arc length, current and ambient pressure on the axial velocity, normalisation factors must be known. Experiments with argon arcs indicate that it is reasonable to take:

(i) $J(0)\simeq 10^8$ A m^{-2} (Guile 1969)
(ii) $J(0)$ is substantially independent of current (Savage *et al* 1965)
(iii) $J(0)\sim P^{0.28}$ where P is pressure in bar (Allum *et al* 1980a).

These give

$$R(0)=0.56\,P^{-0.14}\,(I/100)^{0.5}\ (\text{mm})$$

$$Re=72.4\,P^{0.5}\,(I/100)$$

$$U_0(\infty)=303.1\,P^{-0.36}\,(I/100)^{0.5}\ (\text{m s}^{-1})$$

where a temperature of 10^4 K has been used. Use has also been made of the result that viscosity is independent of pressure at temperatures encountered in TIG arcs (Kannappan and Bose 1977). Numerical solutions obtained using this data show that velocity falls with increasing pressure (less quickly than $P^{-0.36}$), increases with current (quicker than

$\sqrt{I}$) and is only weakly dependent on arc length (figures 2 and 3). Results show that the effect of initial conditions is most noticeable at high arc currents. These correspond to high Reynolds numbers where viscous forces become important at correspondingly larger distances from the cathode. Clearly viscosity acts in such a manner so as to destroy the history of the flow.

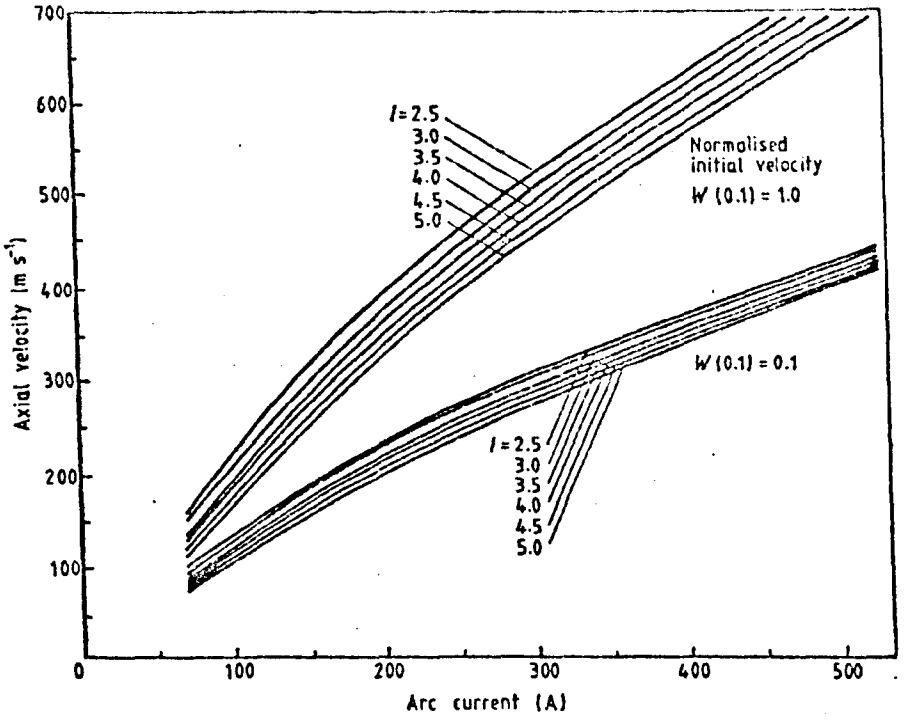

Figure 2. Dependence of axial velocity on arc current and length (l in mm) for a parabolic arc profile (argon at 1 bar).

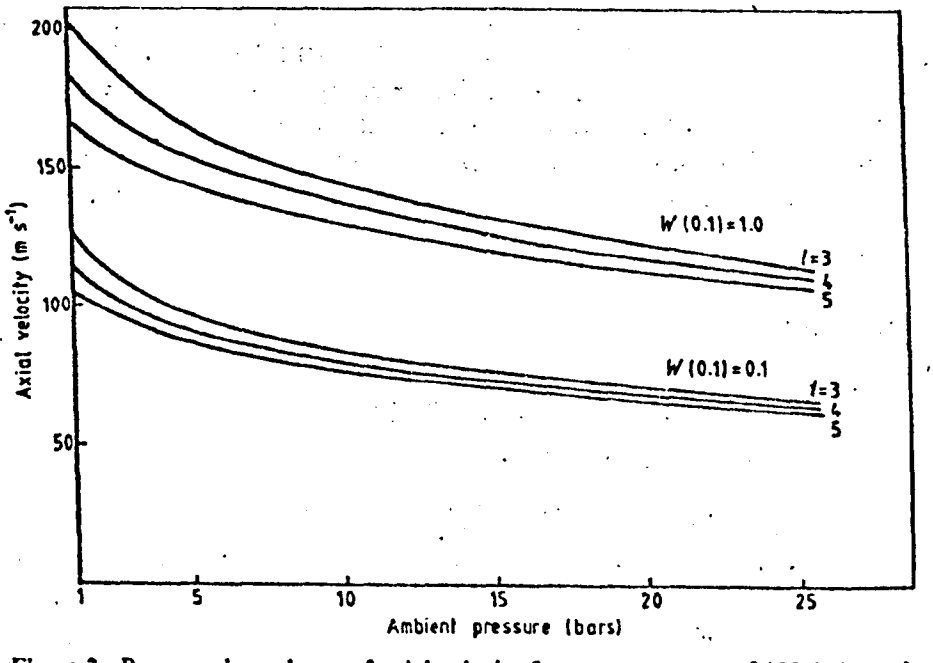

Figure 3. Pressure dependence of axial velocity for an arc current of 100 A (argon).

Results represented graphically in figure 2 are in fair agreement with available experimental results and tend to indicate that a lower bound value of $W(0.1)$ shouldbe adopted. Recently Seeger and Tiller (1979) have reported values of about 110 m s^{-1} at the midplane of an 10 mm 100 A argon TIG arc. Chang *et al* (1979) report a lower bound value for the average axial velocity of a 3 mm, 200 A argon TIG arc of 120 m s^{-1}.

The effect of ambient pressure on the axial velocity of a 100 A argon arc has been computed at different axial positions (figure 3). This shows velocity to fall with pressure despite an observed decrease in the cross-section of the column. Such a result is understood in terms of the weak pressure dependence of the momentum flux compared to that of gas density. It is interesting to note that the pressure dependence is between that predicted by viscous (independent) and inviscid solutions $(J(0)/\rho)^{1/2}$. From figure 3 it is apparent that changes in arc length have less effect on flow velocity at high pressures.

Unfortunately no systematic set of experiments has yet been reported to which the above predictions can be matched. For this reason a series of experiments, measuring the distribution of pressure at the anode of a TIG arc, has been performed and results are given here. Before making a detailed comparison it is appropriate to return and investigate further, the gaussian velocity assumption.

6. Some consequences of the assumed radial velocity dependence

Incompressibility is only a realistic assumption if the momentum flux is confined within the current boundary. A measure of the relative extents of these regions is afforded by the ratio (flow to current) of distribution half widths (Ω). It may be shown from expressions previously obtained that

$$\Omega=\frac{1}{Wr}\left(\frac{W^2(0)+\ln r}{\ln 2}\right)^{1/2}.$$

The axial dependence of W (see figure 1) may be used to show that $\Omega<1$ with the exception of a region close to the origin where a maximum value of $(\ln 2)^{-1/2}$ occurs. The flow region is substantially smaller than the electrical boundary particularly for high initial momentum fluxes and axial portions well removed from the origin. For example, for $Re=100$ and $x=10$ the respective values of Ω at $W(0.1)=0.1$, 0.5 and 1 are 0.86, 0.77 and 0.54. The current boundary has been defined in such a manner it can now be seen that

$$U(R, z)/U(0, z)<0.05$$

therefore momentum diffusion into the heat affected arc zone is negligible and it is reasonable to assume incompressibility (see §2). It is interesting to note that the flow diameter falls, although only marginally, with increasing initial momentum flux. This is thought to be a remnant of the viscous solution where the jet contracts with increasing momentum flux. However, in a free jet the momentum is independent of axial position. This is not the case for the present model. Also the arc boundary increases with arc current. Such an effect is particularly difficult to visualise in terms of the separate solutions in view of the contraction predicted by the viscous model and the essentially one dimensional nature of the inviscid model.

Computations on how pressure effects the flow distribution show that the radius of a 3 mm, 100 A argon arc falls by a factor of more than 2 between 1 and 10 atm. This is stronger than the electrical behaviour and indicates favourable conditions for the domi-

nance of buoyancy in the heat affected arc zone of a high pressure arc. This is a possible mechanism for the observed instabilities in high pressure arcs. Conditions are made all the more favourable by the increasing importance of radiation, i.e. a decreasing temperature gradient from arc to heat affected zone and hence an increase in buoyancy over and above that due to pressure.

By considering the axial mass flow some comment can be made about the energy balance behaviour of the column resulting from the gaussian assumption. The axial mass flow rate $\dot{m}$ is

$$\dot{m}=\int_0^\infty \rho U_z 2\pi r \, dr.$$

Using expressions previously introduced it can be shown that

$$\dot{m}=\dot{m}_0\left(\frac{W(0)+\ln r}{W\cdot W(0)}\right)$$

where $\dot{m}_0$ is the initial mass flux and given by

$$\dot{m}_0=IR(0)\left(\frac{\mu_0\rho(C-1)}{2\,(\ln 2)\ln C}\right)^{1/2} W(0).$$

Data previously introduced allow this to be written as:

$$\dot{m}_0=6.6\times 10^{-3}\, I^{1.5}P^{0.36}\, W(0) \text{ mg s}^{-1}.$$

The mass flow rate for a typical TIG arc (100 A, 3 mm) is now readily found to be about 20 mg s^{-1} and substantially independent of initial conditions. Under similar conditions the free jet solution is in surprisingly good agreement and gives 17 mg s^{-1}. However, only half this flow is substantially parallel to the arc axis. The enthalpy associated with a flow of 20 mg s^{-1} corresponds to about 120 W (Metcalfe and Quigley (1975) quote a value of 6.12 MJ kg^{-1} for the enthalpy of argon at 10^4 K). Such a figure compares favourably with estimates of the power lost from the column of a TIG arc. Taking an electric field strength of 8 V cm^{-1} (Glickstein 1979) gives 240 W for a 100 A, 3 mm arc. This is certainly not in conflict with the previous result and suggests that about 50% of the energy supplied is used to heat entrained gas flow.

It is known that the operating voltage of an arc increases with pressure. Experiments (Allum *et al* 1980b) indicate that the increase with pressure in the arc column electric field strength may be well represented by a $P^{0.5}$ dependence. This compares well with the $P^{0.36}$ dependence of the mass flux.

7. Comparison with experiment

An experimental comparison with the numerical results has been made by passing an arc over a small hole (0.4 mm in radius—about 2% of the arc area at the anode) situated in a water-cooled copper anode and manometrically observing the pressure distribution. In all cases a pointed 1% thoriated tungsten electrode was used with an argon shielding gas flow rate of 10 l min^{-1}. The procedure adopted was to move the arc slowly over the hole, observing the maximum pressure. The arc axis was then incremented a small distance relative to the hole and the procedure repeated. In this manner distributions of pressure similar to those shown in figure 4 were obtained. Pressures measured in this manner have two main components. One, P_t, results from the flow and the other, P_s,

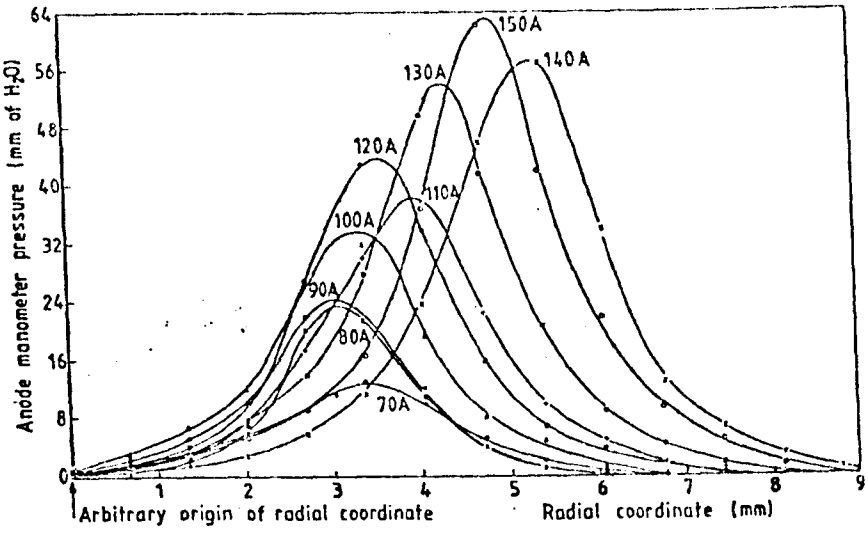

Figure 4. Example of pressure distribution at the anode for an argon arc of length 3 mm. 1% thoriated tungsten electrode; electrode diameter 2.4 mm; Ar gas flow 10 l min^{-1}; 60° vertex angle.

from a local increase in pressure caused by magnetic effects. This last factor has already been calculated and is given by equation (15). If P_m is the measured pressure then

$$P_m = P_t + (\mu_0 I J_0/4\pi) G(\infty, br^2).$$

On the axis P_t becomes the stagnation pressure P_s and therefore

$$P_s = P_m - (\mu_0 I J_0/4\pi) \ln 2.$$

The axial velocity upstream of the stagnation point is

$$U_0 = \left(\frac{2P_s}{\rho}\right)^{1/2} = \left(\frac{2P_m}{\rho}\right)^{1/2} \left(1 - \frac{\mu_0 I J_0 \ln 2}{4\pi P_m}\right)^{1/2}.$$

Experiments (Allum *et al* 1980b) indicate that the maximum current density at the anode of a 3 mm, 100 A argon arc is about 10^7 A m^{-2}. The magnetic component of pressure is therefore about 7 mm of water. This is not insignificant when compared to the respective measured value of 34 mm of water (see figure 4). In this example U_0 is lowered by 10%. Corrections of this sort have been applied to U_0 by taking J_0 to decrease axially in accordance with the parabolic arc envelope (figures 5 and 6). Experimental results here are in broad agreement with the numerical solutions. However, the maximum velocity predicted by equation (29) occurs further downstream than is predicted. This could be explained by the temperature dependence of viscosity. It is known that viscosity exhibits a peak value near the temperature of 11 000 K (Metcalfe and Quigley 1975). This would significantly decrease the local Reynolds number near the cathode, where temperatures are substantially higher (~15 000 K) than those in the bulk of the column. The axial velocity may therefore initially fall more quickly than predicted by the value of viscosity used. Experimentally measured velocities (figure 6) are also in good agreement with the predicted current dependence. This shows the velocity to increase noticeably with decreasing vertex angle. This may be explained theoretically in terms of an increasing initial J. The arc column momentum flux can be found by integrating experimental pressure distributions. However, an overestimate will be made unless the local increase

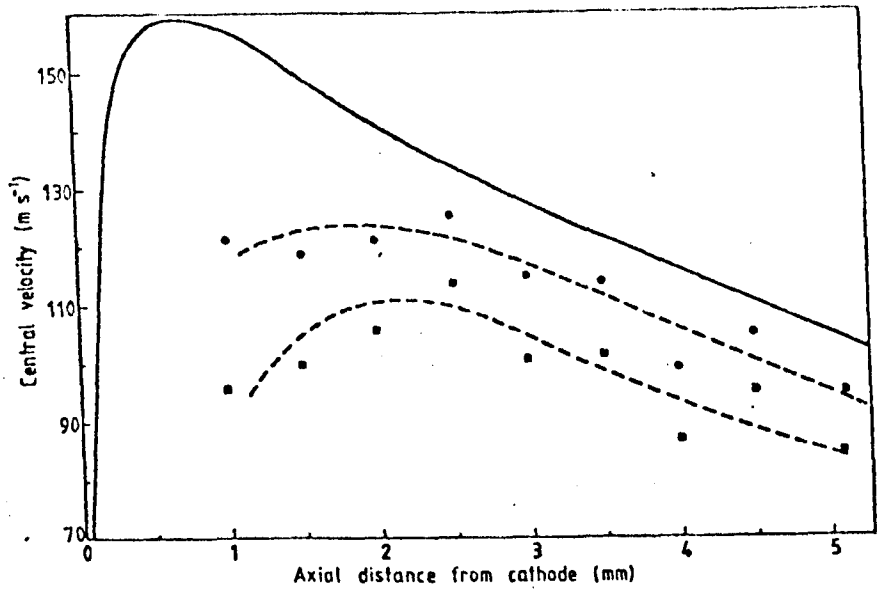

Figure 5. Dependence of axial velocity on the distance from the cathode for an argon arc current of 100 A. Full curve, theory for $W(0.1)=0.1$; points, ● uncorrected and ■ corrected; 90° vertex angle.

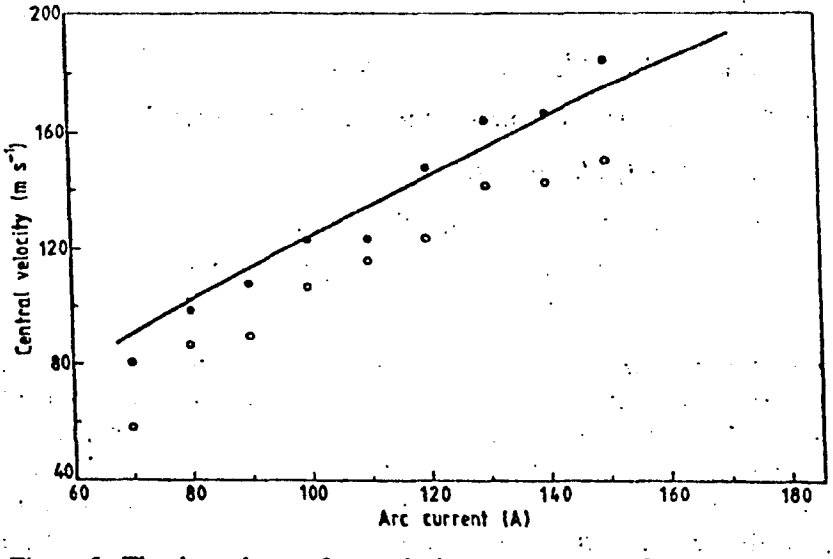

Figure 6. The dependence of arc velocity on arc current for a 3 mm argon arc. Full curve, theory for $W(0.1)=0.1$; ●, 30° vertex angle; ○, 60° vertex angle; (all values corrected).

in pressure associated with the magnetic field is allowed for. If F is the momentum flux due to flow and if F_m is the measured flux then by definition, because of the method of measurement

$$F_m = \int_0^\infty P_m 2\pi r \, dr$$

and substituting for P_m gives

$$F_m = \int_0^\infty P_t 2\pi r \, dr + \tfrac{1}{4}\mu_0 I J_0 \int_0^\infty G(\infty, br^2)\, dr^2$$

or in normalised form

$$f = f_m - \tfrac{1}{2}.$$

The momentum flux is therefore modified in a manner that is independent of arc length and electrode geometry. This correction has been applied to the results shown in figures 7 and 8. These show that F is almost proportional to the square of current and substantially independent of arc length. This is to be expected due to the logarithmic term in equation (28). However, f is quite markedly affected by electrode vertex angle and electrode diameter (table 1). Values shown in table 1 were obtained during a separate set of experiments than those shown graphically and as such can be used to estimate the reproducibility of experimental results presented here. The tendency is for momentum flux to increase with decreasing vertex angle and increasing electrode diameter. The difference between the large diameter, small angled electrode and the small diameter large angled electrode is a factor of about 3 for both 100 and 150 A arcs. These differ-

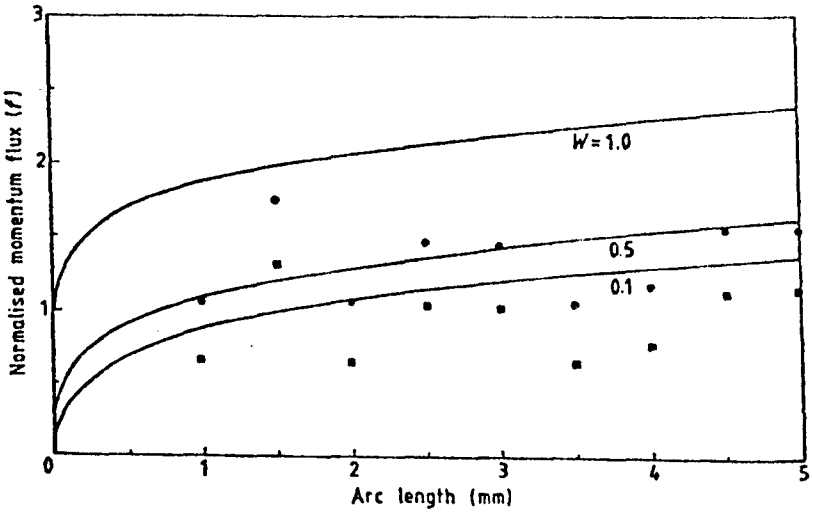

Figure 7. Dependence of the normalised momentum flux f on distance from the cathode for an argon arc current of 100 A. ●, measured values; ■, corrected points; 90° vertex angle.

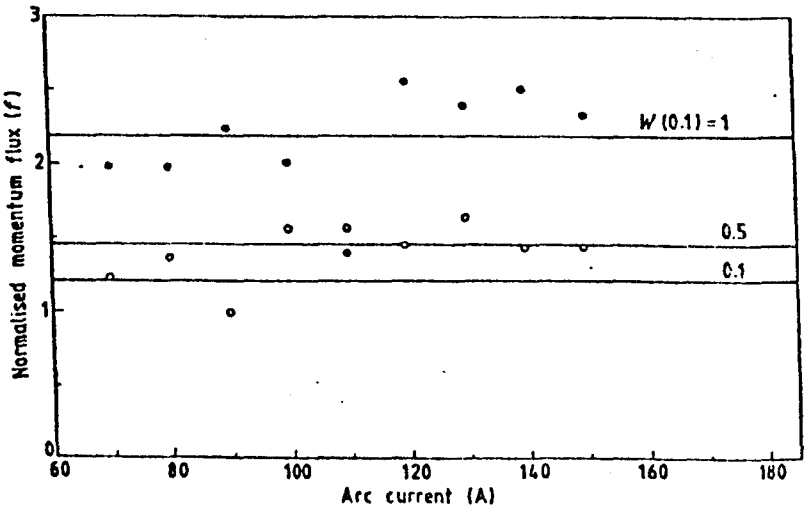

Figure 8. Depencence of the normalised momentum flux f on the arc current for a 3 mm argon arc. ●, 30° vertex angle; O, 60° vertex angle; (all values corrected.)

Table 1. Values (corrected for the magnetic component) of the normalised momentum flux f for different electrodes. Arc length = 3 mm.

I (A)	Electrode diameter (mm)	Vertex angle (deg)		
		30	60	90
100	2.4	1.80	1.77	0.90
100	3.2	2.74	2.23	1.49
150	2.4	1.74	1.53	1.06
150	3.2	2.92	2.37	1.49

ences are thought to be the result of thermal conduction effects modifying thermionic emission near the electrode tip. The structure of the cathode clearly affects arc behaviour. The dependence on electrode diameter suggests that energy balance considerations of the cathode region are required to explain anodic behaviour.

The effect of a plate anode on flow upstream of this object, is not accounted for in the theory presented here. This is the experimental situation to which predictions have been compared. The reasonable agreement between theory and experiment tends to indicate that upstream of the stagnation point, no great influence is felt.

8. Conclusions

The model developed here is based on an assumed form for the radial dependence of the axial velocity. This has made redundant the energy equation. The consequences of this assumption are in agreement with results obtained by considering separately the magnetic and viscous forces. Numerical solutions accounting for both body forces produce a flow field with strong radial entrainment and an axial flow that is confined to the arc column. Such a flow field has made it realistic to assume incompressible flow in the arc. Enthalpy flux considerations based on this radial distribution and the calculated axial dependence are compatible with the situation found to exist in the column of a TIG arc. Calculations show that buoyancy forces are dominant in the outer heat affected zone of the arc and increase in importance with pressure. This gives a possible mechanism for observed instabilities in high pressure arcs.

Experimental results have been presented and are found to be fairly represented by the theory. The effect of electrode characteristics is particularly noticeable. These have been allowed for in the theory by using the idea of an 'equivalent cathode'. This makes possible the general treatment of an arc column if suitable cathodic boundary conditions can be found. However, a more detailed investigation of this region is required.

Appendix

$G(a, b)$ is defined by equation (16) as

$$G(a,b)=\int_b^a \frac{\exp(-x)\,[1-\exp(-x)]}{x}\,dx.$$

The integrand may be expanded and integrated giving

$$G(a,b)=\sum_{n=0}^{\infty}\frac{(-1)^n}{1+n}\,[\exp(-b)\,S_n(b)-\exp(-a)\,S_n(a)]$$

where

$$S_n(a)=1+\frac{a}{1!}+\frac{a^2}{2!}+\ldots+\frac{a^n}{n!}.$$

Two particular results are used in the text. These are

$$G(\infty,0)=\ln 2$$

and

$$\int_0^\infty G(\infty,x)\,dx=\tfrac{1}{2}.$$

Acknowledgments

The author wishes to thank the referees for their comments and the Marine Technology Directorate of the Science Research Council for funding.

References

Allum C J 1980 *Proc. 6th Int. Conf. Gas Discharges and Their Applications, Edinburgh* pt 2 (London: IEE) pp 79–80

Allum C J, Pinfold B E and Nixon J M 1980a *Am. Welding J. Res. Suppl.* July 1980

—— 1980b *Int. Inst. Welding* document XII B-286–80

Chang C W, Eager T W and Szekely J 1979 *Proc. Welding Inst. Conf. Arc Physics and Weld Pool Behaviour.* Paper 13

Glickstein S S 1979 *Proc. Welding Inst. Conf. Arc Physics and Weld Pool Behaviour.* Paper 5

Guile A E 1969 *Int. Inst. Welding* document 212-170-69

Gvozdetskii V S 1974 *Avt. Svarka* **11** 1–8

Kannappan D and Bose T K 1977 *Phys. Fluids* **20** 1668–73

Lancaster J F 1966 *Int. Inst. Welding* document 212-87-66

Loitsyanskii L G 1966 *Mechanics of Liquids and Gases* (London: Pergamon) p 592

Maeker H 1955 *Z. Phys.* **141** 198–216

Metcalfe J C and Quigley M B C 1975 *Am. Welding J. Res. Suppl.* March 1975

Nestor O H 1966 *Proc. Welding Inst. Conf. Physics of the Welding Arc*

Savage W F, Strunk S S and Ishikawa Y 1965 *Am. Welding J. Res. Suppl.* November 1965

Seeger G and Tiller W 1979 *Proc. Welding Inst. Conf. Arc Physics and Weld Pool Behaviour.* Paper 31

Wienecke R 1955 *Z. Phys.* **143** 128–40

Appendix 6

Influence of Plate Size on Bead Geometry

(see figs. A6)

No.	GAS	PRESSURE (bars)	CURRENT (A)	ARC POWER (kω)	PLATE THICKNESS (mm)	Weld Dia. (mm)	Weld Depth (mm)	HAZ Dia. (mm)	HAZ Depth (mm)
3X	Ar	1	100	0.960	13	5.3	2.1	7.0	2.9
15X	Ar	1	100	1.025	25	5.8	2.0	7.5	2.6
4X	Ar	1	150	1.500	13	6.0	2.0	8.8	3.3
16X	Ar	1	150	1.710	25	6.3	2.8	8.5	3.5
1X	Ar	42	100	1.920	13	5.9	2.4	9.0	3.6
5X	Ar	42	100	2.250	25	5.9	2.8	8.3	3.8
2X	Ar	42	150	3.525	13	10.1	4.0	14.3	5.9
6X	Ar	42	150	3.525	25	10.3	4.0	12.3	5.1
9X	He	1	100	1.390	13	4.6	3.3	7.5	3.9
13X	He	1	100	1.360	25	3.9	2.5	7.3	3.4
10X	He	1	150	1.875	13	5.6	3.6	10.0	5.1
14X	He	1	150	1.920	25	5.3	3.3	8.5	4.3
7X	He	10	100	2.140	13	5.0	4.3	10.4	5.3
11X	He	10	100	1.970	25	5.3	3.1	7.8	4.1
8X	He	10	150	3.338	13	8.6	5.0	15.9	7.3
11X	He	10	150	3.338	25	7.5	5.5	11.3	6.5

P = 1 bar
I = 100A

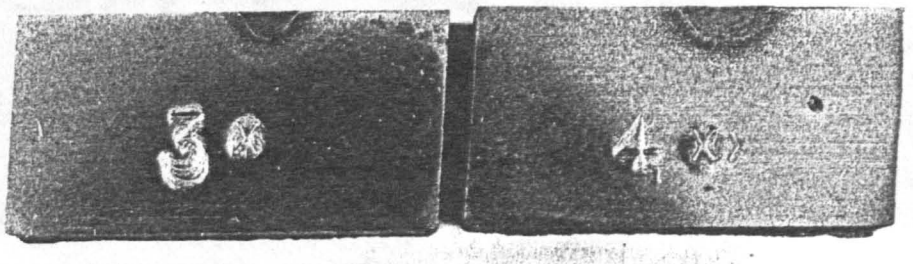

P = 1
I = 150

P = 41.8
I = 100A

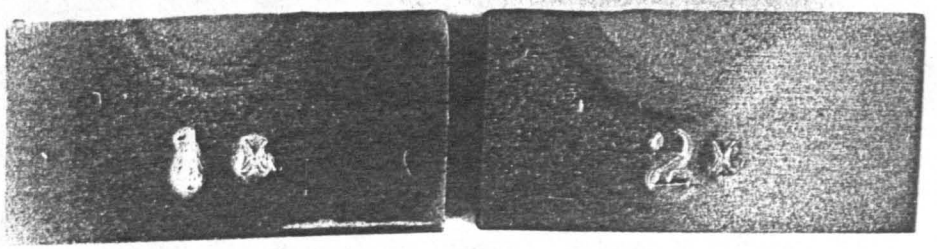

P = 41.8
I = 150

Figure A6(1) Argon Bead Profiles on Thin Plate
(1.38 mm/s table speed, magnification of 2.1)

P = 1 bar
I = 100A

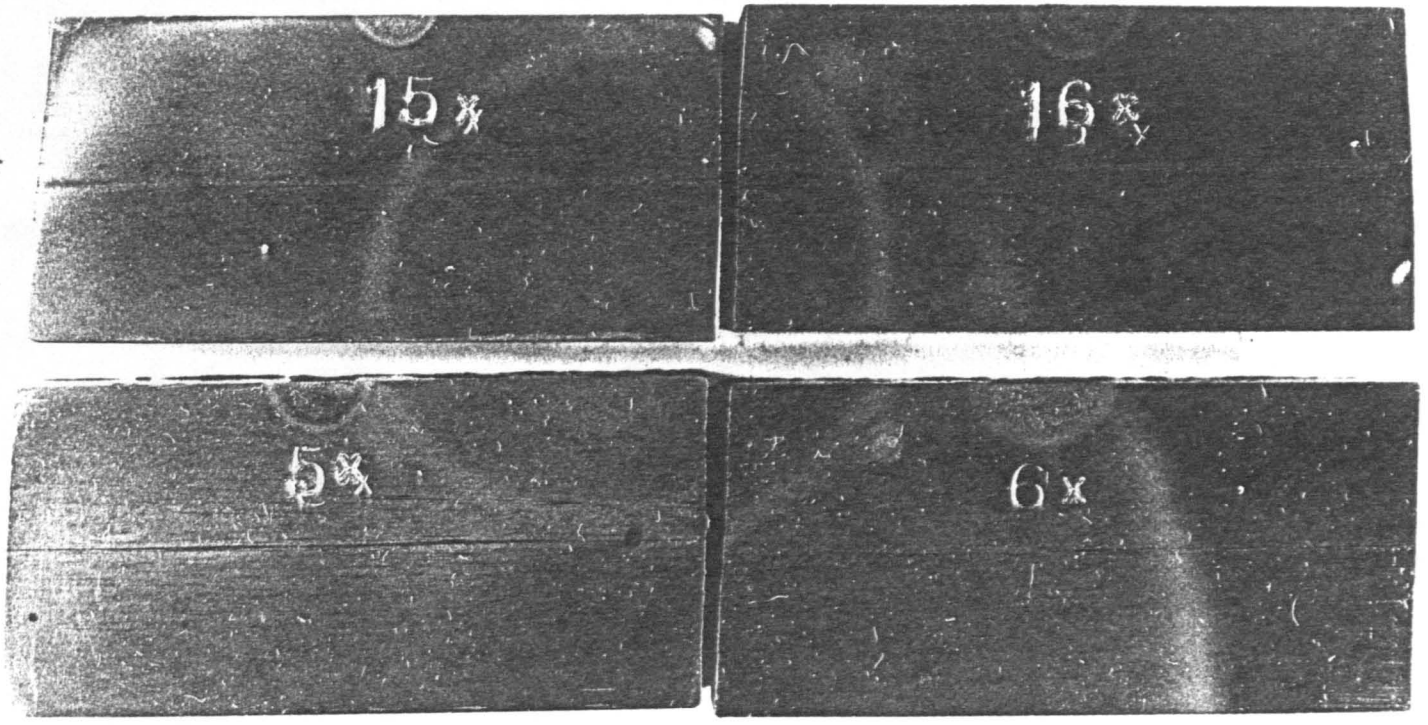

P = 1 bar
I = 150A

P = 41.8
I = 100A

P = 41.8
I = 150A

Figure A6(2) Argon Bead Profiles on Thick Plate (25 mm)
(1.38 table speed, magnification of 1.8)

P = 1 bar
I = 100A

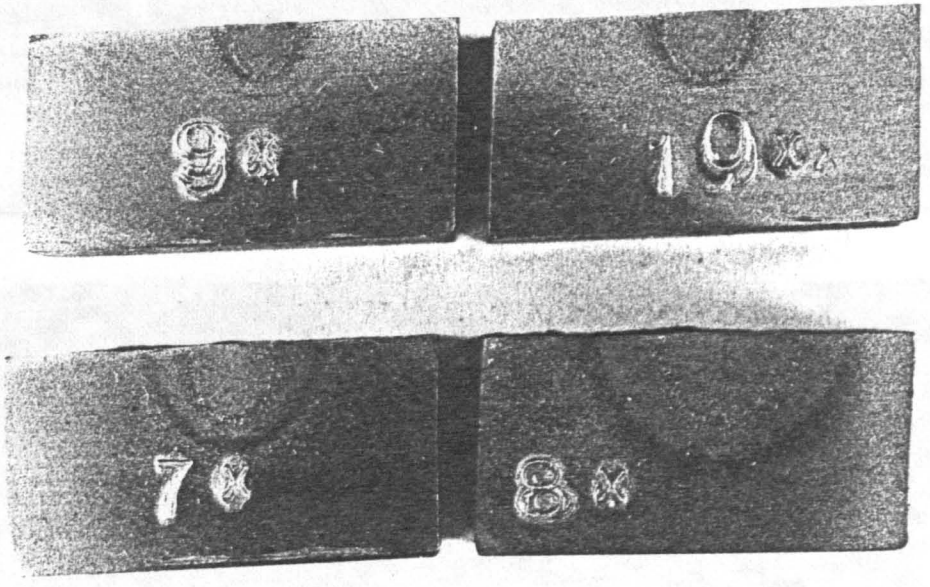

P = 1
I = 150

P = 11.2
I = 100

P = 11.2
I = 150

Figure A6(3) Helium Bead Profiles on Thin Plate (12.5mm)
(1.38 mm/s table speed, magnification: 2.1)

P = 1 bar
I = 100A

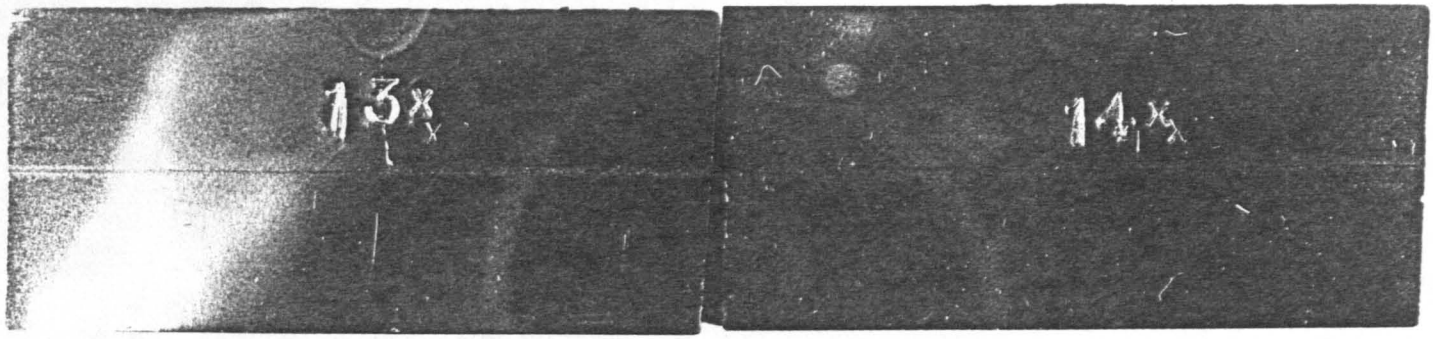

P = 1 bar
I = 150A

P = 11.2
I = 100

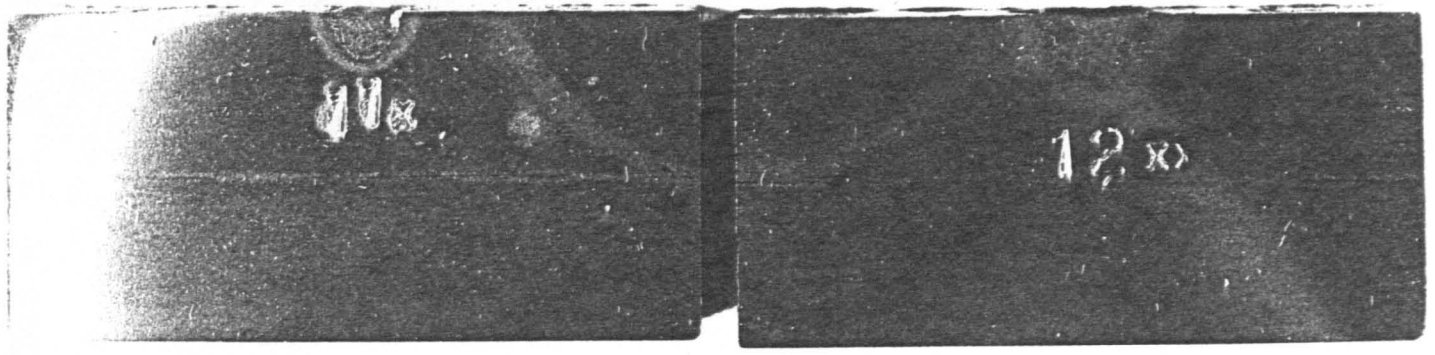

P = 11.2
I = 150

Figure A6(4) Helium Bead Profiles on Thick Plate (25mm)
(1.38 mm/s table speed, magnification: 1.7)